

NAS 1.55:3022/pt.2

NASA Conference Publication 3022
Part 2

NAS 1.55:

Transonic Unsteady Aerodynamics and Aeroelasticity 1987

*Proceedings of a symposium held at
NASA Langley Research Center
Hampton, Virginia
May 20-22, 1987*

NASA

2/DM
COMPLETED

Transonic Unsteady Aerodynamics and Aeroelasticity 1987

Compiled by
Samuel R. Bland
Langley Research Center
Hampton, Virginia

Proceedings of a symposium sponsored by the
National Aeronautics and Space Administration,
Washington, D.C., and held at
NASA Langley Research Center
Hampton, Virginia
May 20-22, 1987



National Aeronautics
and Space Administration

**Scientific and Technical
Information Division**

1989

BLANK PAGE

11

BEST COPY AVAILABLE

Preface

This two-part document contains text and figures for the papers presented at the Symposium on Transonic Unsteady Aerodynamics and Aeroelasticity - 1987, held at the NASA Langley Research Center on May 20-22, 1987. The Symposium, which reviewed the subject area, was the third such meeting at Langley. The previous workshops were held in 1980 and 1983 and were an outgrowth of a meeting held at Columbus, Ohio in 1978 to assess the state of unsteady aerodynamics for use in transonic flutter analysis.

The papers were grouped in five subject areas, which may be described broadly as:

- (1) Transonic small disturbance (TSD) theory for complete aircraft configurations
- (2) Full potential and Euler equation methods
- (3) Methods for vortex and viscous flows
- (4) Aeroelastic applications
- (5) Experimental results and cascade flows

The decade since the Columbus meeting has seen the wide acceptance of computational fluid dynamics methods for transonic aeroelastic analysis. In 1978, calculations with the TSD methods for two-dimensional airfoils (especially the NASA Ames LTRAN code and its derivatives) were well established, and the USAF Flight Dynamics Laboratory had initiated development of the first TSD code (XTRAN3) for three-dimensional wings. As demonstrated in the papers from the 1987 meeting contained herein, the TSD methods (the NASA Langley CAP-TSD code in particular) can now be applied to the aeroelastic analysis of complete aircraft. Methods suitable for situations in which small disturbance theory is inadequate are being aggressively pursued.

Future research should follow three main paths:

- (1) Development of more exact methods using the full potential, Euler, and Navier-Stokes equations
- (2) Evaluation of the TSD methods by detailed comparison with more exact methods and experiment
- (3) Detailed pressure measurements and flutter tests on well-defined aeroelastic models.

Samuel R. Bland

BLANK PAGE

CONTENTS

PREFACE	iii
ATTENDEES	ix

Part 1*

SESSION 1

UNSTEADY AERODYNAMICS AND AEROELASTIC RESEARCH AT AFWAL	1
L. J. Huttell and W. A. Sotomayer	
EXTENSIONS AND IMPROVEMENTS OF XTRAN3S	15
C. J. Borland	
ROLE OF COMPUTATIONAL FLUID DYNAMICS IN UNSTEADY AERODYNAMICS FOR AEROELASTICITY	47
Guru P. Guruswamy and Peter M. Goorjian	
CAP-TSD: A PROGRAM FOR UNSTEADY TRANSONIC ANALYSIS OF REALISTIC AIRCRAFT CONFIGURATIONS	63
John T. Batina, David A. Seidel, Samuel R. Bland and Robert M. Bennett	
CAP-TSD ANALYSIS OF THE F-15 AIRCRAFT	97
Dale M. Pitt	
CALCULATION OF STEADY AND UNSTEADY PRESSURES AT SUPERSONIC SPEEDS WITH CAP-TSD	117
Robert M. Bennett, Samuel R. Bland, John T. Batina, Michael D. Gibbons, and Dennis G. Mabey	

SESSION 2

AN EFFICIENT METHOD FOR COMPUTING UNSTEADY TRANSONIC AERODYNAMICS OF SWEPT WINGS WITH CONTROL SURFACES	139
D. D. Liu, Y. F. Kao, and K. Y. Fung	
APPLICATION OF A FULL POTENTIAL METHOD TO AGARD STANDARD AIRFOILS	157
Woodrow Whitlow, Jr.	
FULL POTENTIAL UNSTEADY COMPUTATIONS INCLUDING AEROELASTIC EFFECTS	175
Vijaya Shankar and Hiroshi Ide	
FLUX-VECTOR SPLITTING FOR UNSTEADY CALCULATIONS ON DYNAMIC MESHES	193
W. Kyle Anderson, James L. Thomas, and Christopher L. Rumsey	
UNSTEADY TRANSONIC FLOW USING EULER EQUATIONS	215
Dave M. Belk and L. Bruce Simpson	

*Part 1 is presented under separate cover.

AGARD STANDARD AEROELASTIC CONFIGURATIONS FOR DYNAMIC RESPONSE	243
E. Carson Yates, Jr.	

Part 2

SESSION 3

SOLUTION OF STEADY AND UNSTEADY TRANSONIC-VORTEX FLOWS USING EULER AND FULL-POTENTIAL EQUATIONS	261
Osama A. Kandil, Andrew H. Chuang, and Hong Hu	
VISCOUS FLOW CALCULATIONS FOR THE AGARD STANDARD CONFIGURATION AIRFOILS WITH EXPERIMENTAL COMPARISONS	313
James T. Howlett	
UNSTEADY TRANSONIC VISCOUS-INVIScid INTERACTION USING EULER AND BOUNDARY-LAYER EQUATIONS	331
Shahyar Pirzadeh and Dave Whitfield	
NUMERICAL SOLUTION OF UNSTEADY ROTATIONAL FLOW PAST FIXED AND ROTARY WING CONFIGURATIONS	351
N. L. Sankar, B. E. Wake, S. Y. Ruo, and J. B. Malone	
UNSTEADY NAVIER-STOKES COMPUTATIONS OVER AIRFOILS USING BOTH FIXED AND DYNAMIC MESHES	375
Christopher L. Rumsey and W. Kyle Anderson	

SESSION 4

THE OBLIQUE-WING RESEARCH AIRCRAFT: A TEST BED FOR UNSTEADY AERODYNAMIC AND AEROELASTIC RESEARCH	395
Glenn B. Gilyard	
STATIC AEROELASTICITY OF A COMPOSITE OBLIQUE WING IN TRANSONIC FLOWS	415
Jonathan D. Bohlmann	
INVESTIGATION AND SUPPRESSION OF HIGH DYNAMIC RESPONSE ENCOUNTERED ON AN ELASTIC SUPERCRITICAL WING	427
David A. Seidel, William H. Adams, Jr., Clinton V. Eckstrom, and Maynard C. Sandford	
THE ROLE OF SHOCK INDUCED TRAILING-EDGE SEPARATION IN LIMIT CYCLE OSCILLATIONS	449
Atlee M. Cunningham, Jr.	
INITIAL APPLICATION OF CAP-TSD TO WING FLUTTER	463
Herbert J. Cunningham, Robert M. Bennett, and John T. Batina	
TRANSONIC FLUTTER CALCULATIONS USING THE EULER EQUATIONS	477
Oddvar O. Bendiksen and Kenneth A. Kousen	

SESSION 5

UNSTEADY PRESSURE MEASUREMENTS ON A SUPERCRITICAL AIRFOIL AT HIGH REYNOLDS NUMBERS	493
R. W. Hess	
AIRFOIL STALL PENETRATION AT CONSTANT PITCH RATE AND HIGH REYNOLDS NUMBER	519
Peter F. Lorber and Franklin O. Carta	
EXPERIMENTAL TRANSONIC STEADY STATE AND UNSTEADY PRESSURE MEASUREMENTS ON A SUPERCRITICAL WING DURING FLUTTER AND FORCED DISCRETE FREQUENCY OSCILLATIONS	543
Douglas S. Piette and Frank W. Cazier, Jr.	
TURBOMACHINERY AEROELASTICITY AT NASA LEWIS RESEARCH CENTER	571
Krishna Rao V. Kaza	
UNSTEADY AERODYNAMICS OF BLADE ROWS	605
Joseph M. Verdon	
COMPUTATIONAL AEROELASTICITY CHALLENGES AND RESOURCES	631
John W. Edwards	

BLANK PAGE

ATTENDEES

Adams, William M., Jr.	NASA Langley
Amos, Anthony K.	USAF AFOSR
Anderson, W. Kyle	NASA Langley
Appa, Kari	Northrop Corporation
Batina, John T.	NASA Langley
Belk, Dave	USAF AD/AFATL/FXA
Bendiksen, Oddvar O.	Princeton University
Bennett, Robert M.	NASA Langley
Beotehond, A.	Hi Tech
Bland, Samuel R.	NASA Langley
Bodapati, Satya	Naval Postgraduate School
Bohlmann, Jonathan D.	General Dynamics
Borland, Christopher J.	Boeing Military Airplane Co.
Brentner, Kenneth S.	NASA Langley
Carta, Franklin O.	United Technologies Research Center
Carter, James E.	United Technologies Research Center
Cazier, Frank W., Jr.	NASA Langley
Chu, Li-Chuan	PRC
Chaung, Hsin-Kung A.	Old Dominion University
Cunningham, Atlee	General Dynamics
Dixon, Sidney C.	NASA Langley
Durham, Michael H.	NASA Langley
Eckstrom, Clinton V.	NASA Langley
Edwards, John W.	NASA Langley
Fuglsang, Dennis F.	Purdue University
Gibbons, Michael D.	PRC
Giesing, Joesph P.	McDonnell Douglas
Gilbert, Michael G.	NASA Langley
Giles, Gary L.	NASA Langley
Gilyard, Glenn B.	NASA Ames-Dryden
Guruswamy, Guru P.	NASA Ames
Haller, Richard L.	General Dynamics
Hassig, Hermann J.	Lockheed-California Co.
Hess, Robert W.	NASA Langley
Howlett, James T.	NASA Langley
Hu, Hong	Old Dominion University
Huttsell, Larry	USAF AFWAL/FIBRC
Kandil, Osama A.	Old Dominion University
Kaza, Krishna R. V.	NASA Lewis
Kousen, Kenneth A.	Princeton University
Layton, Jeffrey B.	Purdue University
Leishman, J. Gordon	University of Maryland
Levine, Mark S.	Purdue University
Liu, Danny D.	Arizona State University
Mohr, Ross W.	Purdue University
Mook, Dean T.	VPI&SU
Mukhopadhyay, Vivekananda	PRC
Mulville, Dan	NASA Headquarters
Noll, Thomas E.	NASA Langley

Pao, S. Paul	NASA Langley
Peele, Elwood L.	NASA Langley (retired)
Perry, Boyd, III	NASA Langley
Piette, Douglas S.	Lockheed-Georgia Co.
Pitt, Dale M.	McDonnell Aircraft Co.
Pototsky, Anthony S.	PRC
Rash, L. C.	Wyle Laboratories
Rivera, Jose A., Jr.	NASA Langley
Robins, Philip C.	Texas A&M University
Rodden, William P.	Consultant
Rumsey, Christopher L.	NASA Langley
Sandford, Maynard C.	NASA Langley
Sankar, Lakshmi	Georgia Tech
Seidel, David A.	NASA Langley
Shankar, Vijaya	Rockwell International
Shifflette, James M.	Old Dominion University
Shimko, A. V.	Northrop Corp.
Shirk, Michael H.	USAF AFWAL/FIBR
Silva, Walter A.	PRC
Simpson, L. Bruce	USAF AFATL/FXA
Smedfjeld, John	Grumman Aircraft
Smith, Gregory E.	Dynamic Engineering
Soistmann, David L.	PRC
Spence, Peter L.	PRC
Strganac, Thomas W.	NASA Langley
Summers, John C.	NASA Langley
Takallu, Mohammed A.	PRC
Tatum, Kenneth E.	PRC
Thomas, James L.	NASA Langley
Tracy, Maureen B.	PRC
Verdon, Joesph M.	United Technologies Research Center
Vinh, Lam-Son	NASA Langley
Vretakis, Nicholas G.	USAF AFSCLO
Watson, Ralph D.	NASA Langley
Weatherill, Warren H.	Boeing Commercial Airplane Co.
Webster, Rosa C.	NASA Langley
Whitfield, David L.	Mississippi State University
Whitlow, Woodrow, Jr.	NASA Langley
Wieseman, Carol D.	NASA Langley
Wynne, Eleanor C.	NASA Langley
Yates, E. Carson, Jr.	NASA Langley
Yurkovich, Rudy	McDonnell Aircraft Co.
Zeiler, Thomas A.	PRC

SOLUTION OF STEADY AND UNSTEADY TRANSONIC-VORTEX FLOWS
USING EULER AND FULL-POTENTIAL EQUATIONS

Osama A. Kandil
Andrew H. Chuang
Hong Hu
Old Dominion University
Norfolk, Virginia

OUTLINE OF TALK

1. Background and Objectives
2. Unsteady Euler Equations in a Rotating Frame of Reference for Transonic Vortex Flows:
 - Formulation (Space Fixed and Rotating Frames of Reference)
 - Method of Solution, Local-Conical Flow, Initial and Boundary Conditions
 - Results:
 - Symmetric Conical Flow
 - Three-Dimensional Steady Transonic-Vortex Flow
 - Uniform Rolling in a Conical Flow
 - Rolling Oscillation in a Conical Flow
3. Transonic Airfoil Computation Using Integral Solution of Full-Potential Eq. With and Without Embedded Euler Domains:
 - Formulation (I.E. Solution of Full-Potential Eq., Euler Equations)
 - Method of Solution (SCSF-Scheme, IEEE-Scheme)
 - Results: SCSF and IEEE Schemes are Applied to NACA 0012 and NACA 64A010A Over a Wide Range of M_∞ .
4. Concluding Remarks

1. Background and Objectives

- As the normal angle of attack, normal Mach number and sweep-back angle are varied, complex flows develop around Delta and Delta-like wings.

These flows are characterized with the formation of large and small scale vortices, weak and strong shock waves, and shock induced separations. The experimental Miller and Wood Classification Diagram shows seven regions of this flow.

- These flows become highly complex when vortex breakdown occurs in the vicinity of the wing or when the wing undergoes unsteady motion due to maneuvering or flutter.
- The main objectives of this ongoing research work are to develop efficient and reliable computational schemes which are capable of predicting the distributed aerodynamic characteristics of these wings in steady and unsteady flows over a wide range of angles of attack, sweep-back angles, Mach numbers and configurations.

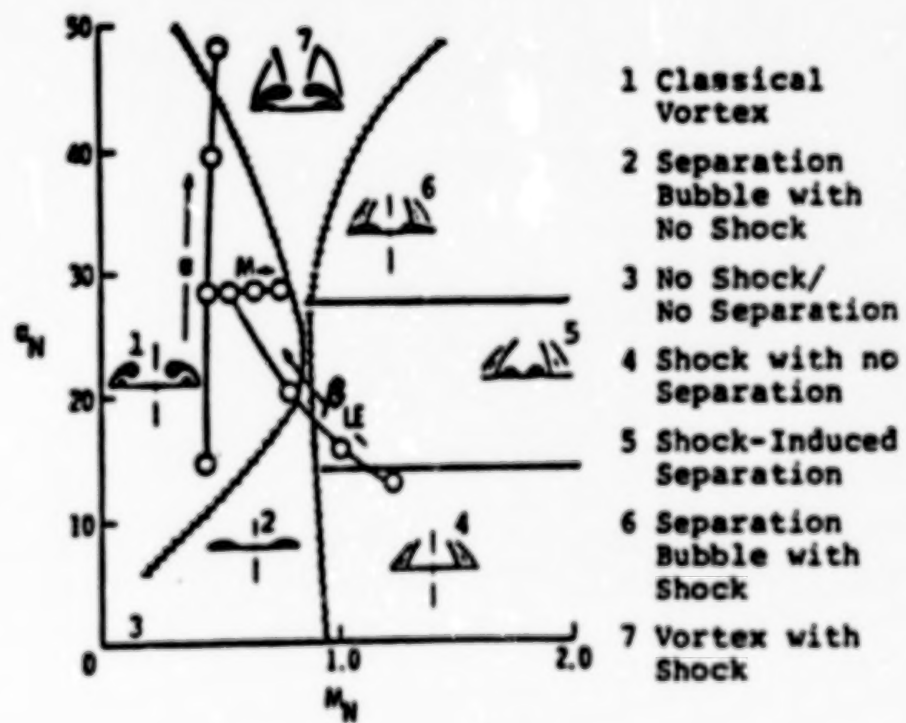


Fig. 1 Miller and Wood¹ Classification Diagram.

2. Unsteady Euler Equations in a Rotating Frame of Reference for Transonic-Vortex Flows

Formulation

- Conservation Form of Euler Equations in a Space-Fixed Frame of Reference

$$\frac{\partial \bar{q}}{\partial t} + \frac{\partial \bar{E}}{\partial x} + \frac{\partial \bar{F}}{\partial y} + \frac{\partial \bar{G}}{\partial z} = 0 \quad (1)$$

where

$$\bar{q} = [\rho, \rho u, \rho v, \rho w, \rho e]^t \quad (2)$$

$$\bar{E} = [\rho u, \rho u^2 + p, \rho uv, \rho uw, \rho uh]^t \quad (3)$$

$$\bar{F} = [\rho v, \rho uv, \rho v^2 + p, \rho vw, \rho vh]^t \quad (4)$$

$$\bar{G} = [\rho w, \rho uw, \rho vw, \rho w^2 + p, \rho wh]^t \quad (5)$$

$$e = p/\rho(\gamma-1) + (u^2 + v^2 + w^2)/2 \quad (6)$$

$$h = e + p/\rho \quad (7)$$

- Rewriting the Equations in the Vector Form

$$\frac{\partial p}{\partial t} + \nabla \cdot (\rho \bar{V}) = 0 \quad (8)$$

$$\frac{\partial(\rho \bar{V})}{\partial t} + \nabla \cdot (\rho \bar{V} \bar{V} + p \bar{I}) = 0 \quad (9)$$

$$\frac{\partial(\rho e)}{\partial t} + \nabla \cdot (\rho h \bar{V}) = 0 \quad (10)$$

And Using the Substantial and Local Derivatives Relations

$$\frac{D\mathbf{a}}{Dt} = \frac{D'\mathbf{a}}{Dt}, \frac{\partial \mathbf{a}}{\partial t} = \frac{\partial' \mathbf{a}}{\partial t} + (\bar{\mathbf{V}}_r - \bar{\mathbf{V}}) \cdot \nabla \mathbf{a} \quad (11)$$

$$\frac{D\bar{\mathbf{A}}}{Dt} = \frac{D'\bar{\mathbf{A}}}{Dt} + \bar{\omega} \times \bar{\mathbf{A}}, \frac{\partial \bar{\mathbf{A}}}{\partial t} = \frac{\partial' \bar{\mathbf{A}}}{\partial t} + (\bar{\mathbf{V}}_r - \bar{\mathbf{V}}) \cdot \nabla \bar{\mathbf{A}} + \bar{\omega} \times \bar{\mathbf{A}} \quad (12)$$

where $\bar{\mathbf{V}} = \bar{\mathbf{V}}_r + \bar{\omega} \times \bar{\mathbf{r}}$; $\frac{D'}{Dt}, \frac{\partial'}{\partial t}$ \equiv Substantial and Local Derivative in the Rotating Frame

- We get the Conservative Form of Euler Equations for the Relative Motion

$$\frac{\partial' \rho}{\partial t} + \nabla \cdot (\rho \bar{\mathbf{V}}_r) = 0 \quad (13)$$

$$\frac{\partial' (\rho \bar{\mathbf{V}}_r)}{\partial t} + \nabla \cdot [\rho \bar{\mathbf{V}}_r \bar{\mathbf{V}}_r + \rho \bar{\mathbf{I}}] = - \rho [\dot{\bar{\omega}} \times \bar{\mathbf{r}} + 2\bar{\omega} \times \bar{\mathbf{V}}_r + \bar{\omega} \times (\bar{\omega} \times \bar{\mathbf{r}})] \quad (14)$$

$$\frac{\partial' (\rho e_r)}{\partial t} + \nabla \cdot [\rho h_r \bar{\mathbf{V}}_r] = - \rho [\bar{\mathbf{V}}_r \cdot (\dot{\bar{\omega}} \times \bar{\mathbf{r}}) + (\bar{\omega} \times \bar{\mathbf{r}}) \cdot (\dot{\bar{\omega}} \times \bar{\mathbf{r}})] \quad (15)$$

where

$$e_r = \frac{p}{\rho(\gamma-1)} + \frac{v_r^2}{2} - \frac{1}{2} |\bar{\omega} \times \bar{\mathbf{r}}|^2 = e - \bar{\mathbf{V}} \cdot (\bar{\omega} \times \bar{\mathbf{r}}) \quad (16)$$

$$h_r = \frac{\gamma p}{\rho(\gamma-1)} + \frac{v_r^2}{2} - \frac{1}{2} |\bar{\omega} \times \bar{\mathbf{r}}|^2 = h - \bar{\mathbf{V}} \cdot (\bar{\omega} \times \bar{\mathbf{r}}) \quad (17)$$

Method of Solution

- The Abstract Conservative Form of the Relative Motion in Terms of Rotating Coordinates are

$$\frac{\partial' \bar{q}_r}{\partial t} + \frac{\partial' \bar{E}_r}{\partial x} + \frac{\partial' \bar{F}_r}{\partial y} + \frac{\partial' \bar{G}_r}{\partial z} = \bar{s} \quad (18)$$

where

$$\bar{q}_r = [\rho, \rho u_r, \rho v_r, \rho w_r, \rho e_r]^t \quad (19)$$

$$\bar{E}_r = [\rho u_r, \rho u_r^2 + p, \rho u_r v_r, \rho u_r w_r, \rho u_r h_r]^t \quad (20)$$

$$\bar{F}_r = [\rho v_r, \rho u_r v_r, \rho v_r^2 + p, \rho v_r w_r, \rho v_r h_r]^t \quad (21)$$

$$\bar{G}_r = [\rho w_r, \rho u_r w_r, \rho v_r w_r, \rho w_r^2 + p, \rho w_r h_r]^t \quad (22)$$

$$\begin{aligned} \bar{s} = [0, 0, \rho(\dot{\omega}z + 2\omega w_r + \omega^2 y), -\rho(\dot{\omega}y + 2\omega v_r - \omega^2 z), -\rho(-v_r \dot{\omega}z + w_r \dot{\omega}y + \omega \dot{\omega}y^2 \\ + \omega \dot{\omega}z^2)]^t \end{aligned} \quad (23)$$

- The Source Term \bar{s} has been written for $\bar{\omega} = \omega \bar{e}_x$, $\dot{\bar{\omega}} = \dot{\omega} \bar{e}_x$

- Eqs. (18)-(23), (16) and (17) are solved using a Central-Difference, Finite-Volume Scheme Using Four-Stage Runge Kutta Time Stepping with Added Second- and Fourth-Order Dissipation Terms.
- The Computer Program is a Three-Dimensional Program.

• Local-Conical Flow Problem

- If the Conical Coordinates are Used to Transform the Relative Motion Equation, Eqs. (18)-(22), the Resulting Equations will not Represent a Conical Flow.
- If the Conical Coordinates are Used to Transform the Absolute Motion Equations, Eqs. (1)-(7), the Resulting Equations will Represent a Conical Flow for the Steady Flow. For the Unsteady Flow, the Problem is Made "Locally Conical" if it is Solved at a Fixed Axial Location.
- In the Three-Dimensional Program, Local Conical Flow Solutions are Obtained at $x=1$ by Equating the Absolute Motion in the First and Third Planes:

$$(\rho \bar{V})_{i \pm 1} = (\rho \bar{V})_i + (\rho \bar{V}_r)_{i \pm 1} = (\rho \bar{V}_r)_i = (\rho \bar{V}_r)_i + \bar{\omega} \times (\rho_i \bar{r}_i - \rho_{i \pm 1} \bar{r}_{i \pm 1}) \quad (24)$$

$$(\rho E)_{i \pm 1} = (\rho E)_i + (\rho E_r)_{i \pm 1} = (\rho E_r)_i + (\bar{V}_r i + \bar{\omega} \times \bar{r}_i) \cdot [\bar{\omega} \times (\rho_i \bar{r}_i - \rho_{i \pm 1} \bar{r}_{i \pm 1})] \quad (25)$$

where $i = 2$.

1. Initial Condition:

- For Constant Rolling Problem ($\bar{\omega} = -\omega_0 \hat{e}_x$), the Flow Corresponds to a Uniform Translation Plus a Rigid Body Rotation $\bar{\omega}x\bar{r}$.
- For Rolling Oscillation ($\bar{\omega} = -\omega_0 \sin kt \hat{e}_x$), the Flow Corresponds to a Uniform Translation Only.

2. Boundary Conditions:

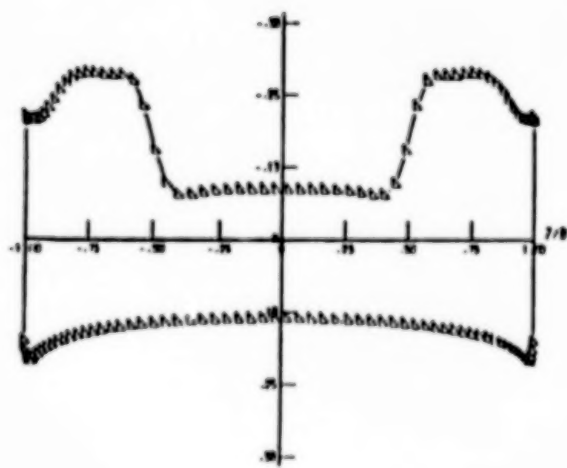
- Normal Momentum Equation is Used on the Wing Surface
 $(\frac{D}{Dt} (\bar{V}_r \cdot \hat{n}) = 0, \frac{\partial \hat{n}}{\partial t} = 0)$

$$\rho \bar{V}_r \cdot (\bar{V}_r \cdot \hat{n}) = \frac{\partial P}{\partial n} + \rho \hat{n} \cdot [2\bar{\omega}x\bar{V}_r + \bar{\omega}x\bar{r} + \bar{\omega}x(\bar{\omega}x\bar{r})] \quad (26)$$

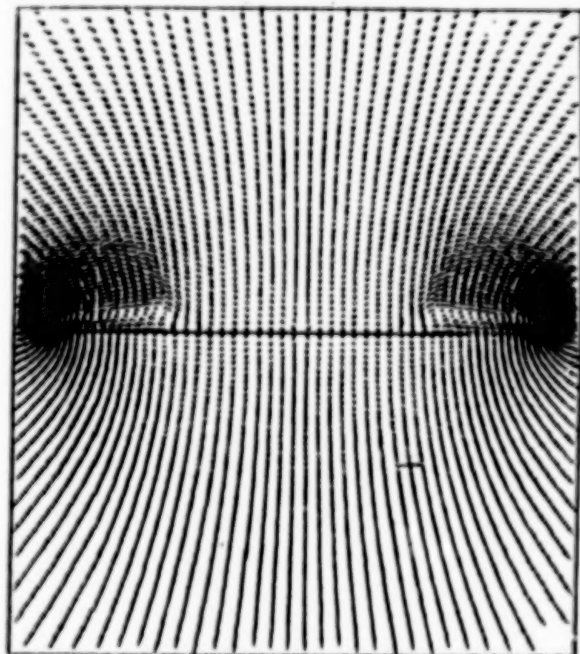
- In the Farfield, a Uniform Translation Plus the Corresponding Rotation are Imposed Outside of the Bow Shock.

SYMMETRIC CONICAL FLOW

This is a verification test case for the three-dimensional program which has been solved earlier by using a conical flow program². Figure 2 shows the results for a flat plate sharp-edged delta wing at $M_{\infty} = 2$, $\alpha = 10^0$ and β (sweep angle) using a modified Joukowski transformation² of 128x64 cells around and normal to the wing has been used for the whole computational region. Figure 2 (a--d) shows the surface pressure, cross-flow velocity, cross-flow Mach contours and static pressure contours. It is clear that two symmetric leading-edge vortices have been captured on the suction side along with a weak cross-flow shock under each vortex. The outer bow shock is clearly visible in the lower portions of the cross-flow Mach and static pressure contours. The surface pressure, Mach contours and static-pressure contours match those obtained by using the conical flow program for half of the computational region.

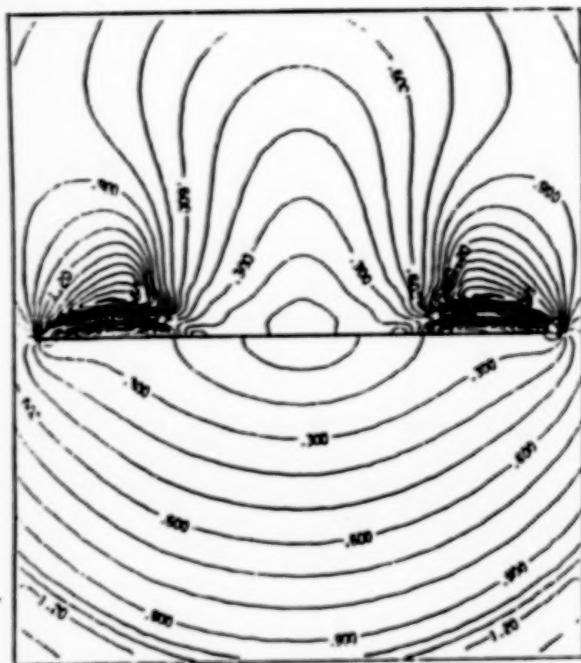


a. surface pressure

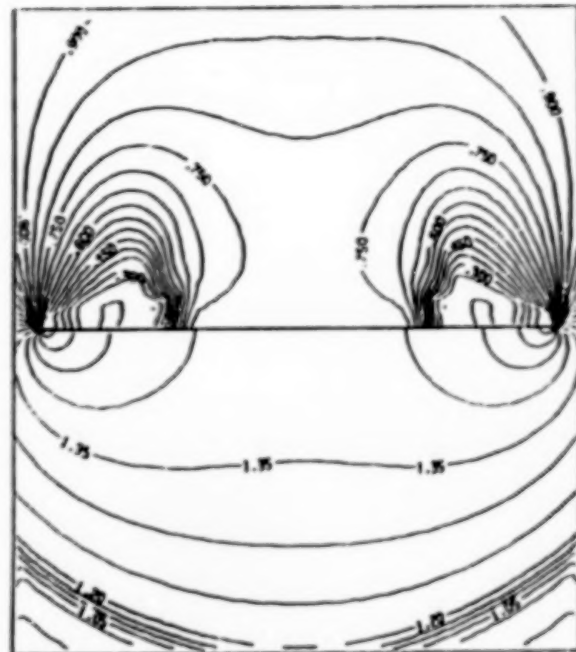


b. cross-flow velocity

Fig. 2 Steady symmetric flow around a delta wing, $M_{\infty} = 2$, $\alpha = 10^0$, $\beta = 70^0$



c. cross-flow Mach



d. static pressure

Fig. 2 Steady symmetric flow around a delta wing, $M_\infty = 2$, $\alpha = 10^\circ$, $\beta = 70^\circ$

THREE-DIMENSIONAL TRANSONIC FLOW

Figure 3 shows the results of a sharp-edged delta wing for $M_\infty = 0.7$, $\alpha = 10^\circ$ and aspect ratio of 1.5 using a number of cells of $80 \times 38 \times 48$ in the x , y and z directions; respectively. The results of Figures 3a and 3b show, from left to right, the surface pressure, the static pressure contours and the cross-flow velocity; each at the chord stations of 0.52 and 0.81. Figure 3c shows the static pressure contours and the cross-flow velocity at the chord station of 1.01 and Figure 3d shows the static pressure contours and the cross-flow velocity at the chord station of 1.25. At $x = 0.81$, comparisons of the computed surface pressure with the experimental data³ shows that the location of vortex core is well predicted, while the value of peak suction pressure under the vortex core is slightly underpredicted. At $x = 1.25$, the static pressure contours and the cross-flow velocity show the formation of trailing-edge vortex core and its interaction with the leading-edge vortex core. Our cross-flow planes are taken normal to the wing surface.

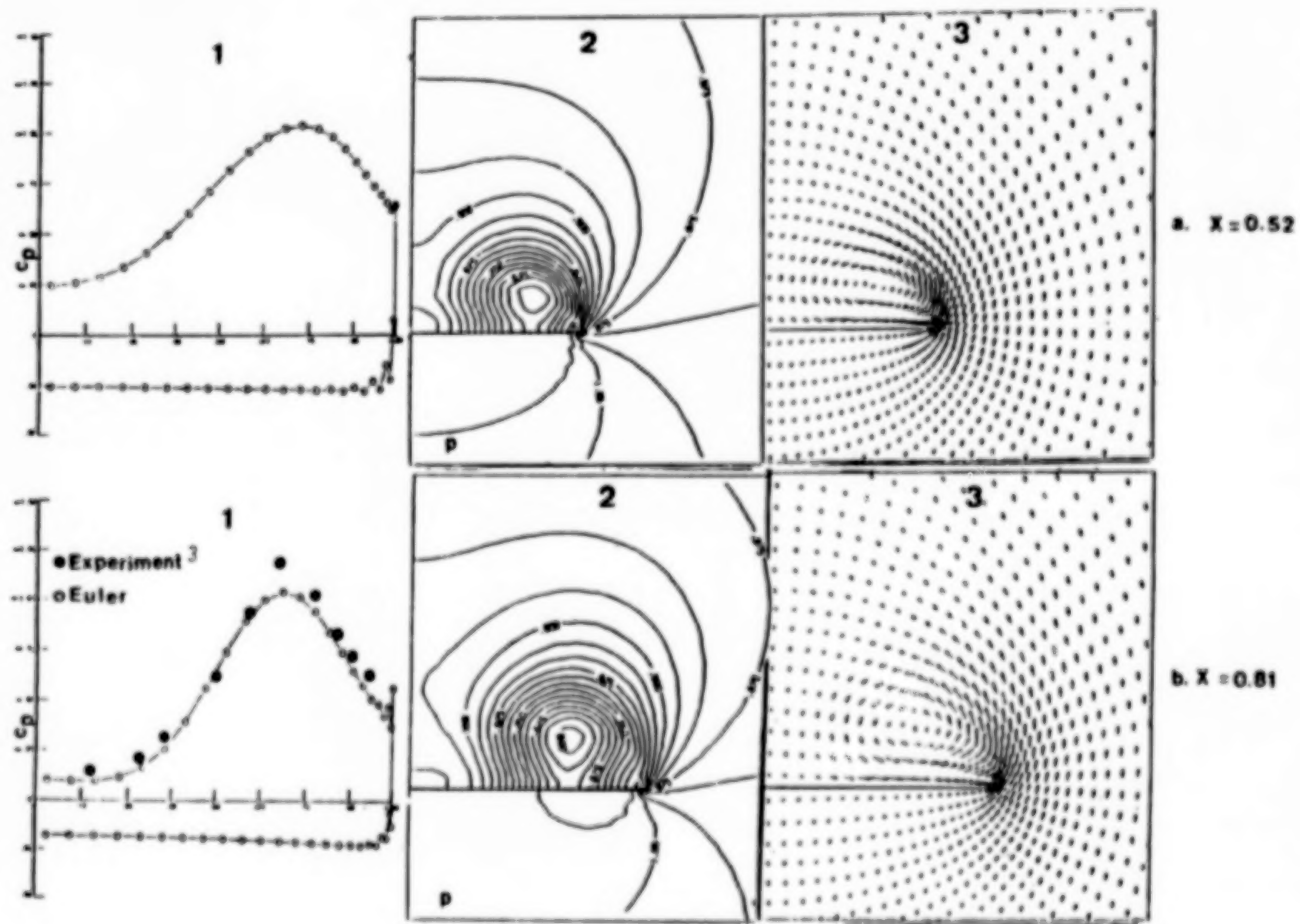


Figure 3 . Three-Dimensional Transonic Flow, Standard Euler Set, Sharp-edged delta wing, $80 \times 38 \times 48$ cell, $M_\infty = 0.7$, $\alpha = 10^\circ$, $AR = 1.5$, $c_2 = 0.12$, $c_4 = 0.005$,
 (a,b) 1. Surface Pressure, 2. Static Pressure Contours, 3. Crossflow velocity
 (c,d) 1. Static pressure Contours, 2. Crossflow velocity

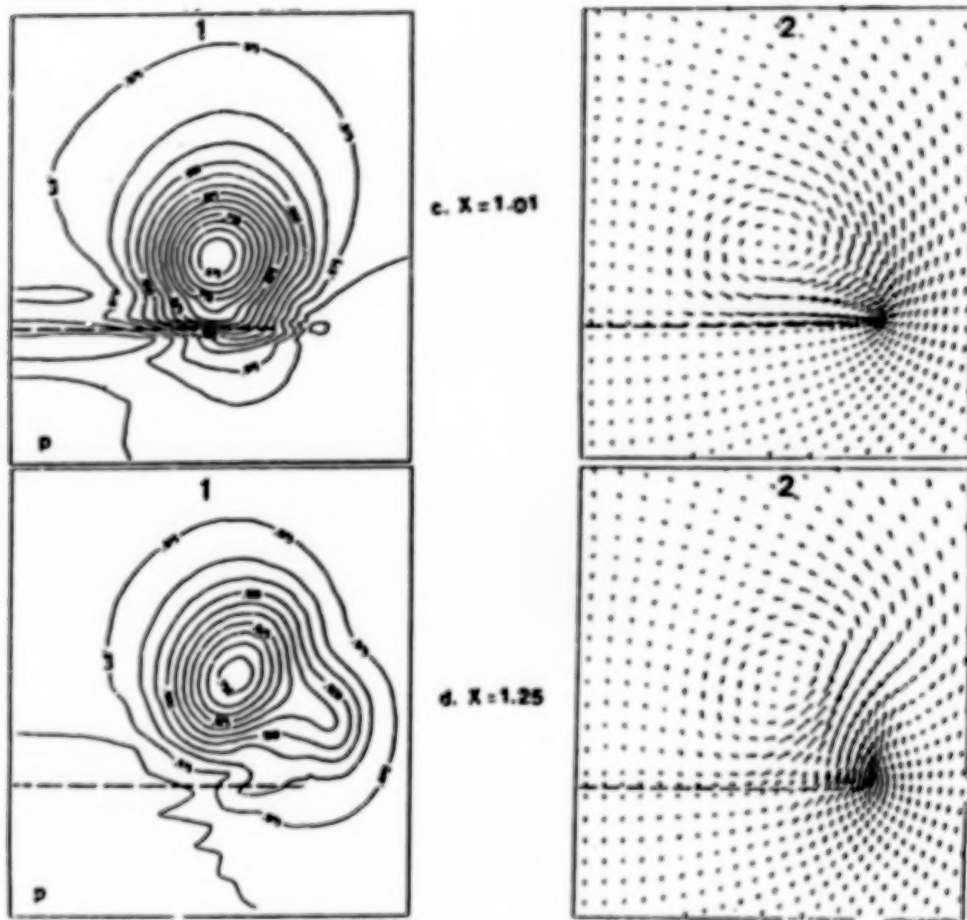


Figure 3. Three-Dimensional Transonic Flow, Standard Euler Set, Sharp-edged delta wing, $80 \times 38 \times 48$ cell, $M_\infty = 0.7$, $\alpha = 15^\circ$, $AR = 1.5$, $c_2 = 0.12$, $c_4 = 0.005$,
 (a, b) 1. Surface Pressure, 2. Static Pressure Contours, 3. Crossflow velocity
 (c, d) 1. Static pressure Contours, 2. Crossflow velocity

THREE-DIMENSIONAL LOW-SPEED FLOW

Figure 4 shows the results of a sharp-edged delta wing for $M_\infty = 0.3$, $\alpha = 20.5^\circ$ and aspect ratio of 1 using a number of cells of $80 \times 38 \times 48$ in the \bar{x} , \bar{y} , and \bar{z} directions; respectively. The results of Figures 4a and 4b show, from left to right, the surface pressure and the experimental data of Hummel⁴ the static-pressure-coefficient contours and the cross-flow velocity at the chord stations of 0.52 and 0.81. The results of Figures 4c and 4d show, from left to right, the experimental static-pressure-coefficient contours⁴ (cross-flow planes are normal to wind direction), the computed static-pressure-coefficient (cross-flow planes are normal to wing surface) and the computed cross-flow velocity at the chord stations 1.02 and 1.25.

The results show that the location of leading-edge vortex core is accurately predicted, the suction pressure peak is accurately predicted at $x = 0.52$ but it is overpredicted at $x = 0.81$, the location of the trailing-edged vortex core is slightly off that of the experimental data. A finer grid than the one used in this example is expected to give a more accurate prediction.

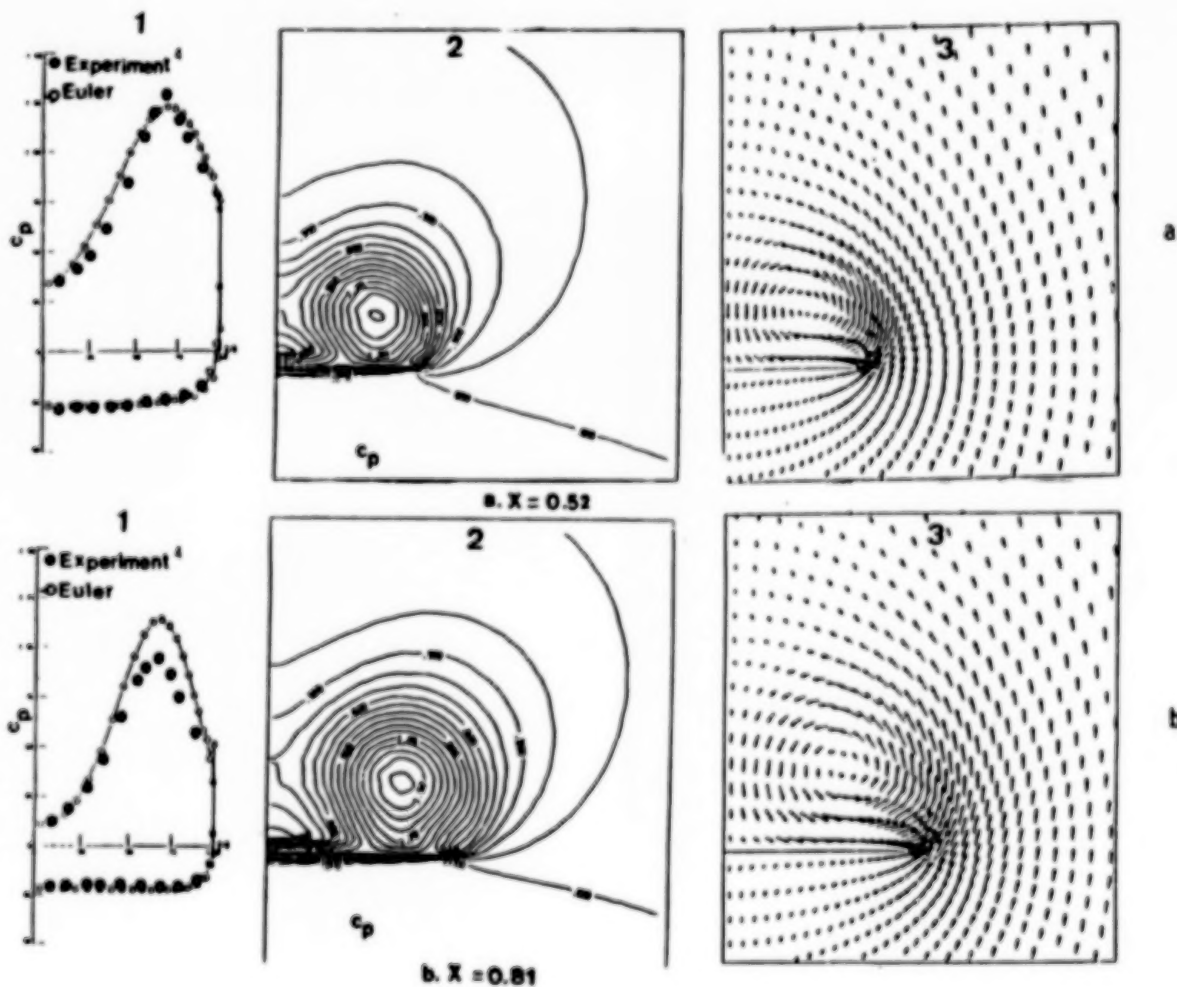


Figure 4. Three-dimensional subsonic flow, isentropic Euler set, sharp-edged delta wing, $80 \times 38 \times 48$ cell, $M_\infty = 0.3$, $\alpha = 20.5^\circ$, $AR = 1$, $c_2 = 0.12$, $c_4 = 0.005$, (a.,b.) 1. surface pressure, 2. static pressure coefficient, C_p , 3. crossflow velocity

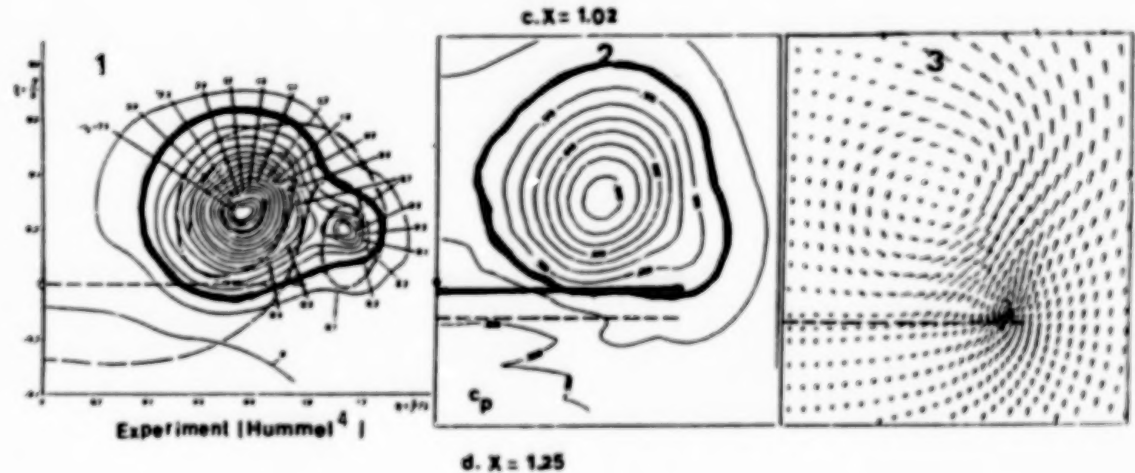
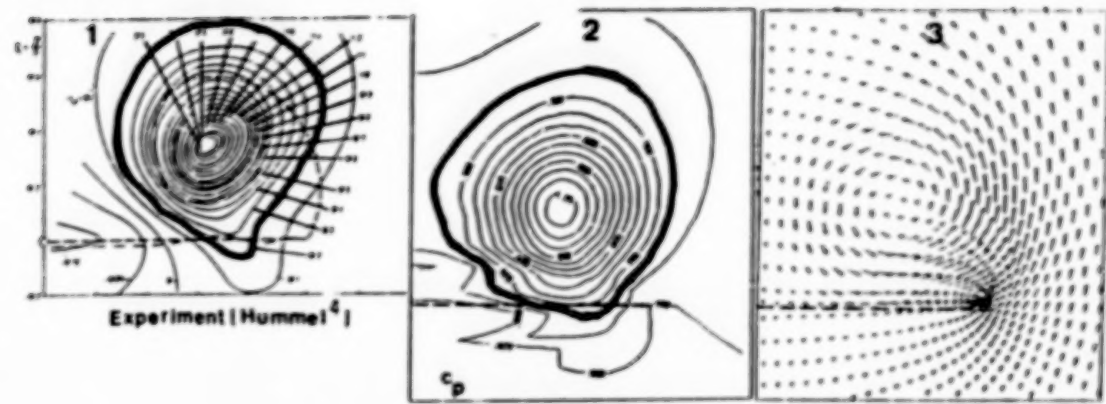
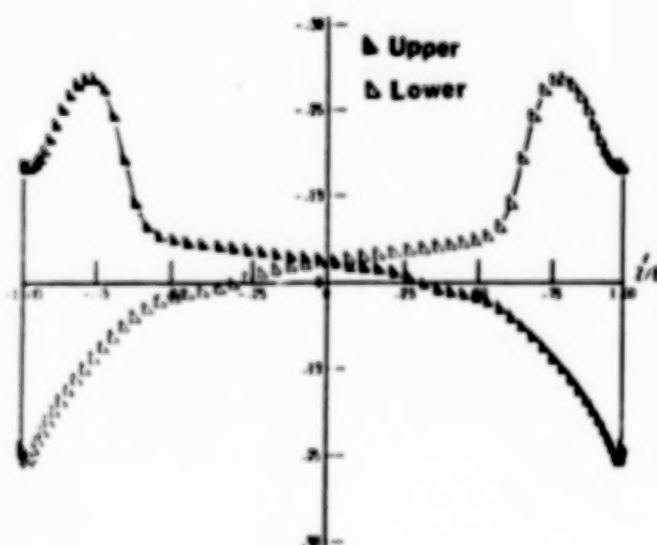


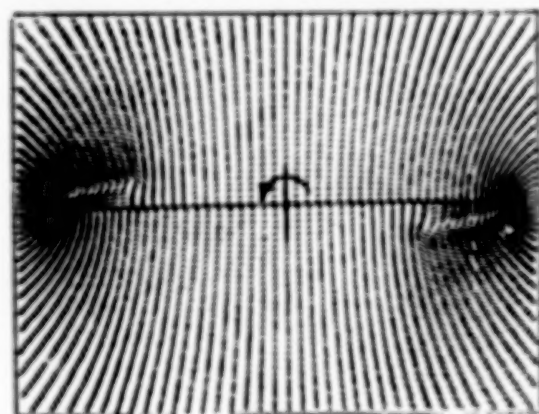
Figure 4. Three-dimensional subsonic flow, isentropic Euler set, sharp-edged delta wing, $80 \times 38 \times 48$ cell, $M_\infty = 0.3$, $\alpha = 20.5^\circ$, $AR = 1$, $\epsilon_2 = 0.12$, $\epsilon_4 = 0.005$, (c.d.) 1. experimental static pressure contours, C_p , (normal to wind direction), 2. static pressure contours, C_p , (normal to wing surface), 3. crossflow velocity.

UNIFORM ROLLING IN A CONICAL FLOW

Figure 5 shows the results for a flat plate sharp-edged delta wing which is undergoing uniform rolling in the counter-clockwise direction around its axis ox' at a constant angular speed $\omega = \frac{\dot{\theta}U}{c} = 0.5$; where ω and $\dot{\theta}$ are the dimensional and dimensionless angular speeds, c is the wing root chord and U is the freestream speed. The wing angle of attack $\alpha = 0$ and hence the flow is steady in the rotating frame of reference. Figure 5a shows the upper "▲" and lower "△" surface pressure. As symmetric surface pressure. Figures 5b, 5c and 5d show the corresponding cross-flow velocity, cross-flow Mach contours and static pressure contours. On the cross-flow Mach contours and under the anti-symmetric leading-edge vortices, one notices a weak cross-flow shock.

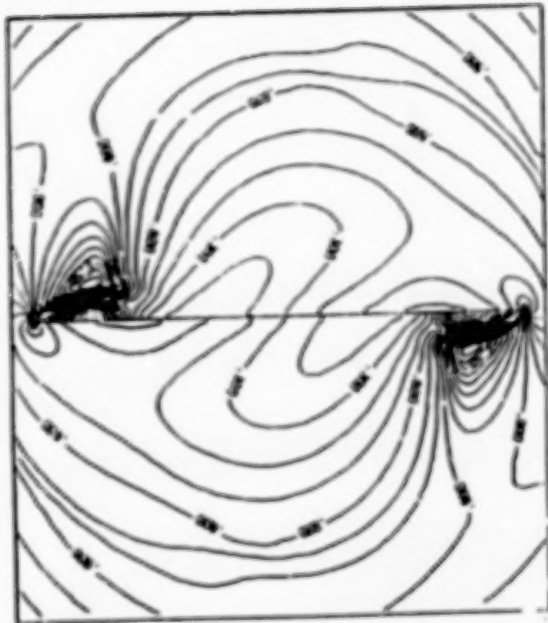


a. surface pressure

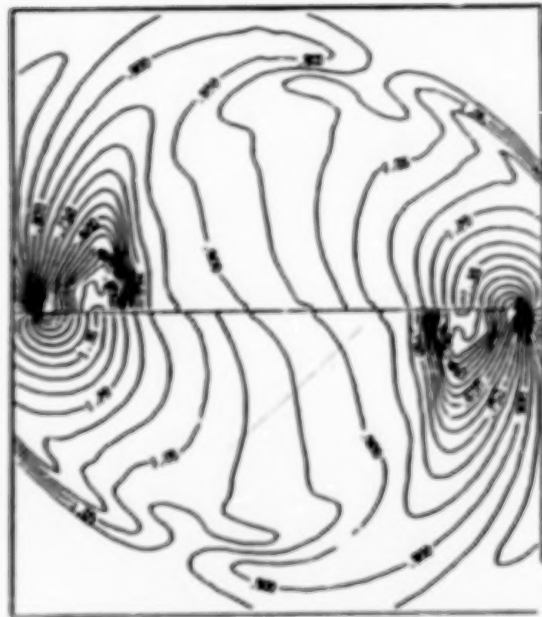


b. cross-flow velocity

Fig. 5. Uniform rolling of a delta wing,
 $M_\infty = 2$, $\alpha = 0^\circ$, $\beta = 70^\circ$, $\omega = 0.5$



c. cross-flow Mach



d. static pressure

Fig. 5. Uniform rolling of a delta wing.
 $M_\infty = 2$, $\alpha = 0^\circ$, $\beta = 70^\circ$, $\omega = 0.5$

ROLLING OSCILLATION IN A LOCALLY-CONICAL FLOW

The wing is given a rolling sinusoidal oscillation of $\dot{\theta}$ and θ of $\dot{\theta} = -\omega_0 \cos kt$ \hat{e}_x , and $\theta = -\theta_{\max} \sin kt$, where $\theta_{\max} = \omega_0/k$ and k is the dimensionless reduced frequency of oscillation ($K = \frac{kL}{U}$ is the dimensional frequency). Choosing $\theta_{\max} = \pi/12$ and $\omega_0 = 0.35$, the corresponding $k = 1.337$ and the period of oscillation $\tau = 4.699$. Figure 6 shows the rolling oscillation motion.

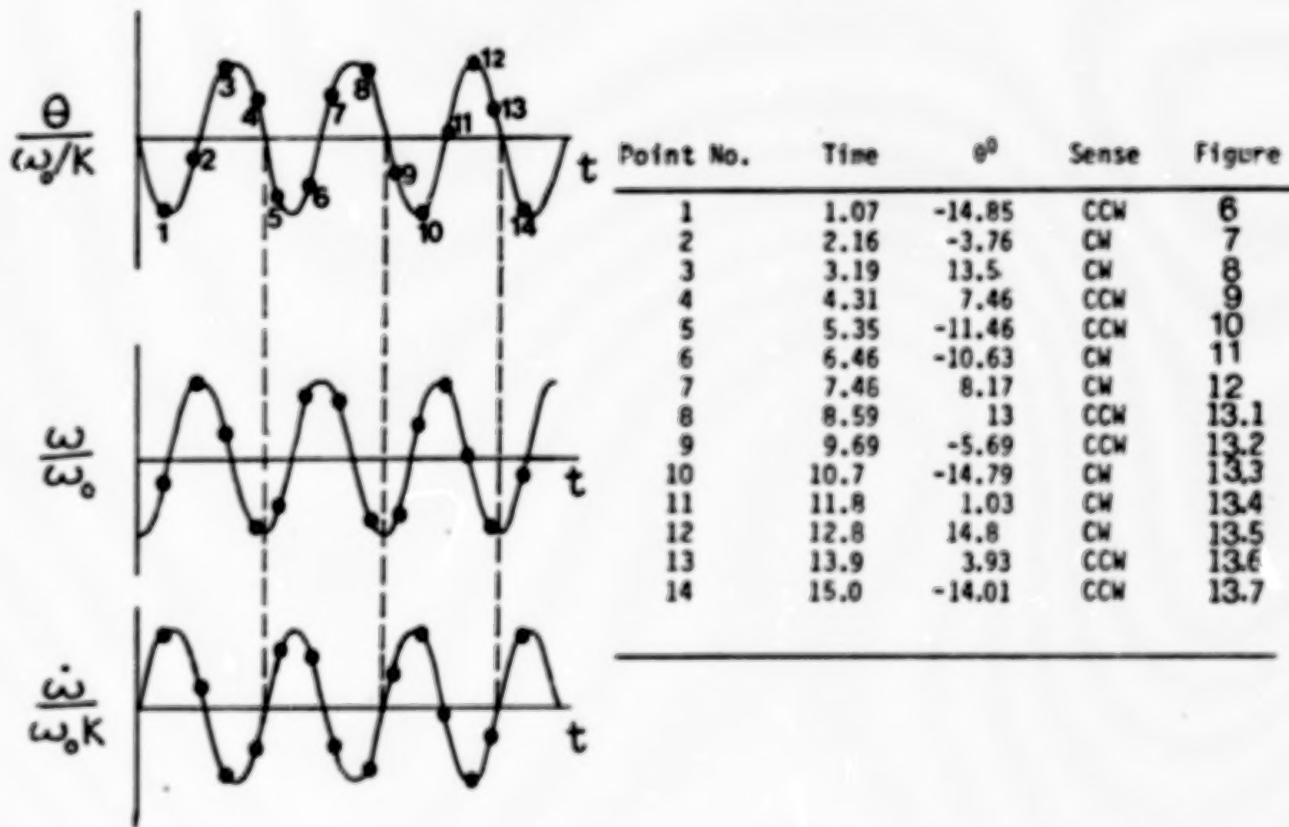
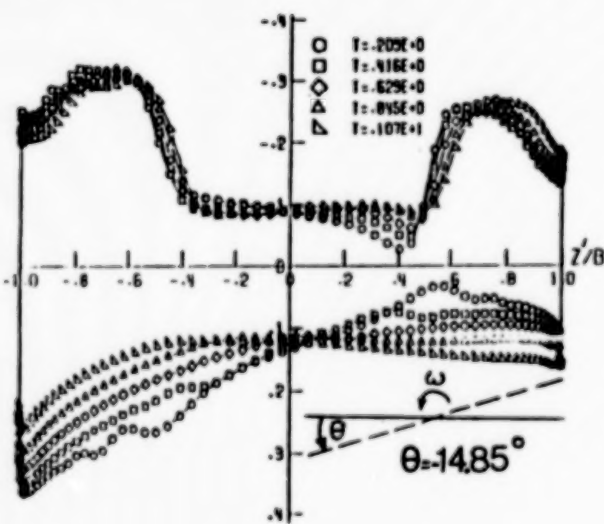


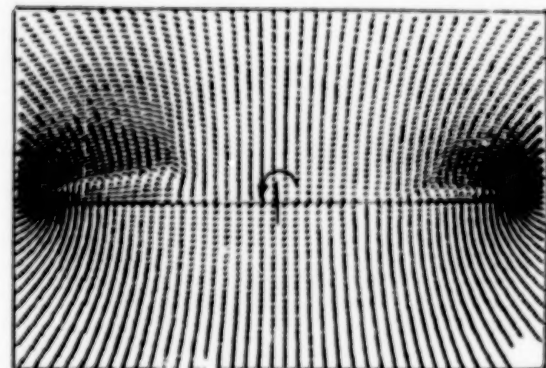
Fig. 6. Roll angle, angular speed and angular acceleration of the rolling oscillation motion.

ROLLING OSCILLATION (CONTINUED)

Figure 7 shows the results for the time range $t = 0 - 1.07$. By the end of this time, the wing has rolled through an angle $\theta = -14.85^\circ$ which corresponds to the end of the first quarter of the cycle. At $t = 0$, $|\omega| = \omega_0$, and $|\omega|$ decreases in the counter-clockwise direction within that time. Figure 7a shows the surface pressure after each 400 time steps covering a total of 2000 time steps. On the upper surface, the suction pressure on the left is higher than that on the right, and the suction peak is moving in the spanwise direction in the positive z direction. On the lower surface, the surface pressure is decreasing on the left side while it is increasing on the right side. Figures 7b, 7c and 7d show the cross-flow velocity, cross-flow Mach contours and static pressure contours at $t = 1.07$ and $\theta = -14.85^\circ$. At this moment, a large leading-edge vortex appears on the left and a small leading-edge vortex appears on the right. The cross-flow Mach contours show shocks above and below the left leading-edge vortex. It also shows the outer bow shock with varying strength (lower portion of the figure).

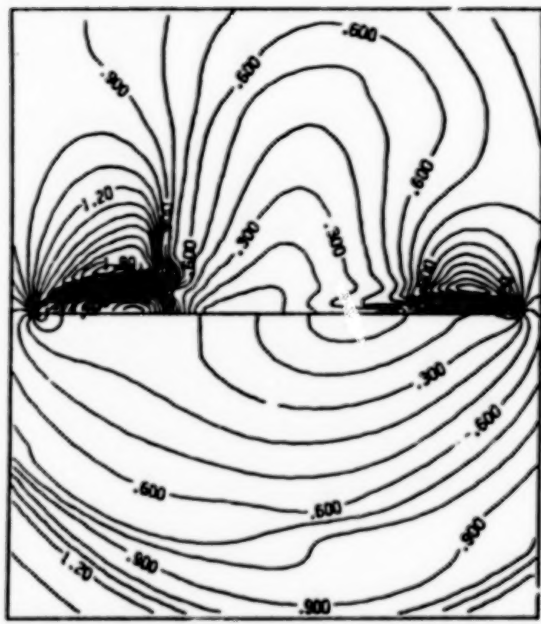


a. surface pressure

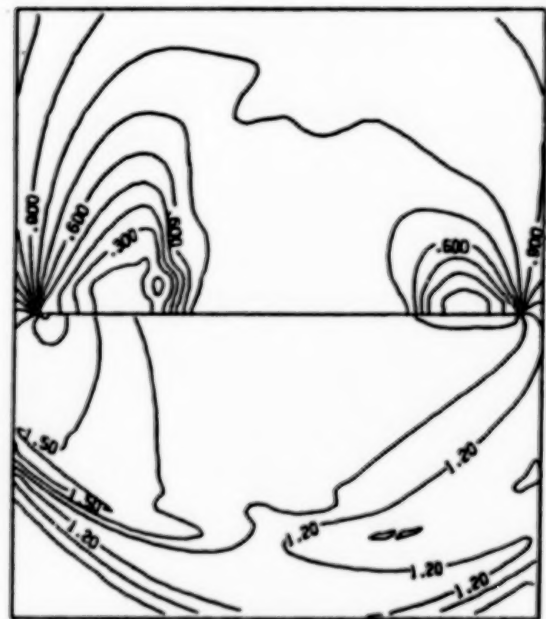


b. cross-flow velocity

Fig. 7 . Rolling oscillation of a delta wing,
 $M_\infty = 2$, $\alpha = 10^\circ$, $\beta = 70^\circ$, $\omega = 0.35$, $k = 1.337$,
 $\theta_{\max} = 15^\circ$, $t = 0 - 1.07$, $\theta = 0 - (-1485^\circ)$



c. cross-flow Mach



d. static pressure

Fig. 7 . Rolling oscillation of a delta wing.
 $M_\infty = 2$, $\alpha = 10^\circ$, $\beta = 70^\circ$, $\omega = 0.35$, $k = 1.337$,
 $\theta_{\max} = 15^\circ$, $t = 0-1.07$, $\theta = 0-(-1485^\circ)$

ROLLING OSCILLATION (CONTINUED)

Figure 8 shows the results for the time range $t = 1.07^+ - 2.16$. Within this time, the wing has reversed its direction $|\omega|$, and by the end of this time, the wing roll angle $\theta = -3.76^\circ$. Figure 8a shows the surface pressure after each 400 time steps covering the range of time steps from 2,001-4,000. The peak suction pressure on the left is decreasing corresponding to a decrease in size of the left vortex while that on the right is increasing corresponding to an increase in size of the right vortex. Figures 8b, 8c and 8d show the cross-flow velocity, cross-flow Mach contours and static-pressure contours at $t = 2.16$, $\theta = -3.76^\circ$.

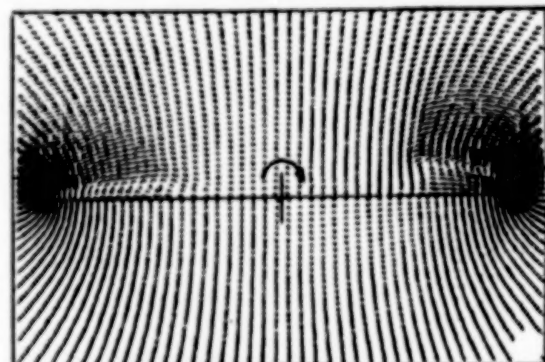
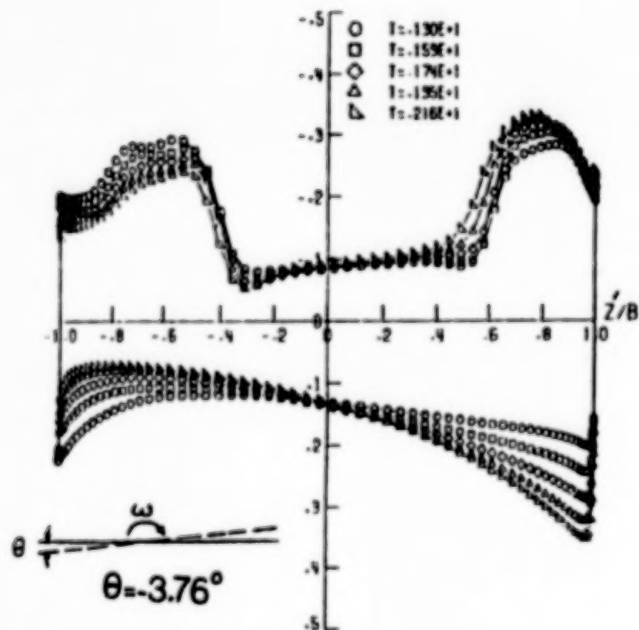
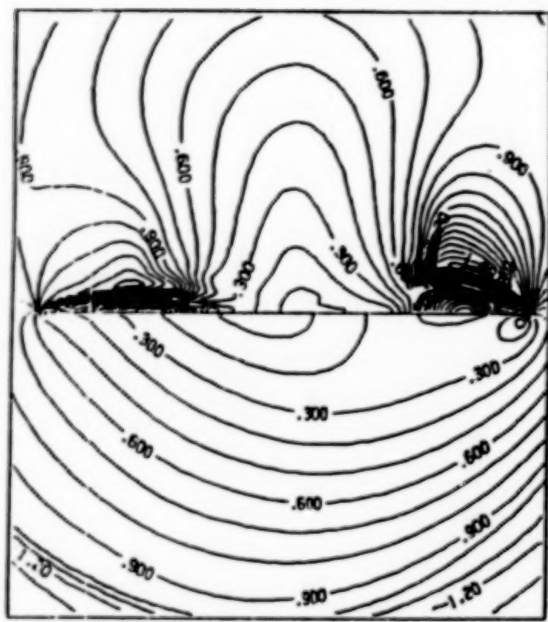
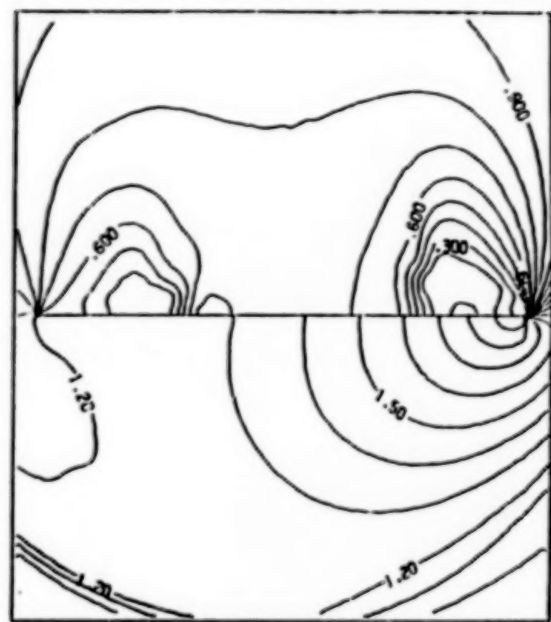


Fig. 8 . Rolling oscillation of a delta wing,
 $M_\infty = 2$, $\alpha = 10^\circ$, $\beta = 70^\circ$, $\omega = 0.35$, $k = 1.337$,
 $\theta_{\max} = 15^\circ$, $t = 1.07^+ - 2.16$, $\theta = (-14.85^\circ) - (-3.76^\circ)$



c. cross-flow Mach

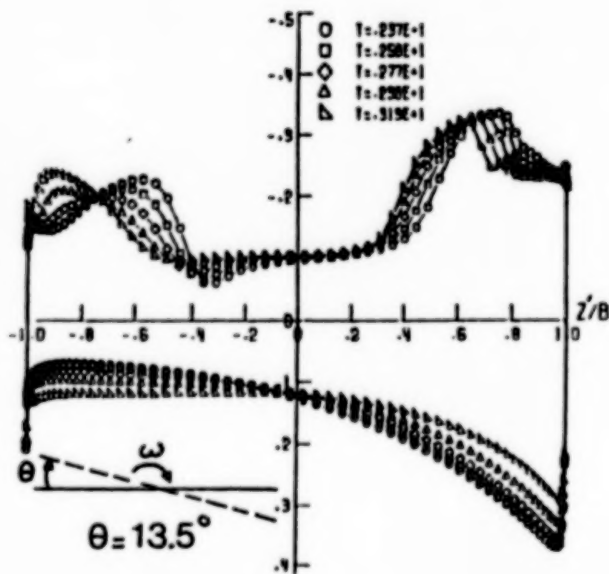


d. static pressure

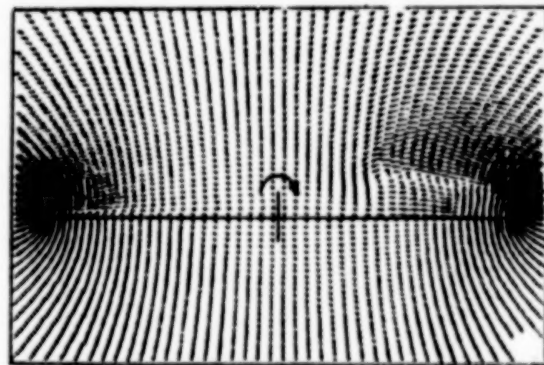
Fig.8 . Rolling oscillation of a delta wing,
 $M_\infty = 2$, $\alpha = 10^\circ$, $\beta = 70^\circ$, $\omega = 0.35$, $k = 1.337$,
 $\theta_{\max} = 15^\circ$, $t = 1.07^+ - 2.16$, $\theta = (14.85^\circ) -$
 (-3.76°)

ROLLING OSCILLATION (CONTINUED)

Figure 9 shows the results for the time range $t = 2.16^+ - 3.19$ during which the wing is rotating in the clockwise direction with decreasing $|\omega|$. By the end of this time, the roll angle is $\theta = 13.5^\circ$. Figure 9a shows the surface pressure covering the range of time steps 4,001-6,000. The peak suction pressure on the left is moving to the left as the vortex is disappearing, and an attached flow is forming. The peak suction pressure on the right is moving inwards to the left, while the shock under the vortex is growing. Figures 9b, 9c and 9d show the cross-flow velocity, cross-flow Mach contours and static pressure contours at $t = 3.19$ and $\theta = 13.5^\circ$.

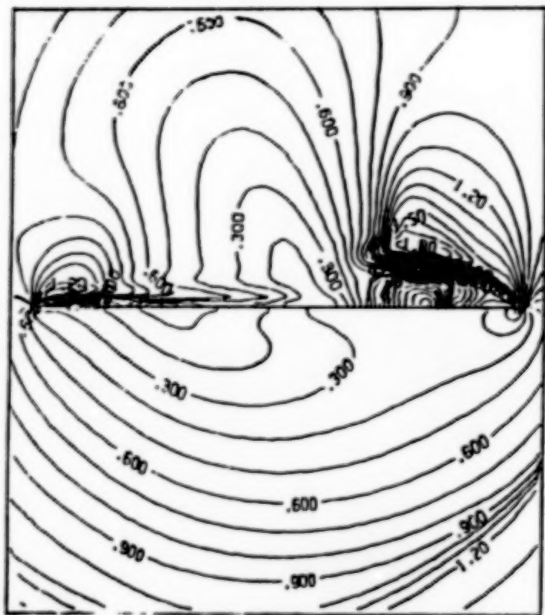


a. surface pressure

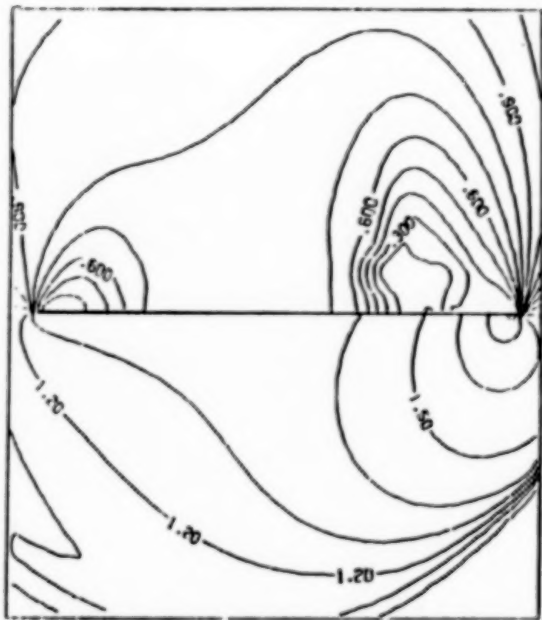


b. cross-flow velocity

Fig. 9. Rolling oscillation of a delta wing.
 $M_\infty = 2$, $\alpha = 10^\circ$, $\beta = 70^\circ$, $\omega = 0.35$, $k = 1.337$,
 $\theta_{\max} = 15^\circ$, $t = 2.16^+ - 3.19$, $\theta = (-3.76^\circ) -$
 $(+13.6^\circ)$



c. cross-flow Mach

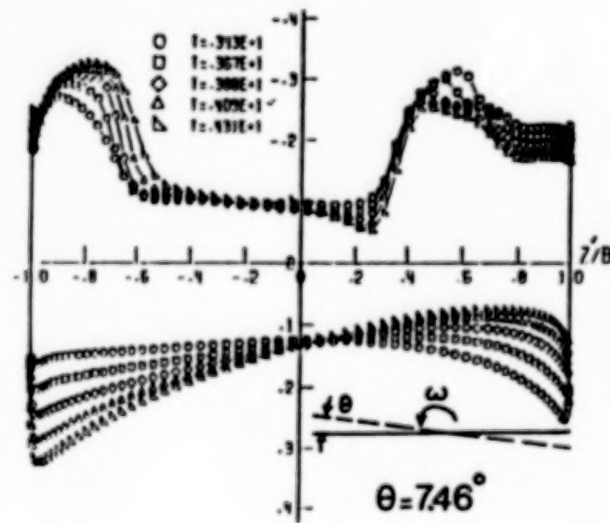


d. static pressure

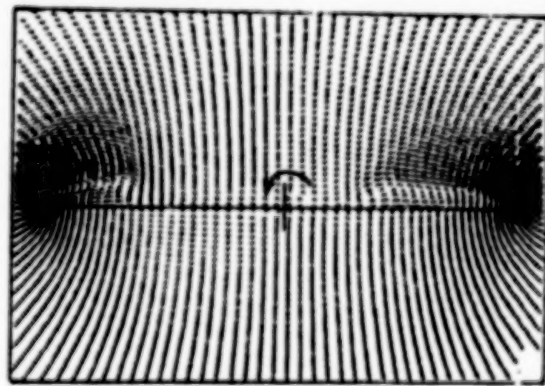
Fig. 9. Rolling oscillation of a delta wing,
 $M_\infty = 2$, $\alpha = 10^\circ$, $\beta = 70^\circ$, $\omega = 0.35$, $k = 1.337$,
 $\theta_{\max} = 15^\circ$, $t = 2.16^\circ - 3.19^\circ$, $\theta = (-3.76^\circ) -$
 $(+13.5^\circ)$

ROLLING OSCILLATION (CONTINUED)

Figure 10(a-d) shows the results for the time range $t = 3.19^+ - 4.31$ during which the wing has reversed the direction of rotation from the CW to CCW, and $|\omega|$ has reached a zero value and then increases. The vortex on the left is growing, and the corresponding peak suction pressure is increasing and moving inboards to the right. The vortex on the right is flattening, and its peak suction pressure is decreasing and moving inboards to the left. By the end this time $t = 4.31$; the roll angle $\theta = 7.46^\circ$.

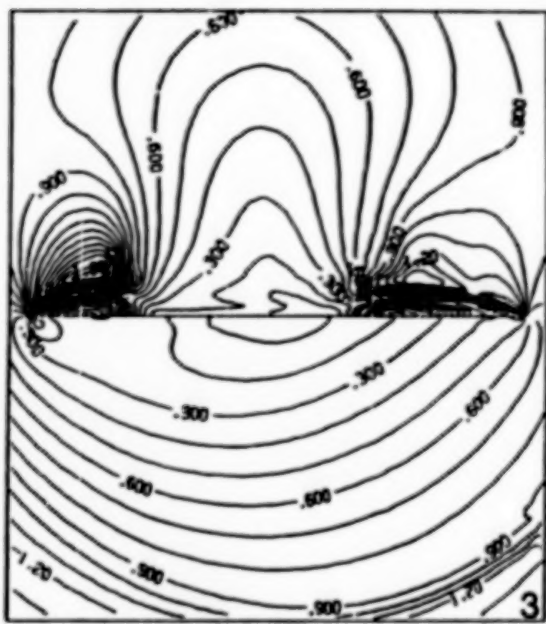


a. surface pressure

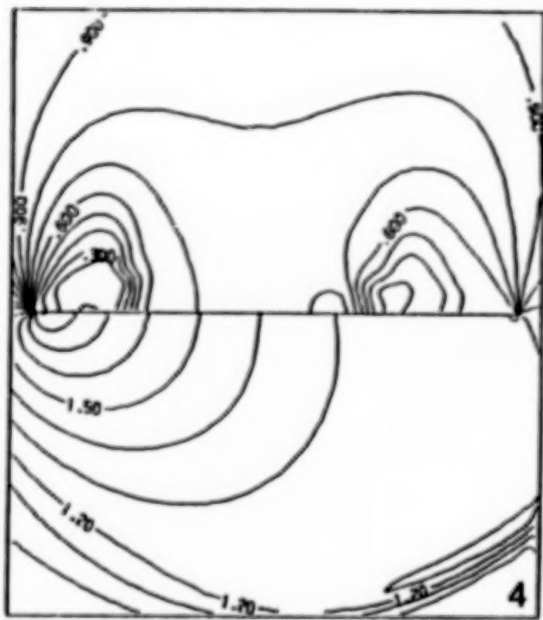


b. cross-flow velocity

Fig. 10. Rolling oscillation of a delta wing,
 $M_\infty = 2$, $\alpha = 10^\circ$, $\beta = 70^\circ$, $\omega = 0.35$, $k = 1.337$,
 $\theta_{\max} = 15^\circ$, $t = 3.19^+ - 4.31$, $\theta = (+13.5^\circ) - (+7.46^\circ)$



c. cross-flow Mach

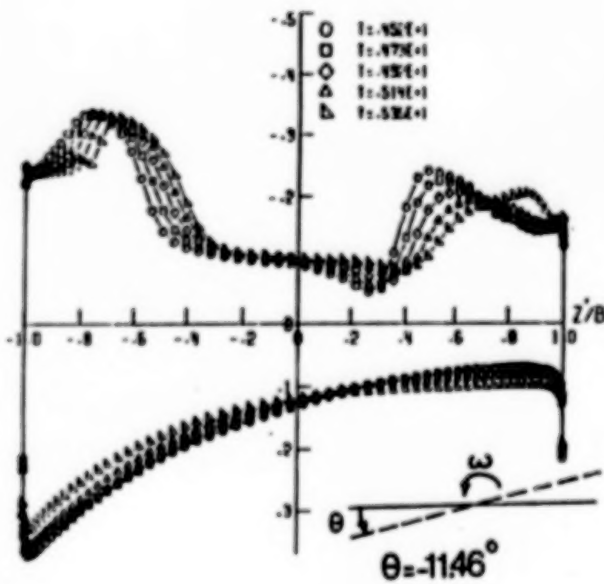


d. static pressure

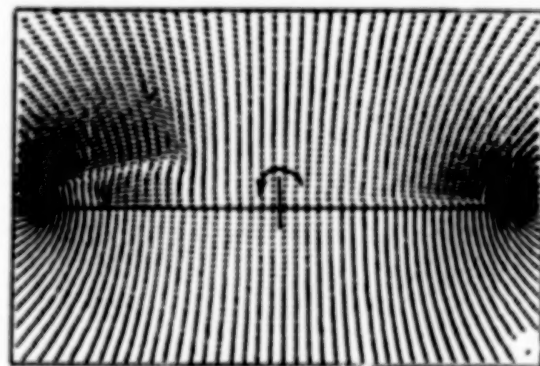
Fig.10. Rolling oscillation of a delta wing,
 $M_\infty = 2$, $\alpha = 10^\circ$, $\beta = 70^\circ$, $\omega = 0.35$, $k = 1.337$,
 $\theta_{\max} = 15^\circ$, $t = 3.19^\dagger - 4.31$, $\theta = (+13.5^\circ) -$
 $(+7.46^\circ)$

ROLLING OSCILLATION (CONTINUED)

Within the time range $t = 4.31^+ - 5.35$, the wing is still rotating in the CCW, and $|\omega|$ has reached its maximum value and then decreases. At $t = 4.7$, the wing has already completed one cycle of oscillation. The peak suction pressure on the left is moving inwards to the right, and the peak suction pressure on the right is moving outwards to the right, Figure 11 (a--d). By the end of this time $t = 5.35$, the roll angle $\theta = -11.46^\circ$.

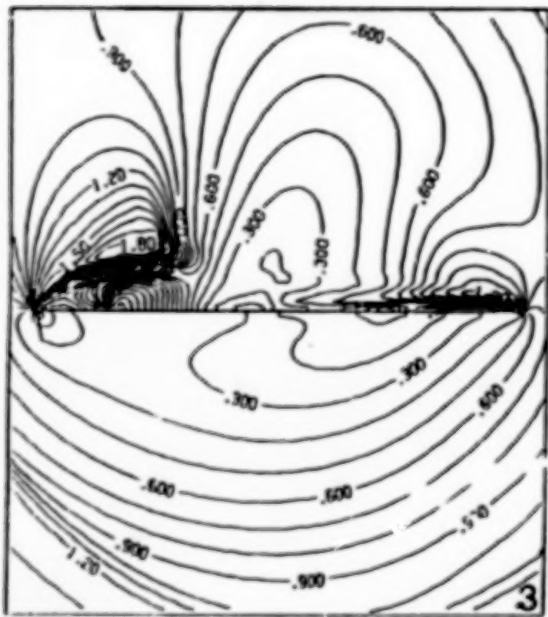


a. surface pressure

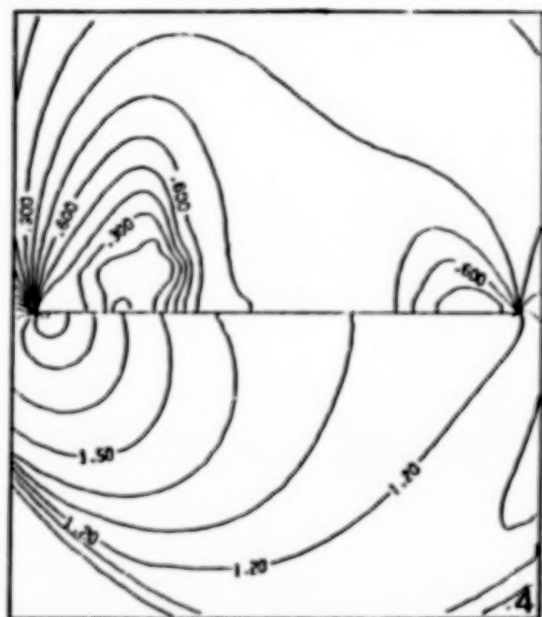


b. cross-flow velocity

Fig.11. Rolling oscillation of a delta wing,
 $M_\infty = 2$, $\alpha = 10^\circ$, $\beta = 70^\circ$, $\omega = 0.35$, $k = 1.337$,
 $\theta_{\max} = 15^\circ$, $t = 4.31^+ - 5.35$, $\theta = (+7.46^\circ) - (-11.46^\circ)$



c. cross-flow Mach

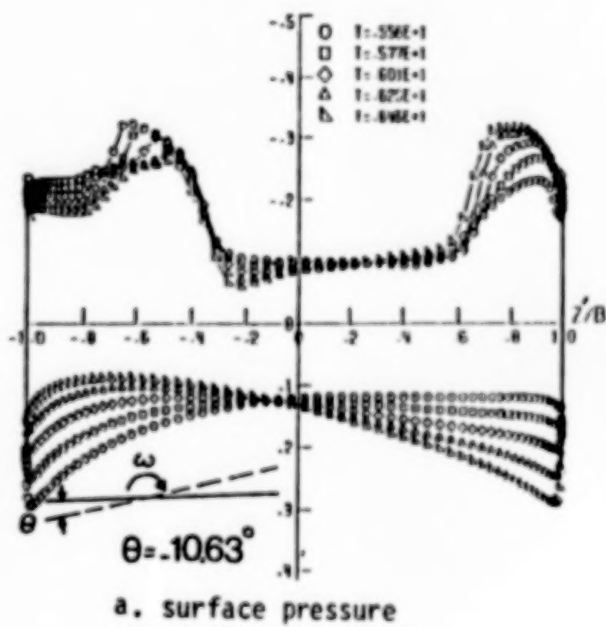


d. static pressure

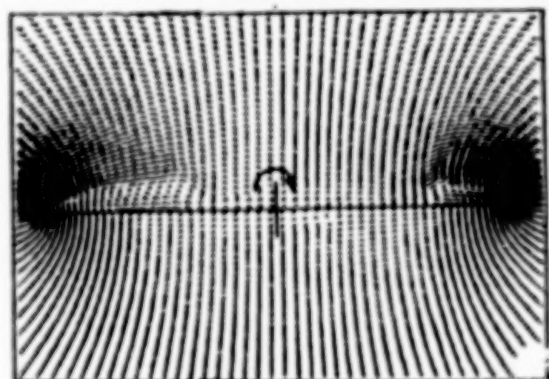
Fig.11. Rolling oscillation of a delta wing,
 $M_\infty = 2$, $\alpha = 10^\circ$, $\beta = 70^\circ$, $\omega = 0.35$, $k = 1.337$,
 $\theta_{\max} = 15^\circ$, $t = 4.31^\circ - 5.35^\circ$, $\theta = (+7.45^\circ) -$
 (-11.46°)

ROLLING OSCILLATION (CONTINUED)

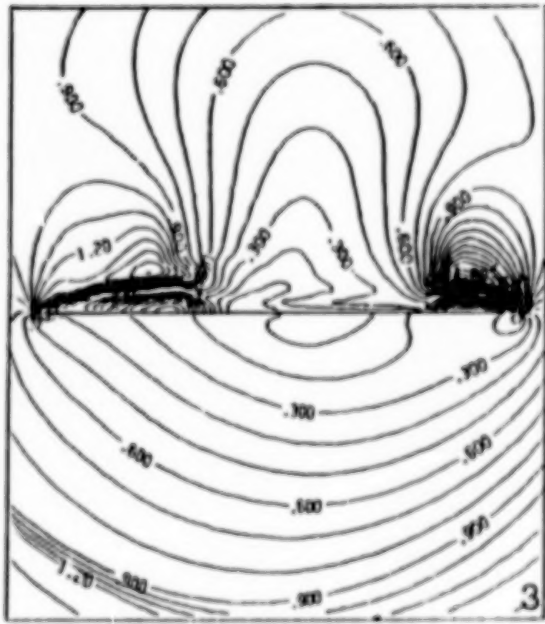
Figures 12a-12d and 13a-13d show the results covering the ranges of time steps 10,001-12,000 and 12,001-14,000, respectively. Figures 5-11 cover a total of 1.56 cycles of oscillation. The results show the successive increase, decreased and motion of the left and right vortices and their corresponding peak suction pressure. They also show the formation and disintegration of the shocks below and above the vortices, and the motion and strength variation of the outer bow shock.



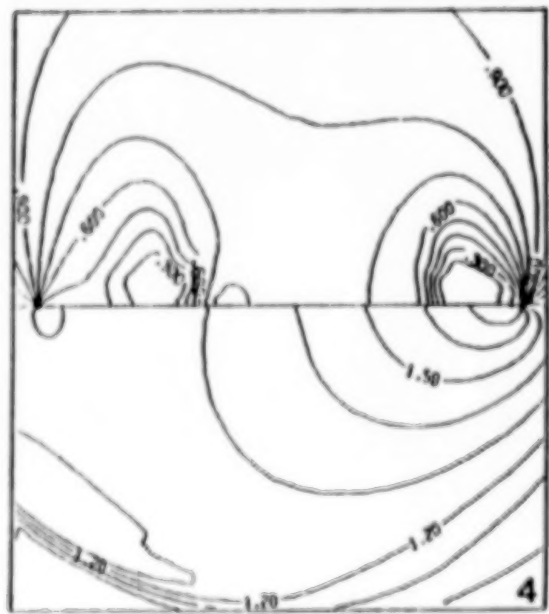
a. surface pressure



b. cross-flow velocity

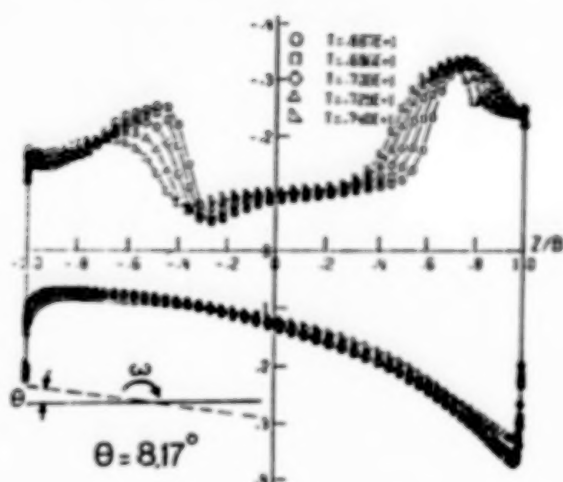


c. cross-flow Mach

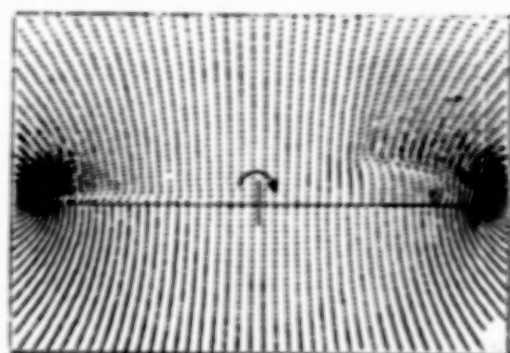


d. static pressure

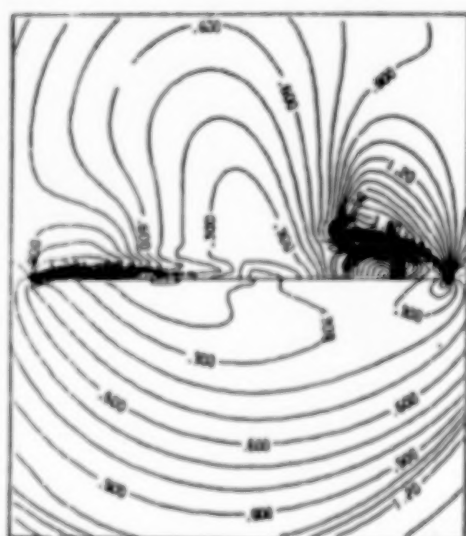
Fig.12. Rolling oscillation of a delta wing,
 $M_\infty = 2$, $\alpha = 10^\circ$, $\beta = 70^\circ$, $\omega = 0.35$, $k = 1.337$,
 $\theta_{\max} = 15^\circ$, $t = 5.35^\circ - 6.46^\circ$, $\theta = (-11.46^\circ) - (-10.63^\circ)$



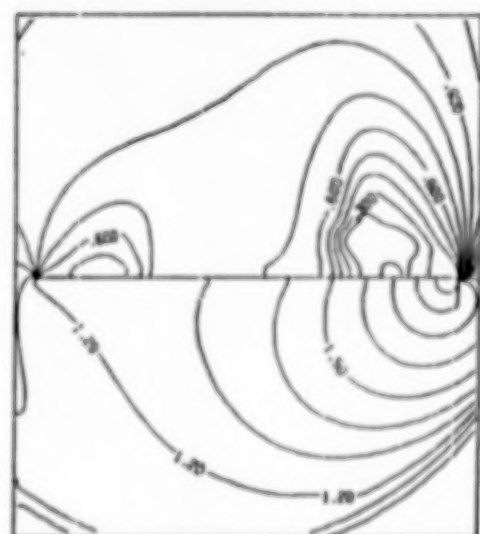
a. surface pressure



b. cross-flow velocity



c. cross-flow Mach



d. static pressure

Fig. 13. Rolling oscillation of a delta wing,
 $M_\infty = 2$, $\alpha = 10^\circ$, $\beta = 70^\circ$, $\omega = 0.35$, $k = 1.337$,
 $\theta_{\max} = 15^\circ$, $t = 6.46^\circ - 7.48$, $\theta = (10.63^\circ) - (+8.17^\circ)$

ROLLING OSCILLATION (CONCLUDED)

Steady state oscillation response is reached after 3 cycles of transient response, Figure 14 (a--g).

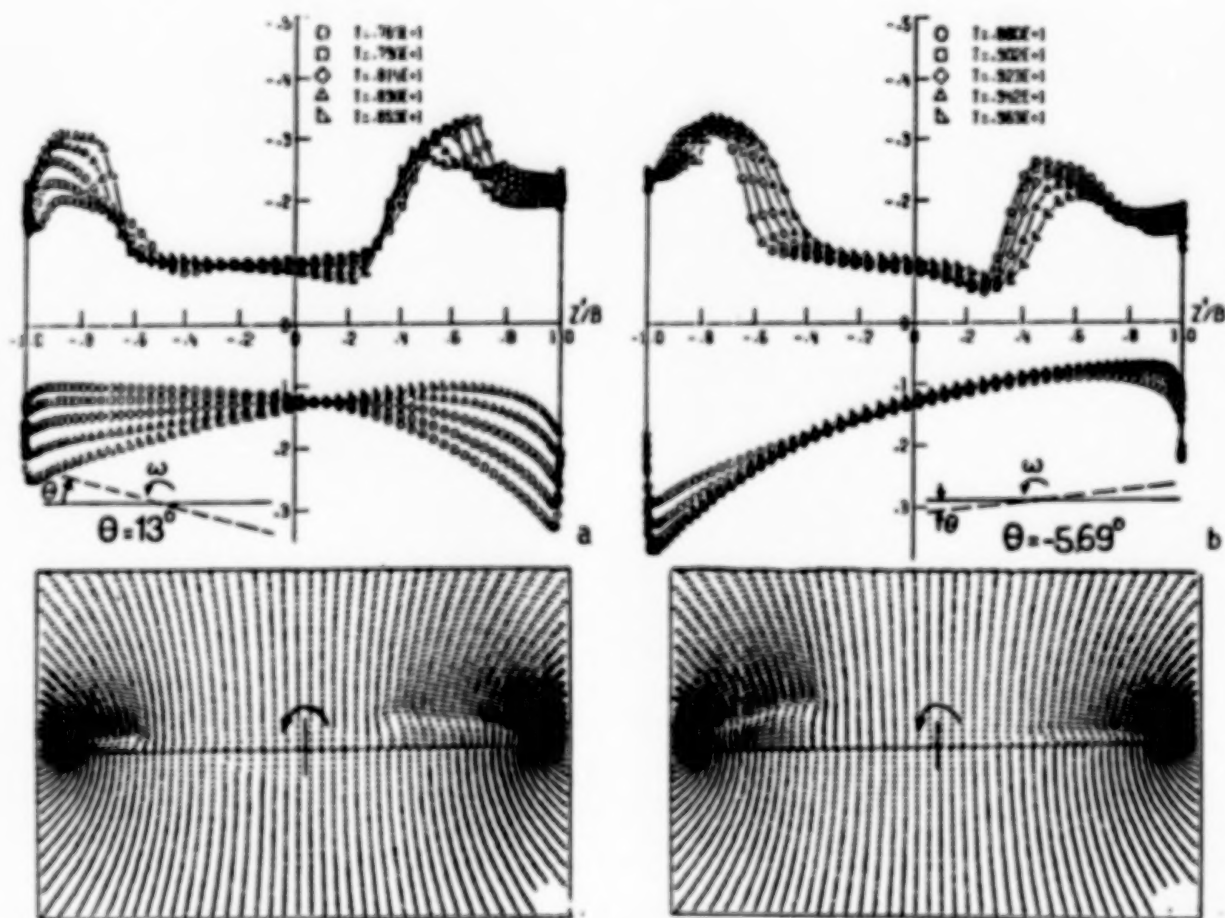


Fig. 14. Rolling oscillations from $t = 7.48^+$ to $t = 15.0$, steady state oscillation is reached.

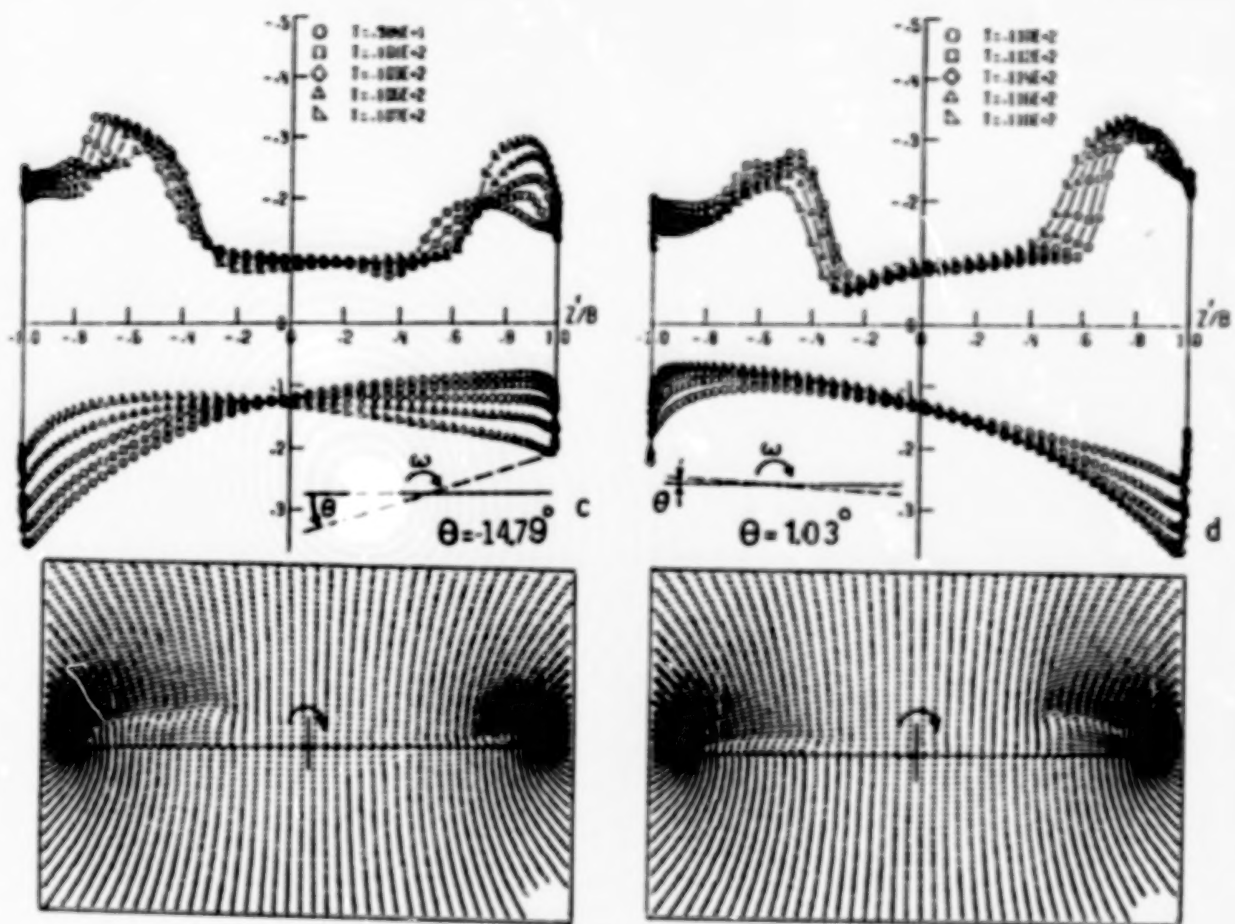
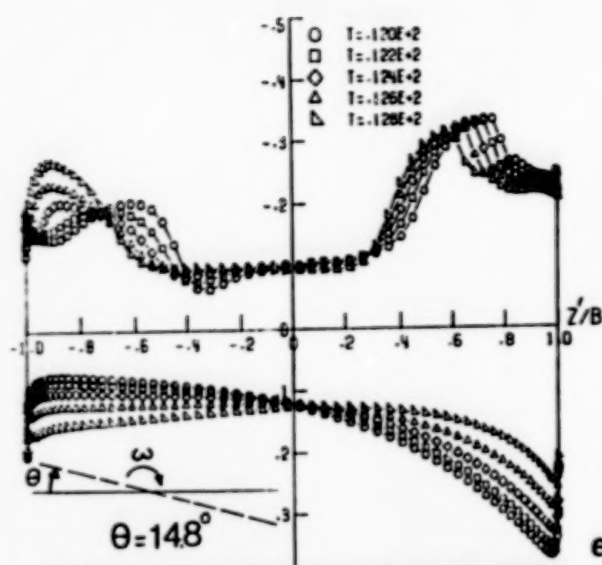
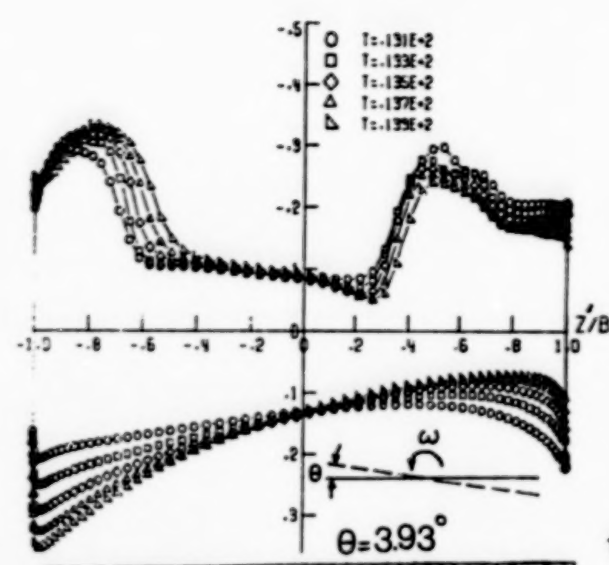


Fig. 14. Continued.



e



f

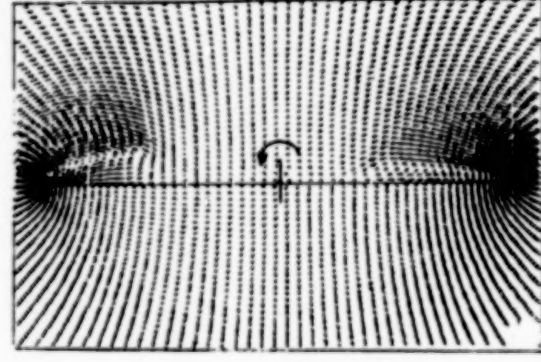
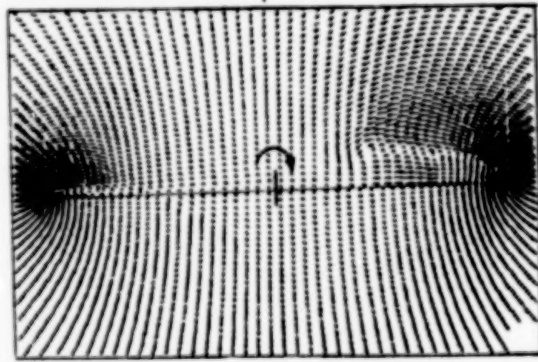


Fig. 14. Continued.

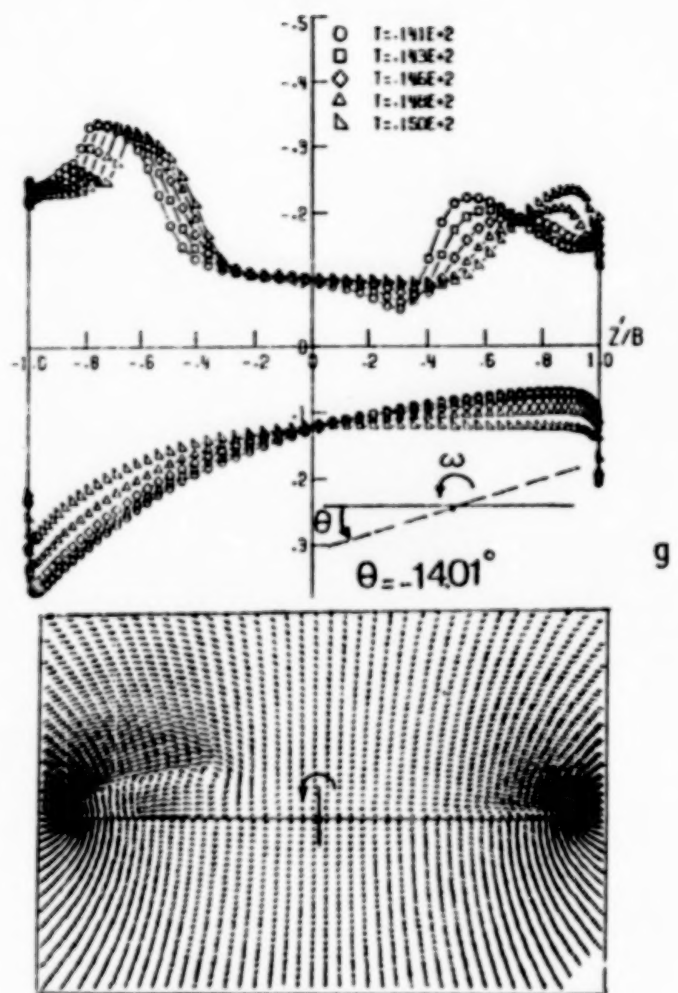


Fig. 14. Concluded.

ROLLING OSCILLATION, LIFT AND ROLLING-MOMENT COEFFICIENTS

Figure 15 shows the time history of the lift and rolling-moment coefficients along with roll angle variation. Steady-state oscillation response is reached by the third cycle. While the phase angle between C_M and θ is 90° , C_M is in phase with ω . Although C_M and θ have the same frequency, C_L shows twice the value of that frequency.

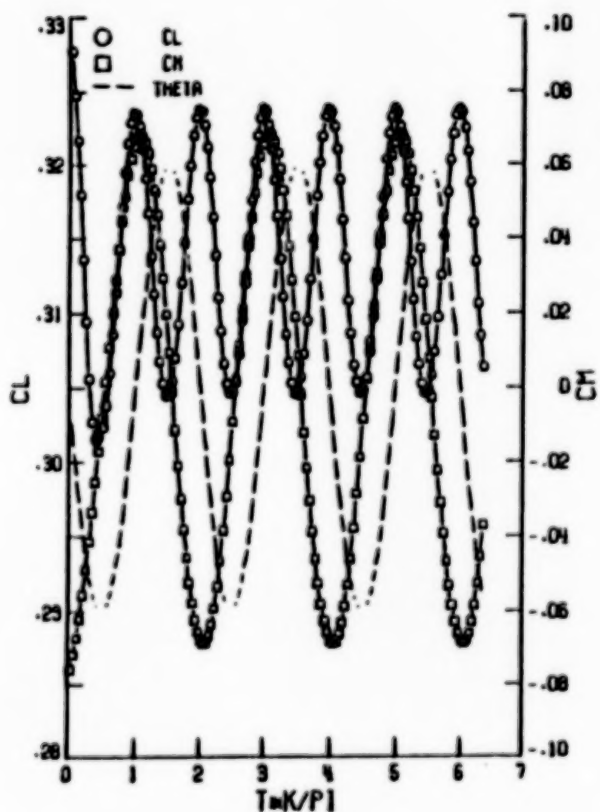


FIGURE 15. TIME HISTORY OF THE LIFT AND ROLLING-MOMENT COEFFICIENTS

3. Integral Solution of Full-Potential Equation With and Without Embedded Euler Domains

Formulation

Full Potential Equation (Shock Capturing, SC; Shock Capturing-Shock Fitting, SCSF)

$$\Phi_{xx} + \Phi_{yy} = G \quad (1)$$

$$G = \frac{-1}{\rho} (\rho_x \Phi_x + \rho_y \Phi_y) \quad (2)$$

$$\rho = [1 + \frac{\gamma-1}{2} M_\infty^2 (1 - \Phi_x^2 - \Phi_y^2)]^{1/\gamma-1} \quad (3)$$

$$\nabla \Phi \cdot \hat{n} = 0 \quad \text{on } g(x, y) = 0 \quad (4)$$

$$\nabla \Phi \rightarrow \bar{e}_\infty \quad \text{away from } g \quad (5)$$

$$\Delta C_p|_{TE} = 0 \quad (6)$$

Integral Solution of Velocity Field With Explicit Shock Surface Contribution

$$\begin{aligned} \nabla \Phi(x, y) = & \bar{e}_\infty + \frac{1}{2\pi} \oint_g q_g(s) \frac{(x-\xi) \bar{i} + (y-\eta) \bar{j}}{(x-\xi)^2 + (y-\eta)^2} ds \\ & + \frac{1}{2\pi} \oint_g \gamma_g(s) \frac{(y-\eta) \bar{i} - (x-\xi) \bar{j}}{(x-\xi)^2 + (y-\eta)^2} ds \\ & + \frac{1}{2\pi} \iint S G(\xi, \eta) \frac{(x-\xi) \bar{i} + (y-\eta) \bar{j}}{(x-\xi)^2 + (y-\eta)^2} d\xi d\eta \\ & + \frac{1}{2\pi} \oint_S q_S(s) \frac{(x-\xi) \bar{i} + (y-\eta) \bar{j}}{(x-\xi)^2 + (y-\eta)^2} ds \quad (7) \end{aligned}$$

Shock Fitting

$$q_S = - (v_{1n} - v_{2n}) = - \frac{2 v_{1n}}{\gamma + 1} \left(1 - \frac{1}{M_{1n}^2}\right) \quad , \quad M_{1n} > 1 \quad (8)$$

$$v_{2n} = \frac{(\gamma - 1) M_{1n}^2 + 2}{(\gamma + 1) M_{1n}^2} v_{1n} \quad (9)$$

$$v_{2t} = v_{1t} \quad (10)$$

$$\rho_2 = \frac{(\gamma + 1) M_{1n}^2}{(\gamma - 1) M_{1n}^2 + 2} \rho_1 \quad (11)$$

$$\beta = \sin^{-1} \left[\frac{1.2 \sin\beta \sin\theta}{\cos(\beta-\theta)} + \frac{1}{M_1^2} \right]^{1/2} \quad (12)$$

$$M_1 = M_\infty \left| \nabla \Phi \right|_1^{1/2} \quad , \quad M_{1n} = M_\infty \nabla \Phi_1 \cdot \hat{n}_S / \rho_1^{1/2} \quad (13)$$

Pressure Coefficient

$$c_p = \frac{2}{\gamma M_\infty^2} \left\{ \left[1 + \frac{\gamma - 1}{2} M_\infty^2 (1 - \Phi_x^2 - \Phi_y^2) \right]^{(\gamma - 1)/\gamma} - 1 \right\} \quad (14)$$

Euler Equations (Integral Equation With Embedded Euler Domains)

$$\frac{\partial \bar{q}}{\partial t} + \frac{\partial \bar{E}}{\partial x} + \frac{\partial \bar{F}}{\partial y} = 0 \quad (15)$$

$$\bar{q} = [\rho, \rho u, \rho v, \rho e]^t \quad (16)$$

$$\bar{E} = [\rho u, \rho u^2 + p, \rho uv, \rho uh]^t \quad (17)$$

$$\bar{F} = [\rho v, \rho uv, \rho v^2 + p, \rho vh]^t \quad (18)$$

$$e = \frac{p}{(\gamma+1)\rho} + (u^2 + v^2)/2, \quad h = e + p/\rho \quad (19)$$

Method of Solution

- Shock-Capturing Shock-Fitting (SCF) Scheme:

- Shock Capturing Part

1. In Eq. (7), Set $G = q_s = 0$, Use Eq. (7) to Satisfy B.C.S; Eqs. (4), (6). Find q_g and γ_g (piecewise linear distribution).
2. Calculate Initial Values of G at the Centroids of Field Elements ($G = M_\infty^2 u_x$).
3. With $q_s = 0$, Eq. (7) is Used to Satisfy R.C.S.
4. Calculate ρ and G Using Eqs. (2), (3) (Type Finite Difference is Used for ρ_x, ρ_y).
5. Steps (3) and (4) are Repeated Until Captured Shock Location is Fixed.

- Shock Fitting Part

6. Shock Panels are Introduced, q_s - term in Eq. (7) is activated.
7. Eqs. (8) and (12) are Used to Find q_s and β , and Eqs. (9)-(12) are Used to Cross the Shock.
8. Iterative Procedure is Continued Until Convergence.

- Integral Equation With Embedded Euler (IEEE) Scheme (For Strong Shocks)

1. Shock Capturing is used to Locate the Shock.
2. A Computational Fine-Grid Domain is Constructed Around the Shock for Euler Computations.
3. With B.C. and I.C. Found From Step (1), Euler Eqs. (15)-(19) are solved by Using a Central-Difference Finite-Volume Solver with Four-Stage Runge-Kutta Time Stepping and Added Second- and Fourth-Order Dissipation.
4. Fixing \bar{q} Values Found From the Euler Calculations, the Integral Eq. is used to Update the B.C.
5. The Iterative Procedure is Continued Until Convergence is Achieved.

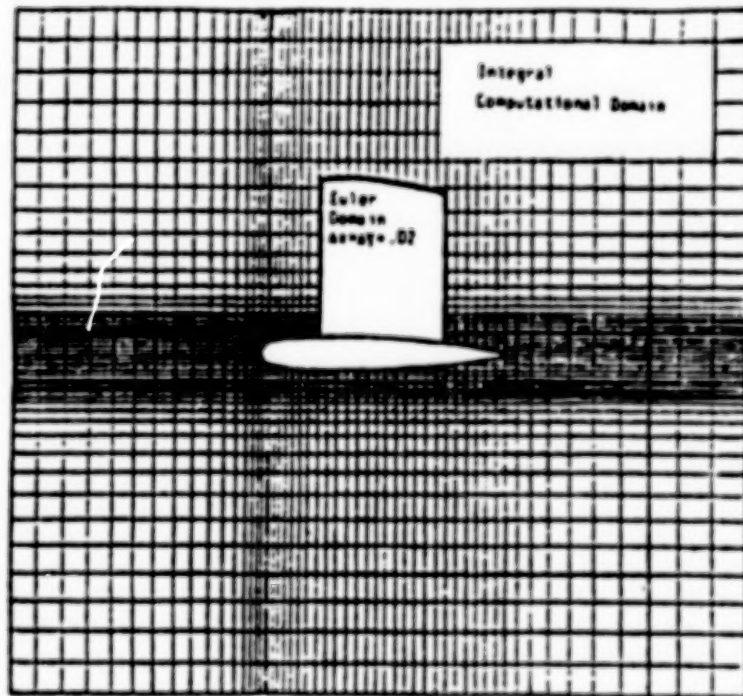


Fig.16 Integral Equation Grid with an Embedded-Euler Domain.

SHOCK-FREE FLOW

The first step to validate the computer program is to check the sensitivity of the IE solution to the size of the computational domain. Figure 17 shows the solutions for the NACA 0012 airfoil at $M_\infty = 0.72$ and $\alpha = 0^\circ$ using vortex panels only on the airfoil surface. We used a total of 140 vortex panels on the airfoil surface and a 64×60 field elements around the airfoil. The solutions show the surface pressure using two sizes of the computational domains; 2×1.5 and 3×2.5 . In Figure 18, we repeat the same test for a lifting case of the same airfoil at $M_\infty = 0.63$ and $\alpha = 2^\circ$. The results of these two cases show that a computational domain of 2×1.5 gives as accurate solutions as those of the 3×2.5 computational domain.

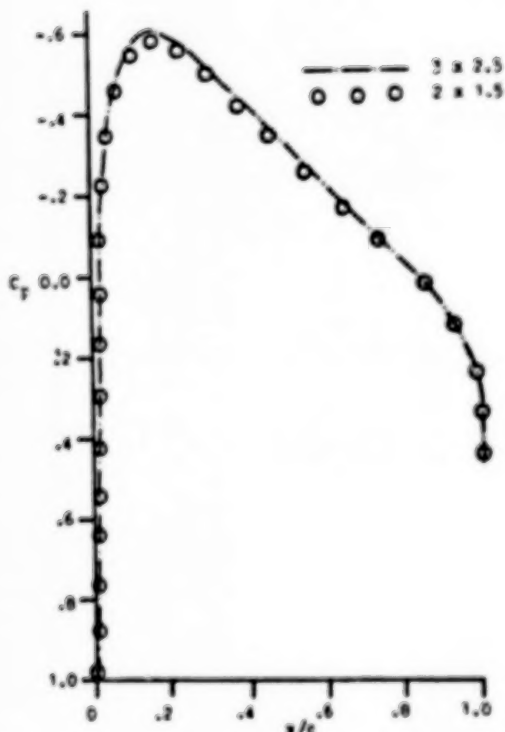


Fig. 17 Effect of the Computational Domain Size, Surface Vortex Panels, NACA 0012, $M_\infty = 0.72$, $\alpha = 0^\circ$.

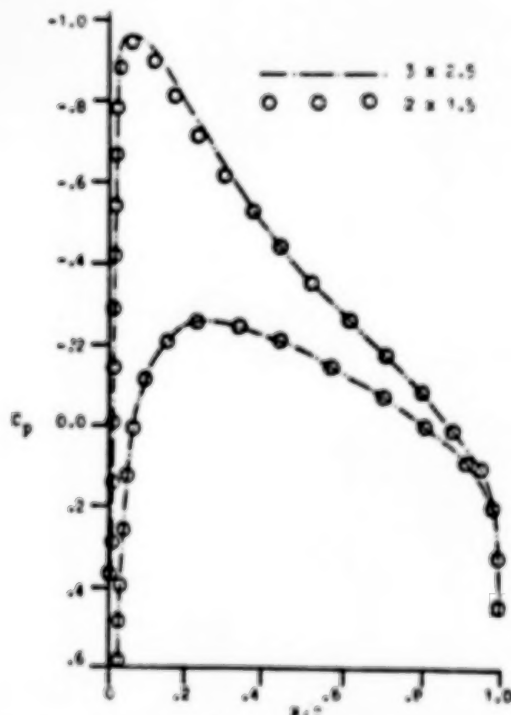


Fig. 18 Effect of the Computational Domain Size, Surface Vortex Panels, NACA 0012, $M_\infty = 0.63$, $\alpha = 2^\circ$.

SHOCK-FREE FLOW

The second numerical test is aimed at comparing the results of the IE solution using vortex panels only and source panels only with the solution of Euler equations⁵. Figure 19 shows the results of this test for the NACA 0012 airfoil at $M_\infty = 0.7$ and $\alpha = 0^\circ$. The computational domain is 2×1.5 , and the same numbers of surface panels and field elements as those of Figure 17 have been used. It is clear that the IE solution with surface vortex panels is superior to that of the source panels.

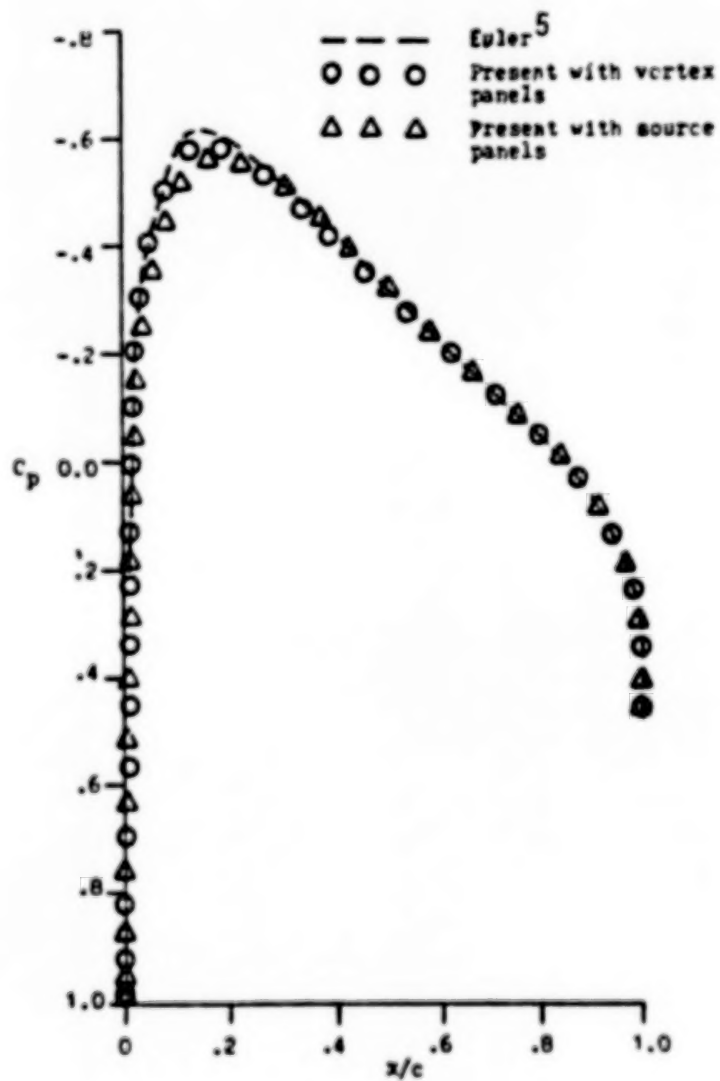


Fig. 19 Comparisons of IE Solution with Surface Vortex Panels and Surface Source Panels with Euler Solution, NACA 0012, $M_\infty = 0.72$, $\alpha = 0^\circ$.

TRANSONIC FLOW

First, we present a numerical test case to show the effect of introducing the shock panels and their fitting as explained earlier. Figure 20 shows a comparison between the shock capturing results and the SCSF-scheme results for the NACA 0012 airfoil at $M_\infty = 0.8$ and $\alpha = 0^\circ$. It is clear that the SCSF-scheme sharpens the shock, as expected, with this relatively coarse grid. Next, we compare the SCSF-scheme with the experimental data and other computational results. Figure 21 shows the results of the SCSF-scheme for NACA 0012, $M_\infty = 0.8$ and $\alpha = 0^\circ$, along with comparisons with the computational results of Garabedian, Korn and Jameson⁶ and the experimental data taken from reference 7. The SCSF-scheme took 12 iteration cycles of shock capturing (SC) and 13 cycles of shock fitting (SF) to achieve convergence.

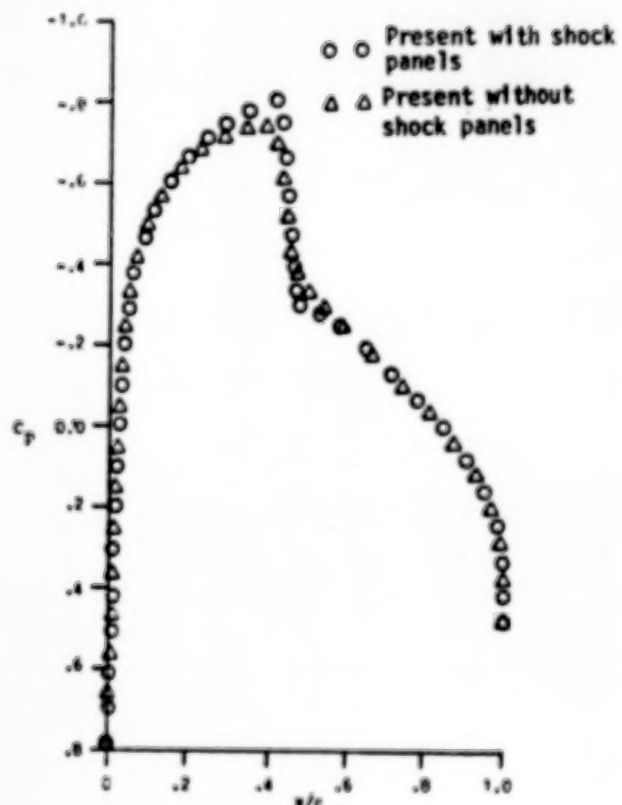


Fig. 20 Shock Capturing vs. SCSF-Scheme, NACA 0012, $M_\infty = 0.8$, $\alpha = 0^\circ$.

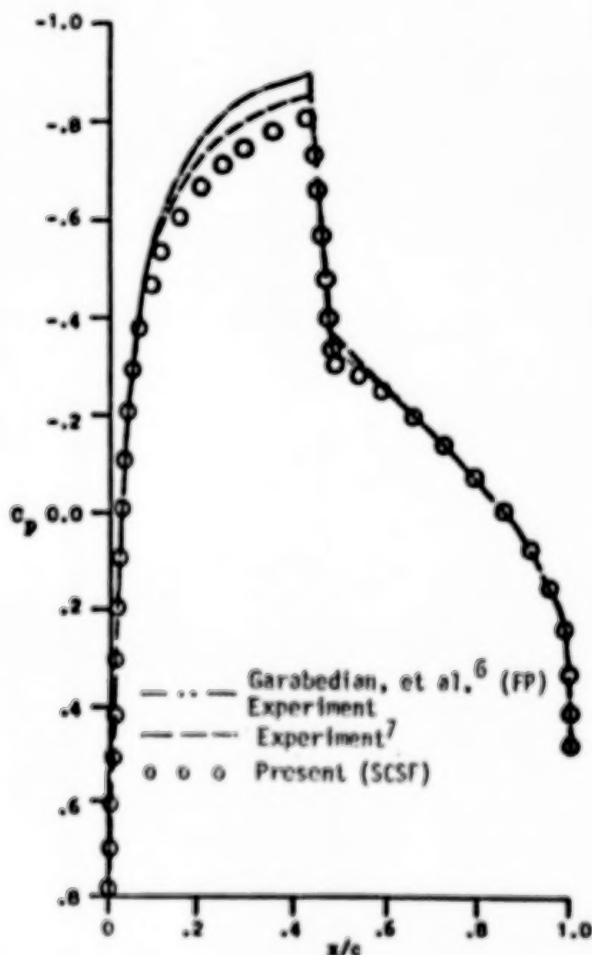


Fig. 21 Integral Equation Solution with SCSF-Scheme, NACA 0012, $M_\infty = 0.8$, $\alpha = 0^\circ$.

TRANSONIC FLOW

Figure 22 shows the results of the IFFE-scheme for the same case along with a comparison with the computational results of Jameson⁸, who also used the finite-volume Euler scheme with four-stage Runge-Kutta time stepping. In the present IEEE-scheme, the embedded Euler domain has a size of 0.5×0.6 around the shock region with a grid of 25×30 . This case took 10 iteration cycles of SC, 250 times cycles of Euler iterations to achieve a residual error of 10^{-3} and 5 IE cycles to update the Euler domain boundary conditions.

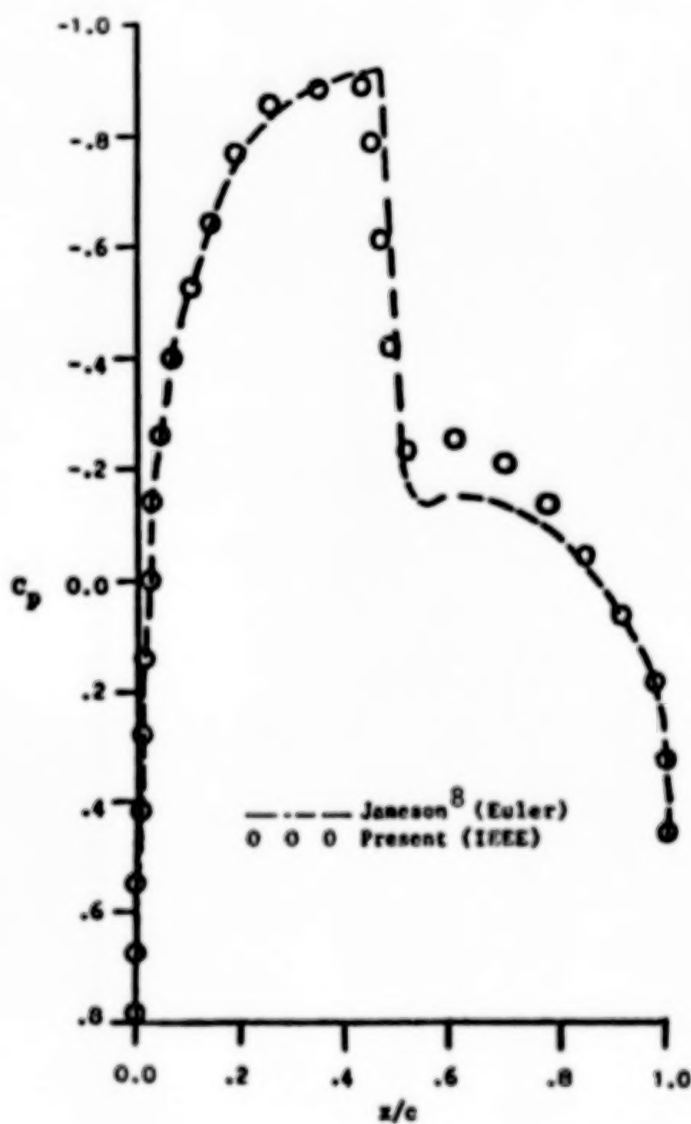


Fig.22 Integral Equation with Embedded-Euler Domain Solution, NACA 0012, $M_\infty = 0.8$, $\alpha = 0^\circ$.

TRANSONIC FLOW

Figures 23 and 24 show the results of the SCSF-and IEEE-schemes for NACA 64A010A, $M_\infty = 0.796$, $\alpha = 0^\circ$ along with comparisons with the computational results of Edwards, Bland and Seidel⁹ who used the TSP-equation, and the experimental data taken from reference 9. With the SCSF-scheme, the numbers of SC and SF iteration cycles to achieve convergence are the same as those of the case presented in Figure 21. With the IEEE-scheme, the embedded Euler domain has a size of 0.7×0.6 with a grid size of 35×30 . This case, Fig. 24, took 10 iteration cycles of SC, 130 time cycles of Euler iterations to achieve a residual error of 10^{-3} and 3 IE cycles to update the Euler domain boundary conditions.

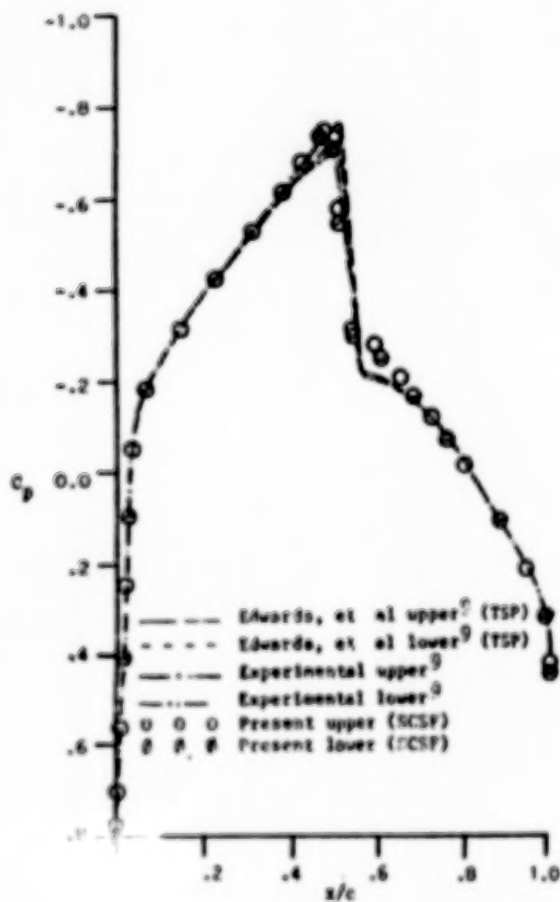


Fig. 23 Integral Equation Solution with SCSF-Scheme, NACA 64A010A, $M_\infty = 0.796$, $\alpha = 0^\circ$.

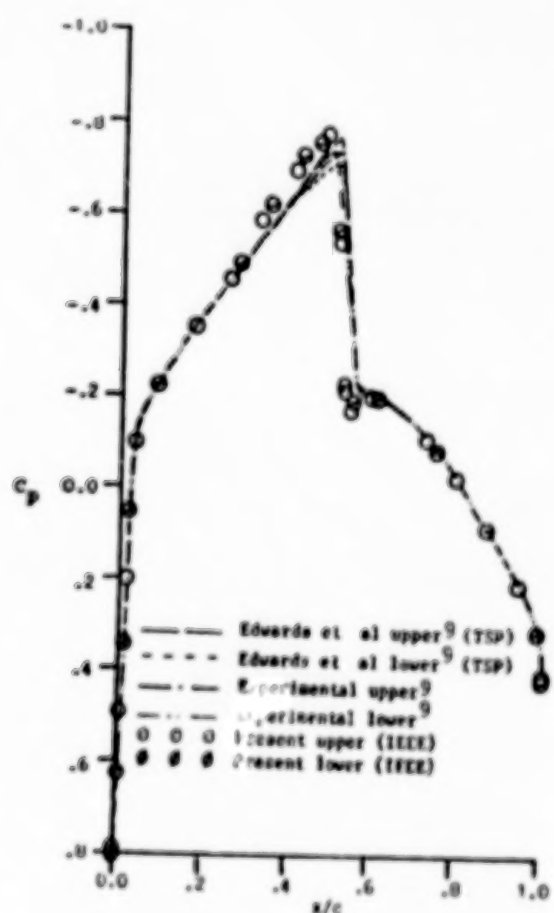


Fig. 24 Integral Equation with Embedded-Euler Domain Solution, NACA 64A010A, $M_\infty = 0.796$, $\alpha = 0^\circ$.

TRANSOMIC FLOW

Figures 25 and 26 show the results of the SCSF- and IEEE-schemes for the lifting case of NACA 0012, $M_\infty = 0.75$ and $\alpha = 2^\circ$ along with the computational results of Steger and Lomax¹⁰, and the experimental data taken from the same reference. The size of the grids and the number of iteration cycles used to achieve convergence are the same as those of the cases given in Figures 21 and 22.

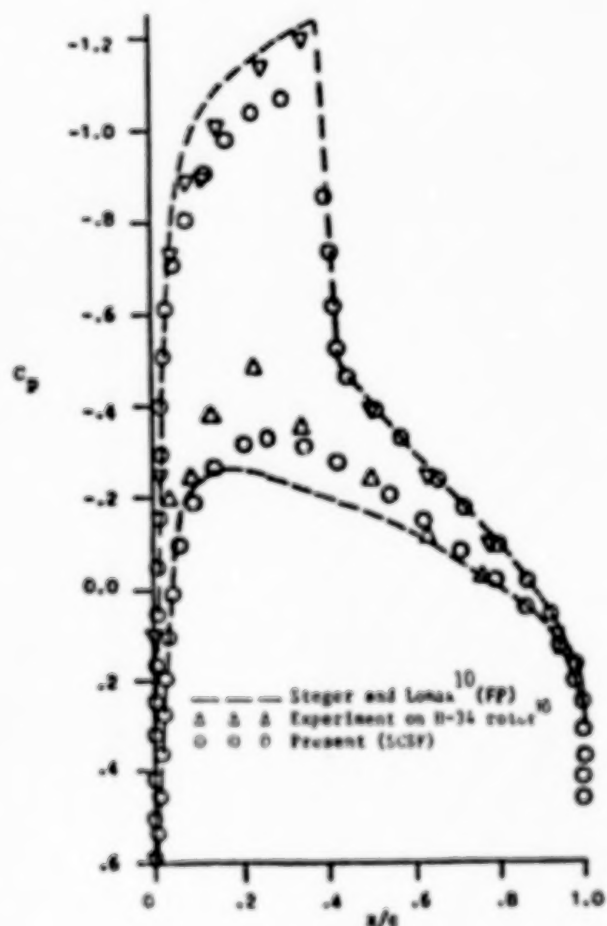


Fig. 25 Integral Equation Solution with SCSF-Scheme, NACA 0012, $M_\infty = 0.75$, $\alpha = 2^\circ$.

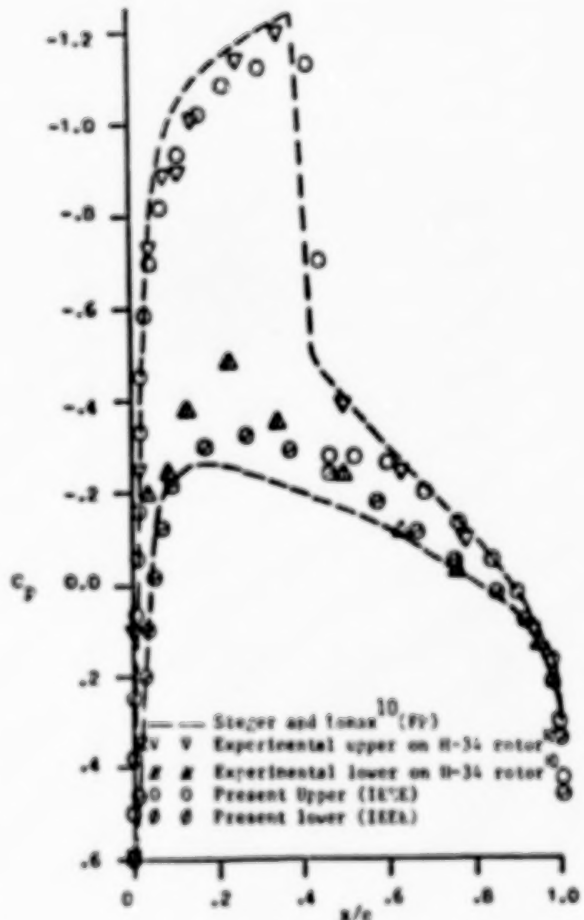


Fig. 26 Integral Equation with Embedded-Euler Domain Solution, NACA 0012, $M_\infty = 0.75$, $\alpha = 2^\circ$.

TRANSONIC FLOW WITH STRONG SHOCKS

For stronger shocks than those considered above the IE computational domain is extended in the longitudinal and lateral directions and so is the embedded Euler computational domain. The Euler domain is extended beyond the trailing edge to allow for the vorticity to be shed downstream where the overlapping region with the IE equation exists. Figure 27 shows a typical computational domain with details of the embedded Euler domain.

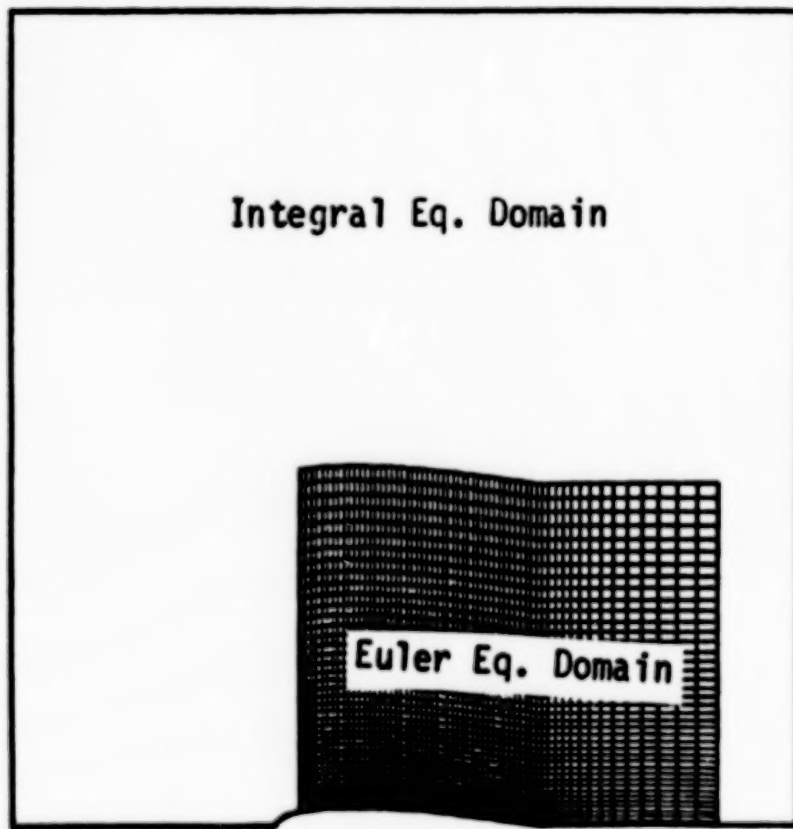


Fig. 27 Embedded Euler Domain and Grid for Strong Shocks.

TRANSONIC FLOW WITH STRONG SHOCKS

Figure 28 shows the results of the IEEE for NACA 0012, $M_{\infty} = 0.812$ and $\alpha = 0^0$ along with the experimental data of reference 7. In Figure 29, the results of the IEEE for NACA 0012, $M_{\infty} = 0.82$ and $\alpha = 0^0$ are shown along with the three-dimensional solution at the wing root chord of Tseng and Morino¹², who use the IE for the TSP, and the results of reference 11. The size of the embedded Euler domain for these cases is 0.8x0.8 and its grid size is 40x40.

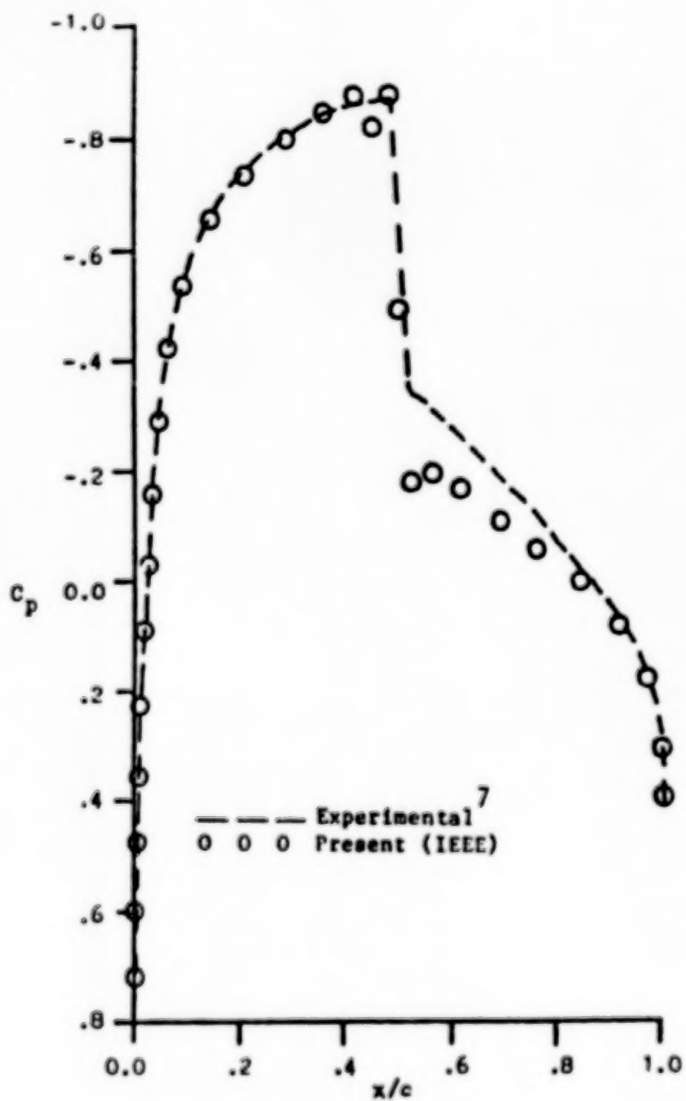


Fig. 28 Integral Equation with Embedded-Euler Domain Solution, NACA 0012, $M_{\infty} = 0.812$, $\alpha = 0^0$.

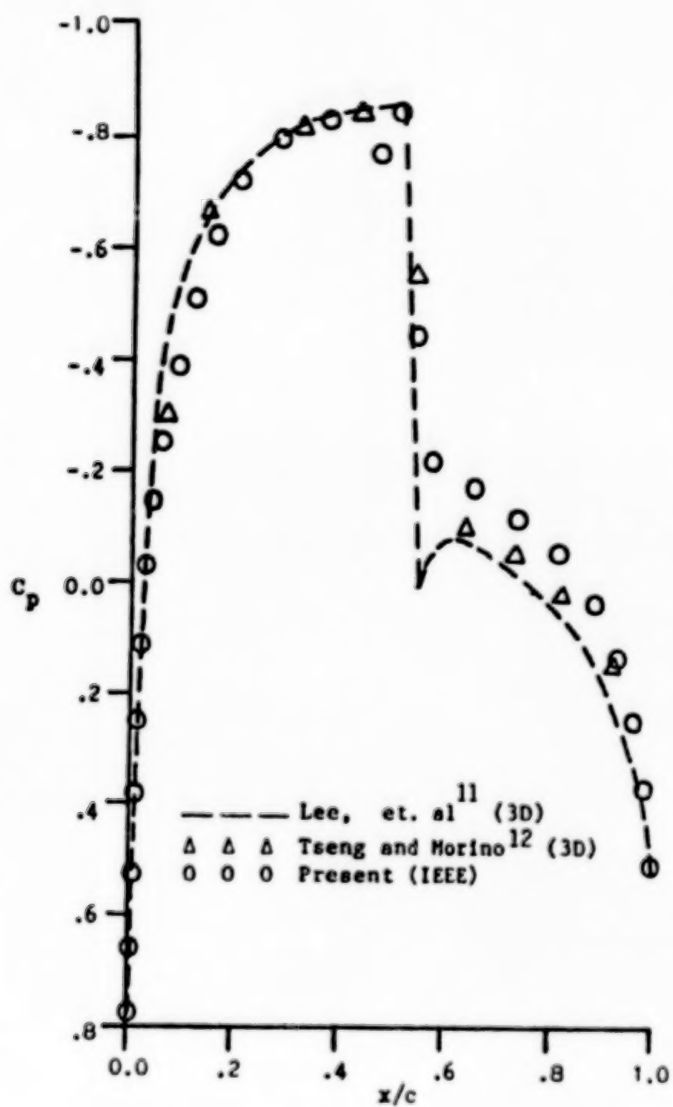


Fig. 29 Integral Equation with Embedded-Euler Domain Solution, NACA 0012, $M_{\infty} = 0.82$, $\alpha = 0^{\circ}$.

TRANSONIC FLOW WITH STRONG SHOCKS

Figure 30 shows the results of the IEE for NACA 0012, $M_\infty = 0.84$ and $\alpha = 0^\circ$ along with comparisons with the nonisentropic FP-solution of Whitlow, et al.¹³ and the Euler equations solution of Jameson⁸. The size of the embedded Euler domain for this case is 1.5x1.0 and its grid size is 60x40. This case took 10 IE iteration, 300 time cycles of Euler iterations and 3 IE cycles to update the Euler domain boundary conditions.

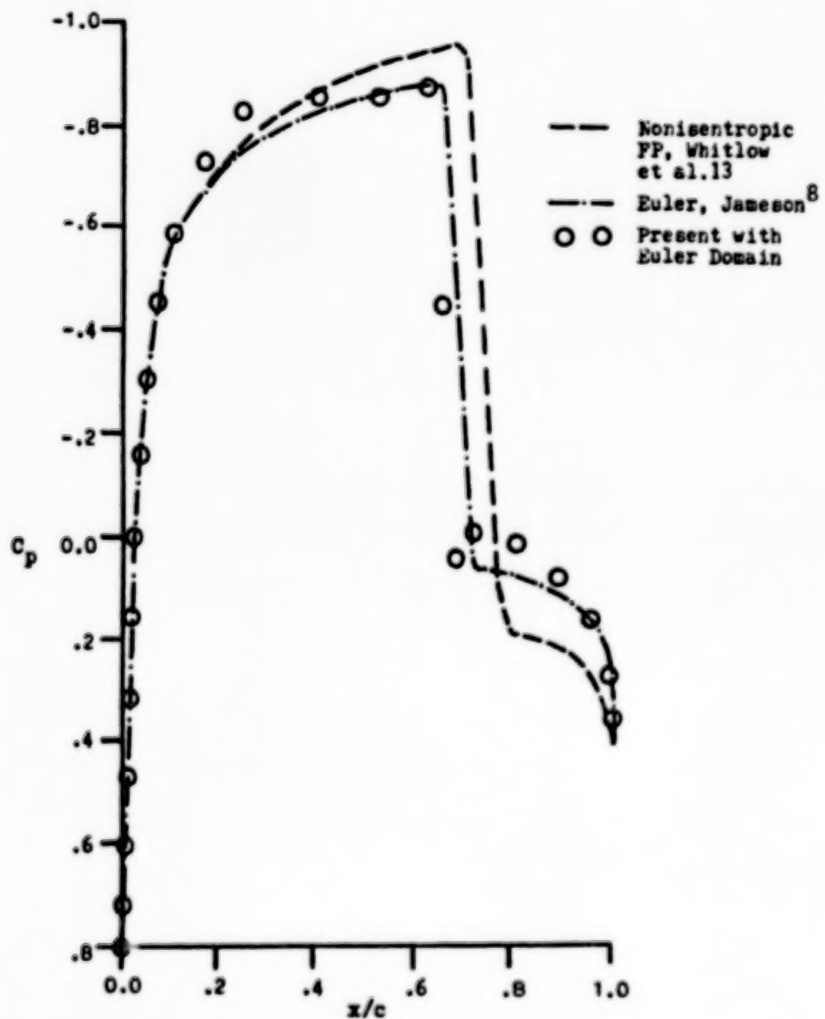


Fig. 30 Integral Equation with Embedded-Euler Domain Solution, NACA 0012, $M_\infty = 0.84$, $\alpha = 0^\circ$.

4. Concluding Remarks

- Two Methods have been Presented for Inviscid Transonic Flows:
 - Unsteady Euler Equations in a Rotating Frame of Reference for Transonic-Vortex Flows.
 - Integral Solution of Full-Potential Equation with and without Embedded Euler Domains for Transonic Airfoil Flows.
- The Computational Results Covered:
 - Steady and Unsteady Conical Vortex Flows
 - Three-Dimensional Steady Transonic Vortex Flow
 - Transonic Airfoil Flows
- The Results are in good agreement with Other Computational Results and Experimental Data.
- The Rotating Frame of Reference Solution is Potentially Efficient as Compared with the Space-Fixed Reference Formulation with Dynamic Gridding.
- The Integral Equation Solution with Embedded Euler Domain is Computationally Efficient and as Accurate as the Euler Equations.
- Currently the Rotating Frame of Reference Euler Solver is Applied to Three-Dimensional Unsteady Transonic-Vortex Flows. The IEEE-Scheme is Being Extended to the Unsteady Transonic Airfoil Calculations.

ACKNOWLEDGMENT

This research work has been supported by NASA-Langley Research Center under Grant No. NAG-1-648.

REFERENCES

1. Miller, D. S. and Wood, R. W.: Lee-Side Flow Over Delta Wings at Supersonic Speed. NASA TP-2430, 1985.
2. Kandil, O. A. and Chuang, A. H.: Influence of Numerical Dissipation in Computing Supersonic Vortex-Dominated Flows. AIAA Paper 86-1073, May 1986. Also to appear in the AIAA Journal, Vol. 25, No. 9, September 1987.
3. Rizzi, A., Eriksson, L. E., Schmidt, W. and Hitzel, S. M.: Simulating Vortex Flows Around Wings. AGARD CP No. 342, April 1983, pp. 21.1-21.14.
4. Hummel, D.: On the Vortex Formulation Over a Slender Wing at Large Angles of Incidence. AGARD CP-247, January 1979, pp. 15.1-15.17.
5. Sells, C. L.: Plane Subcritical Flow Past a Lifting Airfoil. Proceedings of the Royal Society, London, No. 308 (Series A), 1968, pp. 377-401.
6. Garabedian, P., Korn, D. G. and Jameson, A.: Supercritical Wing Sections. Lecture Notes in Economic and Mathematical Systems, Vol. 66, 1972.
7. Hall, M. G.: Transonic Flows. IMA, Controller, HMSO, London, 1975.
8. Jameson, A.: Transient Airfoil Calculations Using the Euler Equations. Numerical Methods in Aeronautical Fluid Dynamics (Ed. P. L. Roe), Academic Press, London and New York, 1982, pp. 289-309.
9. Edwards, J. W., Bland, S. R. and Seidel, D. A.: Experience with Transonic Unsteady Aerodynamic Calculations. NASA TM 86278, Langley Research Center, Hampton, VA, 1984.
10. Steger, J. L. and Lomax, H.: Transonic Flow about Two-Dimensional Airfoils by Relaxation Procedures. AIAA Journal, Vol. 10, 1972, pp. 49-54.
11. Lee, K. D., Dickson, L. J., Chen, A. W. and Rubbert, P. E.: An Improved Matching Method for Transonic Computations," AIAA Paper 78-1116, 1978.
12. Tseng, K. and Mornio, L.: Nonlinear Green's Function Methods for Unsteady Transonic Flows. Transonic Aerodynamics (edited by D. Nixon), AIAA, New York, 1982, pp. 565-603.
13. Whitlow, W., Jr., Hafez, M. M. and Osher, S. J.: An Entropy Correction Method for Unsteady Full Potential Flows with Strong Shocks. NASA TM 87769, Langley Research Center, Hampton, VA, 1986.

**VISCOUS FLOW CALCULATIONS FOR THE
AGARD STANDARD CONFIGURATION AIRFOILS
WITH EXPERIMENTAL COMPARISONS**

**JAMES T. HOWLETT
UNSTEADY AERODYNAMICS BRANCH
NASA Langley Research Center**

This paper reports on recent experience in calculating unsteady transonic flows by means of viscous-inviscid interactions with the XTRAN2L computer code (ref. 1). The boundary-layer method for attached flows is based upon the work of Rizzetta (ref. 2) as implemented in reference 3. The non-isentropic corrections of Fuglsang and Williams (ref. 4) have also been incorporated along with the viscous interaction for some cases and initial results are presented. For unsteady separated flows, the inverse boundary-layer equations developed by Vatsa and Carter in reference 5 are used in a quasi-steady manner and preliminary results are presented. Currently, efforts are underway to include the viscous interactions in 3-D calculations in a stripwise fashion although no results for the 3-D work are presented herein.

UNSTEADY TRANSONIC VISCOUS-INVISCID INTERACTIONS

○ ATTACHED FLOW (ARC, RIZZETTA)

- THEORY WELL-DEVELOPED
- EXTENSIVE APPLICATIONS

○ NONISENTROPIC CORRECTIONS WITH VISCOUS EFFECTS

- INITIAL THEORY
- LIMITED APPLICATIONS

○ SEPARATED FLOW

- PRELIMINARY THEORY
- LIMITED APPLICATIONS

○ 3-D FLOW

- XTRAN3
- CAP-TSD

The inviscid code used in this study is the XTRAN2L computer code described in reference 1. The viscous boundary layer analysis is based upon Green's lag-entrainment equations as described in reference 2. For attached flow, the equations are used in the direct form: pressure from the inviscid analysis is specified and the equations are integrated to obtain the boundary-layer displacement thickness δ^* . For separated flows, the equations are inverted as described in reference 5 and the mass flow \bar{m} is specified as input. In the inverse method, the boundary-layer displacement thickness δ^* is updated using Carter's method (ref. 6). For both the direct and the inverse method, the effect of the viscous boundary layer is included in the inviscid analysis by means of the airfoil surface tangency boundary condition.

BOUNDARY LAYER ANALYSIS

DIRECT

$$\begin{Bmatrix} \theta \\ \bar{H} \end{Bmatrix}_x = \{A_1\} + \{A_2\} \phi_{xx}$$

INVERSE

$$\begin{Bmatrix} \phi_x \\ \bar{H} \end{Bmatrix}_x = \{A_3\} + \{A_4\} \bar{m}_x$$

$$\bar{m} = \rho u \delta^*$$

$$(C_E)_x = A_5 + A_6 \phi_{xx}$$

$$\delta^{*n+1} = H^n \theta^n$$

$$\delta^{*n+1} = \delta^{*n} + \omega \delta^{*n} \left(\frac{u_v}{u_l} - 1 \right) \text{ (CARTER)}$$

AIRFOIL BOUNDARY CONDITION

$$\phi_y = F_x + F_t + \delta_x^*$$

Non-isentropic modifications to the transonic small disturbance (TSD) equation were developed by Fuglsang and Williams in reference 4. These modifications include a streamwise flux that satisfies the Prandtl relations at shock jumps, convection of shock generated entropy in the wake, and an entropy correction in the pressure coefficient. The non-isentropic modifications have been incorporated into the computer code along with the viscous-inviscid interactions and some initial calculations are presented.

NONISENTROPIC MODIFICATIONS TO TSD EQUATION (FUGLSANG AND WILLIAMS)

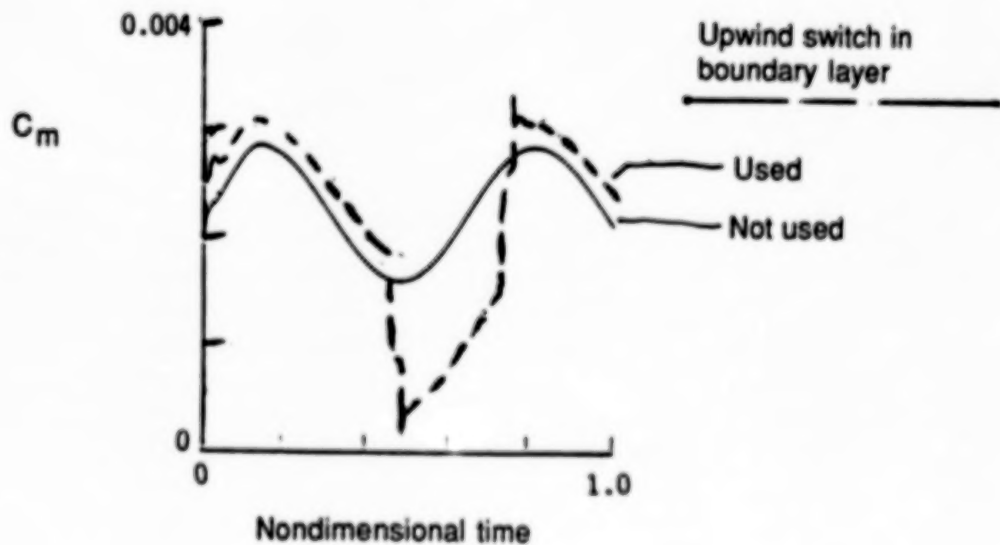
- MODIFIED STREAMWISE FLUX SATISFYING PRANDTL RELATION AT SHOCK JUMPS
- CONVECTION OF SHOCK GENERATED ENTROPY IN WAKE
- ENTROPY CORRECTION IN PRESSURE COEFFICIENT

This figure illustrates one of the numerical difficulties encountered with the interacting boundary-layer calculation. The original version of the computer code included an upwind switch in the evaluation of the pressure gradient term ϕ_{xx} for input to the boundary-layer equations. This upwind switch introduced a discontinuity in the unsteady forces when the shock moved across a grid point. The dashed line in the figure shows this discontinuity in the moment coefficient for a typical case. The purpose of upwind switching in computational fluid dynamics is to account properly for the domain of dependence in the numerical solution of partial differential equations. However, the present application merely requires numerically computing the derivative of a known function. Hence, upwind switching is not required. The solid line in the figure shows that the moment coefficient varies smoothly in time when upwind switching is not used. For all results presented in this paper, upwind switching is not used in the boundary-layer calculation. However, the inviscid solution algorithm does use upwind switching in the standard manner.

EFFECT OF UPWIND SWITCH IN BOUNDARY LAYER CALCULATION

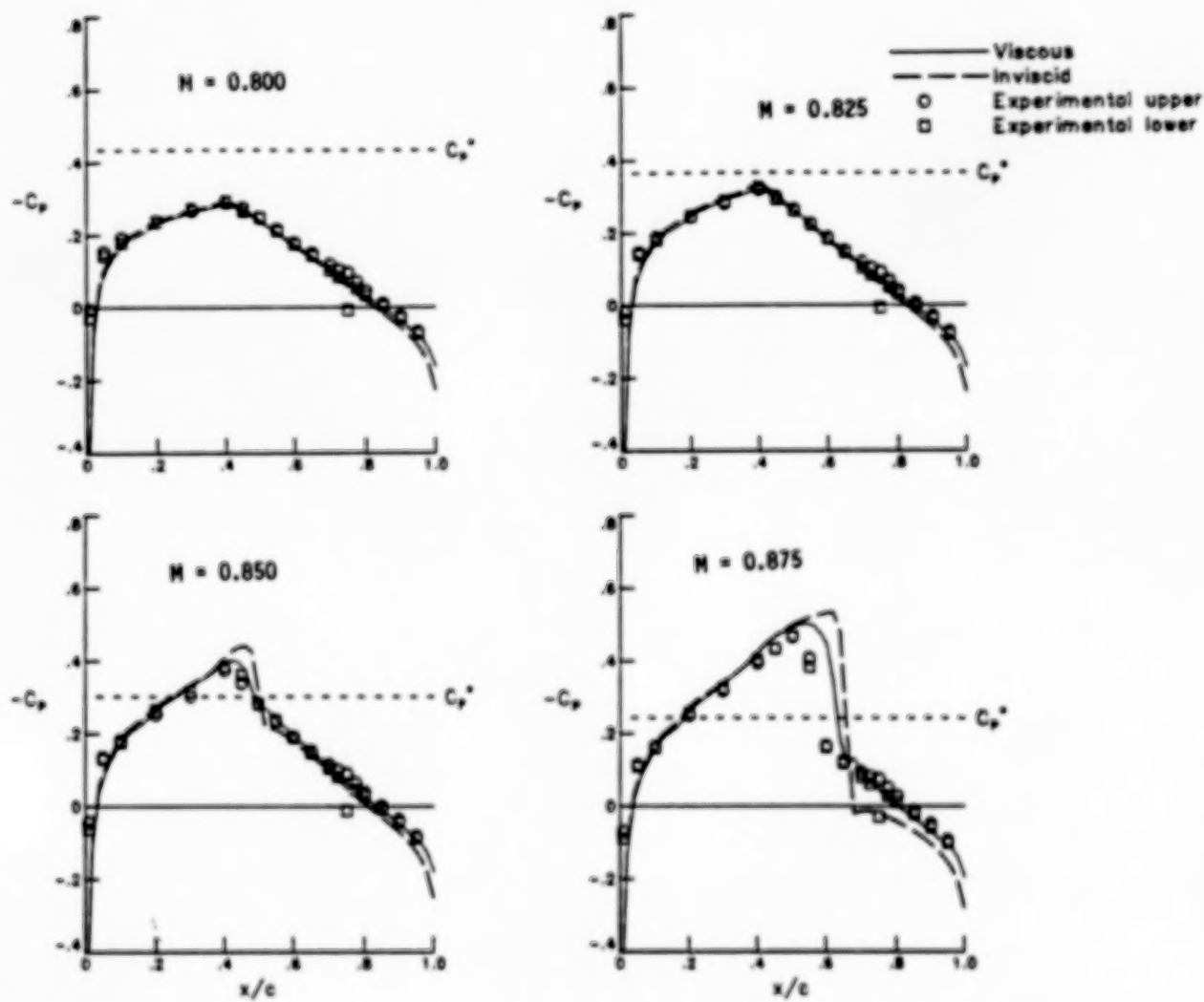
NACA 64A010A

$M = 0.796$



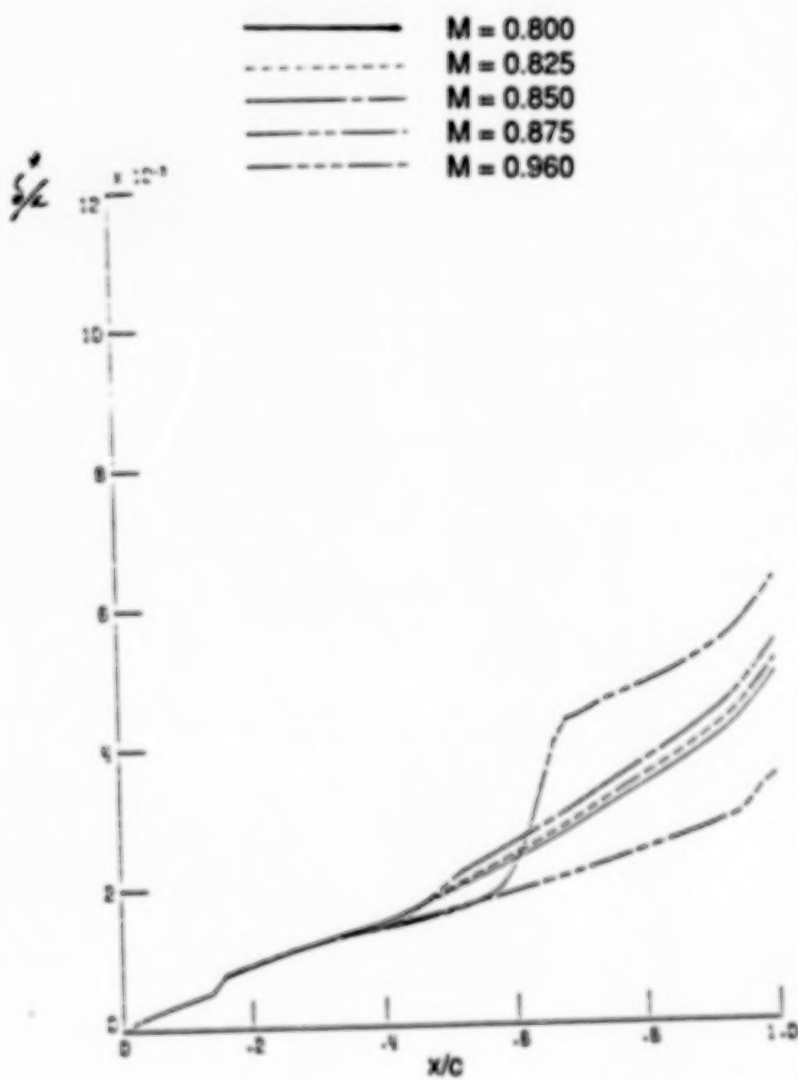
This figure shows steady pressure distributions for the NACA 64A006 airfoil for a range of Mach numbers. For the subsonic cases, the viscous and inviscid results are nearly identical except for small differences near the trailing edge where the viscous results more closely match the experiment. At $M = 0.850$, a shock wave develops near midchord and the viscous calculation agrees much better with the experiment than the inviscid result. For $M = 0.875$, the shock strengthens and moves aft. In this case, both the viscous and inviscid calculations exhibit differences from the experiment although the viscous result is closer to the experiment in the vicinity of the shock. Downstream of the shock the viscous result is in good agreement with the experiment.

STEADY PRESSURE DISTRIBUTION FOR NACA 64A006 AIRFOIL



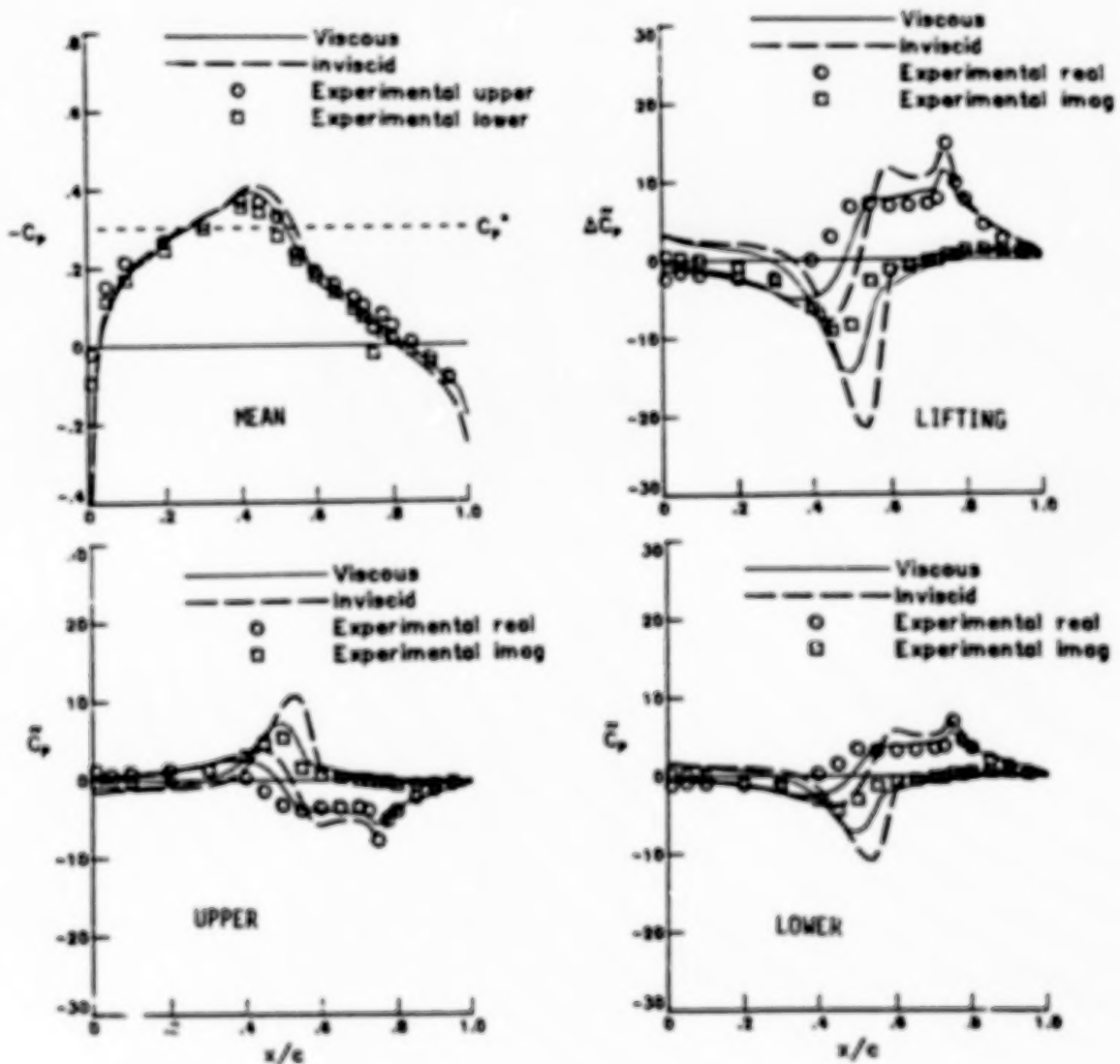
This figure shows plots of the boundary-layer displacement thickness for several mach numbers for steady calculations for the NACA 64A006 airfoil. For the two lowest values of Mach number, the results are subcritical and the displacement thickness increases smoothly in the downstream direction as Mach number is increased. At $M = 0.850$, the displacement thickness shows a slight increase due to the shock wave near midchord. For $M = 0.875$, the calculated result has a strong shock near 60% chord and the displacement thickness increases significantly across this shock. A further increase in Mach number to 0.960 moves the shock off the trailing edge and the displacement thickness increases slowly as the trailing edge is approached.

EFFECT OF MACH NUMBER ON DISPLACEMENT THICKNESS FOR NACA 64A006 AIRFOIL



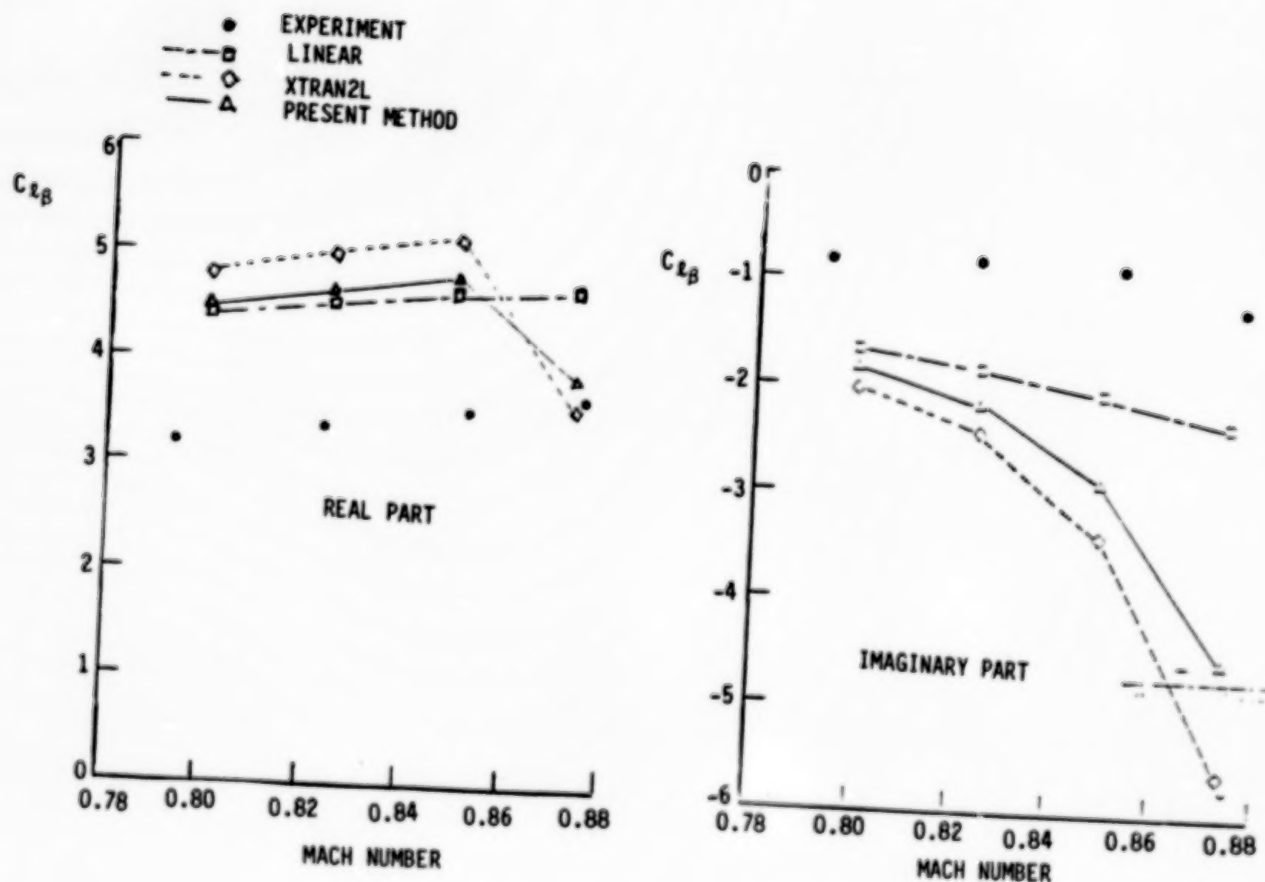
Unsteady pressure distributions are plotted for the NACA 64A006 airfoil with an oscillating flap for $M = 0.850$ and $k = 0.242$. The calculated mean pressures are similar to the steady pressure distributions for this Mach number. The effect of the viscous boundary layer can be seen in the results for the upper surface pressure distribution in the lower left hand side of the figure. The viscous unsteady pressure distributions agree very well with the experimental results, especially in the vicinity of the shock where the inviscid calculation shows the largest discrepancy. The interacting viscous boundary layer gives a substantial improvement over inviscid calculations in predicting the unsteady pressure distributions for this airfoil.

UNSTEADY PRESSURE DISTRIBUTION FOR NACA 64A006 AIRFOIL
 $M = 0.850 \quad K = 0.242$



This figure shows plots of the unsteady lift as a function of mach number for the NACA 64A006 airfoil for a reduced frequency of 0.060. The results indicate that the viscous boundary layer corrects up to 25% of the differences between the inviscid results and the experiments for the lower values of Mach number. The linear theory results, also shown on the figure, are competitive with the CFD calculations for predicting the unsteady lift for most of the cases investigated for this airfoil.

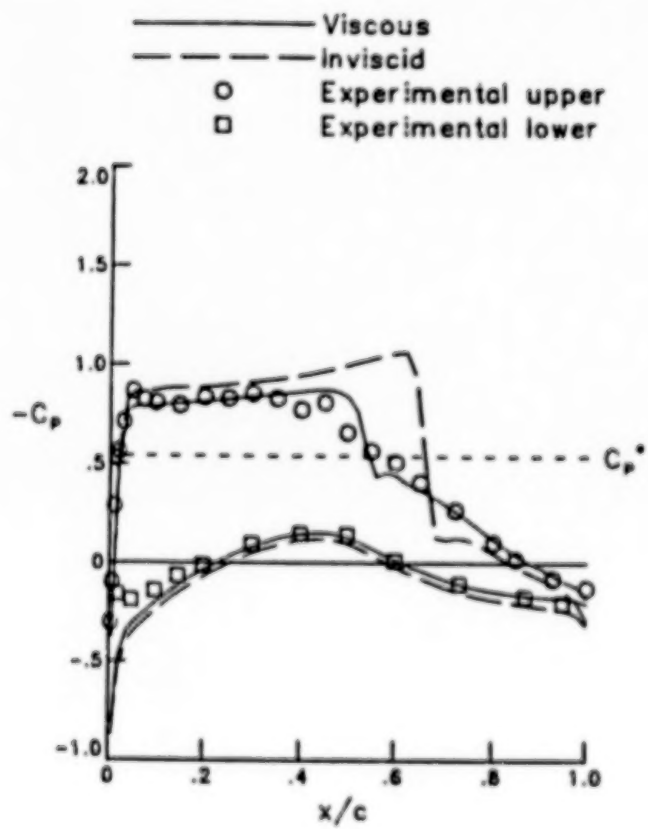
**COMPARISON OF UNSTEADY LIFT FOR
NACA 64A006 AIRFOIL
 $K = 0.060$**



The steady pressure distributions for the MBB-A3 supercritical airfoil at the supercritical design point ($M = 0.765$, $\alpha_0 = 1.5^\circ$) are plotted in this figure. The calculated cases are for the actual experimental values of Mach number and angle of attack rather than values adjusted to match flow conditions in the wind tunnel as is frequently done in comparison with this particular data. The experiment shows supercritical flow without a discernable shock wave typical of flow at the design point. The region of supercritical flow terminates at about $x/c = 0.53$. The viscous calculation indicates a moderate strength shock wave at nearly the same location. Away from the shock, agreement between the viscous calculation and the experiment is very good, although some discrepancies are noted near the leading edge on the lower surface. For this case, the inclusion of viscous effects yields a significant improvement in the calculation of the steady pressure distribution.

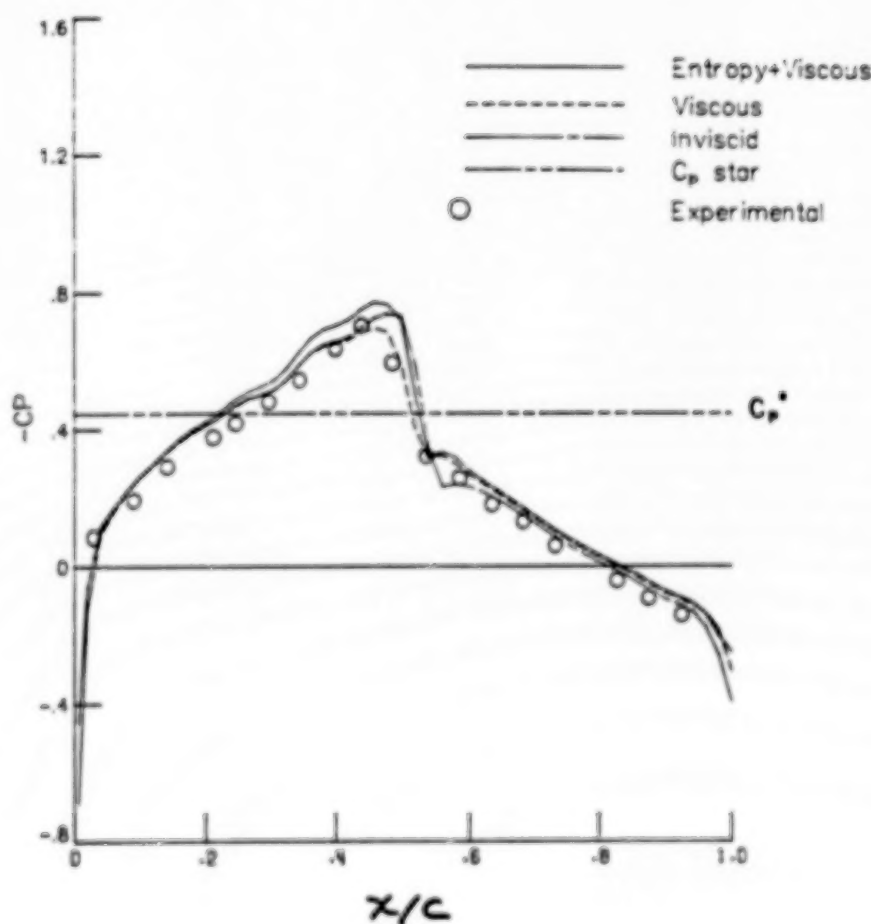
STEADY PRESSURE DISTRIBUTION FOR MBB-A3 AIRFOIL

$M = 0.765$ $\alpha_0 = 1.5^\circ$



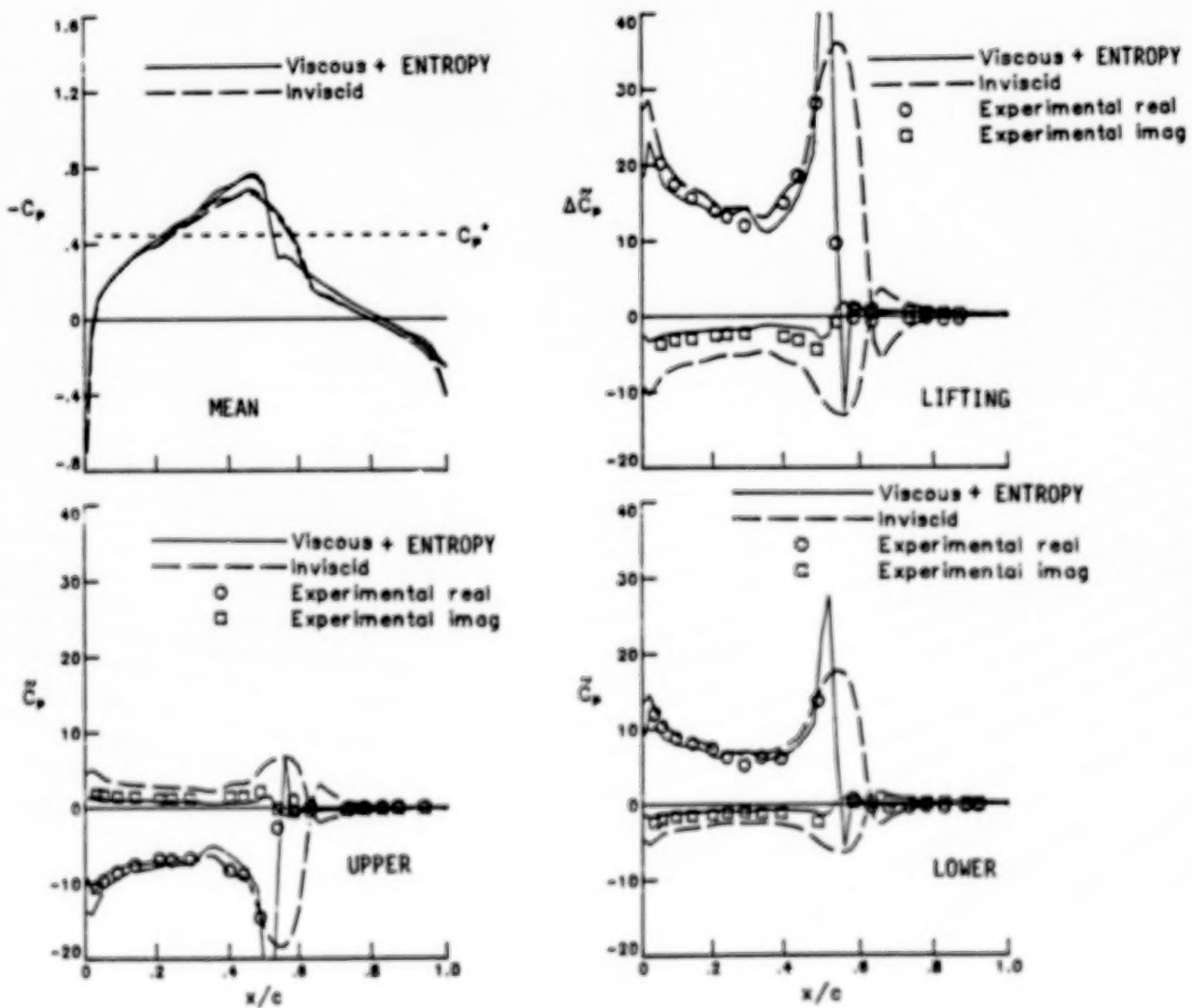
Steady pressure distributions for the NACA 64A010A (Ames) airfoil at $M = 0.796$ and $\alpha_0 = 0^\circ$ have been calculated with the inviscid code, the viscous interaction theory, and non-isentropic corrections to the viscous interaction results. As the figure shows, the viscous calculation agrees better with the experimental results in so far as shock location and strength is concerned. The non-isentropic corrections move the shock position downstream about 1% chord and increase the shock strength slightly. In general however, differences between the experiment and all three calculated results are small.

**STEADY PRESSURE DISTRIBUTION FOR NACA 64A010 AIRFOIL
WITH NON-ISENTROPIC CORRECTIONS**
 $M = 0.796$



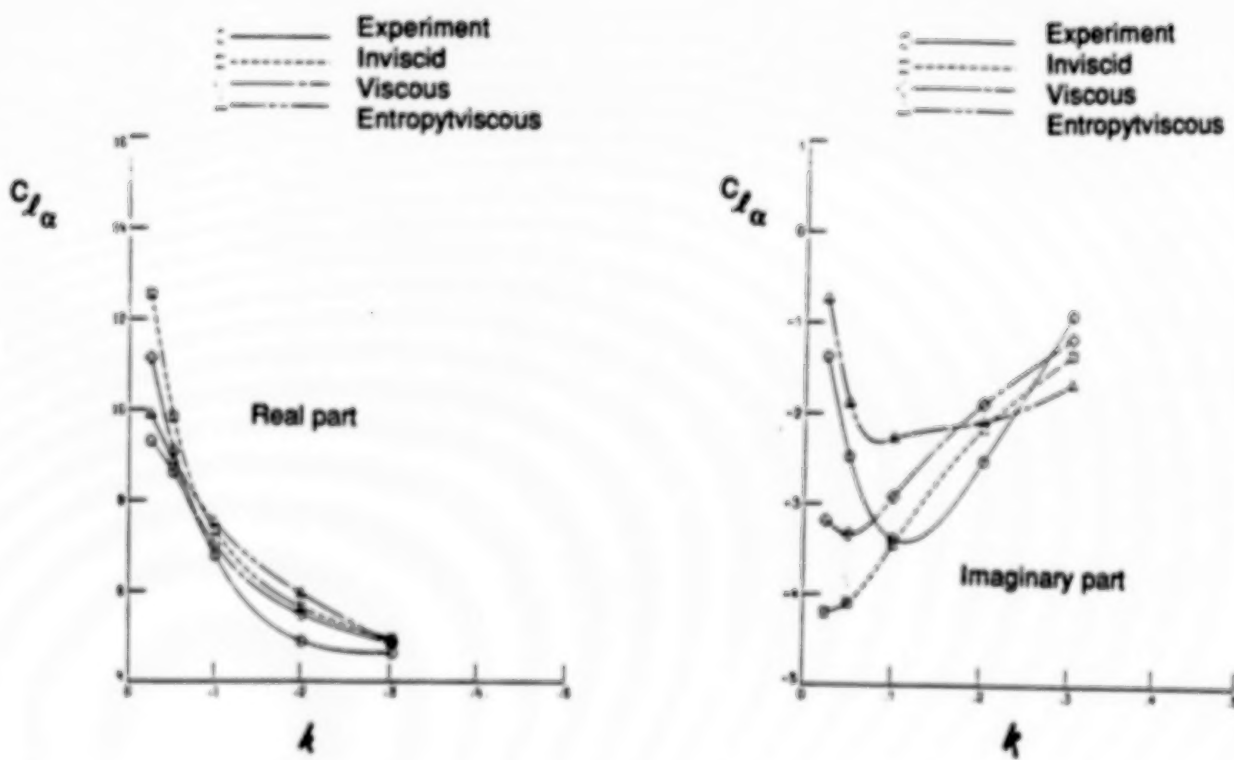
This figure shows plots of the unsteady pressure distributions for the NACA 64A010A (Ames) airfoil oscillating in pitch at $M = 0.796$ and $k = 0.025$. In contrast to the small effect the non-isentropic corrections have on the steady pressure distributions, these corrections to the viscous interaction theory give substantially better agreement with the unsteady experimental results. In the vicinity of the shock wave, the modified theory matches the experimental points very well, whereas the inviscid calculation is quite different. The significant improvement of calculated unsteady pressure distributions for this case due to the inclusion of non-isentropic and viscous effects is particularly interesting because the shock wave has only moderate strength.

**UNSTEADY PRESSURE DISTRIBUTION WITH NON-ISENTROPIC
CORRECTIONS FOR NACA 64A010 AIRFOIL**
 $M = 0.796 \quad K = 0.025$



This figure presents comparisons of unsteady lift for calculated and experimental results for the NACA 64A010A (Ames) airfoil oscillating in pitch. The non-isentropic and viscous corrections give substantial improvements in the calculated values for low values of reduced frequency. This is especially evident in the imaginary part of the unsteady lift. Neither the inviscid nor viscous calculations predict the upward trend of the experimental results for low values of reduced frequency. The non-isentropic and viscous calculations show this low frequency upward trend very well, although some discrepancies are evident in the mid-frequency range. This significant improvement in lift predictions for low frequency cases re-emphasizes the importance of non-isentropic corrections even when the flow field does not exhibit strong shock waves.

**COMPARISON OF UNSTEADY LIFT WITH NON-ISENTROPIC
CORRECTIONS FOR NACA 64A010 AIRFOIL**
M = 0.796

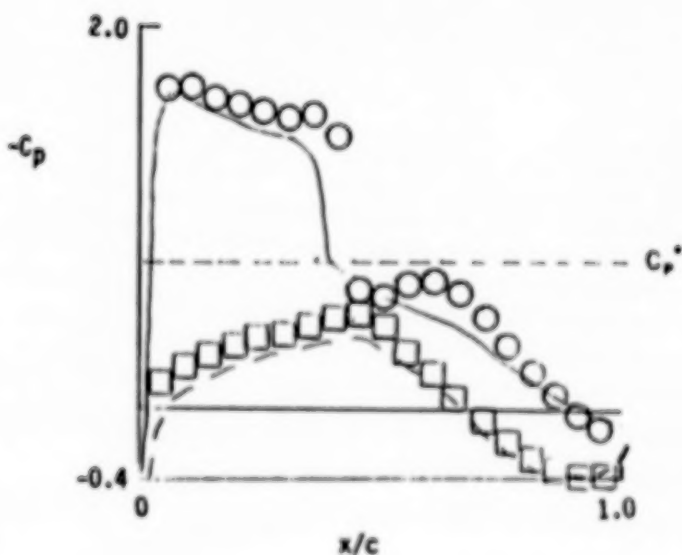


The inverse boundary-layer code has been used to calculate several test cases in which the flow is separated, or close to separation, in order to demonstrate the capabilities of the method. This figure shows plots of the steady pressure distributions for the NLR 7301 airfoil at $M = 0.70$ and $\alpha_0 = 3^\circ$. Note the mean angle of attack is the actual experimental angle of 3° and not the corrected value of 2° which is specified in the AGARD conditions for this case. As the figure shows, the inverse boundary-layer code predicts a pressure distribution which agrees reasonably well with the experiment for this very difficult case. The calculated shock wave is about 5% chord upstream of the experiment and slightly weaker. The calculation also indicates a small region of separation at the trailing edge whereas the experimental pressures show no evidence of trailing edge separation.

**STEADY PRESSURE DISTRIBUTION CALCULATED WITH INVERSE BL CODE
FOR NLR 7301 AIRFOIL**

$M = 0.70 \quad \alpha_0 = 3^\circ$

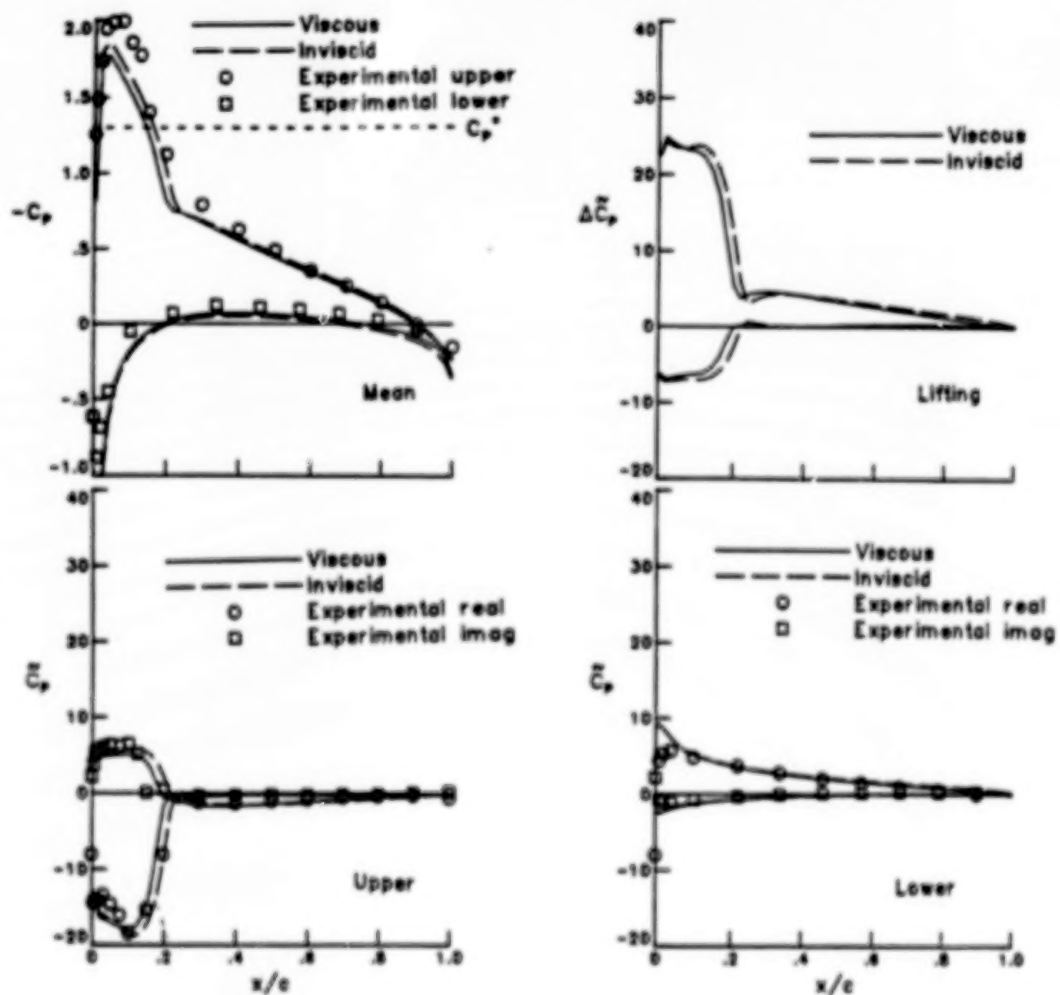
—	Viscous upper
-	Viscous lower
○	Experimental upper
□	Experimental lower



This figure shows unsteady pressure distributions for the NACA 0012 airfoil oscillating in pitch at $M = 0.599$. The mean angle of attack is 4.86° and the reduced frequency is $k = 0.081$. For the viscous calculation with the inverse boundary-layer method, transition is specified to be at 20% chord. The mean pressure distributions show the calculated results underestimating the suction peak near the leading edge with the inviscid calculation being slightly closer to the experiment in this region. Over the rest of the airfoil, both viscous and inviscid calculations agree well with the experiment. The unsteady pressure distributions on the airfoil upper surface are well predicted by both viscous and inviscid calculations with the viscous shock location slightly upstream of the inviscid result. The viscous calculation indicates that the flow is very close to separation near the maximum angle of attack of 7.3° . In fact, as shown in the next figure, a small change in the specified position of transition for the viscous calculation can result in flow separation during part of the oscillation cycle.

UNSTEADY PRESSURE DISTRIBUTION CALCULATED WITH INVERSE BL CODE FOR NACA 0012 AIRFOIL

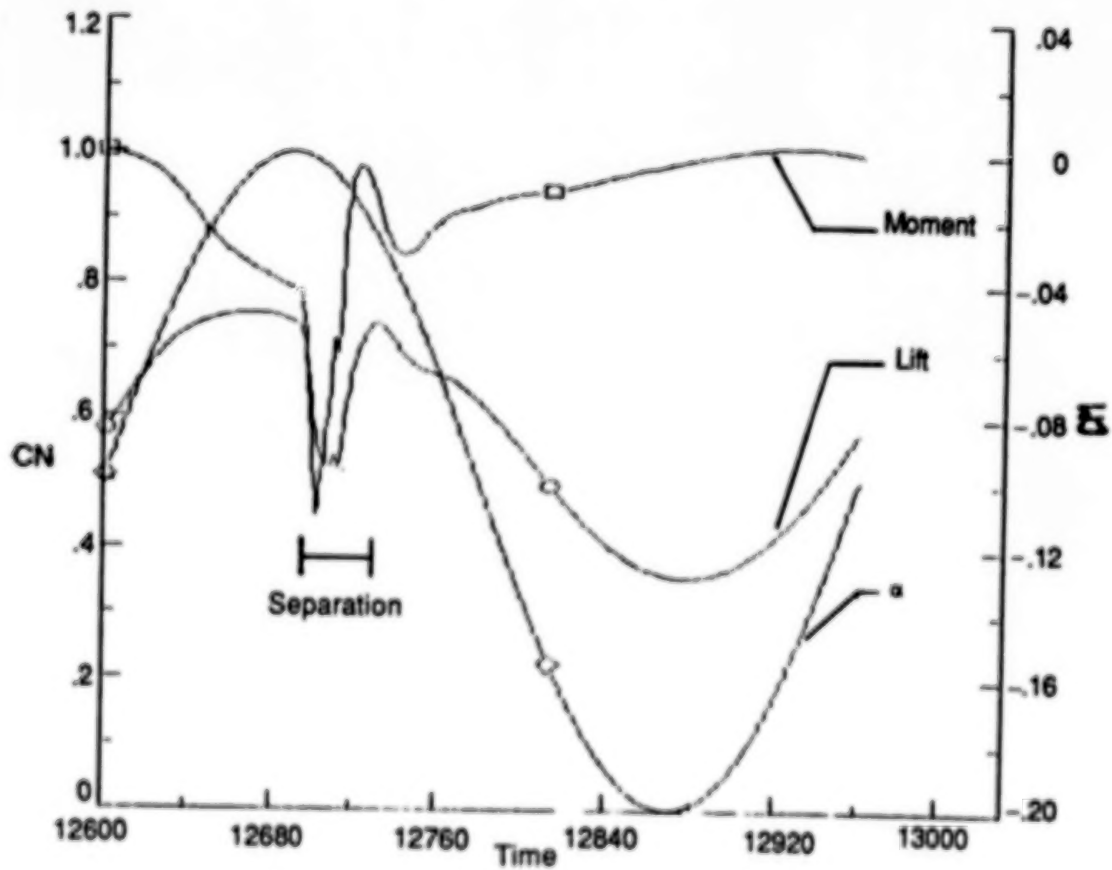
$$M = 0.599 \quad \alpha_0 = 4.86^\circ \quad \alpha_1 = 2.44^\circ \quad K = 0.081$$



This figure shows plots of the unsteady lift and moment coefficients for the NACA 0012 airfoil as calculated by the inverse boundary-layer method with transition specified at 10% chord. With transition at this location, which is upstream of the shock wave, the boundary-layer displacement thickness increases significantly across the shock wave. This increased displacement thickness causes the flow to separate just after maximum lift. The lift coefficient plotted in the figure clearly shows the sudden decrease in lift associated with flow separation and the corresponding increase in lift upon reattachment. After the flow reattaches, the lift coefficient continues to vary smoothly throughout the rest of the cycle. The inverse boundary-layer method successfully captures this flow separation and reattachment without difficulty.

**UNSTEADY LIFT CALCULATED WITH INVERSE BL CODE
FOR NACA 0012 AIRFOIL**

$$M = 0.599 \quad \alpha_0 = 4.86^\circ \quad \alpha_1 = 2.44^\circ \quad K = 0.81$$



This paper has presented comparisons of calculated and experimental results for unsteady transonic flows over airfoils. The calculations include results obtained from a viscous-inviscid interaction method based upon the 2-D XTRAN2L inviscid transonic computer code. Non-isentropic corrections have been included in some cases. The viscous boundary-layer equations have been solved in the direct mode for attached flow and an inverse mode for separated flow. The results have demonstrated that pressures and forces calculated by the viscous-inviscid interaction method compare well with experimental results for steady and unsteady attached flows. The non-isentropic corrections with the viscous interaction method provided improved comparisons with experiments for unsteady low frequency oscillations in cases involving moderate strength shock waves. Initial applications of the inverse boundary-layer method have demonstrated that this method can calculate unsteady flow fields involving flow separation and reattachment. The results indicate that the viscous-inviscid interaction method can provide accurate predictions of viscous effects in unsteady transonic flow fields.

CONCLUSIONS

- PRESSURES AND FORCES CALCULATED BY VISCOUS-INVISCID INTERACTION COMPARE WELL WITH EXPERIMENTS FOR STEADY AND UNSTEADY ATTACHED FLOW
- NON-ISENTROPIC CORRECTIONS WITH VISCOUS INTERACTION YIELD IMPROVED COMPARISONS WITH EXPERIMENTS FOR UNSTEADY LOW FREQUENCY OSCILLATIONS
- INVERSE BOUNDARY LAYER METHOD HAS POTENTIAL FOR CALCULATING UNSTEADY FLOW SEPARATION AND REATTACHMENT

REFERENCES

1. Whitlow, Woodrow, Jr.: XTRAN2L: A Program for Solving the General-Frequency Unsteady Transonic Small Disturbance Equation. NASA TM 85723, November 1983.
2. Rizzetta, Donald P.: Procedures for the Computation of Unsteady Transonic Flows Including Viscous Effects. NASA CR 166249, January 1982.
3. Howlett, James T.: Efficient Self-Consistent Viscous-Inviscid Solutions for Unsteady Transonic Flow. AIAA Paper No. 85-0482, 23rd Aerospace Sciences Meeting, Reno, Nevada, January 14-17, 1985.
4. Fuglsang, Dennis F; and Williams, Marc H.: Non-Isentropic Unsteady Transonic Small Disturbance Theory. AIAA Paper No. 85-0600, AIAA/ASME/ASCE/AHS 26th Structures, Structural Dynamics and Materials Conference, Orlando, Florida, April 1985.
5. Vatsa, V. N.; and Carter, J. E.: Development of an Integral Boundary-Layer Technique for Separated Turbulent Flow. United Technologies Research Center, Report No. UTRC 81-28, April 1981.
6. Carter, James E.: A New Boundary-Layer Inviscid Iteration Technique for Separated Flow. AIAA Computational Fluid Dynamics Conference, Williamsburg, VA, July 23-25, 1979.

UNSTEADY TRANSONIC VISCOUS-INVISCID INTERACTION
USING EULER AND BOUNDARY-LAYER EQUATIONS *

SHAHYAR PIRZADEH
AND
DAVE WHITFIELD
MISSISSIPPI STATE UNIVERSITY

*This research was sponsored by NASA Langley Research Center. It is a report on work in progress.

OBJECTIVES

This list is obvious for a symposium on transonic unsteady aerodynamics. The last three are the most difficult to achieve. Turbulence is in its usual state of affairs.

- VISCOSUS-INVISCID INTERACTION
- TRANSONIC
- UNSTEADY
- TURBULENT
- THREE-DIMENSIONAL
- EFFICIENT
- ROBUST

APPROACH

The Euler code is one we've used extensively for some time now. The boundary-layer code solves the three-dimensional, compressible, unsteady, mean flow kinetic energy integral boundary-layer equations in the direct mode. Inviscid-viscous coupling is handled using porosity boundary conditions.

- EULER EQUATIONS
 - IMPLICIT
 - FINITE VOLUME
 - UNSTEADY
 - FLUX-VECTOR SPLIT
 - THREE-DIMENSIONAL
- BOUNDARY-LAYER EQUATIONS
 - COMPRESSIBLE
 - THREE-DIMENSIONAL
 - UNSTEADY
 - MEAN FLOW KINETIC ENERGY
 - INTEGRAL
 - DIRECT

OUTLINE OF RESULTS

This slide outlines the order of the results to follow. Steady-state results are considered first to validate the basic inviscid and viscous codes, followed by the unsteady results that have been obtained to date.

- STEADY-STATE
 - 3-D EULER, 2-D BOUNDARY-LAYER (WING-FUSELAGE)
 - 3-D EULER, 3-D BOUNDARY-LAYER (WING)
- UNSTEADY
 - 3-D EULER, 3-D BOUNDARY-LAYER (WING)
 - 3-D EULER, 3-D BOUNDARY-LAYER (QUASI-STEADY AIRFOIL)
 - 3-D NAVIER-STOKES (AIRFOIL)

A two-dimensional steady version of the turbulent boundary-layer code was used with the three-dimensional Euler code in a strip-theory fashion to compute the flow about the supercritical Pathfinder wing with fuselage. The results are shown in Figure 1. These results are included simply to illustrate the type of results that might be obtained using the boundary-layer in a strip-theory fashion. The results were obtained by Dr. Keith Koenig, Mississippi State, under a NASA Langley grant.

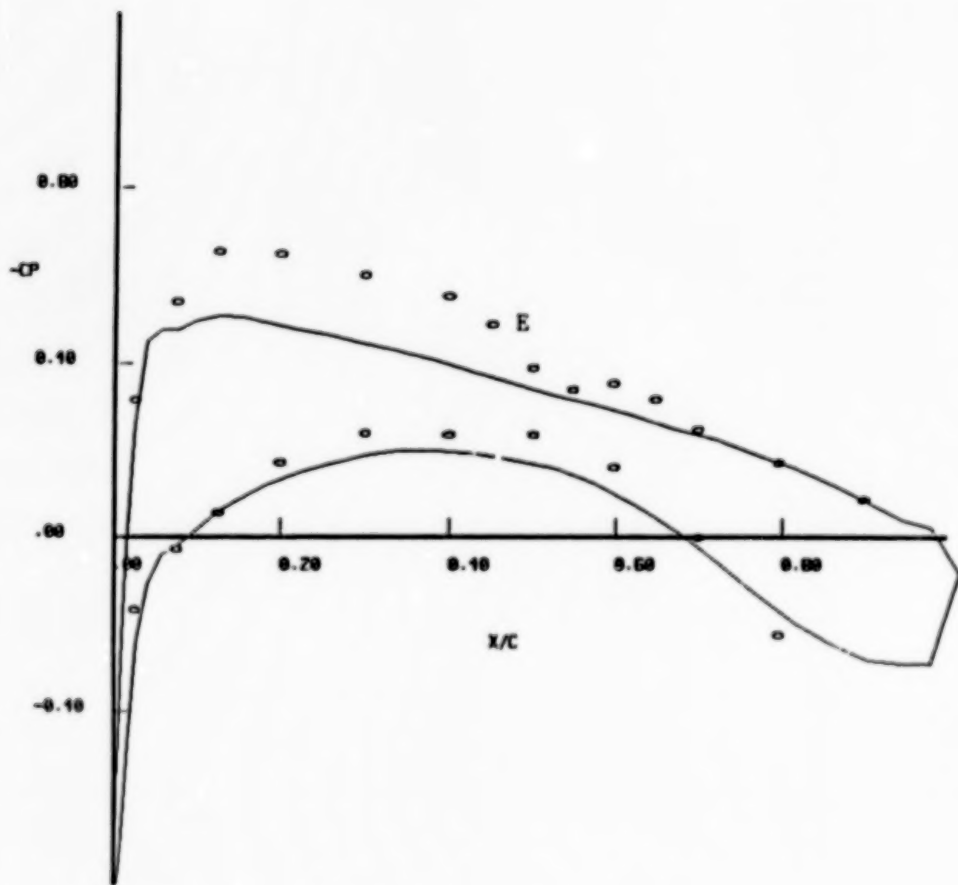


Figure 1a. Section pressure distribution, $M_\infty=0.7$, $\alpha=2^\circ$, $Re=5.3 \times 10^6$;
 E = experiment, 13.1% span; —, viscous, 15% span.

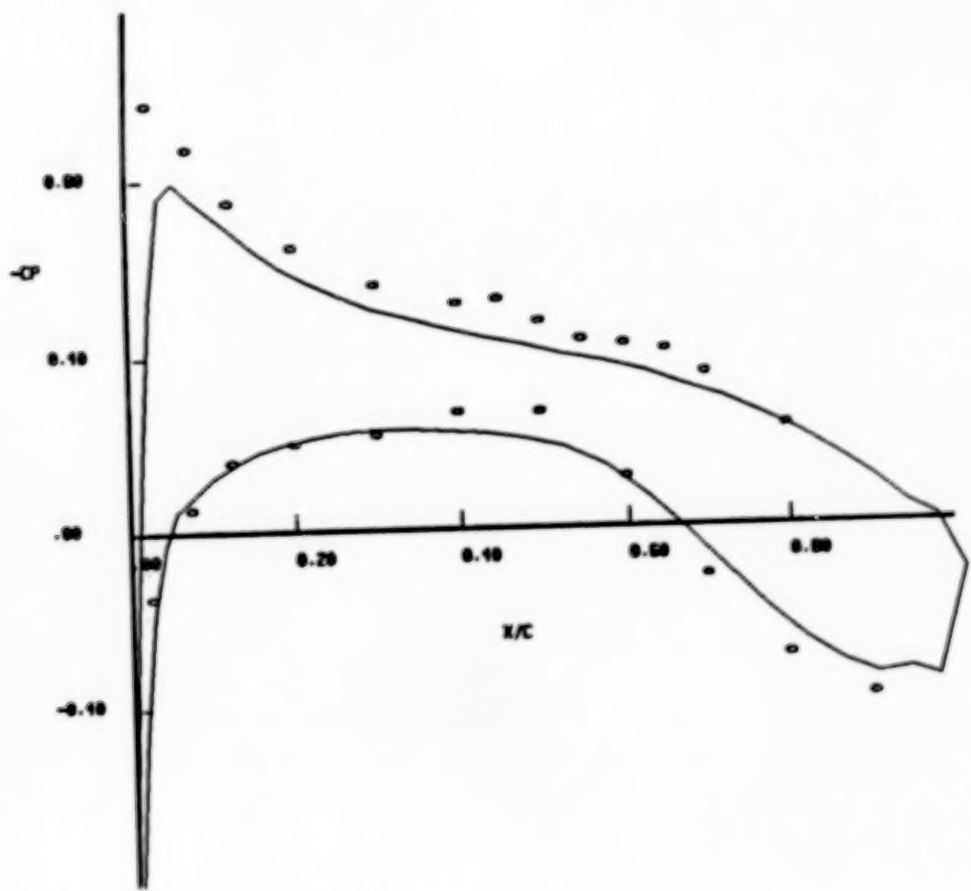


Figure 1b. α , 29.2%; calculation, 25%.

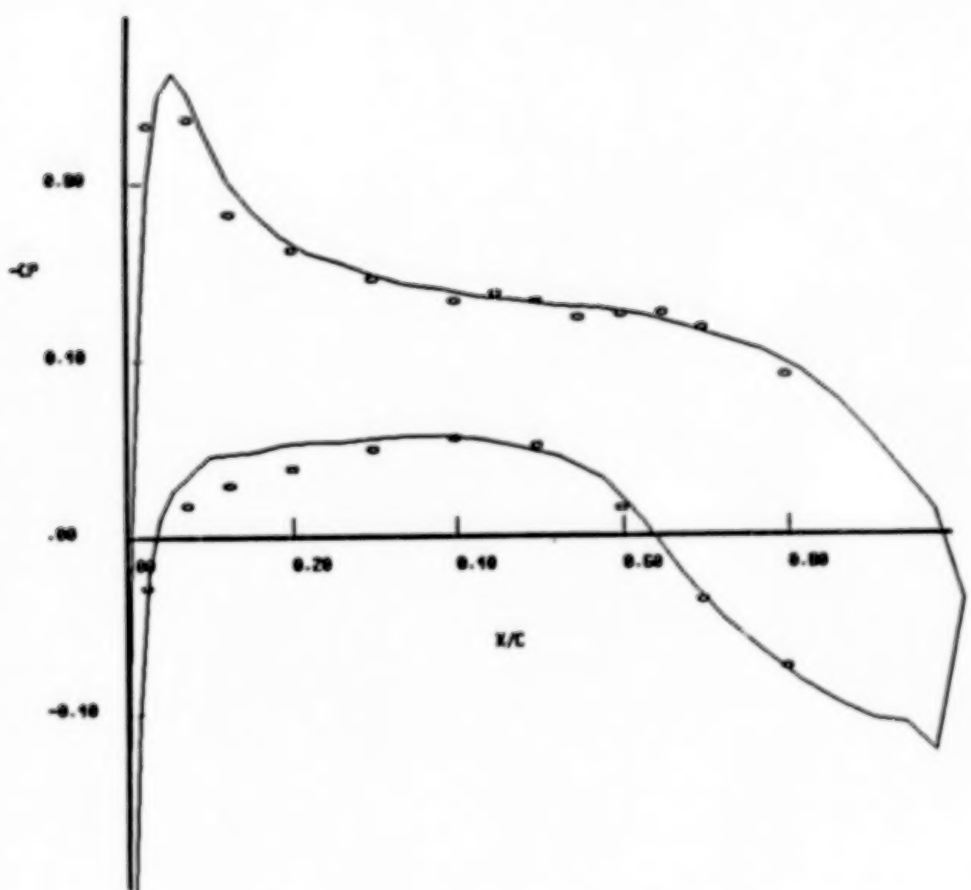


Figure 1c. E, 43.2%; calculation, 45%.

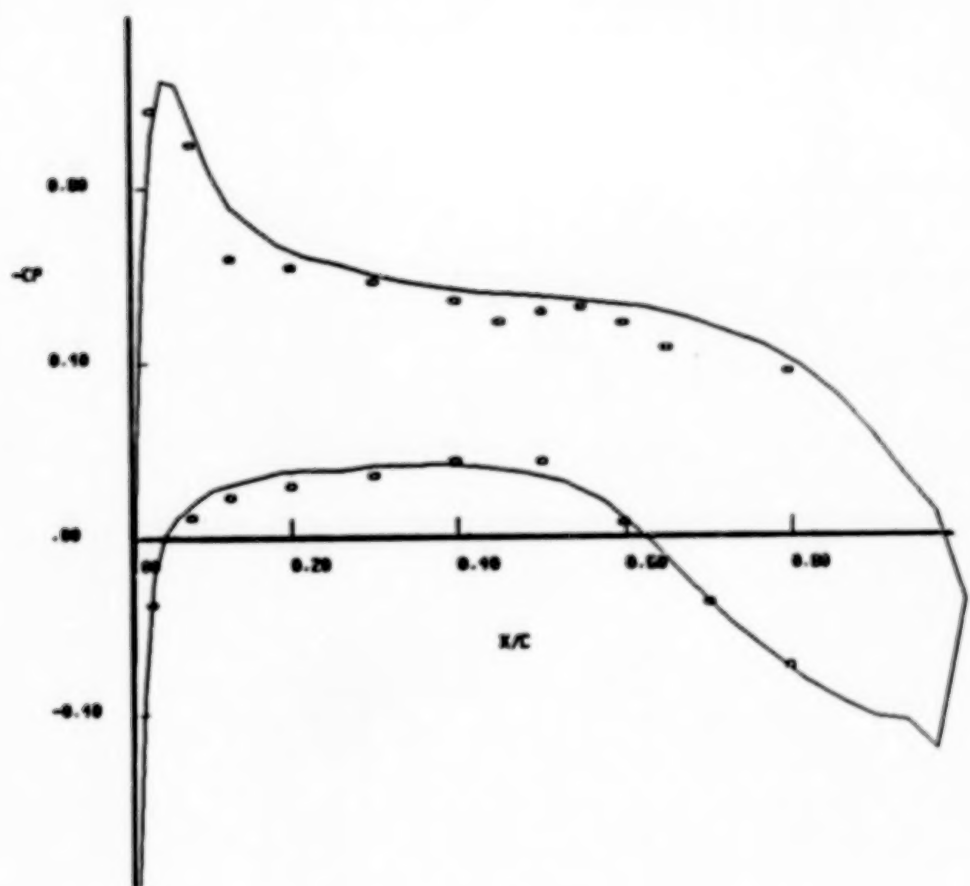


Figure 1d. E, 64%, calculation, 65%.

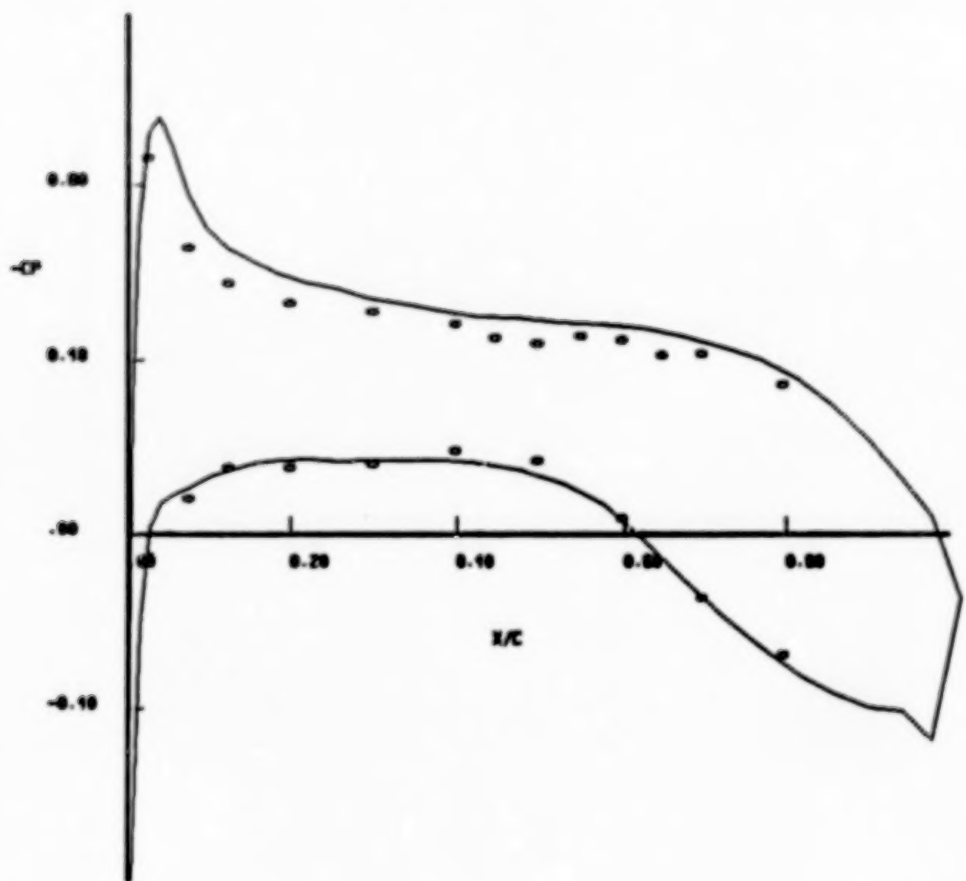


Figure 1e. E, 84%; calculation, 84%.

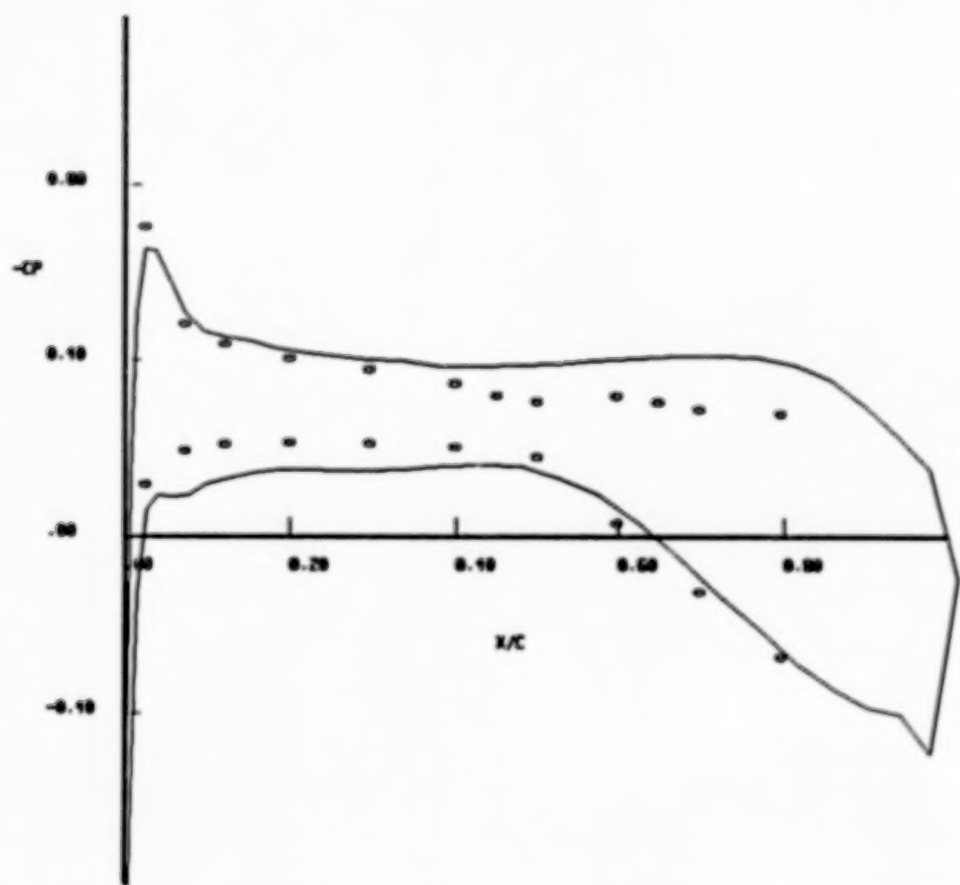


Figure 1f. E, 96.1%; calculation, 95%.

A steady-state interactive solution using the three-dimensional unsteady Euler and boundary-layer codes was obtained for the ONERA M6 wing. The streamwise momentum thickness and shape factor distributions at about fifty percent semi-span location are compared in Figure 2 with the calculations of Schmitt, Destarac, and Chavmet. An isolated experimental data point at sixty percent chord location is also shown.

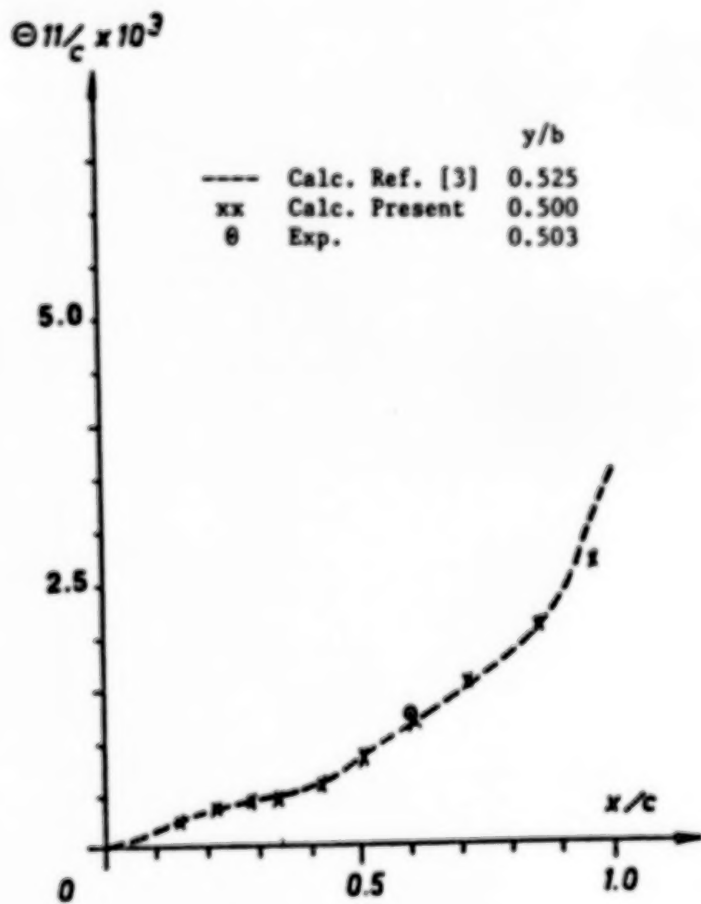


Fig. 2a. Boundary layer characteristics on the upper surface of the ONERA M6 wing. $M=0.84$, $Re_c = 11.7 \times 10^6$, $\alpha=3^\circ$.

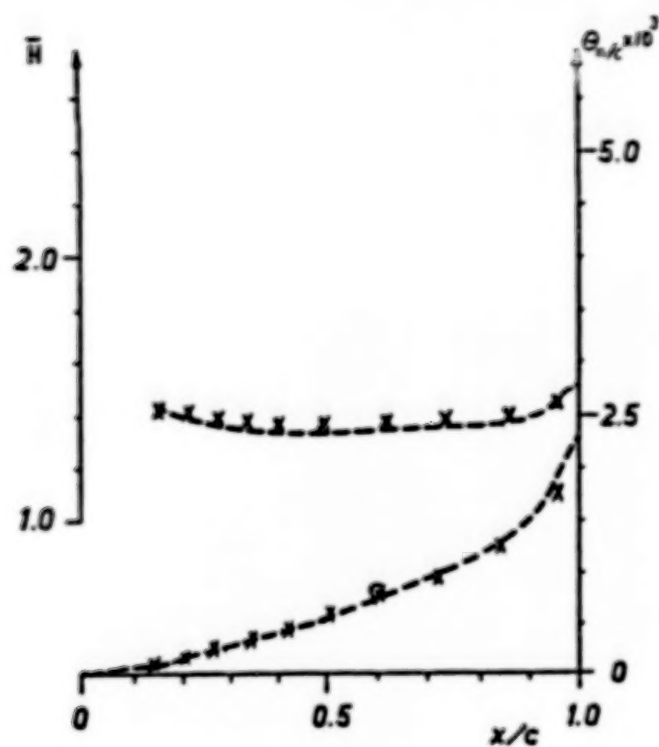
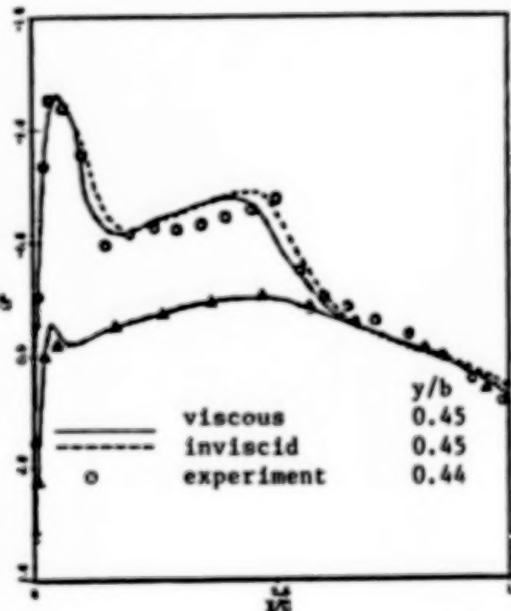


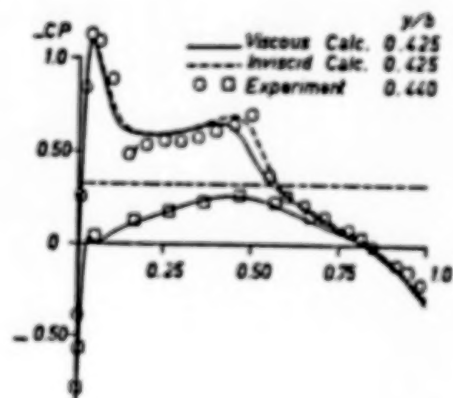
Fig. 2b. Boundary layer characteristics

on the lower surface of the ONERA
 M6 wing, $M=0.84$, $Re_c = 11.7 \times 10^6$,
 $\alpha=3^\circ$.

Surface pressure distributions for the same solution as shown in Figure 2 are compared in Figure 3 with the computations of Schmitt, et al., and experimental data at about forty-five percent semi-span location. The computations of Schmitt et al. used potential flow and a steady state three-dimensional integral boundary-layer code.



(a) Present calculation



(b) Ref. [3]

Fig. 3. Steady pressure distribution on the ONERA M6 Wing. $M=0.84$, $\alpha=3^\circ$

A complete three-dimensional unsteady viscous-inviscid interaction solution was obtained on a relatively coarse grid for the ONERA M6 wing as shown in Figures 4 through 6. The wing was oscillated in pitch ± 2 degrees (mean angle of attack was 0°) about the mid-chord at a reduced frequency of 0.3. For this case there was little viscous effect. Figure 4 shows unsteady viscous and inviscid surface pressure distributions at forty-five percent semi-span location. It is a snapshot at $\alpha = 1.94^\circ$.

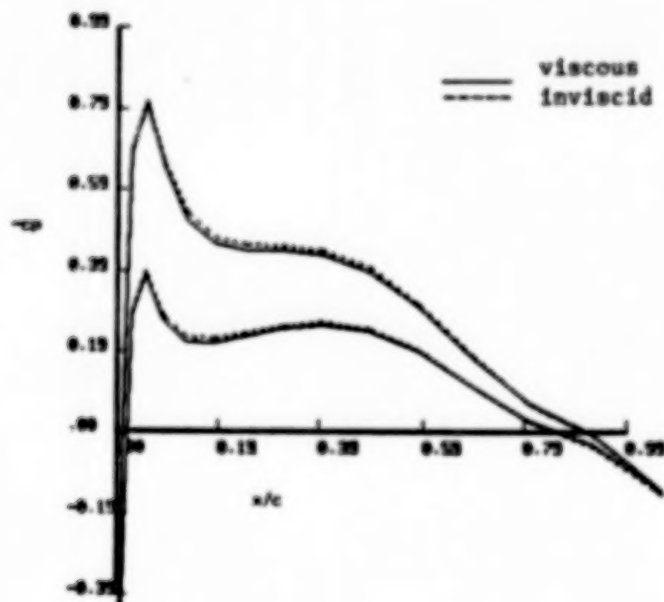


Fig. 4. Unsteady pressure distributions on the ONERA M6 wing at $M=0.84$, $k=0.3$, $\alpha=1.94^\circ$, and $y/b=0.45$. Pitch oscillation about mid-chord $-2^\circ < \alpha < 2^\circ$.

Figure 5 shows the phase shift of the viscous solution described on Figure 4.

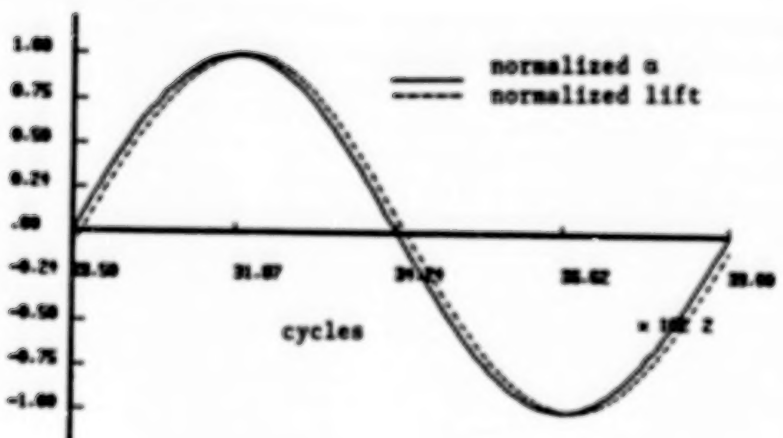


Fig. 5. Phase shift of the ONERA M6 wing lift coefficient (viscous solution). Pitch oscillation.
 $M=0.84$, $k=0.3$, $-2^\circ \leq \alpha \leq 2^\circ$.

Figure 6 shows the viscous and inviscid results of drag coefficient and number of supersonic cells for the computation described on Figure 4.

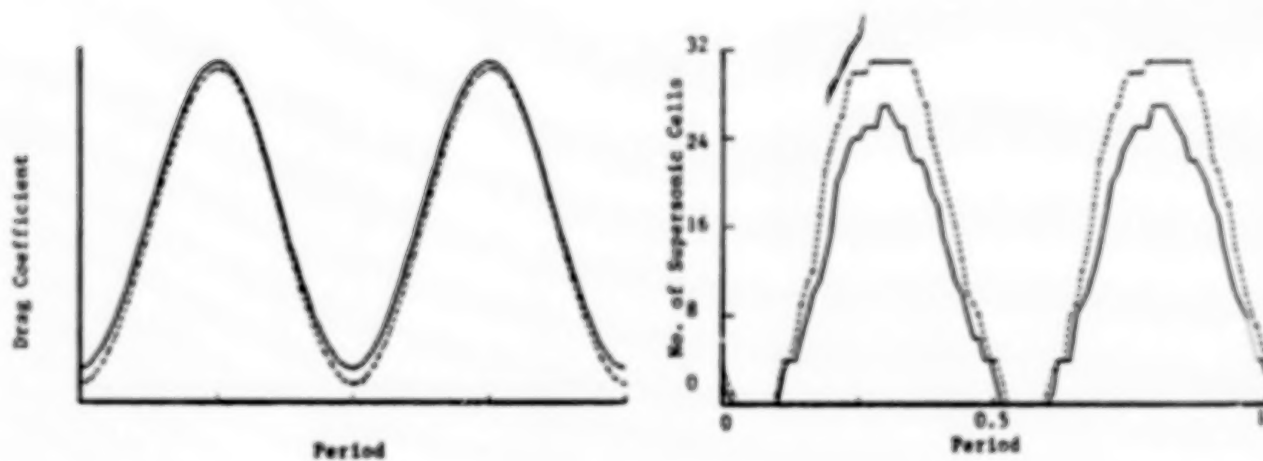


Fig. 6. Drag coefficient and number of supersonic cells. ONERA M6 wing pitch oscillation. $M=0.84$, $k=0.3$, $-2^\circ < \alpha < 2^\circ$.

Figure 7 is a plot of normalized lift and drag versus period for an NACA 0012 airfoil at $M_\infty = 0.776$, Reynolds number of 23.7×10^6 , oscillating ± 1 degree in pitch about the quarter-chord point at a reduced frequency of 0.3 using quasi-steady interaction (that is, unsteady Euler calculation with steady-state boundary-layer calculation).

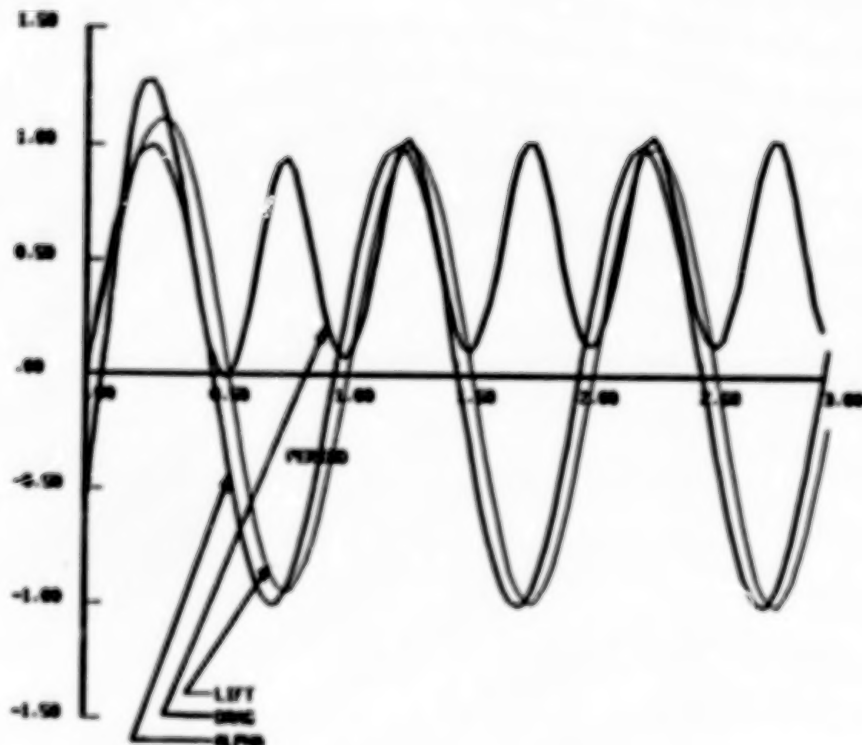


Fig. 7 Quasi-steady interaction for an NACA 0012 airfoil oscillating in pitch ± 1 degree about the quarter-chord point for $M = 0.776$ and $Re = 23.7 \times 10^6$ at a reduced frequency of 0.3.

Figure 8 is a comparison of absolute values of lift versus period resulting from the quasi-steady interaction solution described in Figure 7 and an unsteady Navier-Stokes solution for the same conditions. The Navier-Stokes solution is courtesy of Bruce Simpson, Eglin Air Force Base, FL.

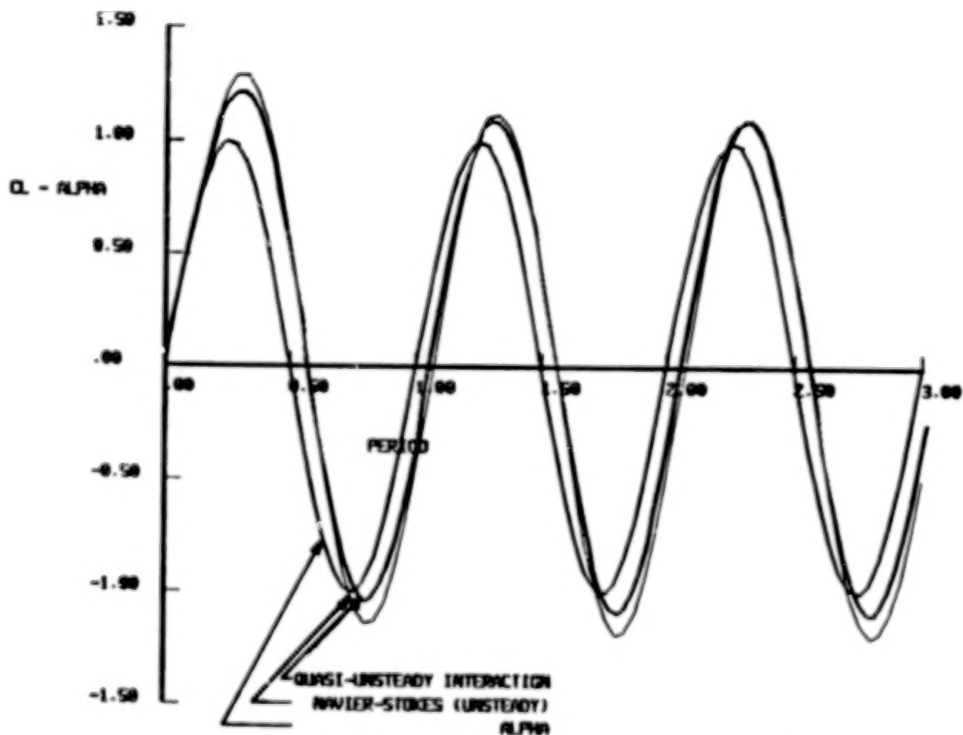


Fig. 8 Lift coefficients for quasi-steady interaction and unsteady Navier-Stokes for an NACA 0012 airfoil oscillating in pitch ± 1 degree about the quarter-chord point for $M = 0.776$ and $Re = 23.7 \times 10^6$ at a reduced frequency at 0.3.

CONCLUSIONS

This slide compares some of the advantages and disadvantages of using the Euler and boundary-layer equations for investigating unsteady viscous-inviscid interaction.

<u>ADVANTAGES</u>	<u>DISADVANTAGES</u>
• ENGINEERING ANSWERS	• MUCH MORE DIFFICULT
• FASTER	• SEPARATION (UNSTEADY)
• LESS STORAGE	• DEVOTED LABOR (PARTICULAR EXPERTISE)
• GRIDDING	• COUPLING
	• ROBUST
	• FEWER PEOPLE WORKING THE PROBLEM

NUMERICAL SOLUTION OF UNSTEADY ROTATIONAL FLOW
PAST
FIXED AND ROTARY WING CONFIGURATIONS

N. L. Sankar and B. E. Wake
Georgia Institute of Technology
Atlanta, GA

S. Y. Ruo and J. B. Malone
Lockheed Georgia Company
Marietta, GA

INTRODUCTION

This work describes the application of unsteady 3-D Euler and Navier-Stokes equations to transonic flow past rotor blades, and wing-alone configurations. The computer code used in this study was developed under the U. S. Army Research Office support at Georgia Tech. The transonic wing-alone calculations were supported by the Lockheed Georgia Company under the IRAD program.

OBJECTIVES

Methods based on the transonic small disturbance theory, and the full potential equation have matured to a point where they may be used by the industries for routine aeroelastic calculations. There is now the need to look at higher order techniques based on the Euler and the Navier-Stokes equations. The higher order solvers can serve two purposes. First, they provide a second estimate in situations where potential flow theory may fail (high transonic Mach numbers, strong shock waves), and provide benchmark runs for the validation of potential flow codes. Secondly, they allow the designer to study phenomena such as high angle of attack transonic maneuvers, supersonic fighter aerodynamics, and 3-D separated flow around highly loaded rotor blades.

1. To Describe a Solution Procedure for the Numerical Solution of the 3-D Compressible Viscous or Inviscid Flow
2. Apply this procedure to a number of fixed and rotary wing problems of interest

Figure 1

GOVERNING EQUATIONS

The equations governing three-dimensional unsteady compressible flow are the Navier-Stokes equations. If the viscous terms are neglected, the Euler equations result. The present solution techniques are designed to work efficiently with both the Navier-Stokes and the Euler equations. All calculations have been done on an algebraically generated body-fitted coordinate system (ξ, η, ζ) , which is allowed to move with time and follow the motion of the solid. The flow properties of interest at a given time level are ρ : the density, u, v, w : the velocity of the fluid in an inertial coordinate system, and e : the total energy of the fluid per unit volume. The quantities U, V and W are the contravariant components of velocity along the ξ -, η - and ζ - directions respectively. Also, p is the pressure.

EULER EQUATIONS

$$q_\tau + E_\xi + F_\eta + G_\zeta = 0$$

$$q = J^{-1} \begin{vmatrix} \rho \\ \rho u \\ \rho v \\ \rho w \\ e \end{vmatrix} \quad E = J^{-1} \begin{vmatrix} \rho U \\ \rho u U + \xi_x P \\ \rho v U + \xi_y P \\ \rho w U + \xi_z P \\ (e + P)U - \xi_t P \end{vmatrix}$$

$$F = J^{-1} \begin{vmatrix} \rho V \\ \rho u V + \eta_x P \\ \rho v V + \eta_y P \\ \rho w V + \eta_z P \\ (e + P)V - \eta_t P \end{vmatrix} \quad G = J^{-1} \begin{vmatrix} \rho W \\ \rho u W + \zeta_x P \\ \rho v W + \zeta_y P \\ \rho w W + \zeta_z P \\ (e + P)W - \zeta_t P \end{vmatrix}$$

$$P = (\gamma - 1)(e - \frac{1}{2}\rho(u^2 + v^2 + w^2))$$

Figure 2

GOVERNING EQUATIONS (CONTD.)

The quantities ξ_x , ξ_y , ξ_z etc. are the metrics of the transformation computed numerically using standard second order accurate finite difference formulas. The quantity J is the Jacobian of transformation.

NAVIER-STOKES EQUATIONS

$$q_r + (E - E_v)_{\xi} + (F - F_v)_{\eta} + (G - G_v)_{\zeta} = 0$$

$$E_v = J^{-1} \begin{vmatrix} 0 \\ \xi_x \tau_{xx} + \xi_y \tau_{xy} + \xi_z \tau_{xz} \\ \xi_x \tau_{yx} + \xi_y \tau_{yy} + \xi_z \tau_{yz} \\ \xi_x \tau_{zx} + \xi_y \tau_{zy} + \xi_z \tau_{zz} \\ \xi_x \beta_x + \xi_y \beta_y + \xi_z \beta_z \end{vmatrix}$$

$$F_v = J^{-1} \begin{vmatrix} 0 \\ \eta_x \tau_{xx} + \eta_y \tau_{xy} + \eta_z \tau_{xz} \\ \eta_x \tau_{yx} + \eta_y \tau_{yy} + \eta_z \tau_{yz} \\ \eta_x \tau_{zx} + \eta_y \tau_{zy} + \eta_z \tau_{zz} \\ \eta_x \beta_x + \eta_y \beta_y + \eta_z \beta_z \end{vmatrix}$$

$$G_v = J^{-1} \begin{vmatrix} 0 \\ \zeta_x \tau_{xx} + \zeta_y \tau_{xy} + \zeta_z \tau_{xz} \\ \zeta_x \tau_{yx} + \zeta_y \tau_{yy} + \zeta_z \tau_{yz} \\ \zeta_x \tau_{zx} + \zeta_y \tau_{zy} + \zeta_z \tau_{zz} \\ \zeta_x \beta_x + \zeta_y \beta_y + \zeta_z \beta_z \end{vmatrix}$$

Figure 3

TURBULENCE MODEL

A two-layer eddy viscosity model developed by Baldwin and Lomax is used in this study (Ref. 1). For the mildly separated flows considered here this model has proved adequate. Here λ_m is the mixing length in the inner layer, proportional to the distance d from the wall, and the van Driest damping factor. In the outer layer, F_{max} is a measure of the velocity scales within the shear layer, while d_{max} is a measure of the length scale. At large distances from the shear layer the eddy viscosity is designed to approach zero through the use of the intermittency factor F_k .

- Baldwin-Lomax two-layer algebraic model used for eddy viscosity.
- Inner Layer:

$$\mu_T = \rho \lambda_m^2 \omega \quad \text{for } d < d_c$$

$$\lambda_m = (\kappa d) [1 - \exp(-d_+ / A_+)]$$

$$d_+ = d(\rho \tau_w)^{1/2} / \mu$$

- Outer Layer:

$$\mu_T = .0168 \rho c_1 F_w F_k \quad \text{for } d > d_c$$

$$F_w = \min(d_{max} F_{max}, c_2 d_{max} Q^2 / F_{max})$$

$$F_{max} = \max[\lambda_m \omega / \kappa]$$

$$F_k = [1 + 5.5(c_3 d / d_{max})^6]^{-1}$$

$$Q = \max|v| - \min|v|$$

Figure 4

HYBRID ALGORITHM

In the present procedure, the time derivatives appearing in the governing equation are discretized using a two-point backward difference formula. The derivatives along the ξ - and ζ directions have been kept at the new time level ($n+1$) where the solution is sought. The spanwise (η -) derivatives have been explicitly evaluated using the latest available information at the inboard station during odd time steps and outboard station during the even time step. Thus, the computational stencil resembles a plane Gauss-Seidel algorithm, where the spanwise sweeps are performed in opposite directions on alternate iteration levels. It may be shown from a linear stability analysis that this technique leads to a stable algorithm.

Implicit Euler rule:

$$q^{n+1} = q^n + \Delta t \frac{\partial q}{\partial t}^{n+1}$$

Evaluate spanwise term explicitly:

$$q^{n+1} = q^n - \Delta t (\delta_\xi E^{n+1} + \delta_\eta F^{n,n+1} + \delta_\zeta G^{n+1})$$

where spanwise term alternates between:

$$\frac{F_{i,j+1,k}^{n+1} - F_{i,j-1,k}^n}{2\Delta\eta} \quad \text{and} \quad \frac{F_{i,j+1,k}^n - F_{i,j-1,k}^{n+1}}{2\Delta\eta}$$

Figure 5

TIME LINEARIZATION

The fact that some of the quantities are to be computed at the new time level ($n+1$) means that the resulting system of equations is algebraic, but highly nonlinear. To avoid an iterative solution of non-linear equations, the well known Beam-Warming linearization (Ref. 2) is applied to the flux terms along the ξ - and ζ directions. The result is a system of linear, block pentadiagonal equations in which the unknown is the 'delta' change in the flow properties between adjacent time levels.

Second-order expansion:

$$\begin{aligned}\mathbf{E}^{n+1} &= \mathbf{E}^n + [\mathbf{A}^n](\mathbf{q}^{n+1} - \mathbf{q}^n) + O(\Delta t^2) \\ \mathbf{G}^{n+1} &= \mathbf{G}^n + [\mathbf{C}^n](\mathbf{q}^{n+1} - \mathbf{q}^n) + O(\Delta t^2)\end{aligned}$$

where \mathbf{A} and \mathbf{C} are the Jacobian matrices:

$$[\mathbf{A}] = \partial \mathbf{E} / \partial \mathbf{q} \quad \text{and} \quad [\mathbf{C}] = \partial \mathbf{G} / \partial \mathbf{q}$$

The following linear system results:

$$\begin{aligned}[\mathbf{I} + \Delta t(\delta_\xi \mathbf{A}^n + \delta_\zeta \mathbf{C}^n)]\Delta \mathbf{q}^{n+1} &= \mathbf{R}^{n,n+1} \\ \Delta \mathbf{q}^{n+1} &= \mathbf{q}^{n+1} - \mathbf{q}^n \\ \mathbf{R}^{n,n+1} &= -\Delta t(\delta_\xi (\mathbf{E}^n - \mathbf{E}_v^{n,n+1}) + \delta_\eta (\mathbf{F} - \mathbf{F}_v)^{n,n+1} + \delta_\zeta (\mathbf{G}^n - \mathbf{G}_v^{n,n+1}))\end{aligned}$$

Figure 6

APPROXIMATE FACTORIZATION

The direct inversion of the pentadiagonal block matrix equations is expensive. In literature, a number of techniques are available, based on the approximate factorization techniques such as L-U decomposition or ADI decomposition. The purpose of these techniques is to break up the coefficient matrix into smaller, easily inverted matrices. In this work an ADI factorization is used to arrive at a system of block tridiagonal equations, which may be inverted using the Thomas algorithm.

ADI Solution in the Airfoil Plane

Approximate factorization:

$$[I + \Delta t(\delta_\xi A + \delta_\zeta C)] = [I + \Delta t \delta_\xi A][I + \Delta t \delta_\zeta C] + O(\Delta t^2)$$

Gives two linear systems with block tridiagonal matrices:

$$[I + \Delta t \delta_\xi A] \Delta q^{*n+1} = R^{n,n+1}$$
$$[I + \Delta t \delta_\zeta C] \Delta q^{*n+1} = \Delta q^{*n+1}$$

At every time step, the solver marches through the radial stations explicitly performing two matrix-inversion sweeps at each station.

Figure 7

ARTIFICIAL DISSIPATION TERMS

The use of pure central differences to advance hyperbolic, or weakly parabolic equations can lead to numerical instabilities. A variety of artificial dissipation forms have been suggested in literature to overcome this instability. In this work, a fourth order explicit dissipation form is used, and to allow large amounts of explicit dissipation to be used without instability, a second order implicit dissipation term is added to the left side.

- Using central differencing alone leads to odd-even decoupling.
- Nonlinearities of the equations produces high-frequency errors which grow.
- Second-order implicit dissipation and fourth-order explicit dissipation used.
- Fourth-order implicit dissipation stabilizes the scheme even more, but results in penta-diagonal systems.
- It can be shown that the dissipation results in an upwinded scheme.

Figure 8

FINAL FORM OF THE DIFFERENCE EQUATIONS

The final form of the discretized equations, used in the computer code are shown below.

$$[I + \Delta t \delta_{\xi} A - \Delta t \epsilon_i J^{-1} \nabla_{\xi} \Delta_{\xi} J] \Delta q^{n+1} = R^{n,n+1} - D_e^{n,n+1}$$

$$[I + \Delta t \delta_{\zeta} C - \Delta t (\epsilon_i + \epsilon_{\mu}) J^{-1} \nabla_{\zeta} \Delta_{\zeta} J] \Delta q^{n+1} = \Delta q^{n+1}$$

where, the explicit dissipation is:

$$D_e^{n,n+1} = \Delta t \epsilon_i J^{-1} [(\nabla_{\xi} \Delta_{\xi})^2 + (\nabla_{\eta} \Delta_{\eta})^2 + (\nabla_{\zeta} \Delta_{\zeta})^2] J q^n$$

and the variable implicit coefficient is:

$$\epsilon_{\mu} = (\mu + \mu_T) (\xi_x^2 + \xi_y^2 + \xi_z^2)$$

As an example,

$$(\nabla_{\xi} \Delta_{\xi})^2 J q^n = (\hat{q}_{i+2} - 4\hat{q}_{i+1} + 6\hat{q}_i - 4\hat{q}_{i-1} + \hat{q}_{i-2})^n$$

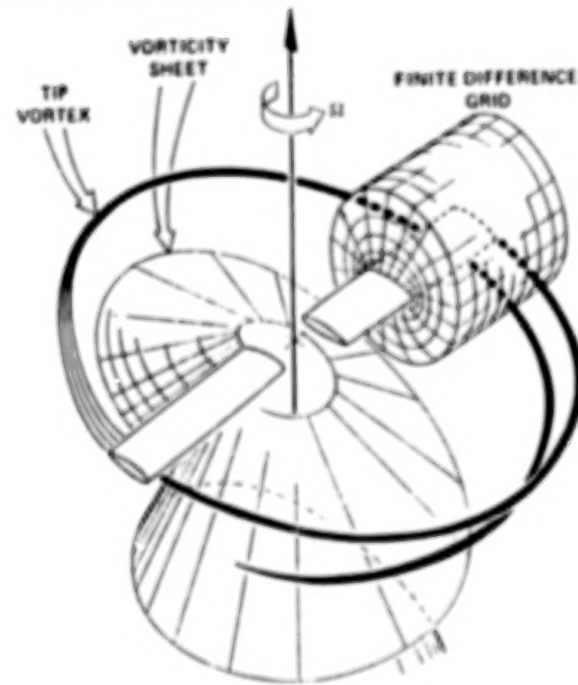
$$(\nabla_{\xi} \Delta_{\xi}) J q^n = (\hat{q}_{i+1} - 2\hat{q}_i + \hat{q}_{i-1})^n$$

Figure 9

TREATMENT OF ROTOR WAKE

In helicopter applications, the treatment of the shed tip vortices requires special considerations. The finite difference grid is usually not large enough or fine enough to capture the many revolutions of the tip vortices shed by several blades. In this work, only the portion of the shed vorticity immediately downstream of the rotor blade is captured by the finite difference scheme. The rest of the vorticity, and the wake behind the other blades is kept track of using a Lagrangean approach. This approach was first proposed by Tung and Caradonna (Ref. 3).

- Downwash due to tip vortex significantly affects the lift of the blade
- Resolving the tip vortex by finite difference techniques is not possible with current computer resources
- Effects of tip vortices lying outside of the computational domain must be included



- Use CAMRAD or some other wake code to obtain effective partial angle of attack distribution

Figure 10

LIFTING VISCOUS FLOW PAST A HOVERING ROTOR

As a first application of the solution technique described, the subsonic lifting flow past a two bladed rotor system in hover is considered. The blades were made of NACA 0012 airfoils and had a rectangular planform. The collective pitch was 8 degrees, and the tip Mach number was 0.44. There is an extensive set of experimental data available for this configuration (Ref. 4). Here, the computed pressure distribution at a number of radial stations is plotted and compared with experimental data. Good agreement is observed at all locations.

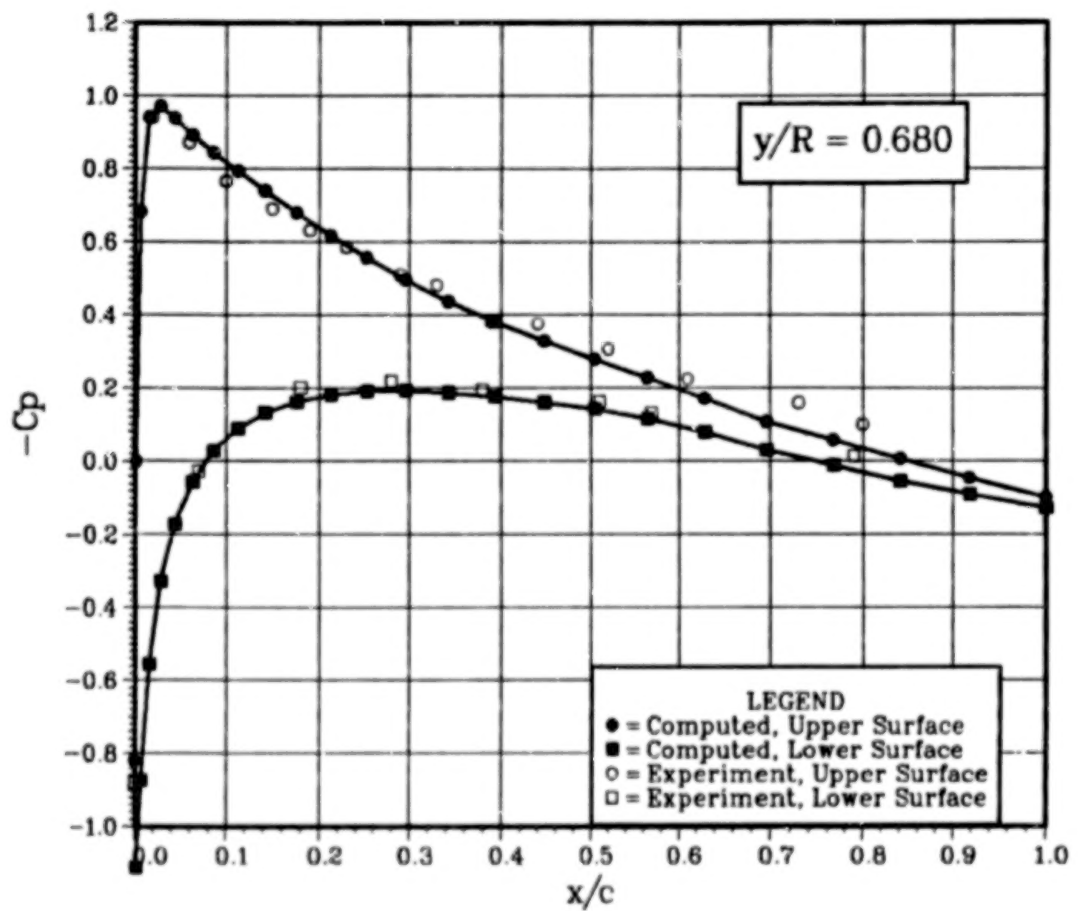


Figure 11

LIFTING SUBSONIC FLOW OVER A HOVERING ROTOR (concluded)

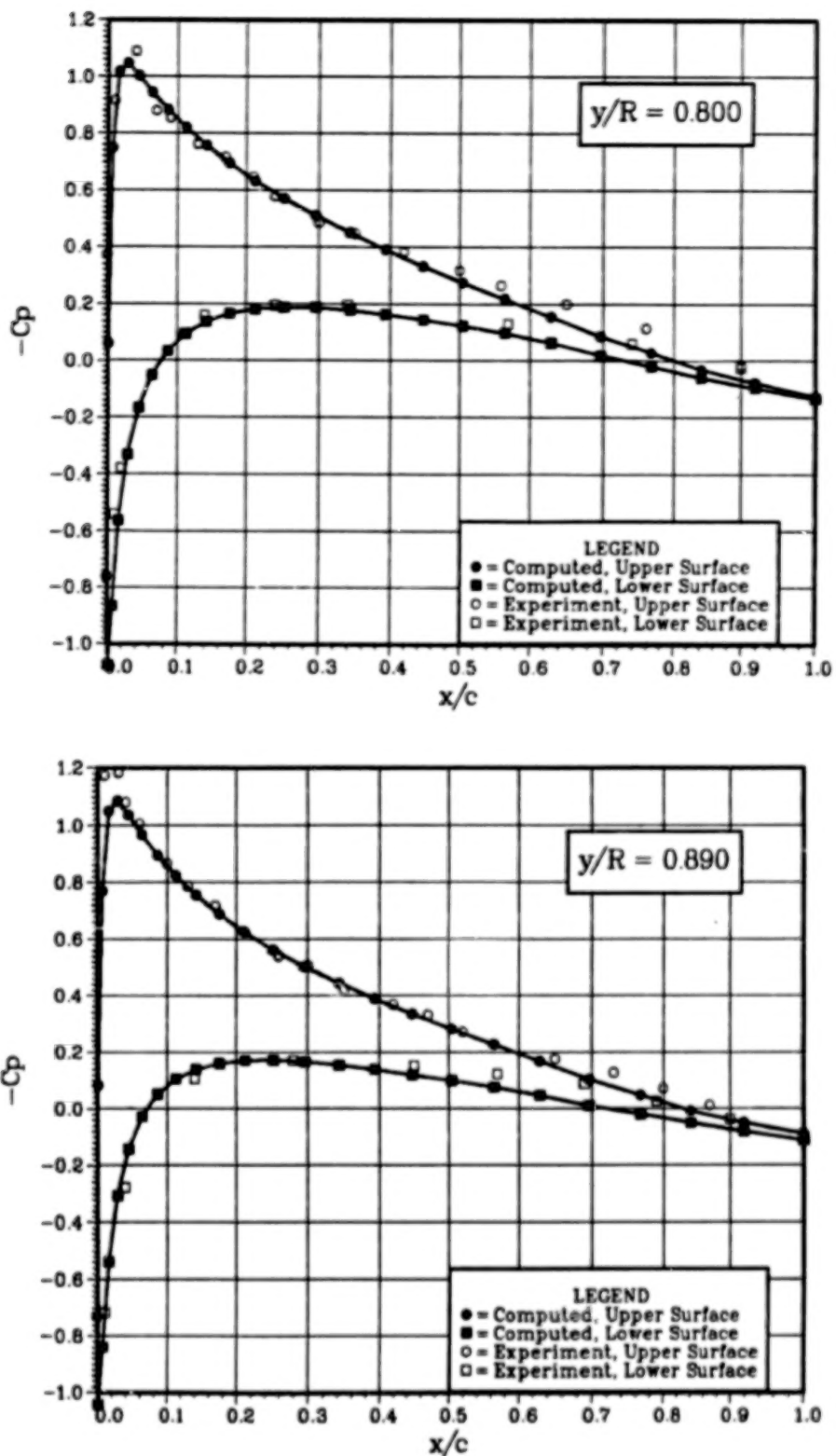


Figure 11 Concluded.

SPANWISE LOADING ON A HOVERING ROTOR

The integrated lift distributions are plotted along the rotor radius below. It is seen that good agreement with experiments is found.

These calculations were done on a $79 \times 23 \times 45$ grid with 50 points at each radial location on the rotor, 11 radial locations on the rotor and 45 points in the normal direction. They required 3.9 seconds per time step on the CRAY XMP.

Lift Coefficient Distribution

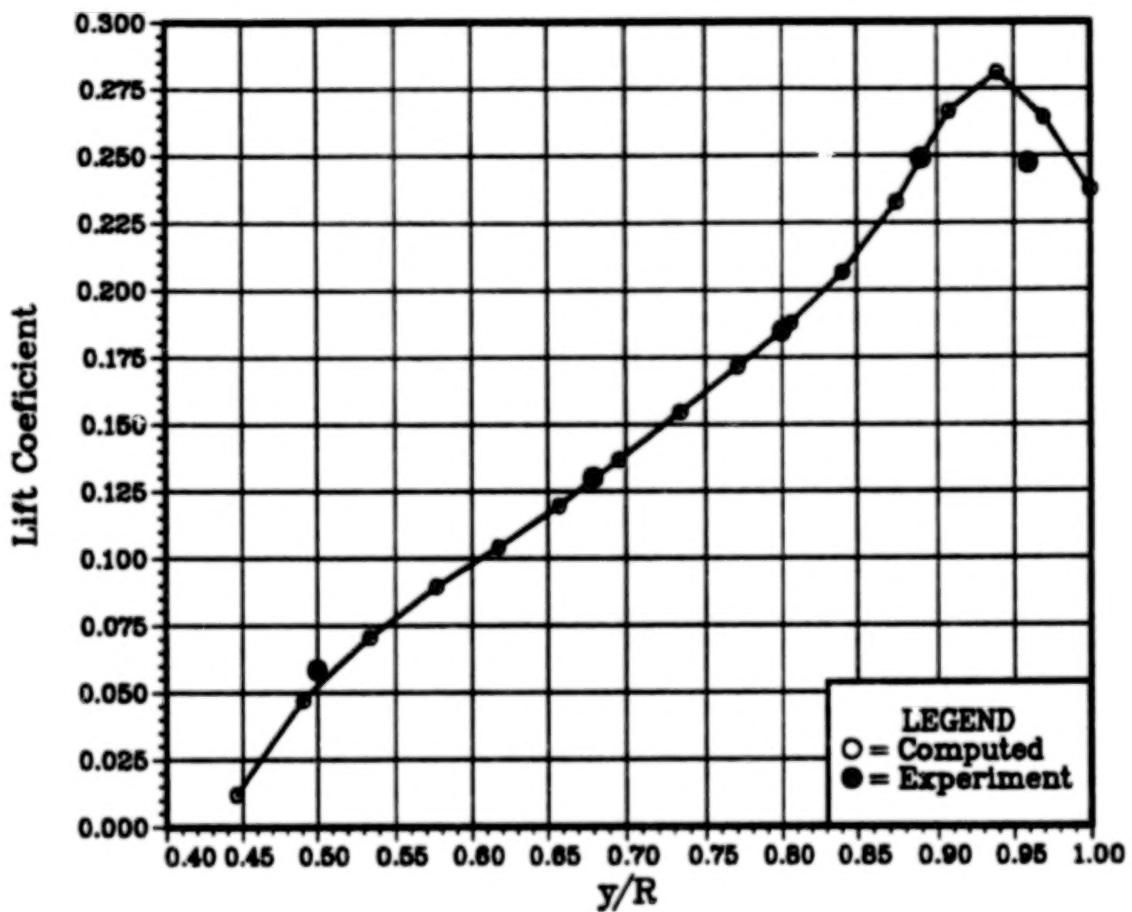


Figure 12

NON-LIFTING TRANSONIC FLOW OVER AN ADVANCING ROTOR

As a second example, the transonic viscous flow past a rotor blade tested at ONERA is considered. The tip Mach number in this case was 0.6, while the advance ratio (forward speed/tip speed) was 0.45. In the next several pages, comparisons between experiments and the Navier-Stokes solutions are given at the 84% span station. For the sake of completeness some Euler solutions are also shown. It is seen that both the Euler and the Navier-Stokes solutions give acceptable agreement with experiments. It is also seen that the Navier-Stokes results predict the shock locations and strength more accurately. These calculations were done on a $121 \times 19 \times 45$ grid and required 4.6 sec per iteration on a CRAY XMP. Several thousand time steps were needed to advance the solution from zero degree azimuth to 360 degree azimuth in time, (through a full revolution).

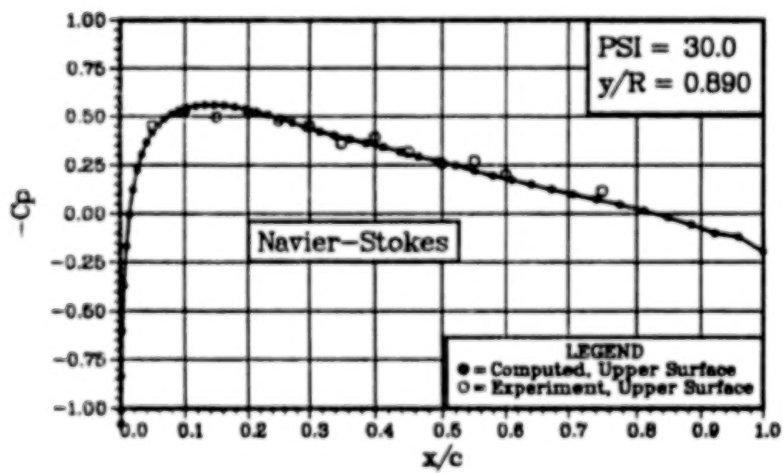
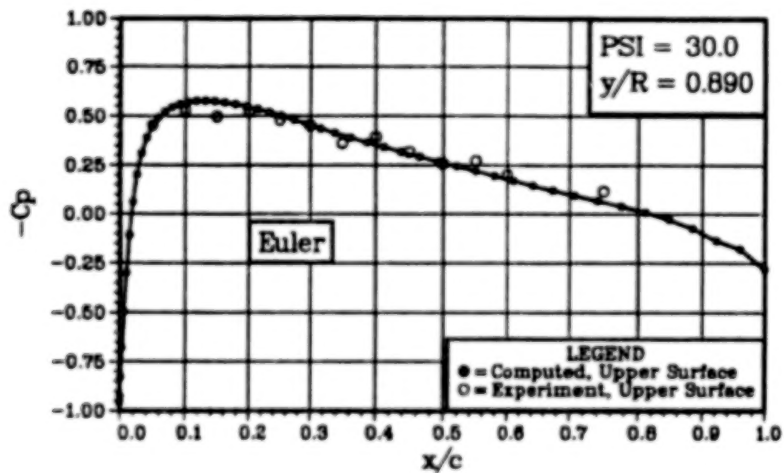


Figure 13

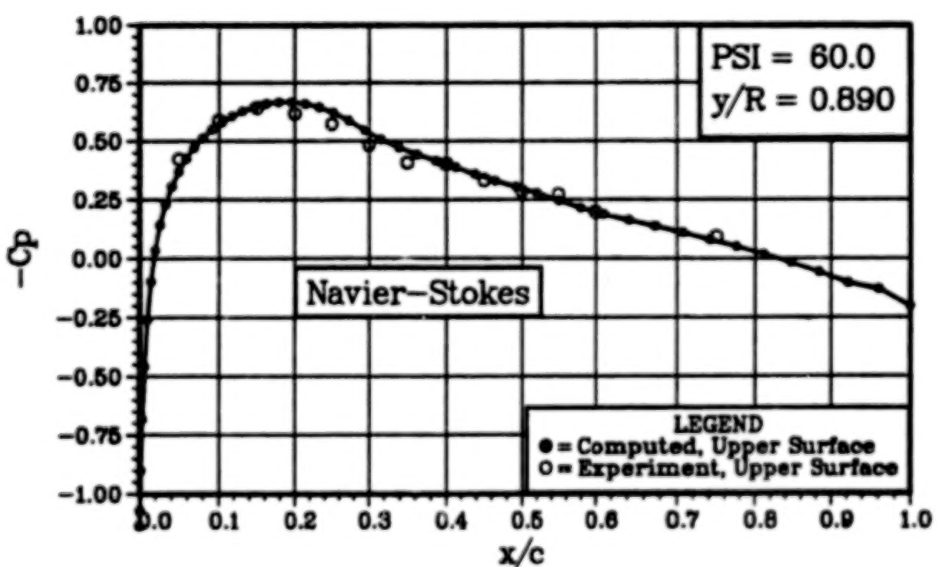
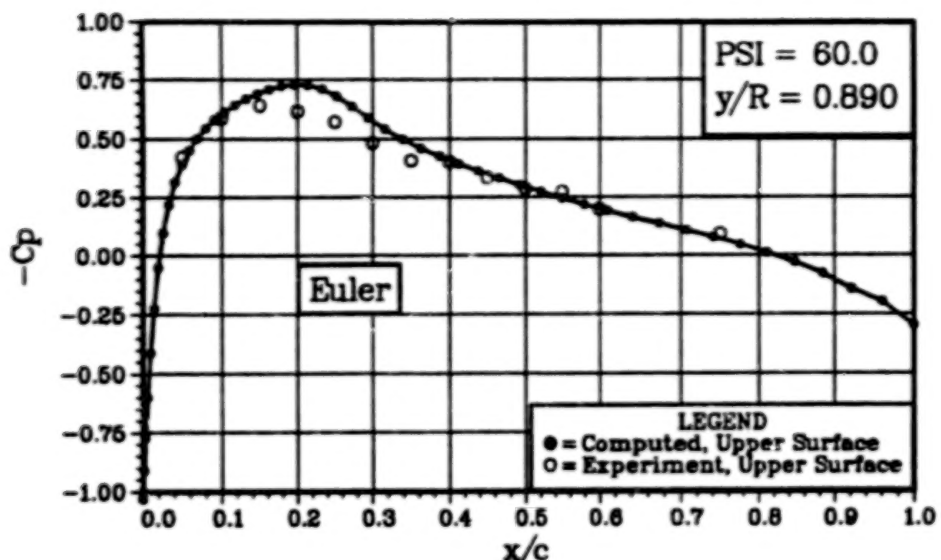


Figure 13 Continued.

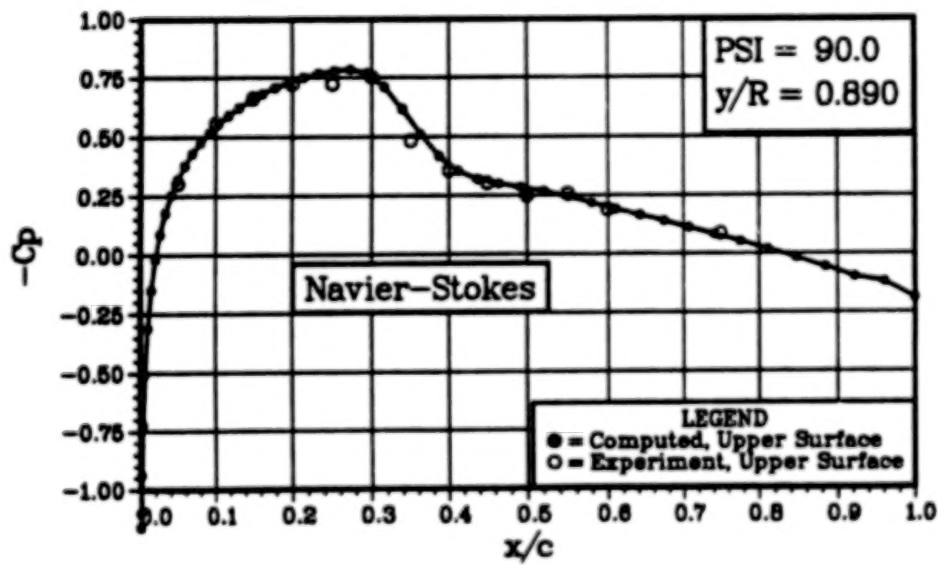
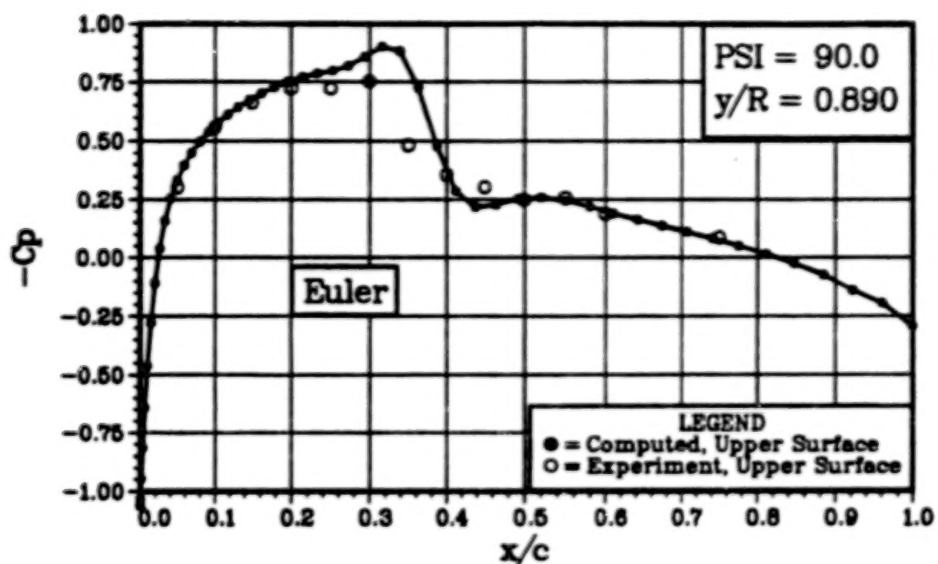


Figure 13 Continued.

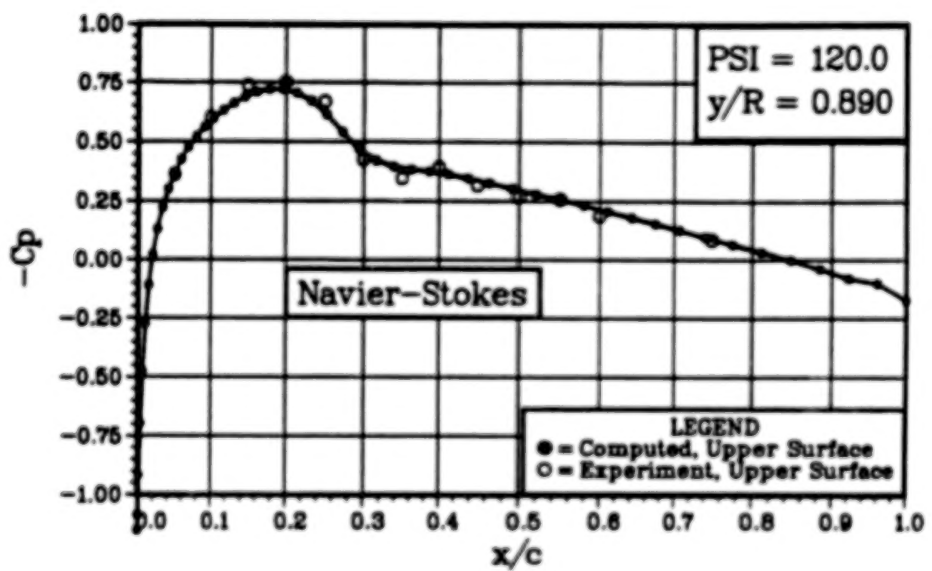
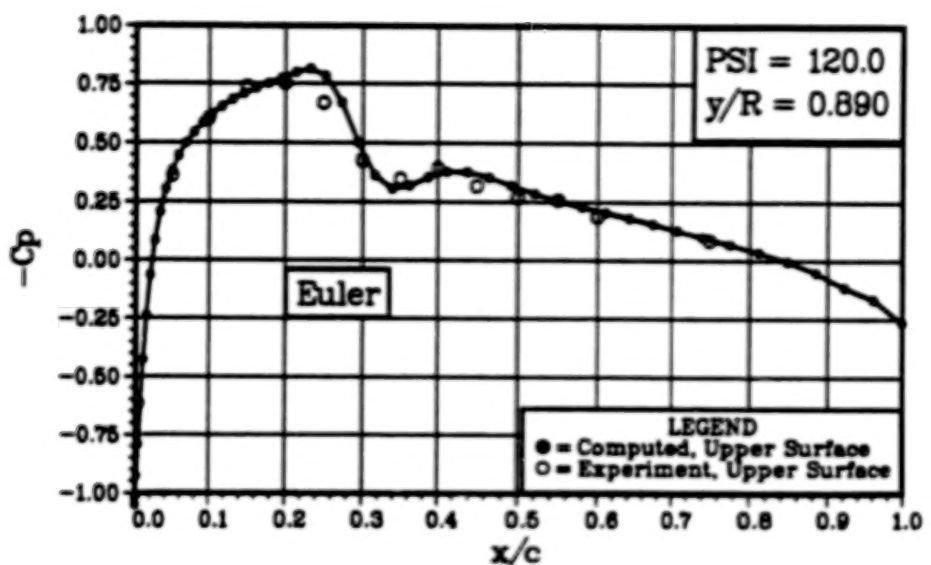


Figure 13 Continued.

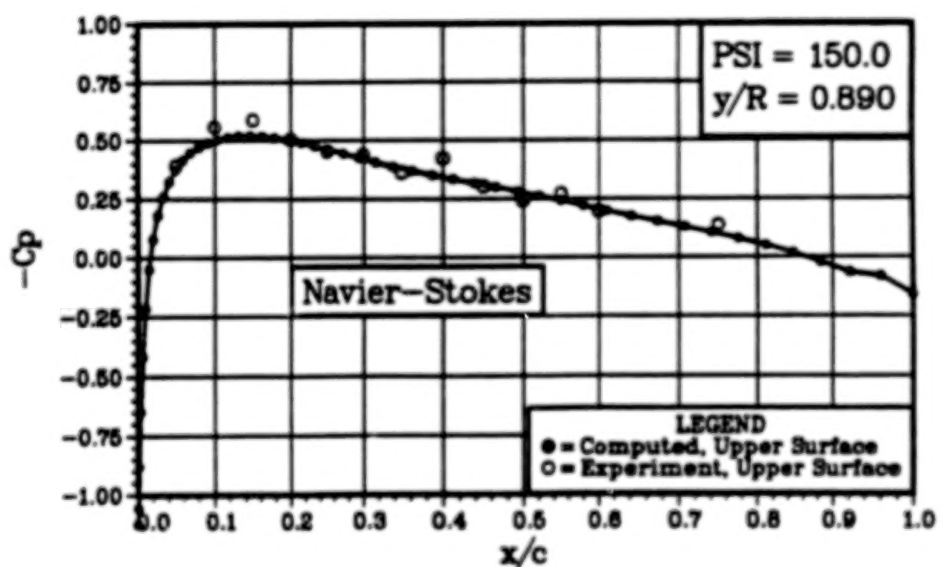
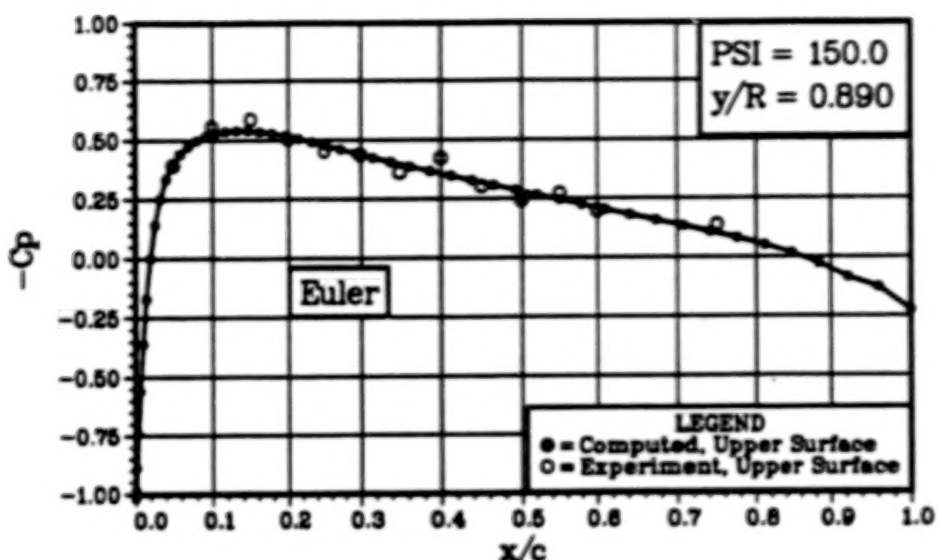


Figure 13 Concluded.

LIFTING TRANSONIC FLOW PAST A RECTANGULAR WING

As a final application of the present approach, the unsteady transonic flow past a rectangular supercritical wing tested at NASA Langley Research Center is presented. The freestream Mach number was 0.7 and the mean angle of attack was 1.98 degrees. The wing was constrained to oscillate in pitch at a frequency of 10 Hz. In the following figures, the in-phase and the out-of-phase components of the surface pressure distribution are plotted at several locations. Overall, a reasonably good agreement is observed.

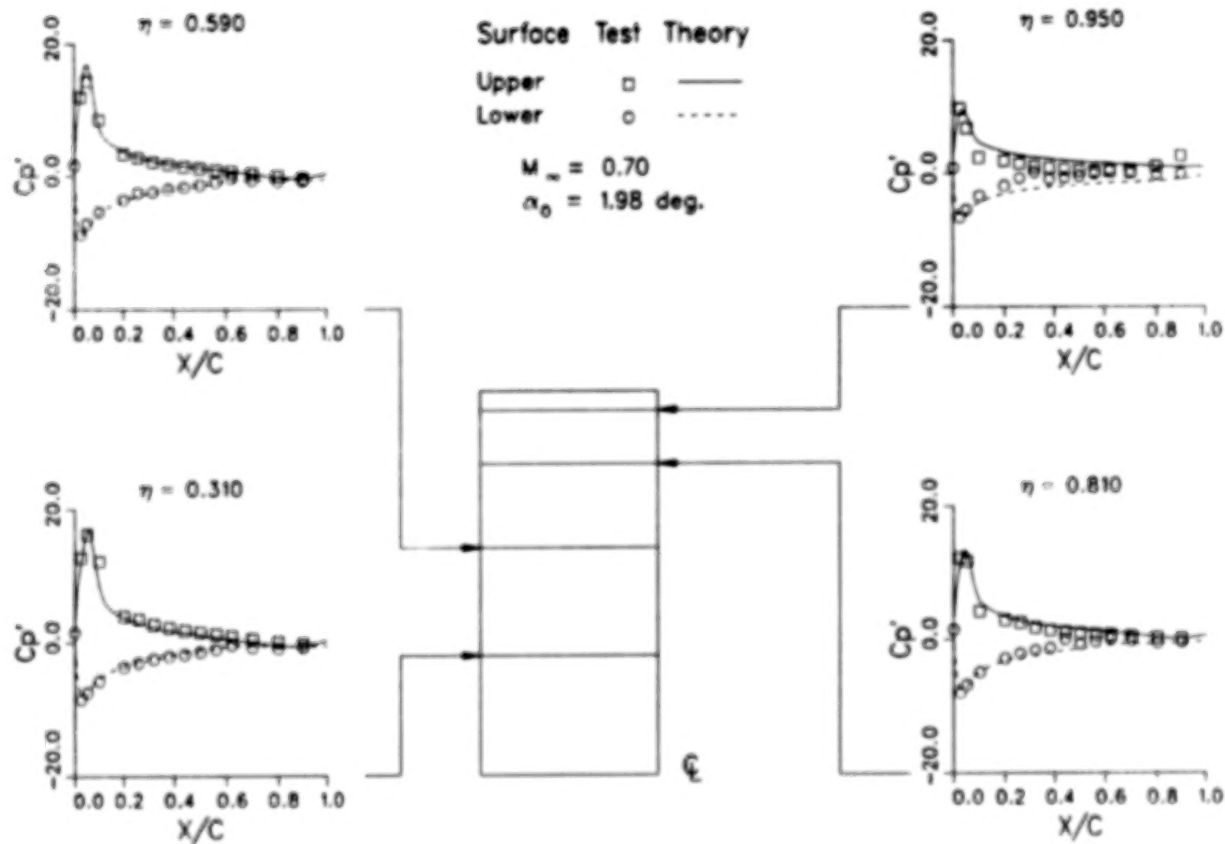


FIGURE 14. R376E21 INVISCID REAL AMPL=1.044 2000 S/C 5000 S, $M_\infty = 0.70$, $\alpha_0 = 2.0$ deg.

LIFTING TRANSONIC FLOW PAST A RECTANGULAR WING (concluded)

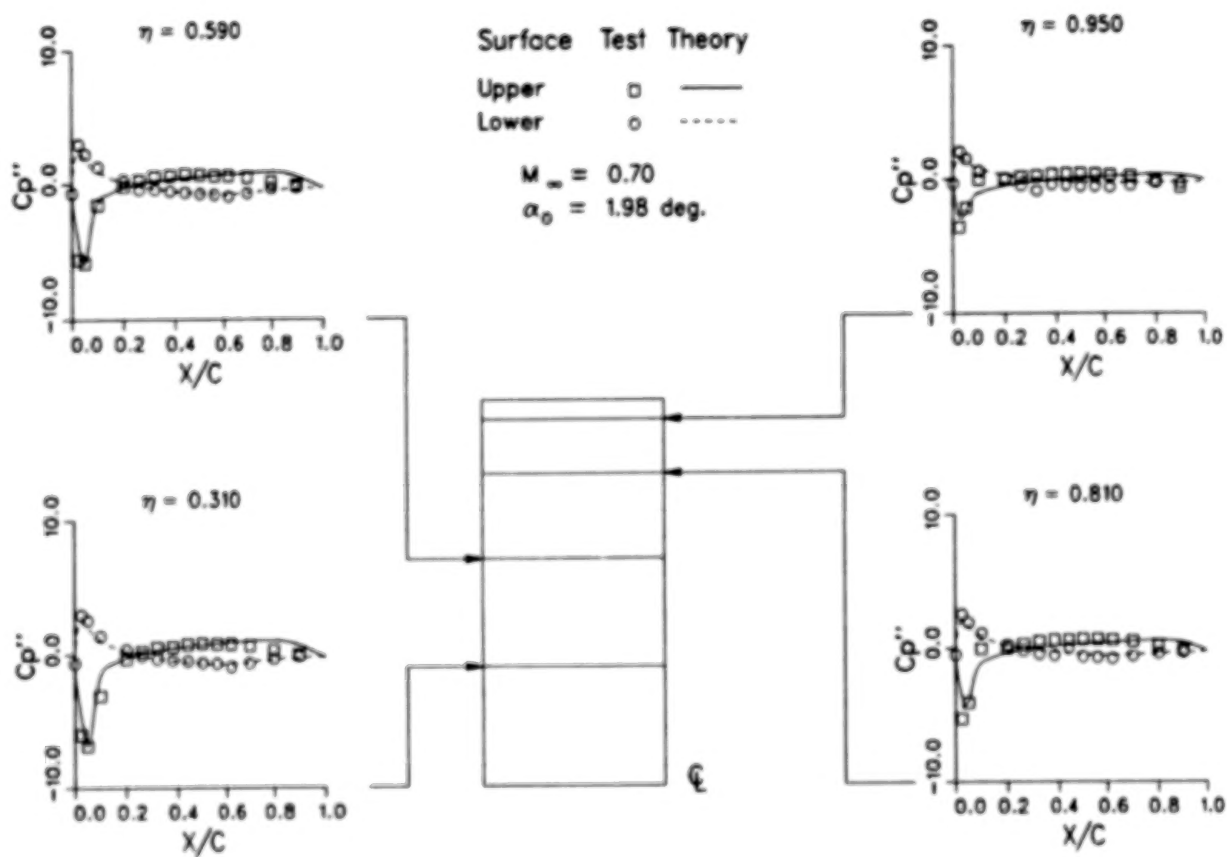


FIGURE 14. R376E21 INVISCID IMAGINARY AMPL=1.044 2000 S/C 5000 S
(Concluded)

CONCLUDING REMARKS

A promising approach for the numerical solution of three-dimensional Euler and Navier-Stokes equations has been described. Additional work is needed for improving the efficiency of the present procedure. It is hoped that the techniques presented here will find use in fixed and rotary wing aircraft analysis. For additional studies and code correlations the reader is referred to Refs. 5-8.

1. A solution technique for the 3-D Euler and Navier-Stokes equations has been developed.
2. A number of interesting fixed and rotary wing applications have been presented.
3. Additional work towards improving the solution efficiency is now underway.

Figure 15

REFERENCES

1. Baldwin, B.S. and Lomax, H., "Thin Layer Approximation and Algebraic Model for Separated Turbulent Flows," AIAA Paper 78-0257.
2. Beam, R.F. and Warming, R.M., "An Implicit Finite-Difference Algorithm for Hyperbolic System in Conservation Law Form," Journal of Computational Physics, Vol. 22, p. 87, 1975.
3. Tung, C., Caradonna, F.X., Boxwell, D.A. and Johnson, W.R., "The Prediction of Transonic Flows on Advancing Rotors," Proceedings of the American Helicopter Society Annual Forum, May 1984.
4. Caradonna, F.X. and Tung, C., "Experimental and Analytical Studies of a Model Rotor in Hover," NASA TM 81232.
5. Sankar, L.N., Wake, B.E. and Lekoudis, S.G., "Solution of the Euler Equations for Fixed and Rotary wing Configurations," Journal of Aircraft, Vol. 23, NO. 4, pp. 283-289, 1986.
6. Sankar, L.N., Malone, J.B. and Schuster, D., "Euler Solutions for Transonic Flow past a Fighter Wing," Journal of Aircraft, Vol. 24, No. 1, pp. 10-16, 1987.
7. Sankar, L.N. and Tung, C., "Euler Calculations for Rotor Configurations in Unsteady Forward Flight," Proceedings of the American Helicopter Society Annual Forum, June 1986.
8. Wake, B.E., "Solution Procedure for the Navier-Stokes Equations applied to Rotors," Ph.D. Dissertation, Georgia Institute of Technology, April 1987.

UNSTEADY NAVIER-STOKES COMPUTATIONS OVER AIRFOILS
USING BOTH FIXED AND DYNAMIC MESHES

Christopher L. Rumsey
W. Kyle Anderson
NASA Langley Research Center
Hampton, Virginia

OUTLINE

- PURPOSE
- GOVERNING EQUATIONS
- NUMERICAL METHOD
- CONSTANT ANGLE-OF-ATTACK UNSTEADY SOLUTIONS
- FORCED PITCHING SOLUTIONS
 - SINUSOIDAL PITCH
 - CONSTANT-RATE PITCH
- CONCLUSIONS

PURPOSE

The purpose of the present investigation is to solve the Navier-Stokes equations for unsteady airfoil flows. Two primary types of unsteady flows are considered. The first is unsteady periodic flow over an airfoil at a fixed angle-of-attack past stall. The second is unsteady flow over an airfoil which is pitching either sinusoidally or with a constant-rate pitch-up motion. For the pitching airfoil solutions, a dynamic mesh is employed in the computations. All results are compared with experiment.

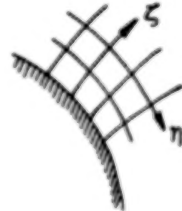
- NAVIER-STOKES EQUATIONS APPLIED TO UNSTEADY FLOWS ON FIXED MESHES
- NAVIER-STOKES EQUATIONS APPLIED TO UNSTEADY FLOWS ON DYNAMIC MESHES
 - INCLUDE TIME TERMS IN FLUX VECTORS
 - SINUSOIDAL PITCH SOLUTIONS
 - CONSTANT-RATE PITCH SOLUTIONS
- COMPARISON WITH EXPERIMENT

GOVERNING EQUATIONS

The governing equations used in the present analysis are the two-dimensional Reynolds averaged thin-layer Navier-Stokes equations. They are written in generalized coordinates, with the η -coordinate direction along the body and the ζ -coordinate direction normal to the body. Q represents the conserved flow variables. The flux vectors G and H are split according to the method of Van Leer¹, with the extension to dynamic meshes given by Anderson et al². J is the coordinate transformation Jacobian. For an unmoving mesh, η_t and ζ_t are zero.

$$\hat{\frac{\partial Q}{\partial t}} + \hat{\frac{\partial G}{\partial \eta}} + \hat{\frac{\partial H}{\partial \zeta}} = \overline{Re}^{-1} \partial_{\zeta} [J^{-1} (\zeta_x R + \zeta_y S)]$$

$$\begin{aligned}\hat{Q} &= Q/J \\ \hat{G} &= (\eta_x G + \eta_y H + \eta_t Q)/J \\ H &= (\zeta_x G + \zeta_y H + \zeta_t Q)/J\end{aligned}$$



$$Q = \begin{bmatrix} \rho \\ \rho u \\ \rho v \\ e \end{bmatrix} \quad G = \begin{bmatrix} \rho u \\ \rho u^2 + p \\ \rho u v \\ u(e + p) \end{bmatrix} \quad H = \begin{bmatrix} \rho v \\ \rho u v \\ \rho v^2 + p \\ v(e + p) \end{bmatrix}$$

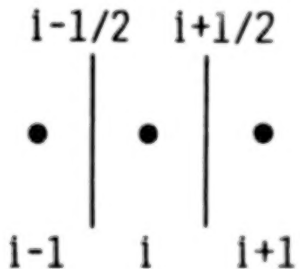
$$R = \begin{bmatrix} 0 \\ \tau_{xx} \\ \tau_{xy} \\ u\tau_{xx} + v\tau_{xy} + \mu Pr^{-1}(\gamma-1)^{-1} \zeta_x (a^2) \zeta \end{bmatrix} \quad S = \begin{bmatrix} 0 \\ \tau_{xy} \\ \tau_{yy} \\ u\tau_{xy} + v\tau_{yy} + \mu Pr^{-1}(\gamma-1)^{-1} \zeta_y (a^2) \zeta \end{bmatrix}$$

FLUX SPLITTING

Fluxes are split into a forward and a backward contribution according to the signs of the eigenvalues of the Jacobian matrices, and differenced accordingly. The split-flux differences are implemented as a flux balance across a cell, corresponding to MUSCL (Monotone Upstream-centered Schemes for Conservation Laws)³ type differencing. For example, the derivative in F at the i node in the figure can be written as $F(Q)_{i+1/2} - F(Q)_{i-1/2}$, where each $F(Q)$ can be split into its forward and backward components F^+ and F^- . State variables on each interface are obtained by interpolation of the conserved variables at the appropriate nodes. Using upwind-biasing, for example, conserved variables at the $i-1$, i , and $i+1$ nodes are used to obtain the positive contribution to $F(Q)$ at the $i+1/2$ interface. The Van Leer splitting has the advantage over more conventional splittings that it is continuously differentiable, and allows shocks to be captured with at most two interior zones.

- Split fluxes into forward and backward contributions

$$F(Q) = F^+(Q^-) + F^-(Q^+)$$
- Use upwind biased approximation to spatial derivatives
- Van Leer splitting
 - Continuously differentiable
 - Allows shocks to be captured with at most two (usually one) interior zones



NUMERICAL METHOD

An implicit, upwind-biased, finite-volume scheme is used to numerically solve the thin-layer Navier-Stokes equations. The system of equations is approximately factored and solved in two sweeps. The (+) and (-) superscripts indicate positive and negative flux split quantities. All viscous terms are centrally differenced. The A, B, and M matrices arise from linearizations of the G flux, H flux, and the viscous terms, respectively. The method is second order accurate in space and first order accurate in time. The algebraic eddy viscosity Baldwin-Lomax turbulence model⁴ is used for all turbulent flow computations. Boundary conditions are applied explicitly.

Upwind Finite-Volume Approximate-Factorization

$$[\frac{I}{J\Delta t} + \partial_\eta^- A^+ + \partial_\eta^+ A^-] \Delta Q^* = -RHS$$

$$[\frac{I}{J\Delta t} + \partial_\zeta^- B^+ + \partial_\zeta^+ B^- - \overline{Re}^{-1} \partial_\zeta J^{-1} M(\zeta)] \Delta Q^n = \frac{\Delta Q^*}{J\Delta t}$$

$$RHS = \partial_\eta^- \hat{G}^+ + \partial_\eta^+ \hat{G}^- + \partial_\zeta^- \hat{H}^+ + \partial_\zeta^+ \hat{H}^- \\ - \overline{Re}^{-1} \partial_\zeta [J^{-1}(\zeta_x R + \zeta_y S)]$$

TURBULENCE MODEL: BALDWIN-LOMAX

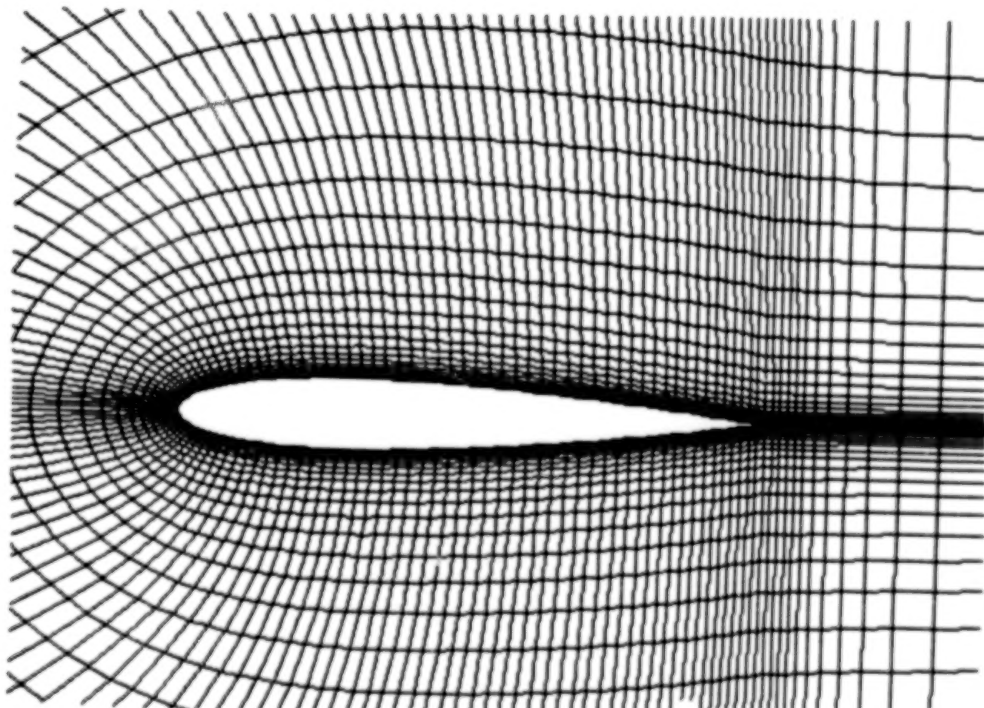
BOUNDARY CONDITIONS: NO-SLIP, ADIABATIC WALL ON BODY

CHARACTERISTIC ANALYSIS IN FARFIELD

AIRFOIL GRID

This figure shows a partial view of a representative grid used in the airfoil calculations. It is a 193 x 65 C-mesh with clustering in the leading and trailing edge regions. Average minimum normal spacing on the body is 6.4×10^{-6} c. The grid extends 30 chords from the airfoil.

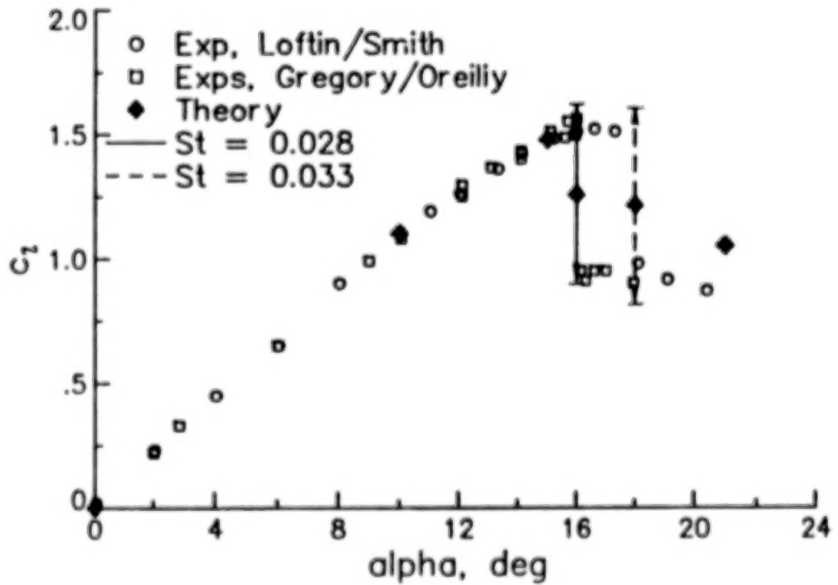
193 x 65 C-mesh



CONSTANT ANGLE-OF-ATTACK UNSTEADY SOLUTIONS

The NACA 0012 airfoil was analyzed at a Reynolds number of 3 million and a Mach number of 0.3 at several angles-of-attack up to and beyond stall. This figure shows computed lift coefficient versus angle-of-attack, α , in comparison with the experiments of Loftin and Smith⁵ and Gregory and O'Reilly⁶. At 0, 10, and 15 deg., computed values are in excellent agreement with experimental results. At both 16 and 18 deg. angle-of-attack, within the region where experiment indicates stall accompanied by a sudden drop in lift, the computed flowfield is unsteady and periodic with lift coefficients varying in the ranges indicated in the figure. The maximum and minimum lift values agree well with the corresponding experimental values before and after stall, respectively. The Strouhal number of the periodic flow is given by $St = nc \sin \alpha / u_\infty$, where n is the frequency of oscillation, c is the airfoil chord, α is the angle-of-attack, and u_∞ is the freestream flow velocity. At 21 deg., the periodic oscillation is no longer present. The results indicate a nearly steady solution, with only a small non-periodic variation in lift coefficient about an average value of about 1.05.

NACA 0012 airfoil, $Re = 3$ million

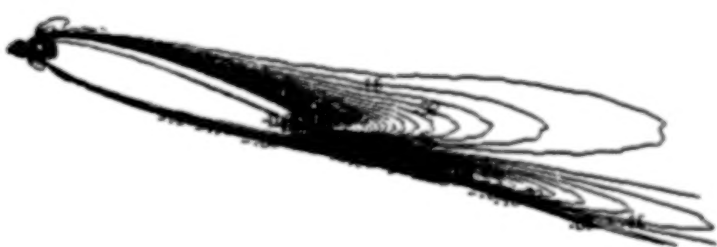


STEADY VORTICITY CONTOURS

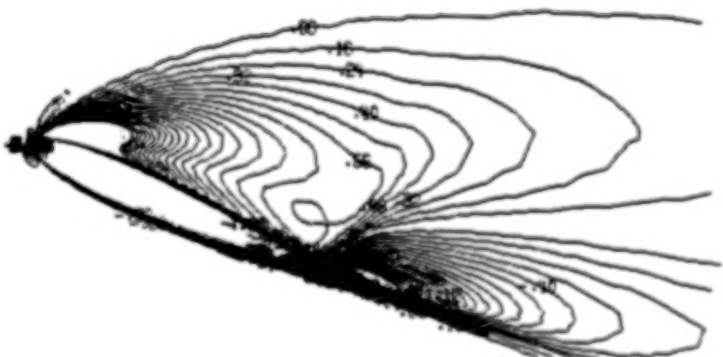
Computed vorticity contours are shown for the NACA 0012 airfoil at 15 and 21 deg. angle-of-attack. At 15 deg., prior to stall onset, the vorticity is concentrated in a relatively thin-layer near the airfoil surface and behind the trailing edge. At 21 deg. the airfoil shows a region of massive separation above the airfoil upper surface. Vorticity levels are much higher than the 15 deg. case, with the strongest clockwise vorticity concentrated near the leading edge on the upper surface and the strongest counterclockwise vorticity again behind the trailing edge.

NACA 0012 airfoil, $Re = 3$ million

$\alpha = 15^\circ$
 $c_L = 1.48$



$\alpha = 21^\circ$
 $c_L = 1.05$



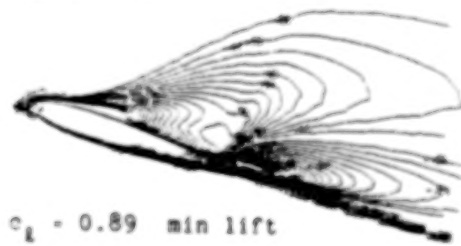
UNSTEADY VORTICITY CONTOURS

At 16 deg. angle-of-attack, the flowfield oscillates in a periodic manner, with the lift varying between a minimum of 0.89 and a maximum of 1.60. Vorticity contours are shown at four points in the unsteady periodic cycle. The cyclic nature of the flowfield is characterized by the shedding of a leading edge vortex near maximum lift.

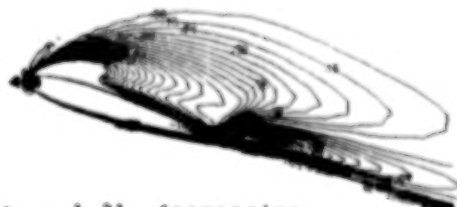
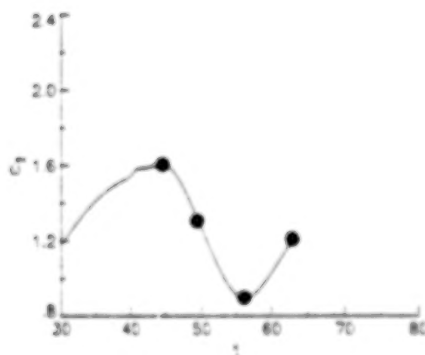
NACA 0012 airfoil, $Re = 3$ million, $\alpha = 16^\circ$



$c_L = 1.60$ max lift



$c_L = 0.89$ min lift



$c_L = 1.31$ decreasing



$c_L = 1.21$ increasing

FORCED PITCHING SOLUTIONS

Computations have been performed in which the airfoil undergoes a forced pitching motion about its quarter chord. Two types of motion have been explored and results compared with experiment. The first is a sinusoidal pitching motion at high Reynolds number (turbulent flow) and the second is a constant-rate pitch from 0 to 60 deg. angle-of-attack at $Re = 45,000$ (laminar flow).

$$\alpha(\tau) = \alpha_0 + \alpha_1 \sin(M_a k\tau) \quad \text{sinusoidal pitch}$$

$$\alpha(\tau) = \alpha_0 + M_a k\tau \quad \text{constant-rate pitch}$$

k = reduced frequency = $\omega c/u_\infty$

ω = frequency (rad/sec)

c = chord

u_∞ = freestream velocity

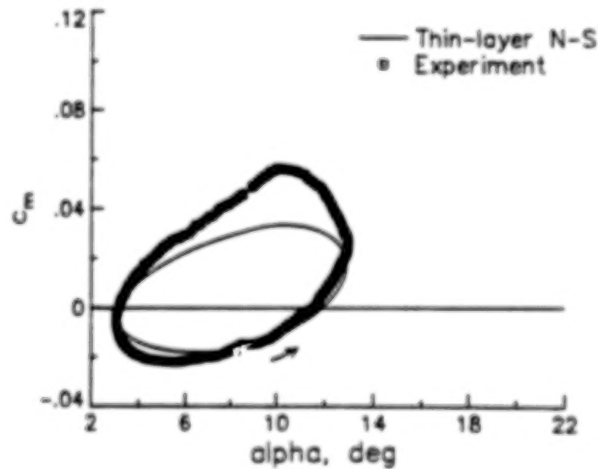
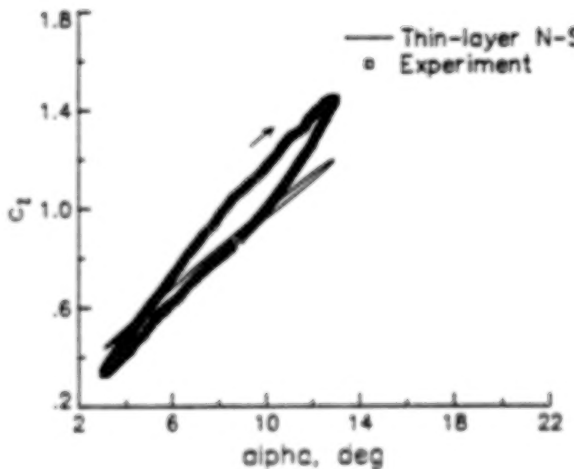
τ = time, nondimensionalized by c/a_∞

a_∞ = freestream speed of sound

SINUSOIDAL PITCH SOLUTION WITH NO STALL

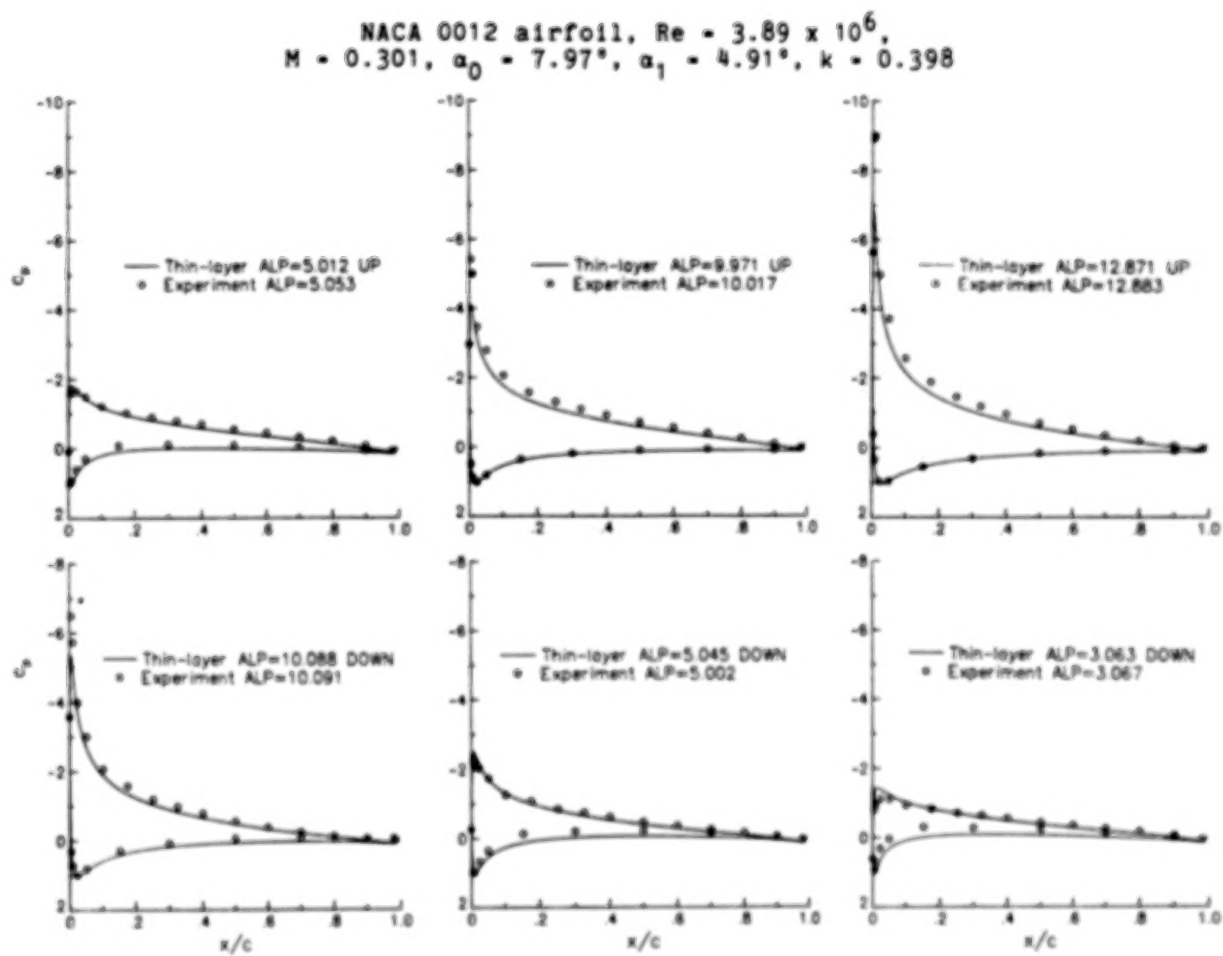
The NACA 0012 airfoil was analyzed at $Re = 3.89 \times 10^6$, $M = 0.301$, $\alpha_0 = 7.97$ deg., $\alpha_1 = 4.91$ deg., and a reduced frequency $k = 0.398$. This corresponds with Case 7111 from McCroskey et al⁷. Transition to turbulence is fixed at the leading edge in the computations but was not fixed in the experiment. The time step taken for the computations is 0.05. This figure shows the lift and moment coefficients as a function of angle-of-attack. The thin-layer Navier-Stokes code predicts a shallower lift versus alpha slope, slightly overpredicting the minimum lift and underpredicting the maximum lift. Lift values for increasing alpha are on the upper half of the lift curve for both theory and experiment. The moment coefficient is in good agreement with experiment when angle-of-attack is increasing (lower half of the curve), but underpredicts the moment when angle-of-attack is decreasing.

NACA 0012 airfoil, $Re = 3.89 \times 10^6$,
 $M = 0.301$, $\alpha_0 = 7.97^\circ$, $\alpha_1 = 4.91^\circ$, $k = 0.398$



PRESSURE COEFFICIENTS

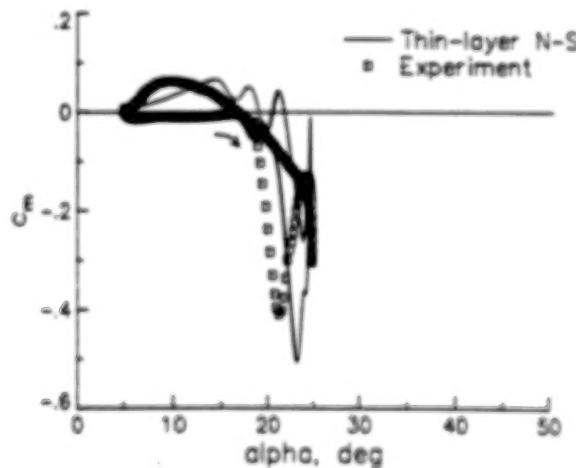
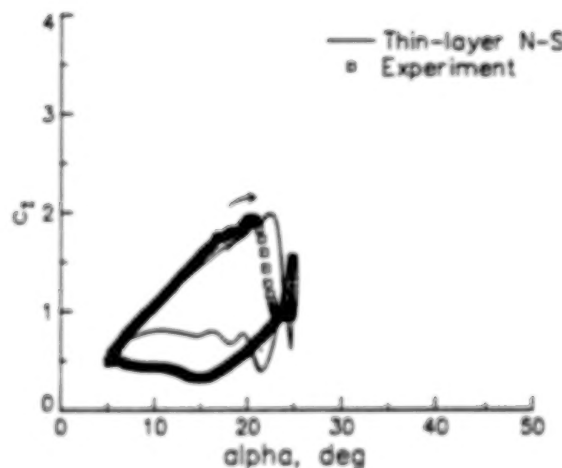
Pressure coefficients are compared with experiment at six times in the pitching cycle for Case 7111. Overall, the present method does well in predicting the shapes of the pressure curves.



SINUSOIDAL PITCH SOLUTION WITH DEEP STALL

A solution with deep stall was computed at $Re = 3.76 \times 10^6$, $M = 0.292$, $\alpha_0 = 14.84$ deg., $\alpha_1 = 9.88$ deg., $k = 0.202$. These conditions correspond with Case 14210 from McCroskey et al⁷. In this case, both theory and experiment fixed transition to turbulence at the leading edge. Time step for the computations is 0.05. As seen from plots of lift and moment coefficient versus angle-of-attack, the computations agree well with experiment only as the angle-of-attack is increasing (upper portion of the lift curve, lower portion of the moment curve). However, theory predicts stall later than experiment. At all other points in the pitching cycle, theory and experiment are only qualitatively similar. Theory shows oscillations, which are not present in the experiment, in the lift and moment curves as the angle-of-attack decreases.

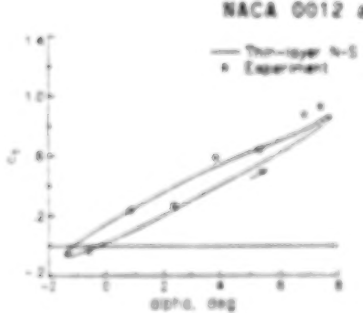
NACA 0012 airfoil, $Re = 3.76 \times 10^6$,
 $M = 0.292$, $\alpha_0 = 14.84^\circ$, $\alpha_1 = 9.88^\circ$, $k = 0.202$



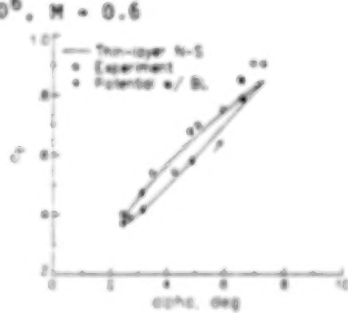
AGARD CASE SINUSOIDAL PITCH SOLUTIONS

Computations were performed to compare with two unsteady solutions from Landon⁸. The first, corresponding with AGARD Case 2, is at $Re = 4.8 \times 10^6$, $M = 0.6$, $\alpha_0 = 3.16$ deg., $\alpha_1 = 4.59$ deg., $k = 0.1622$. The second corresponds with AGARD Case 3: $Re = 4.8 \times 10^6$, $M = 0.6$, $\alpha_0 = 4.86$ deg., $\alpha_1 = 2.44$ deg., $k = 0.1620$. Lift and moment coefficients for each case are shown in the figure. In both cases, for theory and experiment, the lift values for increasing alpha are on the lower portion of the curve. The computations do fairly well to predict lift at the lower angles-of-attack but underpredict the lift at the high end of the cycles. Moment coefficients are underpredicted everywhere in the cycles, although for alpha increasing (lower portion of the curve) results are in closer agreement than for alpha decreasing. Results for Case 3 are very similar to those obtained by Howlett⁹ using a small-disturbance potential code coupled with an inverse boundary-layer method. Howlett found that results near maximum lift are highly sensitive to the transition location. His results shown here have transition set at 20%. The thin-layer Navier-Stokes computations set transition at the leading edge, while experimental transition is unspecified.

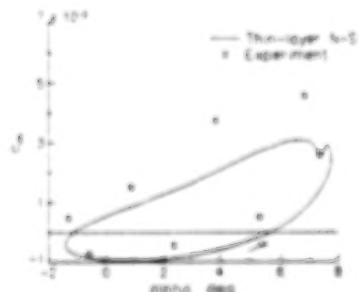
AGARD Case 2



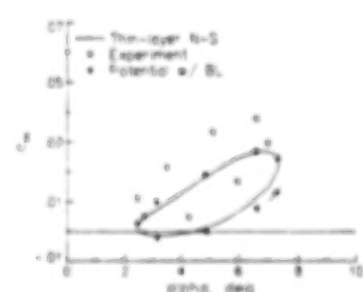
AGARD Case 3



NACA 0012 airfoil, $Re = 4.8 \times 10^6$, $M = 0.6$



$\alpha_0 = 3.16^\circ$, $\alpha_1 = 4.59^\circ$, $k = 0.1622$



$\alpha_0 = 4.86^\circ$, $\alpha_1 = 2.44^\circ$, $k = 0.1620$

FORCE COMPONENTS AND PHASE LAG

The real and imaginary components of lift and drag were computed for AGARD Cases 2 and 3 and compared with experiment. Agreement is fair, with the largest discrepancies in the imaginary component of moment for both cases. The values α_l and α_m are the phase angles by which lift and moment cycles lead or lag the angle-of-attack cycle.

$$c_{laR} = \frac{2}{\alpha_l(t_2 - t_1)} \int_{t_1}^{t_2} [c_l(\tau) - c_{lavg}] \sin(M_k \tau) d\tau$$

$$c_{laI} = \frac{2}{\alpha_l(t_2 - t_1)} \int_{t_1}^{t_2} [c_l(\tau) - c_{lavg}] \cos(M_k \tau) d\tau$$

and similar expressions for c_{maR} and c_{maI}

AGARD Case 2

AGARD Case 3

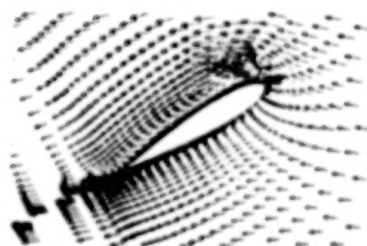
	Exp	Theory	Error	Exp	Theory	Error
c_{laR}	6.616	5.67	14.3%	6.372	5.56	12.7%
c_{laI}	-0.891	-0.88	1.2%	-0.803	-0.75	6.6%
c_{maR}	0.224	0.172	23.2%	0.303	0.258	14.9%
c_{maI}	-0.244	-0.165	32.4%	-0.287	-0.200	30.3%
α_l	-7.7°	-8.8°	14.3%	-7.2°	-7.7°	6.9%
α_m	-47.4°	-43.6°	8.0%	-43.4°	-37.8°	12.9%

CONSTANT-RATE PITCH SOLUTIONS, $\omega = 460$ DEG/SEC

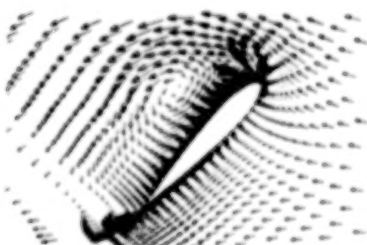
At a Reynolds number of 45,000, laminar flow computations of an NACA 0015 airfoil pitched up at a constant rate of 460 deg./sec ($k = 0.2007$) are compared with smoke wire flow visualizations of Helin and Walker¹⁰. Three angles-of-attack are shown in the figure. Flow is from right to left. With a time step of 0.05, computed velocity vectors show the same general trend as experiment, although the center of the shed leading-edge vortex does not convect downstream as quickly in the computations as it does in the experiment. At both 45 and 60 deg., there is reversed flow over most of the airfoil upper surface, due to the shed vortex.

NACA 0015 airfoil, $Re = 45,000$, laminar flow
 $\omega = 460$ deg./sec

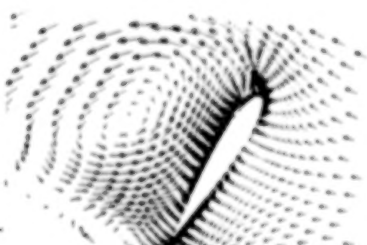
COMPUTATION



$\alpha = 30^\circ$

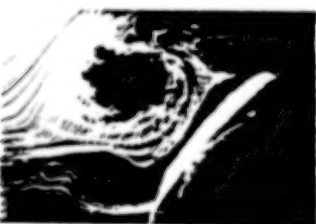
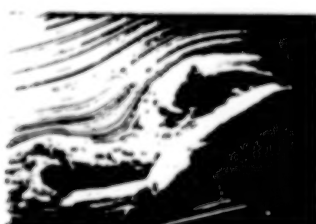


$\alpha = 45^\circ$



$\alpha = 60^\circ$

EXPERIMENT



CONSTANT-RATE PITCH SOLUTIONS, $\omega = 1380$ DEG/SEC

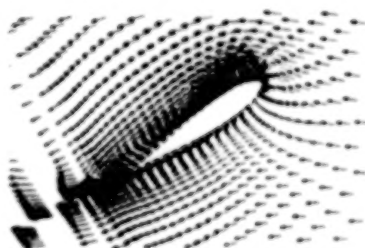
At a higher rate of pitch ($k = 0.6021$), computation with a time step of 0.02 shows a leading-edge vortex growth rate in good agreement with experiment. This vortex is much smaller in size than that for the lower pitch rate of 460 deg./sec. However, the computational analysis does not show the second region of separated flow near the trailing edge that is seen in the flow visualizations.

NACA 0015 airfoil, $Re = 45,000$, laminar flow

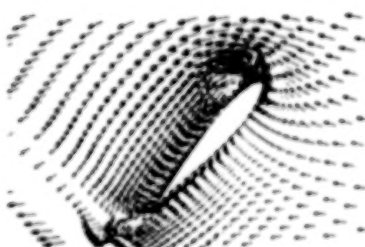
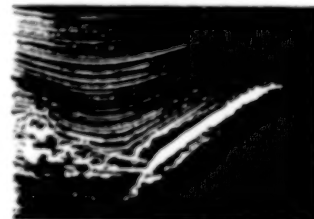
COMPUTATION

$\omega = 1380$ deg./sec

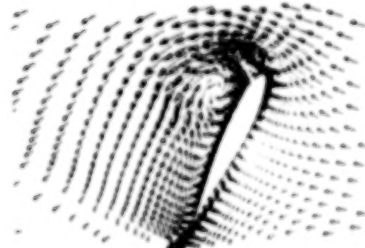
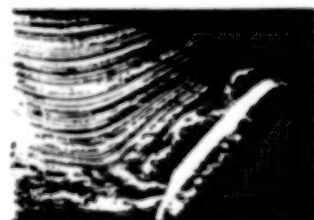
EXPERIMENT



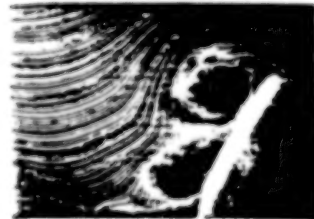
$\alpha = 30^\circ$



$\alpha = 45^\circ$



$\alpha = 60^\circ$



CONCLUSIONS

A finite volume implicit approximate factorization method which solves the thin-layer Navier-Stokes equations has been used to predict unsteady turbulent-flow airfoil behavior. At a constant angle-of-attack of 16 deg., the NACA 0012 airfoil exhibits an unsteady periodic flowfield with the lift coefficient oscillating between 0.89 and 1.60. The Strouhal number is 0.028. Results are similar at 18 deg., with a Strouhal number of 0.033. A leading-edge vortex is shed periodically near maximum lift.

Dynamic mesh solutions for unstalled airfoil flows show general agreement with experimental pressure coefficients. However, moment coefficients and the maximum lift value are underpredicted. The deep stall case shows some agreement with experiment for increasing angle-of-attack, but is only qualitatively comparable past stall and for decreasing angle-of-attack. Laminar-flow computations of a constant-rate pitch-up NACA 0015 airfoil show that increasing pitch rate slows separation. Computed velocity vectors agree qualitatively with experimental flow visualizations.

- CONSTANT ANGLE-OF-ATTACK
 - NACA 0012 FLOWFIELD UNSTEADY AT $\alpha = 16$ AND 18 DEG.
 - lift oscillates within range of experiment
 - $St = 0.03$
 - PERIODICALLY SHED LEADING-EDGE VORTEX
- SINUSOIDAL PITCH
 - UNSTALLED CASES
 - pressure coefficients agree in general with experiment
 - moment coefficients and maximum lift underpredicted
 - DEEP STALL AGREES ONLY FOR α INCREASING
- CONSTANT-RATE PITCH
 - INCREASING PITCH RATE LESSENS SEPARATION
 - QUALITATIVE AGREEMENT WITH EXPERIMENT

REFERENCES

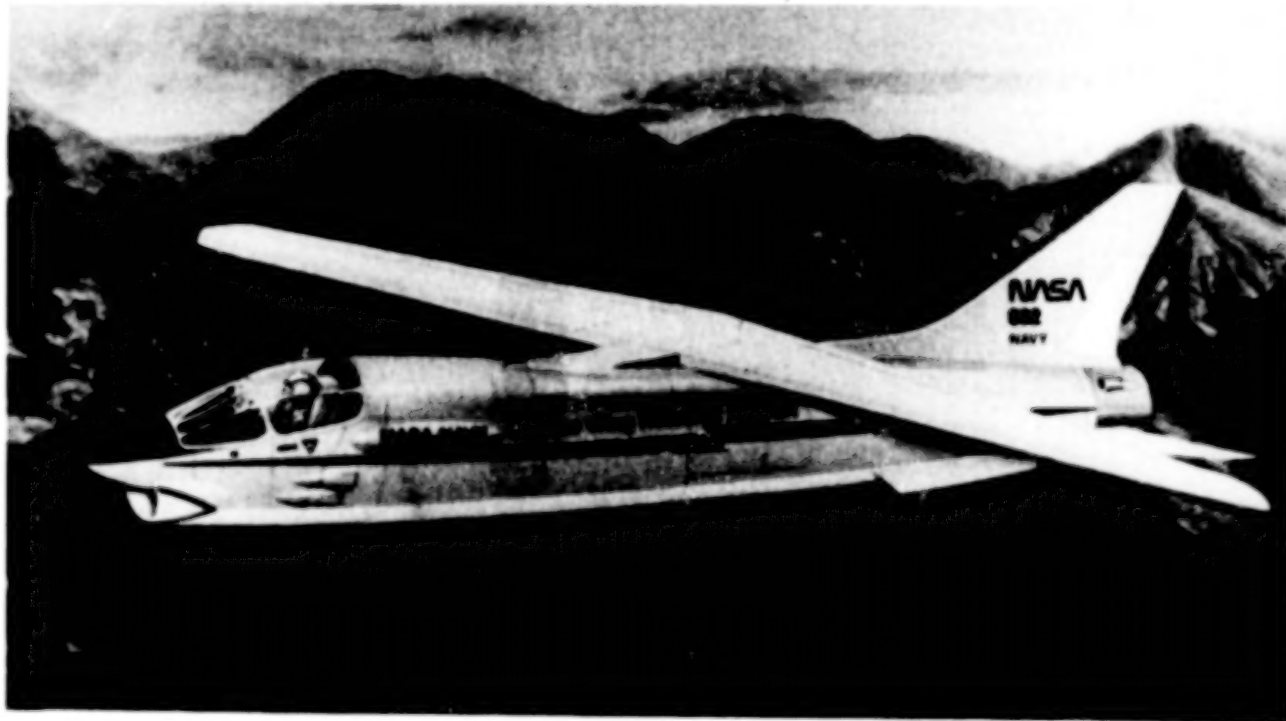
1. Van Leer, B., "Flux-Vector Splitting for the Euler Equations," Lecture Notes in Physics, Vol. 170, 1982, pp. 501-512.
2. Anderson, W., Thomas, J., and Rumsey, C., "Extension and Applications of Flux-Vector Splitting to Unsteady Calculations on Dynamic Meshes," AIAA Paper 87-1152-CP, 1987.
3. Van Leer, B., "Towards the Ultimate Conservation Difference Scheme V. A Second Order Sequel to Gudonov's Method," Journal of Computational Physics, Vol. 32, 1979, pp. 101-136.
4. Baldwin, B. and Lomax, H., "Thin Layer Approximation and Algebraic Model for Separated Turbulent Flows," AIAA Paper 78-257, 1978.
5. Loftin, L., Jr. and Smith, H., "Aerodynamic Characteristics of 15 NACA Airfoil Sections at Seven Reynolds Numbers from 0.7×10^6 to 9.0×10^6 ," NACA TN 1945, 1949.
6. Gregory, N. and O'Reilly, C., "Low-Speed Aerodynamic Characteristics of NACA 0012 Aerofoil Section, Including the Effects of Upper Surface Roughness Simulating Hoar Frost," NASA R&M 3726, 1970.
7. McCroskey, W., McAlister, K., Carr, L., and Pucci, S., "An Experimental Study of Dynamic Stall on Advanced Airfoil Sections," NASA TM 84245, 1982.
8. Landon, R., "NACA 0012. Oscillatory and Transient Pitching," Compendium of Unsteady Aerodynamic Measurement, AGARD-R-702.
9. Howlett, J., "Viscous Flow Calculations for the AGARD Standard Configuration Airfoils with Experimental Comparisons," Langley Symposium on Transonic Unsteady Aerodynamics and Elasticity, 1987, NASA CP 3022, pp. 313- 350.
10. Helin, H. and Walker, J., "Interrelated Effects of Pitch Rate and Pivot Point on Airfoil Dynamic Stall," AIAA Paper 85-0130, 1985.

**THE OBLIQUE-WING RESEARCH AIRCRAFT:
A TEST BED FOR UNSTEADY AERODYNAMIC
AND
AEROELASTIC RESEARCH**

**Glenn B. Gilyard, NASA Oblique-Wing Chief Engineer
NASA Ames Research Center
Dryden Flight Research Facility
Edwards, California**

OBLIQUE-WING RESEARCH AIRCRAFT PROGRAM

The advantages of oblique-wings have been the subject of numerous theoretical studies, wind tunnel tests, low speed flight models, and finally a low speed manned demonstrator, the AD-1(ref. 1). An oblique-wing configuration is well suited for a Navy fleet defense mission and a supersonic transport (Mach < 1.6). An excellent review of the historical development of oblique-wing technology is presented in reference 2; references 3 and 4 discuss potential applications. NASA's Oblique-Wing Research Aircraft (OWRA) program is directed at the development and flight test of a full scale supersonic demonstrator which will address the key technological challenges. The specific objectives of the OWRA program are 1) establish the necessary technology base required to translate theoretical and experimental results into practical, mission oriented designs, 2) design, fabrication and flight test an oblique-wing aircraft throughout a realistic flight envelope, and 3) develop and validate design and analysis tools for asymmetric aircraft configurations.



Objectives

- Establish a technology base for oblique wing concepts which can be applied to mission-oriented aircraft designs

- Design, fabricate, and flight test an oblique wing throughout a realistic flight envelope
- Develop and evaluate design tools for asymmetric aero-dynamic configurations

OBLIQUE-WING AERODYNAMIC ADVANTAGES

Theoretical aerodynamic advantages of oblique wings have been the subject of numerous studies over the years. The variable sweep aspect of course permits optimization with Mach number thus yielding efficient flight for the subsonic cruise/loiter condition while also providing for efficient supersonic dash/cruise capability. As shown in the figure the induced drag is minimized for a zero sweep, maximum aspect ratio condition; this advantage is independent of symmetrically swept or obliquely swept aircraft. In the supersonic regime, the oblique type wing has a significant advantage (over a symmetrically swept wing) in that it produces less wave drag since the wing volume is distributed over a greater length.

Surpasses Variable Sweep for Mixed Missions

- Efficient subsonic cruise/loiter

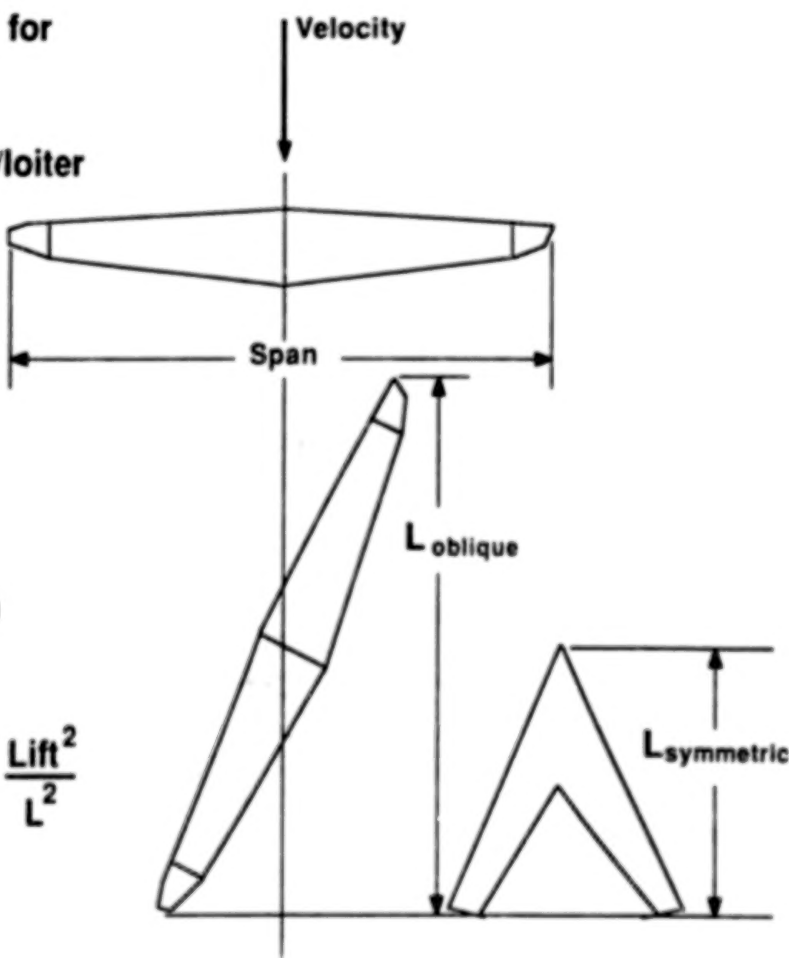
High aspect ratio

$$\text{Drag due to lift} \sim \frac{\text{Lift}^2}{\text{Span}^2}$$

- Efficient supersonic dash

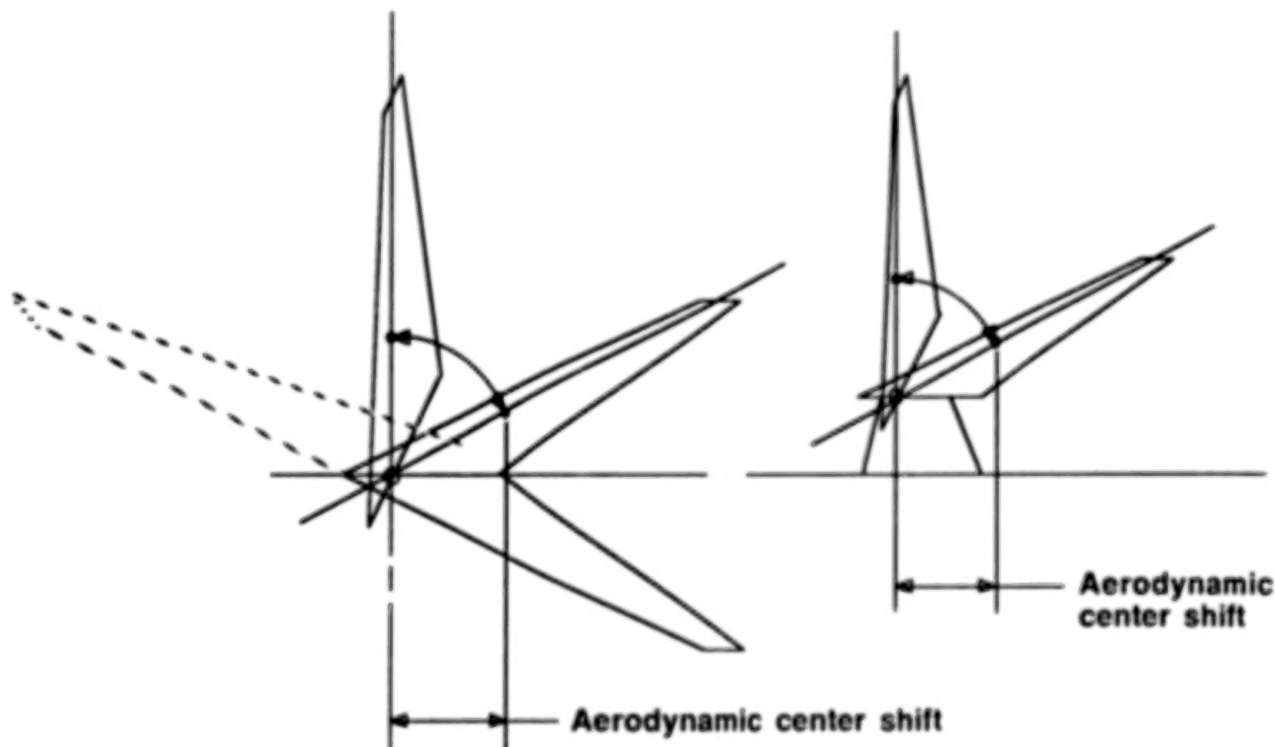
Low aspect ratio

$$\text{Wave drag} \sim \frac{\text{Vol}^2}{\text{L}^4} + \frac{\text{Lift}^2}{\text{L}^2}$$



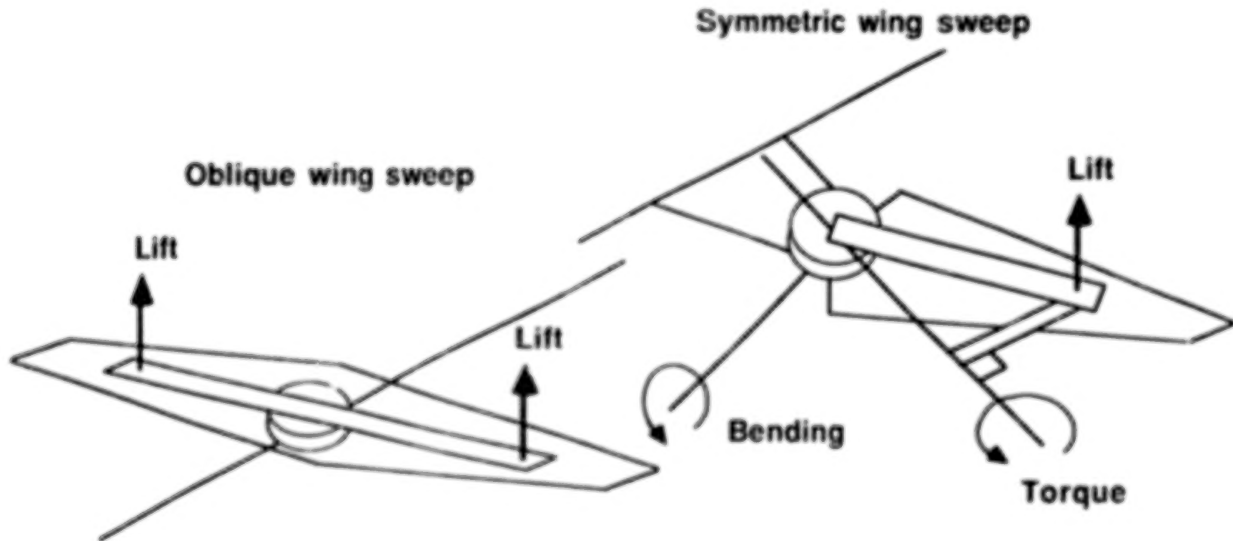
OBLIQUE-WING AERODYNAMIC CENTER SHIFT

An oblique-wing configuration also provides a major advantage in that sweep does not produce an aerodynamic center shift as does a symmetric swept configuration. This minimizes trim drag penalties due to aerodynamic center shifts and reduces tail loads, thus resulting in a lighter structure and eliminating center-of-gravity control as a function of wing sweep.



OBLIQUE-WING STRUCTURAL ADVANTAGE

An oblique-wing configuration has a number of significant structural advantages over a symmetrically swept wing configuration, the most obvious being a single pivot requirement. A single pivot results in both cost and weight savings and other factors that accrue from maintaining one as opposed to two pivots. On an oblique-wing, the lift forces pass essentially through the center of the pivot independent of sweep angle, thus minimizing bending and torque loads transmitted through the pivot. For symmetrical swept configurations, offset lift forces produce significant bending and torque forces transmitted through the pivot, which in turn requires a 'beefed-up' pivot/substructure assembly and results in a major weight penalty.



- Pivot torque and bending loads avoided
- Inboard wing torque loads avoided
- Single pivot

OWRA UNSTEADY PRESSURE MEASUREMENT EXPERIMENT

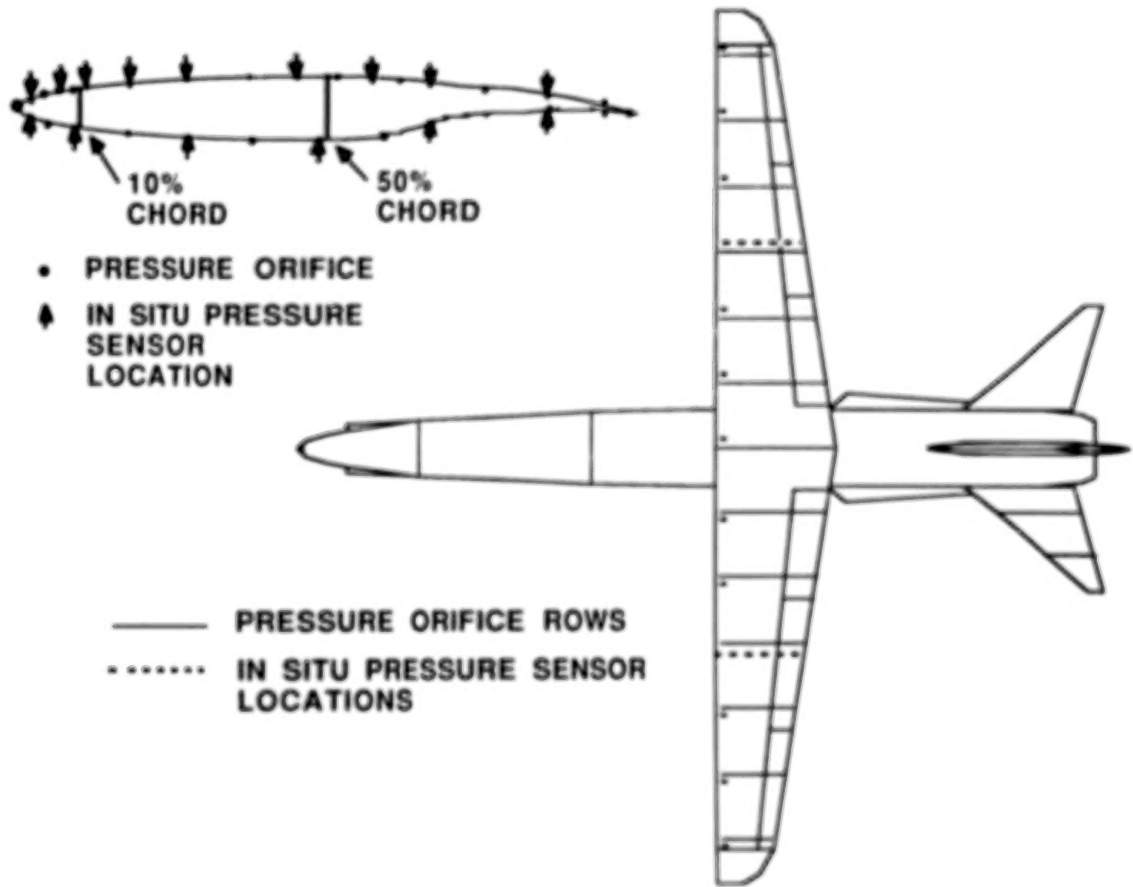
Efficient aircraft design increasingly relies on predictions; therefore, in an attempt to improve vehicle aeroelastic design and prediction techniques, an experiment will be implemented on the OWRA which will measure unsteady pressures. The unsteady pressure survey will use remote sensing (pneumatic lines) to measure pressures on thirteen chords covering the full span of the wing; each chord will consist of approximately 30 orifices and will be sampled 400 times per second. The approach is similar to that reported for the laboratory experiment of reference 5 and the wind tunnel test of reference 6. A limited number of in situ measurements will be taken and used to correct the pneumatic measurements for magnitude and phase. Controlled data will be gathered using preprogrammed aileron excitation algorithms. The data base will be used for correlation with currently used unsteady aero codes and will also provide a valuable data base for evaluation of future codes. It is anticipated that the unsteady pressure measurements will prove valuable in analysis of other unique flow phenomena and provide insight into effects such as vortex flow patterns and vortex and/or shock induced oscillations should they occur.

Objectives:

- **Develop unsteady pressure data base**
 - Full span**
 - 13 chords; 30 orifices/chord**
 - 400 samples per second**
- **Correlation with current unsteady codes**
- **Data base for future code development**
- **Identify unique flow phenomena**
 - Vortex flow**
 - Vortex / shock induced oscillations**

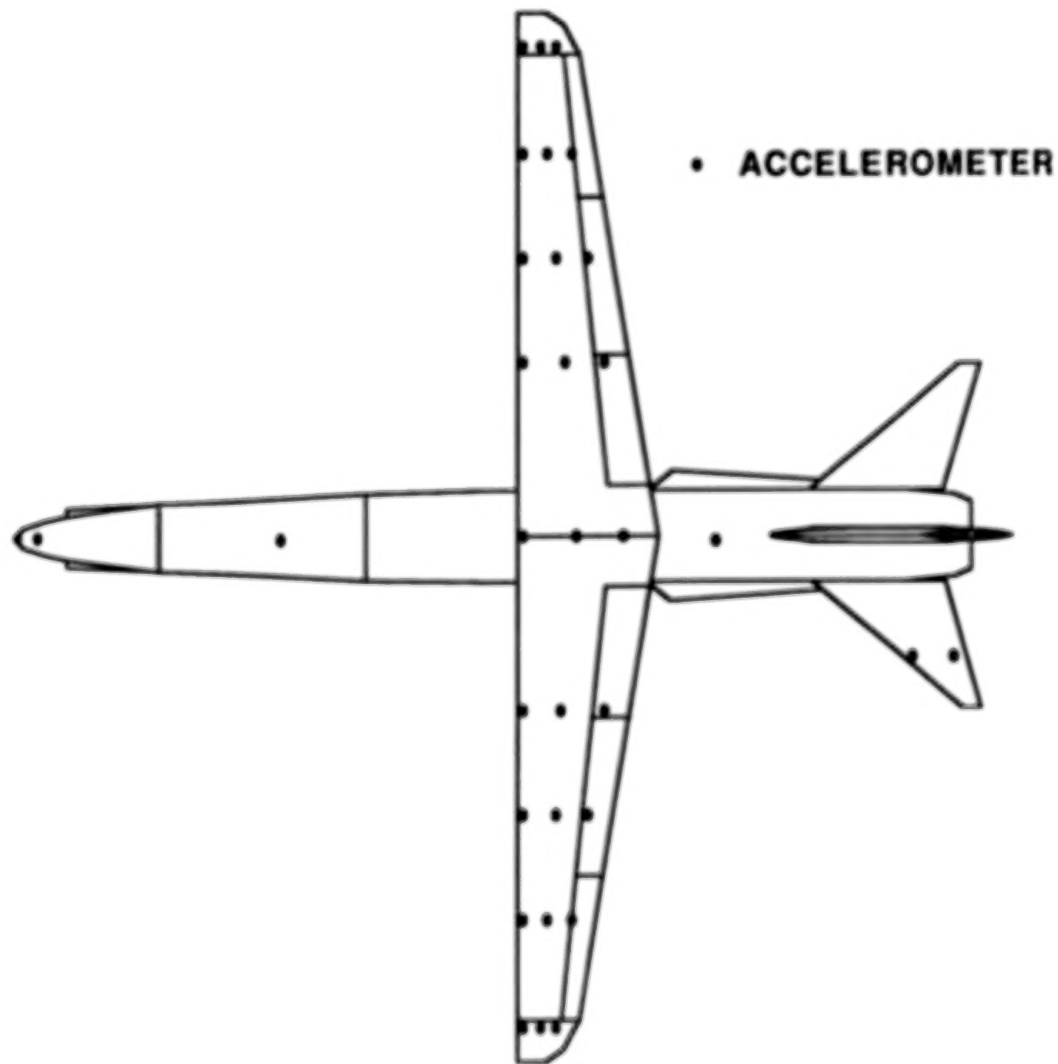
OWRA UNSTEADY PRESSURE SENSOR LAYOUT

A pressure sensing system will be implemented on the OWRA which will be capable of measuring both static and unsteady pressures. The primary system will acquire data pneumatically using remotely located electronically scanned pressure (ESP) modules located either in front of the forward spar or aft of the rear spar. This arrangement will provide a cost effective and readily maintainable system since access to the wing box will not be possible after it is sealed. The pneumatic system will consist of equal lengths of tubing connecting the orifices and the transducer. Current plans call for use of approximately 4 foot lengths of 0.060 " ID tubing. The data will be corrected based on in situ unsteady pressure measurements made at two chord locations and one in situ measurement made for each of the other chord locations. At the maximum skew angle of 65 degrees, the left wing overlays the left horizontal stabilizer and as such, leads to interesting aerodynamic interactions. In order to assist in analysis of this effect, unsteady pressures will also be measured for two horizontal tail chord locations.



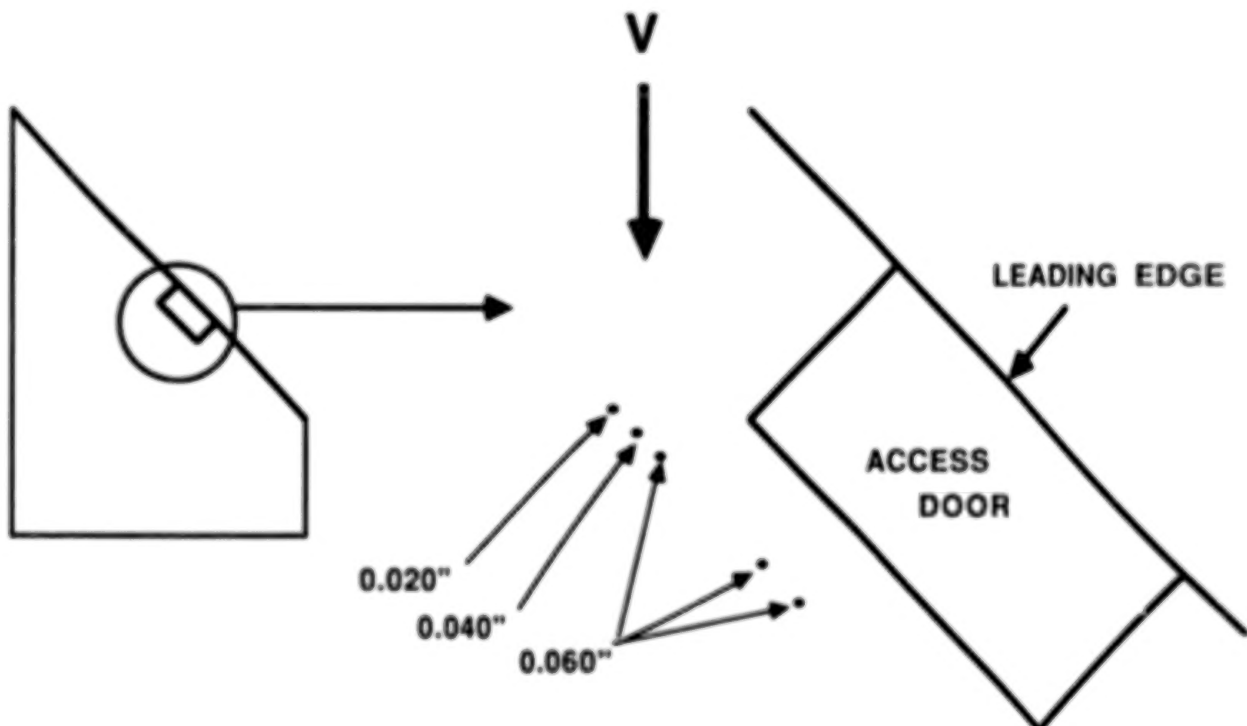
OWRA MODAL RESPONSE SURVEY LAYOUT

Correlation of predicted and experimental unsteady aerodynamics requires an accurate mode shape of the wing. The figure below illustrates the planview layout for accelerometers used for defining the wing mode shape. In addition, these accelerometers will in general meet the requirements for flutter and aeroservoelastic stability clearance work. The unsymmetric nature of the OWRA leads to unsymmetrical leading edge suction forces which could in turn develop significant in-plane wing motion. Therefore triaxial accelerometers will be located along the wing. Additional accelerometers will also be located on the fuselage to identify later bending and torsional characteristics. The sample rate of the accelerometers will be identical to the rate used for unsteady pressure measurements.



F-15 UNSTEADY PRESSURE EXPERIMENT

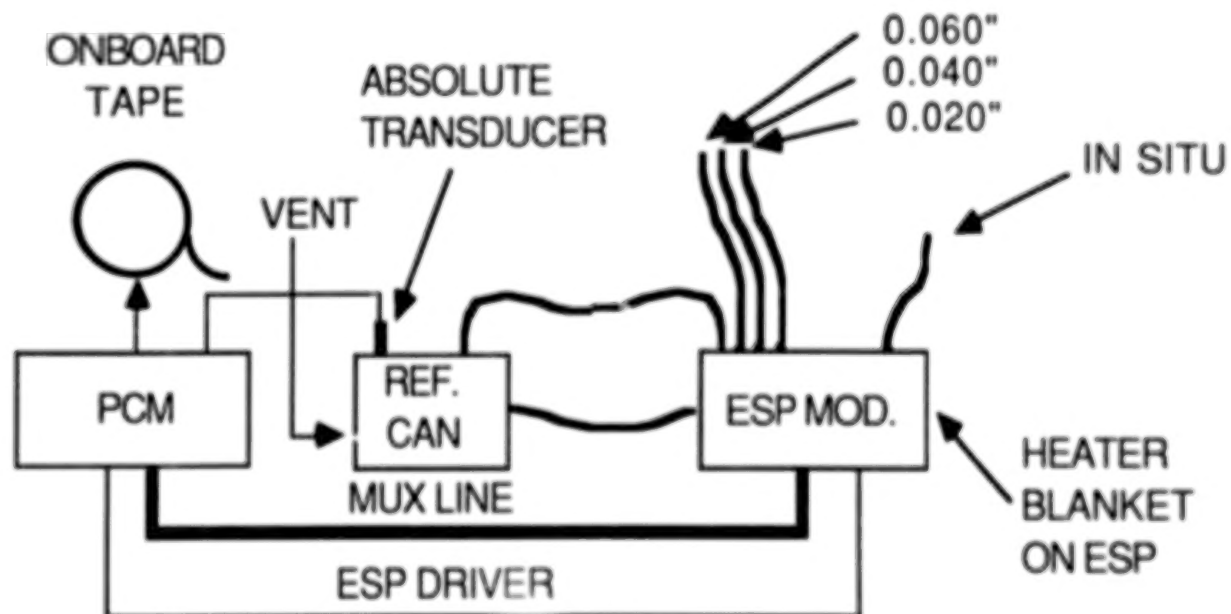
A validation of the unsteady pressure measurement system proposed for the OWRA was conducted on an F-15 experimental aircraft at Dryden. The validation consisted primarily of a parametric evaluation of line length and orifice/tubing diameters. An auxiliary objective was to demonstrate that the ESP module could be driven and data recorded at 500 samples/sec in a flight environment with no adverse effects on data quality. The experiment consisted of orifices located at 10% chord, one-half inch apart, and approximately mid-span on the upper surface of the right wing of the F-15. The orifice/tubing inside diameters evaluated were 0.020, 0.040, and 0.060 inches with tubing lengths of two, four, and eight feet being changeable between flights. An in situ measurement consisted of a 0.060 inch orifice/tubing diameter connected to the same ESP module but with a minimal line length, six inches. Flights to date have obtained excellent quality data for both two and four foot line lengths.



F-15 UNSTEADY PRESSURE SYSTEM SCHEMATIC

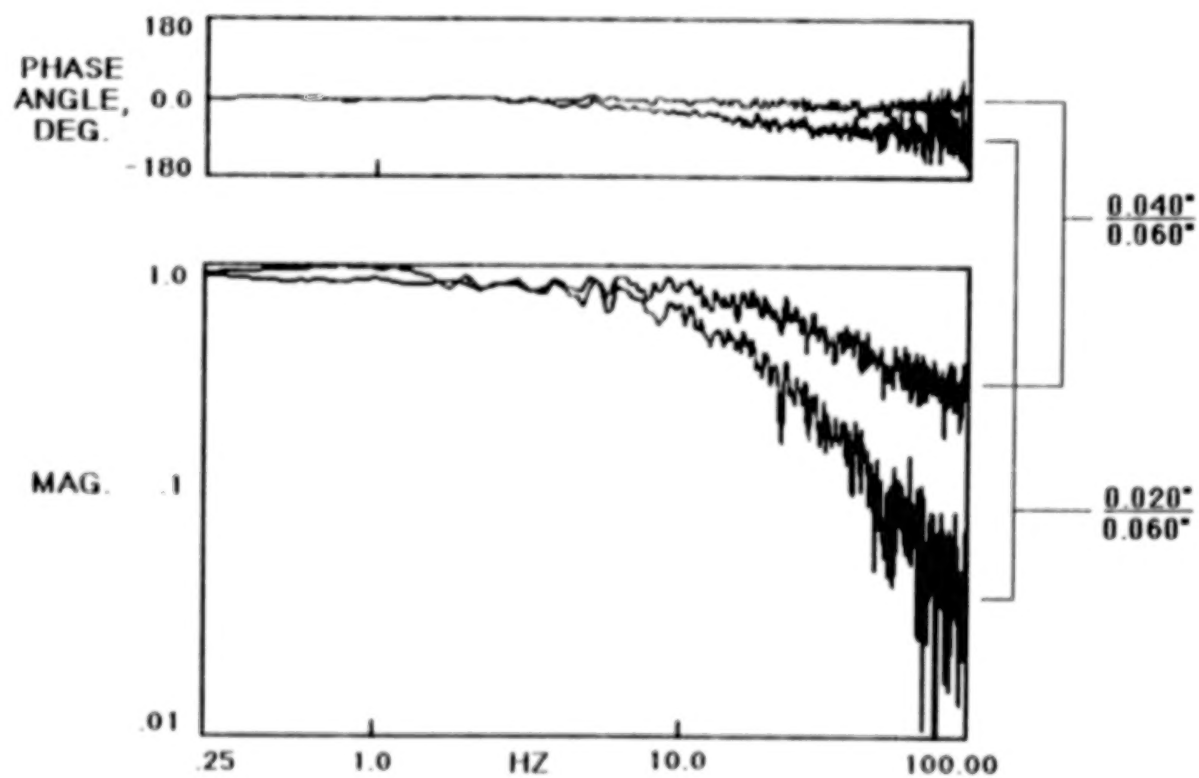
An end-to-end schematic of the instrumentation system used in the F-15 experiment is presented in the figure below. The ESP module consists of 32 flush-diaphragm, strain-gage-type differential-pressure transducers. The reference side of the ESP module is connected to an ambient pressure reservoir which is vented to the interior wing cavity. The purpose of the reservoir is to allow the reference pressure (backside of the ESP differential transducer) to adjust to changes in altitude without any high frequency pressure oscillations. The module multiplexes the individual port measurements with the output routed to a 10 bit PCM system and recorded on on-board tape. There is no signal conditioning of the individual ESP port data prior to multiplexing. The ESP module transducers are ranged for ± 5 psi.

The ESP module is operated and data was recorded at 250 sps for the first few flights and subsequently increased to 500 sps. A heater blanket was installed to maintain a constant temperature on the ESP module. A check on the quality of the PSI transducer is obtained by plumbing one of the ports directly to the reservoir. The absolute transducer on the reference can allows for the absolute chordwise pressure measurements as well. A factor which makes the ESP transducer outstanding for dynamic pressure measurements is its minimal internal volume. The internal diameter of each ESP port is 0.040 inch with no increase in diameter at the diaphragm face and as such the transducer volume can be analytically modeled as a 0.040 inch ID line length extension to the orifice connecting tubing.



F-15 UNSTEADY PRESSURE TRANSFER FUNCTION ANALYSIS

A transfer function analysis was performed on approximately one minute of data obtained in a moderate g wind up turn at a high subsonic Mach number. Using the 0.060" tubing as the reference, both the 0.040" and 0.020" tubing show little attenuation to at least 10 Hz although the 0.020" tubing does attenuate at a much more rapid rate than the 0.040" tubing once the break frequency is past. The poorer characteristics of the 0.020" tubing are also indicated by its significantly worse phase angle. Although not plotted on this figure, the coherence of the two transfer functions was also determined. For the 0.040" transfer function, the coherence starts at one (perfect correlation) for low frequencies and gradually decreases to one-half (reasonably good correlation) at 100 Hz. The 0.020" transfer function also starts at a coherence of one for low frequencies but degrades to a value of zero (no correlation) at approximately 80 Hz.



OWRA FLUTTER MODEL TEST

Unique aerodynamic characteristics of oblique-wing configurations have the potential for producing unusual flutter type characteristics and/or other instabilities. A wind tunnel flutter model test will be performed in the TDT to both provide data for validation of aeroelastic analysis codes prior to first flight and to support an efficient and rapid envelope clearing process. In order to maximize the return on the test, the model will be designed to flutter (or encounter some other type of instability unique to oblique-wing configurations) within the tunnel. Identification of transonic flutter/instability characteristics is of prime importance. There are tentative plans to obtain limited unsteady pressure measurements for both code validation and correlation with flight results. Preliminary studies have been performed to identify critical DOF for flutter model tests of oblique configurations. An 'oblique' mode has been identified with a 5 DOF model which still retains its characteristics with the three rotational DOF's.

Problem: Unique, unsymmetrical configuration presents potential for unusual flutter type instabilities. No flight experience is available for oblique-wing configurations.

Objectives:

- Design model to flutter; test in TDT
- Identify transonic flutter characteristics
- Correlate with predictions
- Identification of unique instability phenomena
- Limited unsteady pressure measurements

Status:

- Identify important DOF
- Preliminary study has identified an 'oblique' mode

FLUTTER/AEROSERVOELASTIC CODE VALIDATION

An interdisciplinary analysis code (STARS), which is capable of performing flutter and aeroservoelastic analyses, has been developed. The structures module has a large library of elements and in conjunction with numerical analysis routines, is capable of efficiently performing statics, vibration, buckling, and dynamic response analysis of structures. In order to accommodate unsymmetrical supersonic conditions, the potential gradient method (PGM) unsteady aero code of Appa is being implemented into the aero module of STARS; subsonic unsteady aero code will continue to be doublet lattice. Linear flutter models are developed and transformed to the body axis coordinate system and are subsequently augmented with the control law. Stability analysis is performed using hybrid techniques. The major research benefit of the OWRA program will be validation of design and analysis tools. As such, the structural model will be validated and updated based on ground vibration test (GVT) results. The unsteady aero codes will be correlated with experimentally measured unsteady pressures.

STARS: In-house analytical code

- **Specialized structural modeling**
- **Efficient matrix manipulation**
- **Implement PGM code**

Validate structural model

- **Fuselage GVT**
- **Wing GVT**
- **Complete A/C GVT**

Validate unsteady aero code with flight data

HIGH ANGLE OF ATTACK AERODYNAMICS

As angle of attack increases, the F-8 OWRA will exhibit non-linearities in all flight axes. At high wing sweeps the increase in spanwise flow and the formation of a leading edge vortex can occur at relatively low angles of attack (6 to 8 deg). Because of the asymmetry of the vehicle these effects will not be balanced in the lateral directional axis. At higher angles of attack, regions of spanwise flow also form in an asymmetric pattern, generally progressing from the trailing wing tip. In addition to these characteristics, which will effect the vehicle flight dynamics, other unusual features have been observed in water tunnel studies such as the interaction of parallel spanwise vortices on the leading wing panel. Further water tunnel studies will be conducted this summer to document the flight configuration and to note distinctions between the various preliminary design planforms. A comprehensive computational fluid dynamics (CFD) analysis is underway at Ames-Moffett to develop a Reynolds averaged Navier-Stokes solution of the complete vehicle. Preliminary results of the wing alone at an angle of attack of 10 deg show good correlation of the spanwise flow and vortex formation with the water tunnel results. During the flight program, unsteady pressure data will be used to identify vortex flow and regions of separated flow. The vehicle is also equipped with a tail mounted camera which can be used for tuft studies and smoke flow visualization. Flight measurements of the vehicle forces and moments will be used for correlation with the flow visualization results. A similar correlation was made during the AD-1 flight program.

Characteristics

- Significant spanwise flow**
- Strong spanwise vortices**
- Asymmetric regions of separated flow**
- Potential dynamic interaction of vortices**

Data Sources

- Water tunnel studies**
- Reynolds averaged Navier Stokes solutions**
- Flight testing**
 - Unsteady pressures**
 - Flow visualization, tufts and smoke**
 - Measured vehicle forces and moments**

OWRA FLIGHT DEFLECTION EXPERIMENT

In order to support research activities on the OWRA, an accurate determination of the wings deflected shape in flight is required to validate the wing stiffness and load distribution predictions which, because of the wings unconventional attitude, could produce some unpredicted pressure distributions. The deflections will also be used for definition of in-flight shape for correlation of CFD codes with flight determined static pressure distributions. The electro-optical system to be used has been developed at Dryden and used quite successfully on both the HiMAT and X-29 aircraft.

OBJECTIVE

Evaluate the ability of analytical codes to predict structural loads and deflections and pressure distributions

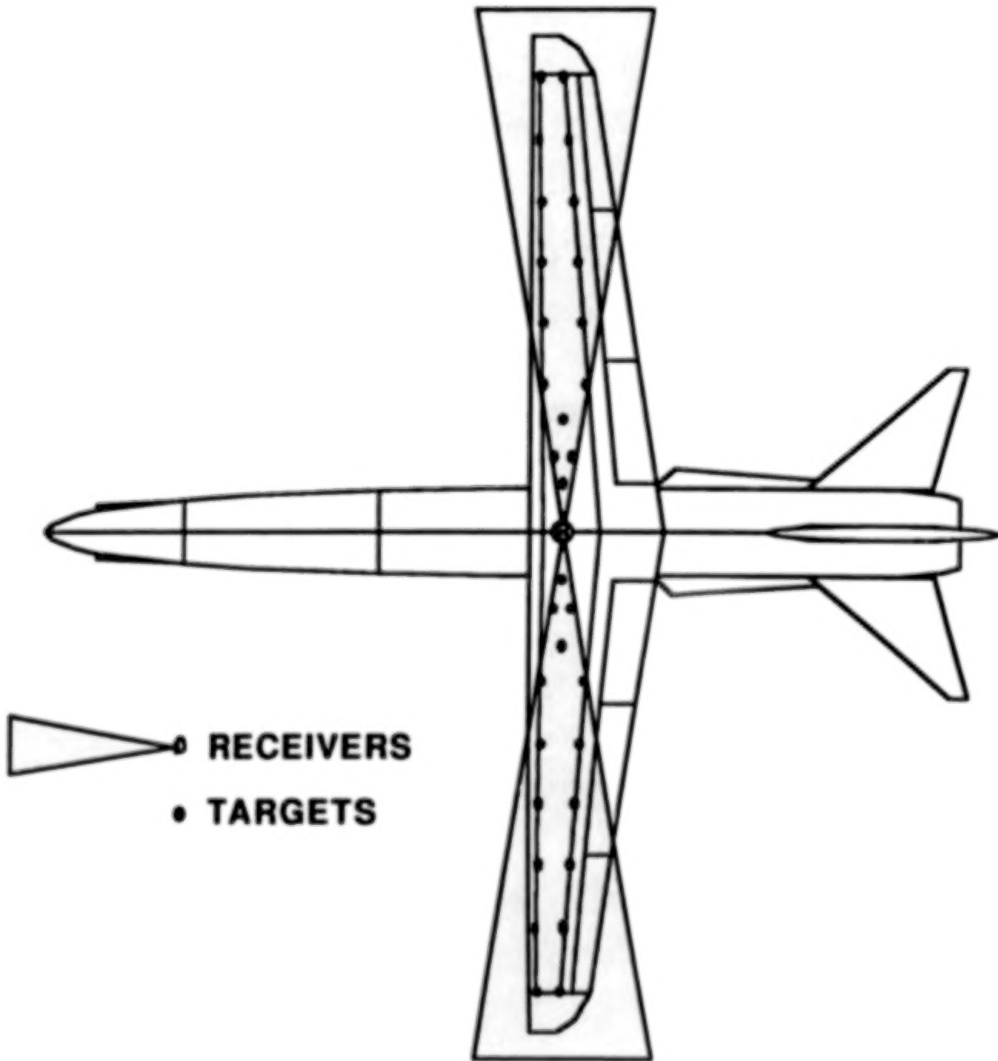
APPROACH

Measure in-flight deflections to correlate with predictions

Define in-flight shape for correlation of pressure data with CFD codes

OWRA FLIGHT DEFLECTION MEASUREMENT SYSTEM

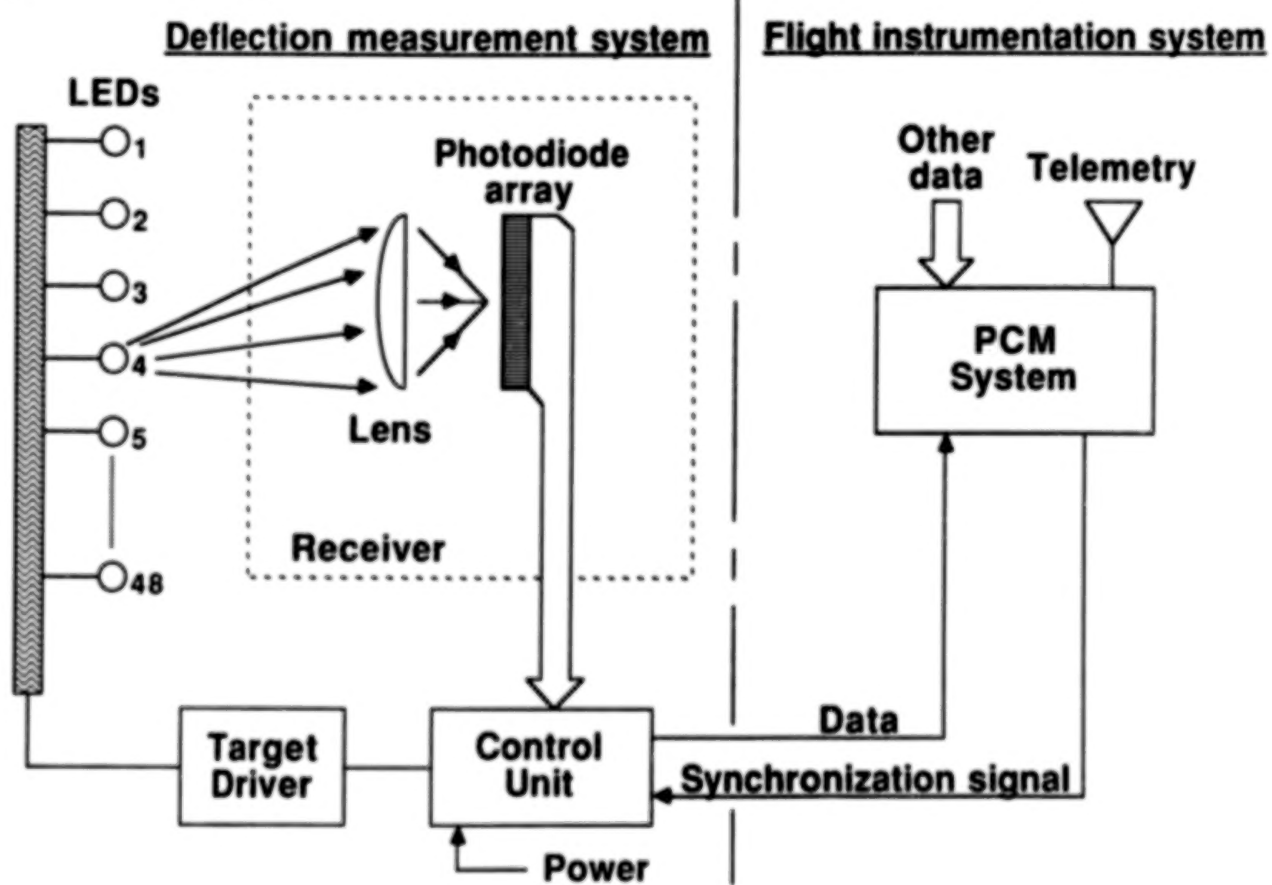
The flight deflection measurement system is electro-optical and consists of wing located targets emitting a light source which is in turn received by a wing center line located receiver. The system to be implemented on the OWRA will have the targets located on the wing upper surface just over the wings fore and aft spars. The system is capable of measuring both bending deflections and twist angles. Sixteen targets per wing semi-span will be installed; the targets have a spherical section shape with a base diameter of approximately 1.5 inches and a height of 1 inch. The receiver (located at the wing pivot) will be housed in an aerodynamically shaped blister with a height of approximately six inches and slightly larger base dimensions. The entire deflection measurement system will be removable so as not to interfere with either the static or unsteady pressure experimental data.



ELECTRO-OPTICAL FLIGHT DEFLECTION MEASUREMENT SYSTEM

The major elements of the deflection measurement system are a control unit, two receivers, two target drivers, and the targets. The targets house an LED which is turned on and off sequentially as a command is cycled through the various targets. Light from the target LED is then sensed by the receiver and is focused on a light sensitive diode array. The signal produced by the diode array is proportional to the wing deflection. This signal is sent to the control unit which, in turn, sends it to the PCMQ system for recording on magnetic tape or telemetering to a ground station for real time display. The control unit contains all of the measuring logic for operation of the system, and the target driver serves as a relay in providing from 2 to 5 amperes of pulsed current to each target. The system has a resolution of approximately 0.03 inch at a 10 foot range and a sample rate of approximately 7 sps for each target.

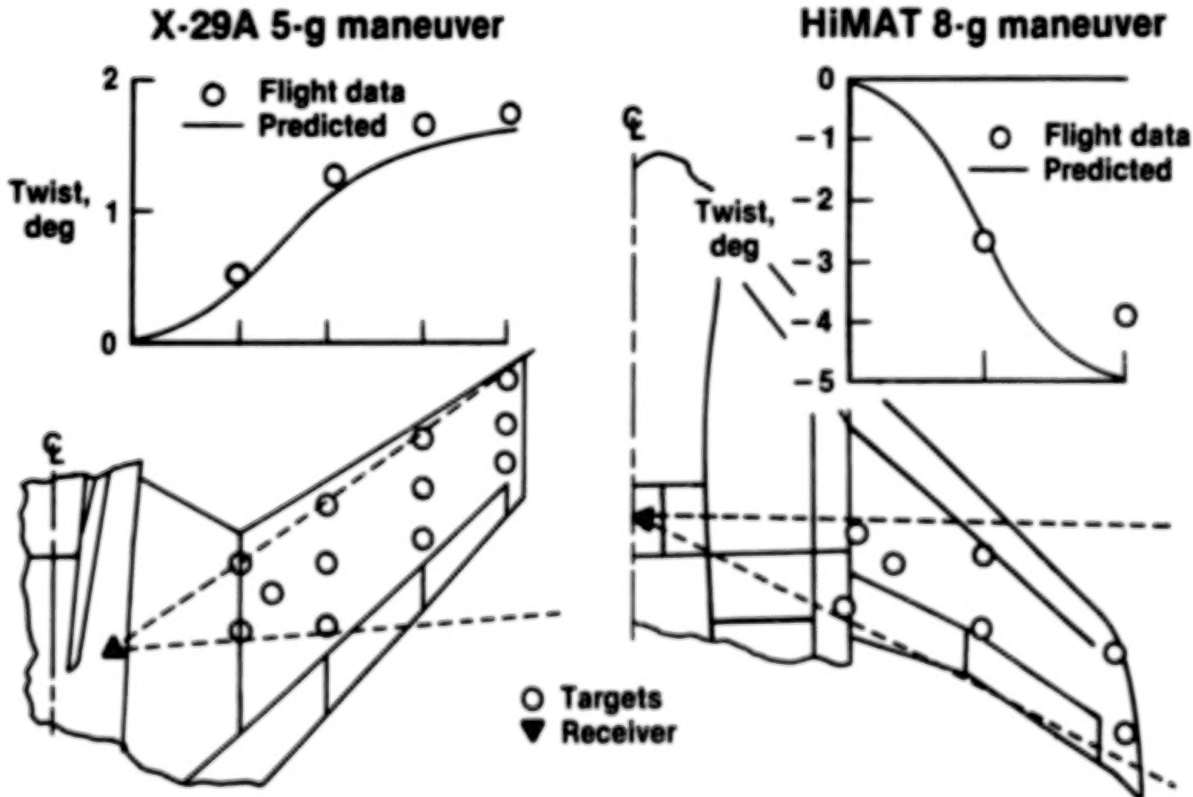
System Diagram



FLIGHT DETERMINED DEFLECTION MEASUREMENT RESULTS

The electro-optical deflection measurement system has been used successfully to obtain flight results on both the HiMAT and X-29A research aircraft as illustrated in this figure. The X-29A flight measured wing panel streamwise twist distributions are derived from front and rear spar deflections measured during a 5 g wind up turn maneuver and are compared to calculated twist data. Also shown are HiMAT flight measurements compared to NASTRAN calculated data for the 8 g maneuver design point. The deflection measurements of the HiMAT wing played a major role in evaluating the performance of the aeroelastically tailored composite wing.

Flight Measurements



OWRA SCHEDULE

The preliminary design phase of the project is complete and has resulted in a wing configuration for which construction is ready to be initiated. The wing area of the current configuration is 300 sq. ft. and is a 50% increase over the feasibility study design. Wing final design and construction will begin this summer and be complete in mid 1990. Testing of the flight configuration force and moment model will begin this fall and upon completion, work can be initiated on the rigid body flight control system. Upon receipt of the wing, extensive ground testing will be conducted to verify loads and dynamic structural modeling. Extensive systems checkout will be conducted with emphasis on the wing and fault tolerant processor (FTP) based flight control system. A first flight is anticipated for early 1991.

Wing construction - July 1987 - July 1990

Systems checkout - July 1990 - April 1991

First flight - May 1991

REFERENCES

1. Curry, R. E., and Sim, A. G., Unique Flight Characteristics of the AD-1 Oblique-Wing Research Airplane, Journal of Aircraft, June 1983, pp. 564-568.
2. Gregory, T., Oblique Wing Ready for Research Aircraft, Aerospace America, June 1985, pp. 78-81.
3. Anon., Military Missions Call for Oblique Wing, Aerospace America, June 1985, pp. 82-84.
4. Wiler, C. D., and White, S. N., Projected Advantage of an Oblique Wing Design on a Fighter Mission, AIAA-84-2474, November 1984.
5. Chapin, William G., Dynamic-Pressure Measurements Using an Electronically Scanned Pressure Module, NASA TM 84650, July 1983.
6. Seidel, D. A., Sanford, M. C., and Eckstrom, C. V., Measured Unsteady Transonic Aerodynamic Characteristics of an Elastic Supercritical Wing With an Oscillating Control Surface, NASA TM 86376, February 1985.

STATIC AEROELASTICITY OF A COMPOSITE OBLIQUE WING
IN TRANSONIC FLOWS

Jonathan D Bohlmann
Purdue University
Currently at General Dynamics
Fort Worth Division

INTRODUCTION

One aircraft configuration that shows great promise in achieving high performance is that of an asymmetrically swept wing, shown in Figure 1 (ref. 1, 2). When compared to conventional swept wings, these advantages include higher lift-to-drag ratios and reduced takeoff and landing speeds, which translate into increased performance in terms of fuel consumption, loiter time, range, etc. However, the oblique wing has a number of disadvantages because of its asymmetric configuration. Referring to Figure 1, consider the swept oblique wing shown to have an upward bending deflection, such that lines AB and A'B' represent lines of constant upward bending displacement. For the aft-swept portion of the wing, the airflow will see line CB. Since point B deflects upward more than point C (due to the bending displacement increasing from the wing pivot to the wing tip), the airflow will see a downward twist along CB due to the bending displacement. This bend-up/twist-down phenomenon is referred to as "wash-out". The forward-swept wing, on the other hand, will have the airflow seeing a nose-up twist due to bending since point C' deflects more than point B'. This bend-up/twist-up is called "wash-in". The increase in angle of attack associated with wash-in will increase the wing load, which will tend to increase the bending deflection and hence wash-in twist even further. Thus, divergence becomes a concern with the forward-swept wing (e.g., the X-29). Also, because the two portions of the wing undergo different bend/twist behaviour, the swept oblique wing will have a roll imbalance due to the different loadings on the forward- and aft-swept portions of the wing.

The question is, then, how to best achieve maximum stability and roll equilibrium without compromising performance. Using aeroelastic tailoring to enhance aeroelastic stability and control has been demonstrated in several analyses, especially for the forward-swept wing (ref. 3, 4, 5). Since the oblique wing has a forward-swept half, aeroelastic tailoring is also potentially beneficial for an oblique wing design. For a basic discussion of aeroelastic tailoring, see references 6 and 7.

TYPICAL ASYMMETRICALLY SWEPT WING

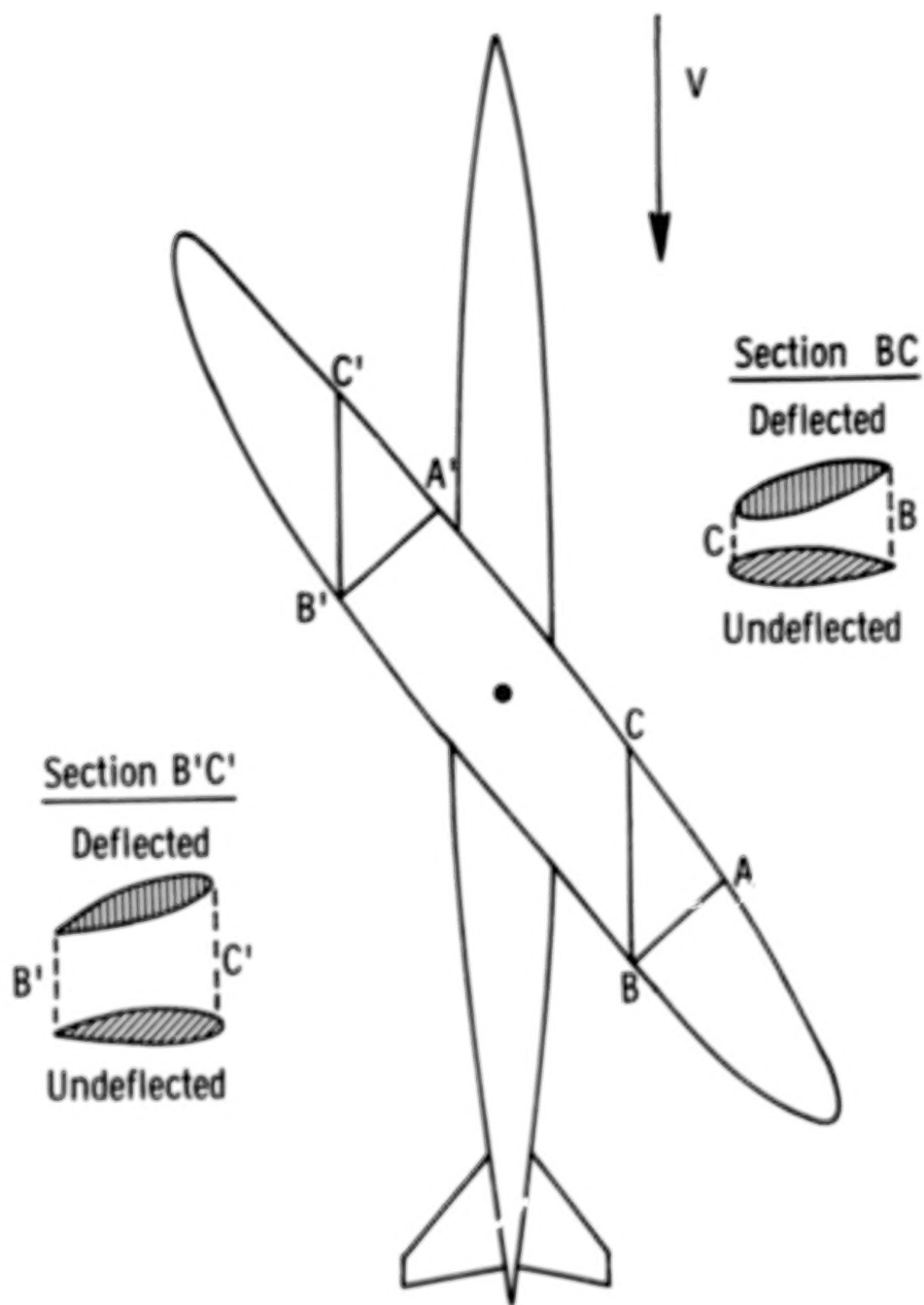


Figure 1

STATIC AEROELASTIC COMPUTATIONAL PROCEDURE

The static aeroelastic computational procedure (Figure 2) was developed to study the basic effects of aeroelastically tailoring an oblique wing through the use of composite materials. First, the geometry is defined for the oblique wing, which may have deflected control surfaces. In this analysis the oblique wing model has two outboard ailerons deflected an equal but opposite amount as input by the user of the computational procedure. This geometry is then submitted to the full potential code FLO22 for aerodynamic analysis (ref. 8, 9, 10). The output is a pressure distribution over the wing. After the pressure load has been converted to equivalent loads P_i , an equivalent plate program, developed by Dr. Gary Giles at NASA-Langley, is invoked for each half of the oblique wing (ref. 11). From the structural definition of the wing (input by the user) and the equivalent loads, the plate program calculates a set of coefficients C_i , from which the displacement of the wing due to the aerodynamic loads is defined in polynomial form. The wing shape is then deflected according to the calculated displacement. This deformed wing geometry is then input to FLO22 for aerodynamic analysis, and the aeroelastic procedure is repeated until a converged deformed shape has been obtained for the flexible composite wing. Usually only 3-4 aeroelastic iterations are required before a converged shape, i.e., a shape consistent with the aerodynamic loads calculated by FLO22, is reached.

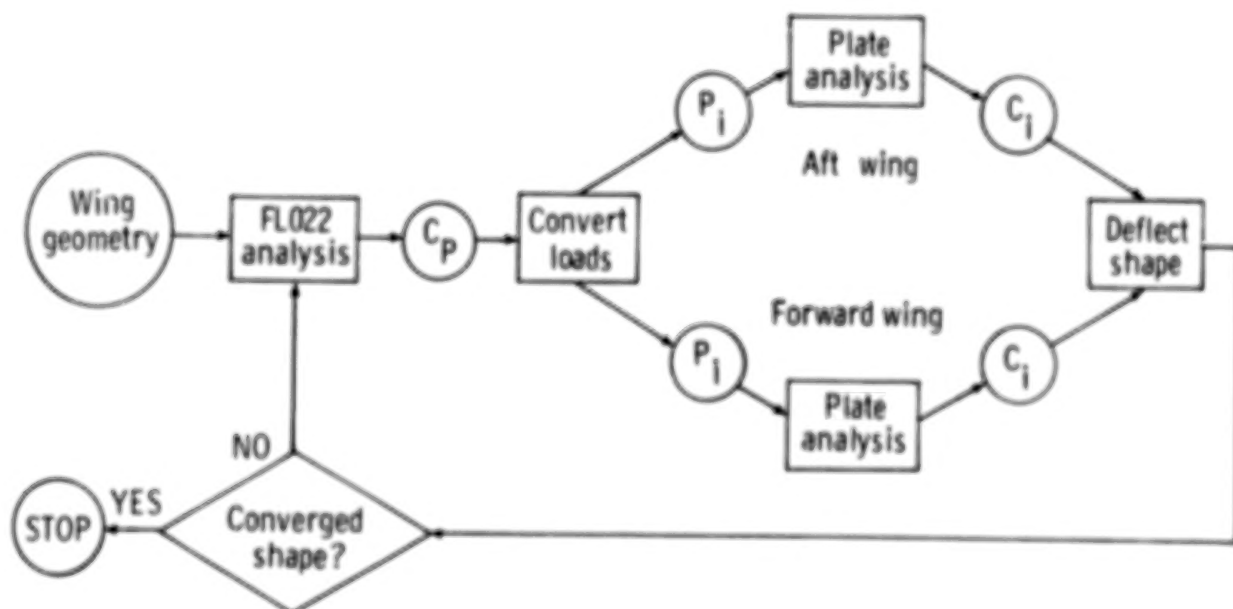


Figure 2

APPLICATION OF AEROELASTIC TAILORING

Each aeroelastic computational run described above involves one aileron deflection and one value of the amount of aeroelastic tailoring applied to the wing. This application of aeroelastic tailoring is achieved in this analysis by simply rotating the basic composite skin laminate of the wing by an angle θ (see figure below). Recall that a swept oblique wing exhibits a roll imbalance. If asymmetric composite tailoring is applied to the wing, i.e., the aft-swept half of the wing is given a wash-in structure to counteract its wash-out twist due to bending (recall figure 1), and the forward-swept half is given a wash-out structure to alleviate its wash-in twist due to bending, the oblique wing will aeroelastically desweep in that it will aeroelastically behave as if the wing had less sweep. This is desired since an unswept oblique wing does not have a roll imbalance. Thus, asymmetric tailoring could alleviate the roll problem of the oblique wing by an aeroelastic desweeping, while the wing would still retain the aerodynamic advantages of being swept. The tailoring is simply applied by rotating the composite laminate an angle θ as shown below. (Figure 3.) The wing can thus be trimmed in roll with aileron deflection or asymmetric tailoring, or a combination of both, as seen next.

APPLICATION OF WASH-OUT/WASH-IN TO COMPOSITE WING

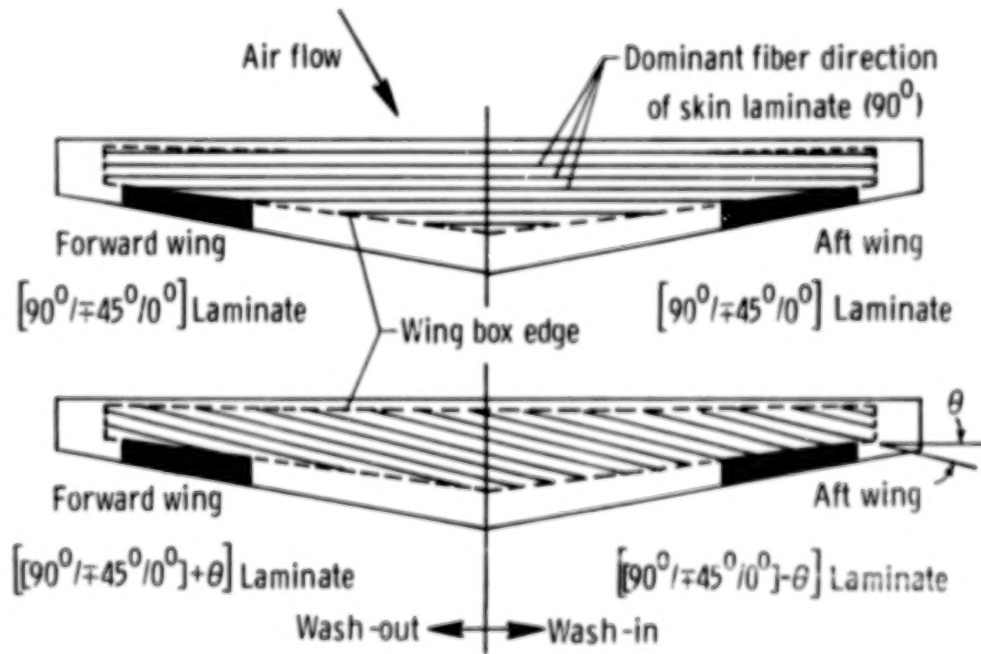


Figure 3

OBLIQUE WING ROLL TRIM ANALYSIS

The main intent of this analysis is to study the performance of an oblique wing in roll trim with asymmetric composite tailoring. Both cruise and maneuver conditions are explored, the cruise case (1g) having a dynamic pressure of 215 psf and an angle of attack of -0.25 deg, and the maneuver case (2.25g) having a dynamic pressure of 280 psf and a 3 degree angle of attack. Both conditions have a Mach number of 0.75. The oblique wing model has an aspect ratio of 10 and a taper ratio of 0.4, and incorporates the supercritical airfoil OW 70-10-12. The wing structure consists of wing skins made of a typical graphite-epoxy composite. The composite lay-up and planform shape were shown in figure 3. The performance of the wing is measured by four aerodynamic, control and structural parameters. Aerodynamically, the pressure (induced) drag is noted to see if aeroelastic tailoring results in an increase or decrease in drag for the wing. From the controls viewpoint, the ability of the ailerons to generate a rolling moment (control effectiveness) and the hinge moments on the control surfaces are used to measure performance. The hinge moments dictate the actuator system for the wing. A decrease in hinge moment could result in a lighter actuator system, which is a benefit because of a decrease in weight. Structurally, the stress level f in the composite skins is noted, defined as

$$f^2 = \left(\frac{\sigma_{11}}{X}\right)^2 + \left(\frac{\sigma_{22}}{Y}\right)^2 - \left(\frac{\sigma_{11}}{X}\right)\left(\frac{\sigma_{22}}{Y}\right) + \left(\frac{\tau_{12}}{S}\right)^2$$

where σ and τ are the stresses in the composite layer, and X , Y and S are material constants (ref. 12). Before noting how these performance parameters are affected by aeroelastic tailoring, conditions for roll equilibrium are first obtained by numerous aeroelastic computational runs. Figure 4 shows combinations of aileron deflection δ and laminate orientation angle θ required to trim the oblique wing in roll.

OBLIQUE WING TRIM CONDITIONS

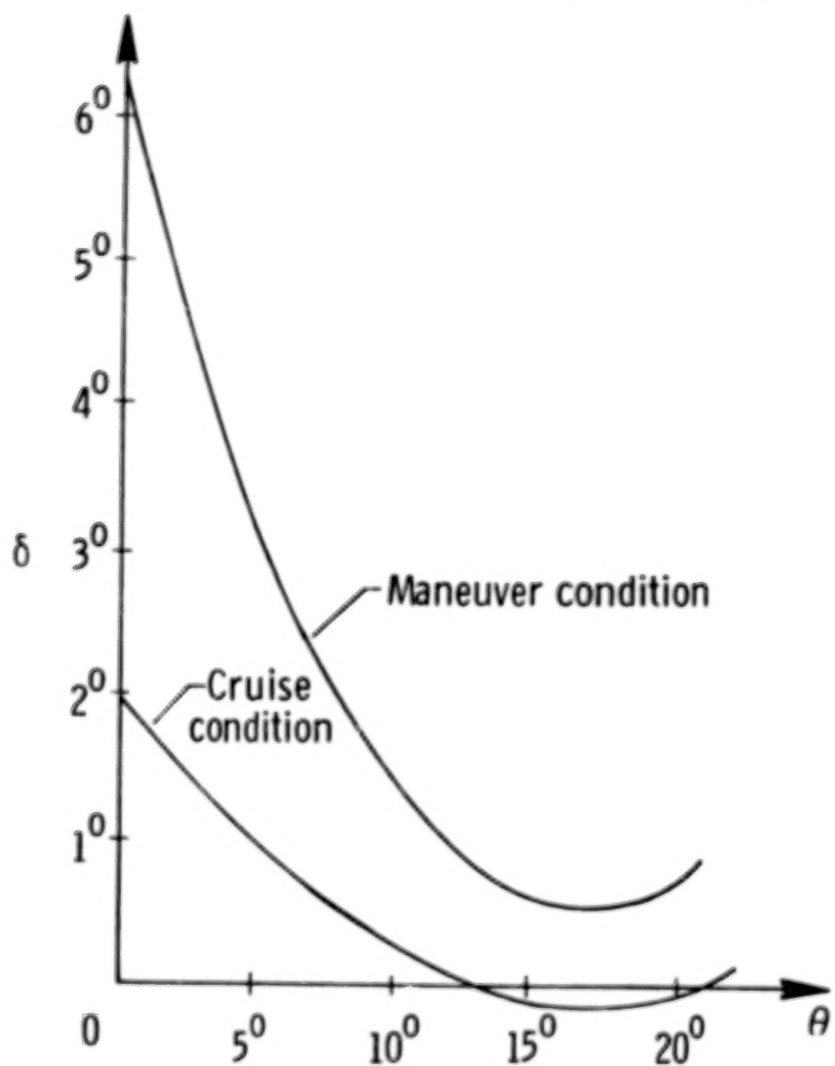


Figure 4

AERODYNAMIC PERFORMANCE

Figure 5 plots the pressure drag coefficient versus the laminate orientation angle for the oblique wing in roll trim. An aileron deflection angle is associated with each laminate orientation angle for cruise and maneuver according to figure 4. For both cruise and maneuver, the pressure drag remains relatively flat. This occurs because the twist distribution across the wing is basically the same for the roll-trimmed oblique wing regardless of what θ - δ combination is used to achieve that roll equilibrium. The drag at $\theta=20$ deg is about 3 or 4 counts higher than at $\theta=0$ deg for the cruise and maneuver conditions (one drag count equals a drag coefficient of 0.0001). However, it must be remembered that the pressure drag does not include boundary-layer effects or drag from flow separation. Referring to Figure 4 again, a fair amount of aileron deflection is required for small laminate orientation angles, especially for the maneuver case. We would suspect that higher aileron deflections would result in a larger boundary layer and a greater likelihood of flow separation, which would result in an increase in drag not accounted for in the aerodynamic analysis of FLO22. Thus, aeroelastic tailoring could potentially result in less drag because of the reduction in aileron deflection needed for roll trim.

PRESSURE DRAG VERSUS θ

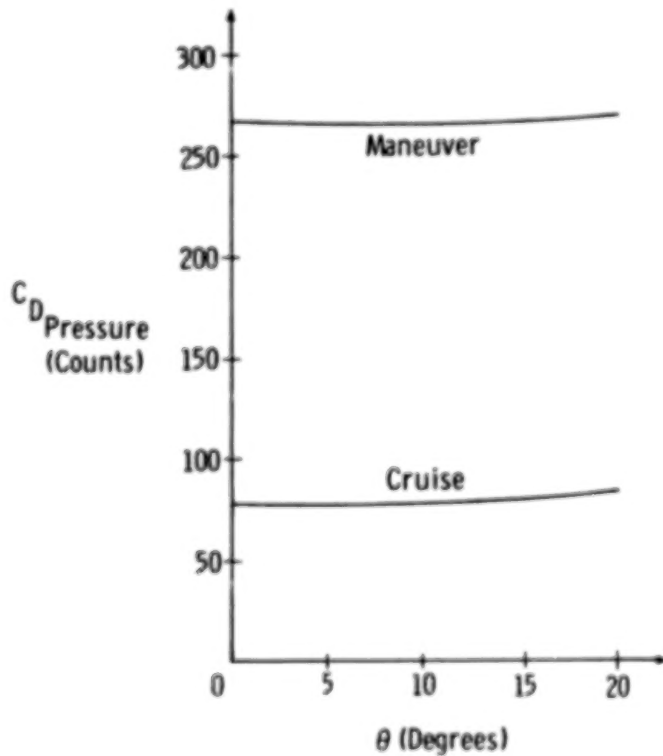


Figure 5

CONTROL PERFORMANCE

The hinge moment coefficient versus laminate orientation angle is plotted in Figure 6 for the oblique wing in roll trim. The hinge moment would determine the actuator system needed for the control surfaces. Since the actuator would be the same for each aileron, consider the higher loaded aileron, which is on the aft wing. We see that for both cruise and maneuver the hinge moment is reduced as the composite laminate is rotated due to the reduction in aileron deflection. Because of the reduced hinge moment, a smaller, lighter actuator could be used giving a weight savings. Aeroelastic tailoring can thus give a performance advantage by not only reduced aileron deflection but also a weight reduction by the resulting decrease in hinge moments. Additional results not shown here also indicate the ailerons will not suffer any significant reduction in their ability to produce a rolling moment if the wing is aeroelastically tailored.

HINGE MOMENT COEFFICIENT VERSUS θ

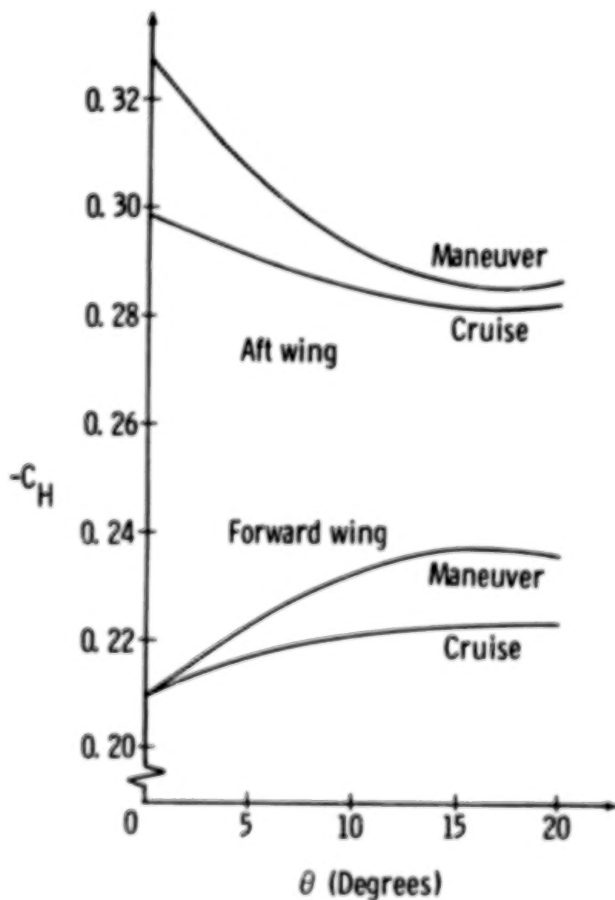


Figure 6

STRUCTURAL PERFORMANCE AND CONCLUSIONS

The effect on the stress level in the composite skins due to changing the laminate orientation angle is shown in Figure 7 for the oblique wing in roll trim. The figure depicts the maximum stress level occurring in the composite laminate, which generally occurs in the composite layer whose fiber direction is directed mainly along the chord of the wing. It is seen that the maximum stress level increases as the composite laminate is rotated. This is viewed as a disadvantage because a higher stress level would imply that the skin thickness must be increased to obtain the desired strength and factor of safety, resulting in more weight.

Thus, performance trade-offs do exist in the application of aeroelastic tailoring to the oblique wing. Tailoring the wing results in a decrease in the aileron requirements on the oblique wing for roll trim, leading to a reduction in aileron hinge moments. This implies a weight reduction since a smaller actuator could be used. The decreased aileron deflection could also mean that aeroelastic tailoring gives a drag reduction because of the smaller boundary layer and less likelihood of flow separation associated with less aileron deflection. However, aeroelastic tailoring also results in an increase in the stress level in the composite wing skins, which could result in a weight increase to maintain the desired strength. Overall it appears that a performance increase is obtained by aeroelastic tailoring. Since trade-offs exist, the use of an integrated design approach incorporating aerodynamic, structural and control considerations would be beneficial (or necessary) for designs with aeroelastic tailoring.

STRESS LEVEL VERSUS θ

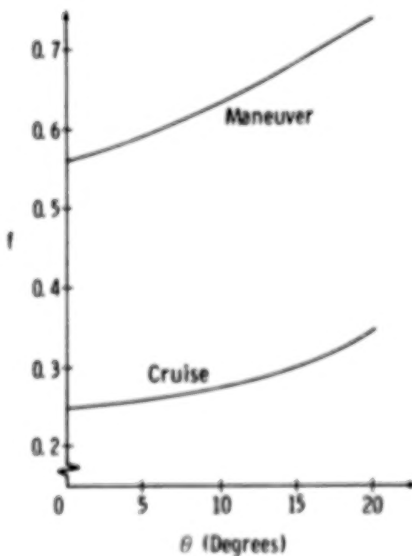


Figure 7

REFERENCES

1. Jones, R.T., "Reduction of Wave Drag by Antisymmetric Arrangement of Wings and Bodies," AIAA Journal, Vol. 10, February 1972, pp. 171-176.
2. Jones, R.T., and Nisbet, J.W., "Transonic Transport Wings-Oblique or Swept," Astronautics and Aeronautics, Vol. 12, January 1974, pp. 40-47.
3. Lynch, R.W., and Rogers, W.A., "Aeroelastic Tailoring of Composite Materials to Improve Performance," Proceedings of the AIAA/ASME/SAE 17th Structural Dynamics and Materials Conference, 1976, pp. 61-79.
4. Weisshaar, T.A., "Aeroelastic Tailoring of Forward Swept Composite Wings," Journal of Aircraft, Vol. 18, August 1981, pp. 669-676.
5. Sensburg, O., and Schmidinger, G., "Integrated Design of Structures," Messerschmitt-Bolkow-Blohm MBB/LKE29/S/PUB/240, April 1986.
6. Shirk, M.H., Hertz, T.J., and Weisshaar, T.A., "Aeroelastic Tailoring--Theory, Practice, and Promise," Journal of Aircraft, Vol. 23, January 1986, pp. 6-18.
7. Weisshaar, T.A., "Aeroelastic Tailoring--Creative Uses of Unusual Materials," Presented at the AIAA/ASME/ASCE/AHS 28th Structures, Structural Dynamics and Materials Conference, April 6-8, 1987.
8. Jameson, A., "Iterative Solution of Transonic Flows over Airfoils and Wings, Including Flows at Mach 1," Communications on Pure and Applied Mathematics, Vol. 27, May 1974, pp. 283-309.
9. Jameson, A., Caughey, D.A., Newman, P.A., and Davis, R.M., "A Brief Description of the Jameson-Caughey NYU Transonic Swept Wing Computer Program - FLO 22," NASA TMX-73996, December 1976.
10. Jameson, A., and Caughey, D.A., "Numerical Calculation of the Transonic Flow Past a Swept Wing," ERDA Mathematics and Computing Laboratory, New York University, COO-3007-140, June 1977 (also available as NASA-CR-153297).
11. Giles, G.L., "Equivalent Plate Analysis of Aircraft Wing Box Structures with General Planform Geometry," Journal of Aircraft, Vol. 23, November 1986, pp. 859-864.
12. Jones, R.M., Mechanics of Composite Materials, McGraw-Hill, New York, 1975, pp. 76-78.

**INVESTIGATION AND SUPPRESSION OF HIGH DYNAMIC RESPONSE
ENCOUNTERED ON AN ELASTIC SUPERCRITICAL WING**

**David A. Seidel, William M. Adams, Jr.,
Clinton V. Eckstrom, and Maynard C. Sandford
NASA Langley Research Center
Hampton, Virginia**

BACKGROUND

The elastic semispan wing used in the present study is from the NASA program Drones for Aerodynamic and Structural Testing (DAST) and is the right wing panel from the second Aeroelastic Research Wing (ARW-2). The DAST ARW-2 wing was designed to flutter within the flight envelope of the drone aircraft to which it was to be attached. The wing had an aspect ratio of 10.3, a leading-edge sweep angle of 28.8°, and a supercritical airfoil. The wing was designed for a cruise condition of $M = 0.80$, $C_L = 0.53$ ($\alpha = 1.3^\circ$), and an altitude of 46,800 feet ($q = 127$ psf). The wing had three hydraulically driven trailing-edge control surfaces and was instrumented with dynamic pressure transducers and accelerometers.

An unusual transonic instability was encountered near $M = 0.9$ during an unsteady pressure test of the DAST ARW-2 wing in October 1983 in the Langley Transonic Dynamics Tunnel (TDT). This unusual transonic instability boundary was predicted using a subcritical response technique. This instability was predicted to occur at an almost constant Mach number of 0.9 for all dynamic pressures tested. The wing motion was primarily first wing bending mode response and was angle of attack dependent. Single degree-of-freedom bending mode oscillations have also been encountered during experiments with several other aircraft configurations. These oscillations have been observed on a low aspect ratio wing with subsonic airfoil shape, on the B-1A during a wind-up turn, on the canard of the HIMAT aeroelastic model at negative angle of attack, and on a forward swept wing force model panel at a negative angle of attack. Linear theory flutter analysis was unable to predict any of these oscillations. (Fig. 1.)

- DAST ARW-2 Wing
 - Aeroelastic wing designed to flutter in flight envelope
 - High-aspect-ratio supercritical wing
 - Design cruise Mach number = 0.8
 - Wing heavily instrumented for unsteady pressure data acquisition
- Wing tested in TDT, October 1983 (AIAA 85-0598-CP)
 - Instability unexpectedly encountered
 - Boundary predicted using subcritical response technique
 - Motion predominantly 1st wing bending
 - Boundary at almost constant Mach number of 0.90
 - Angle-of-attack sensitive
 - Similar phenomena observed for other aircraft

Figure 1

DAST ARW-2 WING IN TDT

Figure 2 shows the wing and fuselage configuration mounted in the wind tunnel. The elastic semispan wing used in the present study is the DAST ARW-2 right wing panel. A half-body fuselage was used to simulate the drone fuselage. This fuselage had shorter nose and tail sections than does the drone fuselage since no supersonic tests were to be made. The center section of the fuselage was similar to the actual drone fuselage in both diameter and wing location to generate the proper airflow over the inboard section of the wing. Both the fuselage and the wing were mounted on a remotely controlled turntable mechanism located on the tunnel sidewall.

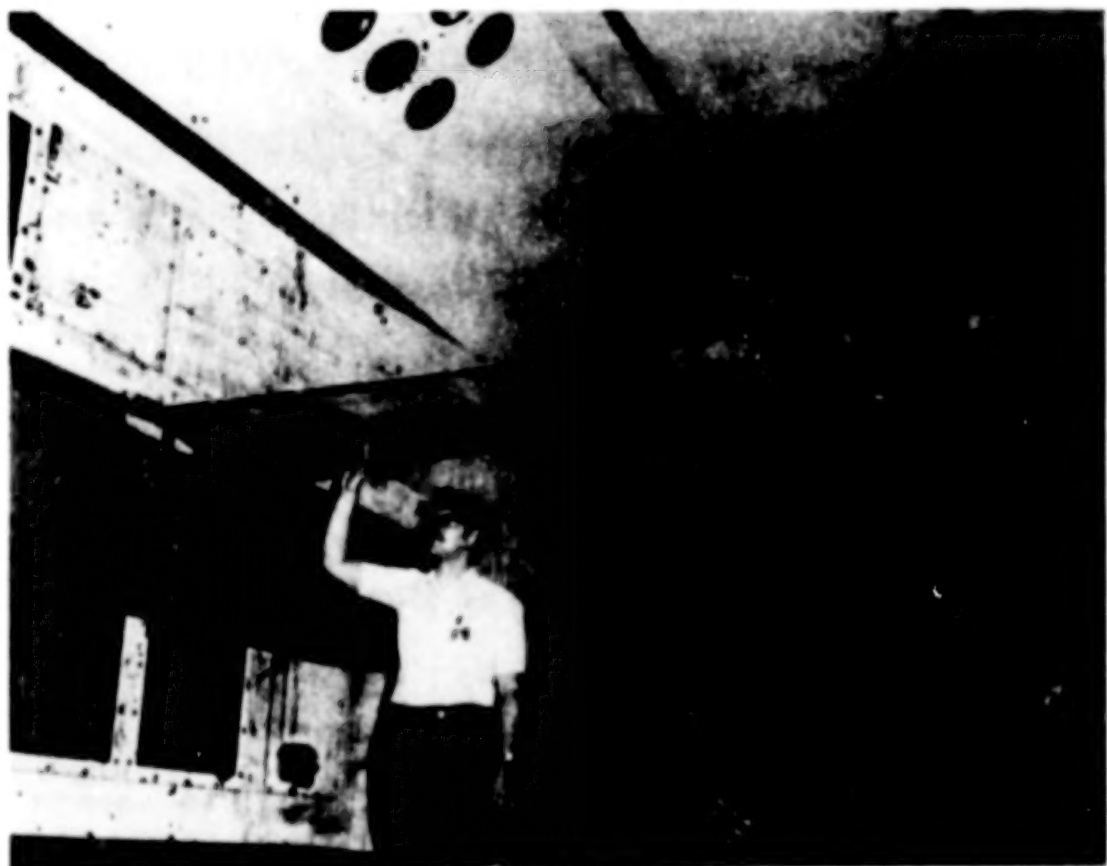


Figure 2

DAST ARW-2 WING

The wing planform is shown in figure 3. The wing had an aspect ratio of 10.3 with a leading-edge sweep angle of 28.8°. The wing was equipped with three hydraulically driven control surfaces, two inboard and one outboard. For this test, the inboard surfaces were held fixed at 0° deflection and only the outboard surface was deflected statically. The outboard surface hinge line was located at 77 percent of local chord.

Also shown in figure 3 are the locations of the wing instrumentation. The instrumentation consisted of 191 dynamic pressure transducers and 10 accelerometers. In addition, strain gauge bridges were located near the wing root to measure bending moments. Small potentiometers were used to measure the control surface angular displacement. The model angle of attack was measured by a servo accelerometer that was mounted near the wing root. Both steady and unsteady pressures were obtained using differential pressure transducers referenced to the tunnel's static pressure. Streamwise rows of upper and lower surface pressure orifices were located at six span stations: $\eta = 0.274, 0.476, 0.599, 0.707, 0.871$ and 0.972 . The fifth row at $\eta = 0.871$ lies along the mid-span of the outboard control surface. All of these surface orifices were connected to pressure transducers by matched tubes having an inner diameter of 0.040 inch and a length of 18 inches. In order to determine the tube transfer functions needed to correct the unsteady pressure data from these matched-tube transducers, simultaneous measurements were also obtained from a row of in situ transducers mounted on the wing upper surface at $\eta = 0.875$, parallel to the fifth row of surface orifices. Dynamic wing deflections were determined using the 10 accelerometers.

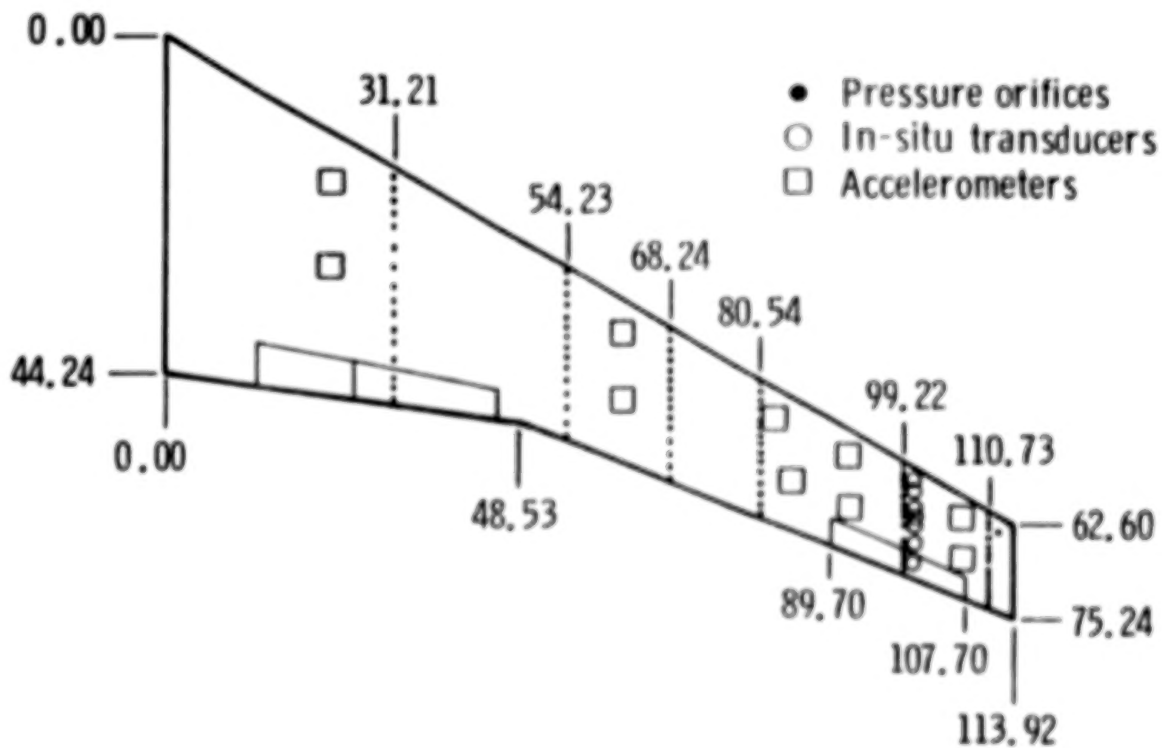


Figure 3

INSTABILITY BOUNDARY PREDICTED DURING FIRST TEST

During the first test of the ARW-2 wing in the TDT an unusual wing instability, with motion similar to the wing first bending mode, was encountered. The boundary was determined for a wing angle of attack and control surface deflection of 0° as shown in figure 4. Also shown in figure 4 as a solid line is the predicted linear theory (doublet lattice theory) flutter boundary, which is of a conventional nature. The measured boundary was determined using a familiar subcritical response technique known as peak-hold. The boundary was predicted to occur at a nearly constant Mach number of 0.90 beginning at a low dynamic pressure of about 50 pounds per square foot (psf) ($R = 874,000$) and rising nearly vertical to over 300 psf ($R = 5,300,000$). The observed wing motion during the instability was similar to the wing first bending mode, the frequency of which was 8.3 Hz wind-off. The instability frequency was 8.6 Hz at the lowest dynamic pressure and increased to about 13 Hz at the highest dynamic pressure.

Because of recent interest in angle-of-attack effects and shock induced effects on wing instabilities, several additional test runs were made. These runs include variation of the wing angle of attack, comparison using air or Freon as the test medium and comparison with and without a transition strip near the wing leading edge. The instability was found to be sensitive to variation in angle of attack and, generally, the minimum damping occurred at or near zero wing root angle of attack. In figure 4 the solid symbol indicates the Mach number and dynamic pressure where the comparison tests were made. The results showed no significant difference in the instability boundary for tests in air or Freon. Reynolds number values in Freon are approximately 3.1 times greater than those obtained in air. There were also no significant differences for tests in Freon with or without a transition strip.

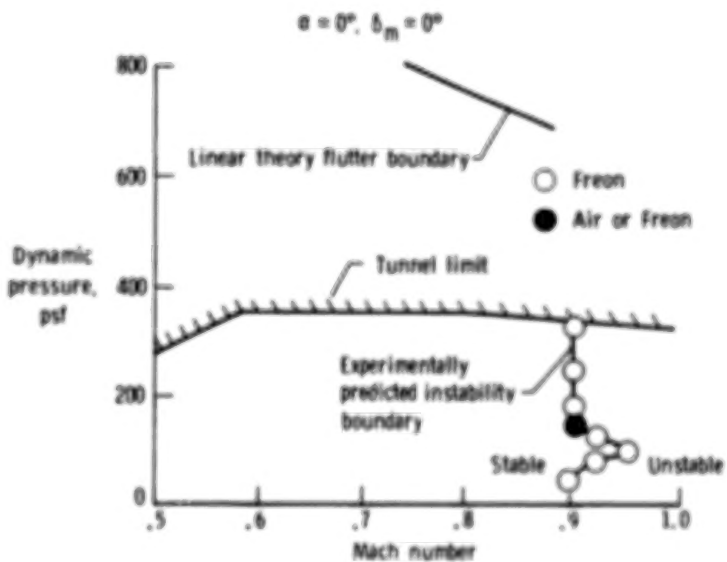


Figure 4

DAST ARW-2 WING RETEST

A second wing tunnel test was performed on the DAST ARW-2 wing to further investigate the unusual instability. The primary purpose of the test was to establish firmly the existence of the instability boundary and to gather wing response data and dynamic pressure measurements to help understand the mechanism forcing the wing oscillations. A secondary purpose was to design an active control system to suppress the wing response using the outboard control surface.

Dynamic pressures and wing deflections were measured for a large number of test conditions in the TDT using Freon as a test medium. Data were taken at Mach numbers from 0.5 to 0.96 for two stagnation pressures. For a Mach number range of 0.8 - 0.96 the two stagnation pressures gave a dynamic pressure variation of 125 - 166 pounds per square foot (psf) and 260 - 340 psf. These two stagnation pressures will be referred to as the low and high density conditions.

Wool tufts were used to visualize the flow patterns on the wing in the instability region. Static wing tip deflection was measured over the range of test conditions. The effect on dynamic wing response of wing angle of attack, static outboard control surface deflection and a spanwise fence on the lower surface were investigated. All dynamic wing response data presented is obtained from the rear wing tip accelerometer. (Fig. 5.)

- Purpose

- Obtain further information on mechanism of non-classical instability
 - Acquire experimental database
- Assess feasibility of active suppression of wing response (AIAA 87-0881-CP)

- Method

- Probe instability region
- Record unsteady pressure and wing acceleration
- Flow visualization
- Measure wing deflection

Figure 5

WING-TIP ACCELEROMETER PEAK-HOLD RESPONSE - MACH EFFECTS

Figure 6 shows the peak-hold results from the wing tip accelerometer for both the low and high density conditions. The wing angle of attack and control surface deflection were held at 0° . The data show that no instability was found but instead a region of high dynamic wing response was observed. For the lower density condition ($q = 125 - 166 \text{ psf}$) the wing motion reaches a maximum at $M = 0.93$ and then rapidly decreases with increasing Mach number. The same trend occurs for the higher density condition ($q = 260 - 340 \text{ psf}$) with maximum wing motion occurring near $M = 0.92$. The observed wing tip maximum dynamic amplitudes are noted in figure 6. At the lower density condition, the amplitude of the wing tip motion was approximately 2 inches peak-to-peak. At the higher density condition, which has double the dynamic pressure, the amplitude of the wing tip motion doubled to approximately 4 inches peak-to-peak.

Also shown in figure 6 at the higher density condition and $M = 0.92$ is a single point for $\alpha = -1^\circ$ where 6 inches peak-to-peak amplitude of wing tip motion was observed. At this condition the wing motion was so severe that the tunnel bypass valves were opened to rapidly reduce the dynamic pressure and associated wing motion.

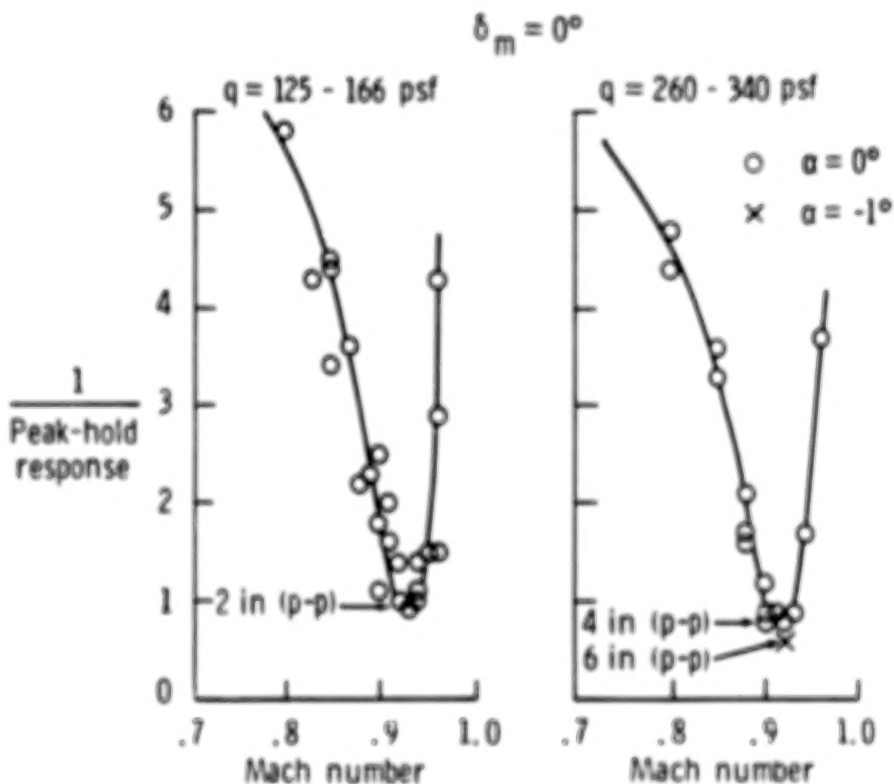


Figure 6

WING-TIP ACCELEROMETER PEAK-HOLD RESPONSE - ANGLE OF ATTACK EFFECTS

Figure 7 shows the peak-hold results from the wing tip accelerometer for three wing angles of attack at the lower density condition. The mean control surface deflection was held at 0° . As shown in the figure, the maximum dynamic wing response occurred for a wing angle of attack of 0° at $M = 0.93$. Changing the wing angle of attack to 2 and -2 degrees decreased the maximum wing response and shifted the corresponding Mach number to 0.94 . Similar angle of attack trend results were seen at the higher density condition. Data were taken for wing angles of attack of 1 , 0 and -1 degrees up to $M = 0.9$ and fell within the scatter of the experimental data observed at 0° as shown in figure 6. Therefore it is believed that for this configuration the maximum wing response occurs when the wing angle of attack is nominally at 0° .

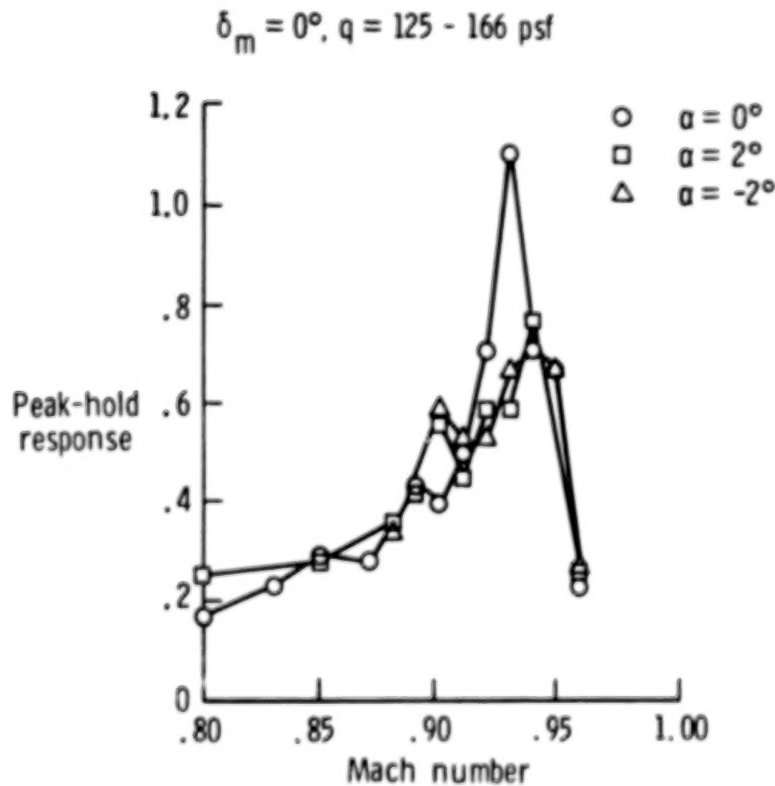


Figure 7

WING-TIP ACCELEROMETER PEAK-HOLD RESPONSE - OUTBOARD CONTROL EFFECTS

Figure 8 shows the peak-hold results from the wing tip accelerometer for three outboard control surface mean deflection angles at the lower density condition. The wing angle of attack was set at 0° . The figure shows a small increase in wing response for the control surface deflection of 6° (trailing-edge down). However, a significant reduction in wing response is shown for a deflection of -6° . The wing tip maximum response peak is reduced by half and shifted to a lower Mach number of 0.91.

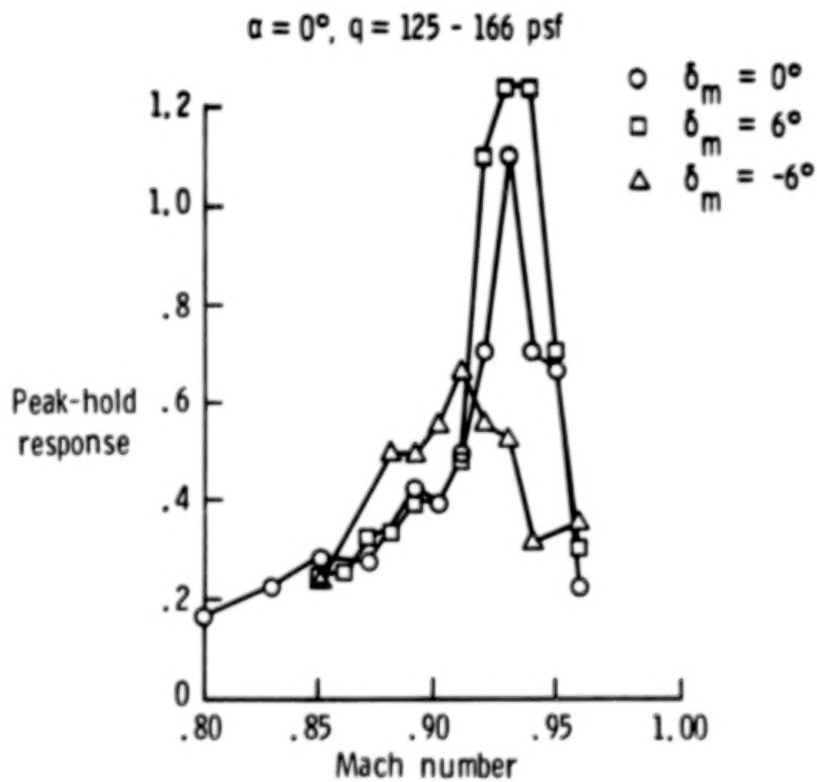


Figure 8

DAST ARW-2 WING WITH LOWER SURFACE SPANWISE FENCE

In an attempt to disturb the flow and change the dynamic wing response, a 1/2-inch high spanwise fence was attached to the lower surface at approximately the 60% local chordline as shown in figure 9. The fence ran from the wing planform break ($\eta = 0.426$) to within 5 inches of the wing tip ($\eta = 0.956$). The fence was made up of 5 separate one foot-long pieces of aluminum placed end to end to minimize increasing the wing stiffness.



Figure 9

WING-TIP ACCELEROMETER PEAK-HOLD RESPONSE - SPANWISE FENCE EFFECTS

The effect of the fence on the wing tip accelerometer peak-hold response at the lower density condition is shown in figure 10. The fence has a significant effect upon the wing response, lowering the amplitude of maximum wing motion and shifting the peak value to a lower Mach number of 0.90.

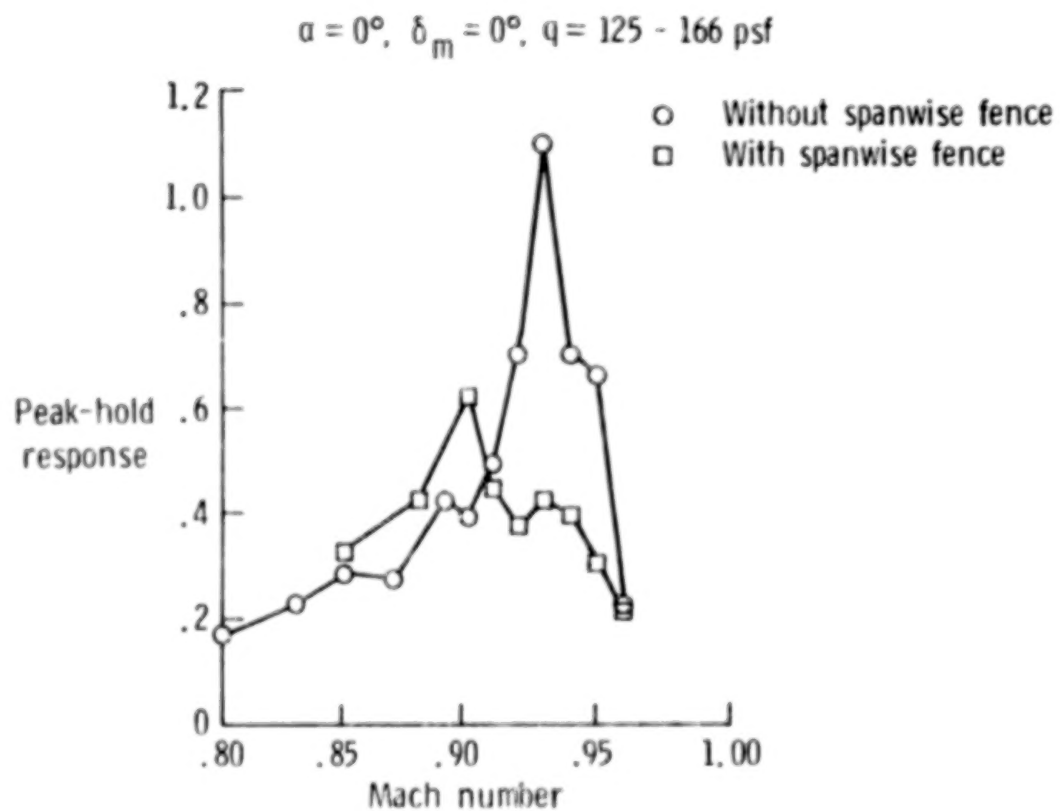


Figure 10

DAST ARW-2 WING WITH WOOL TUFTS

Wool tufts were placed on the upper and lower wing surfaces for several test runs to visualize the flow patterns on the wing. The tufts were placed on eight span stations located at $\eta = .517, .558, .635, .671, .761, .816, .905$ and $.938$, as shown in figure 11. The tufts were one inch long and on the six inboard span stations were located at ever 10% of local chord. On the two outboard span stations the tufts were located between 10 and 90% chord at every 20% of local chord.

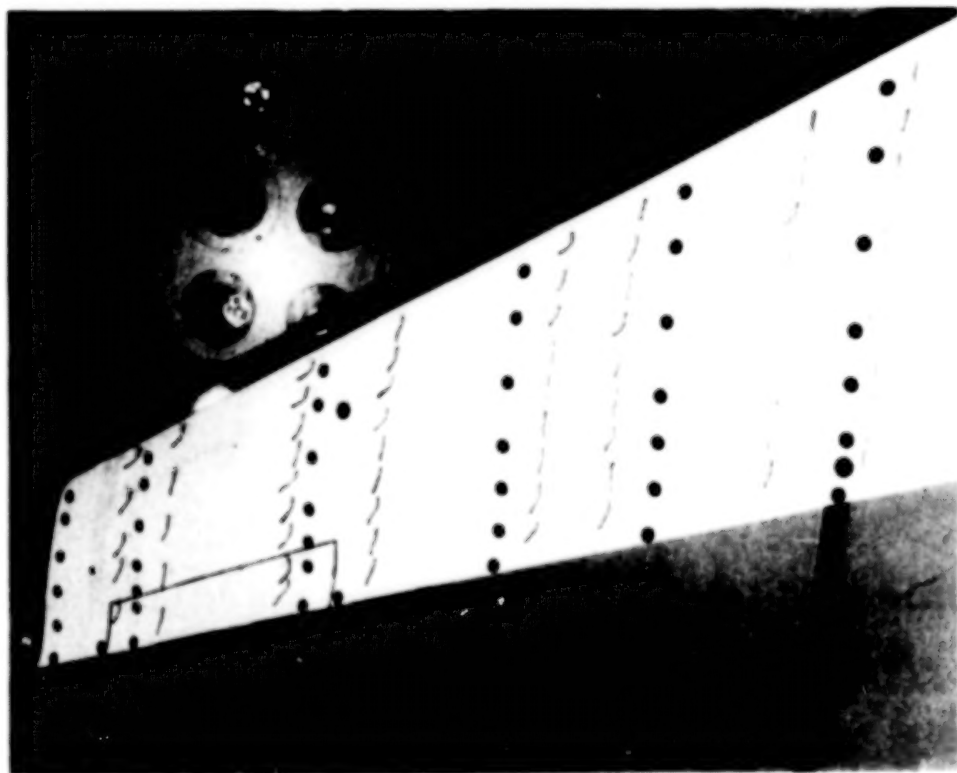


Figure 11

SEPARATED FLOW REGIONS INDICATED BY WOOL TUFTS

Figure 12 lists the regions of separated flow on the wing as indicated by the tuft data for Mach numbers from 0.85 to 0.96 at the lower density condition. Upper surface flow separation is first indicated at $M = 0.88$. The region of separated flow expands upstream and outboard as Mach number increases to 0.94 and then remains constant to $M = 0.96$. Flow separation on the lower surface is initially indicated at $M = 0.90$. The region of separated flow expands upstream and outboard as Mach number increases to 0.94. At $M = 0.96$ the region of separated flow on the lower surface decreases, moving downstream and inboard.

M	Region of separated flow			
	Upper surface		Lower surface	
	x/c	η	x/c	η
.85	-----	-----	-----	-----
.88	.8 - 1.0	.517 - .816	-----	-----
.90	.7 - 1.0	.517 - .905	.6 - 1.0	.635 - .761
.92	.7 - 1.0	.517 - .938	.6 - 1.0	.635 - .938
.94	.6 - 1.0	.517 - .938	.5 - 1.0	.635 - .938
.96	.6 - 1.0	.517 - .938	.6 - 1.0	.635 - .905

Figure 12

MEAN PRESSURE DISTRIBUTIONS

Figure 13 shows the mean chordwise pressure distribution at the 87.1% span station for nine Mach numbers at the lower density condition. The wing angle of attack and outboard mean control surface deflection were 0° . As Mach number increases, a shock develops on the upper surface at $M = 0.85$ and becomes quite strong at $M = 0.89$. The criteria used to determine trailing-edge flow separation from mean pressure measurements is the attainment of negative pressure coefficients at the 95% chord location. When negative pressures are sustained aft of this location, the flow is considered to be separated. Based upon the mean pressure distributions shown in figure 13, it appears that flow separation on the upper surface is evident at $M = 0.92$ and is established strongly at $M = 0.94$. The lower surface develops a strong shock at $M = 0.92$ and the pressure distributions indicate flow separation at $M = 0.96$.

Comparing these data to the separated flow regions indicated by wool tufts shown in figure 12 leads to two conclusions. The first is that the mean pressure data give an incomplete picture of the flow separation. The mean pressure data, taken at $\eta = 0.871$, does not indicate flow separation on the upper surface until $M = 0.92$ while the wool tufts indicate separation in the region of the pressure transducers near $M = 0.89$. Flow separation on the lower surface is not indicated by the mean pressures until $M = 0.96$ while the tufts indicate separation in the region at $M = 0.92$. The second conclusion is that flow separation, as shown by the tuft data, coincides with the occurrence of strong shocks on a surface, as shown by the mean pressure data in figure 13. This flow separation occurs near $M = 0.89$ on the upper surface and $M = 0.92$ on the lower surface at the 87.1% span station.

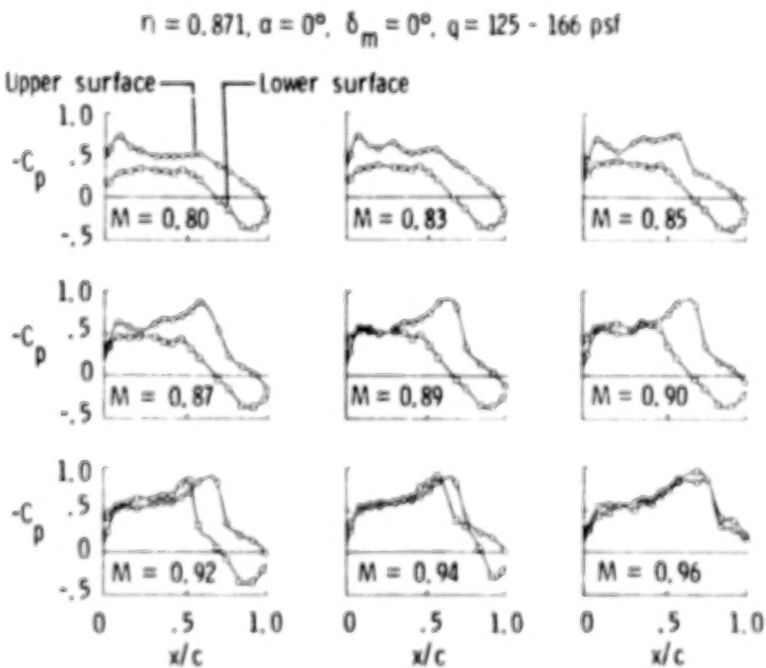


Figure 13

STATIC WING TIP DEFLECTIONS

During the test, measurements of the mean wing tip deflection and twist were made using an optical cathetometer instrument focused on a straight line drawn on the outboard tip of the wing. The results of the wing tip measurements for the lower density condition at a wing angle of attack and mean control surface deflection of 0° are shown in figure 14. The wing tip deflection and twist increase as Mach number increases up to a maximum near $M = 0.85$. At higher Mach numbers the wing tip deflection and twist values decrease rapidly as the Mach number increases. This agrees with the tuft data which show flow separation beginning on the upper surface at $M = 0.88$, causing loss of lift (see figure 13) and the resulting decrease in wing deflection and twist.

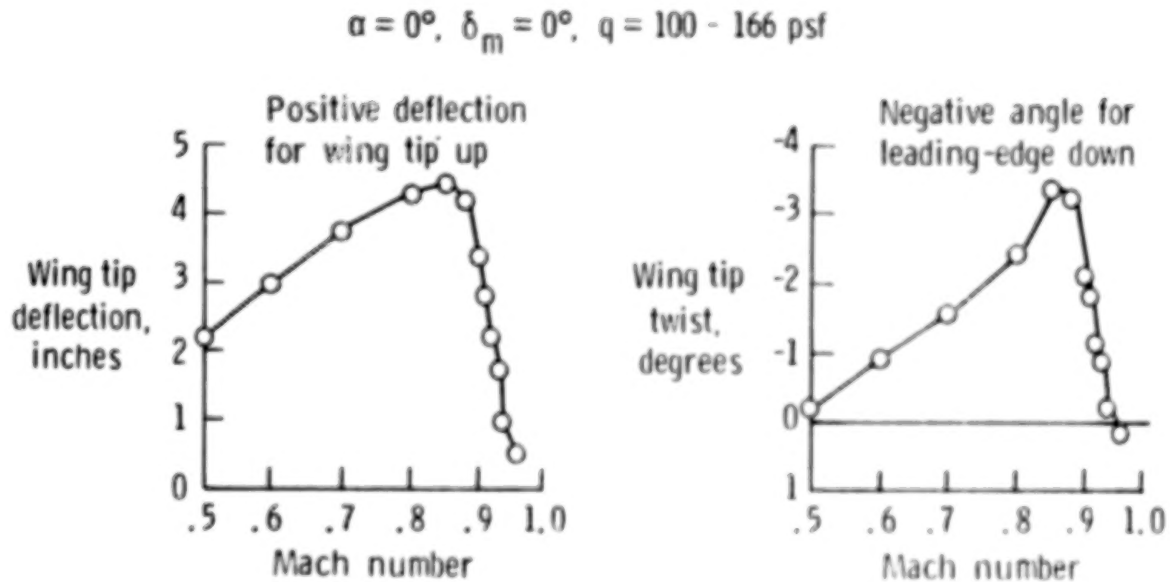


Figure 14

INSTANTANEOUS PRESSURE DISTRIBUTIONS

Figure 15 shows the instantaneous chordwise pressure distribution at the 87.1% span station for $M = 0.92$, $\alpha = -1^\circ$ and $\delta_m = 0^\circ$. This is the condition at which 6 inch peak-to-peak wing tip motion occurred (figure 6). The instantaneous pressure distributions are shown for the maximum and minimum vertical wing tip deflection. Based upon the pressure at 95% chord, at the maximum wing tip deflection the flow aft of the shock is separated on the upper and lower surfaces. The flow is attached on both surfaces when the vertical tip deflection is a minimum.

This figure points out an important feature of this dynamic motion. At conditions where large amplitude dynamic motion is encountered, the trailing-edge flow begins a pattern of separating and reattaching on the wing, which coincides with the shock wave motion. As the Mach number is increased above 0.92 the flow behind the shock remains separated (see figure 13) and the amplitude of the motion rapidly decreases (see figure 6). Thus it appears that the dynamic wing response is related to chordwise shock motion in conjunction with shock induced flow separation and reattachment on both the upper and lower surfaces. This conclusion is supported further by the results obtained when the spanwise fence was attached to the wing lower surface. The fence prevented reattachment of the flow on that surface and the maximum wing motion was found to be dramatically reduced as shown in figure 10.

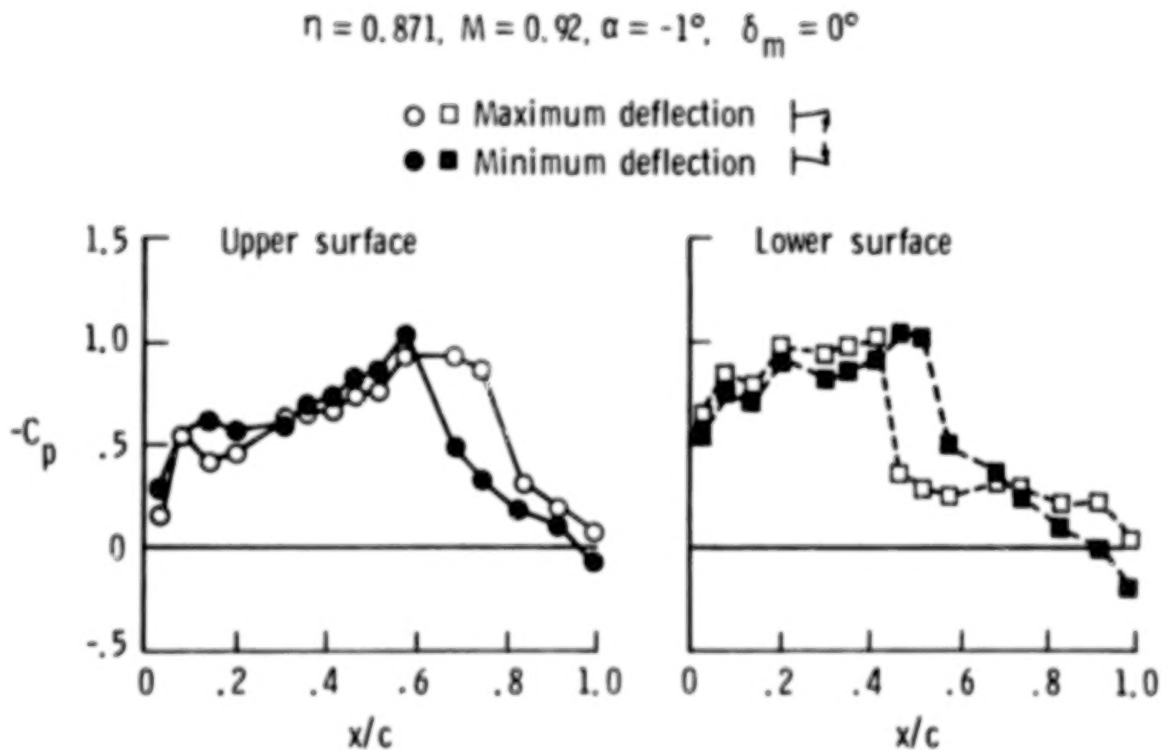


Figure 15

PRESSURE VARIATION WITH TIME

Figure 16 shows a time history of upper and lower surface pressures at the same span station and flow conditions as given in figure 15. All pressures are arbitrarily plotted so that they fit near each other. However, the last chordwise pressures on both surfaces are plotted with a zero reference line. For the last chordwise pressures, the figure clearly shows the separation and reattachment of flow in the trailing-edge region of both surfaces as the pressure values fluctuate above and below zero. The shock motion, as indicated by large pressure variations, is also shown in the figure. For example, the upper surface shock can be seen to move from in front of 68.0% of local chord to behind 74.2%. The lower surface shock moves from in front of 46.0% to behind 51.3%. At the bottom of the figure the measured wing root bending moment time history is plotted for reference. For the observed motion, the wing root bending moment is proportional to wing tip displacement, bending maximum for maximum positive (up) wing tip position.

The alternating separation and reattachment of the flow on the upper and lower surfaces explains the discrepancy between the mean pressure and wool tuft data. The mean pressure data give an average of the pressure values in the trailing-edge region. If, on the average, the flow is attached most of the time, the mean pressure distributions will indicate that the flow is attached. The mean data give an accurate indication of separation only when the flow remains separated most of the time. Another point to note is that while the wool tufts indicate flow separation, they are inadequate for indicating the subsequent flow reattachment.

$$\eta = 0.871, M = 0.92, \alpha = -1^\circ, \delta_m = 0^\circ$$

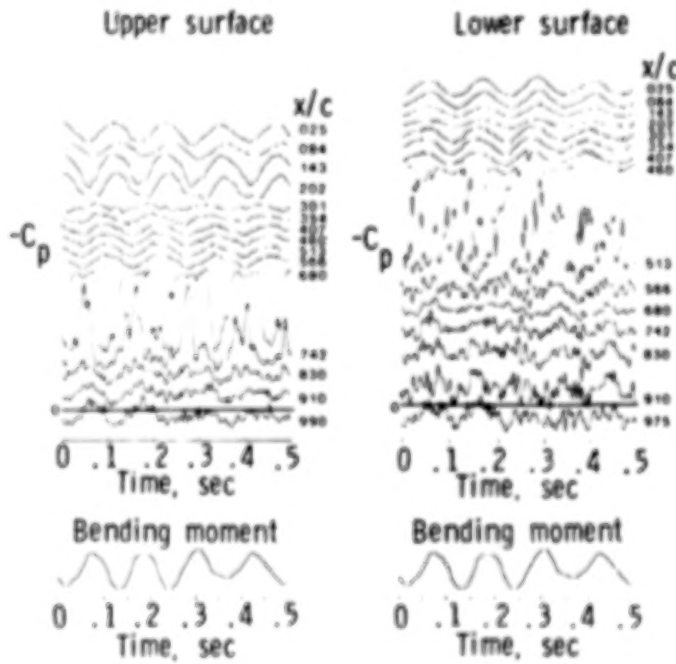


Figure 16

DEMONSTRATION OF ACTIVE SUPPRESSION OF WING RESPONSE

The design of a controller to actively suppress the wing response presented several challenges. Flutter analysis based upon linear potential flow aerodynamic theories did not predict the wing response. The approach adopted was to develop approximate linear models by utilizing forced response data taken during the previous tunnel entry in October 1983. Key transfer functions were estimated from the forced response data for a range of test points as the region of dynamic wing response were approached. Because of the uncertain nature of the transfer function estimates upon which the control law was based, additional transfer function and controller performance data were gathered during the test and used to modify the controller to obtain satisfactory performance. Computer algorithms were written to give near real-time assessment of controller performance.

During the test several sets of fast sine sweep data were taken and averaged for improved transfer function estimation. The loop transfer function was estimated using Fast Fourier Transform (FFT) techniques and, with the feedback loop open, provided a near real-time assessment of controller performance. The controller was modified as necessary and the control loop closed. Fast sine sweep data were again taken to evaluate controller performance. (Fig. 17.)

- Challenges

- Mathematical models more uncertain than normal
- Requirement to estimate key transfer functions from experimental data
- Development/assembly of algorithms that allow near real-time assessment of controller performance during test

- Method

- Upgrade transfer function estimates
- Evaluate controller performance with loop open
- Confirm modified controller performance by closing loop

Figure 17

CLOSED LOOP BLOCK DIAGRAM

The inability of flutter analyses based upon linear potential flow aerodynamic theories to predict the apparent instability led to a decision to attempt to design a control law based upon forced response data from the previous TDT entry (October 1983). Figure 18 depicts the block diagram for the closed-loop single-input/single-output system. The transfer function estimates, \hat{Z}/δ_a , were obtained from response data due to fast sine sweep inputs into the aileron actuator, G_A . These data were available for a number of test points in the range of Mach number $0.7 < M < 0.85$. Unfortunately, the accuracy of the estimates became more suspect as the apparent stability boundary, where good estimates were most needed, was approached. Nevertheless, these transfer function estimates were employed in the preliminary design of a control law, H , to add damping to the critical mode.

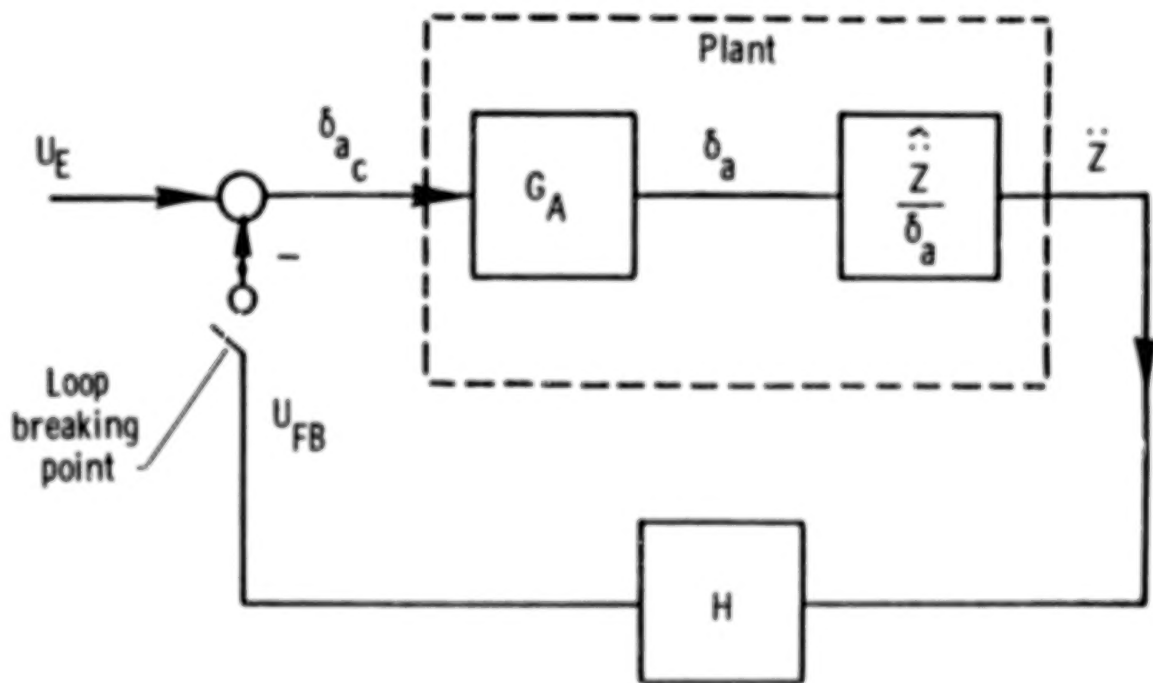


Figure 18

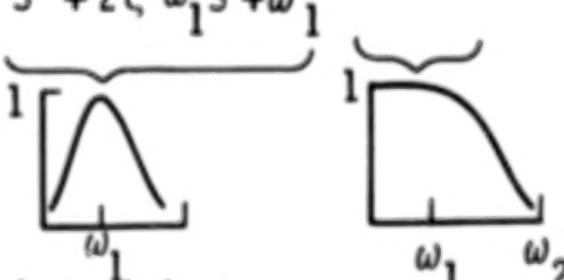
ROBUSTNESS MAXIMIZATION

The objective of the control law design activity was to add damping in the critical frequency range without degrading the stability characteristics of the higher frequency modes. The approach taken was to define, for a range of test points, the compensation, $H(s)$, required to modify the amplitude and phase of the accelerometer outputs such that damping was added in a frequency band centered at the frequency of the first elastic mode. The control law form chosen is shown in figure 19.

$T(s)$ is a fixed low pass filter chosen to attenuate the feedback control so that higher frequency elastic modes were not affected. The factor adjacent to $T(s)$ concentrates the control effort in the frequency region, ω_1 , of the first elastic mode; the frequency, $\omega_1(M, q)$, depended upon Mach number, M , and dynamic pressure q . The parameter ζ was fixed at 0.2. The choice, $\zeta=0.2$, was made to confine the control activity in a narrow band around ω_1 . In retrospect, a larger value of ζ would probably have resulted in more attenuation of the response due to turbulence and could have been used safely since the frequency of the second elastic mode was about 32 Hz. The remaining part of $H(s)$ factor has variable coefficients $\{D_i(M, q), i=1, 5\}$ which were used as control design variables to allow proper amplitude and phasing for robustness.

Values for the variable parameters were found for each test point such that the minimum singular value of the return difference transfer function was maximized subject to gain and phase margin constraints. The search for the optimizing set $\{D_i(M, q)\}$ was done using a nongradient constrained optimization approach.

Find values for the design variables D_i where

$$H = D_1 \frac{(s^2 + D_2 s + D_3)}{(s^2 + D_4 s + D_5)} \underbrace{\frac{2\zeta \omega_1 s}{s^2 + 2\zeta \omega_1 s + \omega_1^2}}_{\text{Phasing adjustment}} T(s)$$


Such that

- Minimum singular value is maximized
- Good gain and phase margins

Figure 19

ACCELEROMETER PEAK-HOLD RESPONSE

Closed-loop performance is shown in figure 20 in terms of frequency domain peak-hold responses. Peak-hold is a subcritical response technique used in predicting flutter boundaries wherein the autospectrum of an output is obtained for a block of data. Subsequent autospectra are taken for a number of blocks of data and the peak value at each frequency out of the entire set of blocks is retained (held). As the point of neutral stability of a mode is approached, the amplitude at its resonant frequency approaches infinity. Thus, by observing the variation in the peaks held, or typically, their reciprocals, as a function of test condition changes, one obtains an indication of changes in damping ratio and a prediction of where an instability might occur.

The figure shows peak-hold responses with the control system loop open and closed both for turbulence only and turbulence plus fast sine sweep excitation. It is seen that the controlled cases have lower responses than the uncontrolled cases over the entire Mach number range. The controlled response is sharply attenuated at the first elastic mode resonant frequency and somewhat amplified on either side of it as compared with the uncontrolled case. The amplification at the slightly higher frequency is due to a lightly damped mode introduced by the controller. Increasing the controller bandwidth by selection of a larger value for ζ , as mentioned earlier, would probably have allowed further reduction in the controlled response. Control effort due to turbulence excitation varied from a peak feedback signal magnitude of approximately 0.25° at $M = 0.70$ to 2.3° at $M = 0.92$ for these cases.

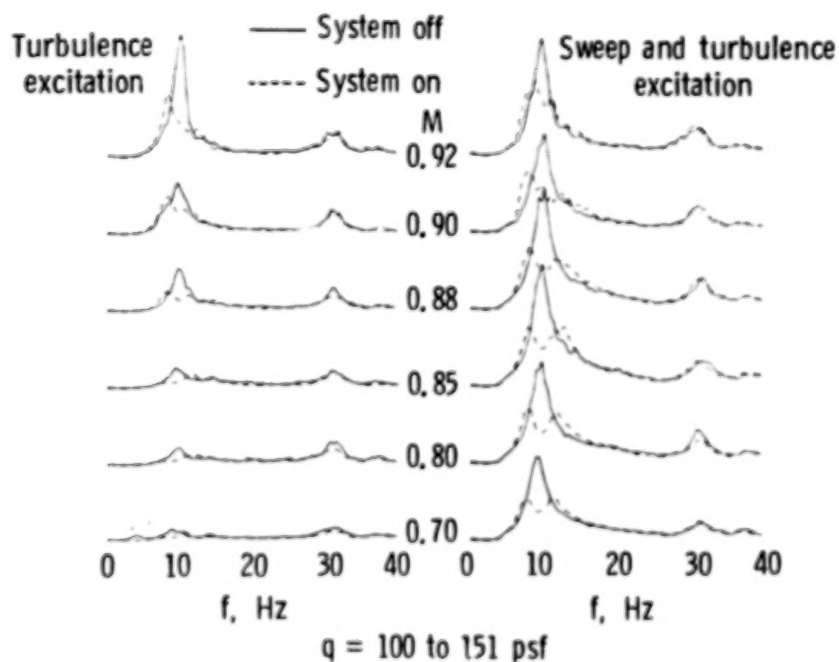


Figure 20

CONCLUDING REMARKS

The DAST ARW-2 wing had been tested previously in the NASA Langley TDT and an unusual instability boundary was predicted based upon subcritical response data. Contrary to the predictions, no instability was found during the present test. Instead a region of high dynamic wing response was observed which reached a maximum value between Mach numbers 0.92 and 0.93. The amplitude of the dynamic response increased directly with dynamic pressure.

The response appears to be related to chordwise shock movement in conjunction with flow separation and reattachment on the upper and lower wing surfaces. The onset of flow separation coincided with the occurrence of strong shocks on a surface. Instantaneous pressure distributions indicated that the flow was intermittently separating and reattaching near the trailing edge under conditions of maximum wing motion. The dynamic wing response was sensitive to angle of attack, with maximum motion occurring near $\alpha = 0^\circ$. Static deflection of the outboard control surface significantly decreased the dynamic response for $\delta_m = -6^\circ$. A spanwise fence installed on the lower surface to disturb the flow pattern resulted in a significant decrease in dynamic wing response.

A controller was designed to suppress the wing response. The control law attenuated the response as compared with the uncontrolled case and added a small but significant amount of damping from $M = 0.70$ to $M = 0.92$ for the lower density condition ($q = 100 - 151 \text{ psf}$).

The unsteady pressure and response data acquired during this test constitute a valuable data base to be used for further study of this unusual phenomena and for validation of unsteady CFD codes. (Fig. 21.)

- No "hard flutter" point obtained although amplitude increases as dynamic pressure increases
- Response coincides with onset of shock-induced separation and reattachment
- Response affected by angle-of-attack, outboard control surface position, and a spanwise fence on the lower surface
- Active suppression successfully demonstrated, significant damping added with feedback loop closed
- Unsteady pressure data acquired during dynamic response for further analysis and use in code validation work

Figure 21

The Role of Shock Induced Trailing-Edge Separation In Limit Cycle Oscillations*

ATLEE M. CUNNINGHAM, JR.
GENERAL DYNAMICS
FORT WORTH DIVISION

*This Work Was Supported Under Contract NAS4-2577

THE ROLE OF SHOCK INDUCED TRAILING EDGE SEPARATION IN LIMIT CYCLE OSCILLATIONS

In figure 1 Limit Cycle Oscillations (LCO) are defined as limited amplitude oscillations which are self-sustaining and are produced by a structural/aerodynamic interaction. The role of shock induced trailing edge separation (SITES) in this phenomenon, as will be discussed in this paper, is to act as a non-linear spring which triggers and drives the LCO. The appearance of SITES coincides with the classical trailing edge pressure divergence which is a well-known indicator of buffet onset. Because of this, LCO has previously been referred to as buffet or, at transonic speeds, Mach buffet. The conditions for transonic LCO are moderate incidence, usually less than 10° , and high transonic Mach numbers, ranging from 0.8 to 1.1. Lowly damped vibration modes tend to respond provided they have the proper characteristics to couple with the SITES type flow. These conditions frequently occur near flutter boundaries which creates considerable anxiety in both test pilots and engineers, especially when the response is in a single mode with a distinct frequency. Since amplitudes can become quite large, even though they are limited, the knowledge of LCO boundaries becomes very important for efficient flight flutter testing.

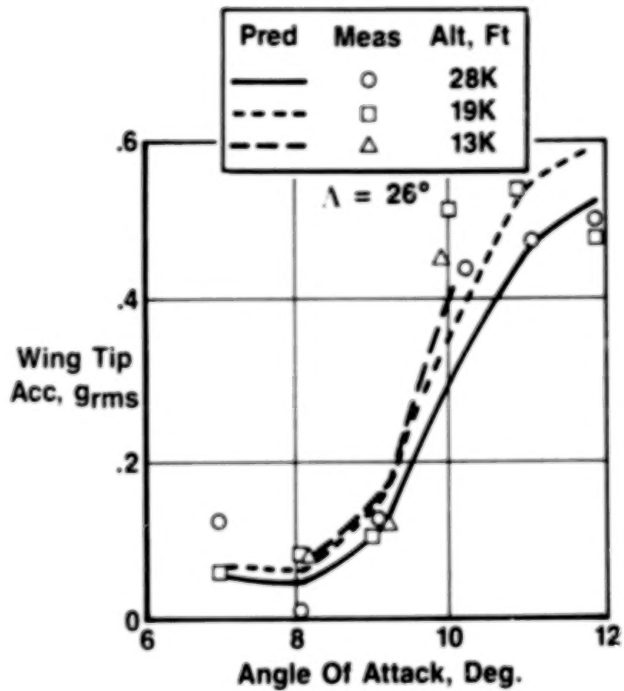
- **LCO Is Defined As A Limited Amplitude Oscillation Which Is Self-Sustaining And Results From A Structural/Aerodynamic Interaction**
- **Shock Induced Trailing Edge Separation (SITES) Coincides With The Classical Trailing Edge Pressure Divergence**
- **The Conditions Are Moderate Incidence And High Transonic Mach Numbers**
- **Lowly Damped Vibration Modes Tend To Respond If They Have The Proper Characteristics**
- **Response Is Single Mode With Distinct Frequency And Limited Amplitude**

Figure 1

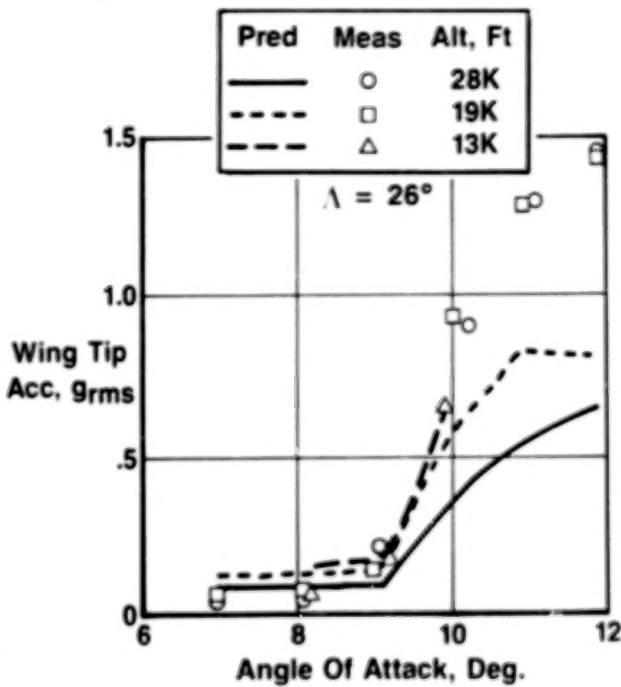
WING BENDING AND TORSION MODE RESPONSE FROM
THE F-111 TACT BUFFET ANALYSIS AT $M=0.8$, $\Lambda_{LE}=26$ DEG

The results shown in figure 2 represent the comparison of predictions and flight test results for buffet response of the F-111 tact aircraft at $M=0.8$ and a leading edge sweep of 26° (ref. 1). The results are wing tip RMS accelerations for the first symmetric wing bending mode and the first wing torsion mode group which includes both asymmetric as well as symmetric modes. Several altitudes are represented which range from 13K ft to 28K ft, for angles varying from 7° to 12° . The interesting feature to note in the comparisons is that (1) the bending mode responses are very well predicted in terms of both angle and altitude effects whereas (2) the torsion mode responses are consistently underpredicted with exception of the lowest altitude. Since the prediction method did not allow for a coupling between the buffeting flow and the structural response, these results led to an investigation of what kind of coupling could exist with the torsion modes. Thus, the role of SITES in LCO was developed as an answer to this question.

(Reference 1)



First Wing Bending
Mode Response



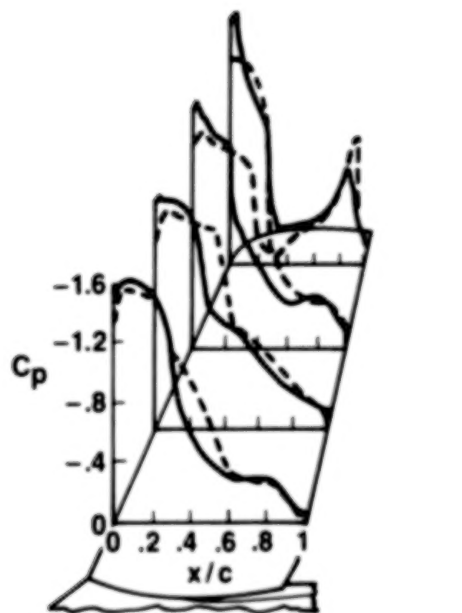
Wing Torsion Mode
Response

Figure 2

STATIC PRESSURE CHANGES ON THE MODEL AND AIRPLANE
WING UPPER SURFACE FOR TRANSITION TO SITES

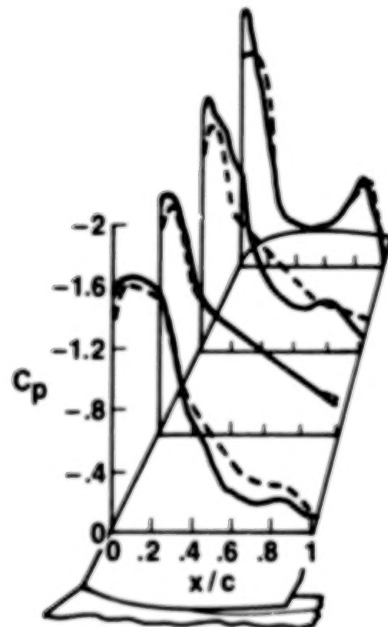
A clue to a possible means for the coupling can be deduced from the static pressures in figure 3. The occurrence of trailing edge pressure divergence at about 10° also corresponds to a large forward movement of the upper surface main shock as shown by comparing the pressures in figure 3 at 9° and at 10° . It will also be noted that the forward shock movement for the aircraft is much larger than that for the model. The condition of this transition is the occurrence of shock-induced trailing edge separation (SITES) which was extensively discussed by Cunningham, et al in reference 2. It was shown that this transition was accompanied by a step change in pitching moment with either increasing or decreasing angle-of-attack. With increasing angle, the forward shock movement produced a loss in lift forward and the trailing edge divergence produced a gain in lift aft. The net result was to provide a step change in pitching moment that was nose down for increasing angle. For decreasing angle, the opposite took place and produced a step change in pitching moment that was nose up.

(Reference 1)



$\alpha = 9.1$ Deg
Pre-SITES

— 1/6 Scale
Model
 $R_{MAC} = 14 \times 10^6$
--- FLT Test
 $R_{MAC} = 25 \times 10^6$
 $M = 0.8$
 $\Lambda_{LE} = 26$ Deg.



$\alpha = 10$ Deg
Post-SITES

Figure 3

EFFECT OF MEAN ANGLE, FREQUENCY AND AMPLITUDE
ON MEASURED UNSTEADY PRESSURES

Dynamic unsteady investigations of SITES flows were conducted by Triebstein (ref. 3) for an NACA 0012 airfoil oscillating in pitch at various mean angles, frequencies and amplitudes as shown in figure 4. These results are the upper surface unsteady pressure distributions for the first harmonic. The effect of varying mean angle is quite pronounced where at $\alpha = 0^\circ$ the distributions are of conventional transonic characteristics, but at $\alpha = 5^\circ$ the distributions are totally different. The most notable change is the trend toward a more nose-down pitching moment. The influence of increasing frequency simply shows an expected increasing lag at either angle. Increasing amplitude at $\alpha = 5^\circ$ with SITES shows a decrease of the shock motion peak amplitude when normalized by the pitching amplitude. This demonstrates the tendency to maintain a constant incremental force with increasing pitch increments so that a limited amplitude motion is inevitable. That is, the viscous damping which is a function of amplitude increases until it balances the destabilizing fixed incremental force due to the SITES transition.

(Reference 2)

Upper Surface Results For An Oscillating NACA 0012 Airfoil, $M = 0.78$

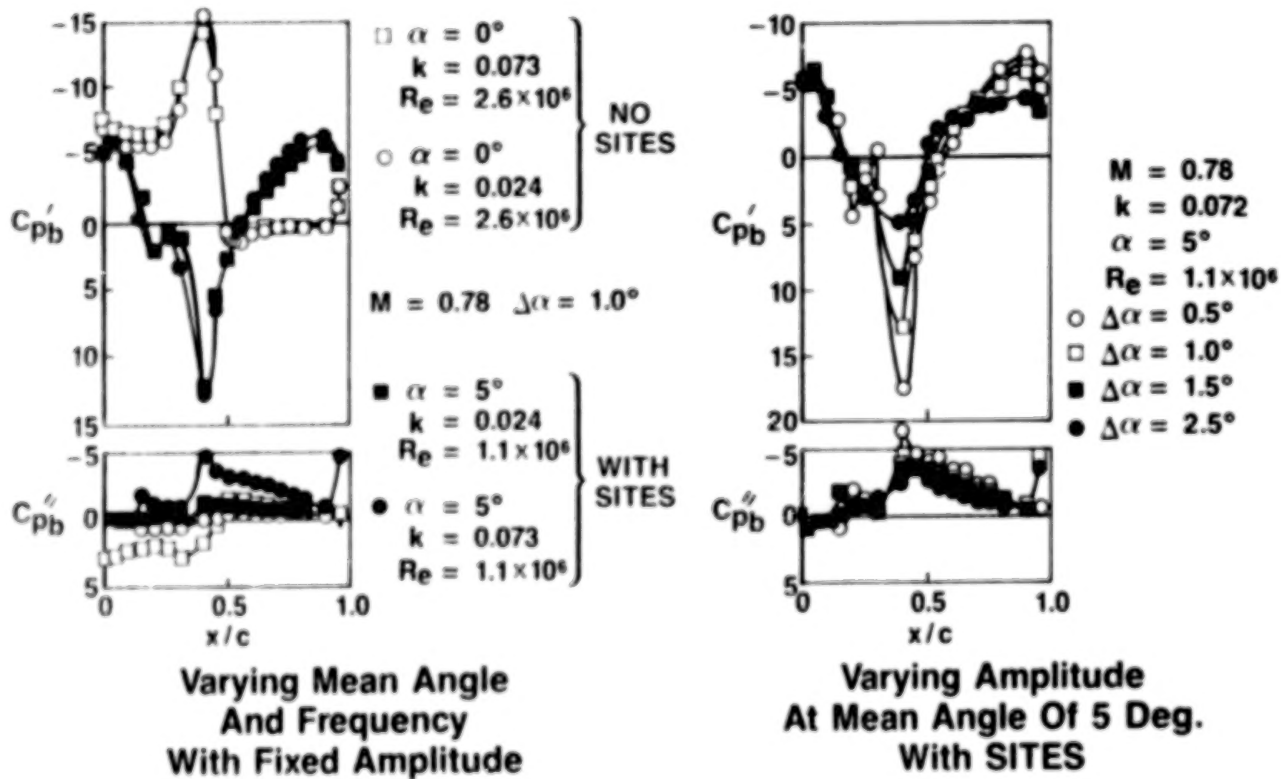


Figure 4

SCHEMATIC DIAGRAM OF THE VARIATION OF THE INCREMENTAL PITCHING MOMENT DUE TO SITES WITH ANGLE AND PITCH RATE

The step change in pitching moment just described in figures 3 and 4 can be cast in the form of a non linear spring that provides a step increase in resisting stiffness as the airfoil passes through SITES. This form is illustrated in figure 5 for a hypothetical situation in which, for simplicity, only the step change is present. (Normally, the pitching moment variation with angle is a nearly constant slope with the discontinuity superimposed to produce a shift in characteristic at the SITES transition point.) The influence of pitch rate that provides the hysteresis is also illustrated. For positive pitch rate, SITES is delayed to a higher angle, whereas for negative pitch rate, re-attachment is delayed to a lower angle.

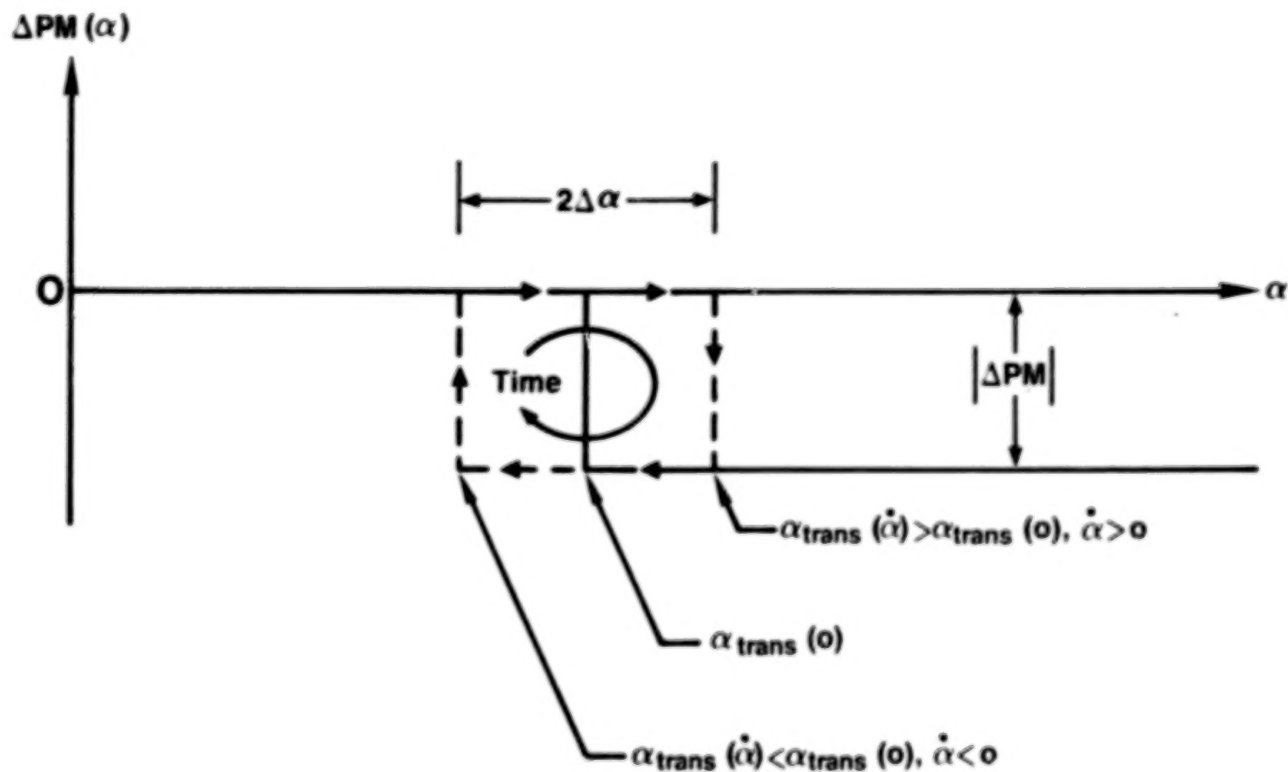


Figure 5

HYPOTHETICAL TIME HISTORY OF AN AIRFOIL
UNDERGOING SITES INDUCED TORSIONAL LCO

The non-linear spring described above can potentially produce a limit amplitude, self-sustaining oscillation. How this is possible can be described by considering an airfoil with a torsion spring undergoing a maneuver of increasing angle until it encounters SITES as shown in figure 6. Slowly increasing incidence at angles below that of SITES allows the torsion spring to attain a continuous state of equilibrium with aerodynamic pitching moment. When SITES is reached, a sudden nose-down increment is imposed on the aerodynamic pitching moment which will tend to reduce wing incidence. This will be a dynamic negative pitch rate which will delay re-attachment and permit the nose-down moment to put work into the system. At some point, re-attachment does take place and the nose-down moment disappears. Accelerations become negative and the wing experiences a reduced pitch rate until it reaches zero and begins nose-up motion. Positive pitch rate now takes over which will produce a delay in SITES and allows an overshoot of the initial starting point due to stored elastic energy during the down stroke. When SITES does occur, the cycle then repeats itself.

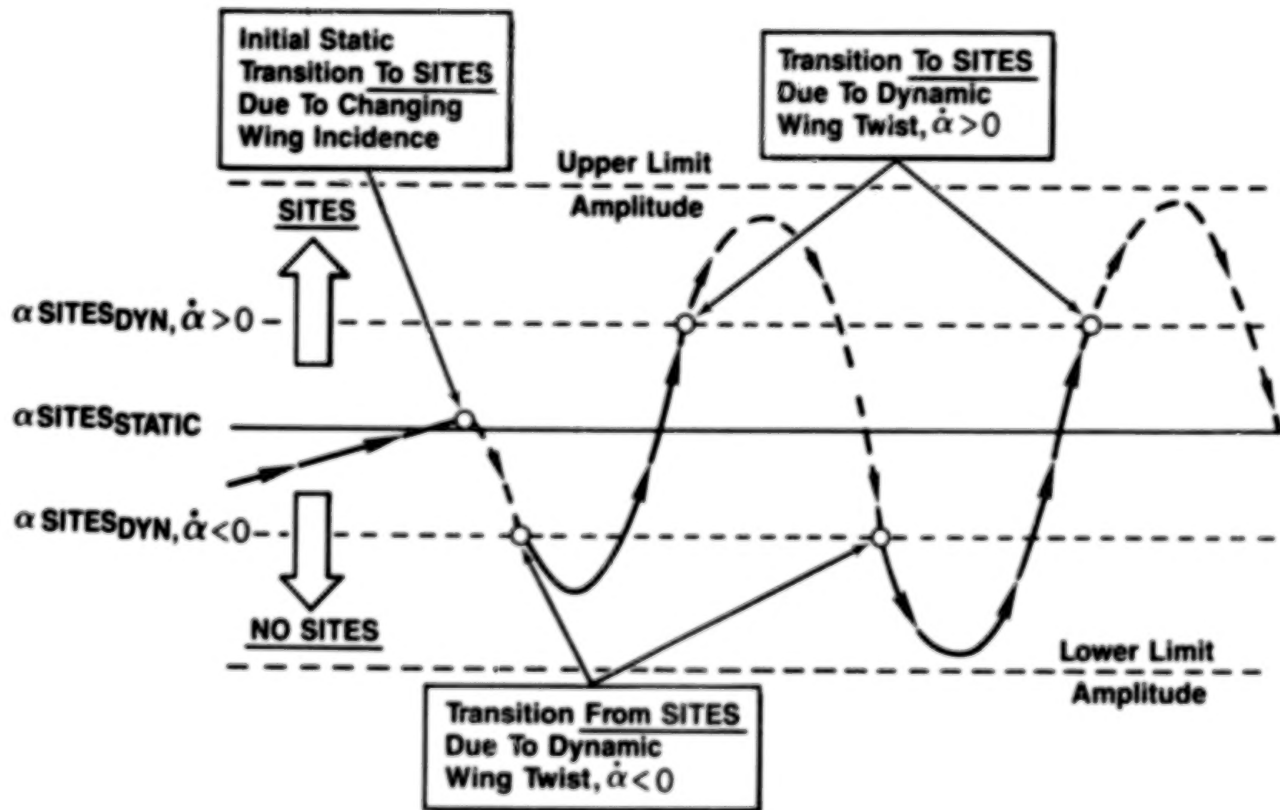


Figure 6

The math model for calculating LCO response was developed and presented in reference 1. The governing equation for a non-linear single DOF spring-mass system is shown in figure 7. The LHS of the equation is the conventional linear equation form for a generalized coordinate response. The RHS is composed of the non-linear step force function as defined for the vibration mode of interest. This force is obtained by integrating the incremental pressure changes due to SITES transition with the mode shape to produce a generalized force. The boundary conditions require that at time zero, the system is in static elastic equilibrium (zero velocity) and that the normalized displacement is equal to zero at the static transition point for SITES. That is, the step function change on the RHS is suddenly imposed on the system at time zero.

- The Non-Linear Single DOF Spring-Mass System

$$M_i \ddot{q} + 2 M_i \omega_i \delta_i \dot{q} + M_i \omega_i^2 q = \Delta F_i(q, \dot{q})$$

- Where

$M_i, \omega_i, \delta_i, q$ = Mass, Frequency, Damping and Response
For The i th Mode

$\Delta F_i(q, \dot{q})$ = Non-Linear Incremental Force
(Due To SITES)

- Is Subject To The Initial Conditions

$$q(t=0) = q_{trans}(\dot{q}=0)$$

$$\dot{q}(t=0) = 0$$

Figure 7

SCHEMATIC DIAGRAM OF THE VARIATION
OF $\Delta F_i(q, \dot{q})$ NEAR SITES

The plot shown in figure 8 illustrates that the form of variation of the step change in generalized force is identical to that shown for pitching moment in figure 5. The influence of pitch rate in the hysteresis is also identical for wing modes that have significant torsional motion. This is consistent with observations to date which indicate that LCO occurrences which are coincident with SITES tend to concentrate on torsional modes or modes with some pitching content.

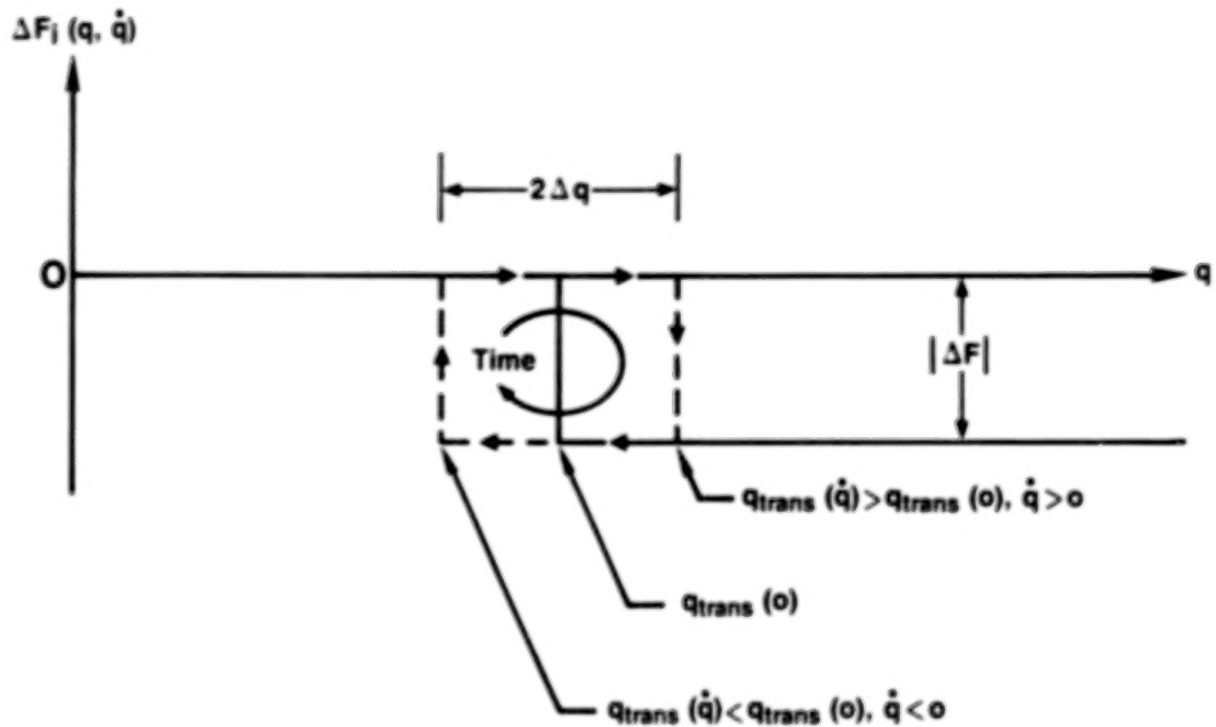


Figure 8

A finite difference solution was developed in reference 1 for the equation of motion discussed in figure 7. The form of the solution is shown in figure 9 where the parameters have all been cast in non-dimensional form with exception of ϵ and q_n . These terms have the dimension of length. The two equations are applicable depending on the response value relative to SITES transition. Hysteresis is included in the model through the use of a transition point that is sensitive to wing motion velocity, \dot{q} . The initial conditions are defined such that the transition actually occurs at the third time step, q_2 .

- A Finite Difference Solution To The Non-Linear Equation Is

$$q_{n+1} = \frac{1}{1+\lambda\delta} [\lambda^2\epsilon + (2 - \lambda^2)q_n - (1 - \lambda\delta)q_{n-1}], \quad q_n \geq q_{\text{Trans}}(\dot{q})$$

$$q_{n+1} = \frac{1}{1+\lambda\delta} [(2 - \lambda^2)q_n - (1 - \lambda\delta)q_{n-1}], \quad q_n < q_{\text{Trans}}(\dot{q})$$

- Where

$$\lambda = \Delta t \omega_i \quad \epsilon = \frac{\Delta F_i}{M_i \omega_i^2}$$

$$\delta = \delta_i$$

Δt = Time Step Size

q_n = Response Of The i th Mode At The n th Time Step

- Subject To The Initial Conditions

$$q_0 = q_1 = 0, q_2 = \frac{\lambda^2\epsilon}{1 + \lambda\delta}$$

Figure 9

SAMPLE OF LCO CALCULATIONS FOR THE F-111 TACT

The algorithm just described was programmed and input data were developed for the right wing torsion mode of the F-111 TACT airplane (ref 1). The conditions were $M=0.8$ and 21K ft altitude. The generalized mass, frequency and damping data were obtained from a conventional dynamic response and flutter analysis. The estimate for ΔF_i was developed by using the pressure distributions at 9° and 10° to obtain the incremental loads due to transition to SITES. The load distribution was combined with the mode deflections, $h_i(x, y)$ to produce the generalized step force value of ϵ . Estimates for Δq , the hysteresis parameter (see fig. 8), were not possible based on available data, hence, a parameter study was conducted by letting Δq vary as a fraction of ϵ . A sample plot for $\Delta q = \epsilon$ shown in figure 10 illustrates how the transient solution quickly approaches a limit amplitude oscillatory motion. It is also interesting to note that the apparent frequency is slightly higher than the right wing torsion mode frequency. (Since the number of time steps shown in the plot represents ten cycles, the apparent frequency can be determined by simply counting cycles.)

- The Parameters For The Right Wing Torsion Mode Were

$$M_i = 565.9 \text{ Lbs}$$

$$\omega_i = (14.17 \text{ Hz}) \times 2\pi$$

$$\delta_i = 0.07 \text{ (From Flutter Solution)}$$

$$\epsilon_i = \frac{Q}{M_i \omega_i^2} \int_{A_{\text{wing}}} h_i(x, y) [C_{p10}(x, y) - C_{p9}(x, y)] dxdy \\ = -0.0127 \text{ Ft}$$

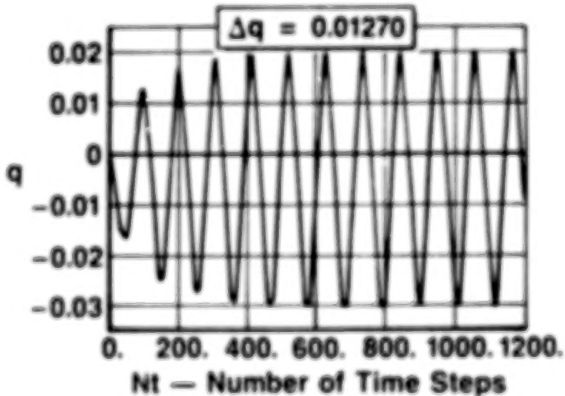


Figure 10

RESULTS OF LCO CALCULATIONS FOR THE F-111 TACT AIRCRAFT
AND 1/6-SCALE MODEL RIGHT WING TORSION MODE

The results shown in figure 11 are for the nominal conditions of $M=0.8$, $\alpha=9^\circ-10^\circ$ as were presented in reference 1. The flight test data were extracted from figure 2 by subtracting the predicted response from the flight measured response for the wing torsion modes. Since the LCO attributed response was assumed to be uncorrelated with the broad-band buffet response, this subtraction was done on an RMS basis. The calculated full scale data were obtained with the LCO algorithm by letting Δq vary as a fraction of ϵ from 0.2 up to 2.0. It is interesting to note that up to a ratio of 1.0, the LCO response increases and the frequency drops. Within this range, the calculated amplitude is within reasonable agreement with the flight data considering that the method should be conservative as it currently exists. For $\Delta q = 2\epsilon$, the response is zero, which states that the conditions for sustained oscillation require that the transition must occur in both directions during the cycles; otherwise, the response is simply a static displacement. Finally, the 1/6-scale model results show that the calculations verify the observation that the model did not experience LCO in the wind tunnel test.

Conf.	Method	ϵ (Fl)	$ \epsilon$ (Deg.)	$ \Delta q/\epsilon $	APP. f, Hz	RWAC. g's Response*
F.S.A.C.	FLT Test	—	—	—	15.0	0.8
F.S.A.C.	Calc.	-0.0127	0.073	0.2	18.4	0.71
				0.4	17.0	1.42
				0.6	16.4	1.79
				0.8	15.1	2.05
				1.0	14.9	2.34
				2.0	14.2	0
1/6-S.M.	Wind Tun.	—	—	—	156.0	≈ 0
1/6-S.M.	Calc.	-0.000253	0.0087	8.4**	156.0	0

*LCO Response From Testing Is Estimated As The Amount That Exceeds Expected Linear Buffet Response

** Δq Assumed As A Constant Angle Determined By F.S.A.C. For $|\Delta q/\epsilon| = 1.0$

Figure 11

As a result of this investigation, the potential role of shock induced trailing edge separation in limit cycle oscillations was established. It was shown that the flip-flop characteristic of transition to and from SITES as well as its hysteresis could couple with wing modes with torsional motion and low damping. This connection led to the formulation of a very simple non-linear math model using the linear equations of motion with a non-linear step forcing function with hysteresis. A finite difference solution with time was developed and calculations were made for the F-111 TACT airplane. Static pressure data for the F-111 TACT were used to determine the step forcing function due to SITES transition. However, no data were available for the hysteresis hence a parameter study was conducted allowing the hysteresis effect to vary. Very small hysteresis effects, which were within expected bounds, were required to obtain reasonable response levels that essentially agreed with flight test results. Also in agreement with wind tunnel tests, LCO calculations for the 1/6-scale F-111 TACT model showed that the model should not have experienced LCO.

- The Role Of Shock Induced Trailing Edge Separation (SITES) In Limit Cycle Oscillations (LCO) Has Been Described
- The Flip-Flop Characteristic Of Transition To SITES and Its Hysteresis Has Been Shown To Be A Potential Source Of LCO
- A Very Simple Non-Linear Math Model Was Assembled and Solved With A Finite-Difference Approach
- The Math Model Used Static Pressure Model Data and Standard Flutter Solution Results; However, Hysteresis Data Were Not Available and Had To Be Assumed For This Study
- Calculations For The F-111 Tact Aircraft Showed Order Of Magnitude Agreement With Flight Test
- Calculations Also Showed That The 1/6-Scale Model Should Not Have Experienced LCO-Which Agrees With Observations

Figure 12

REFERENCES

1. Coe, C. F. and Cunningham, A. M., Jr.: Predictions of F-111 Tact Aircraft Buffet Response and Correlation of Fluctuating Pressures Measured on Aluminum and Steel Models and the Aircraft. NASA CR-4069, May 1987.
2. Cunningham, A. M., Jr., Sheridan, A. E., and Freeman, T. K.: Update Structural Design Criteria, Design Procedures and Requirements for Bomber/Logistic Type Airplane Wing and Tail Loads, Volumes I through VII. AFWAL-TR-82-3084, December 1982.
3. Triebstein, H.: Steady and Unsteady Transonic Pressure Distributions on NACA 0012. Journal of Aircraft, vol. 23, no. 3, March 1986, pp. 213-219.

INITIAL APPLICATION OF CAP-TSD TO WING FLUTTER

**Herbert J. Cunningham, Robert M. Bennett,
and John T. Batina
Unsteady Aerodynamics Branch
NASA Langley Research Center
Hampton, Virginia**

INTRODUCTION

The purpose of this presentation is to present a brief status report on the initial application of the CAP-TSD computer program for wing flutter analysis. The CAP-TSD program (for Computational Aeroelasticity Program - Transonic Small Disturbance) is based on an approximate factorization (AF) algorithm that is stable and efficient on supercomputers with vector arithmetic. The program has been described by Batina* in an earlier presentation. CAP-TSD has been used to calculate steady and unsteady pressures on wings and configurations at subsonic, transonic, and supersonic Mach numbers. Comparisons of these results with other methods and with experimental data have been favorable. However, the CAP-TSD code has been developed primarily for aeroelastic analysis. The present paper reports on the initial efforts for validation of the aeroelastic analysis capability. The initial applications include two series of symmetric, planar wing planforms. Well-defined modal properties are available for these wings; this is vital for accurate flutter calculations. In addition, transonic flutter boundaries are available for evaluation of the transonic capabilities of CAP-TSD. Additional comparisons are also being made with linear theory and with the 2-D code XTRAN2L. (Fig. 1.)

*Batina et al., NASA CP- 3022, 1989, Paper No. 4, pp. 63-96.

- **COMPUTATIONAL AEROELASTICITY PROGRAM - TRANSONIC SMALL DISTURBANCE**
- **PREVIOUS EMPHASIS HAS BEEN ON PRESSURES**
 - GENERALLY GOOD RESULTS
 - HAVE CONSIDERED STEADY AND UNSTEADY CASES
 - CONFIGURATIONS
- **PROGRESS REPORT ON AEROELASTIC VALIDATION**
- **CONSIDERING SYMMETRIC PLANAR WINGS**
 - WELL-DEFINED MODAL PROPERTIES
 - TRANSONIC FLUTTER BOUNDARIES
- **COMPARISONS WITH 2-D CODE XTRAN2L ARE ALSO UNDER WAY (NOT PRESENTED)**

Figure 1

WINGS

Two series of wing planforms are being used for the initial flutter calculations with CAP-TSD. The first set of wings is a series of swept and tapered wings that are being considered as an AGARD standard configuration for aeroelastic analysis. These wings are swept back 45° at the quarter chord. They are described further by Dr. E. C. Yates' presentation* of this workshop. The wings and test data are presented in NASA TN D-1616, dated March 1963.

The other wing planform is a clipped delta wing that was used in some early flutter suppression studies. It is described in NASA TN D-7544, June 1974, and NASA TR R-450, December 1975. The leading edge sweep for this wing is 50.5° and it is highly tapered. (Fig. 2.)

* Yates, E. C., NASA CP-3022, 1989, Paper No. 12, pp. 243-260.

- 45° SWEPT WINGS - NASA TN D-1616 AND YATES' PRESENTATION
- CLIPPED DELTA WING - NASA TN D-7544 AND TR R-450

Figure 2

PLANVIEW OF 45° SWEPT WING

The planview of the 45° swept wing is shown in figure 3. The wings were semispan, wind-tunnel-wall-mounted models that had a quarter chord sweep of 45° (leading-edge sweep of 46.3°), a panel aspect ratio of 1.65, and a taper ratio of 0.66. The wings had an NACA 65A004 airfoil section and were constructed of laminated mahogany. In order to obtain flutter for a wide range of Mach number and density conditions, some of the wings had holes drilled through the wing to reduce the stiffness. To maintain the airfoil shape, the holes were filled with a rigid foam plastic as can be seen in figure 3.

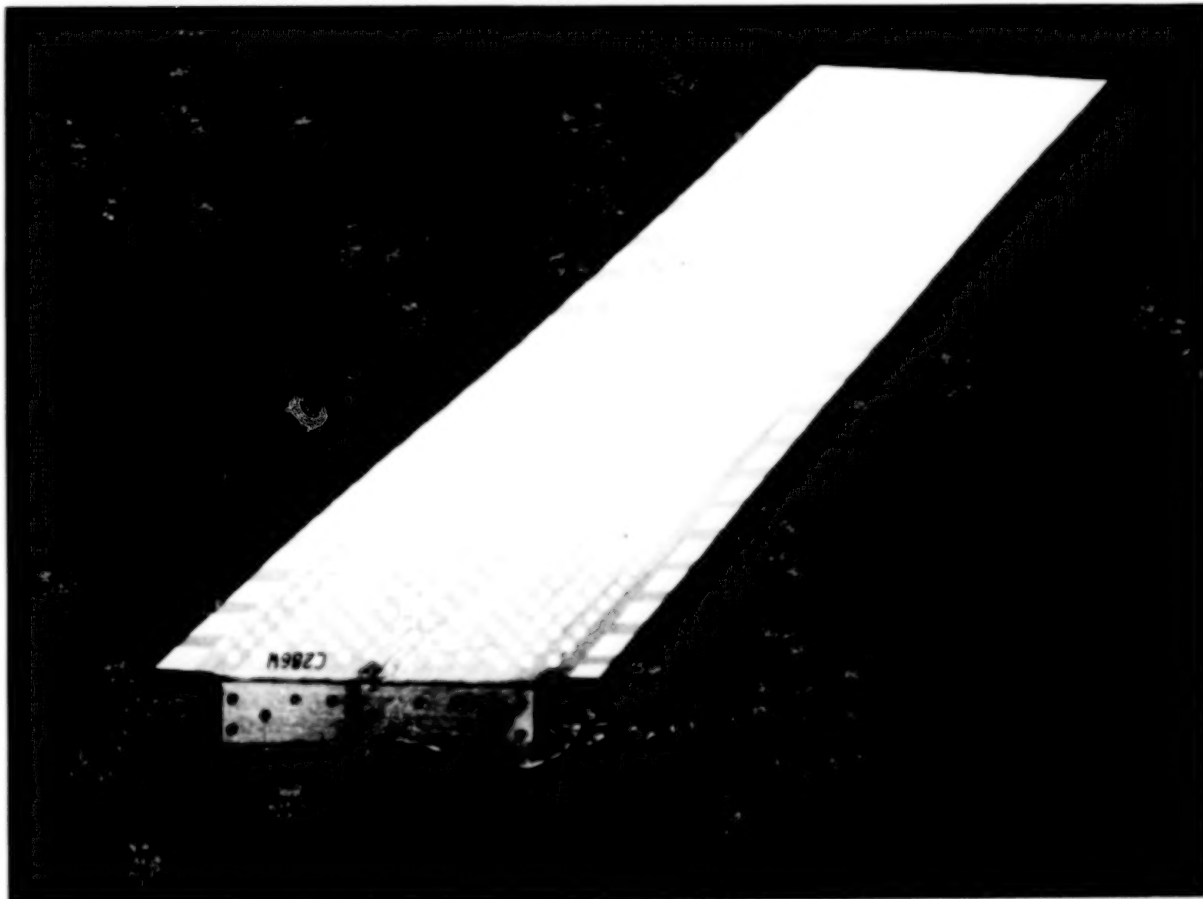


Figure 3

45° SWEPT WING IN THE NASA TRANSONIC DYNAMICS TUNNEL

One of the 45° wings is shown mounted in the Transonic Dynamics Tunnel (TDT) at NASA Langley Research Center in figure 4. The models were tested in air and Freon* test media. The semispan of most of these models was 2.50 feet, which is small compared to the 16-foot test section of the TDT. The models were tested at zero angle of attack.

*Freon: Registered trademark of E. I. duPont de Nemours and Co., Inc.

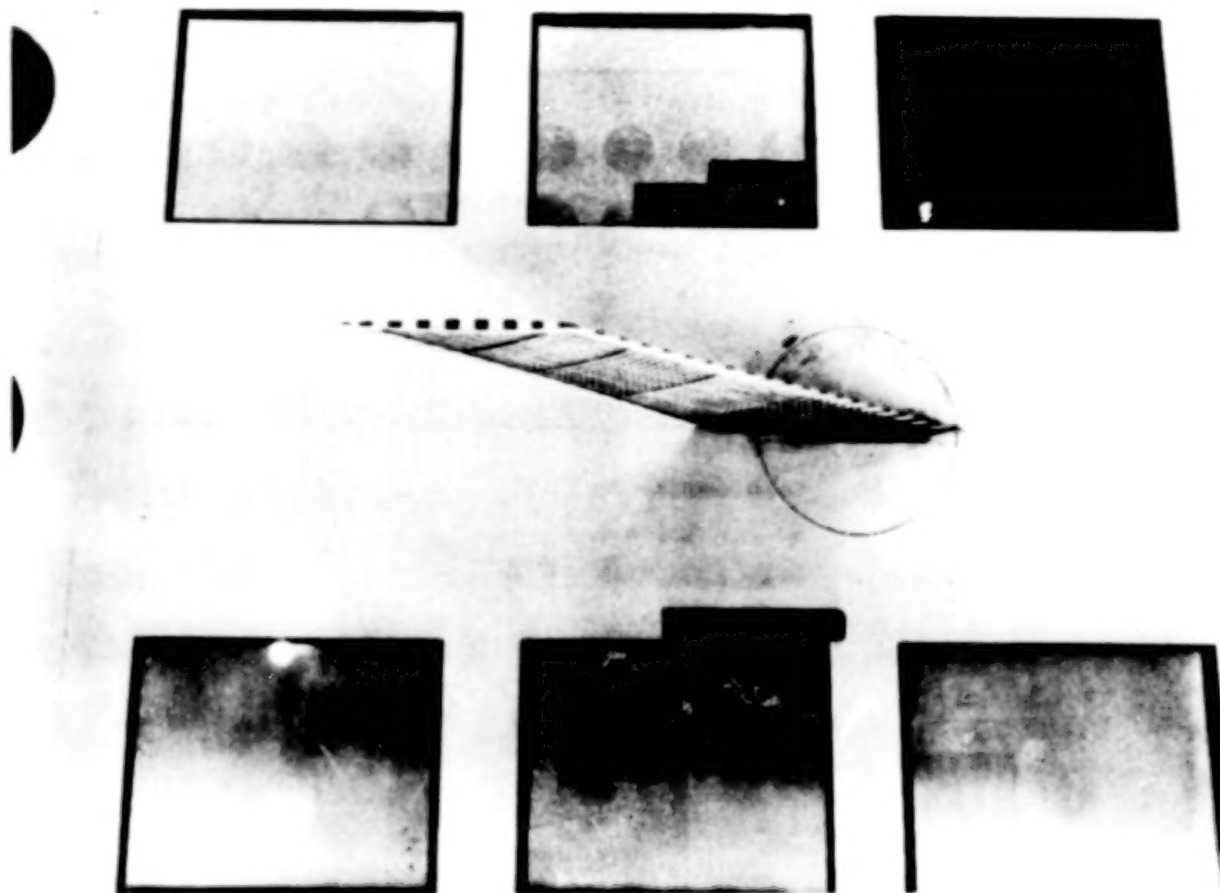


Figure 4

OBLIQUE PROJECTIONS OF NATURAL VIBRATION MODES 45° WING WEAK3

The vibration mode shapes for the 45° wings were not measured, but node lines, frequencies, and stiffnesses are available from the report (NASA TN D-1616, 1963). Mode shapes were calculated with a finite-element analysis and the wing properties were adjusted to match the measured nodes lines and frequencies for the lower vibration modes. Oblique projections for the first four modes for wing WEAK3 are shown in figure 5. The modes numbered 1 through 4 represent first bending, first torsion, second bending, and second torsion, respectively. The modal frequencies range from 9.60 Hz for the first bending mode to 91.54 Hz for the second torsion mode. Similar mode shapes have been calculated for the wing SOLID2.

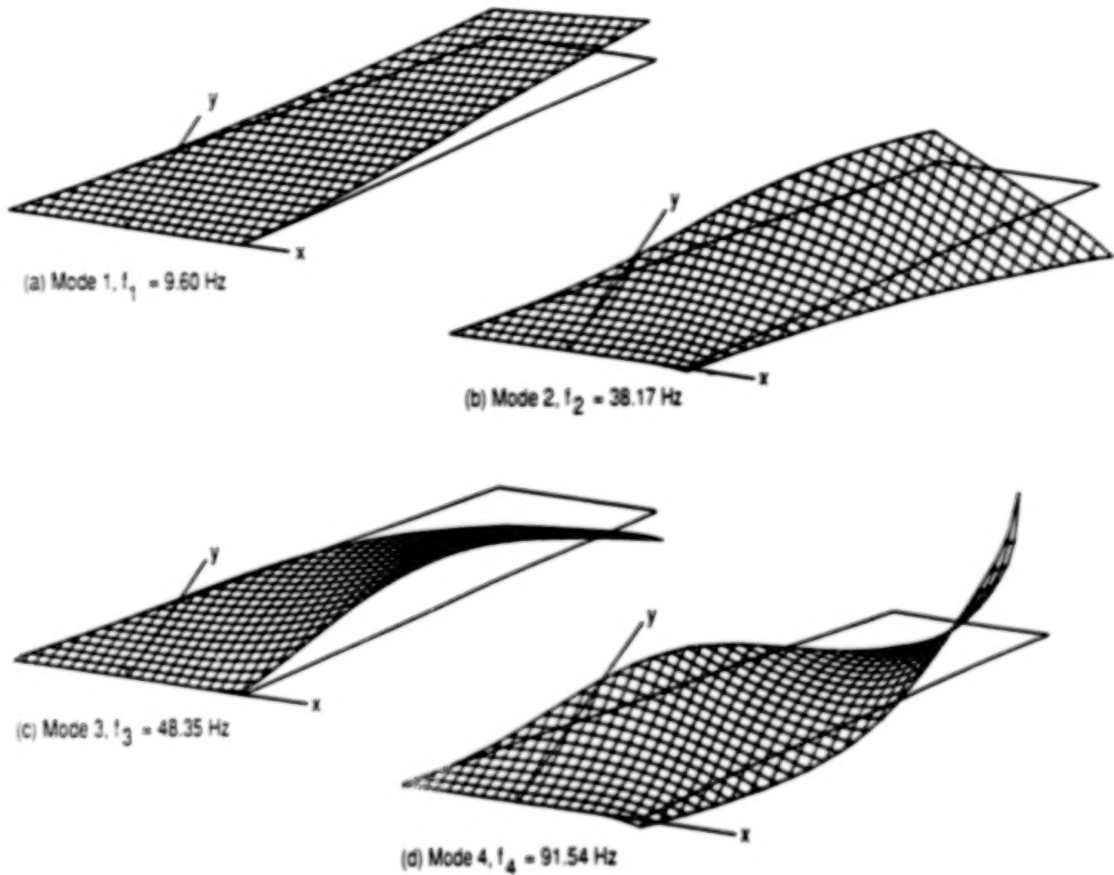


Figure 5

AEROELASTIC TRANSIENT AND LEAST-SQUARES CURVE FIT

For aeroelastic analysis, the steady state flow field is first calculated to account for wing thickness, camber, and mean angle of attack. The wing is then disturbed with an initial condition and free decay transients are calculated. The resulting transients are then analyzed to determine growth or decay for aeroelastic stability. Dynamic pressure is changed, and the transients computed again to determine the variation of stability with dynamic pressure.

An example transient for the 45° wing calculated by CAP-TSD is shown in figure 6. All four modes used in the analysis were excited by specifying an initial condition for each modal velocity which produces a complicated decay record. This record is analyzed using a least-squares curve-fit of the response data with complex exponential functions. The program utilized is a derivative of the one described by Bennett and Desmarais in NASA SP-415, May 1975.

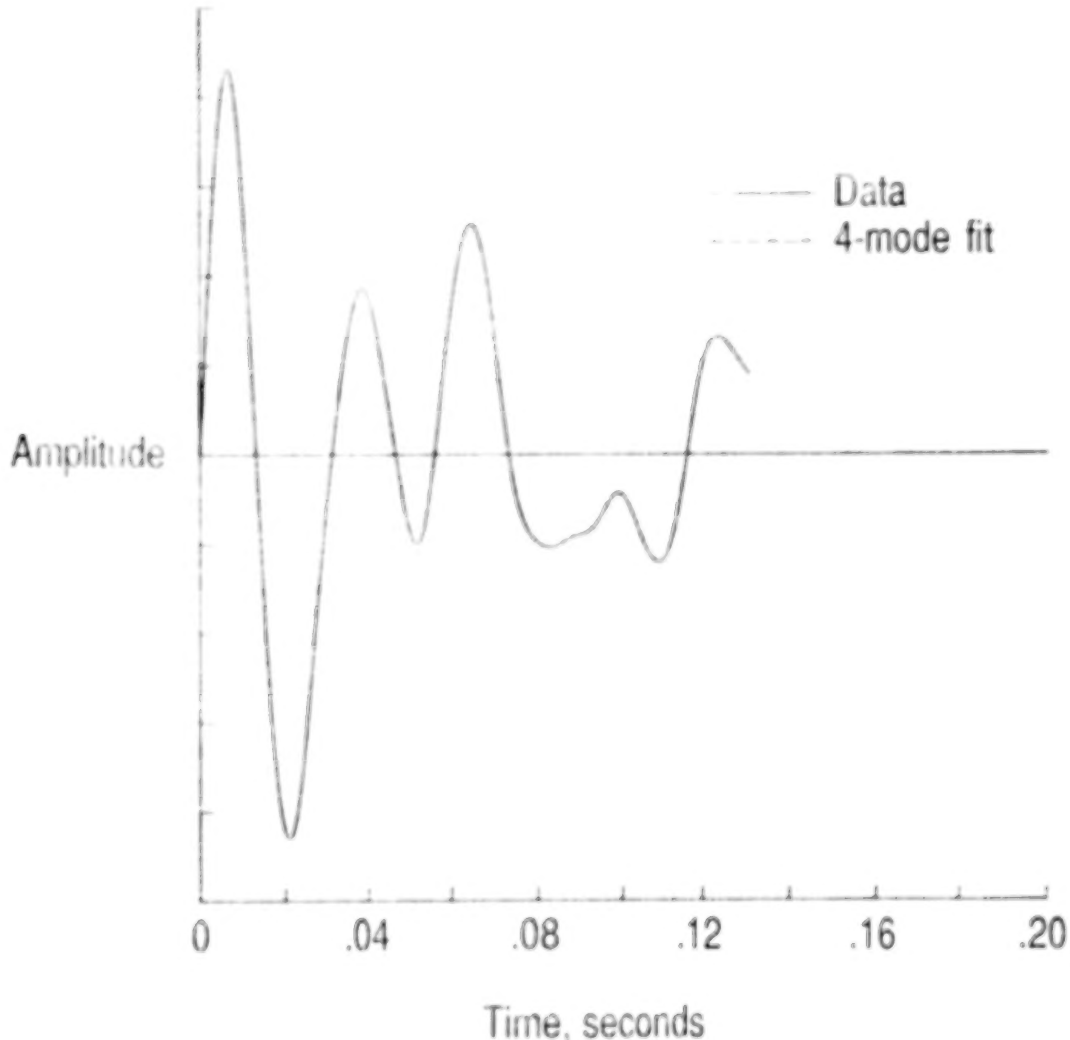


Figure 6

COMPONENT MODES FROM CURVE FIT

The components of the transient presented in the previous figure are shown in figure 7 to the same scale as that used in figure 6. The free decay properties of each mode for this condition are readily apparent after the least-squares fit, whereas the complexity of the complete decay record is such that the stability is not recognizable in the previous figure. The instability of the first mode might have been missed unless many more time steps were run. A post-processing program of this type is essential to efficient use of these types of programs where large resources are used for the CFD flow field calculations.

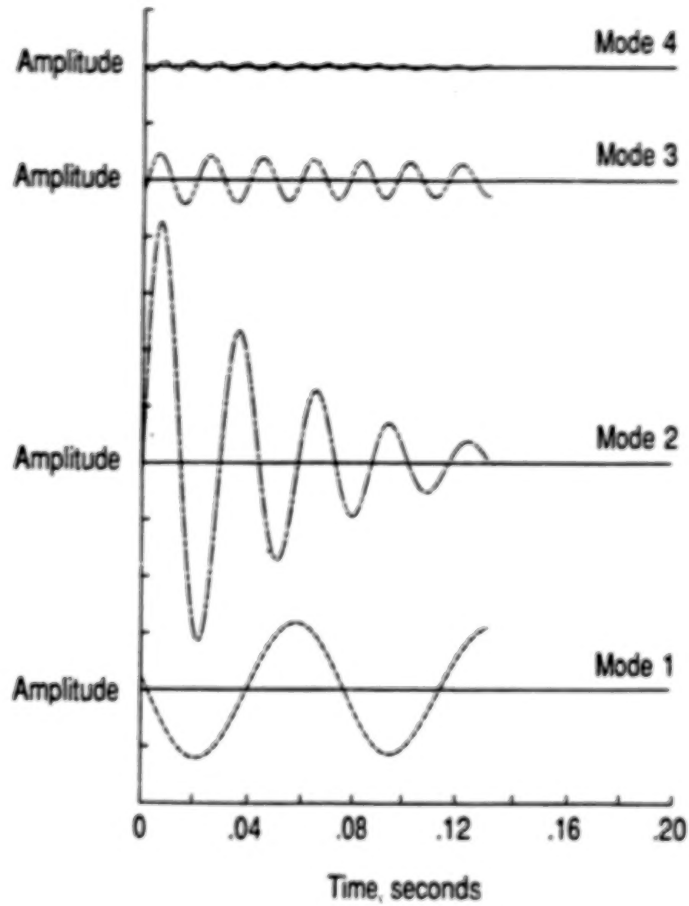


Figure 7

EXAMPLE OF ROOT LOCUS FROM CAP-TSD RESULTS

45° WING, $M = 0.499$

The potential of this methodology to produce complete root loci for the aeroelastic system is illustrated in figure 8. The variation of frequency and damping for all four modes used in the analysis is deduced for various dynamic pressures as shown in the figure (note change in frequency scale for the higher modes). It is apparent that the first mode increases rapidly in frequency and flutters, whereas the damping in the other three modes increases rapidly with dynamic pressure.

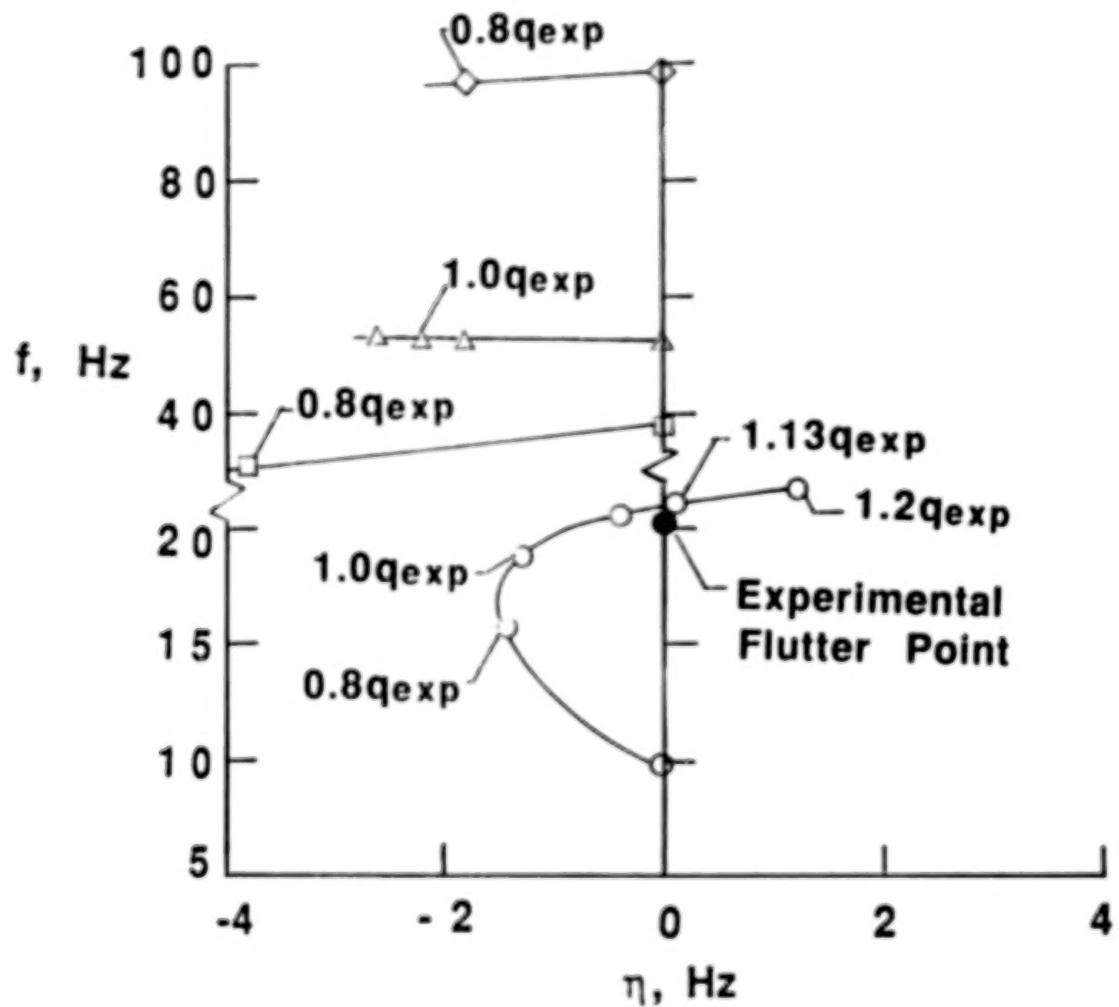


Figure 8

PRELIMINARY FLUTTER CALCULATIONS FOR 45° SWEPT WINGS

Preliminary flutter calculations for the 45° wing WEAK3 in air are shown in figure 9. The circles indicate the measured flutter points which are faired by the solid line. The bottom of the dip near Mach 1.0 is estimated from the no flutter data obtained while going to the point at $M = 1.07$. The squares indicate the results from subsonic kernel function linear theory (program FAST). There is very good agreement of the linear theory with the four data points shown, even for the point near $M = 0.95$. The two diamonds indicate two subsonic points calculated using CAP-TSD. The two points are in fair agreement with the data. Effort to extend these results to other Mach numbers and to obtain direct comparisons with linear theory is continuing. These initial results are encouraging however.

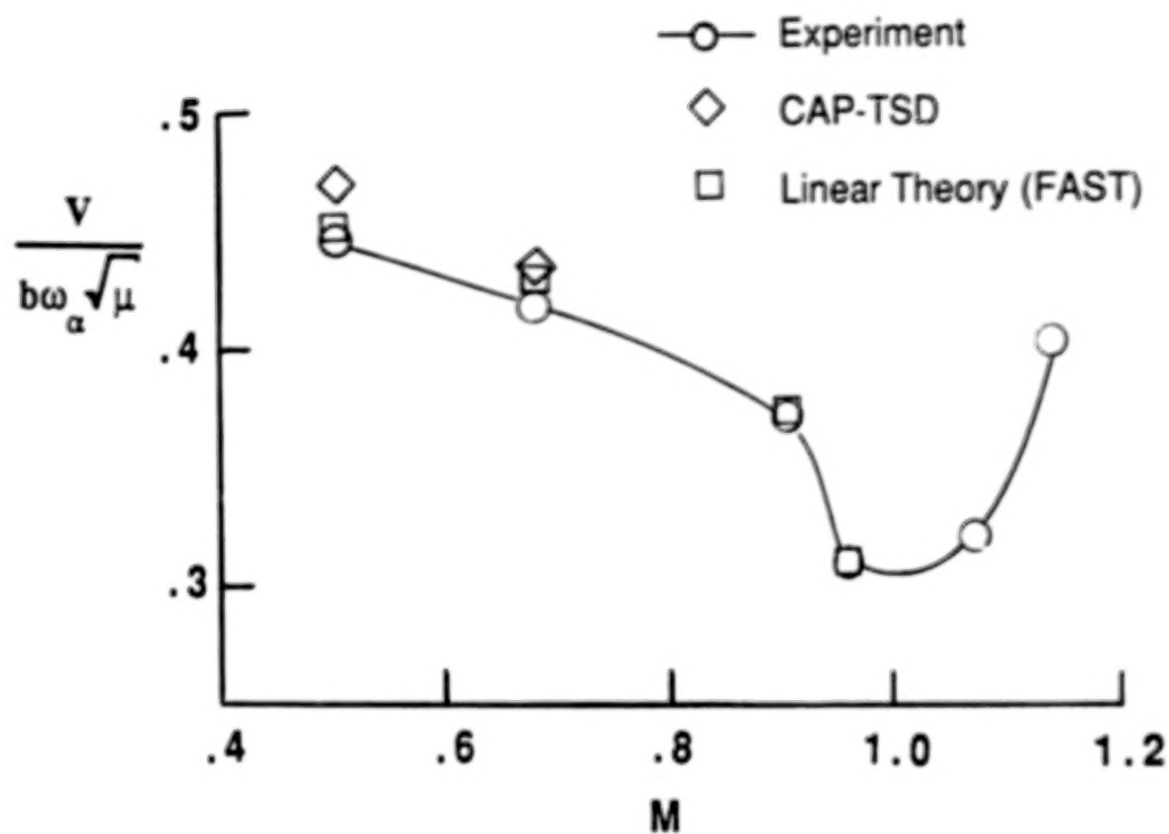


Figure 9

CLIPPED DELTA WING IN THE NASA LANGLEY TRANSONIC DYNAMICS TUNNEL

The second wing to be analyzed is a clipped delta wing model that was also tested in Freon in the Langley Transonic Dynamics Tunnel. A view of the model mounted in the TDT is shown in figure 10. The wing has a leading-edge sweep of 50.5°, a panel aspect ratio of 1.24, and a taper ratio of 0.142. The airfoil section is a circular arc with a maximum thickness of 0.03. The wing was constructed of a load-carrying plate structure with cutouts to simulate a beam structure and was covered with balsa wood which was contoured to the required airfoil shape. The model also had two slender underwing bodies to simulate engine nacelles. The total mass of these bodies was about the same as the total mass of the wing. A fuselage fairing was used to ensure that the wing root was outside the tunnel wall boundary layer. Nine natural vibration modes and their associated generalized masses were measured for this wing.



Figure 10

CLIPPED DELTA WING FLUTTER BOUNDARY
NASA TN D-7544

The experimental flutter boundary for the clipped delta wing is shown in figure 11. Calculations with CAP-TSD are under way, but results have not yet been obtained. The figure shows a composite boundary obtained by normalizing the boundaries for three wings of differing sizes in terms of the flutter speed index. The data for the wing of the previous figure are shown as the diamond symbols. The flutter boundary has a significant transonic dip with a minimum near $M = 0.92$, a rapid rise after the dip, and a supersonic level near that of subsonic speeds.

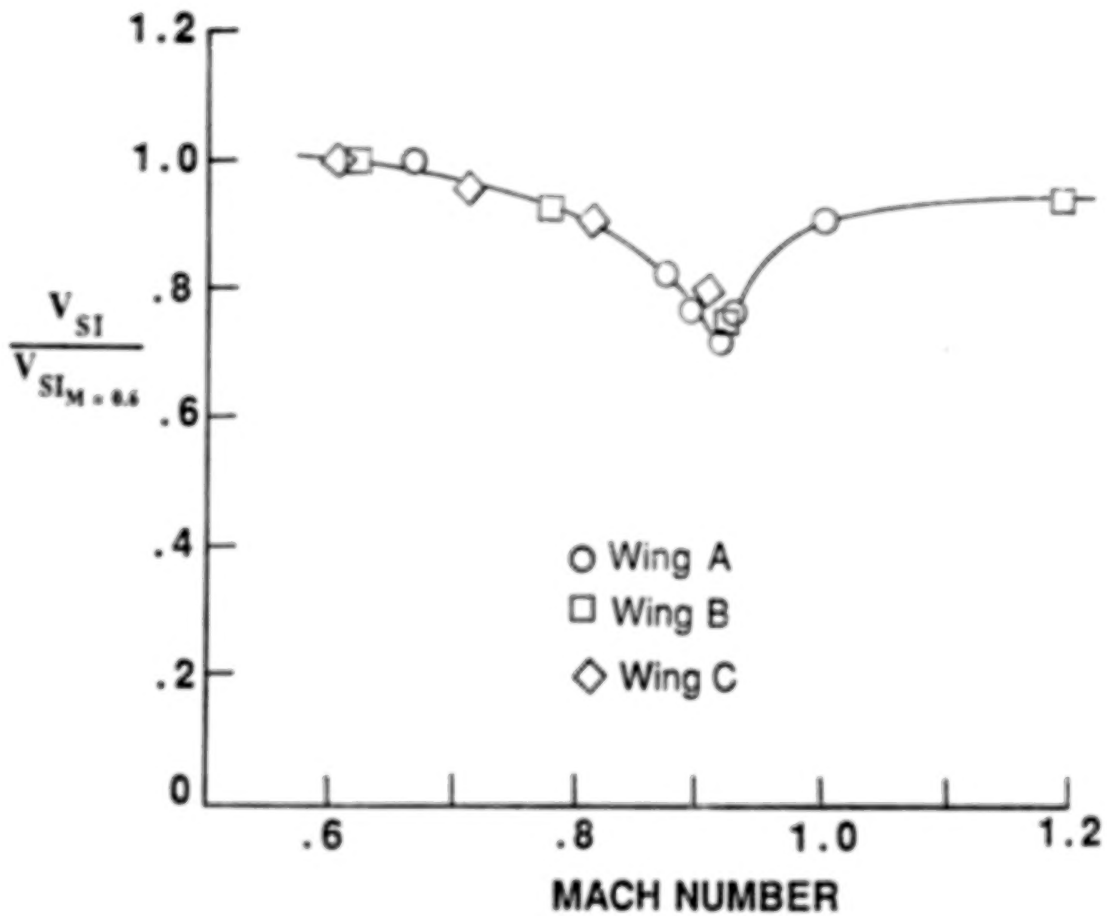


Figure 11

CONCLUDING REMARKS

In an effort to assess the accuracy of the CAP-TSD program for aeroelastic applications, flutter calculations are under way for several wings of two different planforms varying in sweep and taper and with thin airfoil sections. One planform is a series of 45° swept wings which have been proposed as an AGARD standard configuration for aeroelastic analysis. The other planform is a clipped delta wing that was used in some early active controls work. The physical properties and experimental flutter boundaries for these wings are well defined for validation purposes. Some initial results have been obtained and are encouraging. Further effort to extend and refine the results is under way. (Fig. 12.)

- CAP-TSD AEROELASTIC VALIDATION UNDER WAY
- HAVE INITIAL RESULTS WHICH ARE BEING EVALUATED AND REFINED

Figure 12

TRANSONIC FLUTTER CALCULATIONS
USING THE EULER EQUATIONS

Oddvar O. Bendiksen
Kenneth A. Kousen
Princeton University, Princeton, NJ

UNSTEADY EULER EQUATIONS

In transonic flutter problems where shock motion plays an important part, it is believed that accurate predictions of the flutter boundaries will require the use of codes based on the Euler equations. Only Euler codes can obtain the correct shock location and shock strength, and the crucially important shock excursion amplitude and phase lag. (For a discussion of the importance of shocks in transonic flutter, see Ref. 1.) The present study is based on the finite volume scheme developed by Jameson and Venkatakrishnan (Refs. 2,3) for the two-dimensional unsteady Euler equations. The equations are solved in integral form on a moving mesh, Eqs. (1-2). Here the variables p , ρ , u , v and e are the pressure, density, cartesian velocity components, and total energy, respectively, and x_t and y_t are the velocity components of the moving boundary $\partial\Omega$ of an element Ω . By applying Eq. (1) to each element or cell (i,j) , a system of ordinary differential equations is obtained, Eqs. (3), where S_{ij} is the cell area, Q_{ij} is the net flux out of the cell, and D_{ij} represents dissipative terms added to damp numerical oscillations (see Refs. 3,4). A five-stage Runge-Kutta scheme is used to integrate Eqs. (3) forward in time.

FINITE VOLUME FORMULATION

- INTEGRAL FORM ON A MOVING MESH

$$\frac{\partial}{\partial t} \iint_{\Omega} W dx dy + \int_{\partial\Omega} (f dy - g dx) = 0 \quad (1)$$

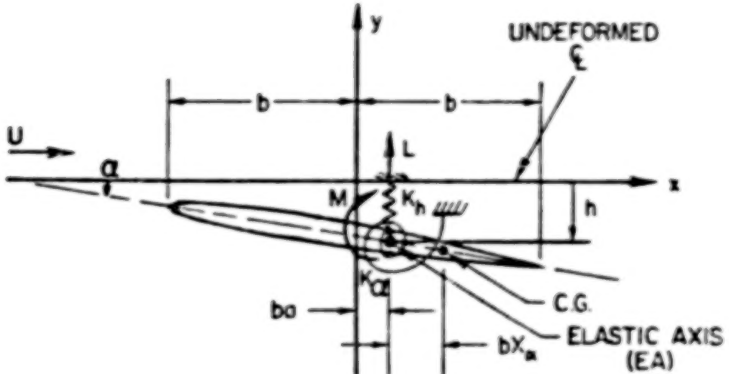
$$W = \begin{Bmatrix} \rho \\ \rho u \\ \rho v \\ \rho e \end{Bmatrix}, \quad f = \begin{Bmatrix} \rho(u-x_t) \\ \rho u(u-x_t)+p \\ \rho v(u-x_t) \\ \rho e(u-x_t)+\rho u \end{Bmatrix}, \quad g = \begin{Bmatrix} \rho(v-y_t) \\ \rho u(v-y_t) \\ \rho v(v-y_t)+p \\ \rho e(v-y_t)+\rho v \end{Bmatrix} \quad (2)$$

- DISCRETIZED FORM WITH DISSIPATION, ADAPTIVE OR TVD-BASED

$$\frac{d}{dt} (S_{ij} W_{ij}) + Q_{ij} - D_{ij} = 0 \quad (3)$$

TYPICAL SECTION MODEL

The wing is modeled as a typical section, with two degrees of freedom (bending h and torsion α), as illustrated in Fig. 1. The usefulness of this model in capturing the fundamental features of bending-torsion flutter is by now well established. In the usual notation, the equations of motion are of the form given by Eqs. (5) and (6), where the lift and moment coefficients C_L and C_M depend on the motion of the airfoil. Because we will consider finite (rather than infinitesimal) amplitude motion, the superposition principle cannot be used. In the present study, C_L and C_M are calculated numerically from the unsteady pressure coefficient on the airfoil surface at the end of each time interval, obtained from the numerical solution of the Euler equations. It should be emphasized that the equations of motion are nonlinear through the dependence of C_L and C_M on the motion h, α of the airfoil (and its time history).



EQUATIONS OF MOTION

$$mh'' + S_\alpha \ddot{\alpha} + K_h h = -L = \frac{1}{2} \rho_\infty U_\infty^2 c^2 C_M \quad (5)$$

$$S_\alpha h'' + I_\alpha \ddot{\alpha} + K_\alpha \alpha = M_{ea} = \frac{1}{2} \rho_\infty U_\infty^2 c C_L \quad (6)$$

FIGURE 1

METHOD OF SOLUTION

Aeroelastic stability is determined by integrating the equations of motion for the coupled fluid-structure system. The structural equations are first transformed to normal coordinates η_r , Eqs. (7)-(8), where the columns of $[\Phi]$ are the eigenvectors of the free vibration problem. The structural integrator is based on the convolution integral solution, Eq. (9), and the generalized aerodynamic forces Q_r are assumed to vary linearly within each time step Δt . Because the multi-stage Runge-Kutta scheme used to integrate the unsteady Euler equations was found to be sensitive to the manner in which the airfoil boundary condition was updated and the mesh moved, the structural integrator has been imbedded within the Runge-Kutta scheme in the Euler code. This permits an efficient implementation of the exact airfoil boundary condition, Eq. (10), on the instantaneous position of the airfoil, given by $B(x,y,t) = 0$. Nonreflective boundary conditions are used in the far field.

- COUPLED EQUATIONS FOR FLUID & STRUCTURE ARE INTEGRATED NUMERICALLY USING NORMAL COORDINATES

$$\{q\} = [\Phi]\{\eta\} \quad (7)$$

$$\ddot{\eta}_r + \omega_r^2 \eta_r = Q_r \quad (8)$$

- STRUCTURAL INTEGRATOR IS BASED ON CONVOLUTION INTEGRAL SOLUTION

$$\begin{aligned} \eta_r(t) &= \eta_r(0) \cos \omega_r t + \frac{\dot{\eta}_r(0)}{\omega_r} \sin \omega_r t \\ &+ \frac{1}{\omega_r} \int_0^t Q_r(\tau) \sin[\omega_r(t-\tau)] d\tau \end{aligned} \quad (9)$$

- STRUCTURAL INTEGRATOR IS IMBEDDED IN FIVE-STAGE RUNGE-KUTTA SCHEME FOR EULER EQUATIONS

- EXACT AIRFOIL B.C. IS SATISFIED

$$\begin{aligned} \frac{DB}{Dt} &= 0 \quad \text{or} \quad \frac{\partial B}{\partial t} + \vec{u} \cdot \nabla B = 0 \\ \text{on } B(x,y,t) &= 0 \end{aligned} \quad (10)$$

- MESH IS MOVED AT EACH STEP

NUMERICAL RESULTS

Flutter calculations have been carried out for the three aeroelastic test cases listed in Table 1, and compared to previously published calculations based on various TSD codes. Case A is the same as studied by Isogai (Refs. 5,6) and later by Edwards et al. (Ref. 7) and also by Weatherill and Ehlers (Ref. 8). Note that the elastic axis location "a" is ahead of the leading edge; the idea here is to simulate the vibratory behavior (in pitch and plunge) of the streamwise sections near the tip of a swept-back wing. Case B has been studied previously by Isogai (Ref. 6) and by Ueda and Dowell (Refs. 9,10). Case C was introduced by Ueda and Dowell as an example where nonlinear (amplitude) effects were clearly discernible, based on LTRAN2 aerodynamics implemented via the describing function method. In all cases, the airfoil is forced for 3-6 cycles in pure torsion at a reduced frequency of interest, released, and the aeroelastic equations are integrated forward in time for another 3-6 cycles. The flutter boundary is located by calculating the logarithmic decrement δ of the transient solutions, and interpolating to $\delta=0$ between adjacent solutions with different $U/b\omega_a$.

TABLE 1
Aeroelastic Test Cases

Case	A	B	C
Airfoil(s)	NACA 64A010	NACA 64A010	NACA 64A006
M_∞	0.7 - 1.0	0.80	0.86
a	-2.0	-0.3	-0.3
x_a	1.8	0.5	0.5
r_a^2	3.48	0.49	0.49
μ	60	60	60
ω_h/ω_a	1.0	0.2	0.2
Refs.	5,6,7,8	6,9	10

MESH GENERATION

The unsteady Euler calculations are carried out on a C-mesh of quadrilateral elements, generated by means of a square root transformation followed by selective stretching to compress the grid near the trailing edge. A near field view of the resulting mesh is shown in Fig. 2. In the far field, the mesh extends to 15-100 chords, depending on direction. The mesh moves with the airfoil as a rigid body, i.e. without deformation. Flutter calculations published earlier by the authors (Ref. 4) were carried out on a 96 x 16 C-mesh, which was found to give adequate engineering accuracy in most, but not all, of the cases studied. In the present study, additional calculations have been performed on both 96 x 16 and 192 x 32 C-meshes, and the results of Ref. 4 have been updated where appropriate.

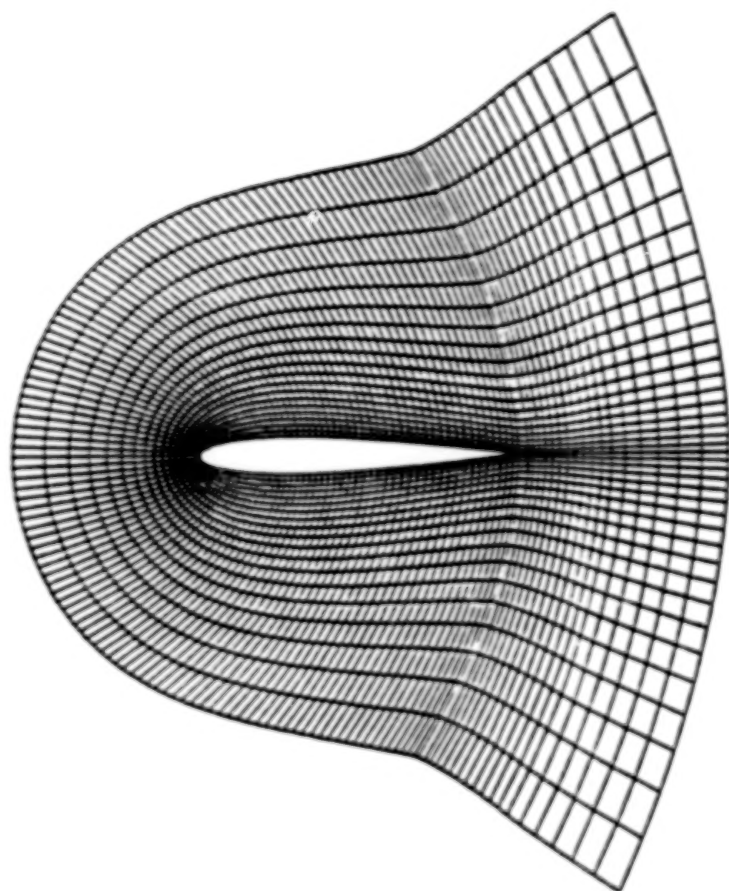


FIGURE 2

FLUTTER BOUNDARIES FOR CASE A

Previous studies (Refs. 5-8), which have been based on a number of different transonic small disturbance (TSD) theories, generally agree that the flutter boundary for Case A exhibits a significant "transonic dip", as shown in Fig. 3. Also shown in this figure are the results of flutter calculations based on the present Euler code, and using an initial forcing amplitude of 0.1 degree in pitch. Overall, the agreement with previous TSD calculations are fairly good. However, the Euler calculations appear to shift the bottom of the "bucket" toward higher Mach numbers. It is interesting to note that the bend-back of the flutter boundary around $M \sim 0.88$ observed by Edwards et al. (Ref. 6) and Weatherill and Ehlers (Ref. 8), is also predicted by the present Euler calculations. Not surprisingly, the precise location of the nose of the curve, where the flutter boundary has a vertical tangent, was found to be sensitive to the mesh size used in the calculations.

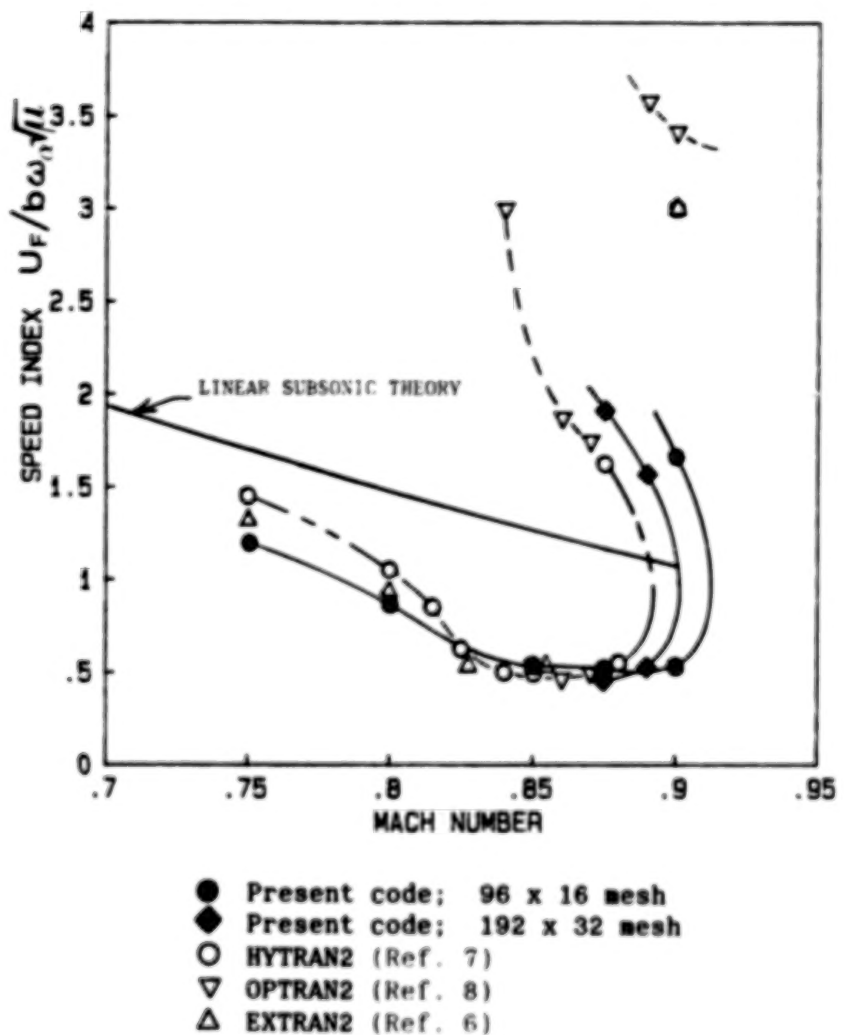


FIGURE 3

FLUTTER FREQUENCIES FOR CASE A

Figure 4 shows the flutter frequencies vs. Mach number, with some comparisons to earlier OPTRAN2 calculations by Weatherill and Ehlers (Ref. 8). As first noted by Isogai (Ref. 5), the flutter mode is essentially the first (predominantly bending) natural mode. The flutter frequency is close to the first coupled natural frequency ω_1/ω_α until the nose of the bend-back is encountered. At this point, the flutter frequency increases to a value between the two coupled natural frequencies and the flutter mode also changes, although it is still associated with the first predominantly bending branch.

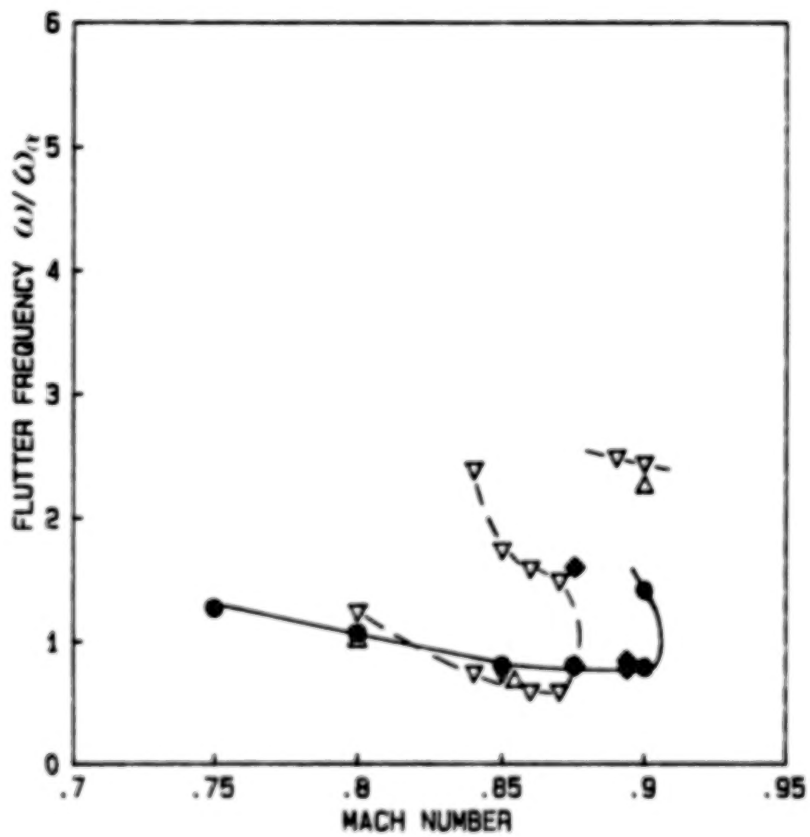


FIGURE 4

TRANSIENT SOLUTIONS FOR CASE A AROUND LOWER FLUTTER BOUNDARY AT $M = 0.9$

Typical transient solutions for Case A are shown in Figs. 5,6. At a Mach No. of 0.9, multiple flutter solutions occur due to the bend-back of the flutter boundary (see Fig. 3). Figure 5 illustrates the dynamic behavior of the airfoil, plotted as $h(t)/b$ and $\alpha(t)$ vs. time, immediately above and below the lower flutter point at $M = 0.9$. In this case, the airfoil is stable below (bottom figure) and unstable above (top figure) the neutral stability boundary ($\bar{U}_F = U_F/b\omega_a$ vs. M). Here, the airfoil has been forced for 3.6 cycles in pure pitch, with an amplitude of 0.1° , and then released at $t=0$.

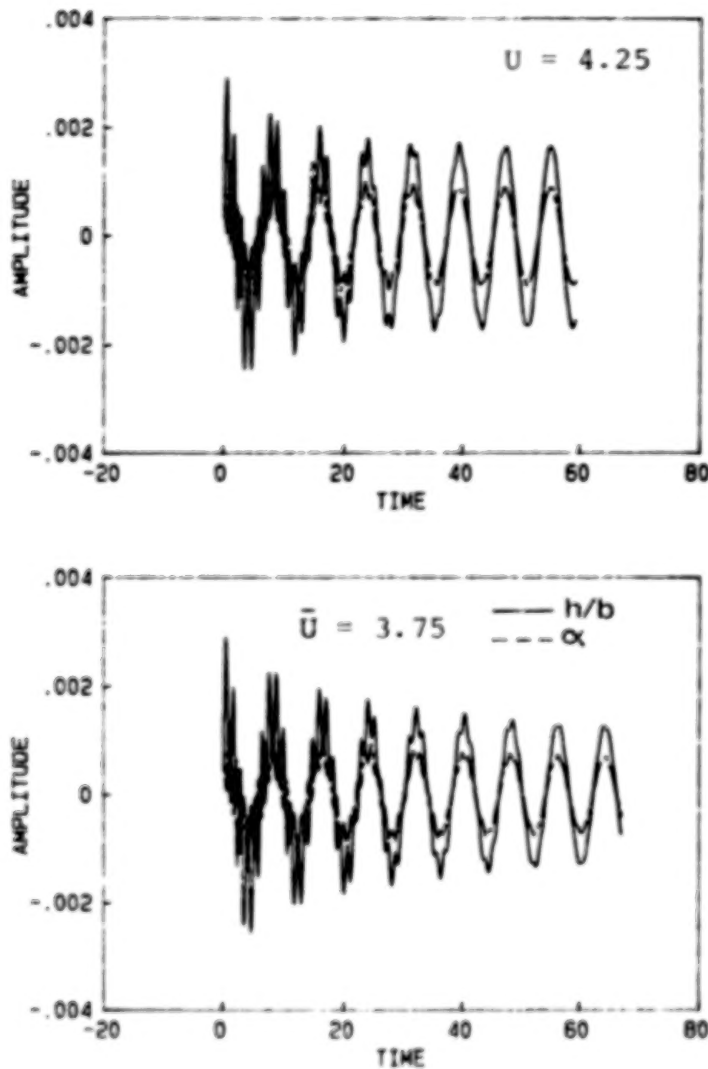


FIGURE 5

TRANSIENT SOLUTIONS FOR CASE A AROUND UPPER FLUTTER BOUNDARY AT $M = 0.9$

In the vicinity of the upper flutter point at $M = 0.9$, the stability behavior is reversed from that observed around the lower point. The airfoil is now stable for values of nondimensional airspeed $U/b\omega_a$, above the neutral stability boundary, as shown in the bottom diagram of Fig. 6. Conversely, the airfoil is unstable for values of $U/b\omega_a$ below the flutter boundary.

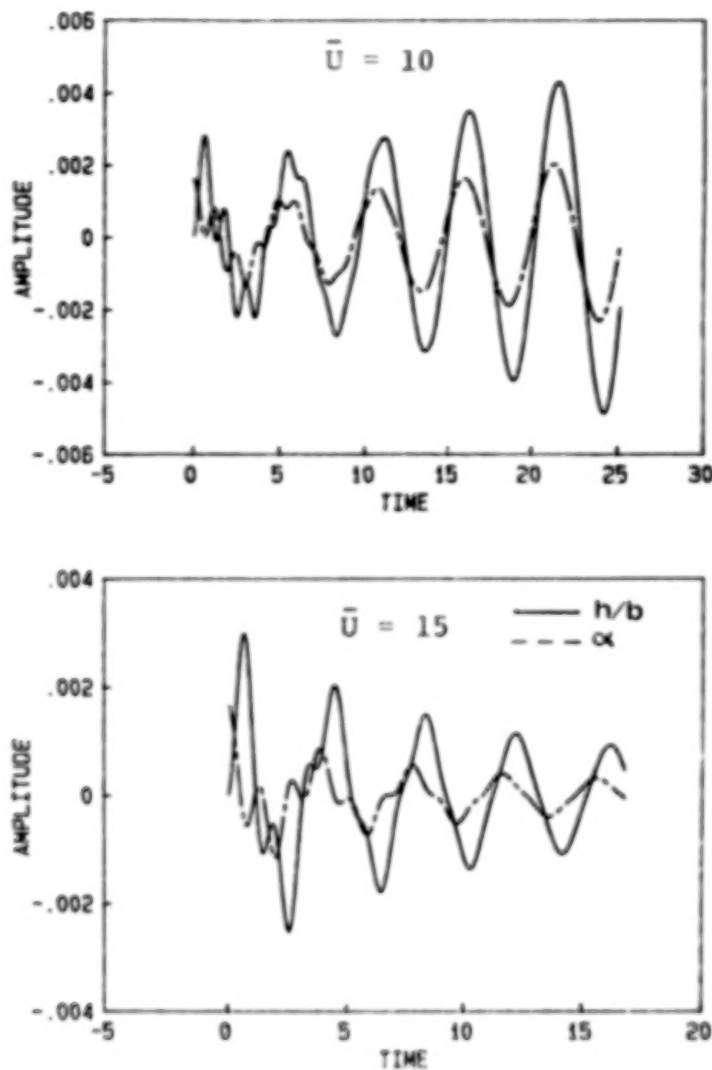


FIGURE 6

FLUTTER CALCULATIONS FOR CASE B

In Table 2, the results from our present flutter calculations for Case B are compared to predictions by previous researchers using various TSD codes. This case is the same as Case B considered by Isogai in Ref. 6. Note that the present Euler calculations predict a somewhat higher flutter speed than the TSD calculation by Isogai, but still below the speed predicted by classical linear theory. The flutter speed predicted by Ueda and Dowell (Ref. 9), using the describing function method based on LTRAN2 aerodynamics, is significantly below the predictions of the Euler code.

TABLE 2
Comparison of Predicted Flutter Speed for Case B

Method	α	$U_F/b\omega_0$	$2k_F$
Present	0.1°	3.43	0.201
Ueda & Dowell ⁹	0.25°(ϕ_1)	2.95	0.221
Isogai ⁶	0.1°	3.25	0.215
Linear Theory	-	3.86	0.210

NONLINEAR DEPENDENCE OF FLUTTER SPEED
ON INITIAL FORCING AMPLITUDE FOR CASE C

In Refs. 9-10, Ueda and Dowell investigated the nonlinear amplitude dependence of the flutter boundary for Case C, Table 1. They found a distinct drop in the flutter speed as the amplitude of the effective induced angle of attack $\phi_1 = \alpha + \dot{h}_c/U$ exceeded about 1° , where \dot{h}_c is the plunging velocity at midchord. Figure 7 shows results from the present Euler calculations, plotted as flutter speed vs. initial forcing amplitude in pitch (prior to release). Note that the flutter boundary is not very sensitive to α in the range 0° - 5° , and that the results obtained are sensitive to the initial forcing frequency.

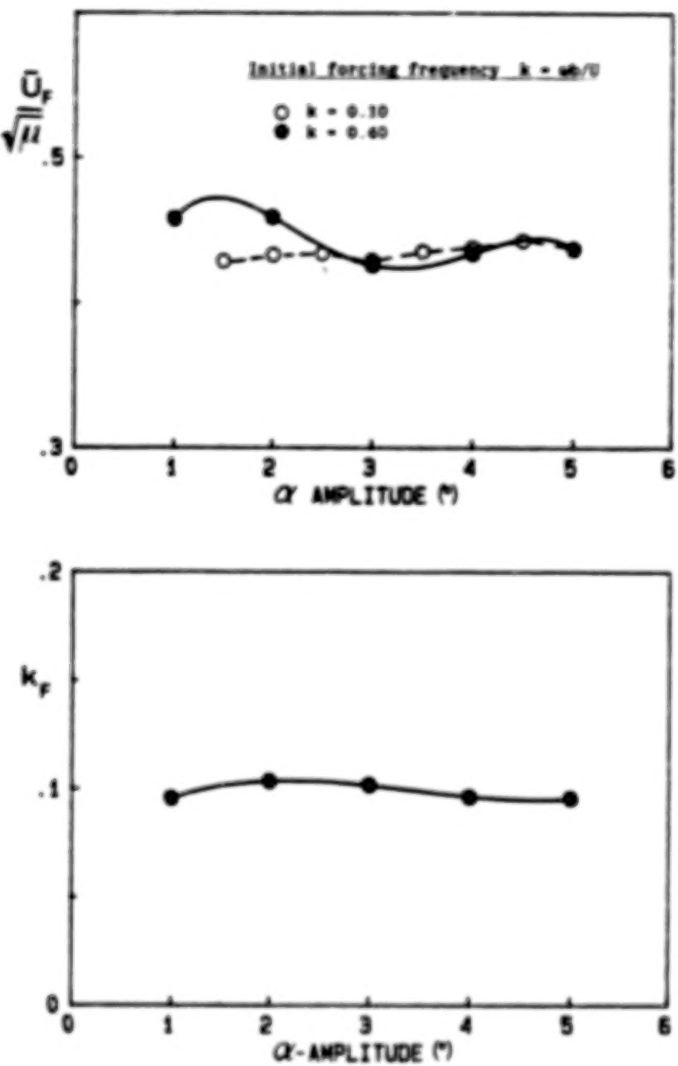


FIGURE 7

TRANSIENT SOLUTIONS FOR CASE C

Typical stable and unstable transient solutions are shown in Figs. 8 and 9, corresponding to initial forcing amplitudes of $\alpha = 1^\circ$ and 4° , respectively. The flutter mode is again a predominantly bending mode and emerges quickly (within a couple of cycles), despite the fact that the initial disturbance is pure torsion. This rapid convergence toward the significant aeroelastic mode was also observed in most of the transient solution of Cases A and B as well.

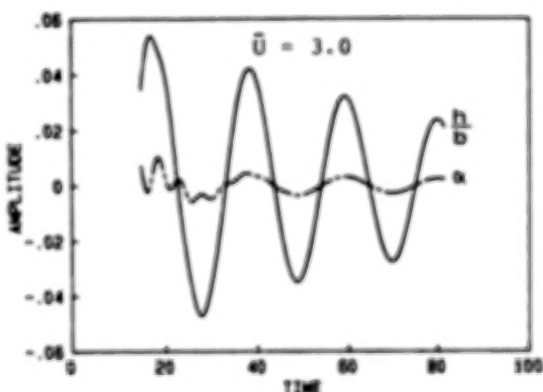
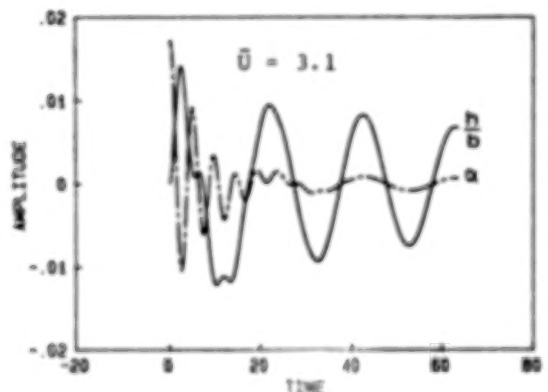
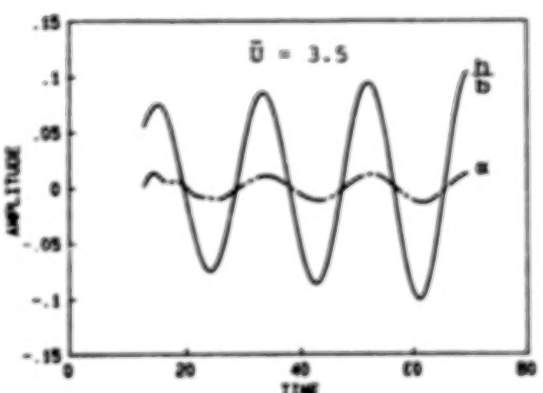
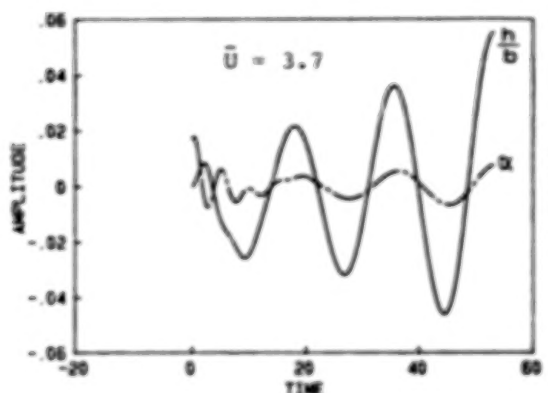


FIGURE 8

FIGURE 9

CONCLUSIONS

1. Typical section flutter calculations based on the two-dimensional unsteady Euler equations are now feasible.
2. Flutter speeds predicted by the present Euler code are in good overall agreement with previous TSD calculations, except in cases where strong shocks are present.
3. The Euler code calculations predict a transonic dip similar to the corresponding dips predicted by TSD codes, but shifted toward higher Mach numbers.
4. Multiple flutter points occur at certain Mach numbers, caused by a bend-back of the flutter boundary.
5. The amplitude dependence of U_F appears to be less than might be expected.

REFERENCES

1. Ashley, H., "Role of Shocks in the 'Sub-Transonic' Flutter Phenomenon," Journal of Aircraft, Vol. 17, March 1980, pp. 187-197.
2. Jameson, A. and Venkatakrishnan, V., "Transonic Flows About Oscillating Airfoils Using the Euler Equations," AIAA Paper No. 85-1514-CP, July, 1985.
3. Venkatakrishnan, V., "Computation of Unsteady Transonic Flows Over Moving Airfoils," Ph.D. Dissertation, Dept. of Mechanical and Aerospace Engineering, Princeton University, Oct. 1986.
4. Bendiksen, O.O. and Kousen, K.A., "Transonic Flutter Analysis Using the Euler Equations," AIAA Paper No. 87-0911-CP, April, 1987.
5. Isogai, K., "Transonic Dip Mechanism of Flutter of a Sweptback Wing: Part II," AIAA Journal, Vol. 19, Sept. 1981, pp. 1240-1242.
6. Isogai, K., "Numerical Study of Transonic Flutter of a Two-Dimensional Airfoil," NAL TR-6177, National Aerospace Institute, Tokyo, Japan, 1980.
7. Edwards, J.W., et al., "Time Marching Transonic Flutter Solutions Including Angle-of-Attack Effects," Journal of Aircraft, Vol. 20, Nov. 1983, pp. 899-906.
8. Weatherill, W.M. and Ehlers, F.E., "A Three Degree-of-Freedom, Typical Section Flutter Analysis using Harmonic Transonic Air Forces," AIAA Paper No. 83-0960, May, 1983.
9. Ueda, T. and Dowell, E.H., "Flutter Analysis Using Nonlinear Aerodynamic Forces," Proc. AIAA/ASME/ASCE/AHS SDM Conf., New Orleans, LA, May 1982, pp. 462-481.
10. Ueda, T. and Dowell, E.H., revised and extended version of Ref. [9], Journal of Aircraft, Vol. 21, No. 2, Feb. 1984, pp. 101-109.

UNSTEADY PRESSURE MEASUREMENTS ON A SUPERCRITICAL
AIRFOIL AT HIGH REYNOLDS NUMBERS

R. W. HESS
UNSTEADY AERODYNAMICS BRANCH
NASA Langley Research Center

MODEL AND TEST CONDITIONS

The supercritical airfoil on which the measurement was made, Sc(2)-0714, was developed at Langley (Ref. 1), was fourteen percent thick, and had a six inch chord and an eight inch span. The model was machined from Vascomax-200 which has superior dimensional stability properties at cryogenic temperatures. The tests were conducted in the Langley 0.3 Meter Transonic Cryogenic Tunnel (Ref. 2), .3-m TCT, at Reynolds numbers, R , which varied from 6×10^6 to 35×10^6 at Mach numbers between 0.65 and 0.74. The higher Reynolds numbers were near the edge of the tunnel operating boundary which has a stagnation temperature of 120° Kelvin (-243°F) and a stagnation pressure 6.5 atm (Ref. 2). This tunnel was used in the Advanced Technology Airfoil Test (Ref. 3) program in extensive steady flow airfoil studies that demonstrated the necessity for high Reynolds number testing.

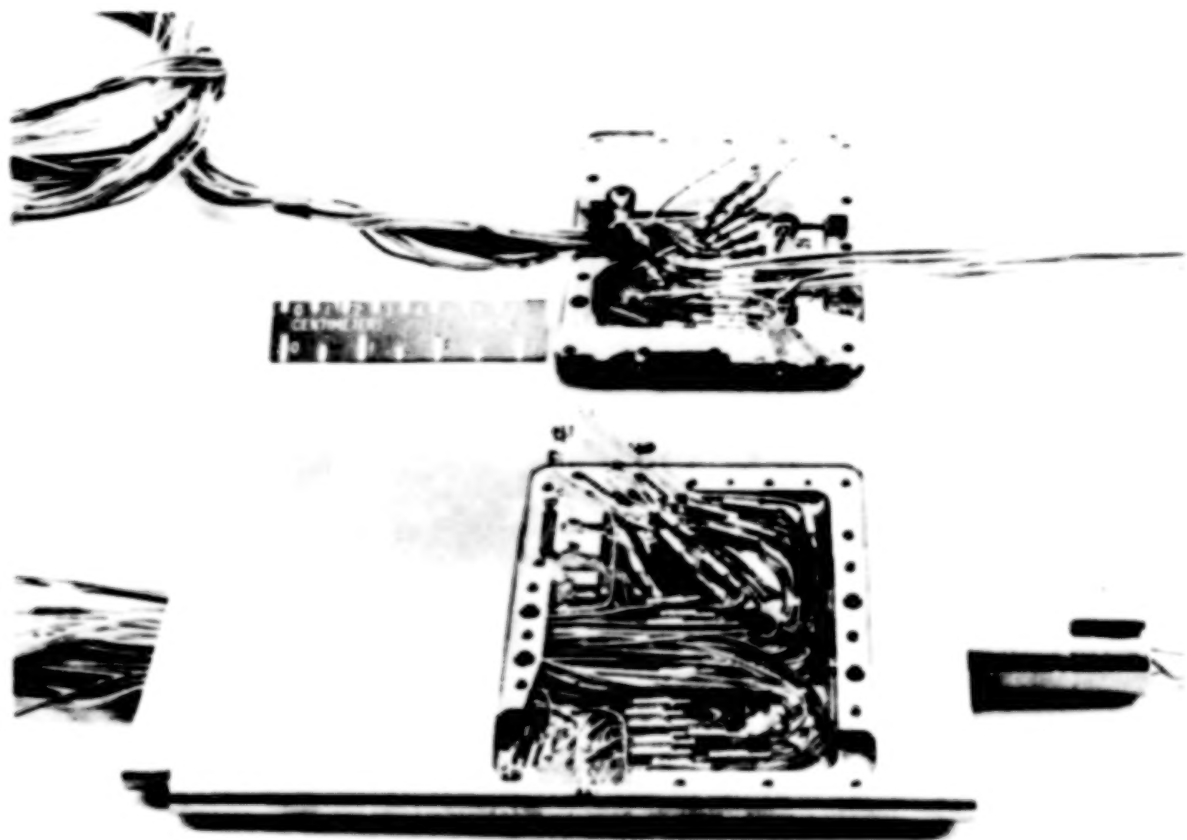
EXTERNAL VIEW OF MODEL



MODEL CONFIGURATION

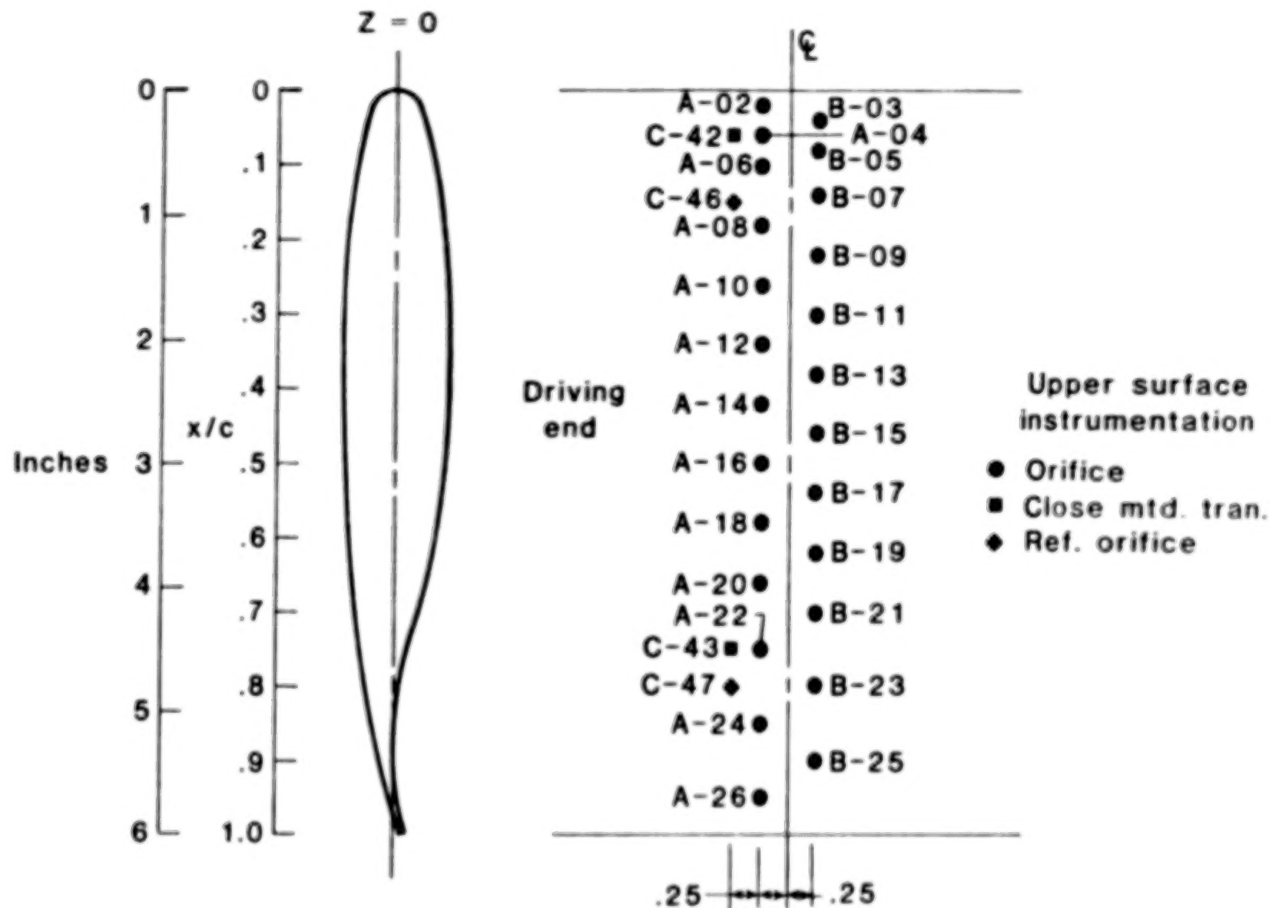
A cavity machined in the underside of the airfoil provided the space necessary to mount the transducers. The cavity was closed by a cover plate on which some lower surface transducers were mounted. The wing was supported on one end by a close-fitting tang fixed to a driving plate with machine screws; this end, on the left of the figure, was sealed with epoxy. The other end was supported by an integral shaft which rotated in a bushing in the tunnel side wall plate. A sliding seal of felt was used to seal the gap between the end of the oscillating airfoil and the fixed tunnel sidewall plate. The position of the supports was designed to locate the pitch axis at thirty-five percent chord.

INTERNAL CONFIGURATION OF MODEL



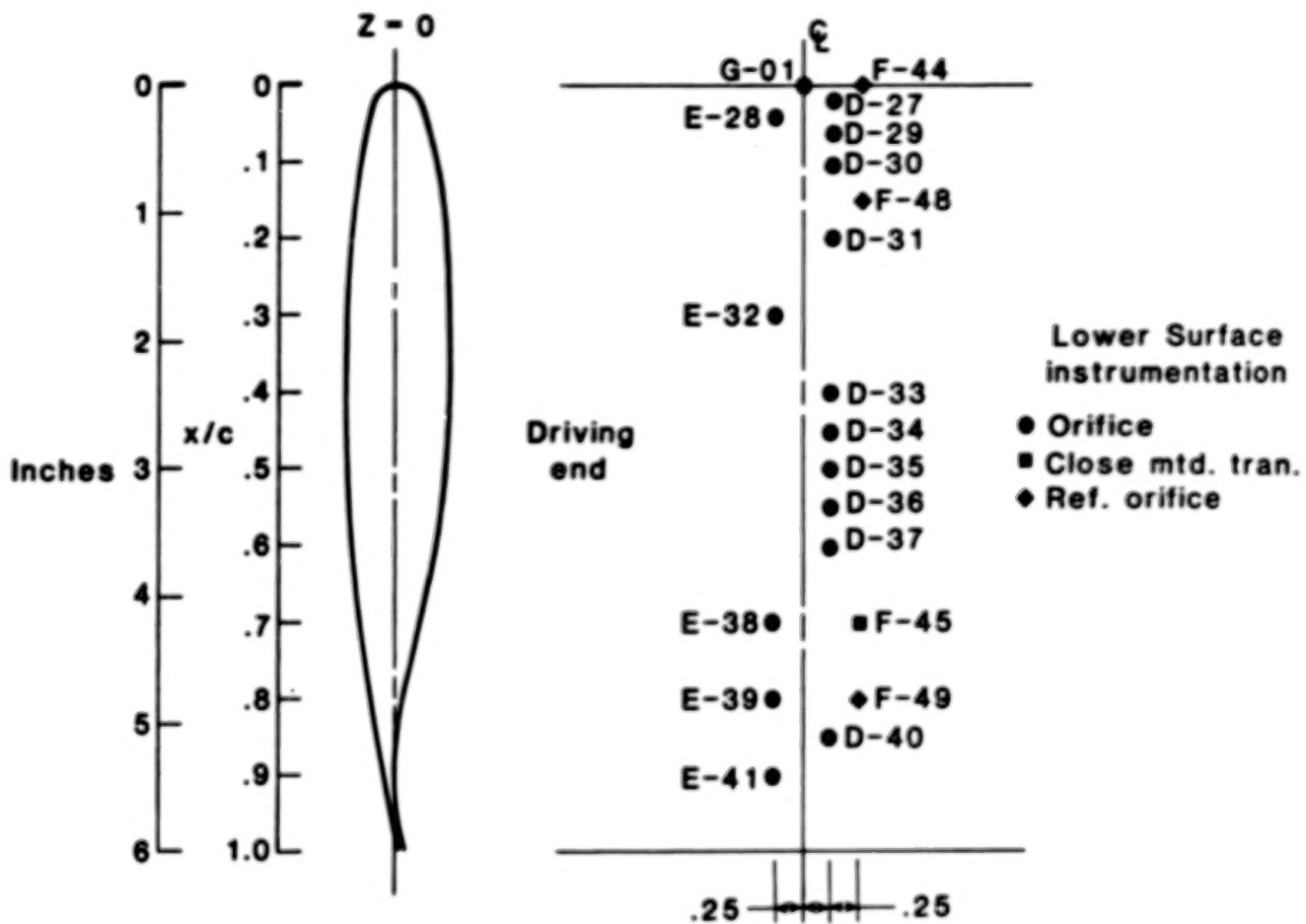
TRANSDUCER LOCATIONS (TOP SURFACE)

Forty-three unsteady pressure transducers were mounted internally in the model. Forty of the transducers were mounted in receptacles connected to the orifice by a short length of tubing. The remaining three transducers, close mounted, were mounted with the transducer head less than 0.1 inch below the surface of the wing. The distribution of the twenty-seven upper surface transducers is shown in the figure. The receptacle mounted transducer orifices were aligned alternately in two rows 0.25 inches on either side of the airfoil center line. The close mounted transducers orifices and reference orifices were located 0.5 inches from the center line. The orifices of the close-mounted transducers were paired with receptacle-mounted transducer orifices for comparison purposes. The orifices were distributed every 2% chord to x/c of 0.1 and 4% chord to x/c of 0.7.



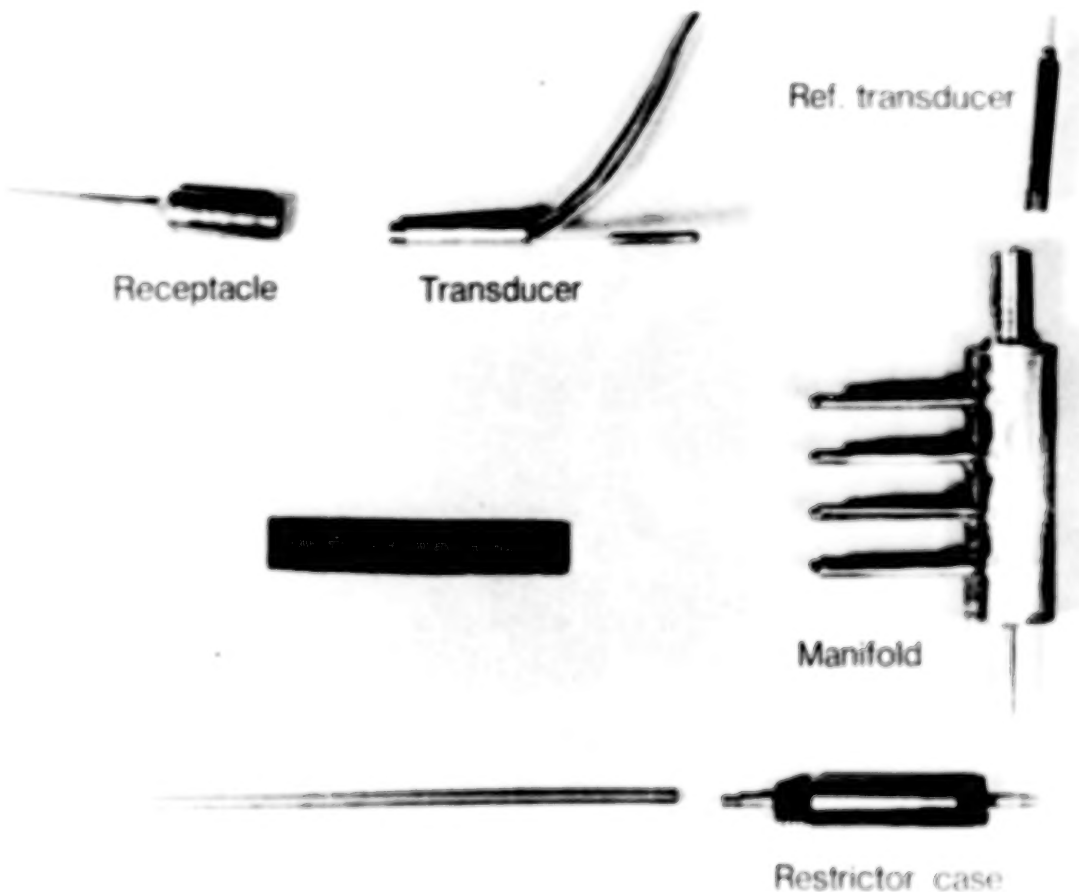
TRANSDUCER LOCATIONS (BOTTOM SURFACE)

This figure shows the distribution of the 16 transducer orifices on the lower surface; the orifice at the leading edge measured only static pressure. The distribution of the 15 receptacle mounted transducers is more sparse than on the upper surface and is concentrated in regions of largest pressure gradient and is 2% to an x/c of 0.1 and 0.5 thereafter.



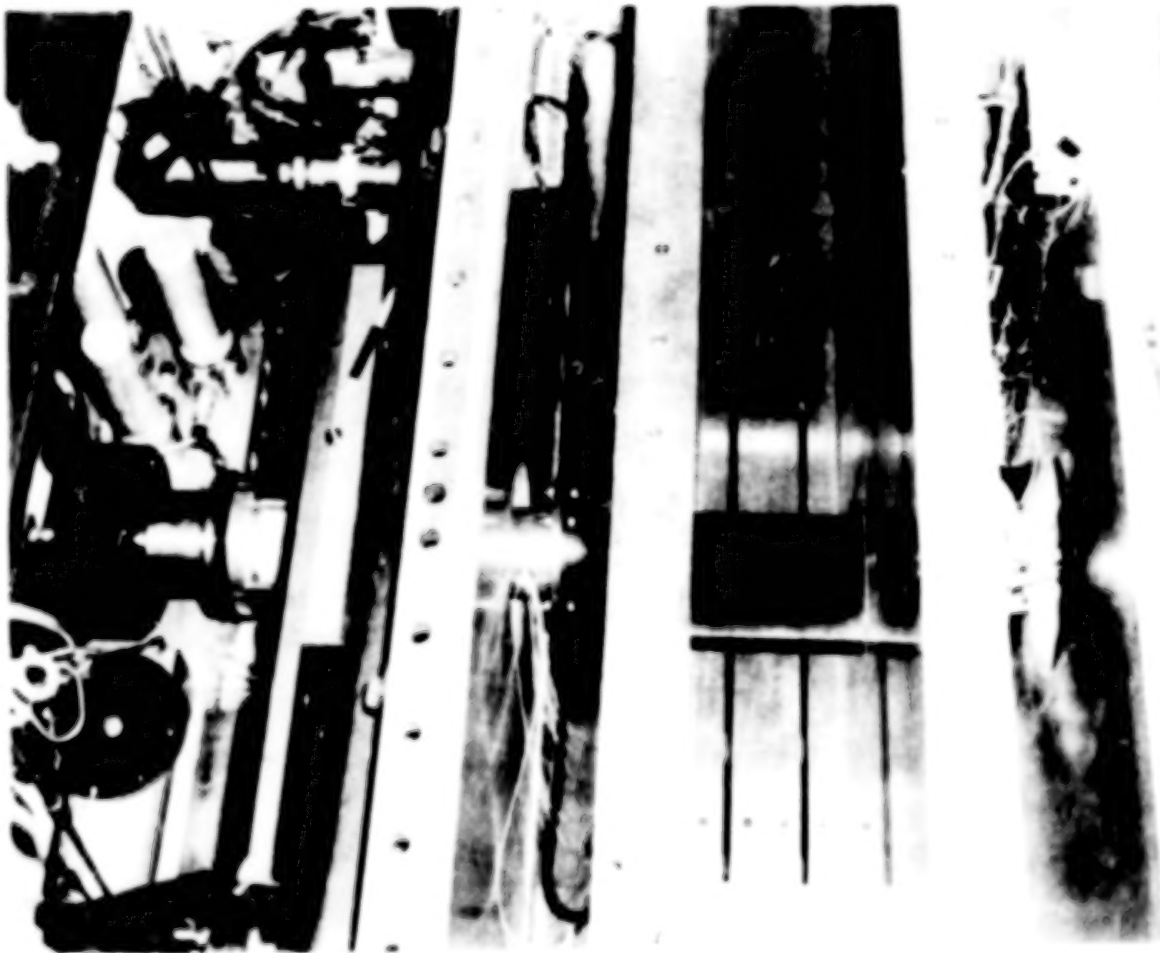
ELEMENTS OF THE TRANSDUCER SYSTEM

The system consisted of transducers, designed for cryogenic application, with a 10 psi range and with outputs of between 5 and 9 mv/psi. Each transducer was mounted in a receptacle which in turn was connected to the 0.015 inch diameter orifice by a 0.75 inch length of 0.030 inch i.d. tubing. Each transducer was referenced to a manifold which in turn was vented to one of five static reference orifices. A reference transducer measured the pressure differential between the manifold and the tunnel static pressure. The connection between the manifold and the reference orifice was interrupted by a porous flow restrictor which damped out the oscillating pressure from the reference orifice. A series of tests were conducted before the model was fabricated to examine the effects of orifice diameter, tube diameter and tube length on the dynamic response of the system. At atmospheric conditions there was no significant reduction of dynamic amplitude response or phase shift of the test configuration up to 100 Hz.



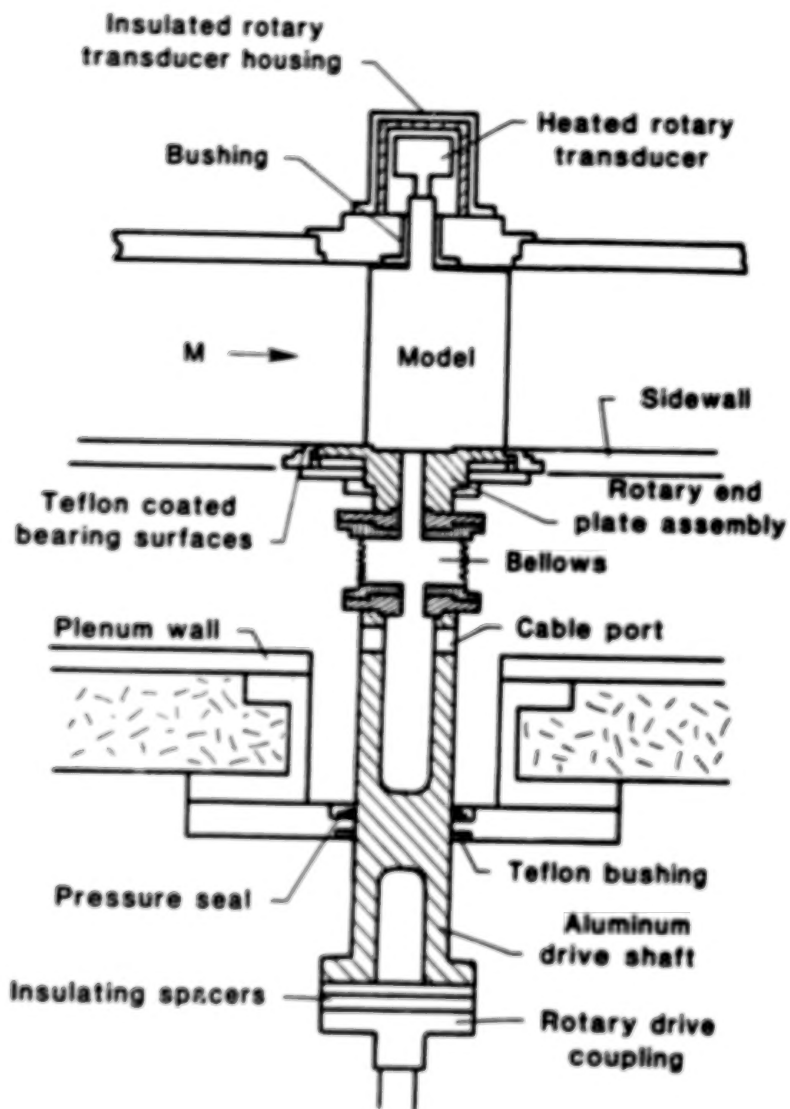
MODEL INSTALLATION

The large variations in temperature (120° K to 320° K) and stagnation pressure (1.4 atm. to 6 atm.) over the operating range of the 0.3-m TCT results in plenum wall deformations that required special consideration in the design of the oscillating drive system. The photograph of the test section, with the ceiling removed, shows the installation of the airfoil and drive system. The hydraulic-rotary actuator required the maintenance of precise alignment during the test. Since the test section floats on a cable suspension system to accommodate thermal contraction, the actuator and supporting structure were also supported by a system of cables and counterweights to enable them to move with the plenum wall.



SCHEMATIC OF MODEL INSTALLATION

The critical elements of the oscillating system are identified in this figure. The hollow aluminum drive shaft had fixed point supports at the rotary shaft and at a Teflon bushing and a pressure seal located on the tunnel plenum wall plate. The shaft was attached to the rotating sidewall wall drive disk through a bellows that allowed in-line shaft movement with the plenum wall. The rotating drive disk was Teflon coated on its circumferential bearing surfaces and had a slot to accommodate the wing tang. The tang was hollow to provide a path for transducer cable and tubing. The other edge of the wing was supported by an integral hollow shaft and a bushing in the sidewall plate. The hollow shaft allowed a path for the remaining transducer cables. The rotary transducer, attached to the shaft, was heated with surface heaters under thermostat control and the assembly was covered by an insulating can.



DATA ACQUISITION AND REDUCTION

Steady Pressures - The airfoil and tunnel instrumentation signals were fed to the tunnel data acquisition system through a 10 Hz low-pass filter, digitized at 20 samples/sec and averaged over a one second interval.

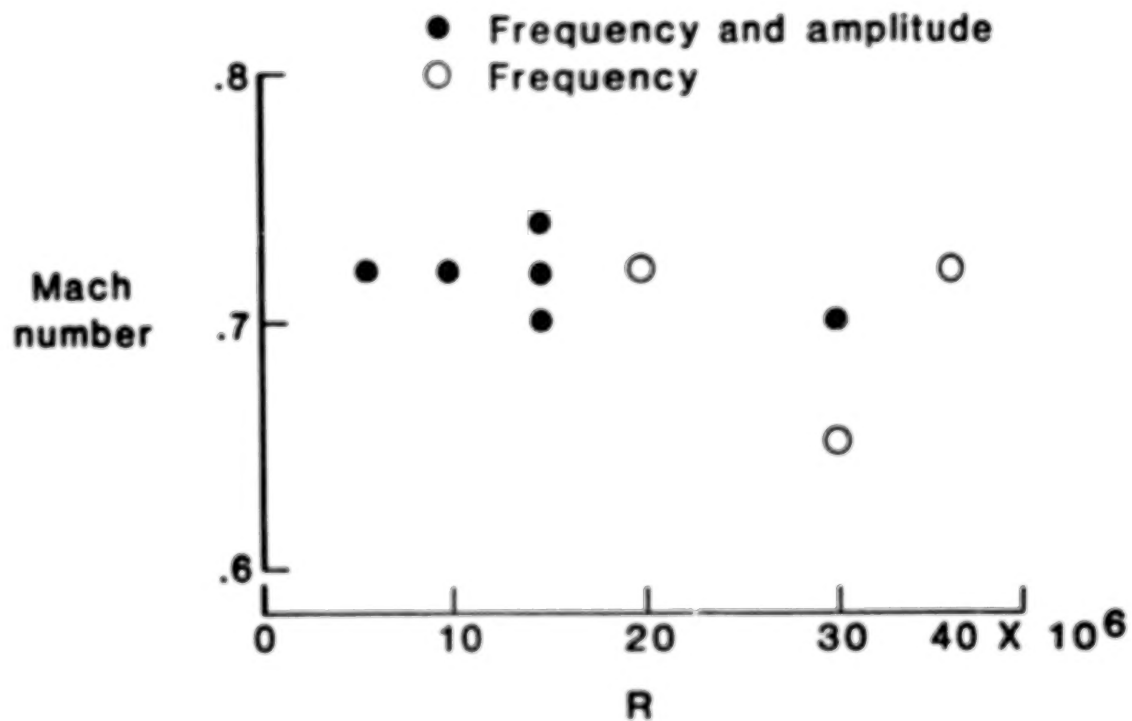
Unsteady Pressures - The signals from the amplifiers were recorded on two 28 channel recorders operating at 15 inches per second. This analog data was then digitized at 32 samples/cyc of oscillatory motion for 64 cycles and the harmonic components of the unsteady pressure were determined from FFT analysis. These components were normalized by the harmonic pitch amplitude in degrees. All phase angles were relative to wing position.

Tunnel Corrections - Sidewall boundary-layer and angle of attack corrections were applied to the measured steady pressure results. The sidewall boundary-layer corrections are based on the analysis of Ref. 4 which is used in Ref. 5 with measured values of sidewall displacement and momentum thickness to compile the tables which were used to correct the experimental values in this paper. The angle of attack corrections described in Ref. 6 (sometimes referred to as the "Barnwell-Davis-Moore" correction) adjust the analysis of Davis-Moore with experimental data. The wall induced downwash over the airfoil in the 0.3-m TCT for $C_l = 1.0$ is:

$$\bar{\delta\alpha} = 1.73245^\circ$$

MACH NUMBER AND REYNOLDS NUMBER TEST CONDITIONS

The test was designed to explore the effects of Reynolds number on unsteady pressures and to generate a data base for validating unsteady-aerodynamic computer codes. The test conditions as defined by Mach number and Reynolds number are shown in the figure. Test points were taken at the design Mach number of 0.72, determined from data of a previous test, at test Reynolds numbers varying from 6×10^6 to 35×10^6 . A total of 976 test points were taken. The primary data base was taken for pitch-oscillation frequency between 5 Hz and 40 Hz at an amplitude of $\pm 0.25^\circ$ as indicated by the open and solid symbols. Once this data was in hand, the pitch amplitude was increased to $\pm 0.5^\circ$ and $\pm 1.0^\circ$ and the pitch frequency increased to 60 Hz at test conditions indicated by the solid symbols.

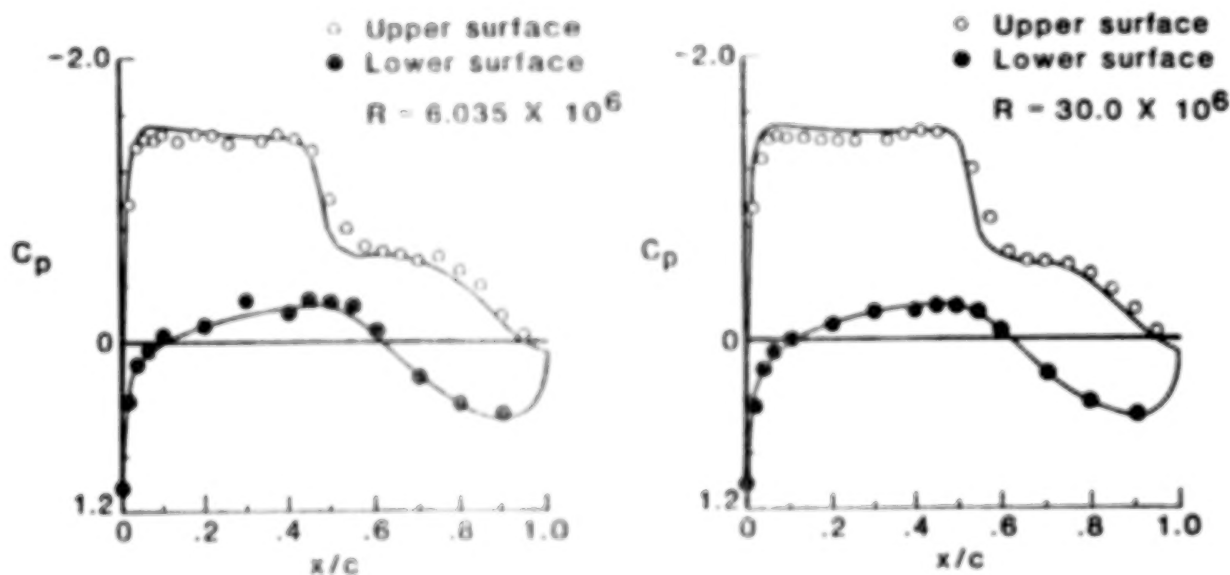


**COMPARISONS OF STEADY TEST RESULTS WITH CALCULATED
RESULTS AT A TUNNEL MACH NUMBER OF 0.72**

$$\bar{\alpha}_t = 2.5 \text{ degrees}$$

The next four figures give the steady pressure distributions for four angles of attack at two Reynolds numbers, 6×10^6 and 30×10^6 . Experimental data, shown as symbols, are compared with calculated results from GRUMFOIL computer code (Ref. 7) which are shown as solid lines. The GRUMFOIL code consists of a full potential equation flow solver integrated with a viscous boundary layer model and may be entered by specifying either $\bar{\alpha}$ or C_l . The corrected values of Mach and C_l were used as the input data for the computed results. Below each figure are listed M , $\bar{\alpha}$, and C_l for the tunnel test conditions, the corrected values, and the values resulting from the GRUMFOIL calculations.

$$\bar{\alpha}_t \approx 2.5 \text{ deg}$$



	Tunnel	Corrected	Grumfoil		Tunnel	Corrected	Grumfoil
M	0.720	0.701	0.701	M	0.719	0.705	0.705
$\bar{\alpha}$	2.504	0.844	1.385	$\bar{\alpha}$	2.51	0.756	1.399
C_l	0.9581	0.9753	0.9837	C_l	1.0123	1.0256	1.0336

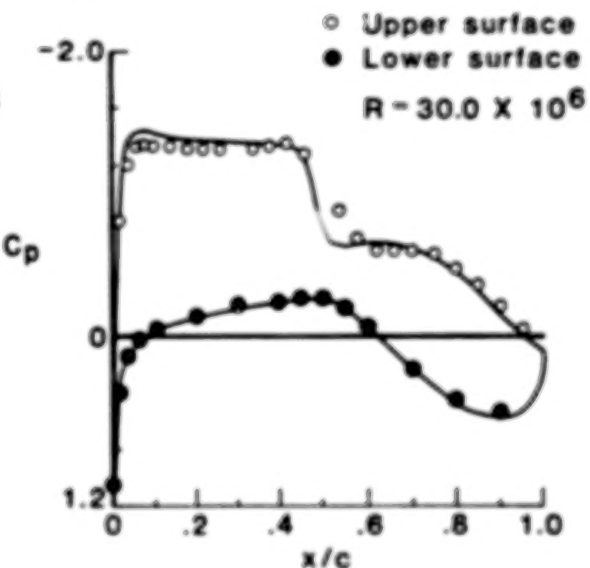
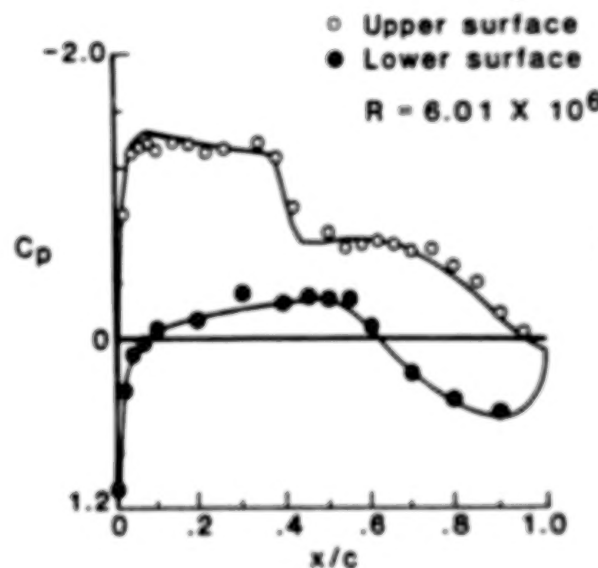
COMPARISONS OF STEADY TEST RESULTS WITH CALCULATED RESULTS AT A TUNNEL MACH NUMBER OF 0.72

$$\bar{\alpha}_t = 2.0 \text{ degrees}$$

The comparisons between the experiment, shown as symbols, and GRUMFOIL calculations, solid lines, are very good. The shock moves aft by approximately 8% to 10% of chord for a given value of tunnel mean angle of attack, $\bar{\alpha}_t$, when Reynolds number is increased from 6×10^6 to 30×10^6 . The code under-predicts the position of the shock at both Reynolds numbers by approximately 2-3% of chord even though C_l is matched.

COMPARISONS OF STEADY TEST RESULTS WITH CALCULATED RESULTS AT A TUNNEL MACH NUMBER OF 0.72

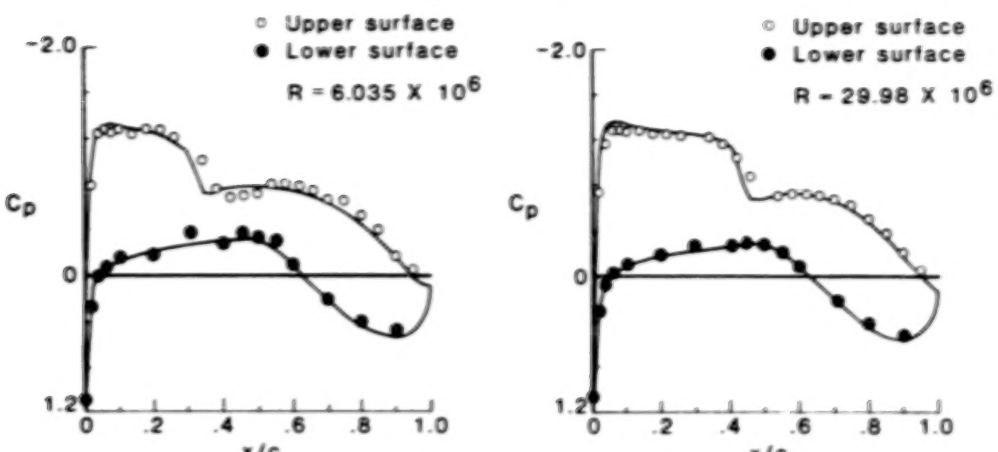
$$\bar{\alpha}_t \approx 2.0 \text{ deg}$$



	Tunnel	Corrected	Grumfoil		Tunnel	Corrected	Grumfoil
M	0.72	0.701	0.701	M	0.721	0.705	0.705
$\bar{\alpha}$	2.002	0.525	0.961	$\bar{\alpha}$	1.997	0.393	0.910
C_l	0.8523	0.8676	0.8757	C_l	0.926	0.939	0.9453

**COMPARISONS OF STEADY TEST RESULTS WITH CALCULATED
RESULTS AT A TUNNEL MACH NUMBER OF 0.72**

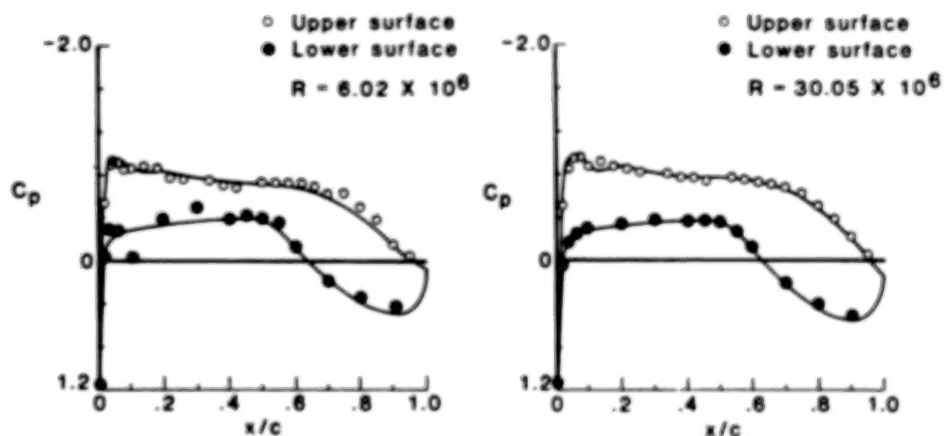
$\alpha_t \approx 1.5 \text{ deg}$



	Tunnel	Corrected	Grumfoil		Tunnel	Corrected	Grumfoil
M	0.719	0.701	0.701	M	0.718	0.705	0.705
α	1.495	0.201	0.493	α	1.501	0.051	0.552
C_1	0.7467	0.7601	0.7680	C_1	.8373	0.849	0.8555

**COMPARISONS OF STEADY TEST RESULTS WITH CALCULATED
RESULTS AT A TUNNEL MACH NUMBER OF 0.72**

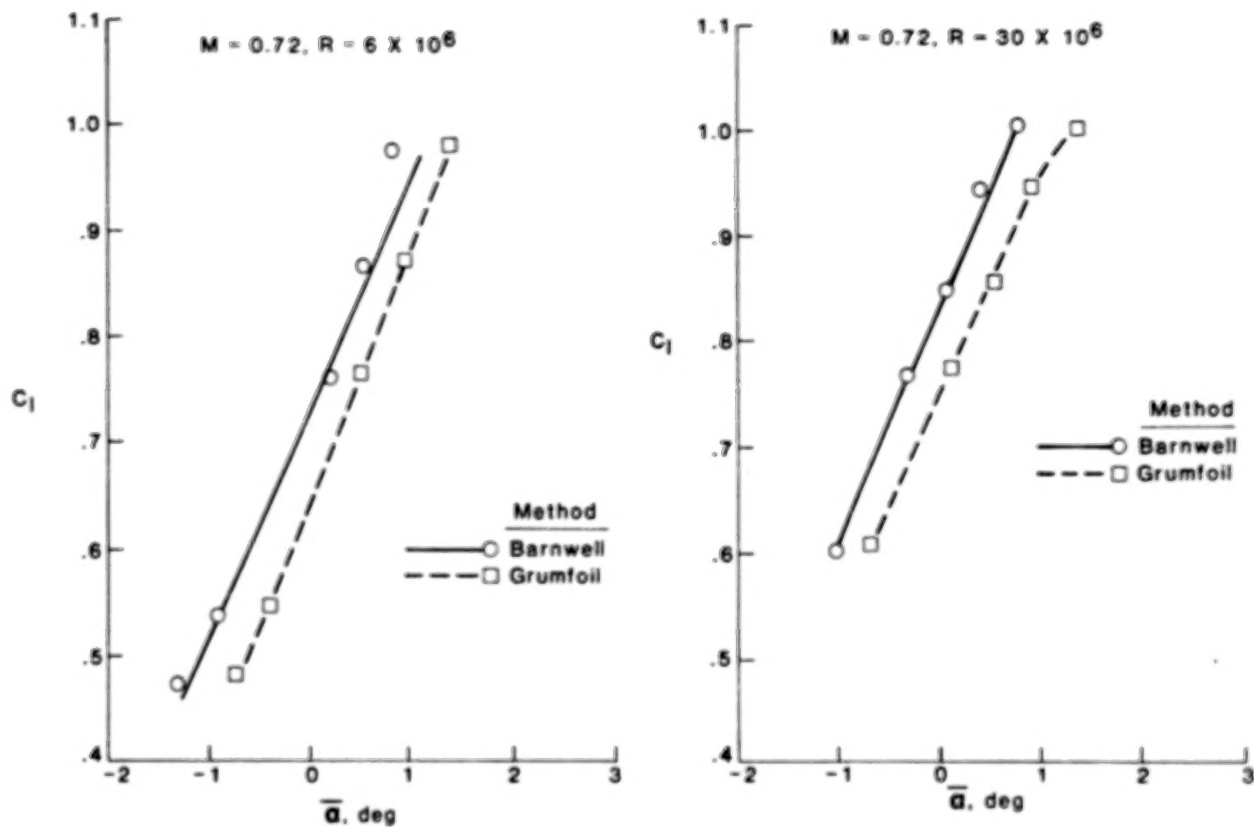
$\alpha_t \approx 0.0 \text{ deg}$



	Tunnel	Corrected	Grumfoil		Tunnel	Corrected	Grumfoil
M	0.720	0.701	0.701	M	.721	0.705	0.705
α	0.004	-0.92	-0.398	α	-0.005	-1.036	-0.715
C_1	0.5288	0.5383	0.5484	C_1	0.5951	0.6034	0.6099

COMPARISON OF LIFT COEFFICIENT VERSUS CORRECTED ANGLE OF ATTACK

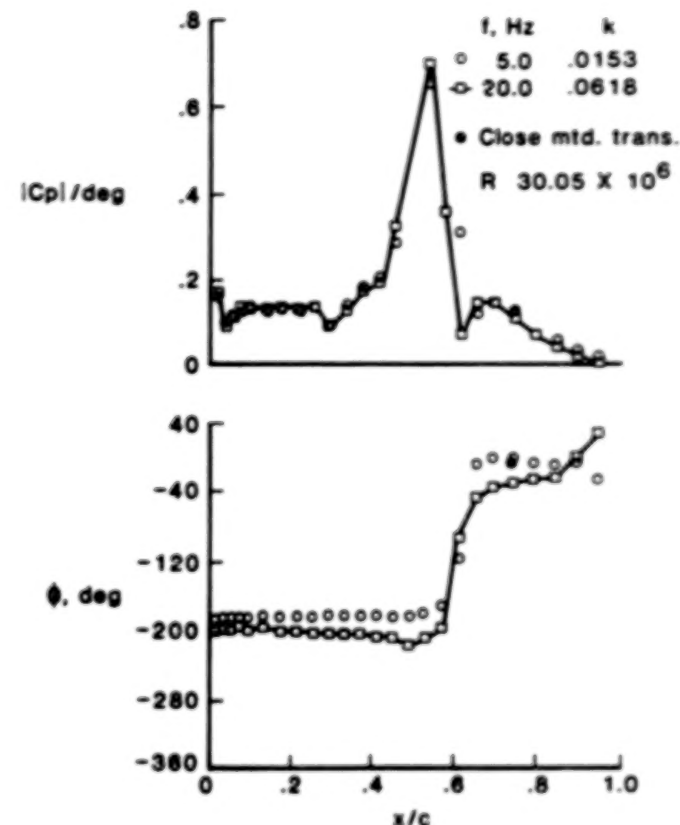
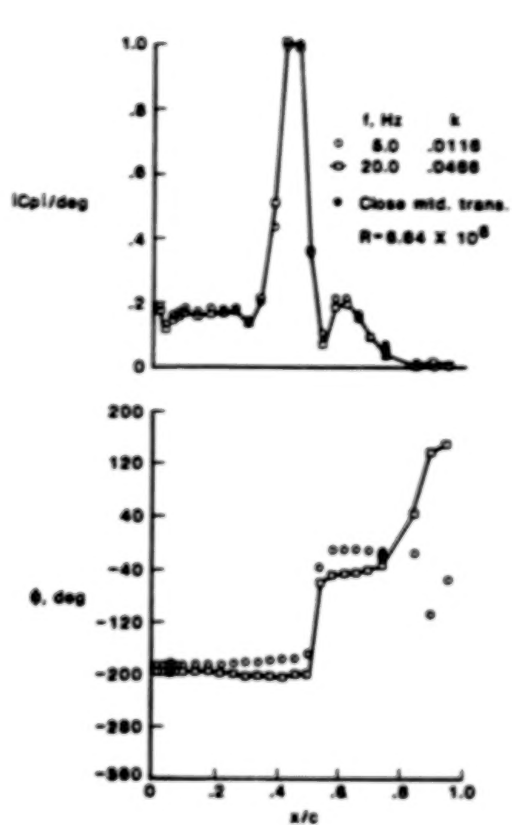
Lift coefficients for several cases are shown in this figure plotted against corrected angle of attack and against angle of attack as computed by GRUMFOIL code for input values of Mach number and C_l for Reynolds numbers of 6×10^6 and 30×10^6 . The angles calculated by the code are consistently larger than those determined by the correction procedure of Ref. 6. Irrespective of angle of attack corrections, an increase in C_l of approximately 0.1 is shown as Reynolds number is increased from 6×10^6 to 30×10^6 . This increase results from the rearward movement of the shock shown in the previous figures.



**UNSTEADY PRESSURE TEST RESULTS AT A TUNNEL
MACH NUMBER OF 0.72 AND AT $\alpha = 0.25$ DEGREES**

$\bar{\alpha}_t = 2.05$ degrees

The effect of Reynolds number and frequency of pitch oscillation on the upper surface unsteady pressure distribution is shown in the next two figures. Results are given in terms of the modulus of the unsteady pressure coefficient normalized by the oscillating pitch angle, α , and the phase angle, ϕ , between the unsteady pressure and the oscillating pitch angle. Results are shown for $\bar{\alpha}_t = 1$ and 2° at $R = 6 \times 10^6$ and 30×10^6 for two oscillation frequencies, 5 Hz and 20 Hz at a pitch amplitude of $\pm 0.25^\circ$.



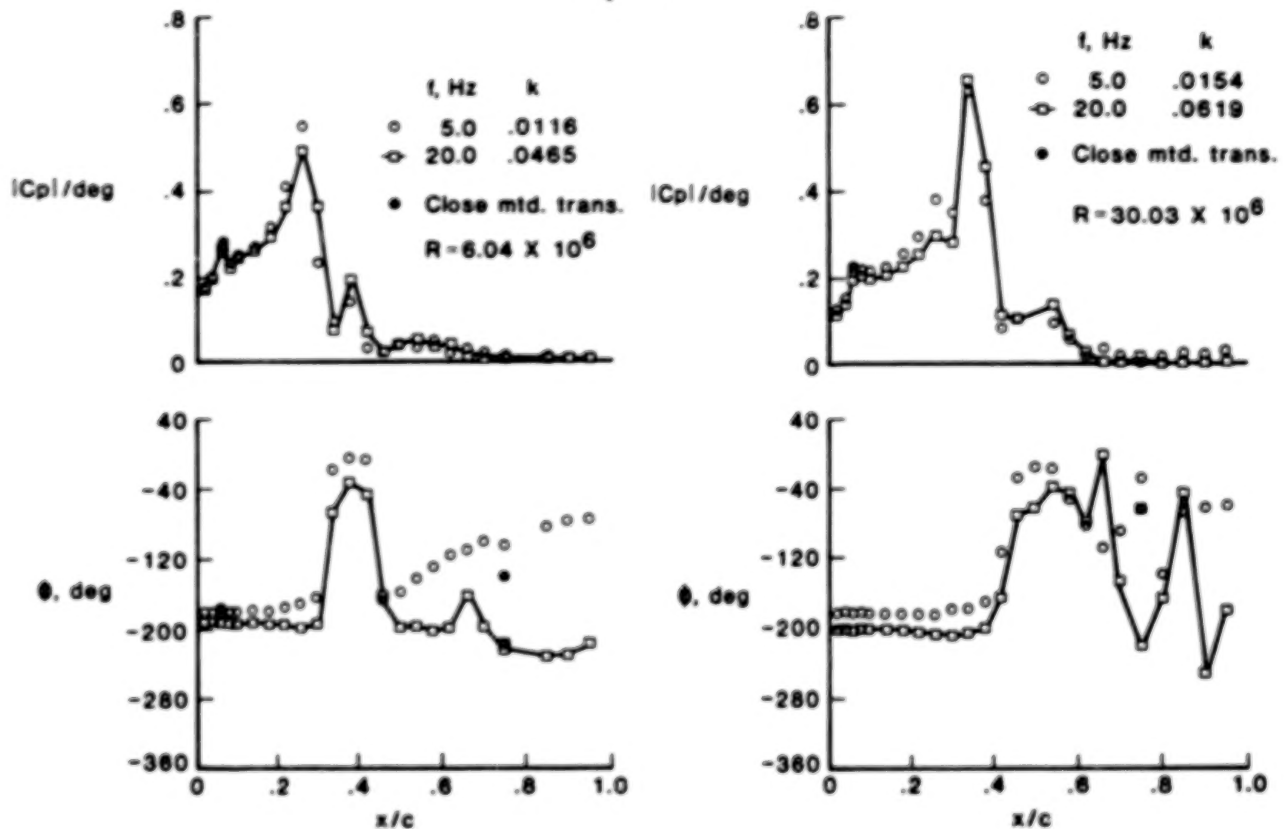
UNSTEADY PRESSURE TEST RESULTS AT A TUNNEL MACH NUMBER OF 0.72 AND AT $\alpha_t = \pm 0.25$ DEGREES

$$\bar{\alpha}_t = 1.04 \text{ degrees}$$

The shock wave, identified by the peak in the unsteady pressures, moves aft about 8% to 10% chord as R is increased from 6×10^6 to 30×10^6 at the same tunnel test angles. The unsteady pressures, at both R , are significantly greater ahead of the shock at $\bar{\alpha}_t = 1^{\circ}$ than at 2° , but there is no significant difference in the pressure modulus due to the change in frequency from 5 Hz to 20 Hz. For both angles of attack and R the pressures ahead of the shock are approximately 180° out of phase with the wing oscillation. At the shock the phase angle abruptly changes from -180° to 0° . Behind the shock the phase angle is erratic at $\bar{\alpha}_t = 1.0^{\circ}$ and is more dependent on frequency than at $\bar{\alpha}_t = 2.0^{\circ}$.

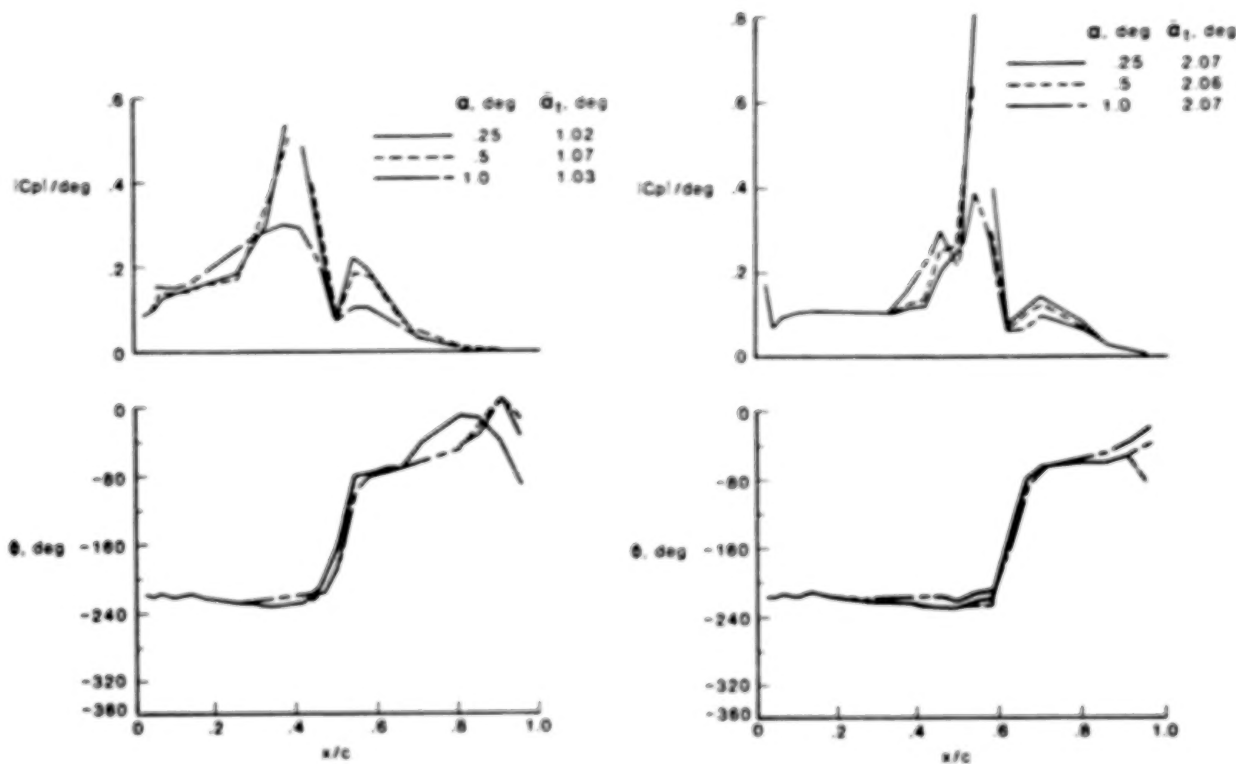
UNSTEADY PRESSURE TEST RESULTS AT A TUNNEL MACH NUMBER OF 0.72 AND AT $\alpha_t = \pm 0.25$

$$\bar{\alpha}_t = 1.04$$



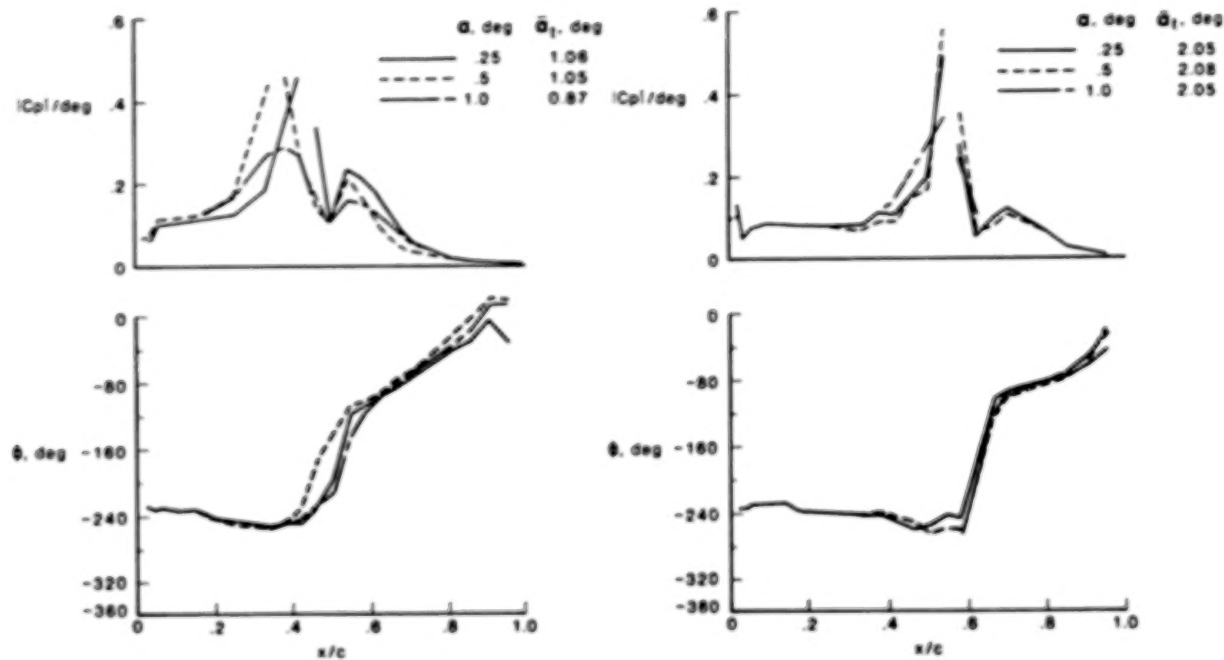
**VARIATION OF $|C_p|/\text{DEGREES}$ AND ϕ WITH PITCH AMPLITUDE
AT $M = 0.72$ AND $R = 30 \times 10^6$
 $f = 40 \text{ Hz}$**

The effect of varying the amplitude of oscillation at $M = 0.72$ and $R = 30 \times 10^6$ is shown in the next two figures. Upper surface pressure modulus and phase are shown for three pitch amplitudes (0.25, 0.5, 1.0°) at mean angles of 1.0 and 2.0° at $f = 40$ and 60 Hz. A reduction and broadening of the shock-generated peak amplitude is evident as the pitch amplitude, α , is increased at both frequencies and mean angles.



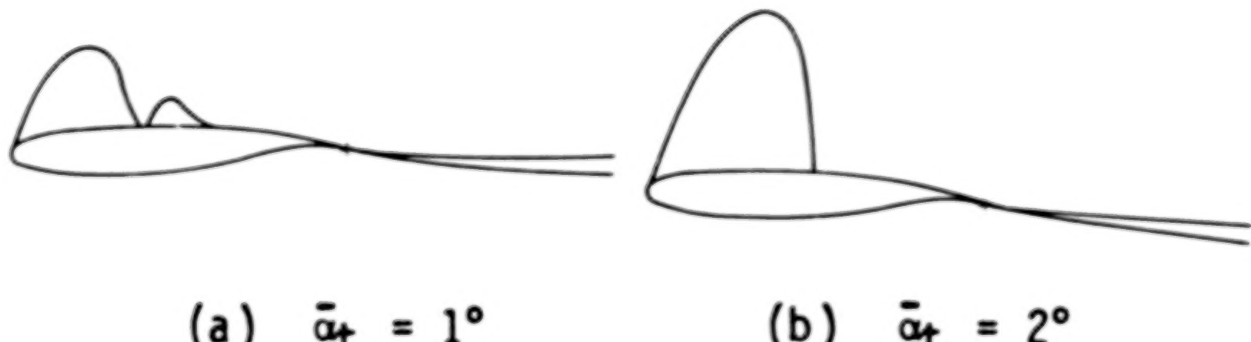
**VARIATION OF $|C_p|$ /DEGREES AND ϕ WITH PITCH AMPLITUDE
AT $M = 0.72$ AND $R = 30 \times 10^6$
 $f = 60$ Hz**

A secondary peak in the modulus of the oscillating pressure is evident immediately behind the shock in this and the other unsteady pressure distribution figures. The amplitude of this second peak is greater at $\bar{\alpha}_1 = 1.0^\circ$ than at $\bar{\alpha}_1 = 2.0^\circ$. The phase angle between pressure and wing motion is approximately -180° between the leading edge and immediately behind the shock, at which point there is a sudden decrease to below -360° . There is less deviation in phase for the $\bar{\alpha}_1 = 2.0^\circ$ data than for the $\bar{\alpha}_1 = 1.0^\circ$ data.



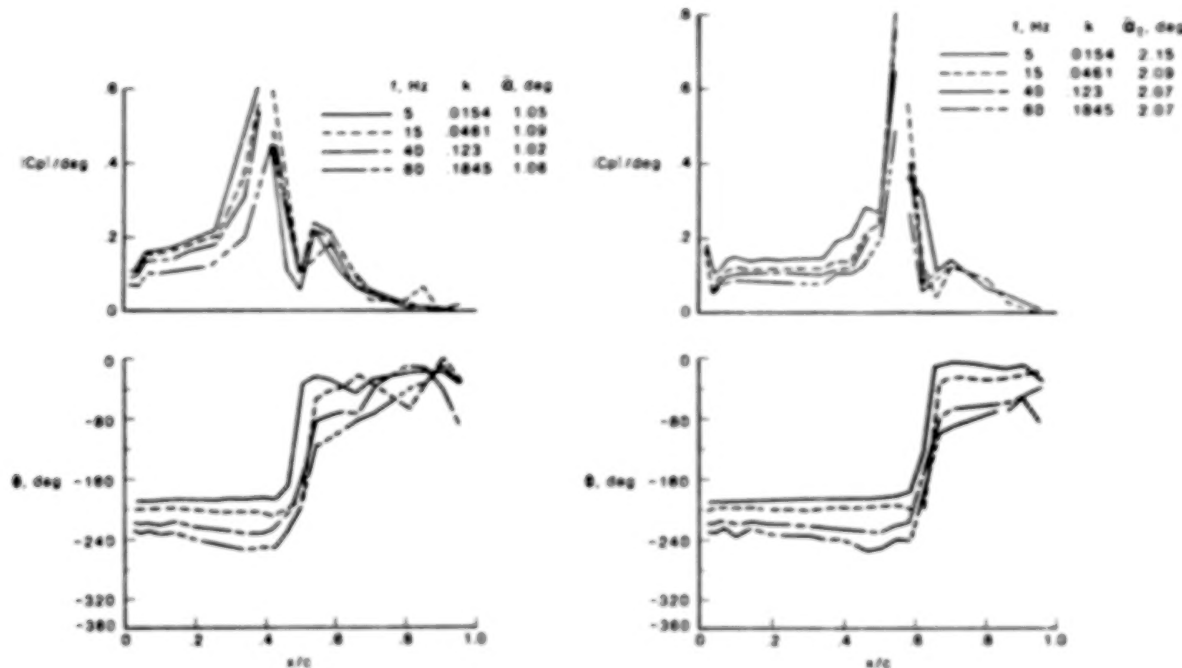
SONIC REGIONS AT M = 0.72 CALCULATED BY GRUMFOIL CODE

The secondary peak in the pressure modulus could be attributed to flow separation and reattachment as discussed in Ref. 9. However, an inviscid calculation using XTRAN2L (Refs. 10,11) computer code predicts this secondary peak in the same relative location. The sonic regions calculated from GRUMFOIL suggests that a more probable reason for the secondary response derives from the supersonic region above the airfoil. At $\alpha_t = 1.0^\circ$ there is a secondary supersonic region behind the shock which is engulfed by the primary supersonic region when the angle of attack is increased to $\alpha_t = 2.0^\circ$. Tijdeman (12) and others have noted that the flow in the supersonic region prior to the formation of a shock is characterized by a substantial increase in unsteady pressure.



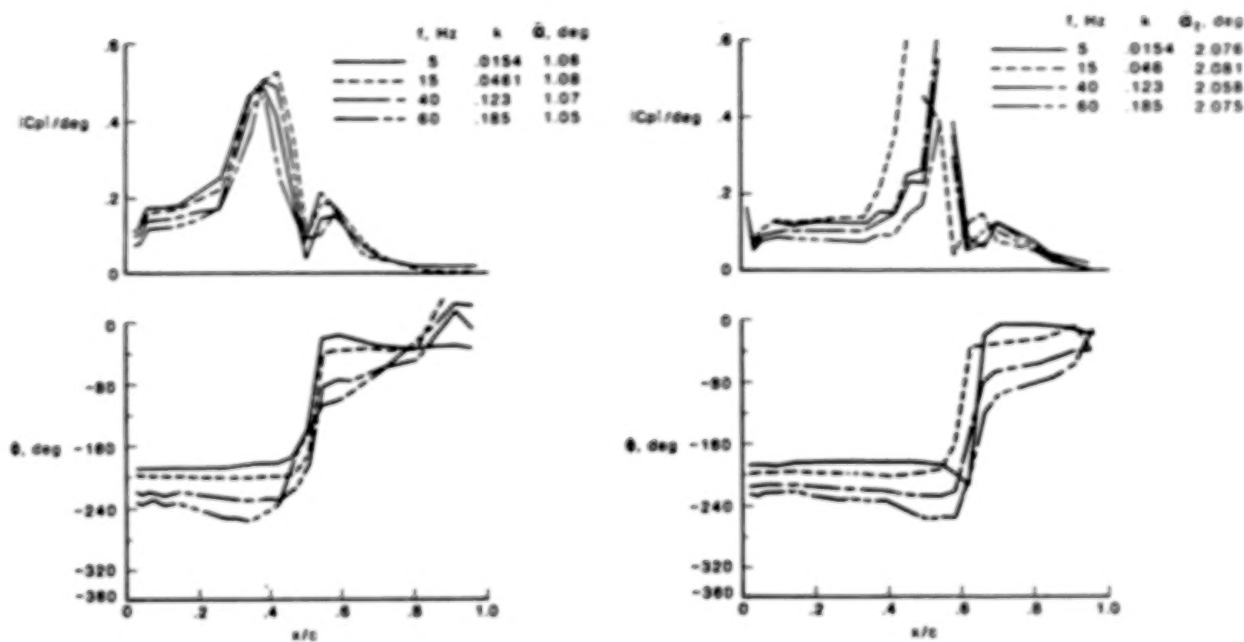
**VARIATION OF $|C_p|$ /DEGREES AND ϕ WITH FREQUENCY
AT $M = 0.72$ AND $R = 30 \times 10^6$
 $\alpha = 0.25$ DEGREES**

The effect of frequency on the modulus and phase of the upper surface unsteady pressures is shown in the next two figures for $M = 0.72$ and $R = 30 \times 10^6$. The measurements are shown for frequencies of 5, 15, 40, and 60 Hz at mean pitch angles of 1 and 2° and at amplitudes of 0.25 and 0.5° . In general the excursion of the shock is reduced at 60 Hz and again the amplitude of the second peak is reduced for all frequencies as α_1 is increased from 1.0 to 2.0° .



**VARIATION OF $|C_p|$ /DEGREES AND ϕ WITH FREQUENCY
AT $M = 0.72$ AND $R = 30 \times 10^6$
 $\alpha = 0.5$ DEGREES**

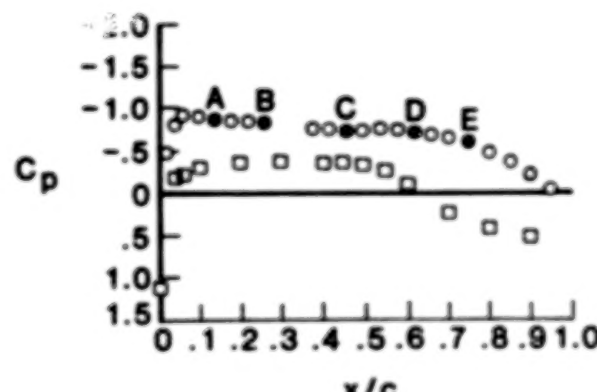
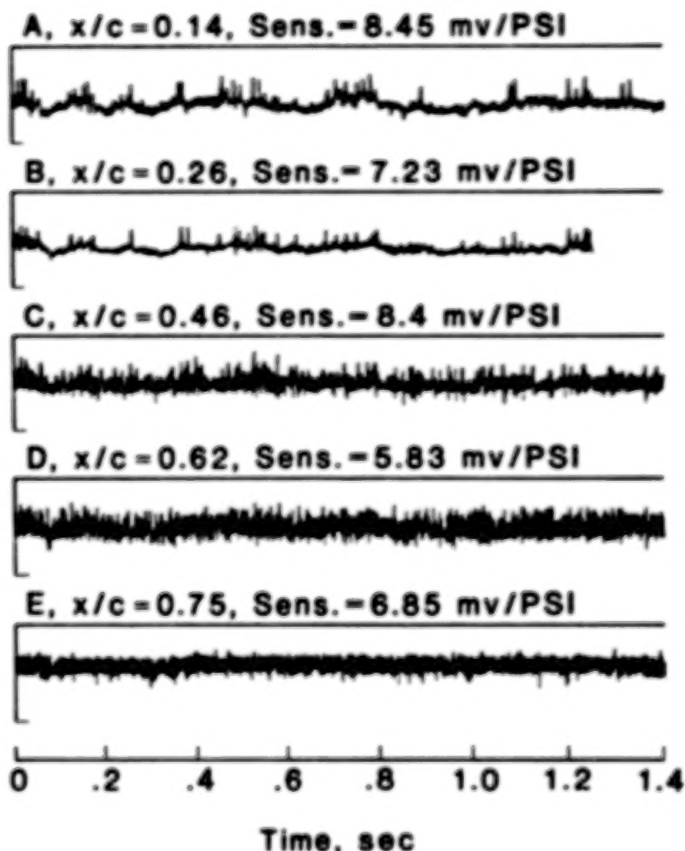
The phase angle shows a dependency on frequency in detailed sense having the same overall characteristics as in the previous figures. The phase angle between the pressure and the airfoil motion is approximately -180° from the leading edge to immediately behind the shock where it increases rapidly to approximately 0° .



TIME HISTORIES AT FIVE CHORD STATIONS FOR
 $A = 0$, $M = 0.72$, AND $R = 35 \times 10^6$

$$\alpha = 0 \text{ degrees}$$

The pressure transducers used to measure unsteady pressures generated by airfoil pitch oscillation were also used to measure unsteady pressures when the wing was held at a fixed angle of attack. The next two figures show time histories at five chord stations whose locations are shown by solid symbols on the plot of the static pressure distribution, on the right of the figures, for the angles of attack (0 and 2°) being considered. The time histories shown in these figures were all taken at a gain of 10, but the transducer sensitivity, given with each trace, has not been applied to put the data in engineering units.



TIME HISTORIES AT FIVE CHORD STATIONS FOR
 $A = 0$, $M = 0.72$, AND $R = 35 \times 10^6$

$\bar{\alpha} = 2$ degrees

At $\bar{\alpha} = 0^\circ$ the time histories have the characteristics of a turbulent boundary layer and are in sharp contrast with the time histories of $\bar{\alpha} = 2^\circ$. At $\bar{\alpha}$ of 2° the pressure is quiescent at x/c of 0.14 and 0.28, at x/c of 0.46 the effect of shock movement on the pressure response is observed, which increases at the foot of the shock, $x/c = 0.62$, where turbulence is also apparent. The observable differences between the flows at the two angles of attack are the more favorable pressure gradient and the presence of a shock wave at $\bar{\alpha} = 2^\circ$. The time histories indicate that laminar flow was present at $\bar{\alpha} = 2^\circ$ and that transition to turbulence was between an x/c of 0.28 and 0.46 corresponding to transition Reynolds numbers between 9.8×10^6 and 16.1×10^6 . The possibility exists that long runs of laminar flow existed intermittently during the tests.

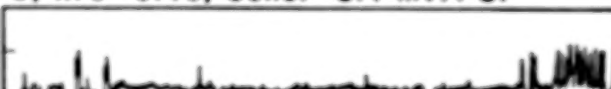
A, $x/c = 0.14$, Sens. = 8.45 mv/PSI



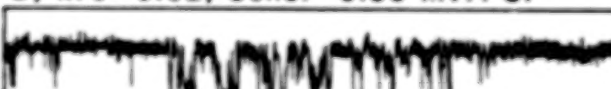
B, $x/c = 0.26$, Sens. = 7.23 mv/PSI



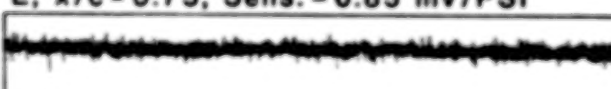
C, $x/c = 0.46$, Sens. = 8.4 mv/PSI



D, $x/c = 0.62$, Sens. = 5.83 mv/PSI

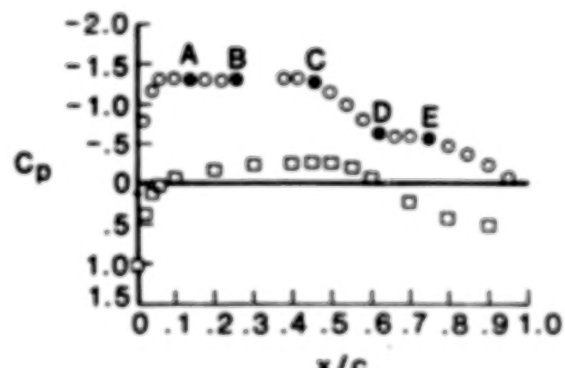


E, $x/c = 0.75$, Sens. = 6.85 mv/PSI



0 .2 .4 .6 .8 1.0 1.2 1.4

Time, sec



CONCLUSIONS

Steady and unsteady pressures have been measured on a 14 percent supercritical airfoil at transonic Mach numbers at Reynolds numbers from 6×10^6 to 35×10^6 . Instrumentation techniques were developed to measure unsteady pressures in a cryogenic tunnel at flight Reynolds numbers. Experimental steady data, corrected for wall effects show very good agreement with calculations from a full potential code with an interacted boundary layer. The steady and unsteady pressures both show a shock position that is dependent on Reynolds number. For a supercritical pressure distribution at a chord Reynolds number of 35×10^6 laminar flow was observed between the leading edge and the shock wave at 45 percent chord.

ACKNOWLEDGMENT

The author wishes to acknowledge the assistance of Clyde Gumbert of the Theoretical Aerodynamics Branch, NASA Langley Research Center, in the Grumfoil calculations.

REFERENCES

¹Harris, C. D.: "Aerodynamic Characteristics of a 14-Percent Thick NASA Supercritical Airfoil Designed for a Normal-Force Coefficient of 0.7." NASA TM X-72712, July 1975.

²Ray, E. J.; Ladson, C. L.; Adcock, J. B.; Lawing, P. L.; and Hall, R. M.: "Review of Design and Operational Characteristics of the 0.3M Transonic Cryogenic Tunnel." NASA TM 80123, 1979.

³Ray, E. J.: "A Review of Reynolds Number Studies Conducted in the Langley 0.4M-Transonic Cryogenic Tunnel." AIAA/ASME 3rd Joint Thermophysics, Fluids, Plasma and Heat Transfer Conference, St. Louis, MO, June 7-11, 1982. AIAA Paper 82-0941.

⁴Sewall, W. G.: "The Effects of Sidewall Boundary Layer in Two-Dimensional Subsonic and Transonic Wind Tunnels." AIAA Journal, Vol. 20, No. 9, September 1982, pp. 1253-1256.

⁵Jenkins, R. V.; and Adcock, J. B.: "Tables for Correcting Airfoil Data Obtained in the Langley 0.3-Meter Transonic Cryogenic Tunnel for Sidewall Boundary Layer Effects." NASA TM 87723, June 1986.

⁶Barnwell, R. W.: "Design and Performance Evaluation of Slotted Walls for Two-Dimensional Wind Tunnels." NASA TM 78648, February 1978.

⁷Mead, H. R.; and Melnik, R. E.: "GRUMFOIL: A Computer Code for the Viscous Transonic Flow Over Airfoils." NASA CR 3806, October 1985.

⁸Gumbert, C. R.; and Newman, P. A.: "Validation of a Wall Interference Assessment/Correction Procedure for Airfoil Tests in the 0.3M-Transonic Cryogenic Tunnel." AIAA 2nd Applied Aerodynamics Conference, August 21-23, 1984.

⁹Mundell, A. R. G.; and Mabey, D. G.: "Pressure Fluctuations Caused by Transonic Shock/Boundary-Layer Interaction." Aeronautical Journal, August/September 1986.

¹⁰Whitlow, W., Jr.: "XTRAN2L: A Program for Solving the General Frequency Unsteady Transonic Small Disturbance Equation." NASA TM 85721, November 1983.

¹¹Seidel, D. A.; and Batina, J. T.: "User's Manual for XTRAN2L (Version 1.2): A Program for Solving the General-Frequency Unsteady Transonic Small-Disturbance Equation." NASA TM 87737, July 1986.

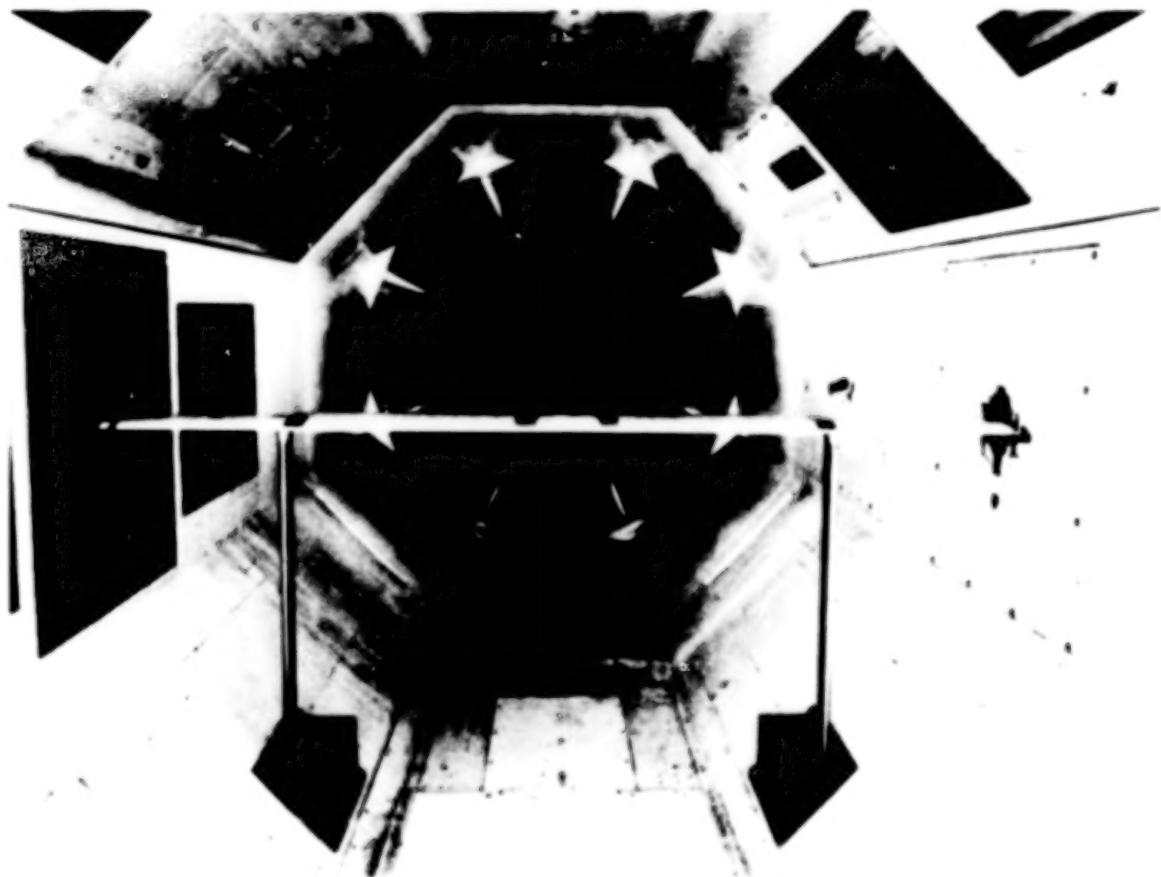
¹²Tijdeman, H.: "Investigation of the Transonic Flow Around Oscillating Airfoils." NLR TR 77090 U, 1977.

AIRFOIL STALL PENETRATION AT CONSTANT PITCH RATE
AND HIGH REYNOLDS NUMBER

Peter F. Lorber and Franklin O. Carta
United Technologies Research Center
East Hartford, Conn.

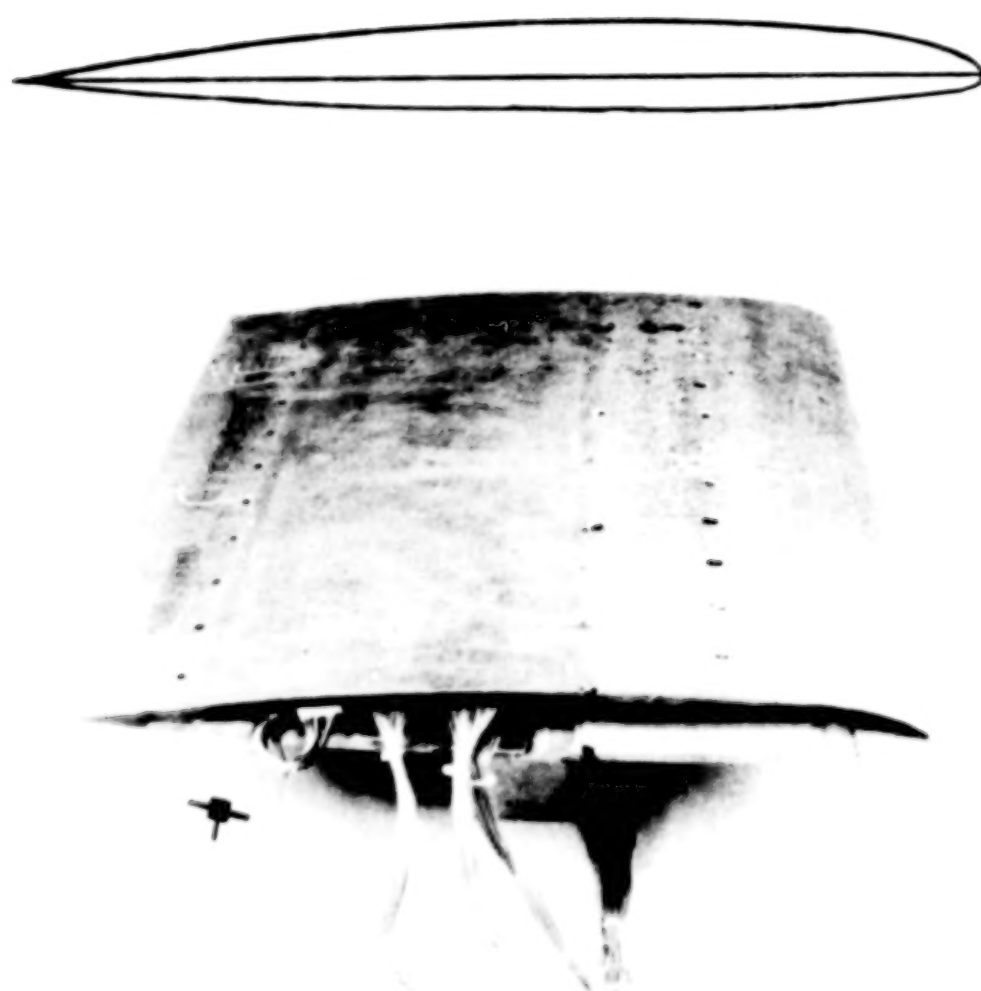
MODEL WING IN WIND TUNNEL

The model wing consists of a set of fiberglass panels mounted on a steel spar that spans the 8 ft. test section of the UTRC Large Subsonic Wind Tunnel. The pitch angle of the model is set by hydraulic actuators attached to each end of the spar and controlled using a dual channel closed-loop system. This allows 1024 samples of each data channel to be acquired at identical positions during each cycle of the wing motion. The first use of this system was to measure surface pressures and flow conditions for a series of constant pitch rate ramps and sinusoidal oscillations at Mach numbers between 0.2 and 0.4, Reynolds numbers between 2 and 4×10^6 , and pitch rates between $A = c\dot{\alpha}/2U = 0.001$ and 0.02.



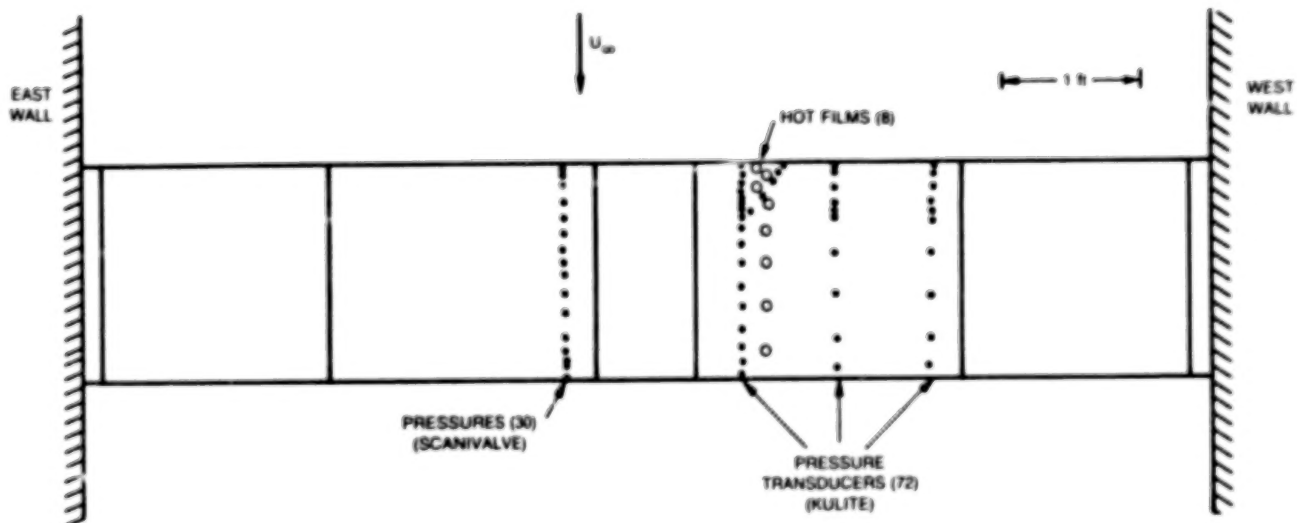
AIRFOIL SECTION

A Sikorsky SSC-A09 airfoil with a 17.3 in. chord was used. This is a 9% thick supercritical section designed for low drag at high subsonic Mach numbers.



INSTRUMENTATION

The wing-mounted instrumentation consists of 72 miniature pressure transducers and 8 surface hot film gages. The pressure transducers are mounted inside the fiberglass skin and are connected to the surface by short pipettes. This technique provides a point measurement on a smooth surface contour. The primary chordwise pressure transducers are located in arrays of 18 on each surface, 0.5 chordlengths from the tunnel centerline, and 2.3 chordlengths from the side wall. The transducers are arranged in a segmented Gaussian array from $x/c = 0.005$ to $x/c = 0.99$. The other 36 transducers are located in additional arrays at 1.8 and 1.4 chordlengths from the wall, intended for use in future swept wing and finite tip experiments. The hot film gages are located in an array parallel to the primary pressure array, from $x/c = 0.026$ to $x/c = 0.88$. Detailed calibrations over both pressure and temperature ranges make it possible to measure both mean and unsteady pressures to within 1% of the calibration range. An interactive data system is used to acquire single samples of time histories, or to obtain an ensemble average of the time histories, based on 20 cycles of the motion. These data are digitized, converted to pressure coefficient, and stored on magnetic tape.



TEST CONDITIONS

Unsteady data were acquired for 36 constant pitch rate ramps and 9 sinusoidal oscillations, as shown in the table. The maximum pitch rate of 360 deg/sec occurred at $A = 0.02$ and $M = 0.2$, and the minimum of 18 deg/sec at $A = 0.001$. The maximum rate is lower than the maximum reached in many smaller scale experiments (Refs. 1-5), but is larger than that for both the "typical" ($A = 0.001$) and "minimum time" ($A = 0.0044$) maneuvers described in Ref. 6. The wing angle of attack was limited by the support system to a maximum of 30 deg, which was less than the maximum obtained in the smaller scale tests, but sufficient to include all of the primary stall-related events at the pitch rates used.

STEADY

$$M = 0.2, \quad -5^\circ \leq \alpha \leq 28^\circ$$

$$M = 0.4, \quad 0^\circ \leq \alpha \leq 20^\circ$$

UNSTEADY RAMPS

M	α -RANGE	A = $C\dot{\alpha}/2U$				
		.001	.0025	.005	.010	.020
0.2	0° → 10°	x	x	x	x	
	0° → 20°	x	x	x	x	
	0° → 30°	x	x	x	x	
	10° → 20°	x	x	x	x	
	12° → 22°	x		x	x	
	14° → 24°	x		x	x	
	20° → 30°	x	x	x	x	
	20° → 10°	x			x	
	30° → 0°	x		x		
0.3	0° → 20°			x		
	0° → 30°				x	
0.4	0° → 10°	x		x		
	0° → 20°	x	x	x	x	
	20° → 0°				x	

(40 RAMPS)

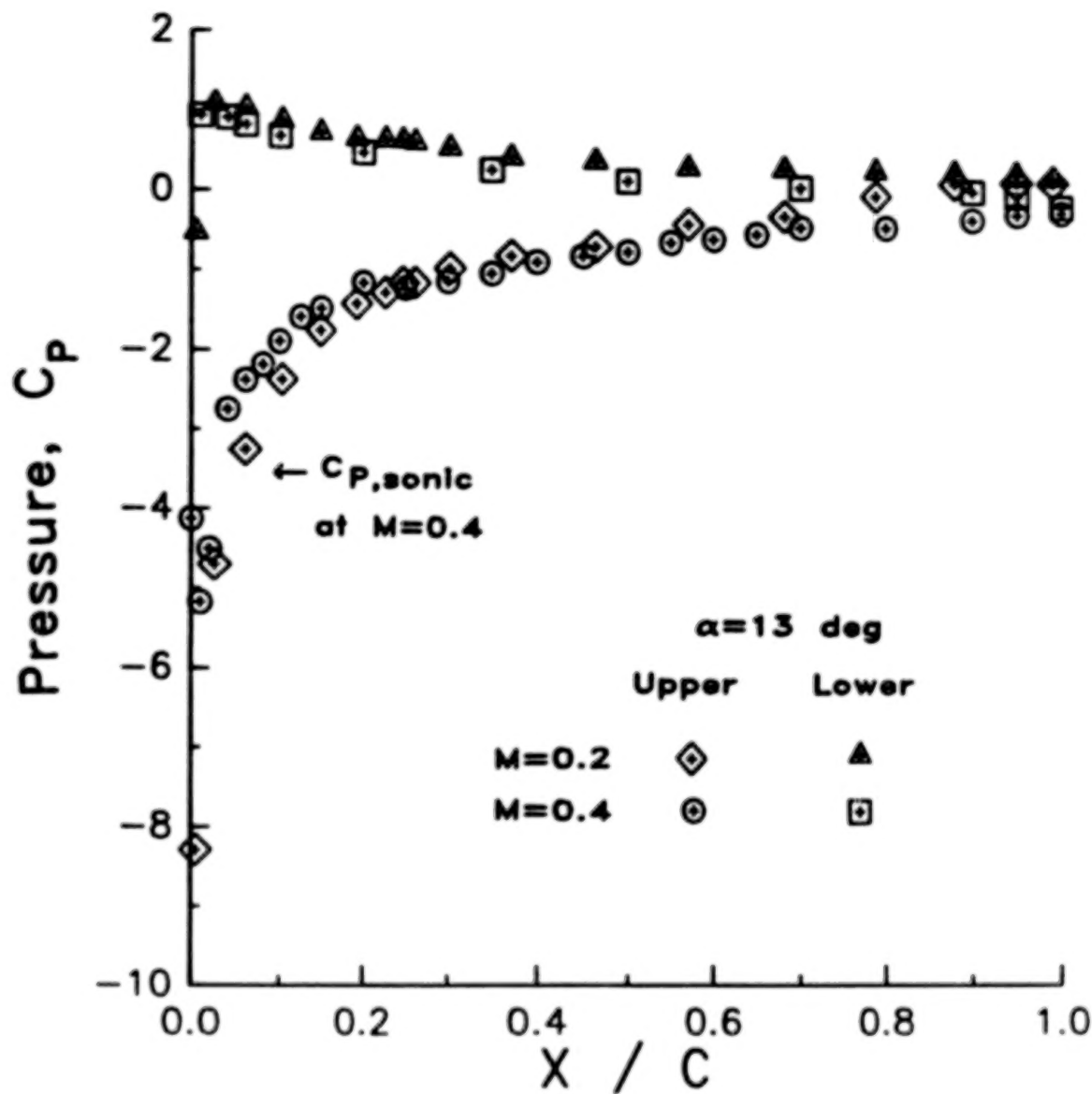
UNSTEADY OSCILLATIONS

M	α	k = $C\omega/2U$		
		.025	.050	.100
0.2	5° + 5°sin ωt	x		
	10° + 10°sin ωt	x	x	x
	20° + 10°sin ωt	x	x	x
0.3	9° + 8°sin ωt		x	
	12° + 8°sin ωt			x

(9 SINUSOIDS)

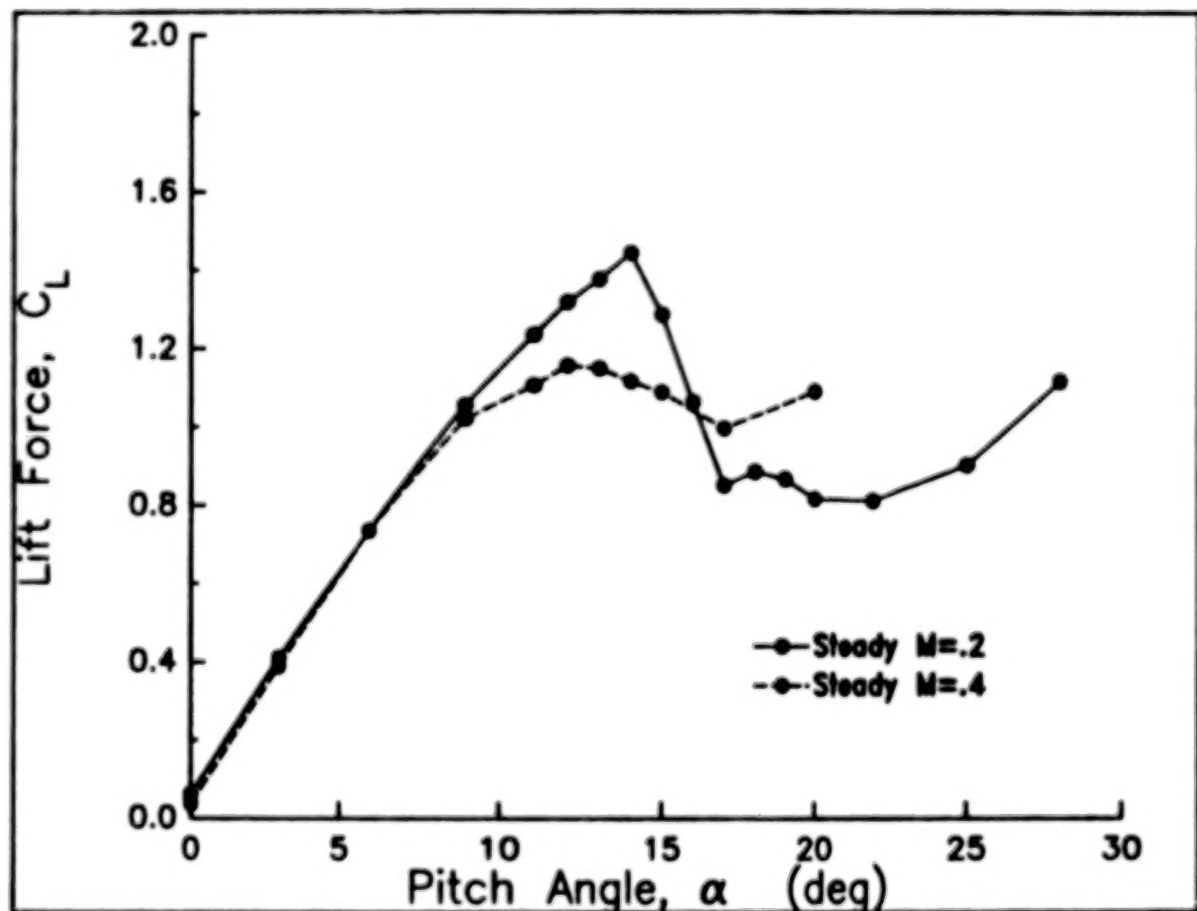
STEADY PRESSURES

The steady pressure distributions have a strong leading edge suction peak prior to stall. Maximum suction occurs at $\alpha = 13$ deg and reaches values of $C_p = -8.2$ at $M = 0.2$, and $C_p = -5.2$ at $M = 0.4$. The sonic pressure coefficient at $M = 0.4$ is -3.7, so a small supersonic zone exists at the leading edge, terminated in a shock near $x/c = 0.03$. The compressibility effects associated with this zone create the lift curve differences seen earlier.



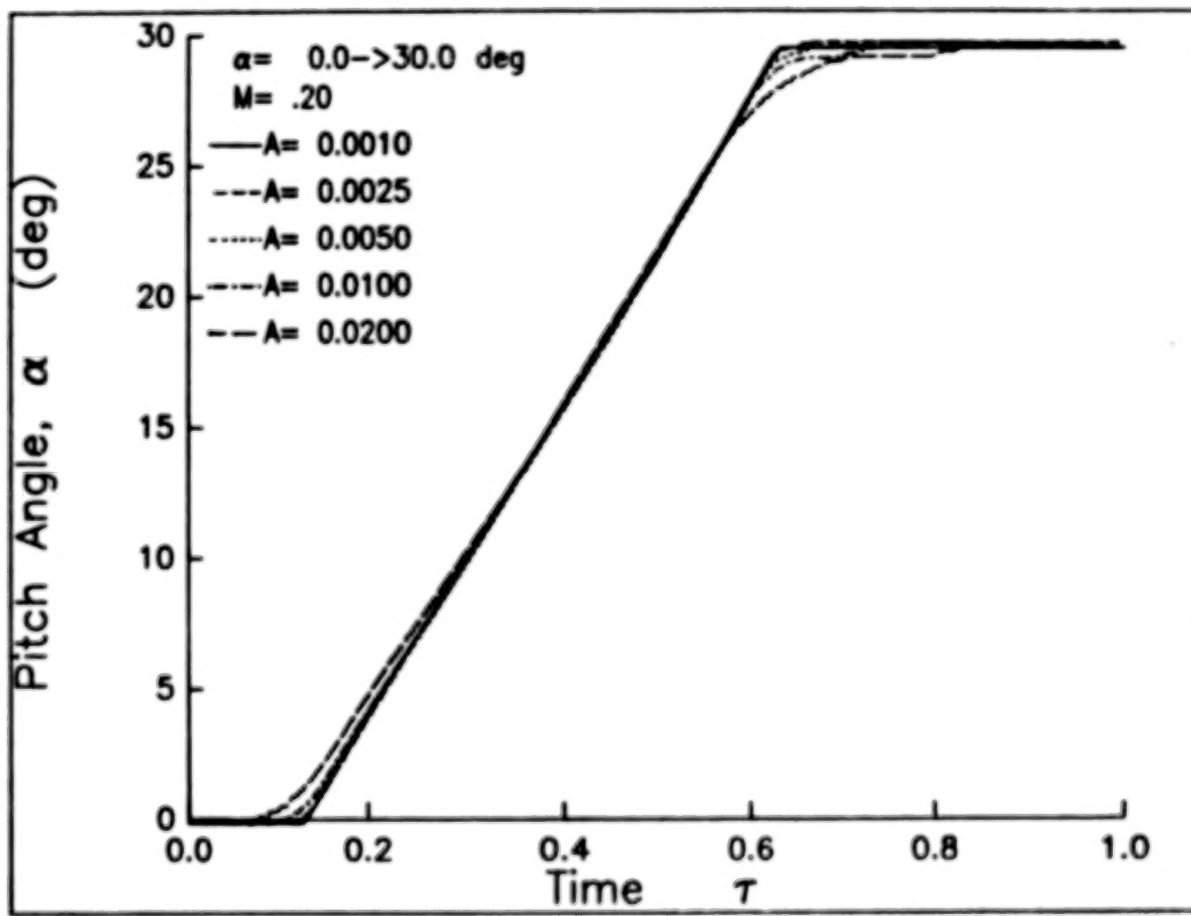
STEADY LIFT FOR $M = 0.2, 0.4$

Steady pressure data acquired at $M = 0.2$ and 0.4 were integrated to yield the lift curves shown in the Figure. At $M = 0.2$ max C_L of 1.4 is reached at $\alpha = 14$ deg, and is followed by a rapid drop to a C_L of 0.9 at $\alpha = 17$ deg. Increasing M to 0.4 reduces max C_L to 1.2 and flattens the stall.



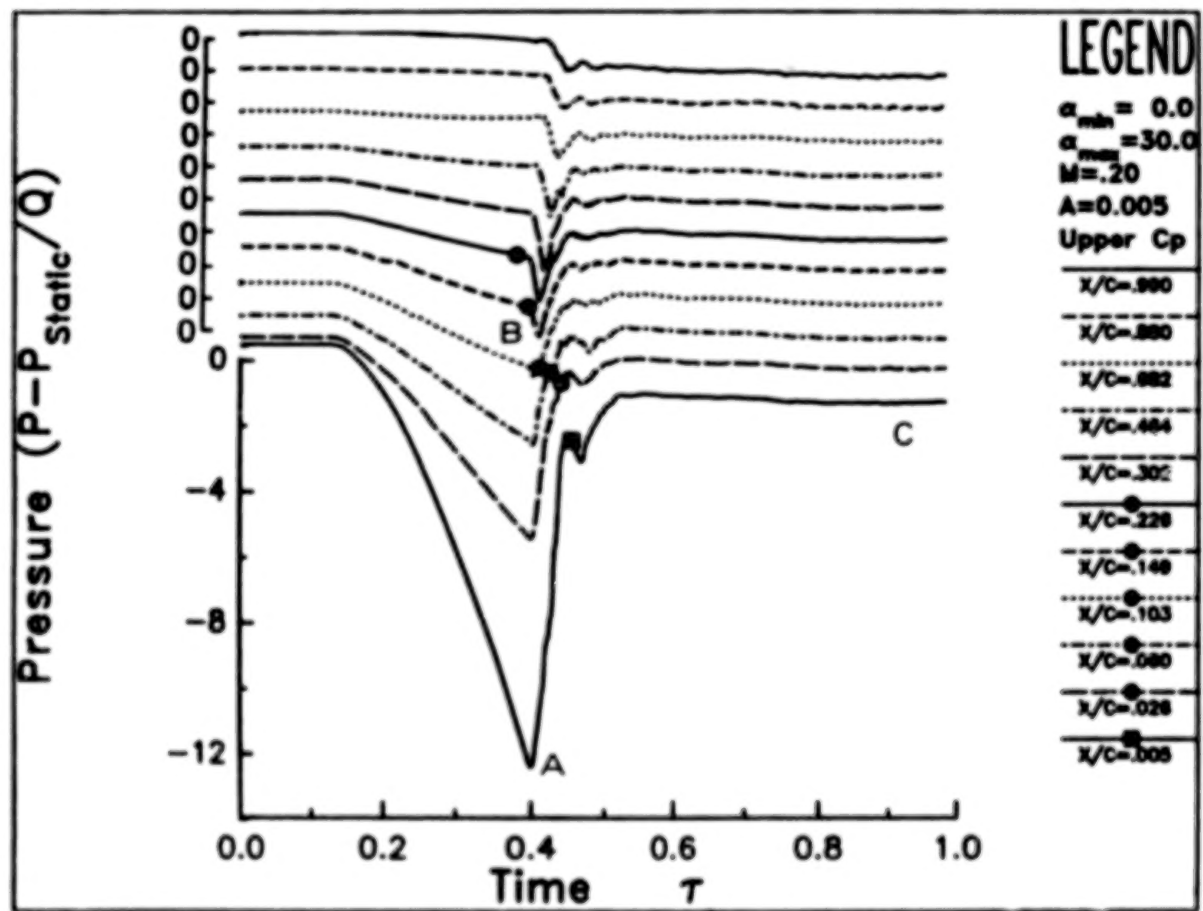
RAMP TIME HISTORIES

Airfoil motion for a ramp consists of an initial delay of several seconds at the minimum angle, a constant rate increase to the maximum angle, a second delay at the maximum angle, and a return to the initial condition. Data are acquired only during a small portion, T , of this cycle. Time histories of the pitch angle during the data acquisition period are shown in the figure for several 0 to 30 deg ramps at $M = 0.2$. The ramp begins at nondimensional time, $\tau = t/T$, of 0.125 and ends at $\tau = 0.625$. The pitch increase is quite linear with time and has sharp corners for $A < 0.005$. At higher pitch rates the damping of the hydraulic system rounds the corners, but still maintains a nearly linear pitch rate near stall.



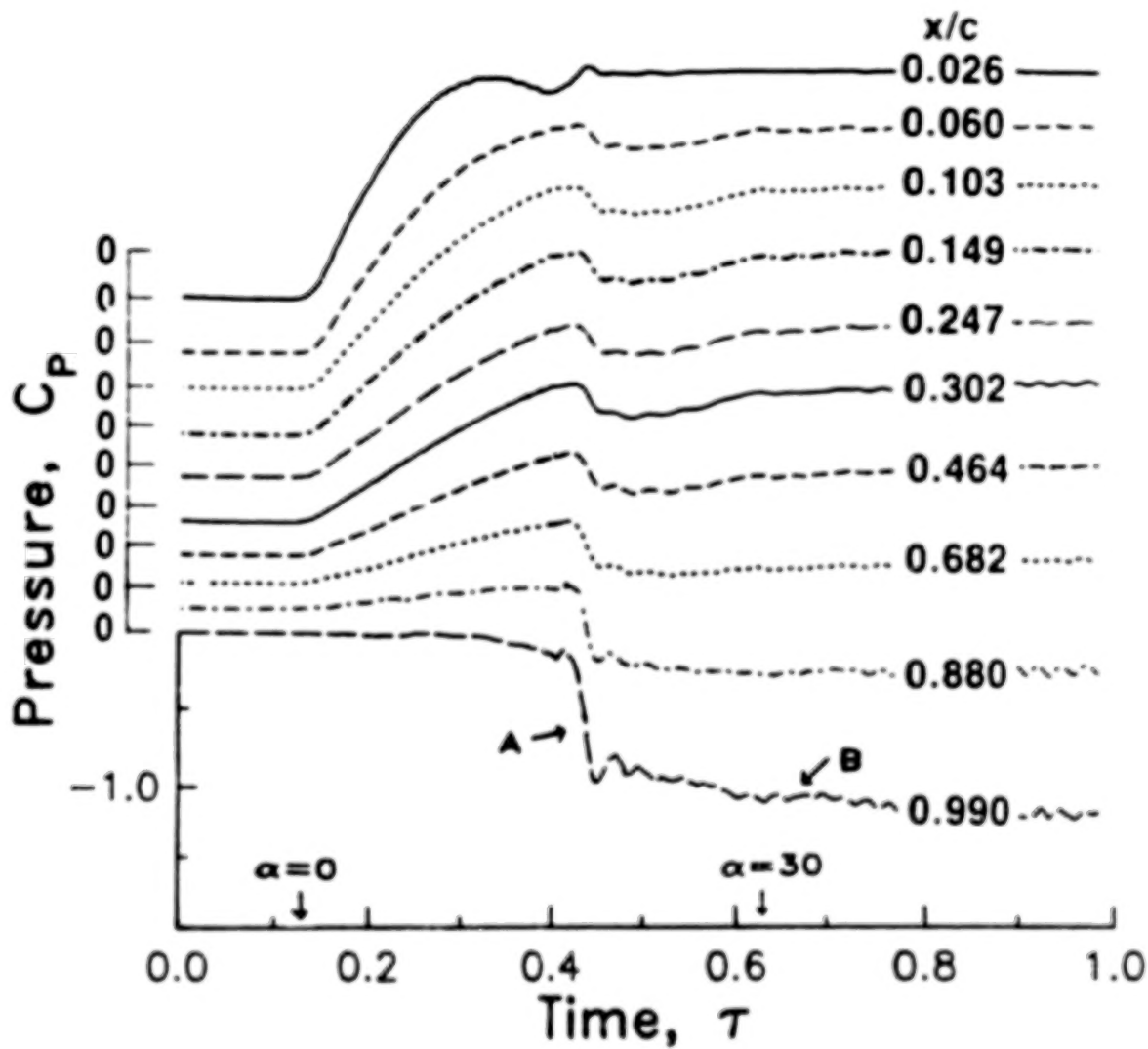
UNSTEADY PRESSURES, UPPER SURFACE

Ensemble averaged upper surface pressure time histories for 11 of the 18 measurement stations are shown for a 0 to 30 deg constant pitch rate ramp at $A = 0.005$, $M = 0.2$. The ordinate scale on the lower left refers absolutely to the $x/c = 0.005$ curve, and all other curves are vertically offset by $\Delta C_p = 1.0$. Each of these curves is referenced to its own origin (upper left scale). The pressure responds smoothly to the imposed pitch angle until maximum suction is reached at $\tau = 0.4$ ($\alpha = 15.5$ deg) at letter A. Peak suction at $x/c = 0.005$ is $C_p = -12.5$, corresponding to a local Mach number of 0.84. The rapid local increase in suction associated with passage of the vortex (letter B) is only observed for $x/c > 0.1$, implying that the vortex forms ahead of this position and travels downstream thereafter. The vortex pressure propagates along the chord at $0.16U$, and reaches the trailing edge at $\tau = 0.45$. For $\tau > 0.50$ the upper surface separation is massive and the pressures are virtually invariant in both time and position (letter C). All events are completed well before the ramp ends at $\tau = 0.625$.



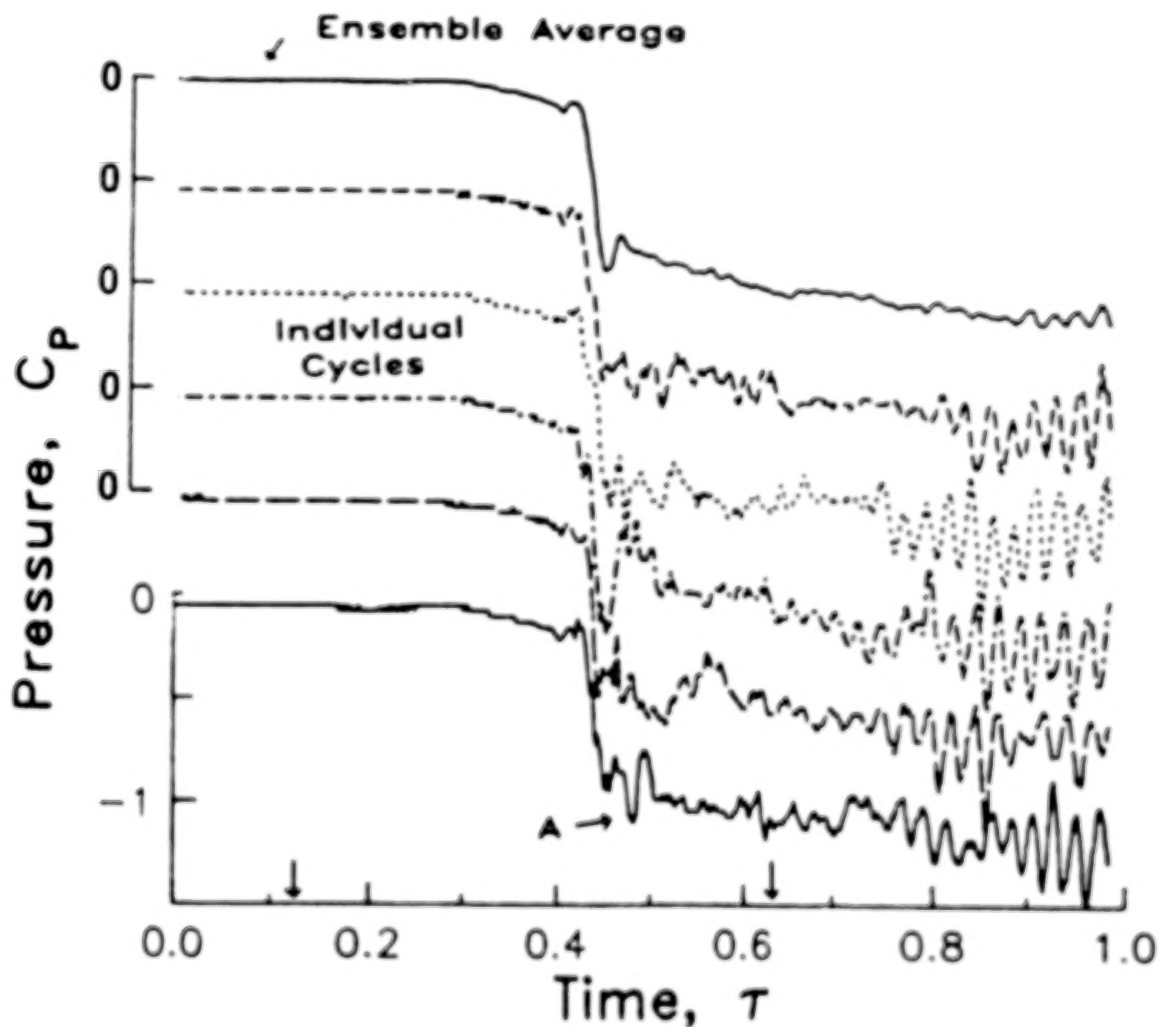
UNSTEADY PRESSURES, LOWER SURFACE

The lower surface does not separate, and responds primarily to the migration of the stagnation point near the leading edge (from motion initiation at $\tau = 0.125$ to $\tau = 0.42$), and to the upper surface massive stall near the trailing edge (letter A), where the pressure is required by continuity to match that on the upper surface. In addition, a periodic oscillation in these ensemble averaged pressures is detected near the lower surface trailing edge (letter B). The oscillation frequency of 62Hz is very close to the 65Hz frequency calculated for the vonKarman vortex street shed by a circular cylinder having a diameter, D, equal to the vertical projection of the airfoil chord, $c \sin \alpha$. From Ref. 7, a cylinder will generate a vortex street at a Strouhal number, Df/U , of 0.21 for Reynolds Numbers less than 10^6 and at $fD/U = 0.27$ for $Re > 3 \times 10^6$. No regular vortex street is formed when the Reynolds number is between these limits. In the present case the Reynolds number of the cylinder is equivalent in projected area to the airfoil at $M = 0.2$ and $\alpha = 30$ deg is 10^6 , near the boundary where periodic oscillations should cease.



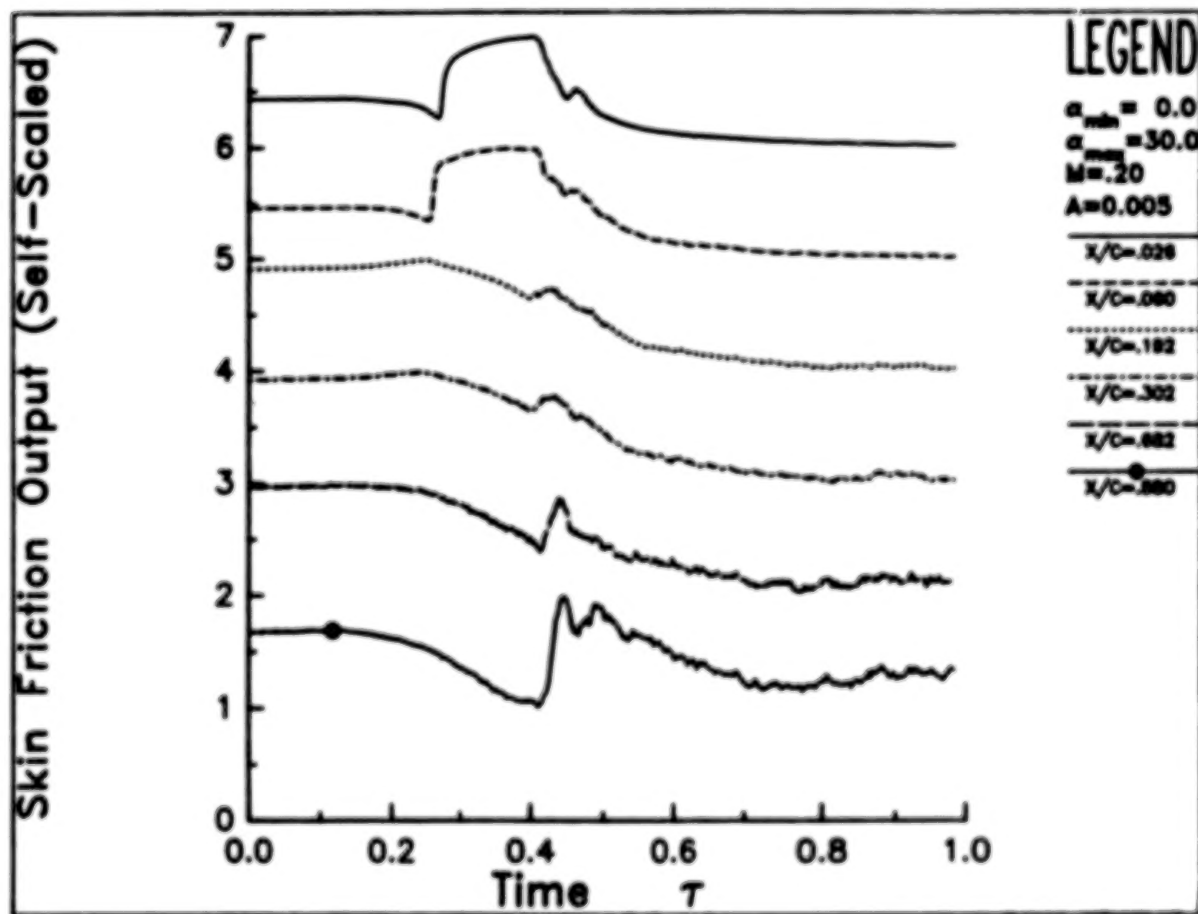
INDIVIDUAL RECORDS, LOWER SURFACE

A larger post-stall oscillation amplitude is found for individual records of the motion than for the ensemble average. The top time history in this figure is the ensemble averaged trailing edge plot from the previous figure, and the remaining curves are a set of (nonconsecutive) individual records at the same location and for the same set of flow conditions. Each curve is offset vertically by $C_p = 0.5$. The oscillations have the same frequency and a similar maximum amplitude during each record, but they are not well correlated in phase. The resulting cancellation reduces the ensemble averaged amplitude. A separate oscillation at a lower frequency is often present immediately following the passage of the stall vortex at $\tau = 0.45$ (letter A), and may result from secondary stall vortices.



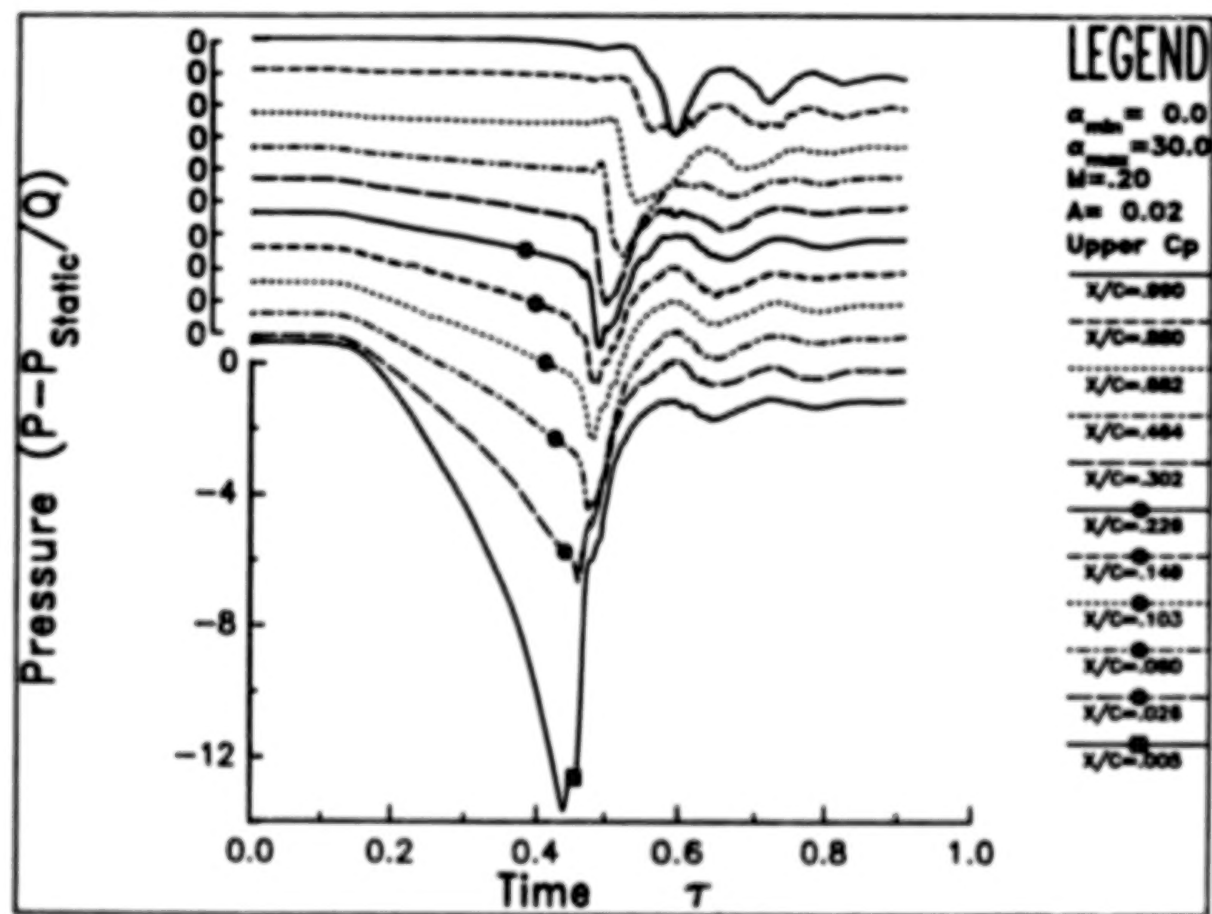
HOT FILM TIME HISTORIES

Hot film gages provide additional information on the surface flow conditions, as shown by the six time histories in this figure. The data are self-scaled, so each varies over one unit. As indicated on the leading edge trace, the boundary layer is initially laminar at the first two stations, goes through transition, becomes turbulent, and eventually becomes separated. From $x/c = 0.192$ and aft the flow is always either turbulent, or separated, and is never laminar. Ahead of the stall vortex release point ($x/c = 0.1$) the heat transfer drops when the boundary layer separates at $\tau = 0.4$. Downstream of the release point the heat transfer drops slightly at separation but then rises rapidly as the high velocities induced by the stall vortex pass each gage. There is excellent agreement between the times of separation as measured by the hot film gages and by the adjacent pressure transducers.



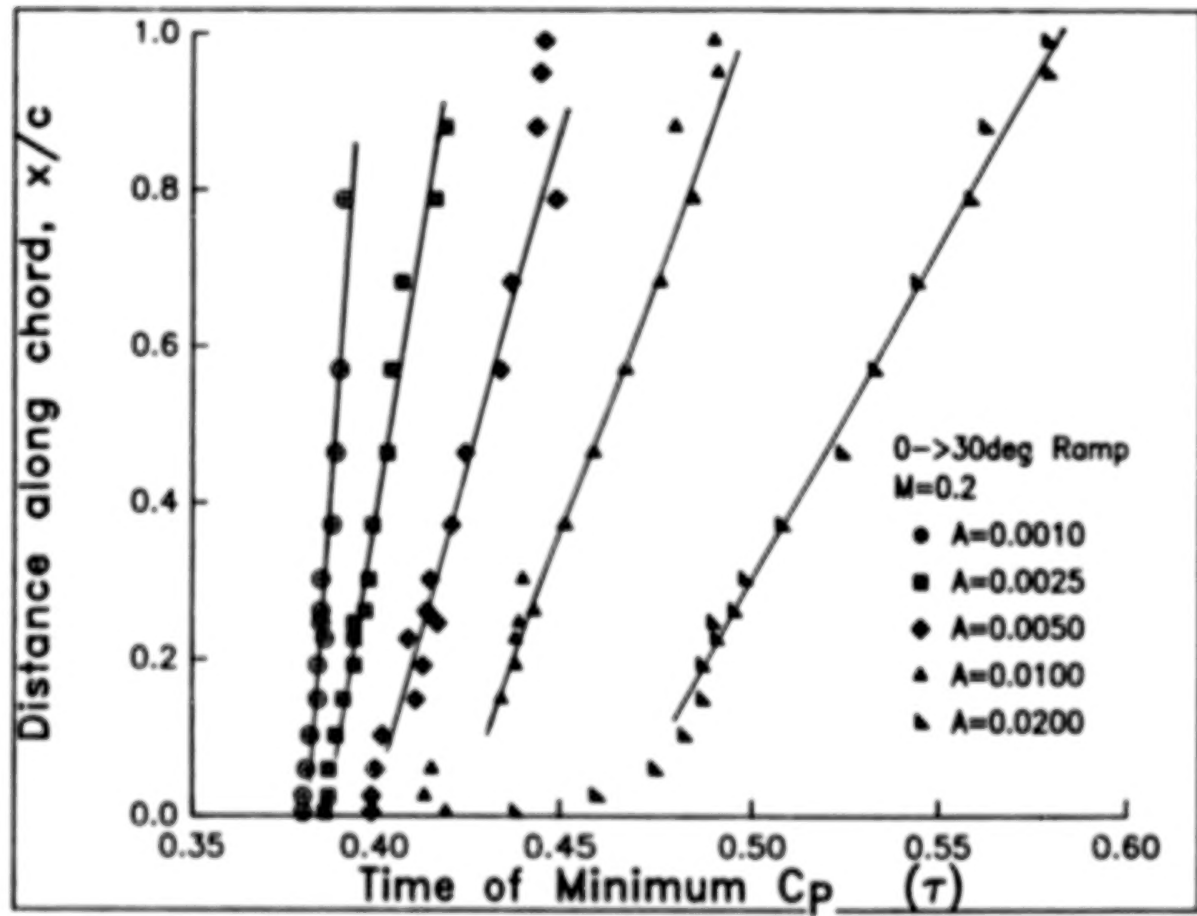
UNSTEADY PRESSURE, UPPER SURFACE, MAX PITCH RATE

At the maximum pitch rate of $A = 0.02$ the upper surface pressure time histories are qualitatively similar to the lower pitch rate results prior to stall, but are significantly different after stall. The unsteady increments to the airloads are strongly influenced by the strength of the stall vortex, which may be estimated by measuring the local change in C_p at some point along the chord downstream of the vortex release point, say at $x/c = 0.302$. This increment increases from $\Delta C_p = 1.0$ at $A = 0.001$ (not shown here) to $\Delta C_p = 1.5$ at $A = 0.005$ and to $\Delta C_p = 2.5$ at $A = 0.020$ (below).



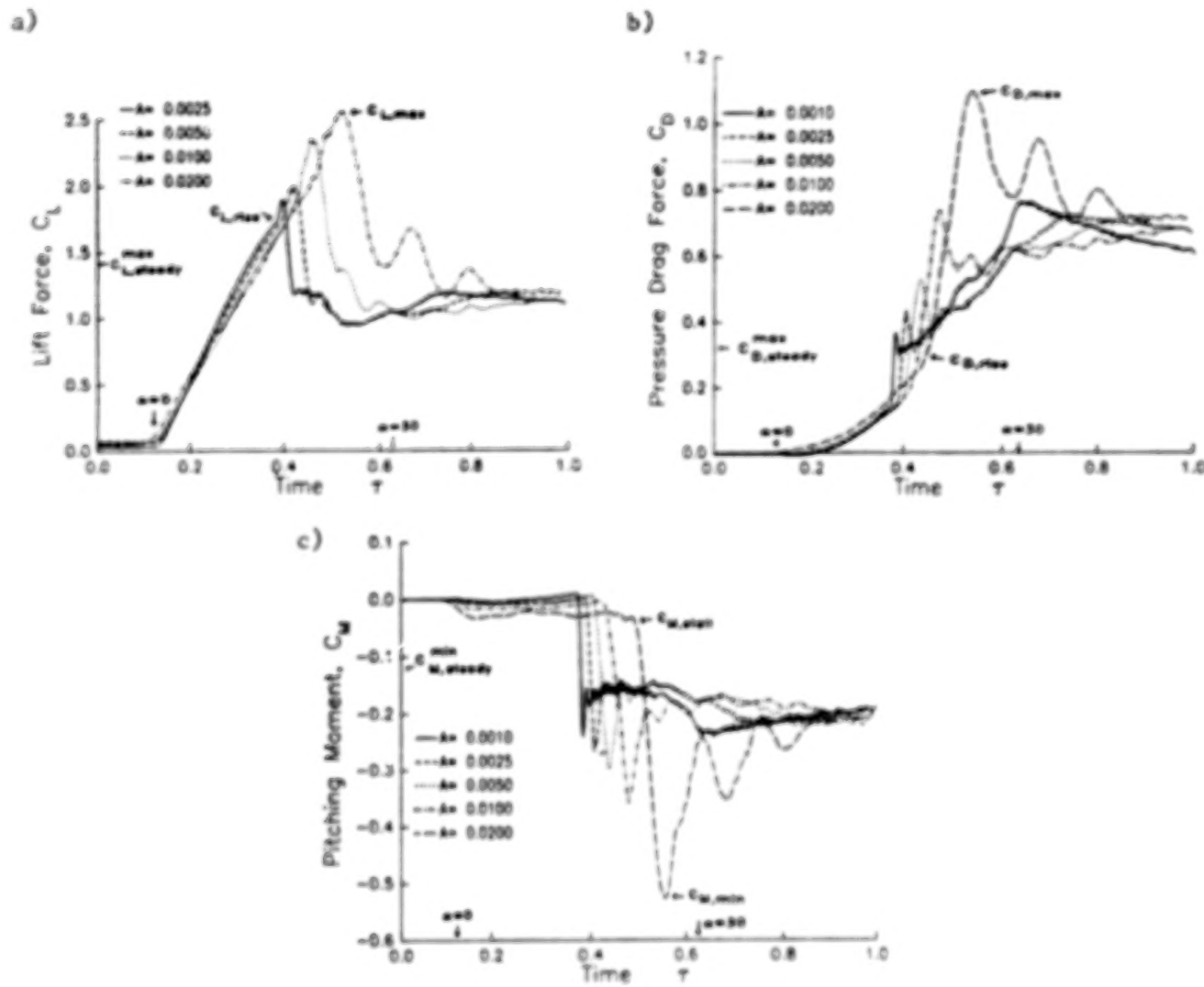
VORTEX PROPAGATION TRACES

The vortex propagation speed along the airfoil may be estimated using the times of minimum pressure at each transducer. These points are plotted below for 5 pitch rates. The region of constant vortex speed generally begins near $x/c = 0.10$ and ends between $x/c = 0.80$ and 0.90 , and the speed in this region increases approximately linearly with pitch rates, from $0.13U$ at $A = 0.001$ to $0.33U$ at $A = 0.020$. These results are consistent with those of previous investigations (Ref. 8 for sinusoidal motions).



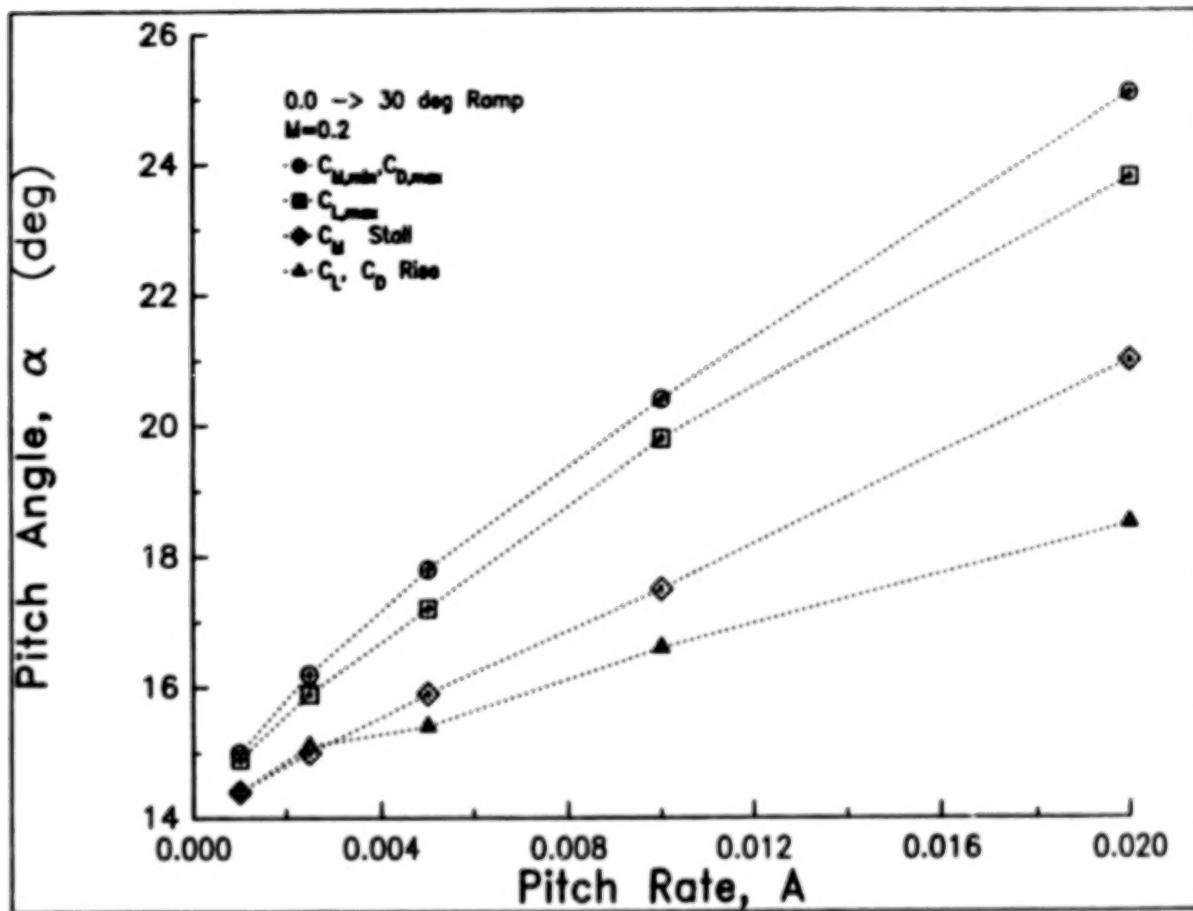
UNSTEADY FORCE AND MOMENT COEFFICIENTS

Integrated lift, pressure drag, and pitching moment (parts a, b, c) exhibit characteristic behavior with increasing pitch rate: (1) Before the stall vortex is formed, increasing pitch rate decreases the lift slope, decreases pitching moment, and increases drag. The lift slope effect agrees with the results of Ref. 2 at lower Reynolds number. (2) There is a rapid buildup of lift as the leading edge vortex forms. The unsteady increment added to the quasi-steady lift increases from $\Delta C_L = 0.4$ at $A = 0.001$ to 1.1 at $A = 0.020$. (3) The pressure drag increases smoothly before stall, rises and falls rapidly as the stall vortex travels over the chord, then increases slowly as the pitching of the airfoil rotates the aerodynamic force vector. (4) The pitching moment in attached flow becomes more negative at higher pitch rate, following the prediction of thin airfoil theory (cf. Eq. 4-171 in Ref. 9). (5) The peak negative C_M after stall increases with pitch rate, from $C_M = 0.22$ at $A = 0.001$ to -0.52 at $A = 0.020$.



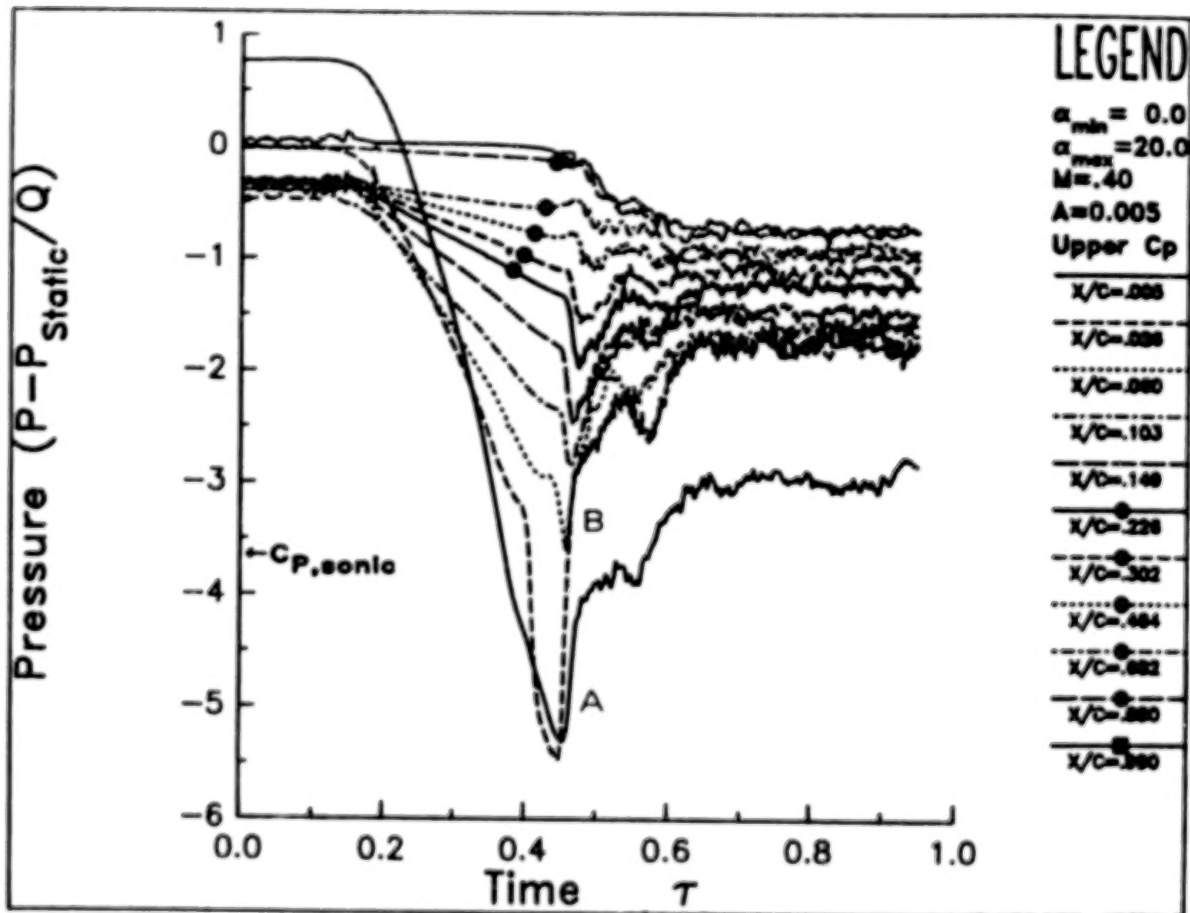
SEQUENCE OF STALL EVENTS

The sequence of stall events is systematic and each appears to be linear with pitch rate. First the stall vortex forms and C_L and C_D start to rise. Moment stall occurs when the vortex is released. Maximum C_L occurs as the vortex travels downstream along the chord, and when the vortex reaches the trailing edge, the minimum C_M and maximum C_D are obtained. At these pitch rates the angle when moment stall occurs increases approximately linearly with A , in agreement with results for a sinusoid at similar peak pitch rates (Ref. 8). This does not agree with the square root correlation postulated by Gormont (Ref. 10).



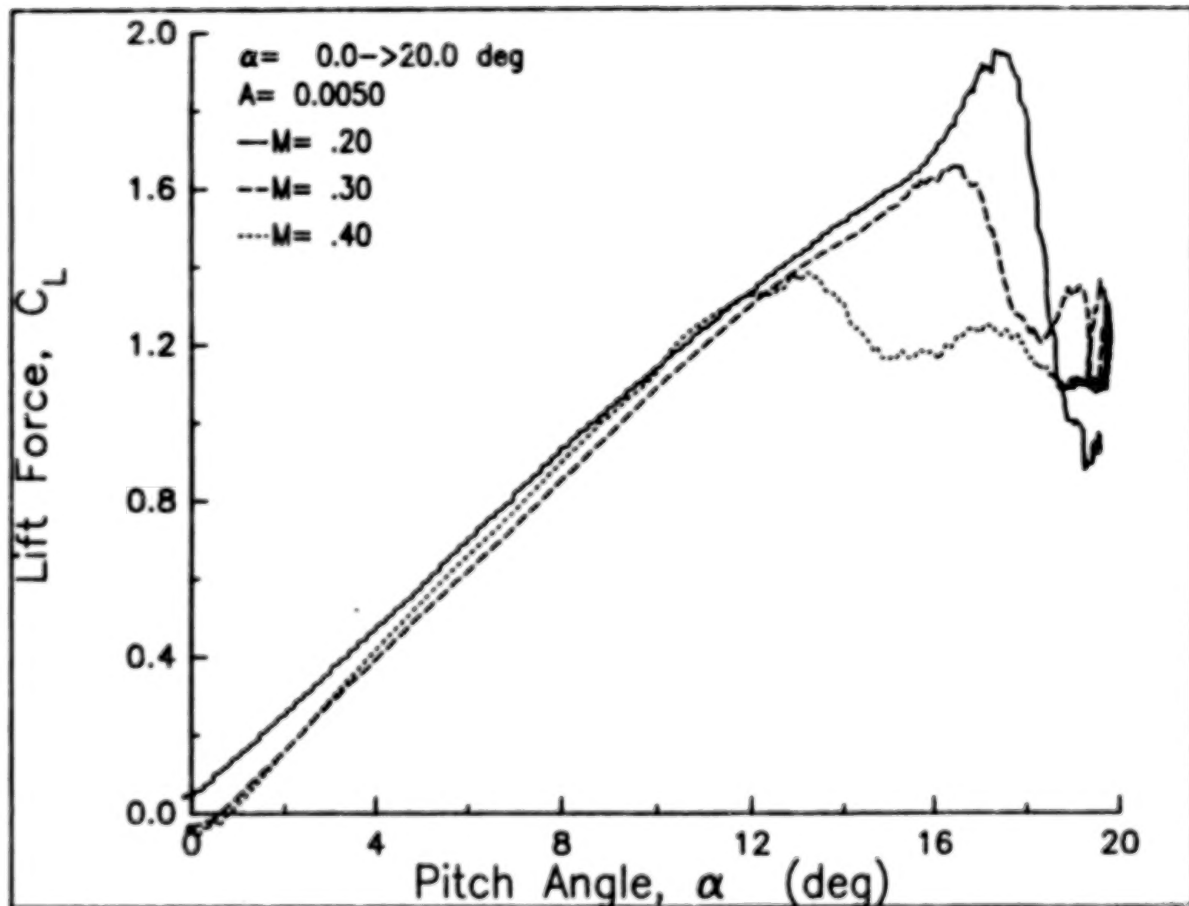
UNSTEADY PRESSURES, UPPER SURFACE, MAX MACH NO.

A supersonic zone at the leading edge has a profound effect on chordwise pressures at freestream Mach number $M = 0.4$. The time histories for this 0 to 20 deg ramp at $A = 0.005$ are not shifted vertically and the ordinate is an absolute measure for all curves. At $x/c = 0.005$ the flow becomes supersonic at $\tau = 0.34$ ($\alpha = 7.6$ deg) and reaches a peak local Mach number of 1.3 at $\tau = 0.45$ ($\alpha = 10.6$ deg). The sharp rise and fall of the pressure at $x/c = 0.026$ (letter A) is caused by the movement of the shock downstream past this station at $\tau = 0.40$ and back upstream at $\tau = 0.46$. A distinct stall vortex is released at $\tau = 0.46$ and $x/c = 0.060$, just downstream of the shock (letter B). Several of the vortex characteristics differ from those at $M = 0.2$: (1) the release point is at $x/c = 0.060$ instead of 0.10; (2) the vortex speed is approximately 10% less than the speed at $M = 0.2$; (3) the strength of the vortex is reduced by approximately 50%; and (4) the pressure signature of the vortex is not observed downstream of $x/c = 0.57$. In addition, no clearly defined oscillations are present after stall at $M = 0.4$. The Reynolds number of the equivalent bluff body is 1.4×10^6 for this case, above the maximum of 1×10^6 for a stable vortex street (Ref. 7).

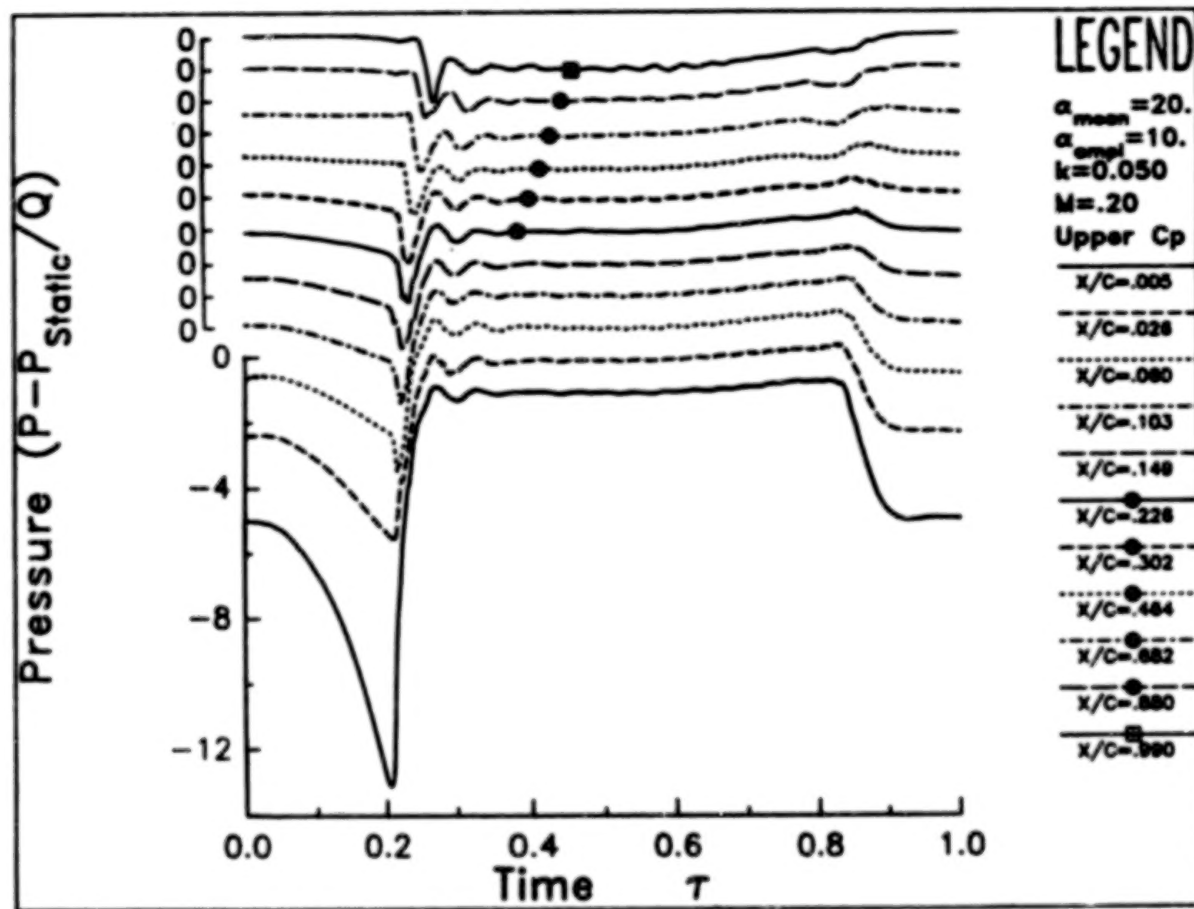


COMPRESSIBILITY EFFECT ON UNSTEADY LIFT

Increasing the Mach number also has a strong effect on the integrated loads. The vortex-induced peak in C_L diminishes markedly as M varies from 0.2 to 0.4, and its position retreats from approximately $\alpha = 16$ deg to 12 deg. This suggests that compressibility prevents the development of the extremely strong suction peak seen at $M = 0.2$, and therefore reduces the strength of the stall vortex.

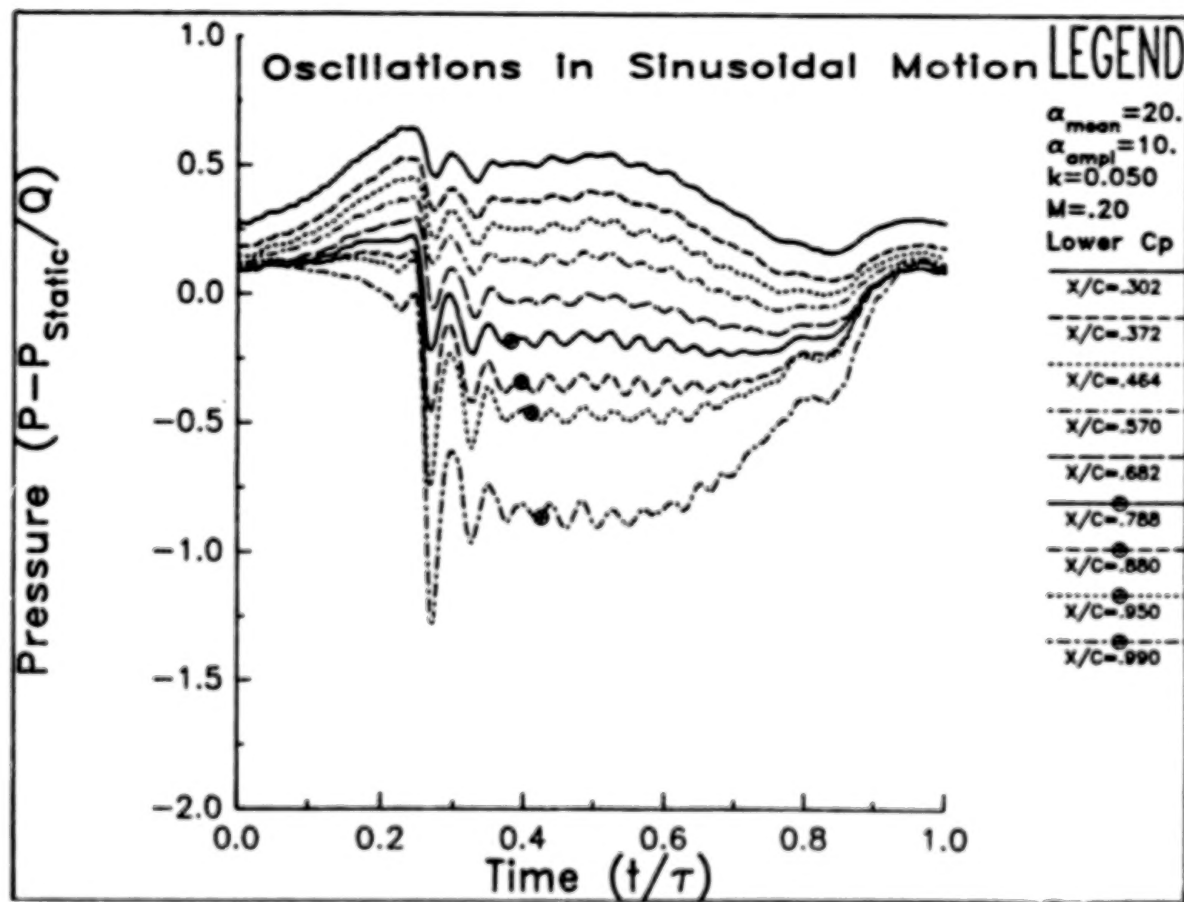


Sinusoidal motion differs from ramp motion in two important aspects: in a sinusoid the airfoil does not start from a steady-state condition, and the pitch rate is constantly changing. Nonetheless, there are many qualitative similarities between the responses to the two motions. For the upper surface time histories shown here ($\alpha = 20 - 10 \cos \omega t$ at $M = 0.2$ and $k = 0.05$) the motion begins at $\tau = 0.0$, reaches maximum pitch angle at $\tau = 0.50$, and returns to the minimum value at $\tau = 1.0$. Each time history here is offset vertically by $\Delta C_p = 1.0$. The characteristics are similar to the constant pitch rate results shown earlier for $A = 0.005$, which is comparable to the instantaneous sinusoidal pitch rate at stall of $A = 0.008$.



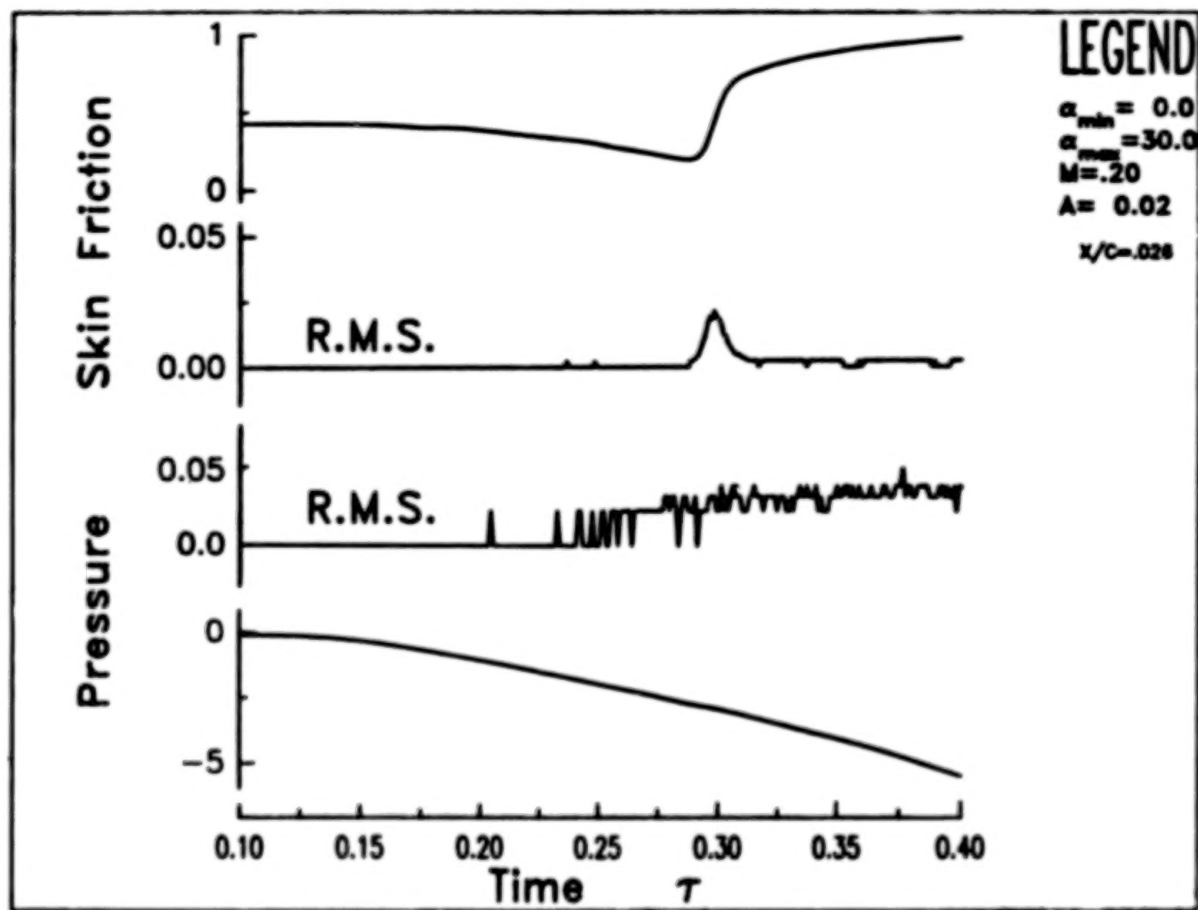
UNSTEADY PRESSURES, LOWER SURFACE, SINUSOID

The lower surface pressures for this same sinusoid are remarkable in that the maximum pressure change occurs at the trailing edge (to match the stalled suction surface pressure level), exhibits an initially damped behavior, and then stabilizes into a coherent vortex street response. The latter is noteworthy because in this ensemble-averaged data set the vortex street frequency must be synchronized with the fundamental frequency of the sinusoid. No single records were taken to permit close examination of the vortex street oscillation.



TRANSITION POINT DETECTION

Accurate determination of the point of boundary-layer transition is critical to many numerical computations. Surface heat transfer gages are usually required to determine the unsteady motion of the transition point. These gages are generally cumbersome to install and each requires a dedicated active anemometer circuit to operate. The techniques developed during the course of this study show that it may be possible to locate the transition point using the local increase in rms pressure measured by the unsteady pressure transducer as the local flow changes its character. An example of the correlation between the hot film and pressure transducer results is shown below. All results are at $x/c = 0.026$ for a 0 to 30 deg ramp at $A = 0.02$ and $M = 0.20$. The vertical pressure scale has been severely foreshortened, and only a small portion of the time scale is displayed. The increase in pressure rms corresponds to the increase in ensemble averaged heat transfer (upper curve) and to the spike in the rms heat transfer (second curve). No change at transition can be discerned in the ensemble-averaged pressure (bottom curve). If these promising early results are confirmed by additional correlations, this method may make it easier to locate transition in complex three-dimensional and unsteady flows.



NOMENCLATURE

A pitch rate, $\dot{\alpha}c/2U$, rad/sec
c airfoil chord, m
 C_D section pressure drag coefficient, D/Qc
 C_L section lift coefficient, L/Qc
 C_M section pitching moment coefficient about $x/c = 0.25$, m/Qc^2
 C_p pressure coefficient, $(P-P_{\text{static}})/Q$
k reduced frequency of sinusoidal motion, $\omega c/2U$
Q freestream dynamic pressure, $0.5 \rho U^2$, Pa
t time from start of data acquisition, sec
T data acquisition period, sec
Re Reynolds number, $c U/\nu$
U freestream velocity, m/sec
x distance from airfoil leading edge, m
 α geometric pitch angle, deg
 ν kinematic viscosity, m^2/sec
 ρ air density, kg/m^3
 τ nondimensional time, t/T
 ω frequency of sinusoidal oscillation, $2\pi f$

CONCLUSIONS

Conclusions - Increased Pitch Rate

- Stall events are delayed
- Stall vortex is strengthened
- Vortex propagation speed increases
- Unsteady airloads increase

Conclusions - $M = 0.3, 0.4$

- Supersonic zone near leading edge
- Stall vortex is weaker
- Unsteady airloads are reduced

Additional Conclusion

- Post stall vortex shedding when $Re_{bluff} < 10^6$
- Shedding synchronized when $A > 0.01$
- Sinusoids and ramps qualitatively similar

Note: This work was supported by the U.S. Air Force Office of Scientific Research under Contract F49620-84-0082 and will be reported in Ref. 11.

REFERENCES

1. Daley, D. C. and Jumper, E. J., "Experimental Investigation of Dynamic Stall for a Pitching Airfoil," *Journal of Aircraft*, Vol. 21, Oct. 1984, pp. 831-832.
2. Jumper, E. J., Schreck, S. J., and Dimmick, R. L., "Lift-Curve Characteristics for an Airfoil Pitching at Constant Rate," *AIAA Paper 86-0117*, Jan. 1986.
3. Walker, J. M., Helin, H. E., and Strickland, J. H., "An Experimental Investigation of an Airfoil Undergoing Large Amplitude Pitching Motions," *AIAA Journal*, Vol. 23, Aug. 1985, pp. 1141-1142.
4. Francis, M. S. and Keesee, J. E., "Airfoil Dynamic Stall Performance with Large Amplitude Motions," *AIAA Journal*, Vol. 23, Nov. 1985, pp. 1653-1659.
5. Strickland, J. H. and Graham, G. M., "Force Coefficients for a NACA 0015 Airfoil Undergoing Constant Pitch Rate Motions," *AIAA Journal*, Vol. 25, April 1987, pp. 622-624.
6. Herbst, W. B., "Supermaneuverability," *Proceedings of the AFOSR-FJSRL-University of Colorado Workshop on Unsteady Separated Flows*, U.S. Air Force Academy, Colorado Springs, Aug. 1983.
7. Schlichting, H., "Boundary Layer Theory," McGraw-Hill, New York, 1979, pp. 31-32.
8. St. Hilaire, A. O. and Carta, F. O., "Analysis of Unswept and Swept Wing Chordwise Pressure Data from an Oscillating NACA 0012 Airfoil Experiment. Volume 1 - Technical Report," *NASA CR-3567*, March 1983.
9. Bisplinghoff, R. L. and Ashley, H., "Principles of Aeroelasticity," John Wiley and Sons, New York, 1962, pp. 120.
10. Gormont, R. E., "A Mathematical Model of Unsteady Aerodynamics and Radial Flow for Applications to Helicopter Rotors," *USAAMRDL Technical Report 72-67*, May 1973.
11. Lorber, P. F. and Carta, F. O., "Unsteady Stall Penetration Experiments at High Reynolds Number," *United Technologies Research Center Report R87-956939-3*, April 1987 (to be released as a technical report by the U.S. Air Force Office of Scientific Research).

EXPERIMENTAL TRANSONIC STEADY STATE AND UNSTEADY
PRESSURE MEASUREMENTS ON A SUPERCRITICAL WING DURING
FLUTTER AND FORCED DISCRETE FREQUENCY OSCILLATIONS

DOUGLAS S. PIETTE

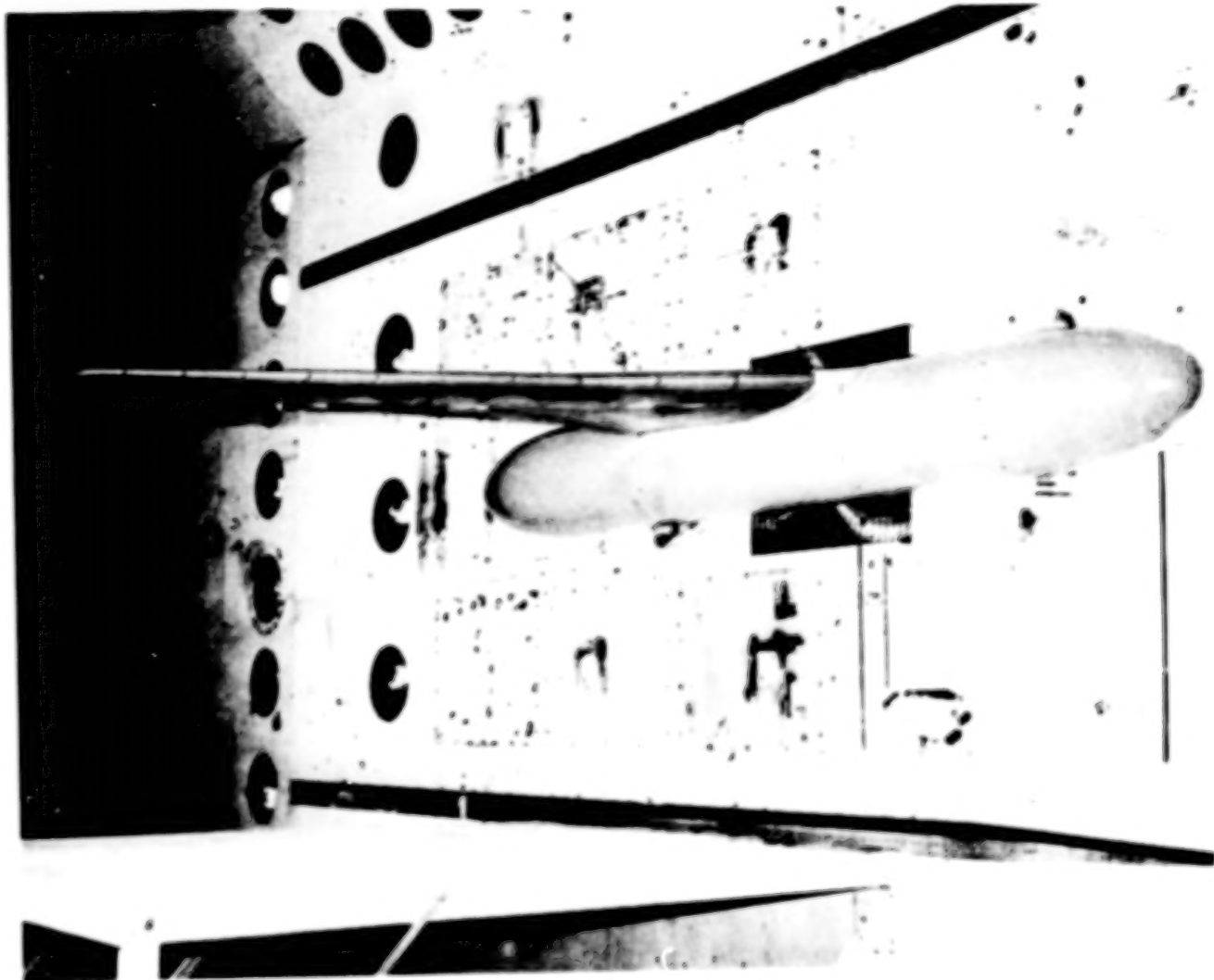
LOCKHEED-GEORGIA COMPANY

FRANK W. CAZIER, JR.

NASA Langley Research Center

PICTURE OF MODEL IN WIND TUNNEL

A joint Langley-Lockheed wind tunnel test was undertaken involving this model. The motivation for this test is explained in the figures to come.



CONVENTIONAL VERSUS SUPERCRITICAL AIRFOILS - GEOMETRIC SHAPE

In 1981 Lockheed conducted a wind tunnel test that compared conventional and supercritical airfoils while holding stiffness, mass, and planform geometric shape constant.

Model Airfoil Profiles for Instrumented Pressure Sections



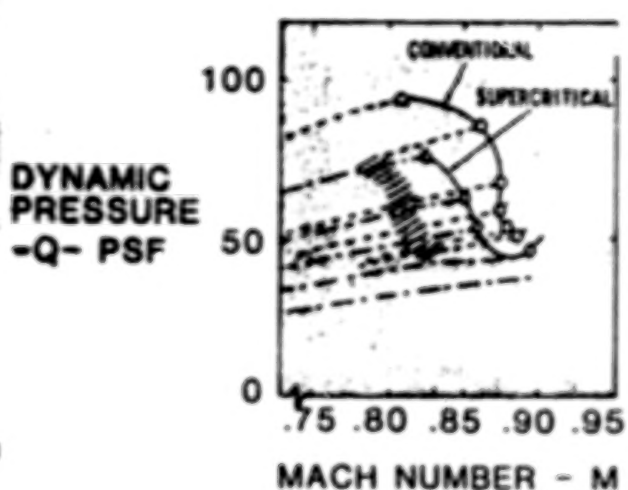
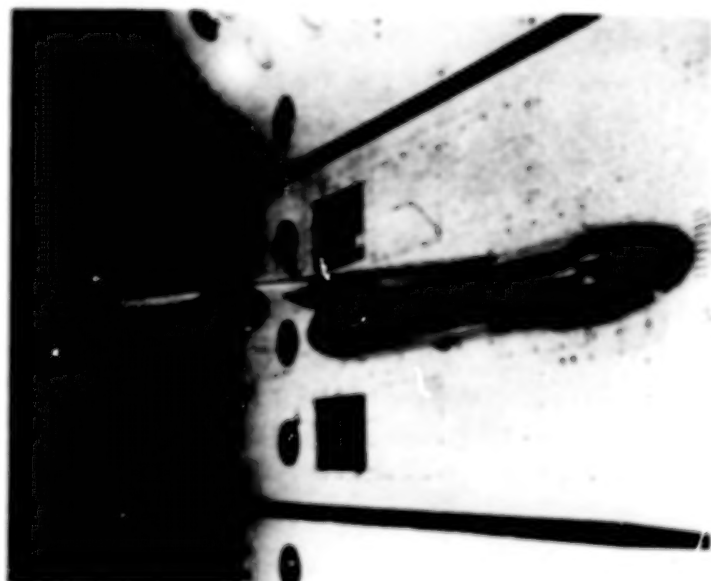
CONVENTIONAL AIRFOIL



SUPERCritical AIRFOIL

CONVENTIONAL VERSUS SUPERCRITICAL AIRFOILS - FLUTTER BOUNDARIES

This test and other tests show that changing from a conventional airfoil shape to a supercritical airfoil shape can greatly reduce the wing's flutter speed. The test also showed that there was a region of low damping within the flight envelope of this wing with supercritical airfoils. This low damping region is shaded in the figure.



PROBLEM

The aerodynamic programs used in flutter analyses do not accurately predict the complex flow around supercritical airfoils in the transonic flow region. This causes the use of long costly wind tunnel tests and empirical weighting factors to modify the analytically predicted flutter speeds. The result can be a stiffer, heavier wing than is needed.

Unsteady transonic aerodynamic programs using Computational Fluid Dynamics (CFD) methods show promise of more accurately predicting transonic flow, but these programs need to be validated before they can be incorporated into a production flutter method.

To validate the programs, analytical predictions must be correlated with steady and unsteady experimental flow data on a flexible, three-dimensional wing. Most of the data available for correlation is from tests on two-dimensional or three-dimensional rigid wings.

In April 1984, Lockheed-Georgia and NASA-Langley conducted a wind tunnel test to obtain all of the types of data needed for CFD program correlation. This included steady state data, forced oscillation data, and oscillatory data during flutter.

- * New Technologies
Have Lower Flutter Speeds
- * Present Analytical Methods
Are Not Accurate
- * Computational Fluid Dynamics (CFD)
- * Verify CFD Programs
- * Lack of Test Data for Correlations

TEST OBJECTIVES

There were three main objectives for this test.

- a) obtain aerodynamic data during flutter for CFD program correlation
- b) obtain a better understanding of supercritical wing flutter
- c) evaluate the effects that pylons and engines have on wing unsteady aerodynamics

- OBTAIN CONGRUENT FLUTTER AND AERO DATA FOR ANALYSIS CORRELATION
- OBTAIN BETTER UNDERSTANDING OF SUPERCRITICAL WING FLUTTER
- EVALUATE EFFECTS OF PYLONS AND ENGINES ON WING AERO DATA

MODEL CONFIGURATIONS

Four different model configurations were tested.

- a) stiffer spar, bare wing
- b) nominal stiffness spar, bare wing
- c) nominal stiffness spar with mass simulated engines
- d) nominal stiffness spar with aerodynamic simulated engines

The first configuration was used only for obtaining forced response oscillatory data. The other three configurations were used for obtaining both forced response oscillatory data and oscillatory data during flutter.

STIFFER WING (FOUR TIMES NOMINAL STIFFNESS)

- BARE WING

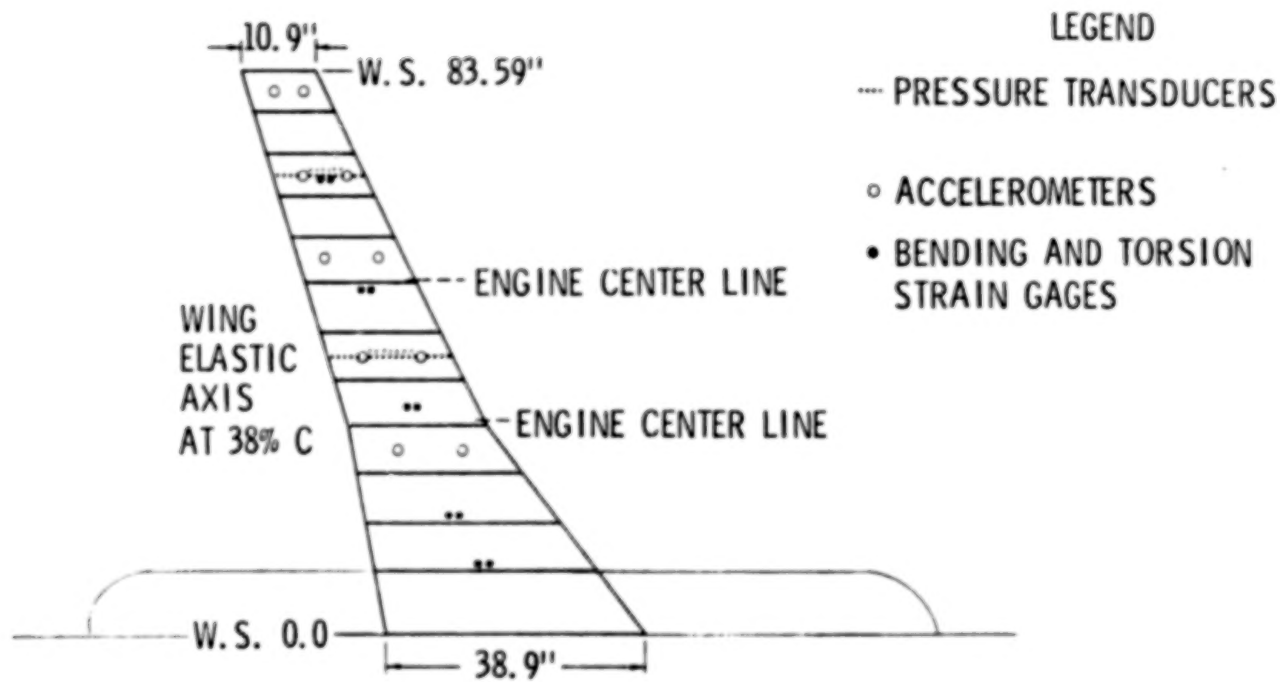
NOMINAL STIFFNESS WING

- BARE WING
- WING PLUS DUMMY NACELLES AND PYLONS
- WING PLUS DUCTED NACELLES AND PYLONS

WING PLANFORM AND INSTRUMENTATION LAYOUT

The wing had an aspect ratio of 7.84. It was constructed on a single aluminum spar with a supercritical airfoil. It had eleven mass ballasted sections. Five bending and torsion strain gage bridges and five pairs of accelerometers were distributed along the wing's span to define the steady and unsteady position of the wing. Instrumentation sections were located at 49.6% and 82.1% span. Each instrumentation section contained 17 delta pressure transducers and 7 upper surface pressure transducers from the leading to the trailing edge.

Aeroelastic Model Wing Planform and Instrumentation Layout



PICTURE OF INSTRUMENTATION SECTION

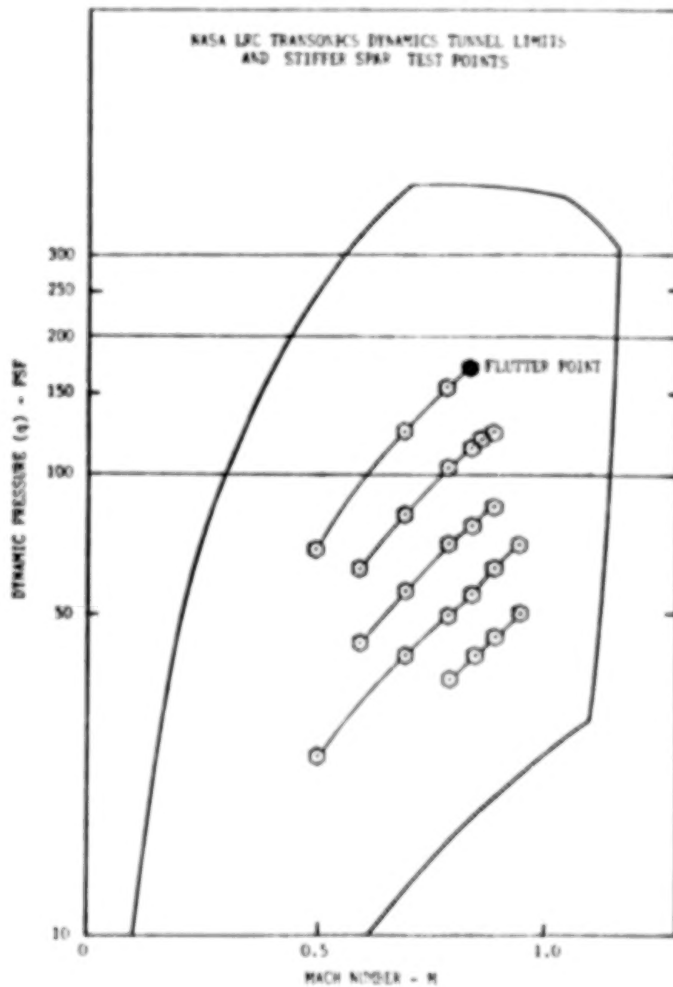
This picture shows an opened up instrumentation section. The holes for the pressure transducers are visible on the wing's surface. Wires from the pressure transducers and the wing's spar are visible inside the model.



STIFFER SPAR TEST POINTS

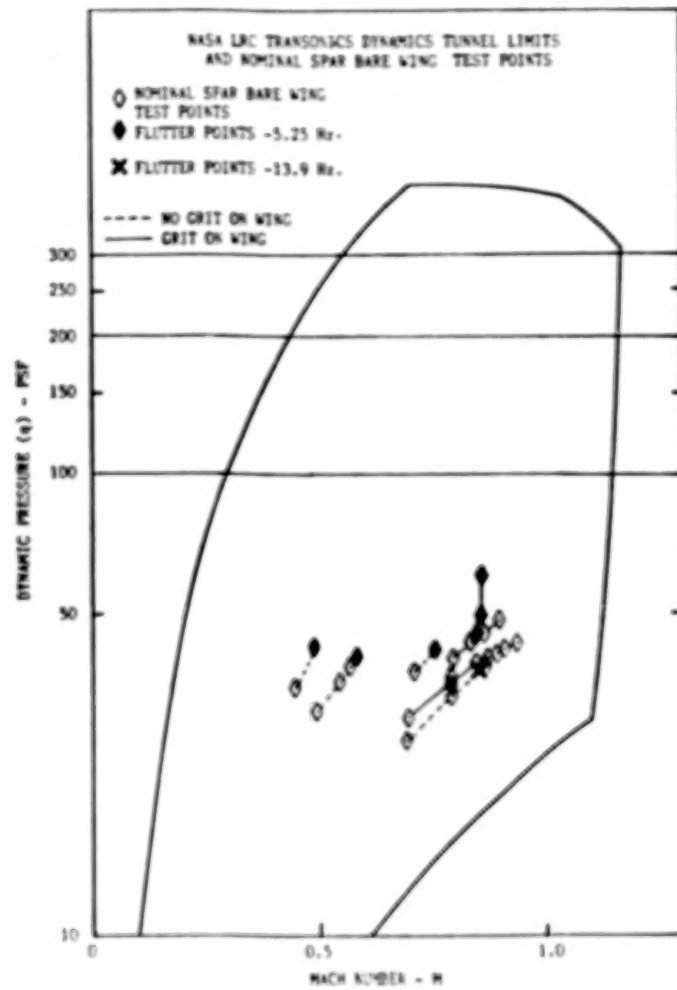
Test points are shown for the stiffer spar, bare wing configuration. The testing procedure is described below.

1. After tunnel was warmed and wind off zero readings were taken, the tunnel speed and density were increased to the desired values.
2. The model was positioned at the desired angle of attack and steady state data was obtained.
3. The wing was oscillated in pitch at 2, 4, 8, and 16 Hertz and unsteady measurements were obtained.
4. The model was positioned at two more steady state angles of attack and oscillated at 2, 4, 8, and 16 Hertz. Steady and unsteady data were measured for each of these conditions.
5. Tunnel speed was increased for testing at other Mach numbers for the same tunnel density.
6. Upon reaching Mach 0.95 or flutter, the tunnel speed was decreased and Freon was pumped in to increase tunnel density to the next desired value.
7. Testing resumed along another constant density line.



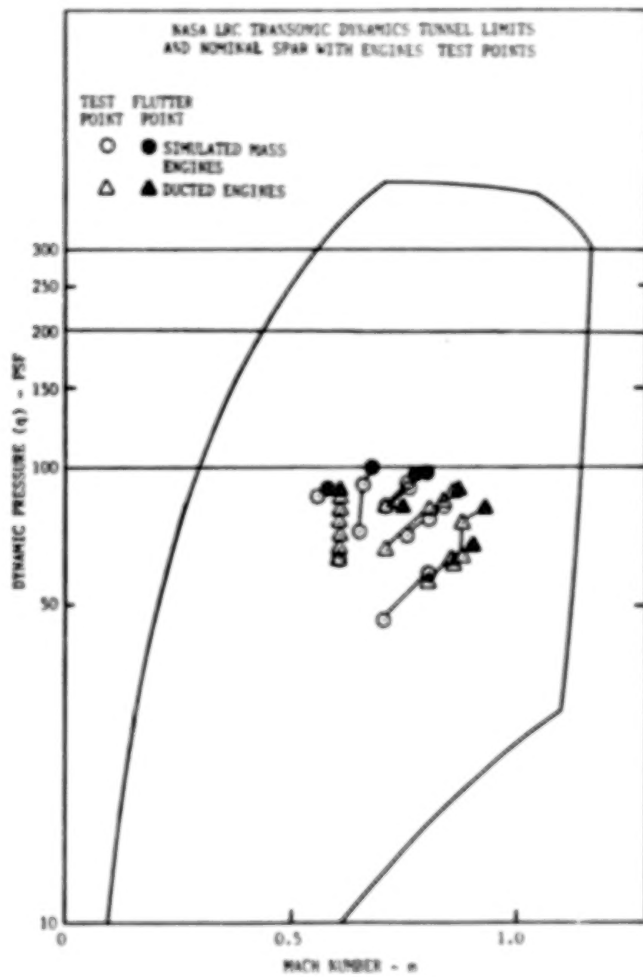
NOMINAL SPAR BARE WING TEST POINTS

Test points are shown for the nominal stiffness spar, bare wing configuration. The flutter boundary for this configuration is also shown. The test procedure was identical to that for the stiff spar, bare wing configuration except forced oscillatory data were measured at fewer than three angles of attack for most test points.



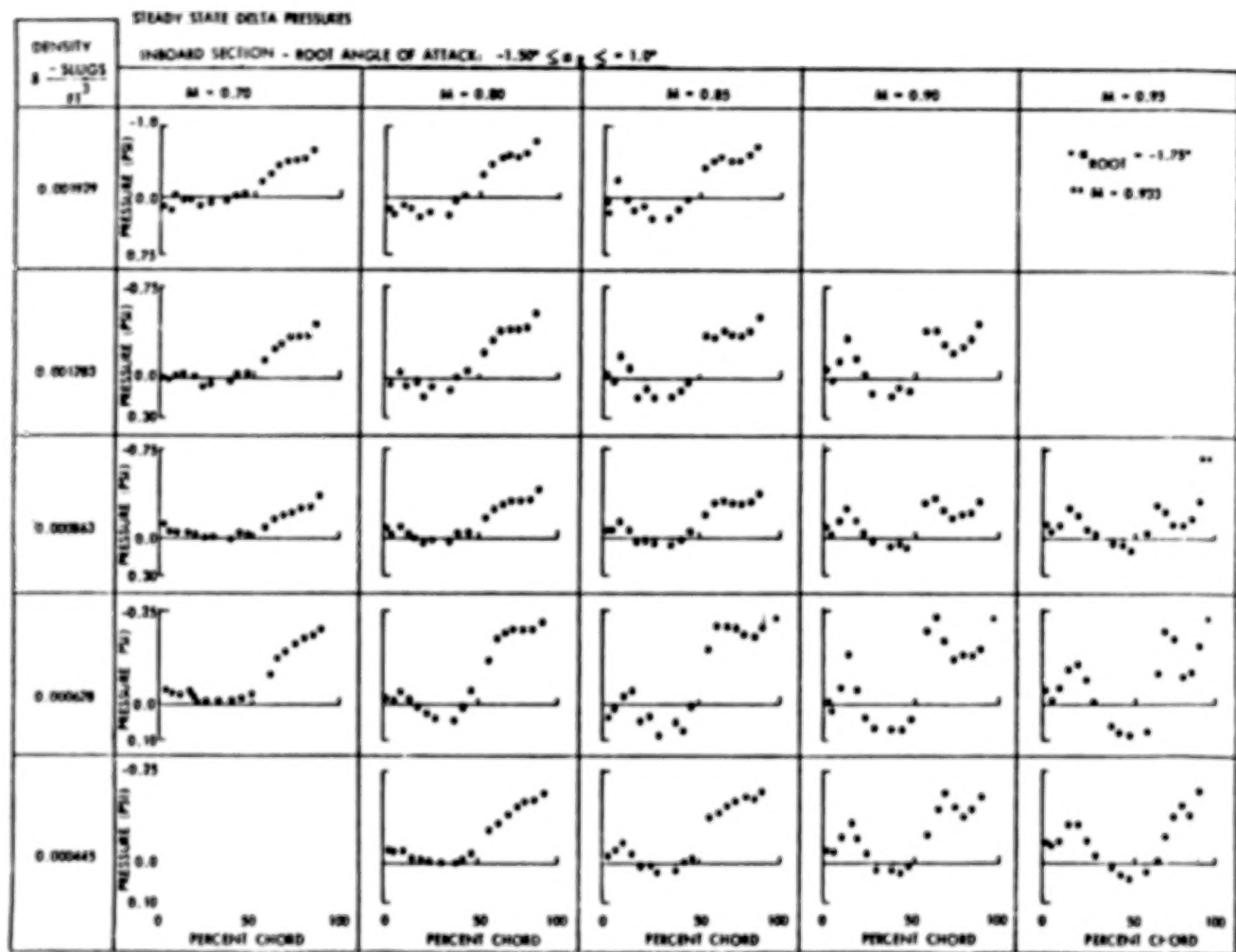
NOMINAL SPAR WITH ENGINES TEST POINTS

Test points are shown for the nominal stiffness spar, with engines configuration. The flutter boundary for this configuration is also shown. The test procedure was identical to that for the nominal stiffness spar, bare wing configuration.



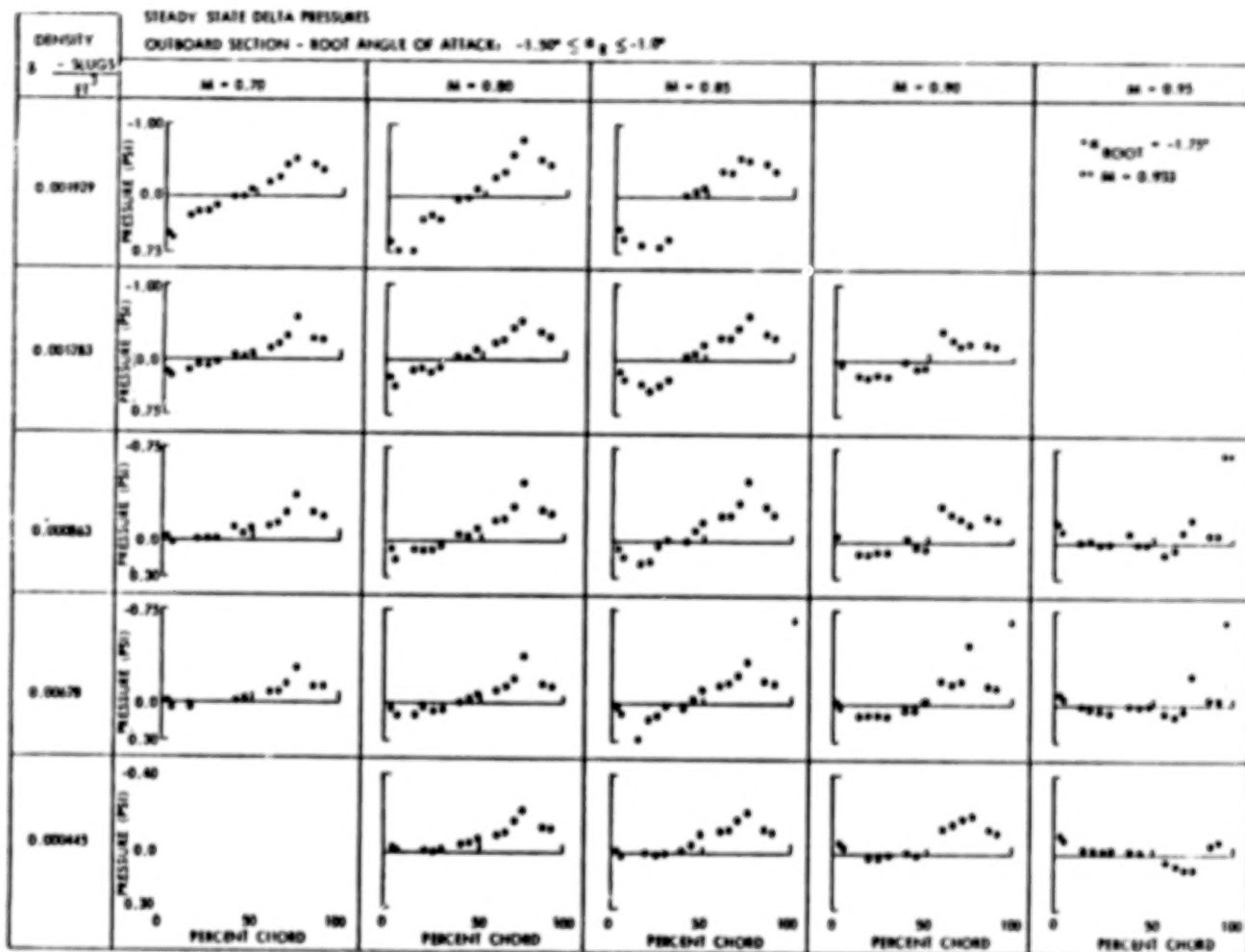
STEADY STATE DELTA PRESSURES - INBOARD SECTION

This is a composite plot showing how the chordwise delta pressure distribution changes with Mach number and tunnel density.



STEADY STATE DELTA PRESSURES - OUTBOARD SECTION

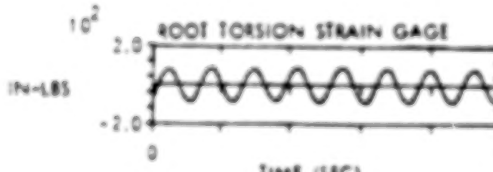
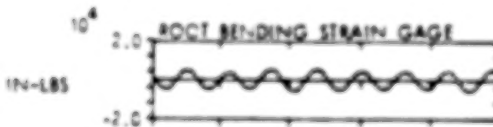
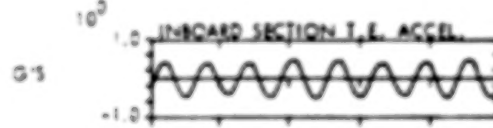
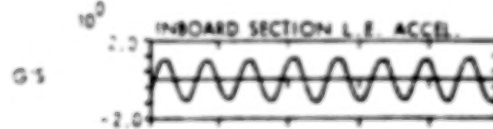
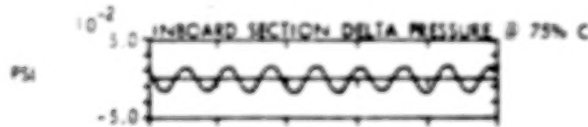
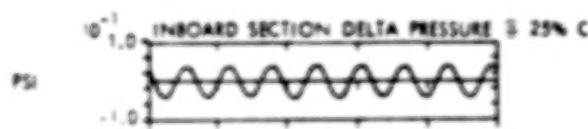
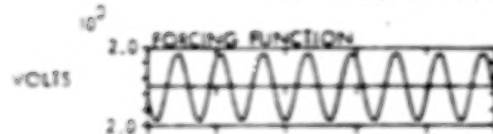
This is a composite plot showing how the chordwise delta pressure distribution changes with Mach number and tunnel density. The differences in chordwise delta pressure distributions between the inboard and outboard sections is due to the difference in local angle of attack caused by the jig twist and the flexibility of the wing.



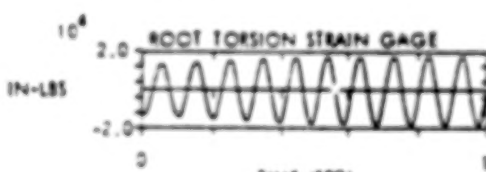
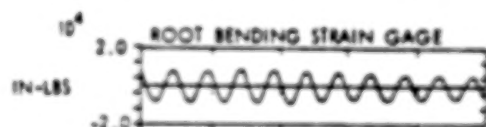
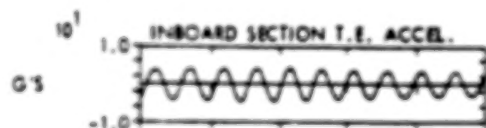
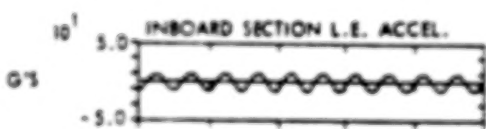
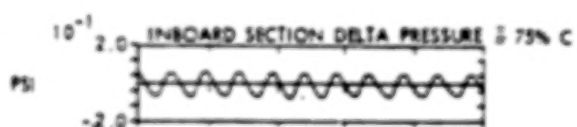
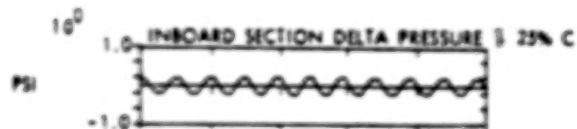
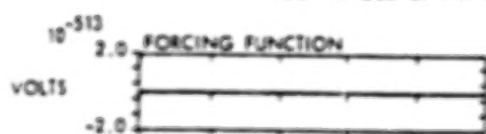
TIME HISTORY PLOTS

This figure shows time history traces for a sample of data channels for both a forced oscillation case and for oscillations during flutter.

FORCED OSCILLATIONS
STIFFER SPAR - BARE WING
MACH = 0.70
DENSITY = 0.00134 SLUGS/FT³
FREQUENCY = 8.0 Hz
ROOT ANGLE OF ATTACK = -1.5°

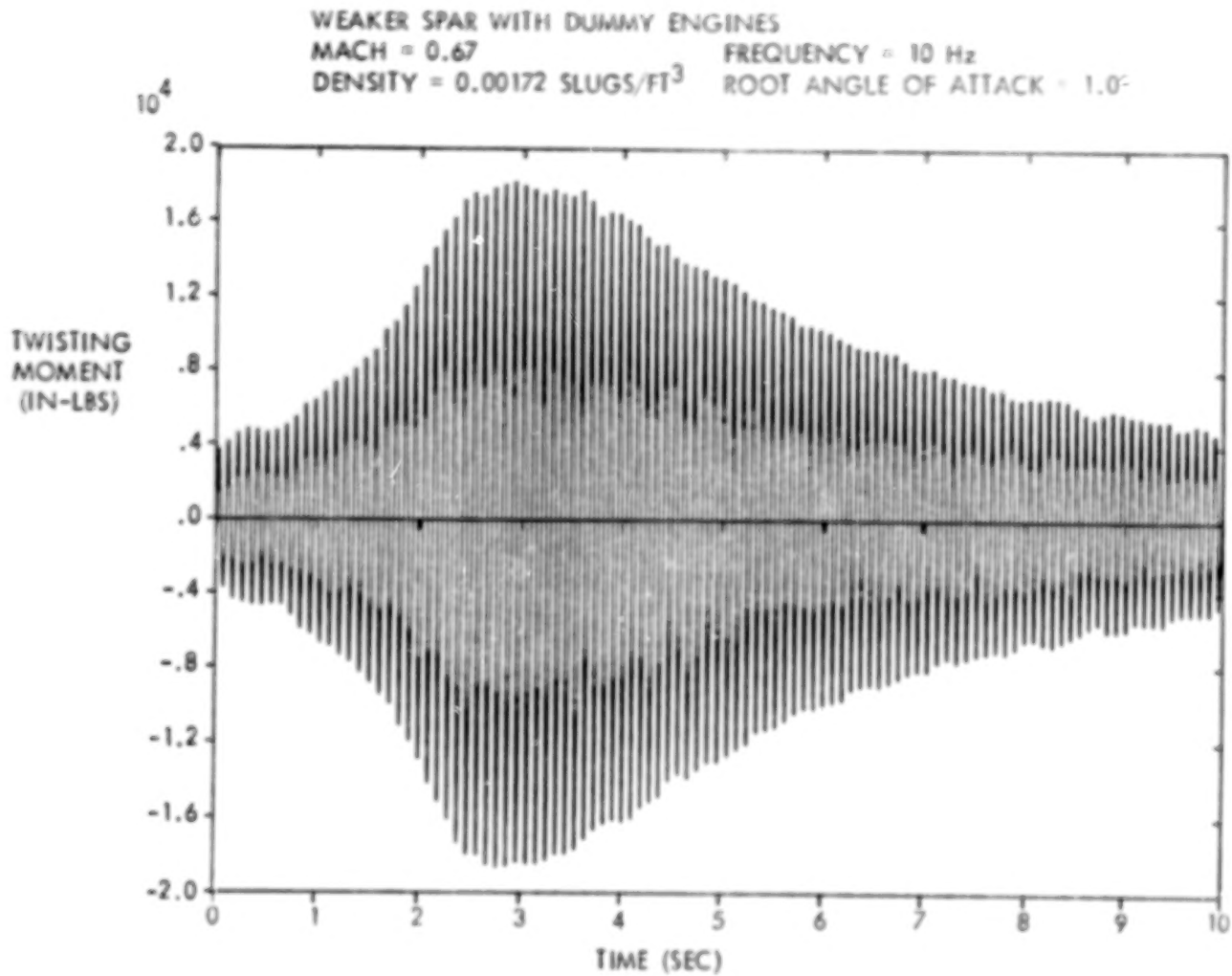


OSCILLATIONS DURING FLUTTER
WEAKER SPAR WITH DUMMY ENGINES
MACH = 0.67
DENSITY = 0.00172 SLUGS/FT³
FREQUENCY = 10 Hz
ROOT ANGLE OF ATTACK = -1.0°



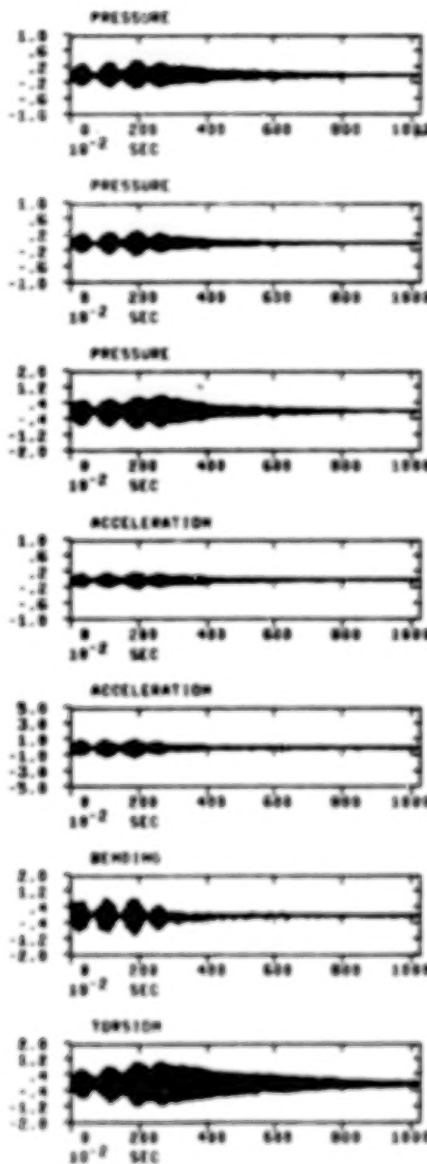
ROOT TORSION STRAIN GAGE - TIME HISTORY DURING FLUTTER

This figure shows a time history plot of the root torsion strain gage during a flutter case. During the first $2\frac{1}{2}$ seconds of this plot the model's deflection is increasing from flutter onset. After $2\frac{1}{2}$ seconds, the tunnel velocity was decreased by about 10% to keep the model from breaking up. The rest of the plot shows the model's response gradually decreasing at the lower tunnel speed.



TIME HISTORIES - BEATING FLUTTER

Aerodynamic data was also measured while the model was beating in and out of flutter. This figure shows a sample of data channels during this beating phenomenon.



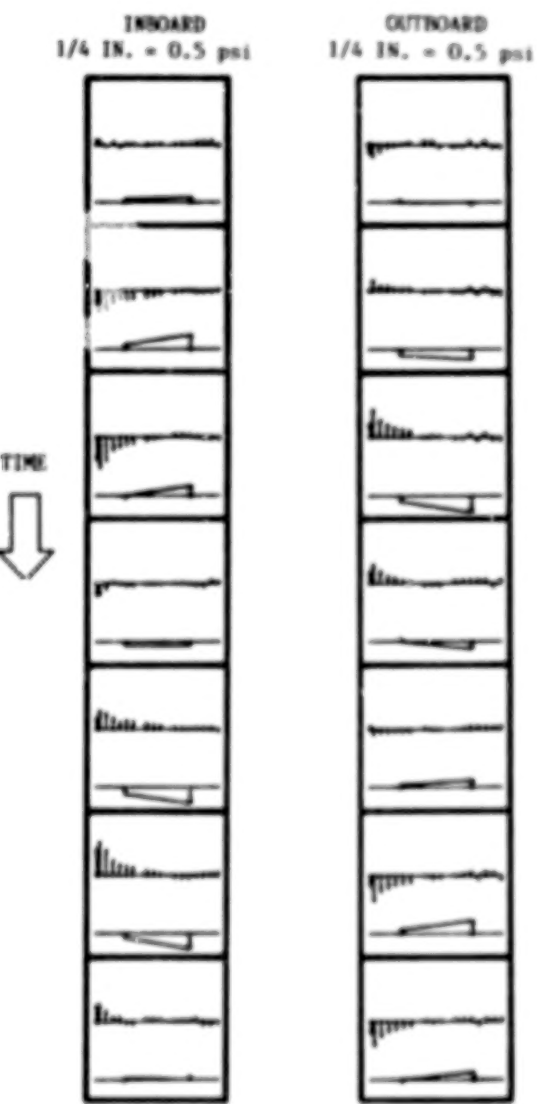
Time Histories; Nominal Spar Self-Sustained
Oscillations 10.4 Hz. ; $M = 0.79$; $q = 97.3$ psf

TIME HISTORY CHORDWISE DELTA PRESSURE OSCILLATIONS DURING FLUTTER

Moving from the top of this figure to the bottom, one cycle of forced response data is shown for both the inboard and the outboard sections. Nine instantaneous "snapshots" are shown to depict how the chordwise delta pressure and airfoil position change with time. In each "snapshot" the top line is a bargraph of the delta pressure measurements (the leading edge is to the left and the trailing edge is to the right). The lower line in each "snapshot" depicts the unsteady airfoil position.

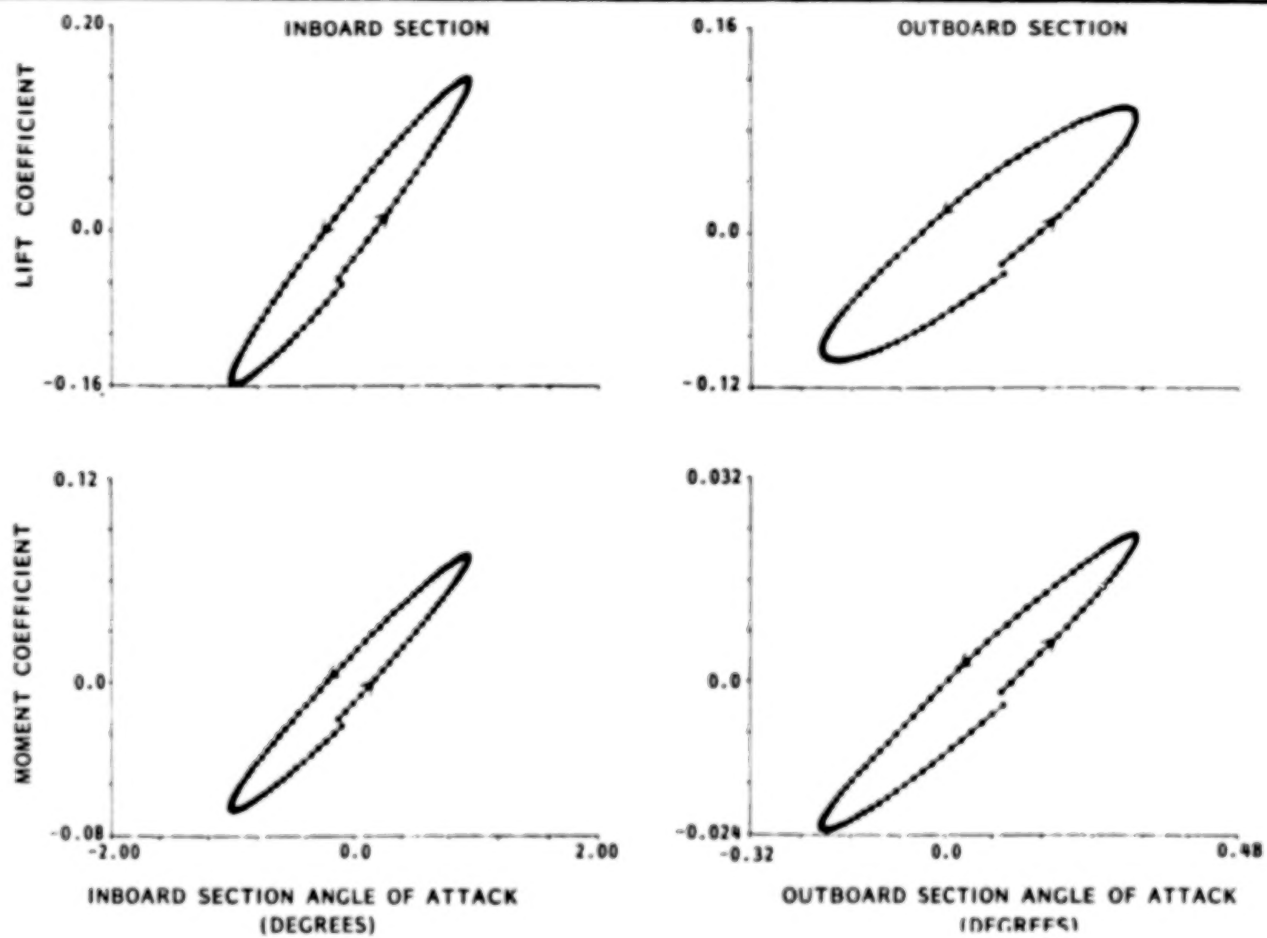
FREQUENCY = 10 Hz DENSITY = 0.00172 SLUGS/FT.³

ROOT ANGLE OF ATTACK = +1.0° MACH = 0.67



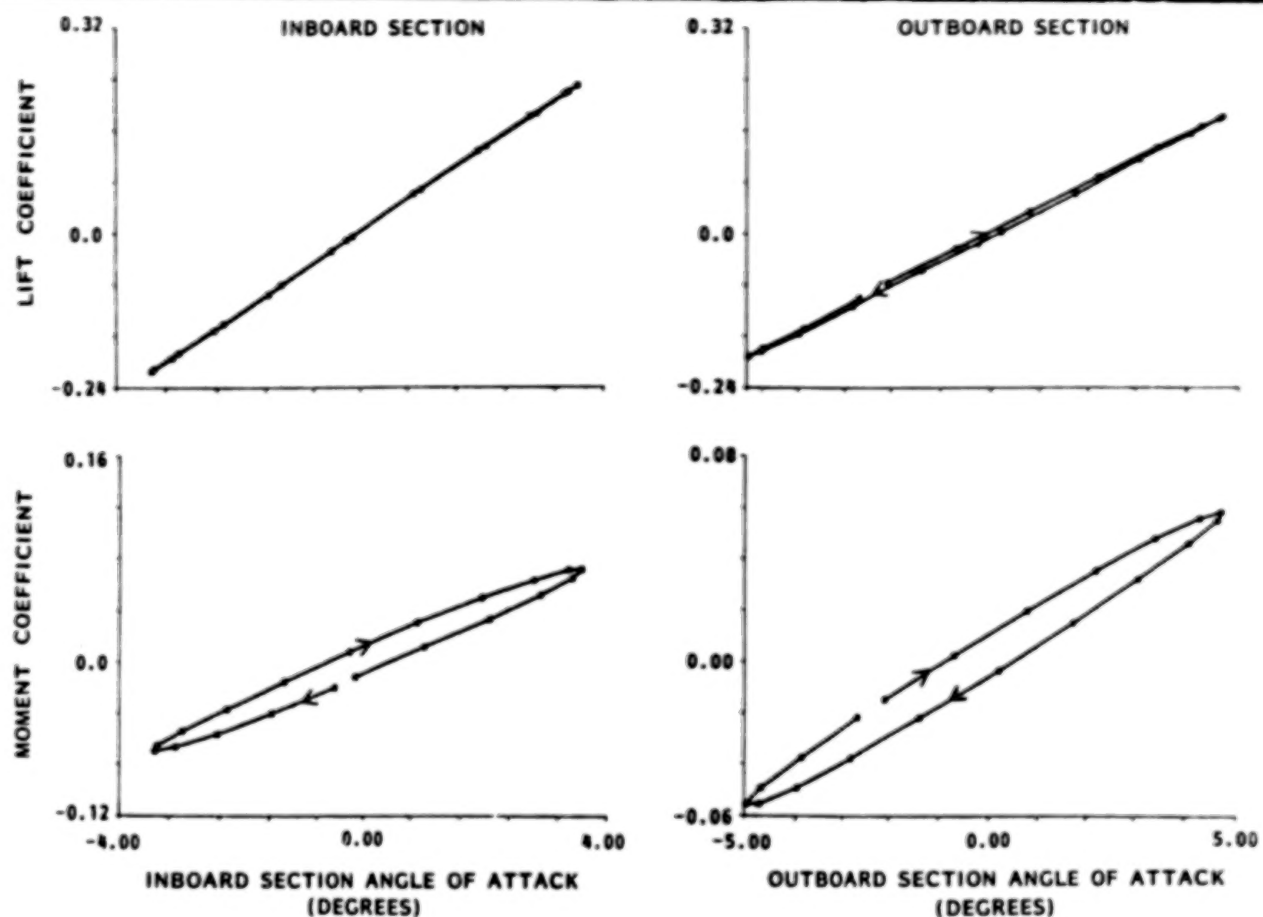
REPRESENTATIVE FORCED RESPONSE AERODYNAMIC COEFFICIENTS

From the instantaneous chordwise delta pressure distribution, the lift and the lift and moment coefficients were calculated. These "instantaneous" coefficients were plotted in this figure versus the section's "instantaneous" angle of attack. For the forced response case, the hysteresis moves in a counter-clockwise rotation indicating that energy is being put into the airstream by the airfoil.



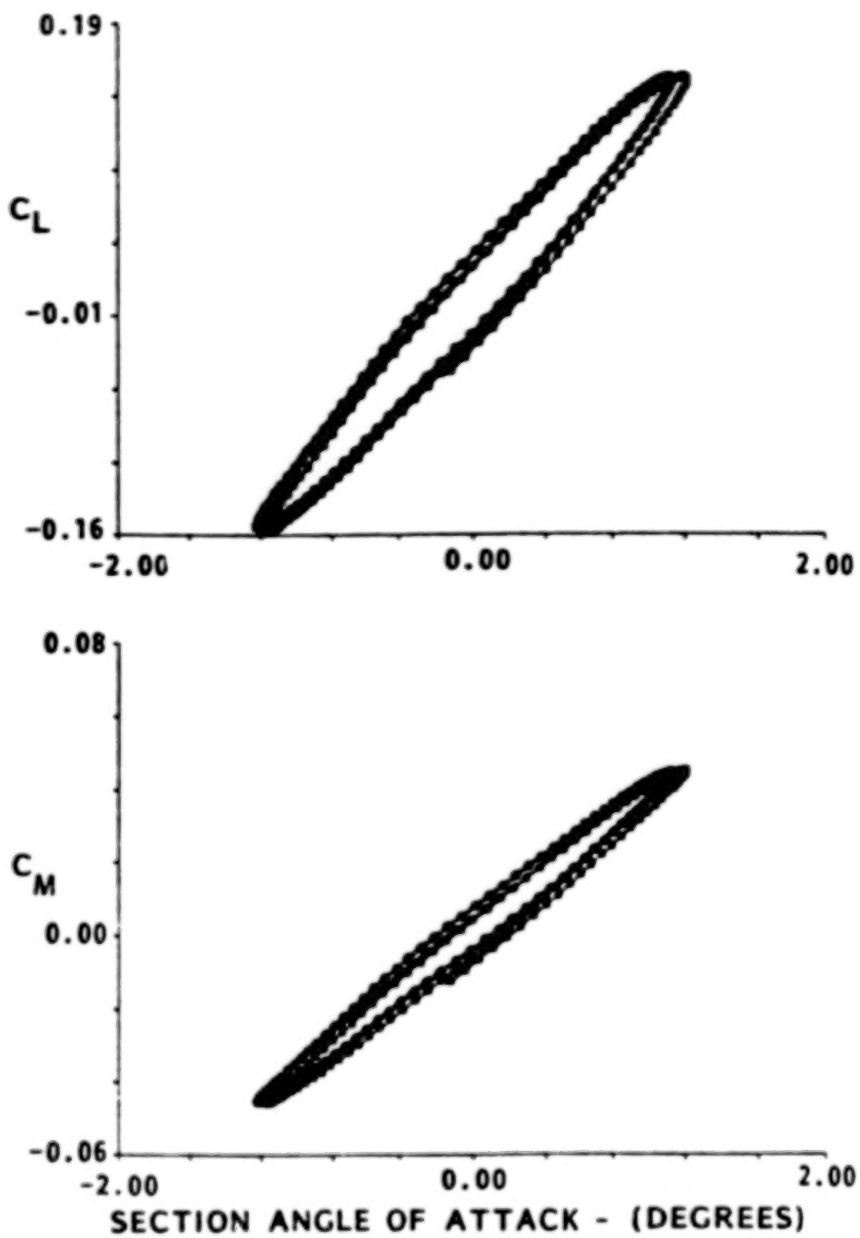
REPRESENTATIVE AERODYNAMIC COEFFICIENTS DURING FLUTTER

This is the same type of data from oscillations during flutter. Note that the hysteresis is moving in a clockwise rotation indicating that energy is being extracted from the airstream by the airfoil.



REPRESENTATIVE MULTICYCLE AERODYNAMIC DATA

Three cycles of data have been plotted to show the repeatability of the data. The case shown is during forced oscillations. During a divergent flutter case, the model's amplitude is building so the plotted data would also increase in magnitude.

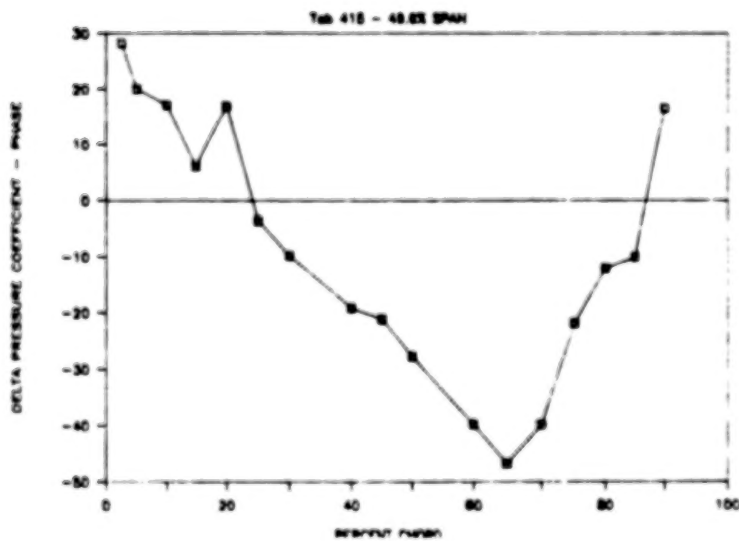
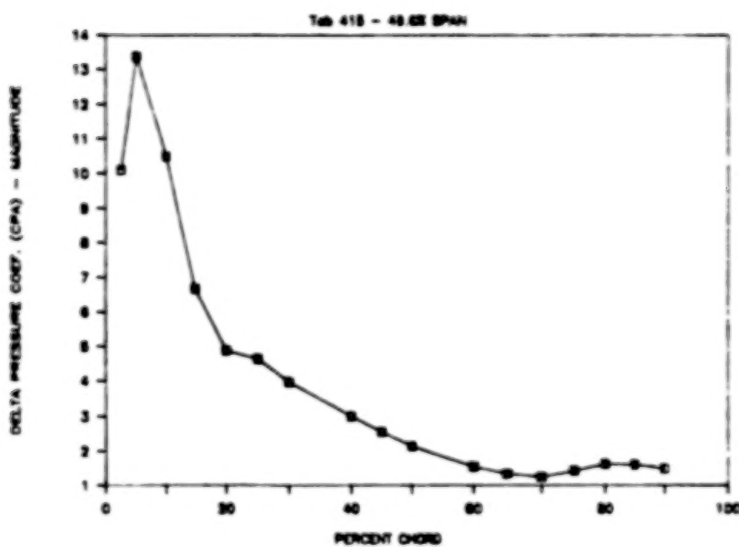


CHORDWISE DELTA PRESSURE COEFFICIENTS - 49.6% SPAN

Unsteady chordwise delta pressures are presented in magnitude/phase plots for representative measurements during flutter.

$$C_{dp} = dp_{max} / (Q * \alpha_{max})$$

Mach = 0.670 Q = 99.000
 Root Alpha = 1.000 Inboard Section Alpha = 4.809

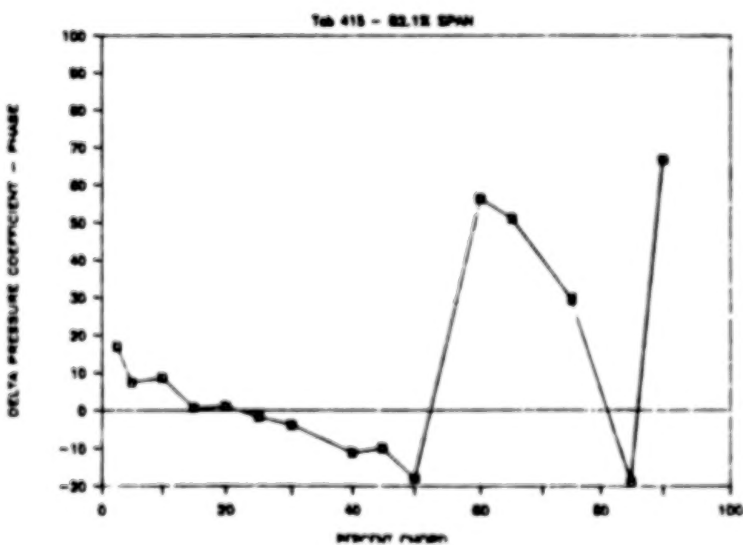
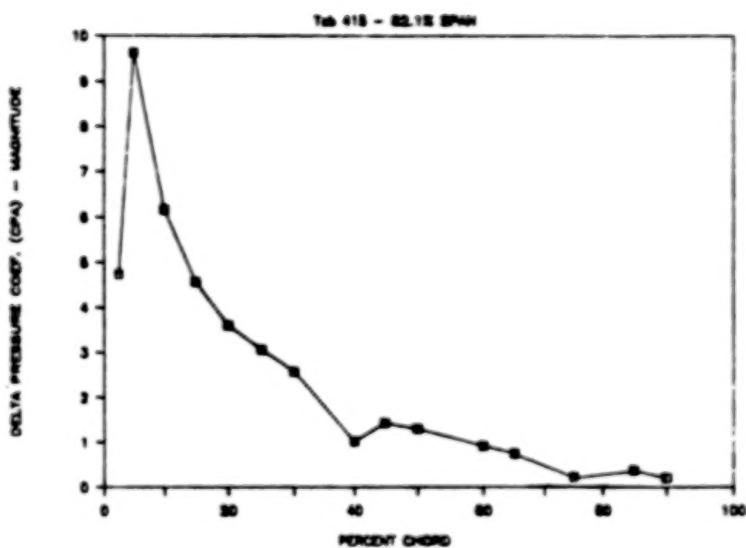


CHORDWISE DELTA PRESSURE COEFFICIENTS - 82.1% SPAN

Unsteady chordwise delta pressures are presented in magnitude/phase plots for representative measurements during flutter.

$$C_{dp} = dp_{max} / (Q * \alpha_{max})$$

Mach = 0.670 Q = 99.000
 Root Alpha = 1.000 Outboard Section Alpha = 1.145

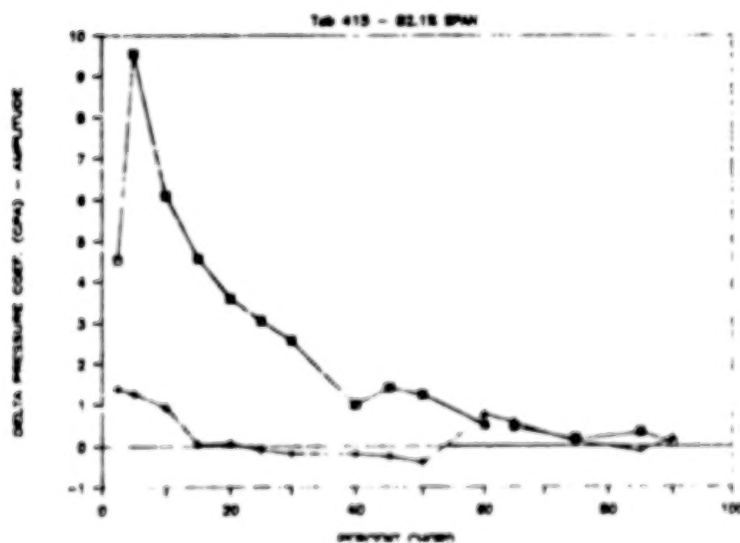
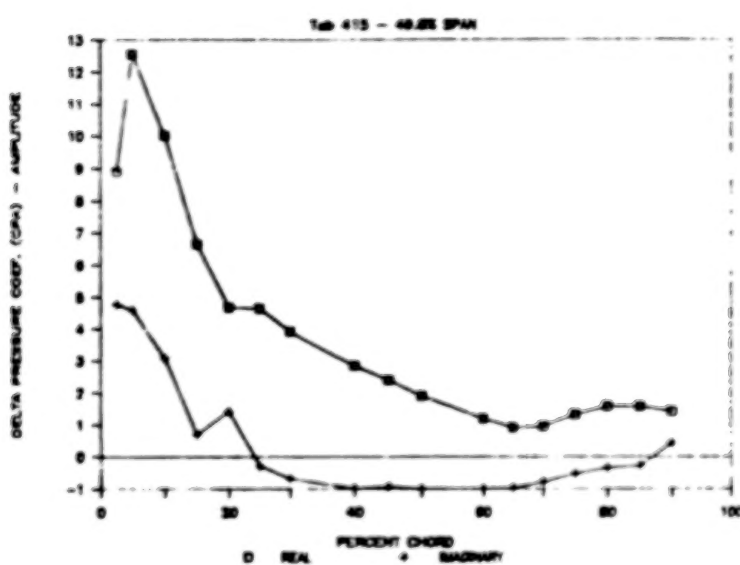


CHORDWISE DELTA PRESSURE COEFFICIENTS

Unsteady chordwise delta pressures are presented in real/imaginary plots for representative measurements during flutter.

$$C_{dp} = dp_{max} / (Q^* \alpha_{max})$$

Mach = 0.670 Q = 99.000
Root Alpha = 1.000 Inboard Section Alpha = 4.809
Outboard Section Alpha = 6.657



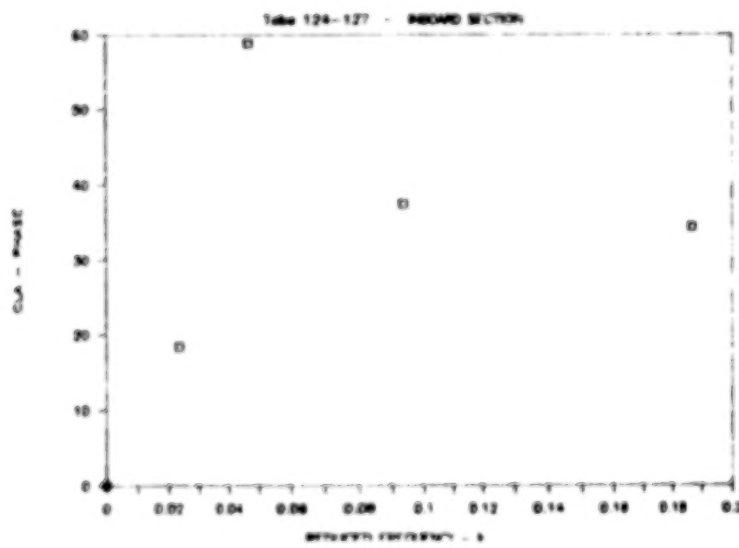
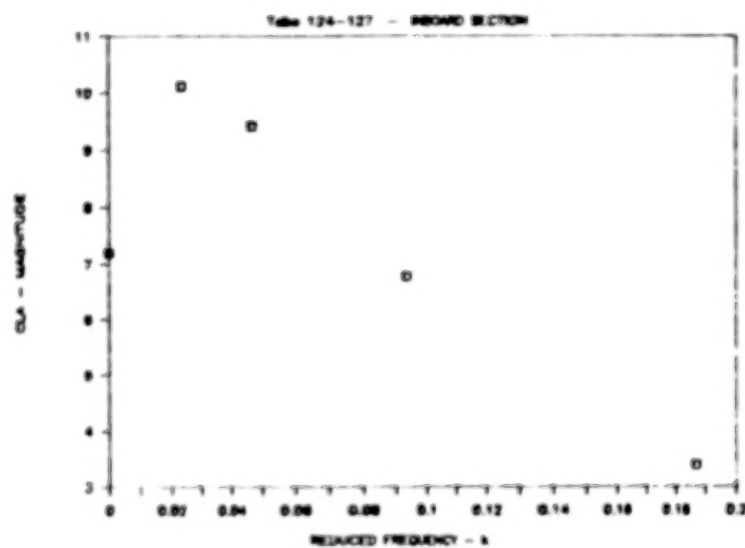
UNSTEADY LIFT COEFFICIENT - 49.6% SPAN

$C_{f\alpha}$'s are plotted for steady state, 2, 4, 8, & 16 Hertz at $\alpha_{root} = -1.5$ degrees. Magnitude/phase plots are shown for measurements at 49.6% span. Plots are made versus reduced frequency - k .

$$C_{f\alpha} = C_{f_{max}} / \alpha_{max}$$

$$k = b\omega/V = \frac{(c/2) \cdot 2\pi f}{\sqrt{2Q/\rho}}$$

Mach = 0.859 Q = 40.68
 Root Alpha = -1.500 Inboard Section Alpha = -0.801



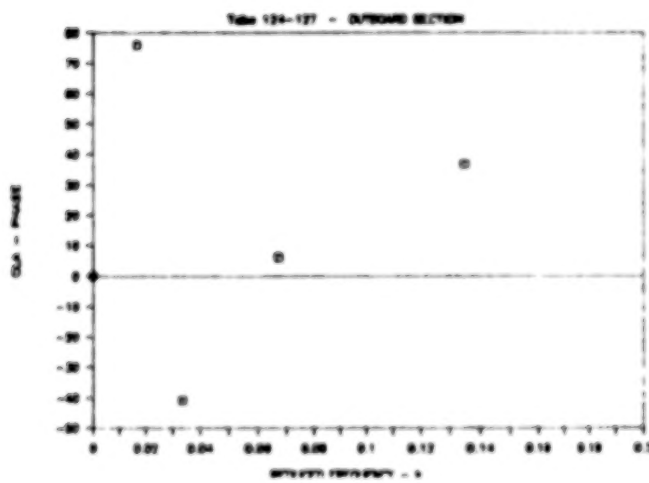
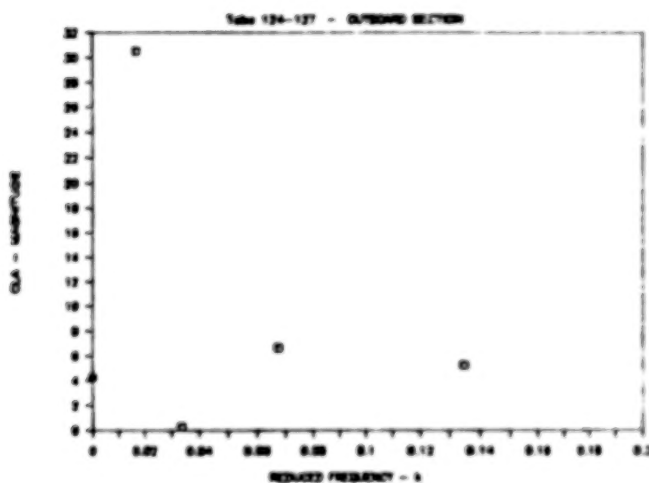
UNSTEADY LIFT COEFFICIENTS -82.1% SPAN

$C_{l\alpha}$'s are plotted for steady state, 2, 4, 8, & 16 Hertz at $\alpha_{root} = -1.5$ degrees. Magnitude/phase plots are shown for measurements at 82.1% span. Plots are made versus reduced frequency - k .

$$C_{l\alpha} = C_{l\alpha_{max}} / \alpha_{max}$$

$$k = b\omega/V = \frac{(c/2) \cdot 2\pi f}{\sqrt{20/P}}$$

Mach = 0.859 $\alpha = 40.68$
 Root Alpha = -1.500 Outboard Section Alpha = -0.357



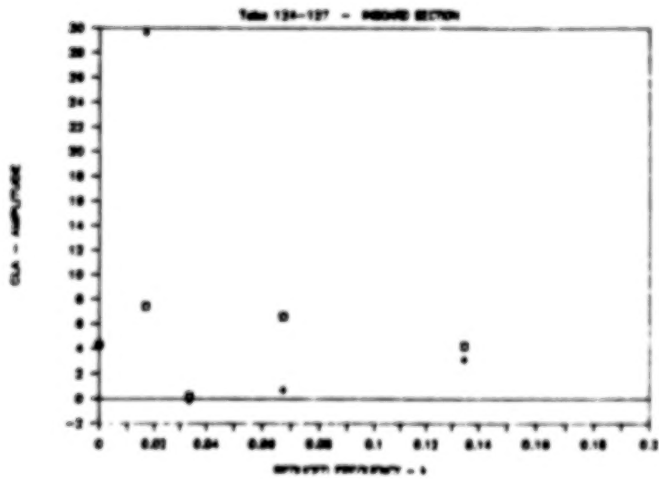
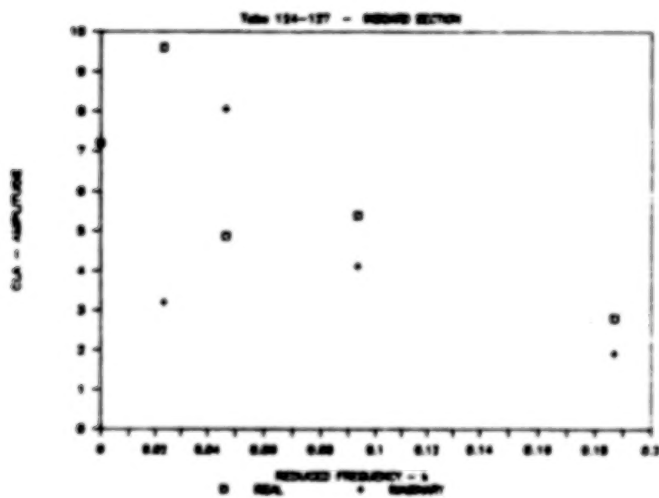
UNSTEADY LIFT COEFFICIENTS

$C_{l\alpha}$'s are plotted for steady state, 2, 4, 8, & 16 Hertz at $\alpha_{root} = -1.5$ degrees. Real/imaginary plots are shown for measurements at 49.6% and 82.1% spans. Plots are made versus reduced frequency $-k$.

$$C_{l\alpha} = C_{l_{max}} / \alpha_{max}$$

$$k = b\omega/V = \frac{(c/2) \cdot 2\pi f}{\sqrt{2Q/\rho}}$$

Mach = 0.659 Q = 40.68
 Root Alpha = -1.500 Inboard Section Alpha = -0.601
 Outboard Section Alpha = -0.357



SUMMARY

1. Present flutter analysis methods do not accurately predict the flutter speeds in the transonic flow region for wings with super-critical airfoils.
2. Aerodynamic programs using CFD methods are being developed, but these programs need to be verified before they can be used with confidence.
3. A wind tunnel test was performed to obtain all types of data necessary for correlating with CFD programs to validate them for use on high aspect ratio wings. The data include steady state and unsteady aerodynamic measurements on a nominal stiffness wing and a wing four times that stiffness. There is data during forced oscillations and during flutter at several angles-of-attack, Mach numbers, and tunnel densities.
4. The test data is being compiled and will be published in a NASA report. Data will also be available through NASA on magnetic tape.
5. The data is intended to be used for correlating with and verifying CFD aerodynamic programs.

- IMPROVED TRANSONIC FLUTTER ANALYSES NEEDED
- COMPUTATIONAL FLUID DYNAMIC CODES
- PRESSURE / FLUTTER MODEL TEST CONDUCTED
- COMPILATION OF TEST DATA
- CORRELATION OF TEST DATA WITH CFD CODES

TURBOMACHINERY AEROELASTICITY AT
NASA LEWIS RESEARCH CENTER

Krishna Rao V. Kaza
Structural Dynamics Branch
Structures Division
NASA Lewis Research Center
Cleveland, Ohio

Aeroelastic Stability and Response of Propulsion Systems (ASTROP)

The turbomachinery aeroelastic effort at NASA Lewis Research Center is focused on unstalled and stalled flutter, forced response, and whirl flutter of both single-rotation and counter-rotation propfans (figs. 1 & 2). It also includes forced response of the space shuttle main engine (SSME) turbopump blades (fig. 1). Because of certain unique features of propfans and the SSME turbopump blades, it is not possible to directly use the existing aeroelastic technology of conventional propellers, turbofans or helicopters. Therefore, reliable aeroelastic stability and response analysis methods for these propulsion systems must be developed. The development of these methods for propfans requires specific basic technology disciplines, such as 2D and 3D steady and unsteady (unstalled and stalled) aerodynamic theories in subsonic, transonic and supersonic flow regimes; modeling of composite blades; geometric nonlinear effects; and passive or active control of flutter and response. These methods for propfans are incorporated in a computer program ASTROP (fig. 3). The program has flexibility such that new and future models in basic disciplines can be easily implemented. The forced response analysis method for turbine blades will be discussed later.

UNSTEADY AERODYNAMICS AND AEROELASTICITY

SR LARGE SCALE
AERODYNAMICS AND FLUTTER
SR 7 L



SR-3 RESEARCH MODEL
FLUTTER, FORCED
RESPONSE, AND MISTUNING



CR PROPFAN WIND TUNNEL MODEL
AERODYNAMICS AND FLUTTER



SSME TURBOPUMP BLADE
FORCED RESPONSE



Figure 1

UNSTEADY AERODYNAMIC AND AEROELASTICITY FLIGHT TEST PROGRAM

SR PROPFAN



CR PROPFAN



CD-87-26577

Figure 2

ASTROP

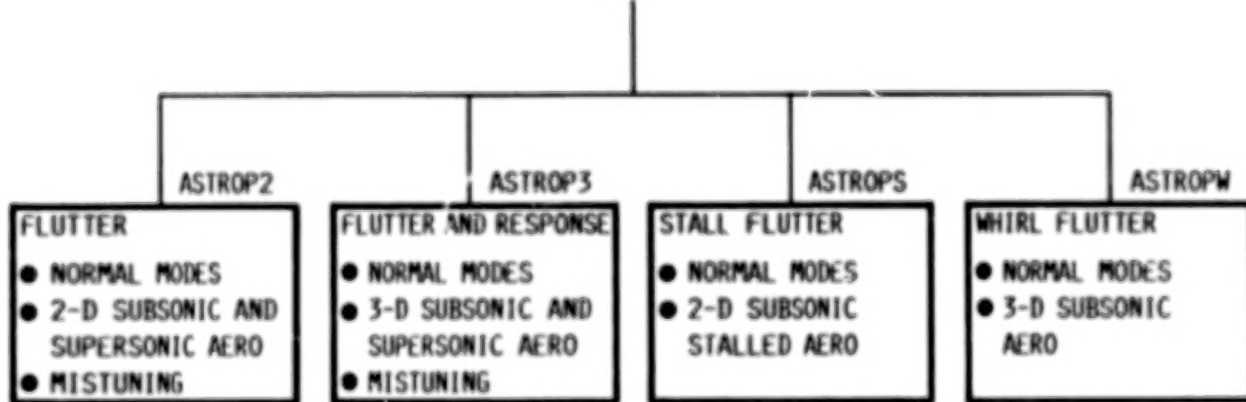
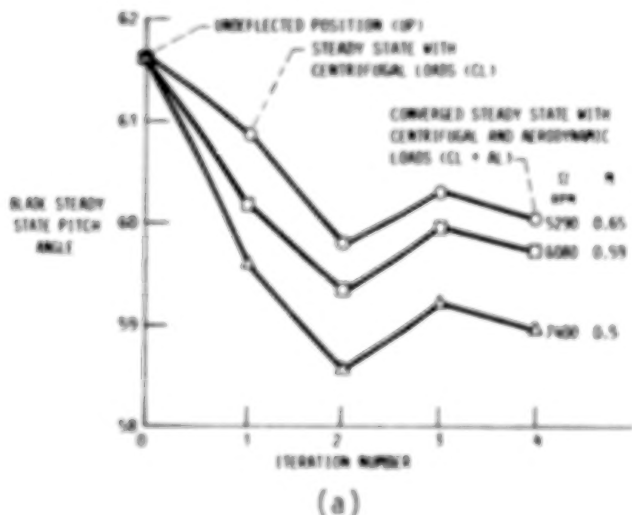


Figure 3

Application of the ASTROP Code to Investigate Flutter of a Composite SR Propfan Model

One version of the code called ASTROP3 (ref. 1) uses three-dimensional subsonic steady and unsteady cascade aerodynamics (ref. 2) and NASTRAN (ref. 3) finite element model to represent the blade structure. The equivalent anisotropic material properties for each finite element are generated by using a preprocessor code COBSTRAN (ref. 4). The effect of centrifugal loads and steady-state airloads on the steady-state geometry of a composite wind tunnel model (SR3C-X2) blade is shown in figure 4(a). The aerodynamic cascade effects (or the effect of number of blades) on the eigenvalues are shown in figure 4(b). Both centrifugal loads and aerodynamic loads untwist the blades and this untwist increases with rotational speed. It is evident from figure 4(b) that the number of blades or the cascade effect is very significant on the real part of the eigenvalue and hence on stability.

EFFECT OF CENTRIFUGAL AND AERODYNAMIC LOADS ON BLADE PITCH ANGLE



EFFECT OF NUMBER OF BLADES ON EIGENVALUES

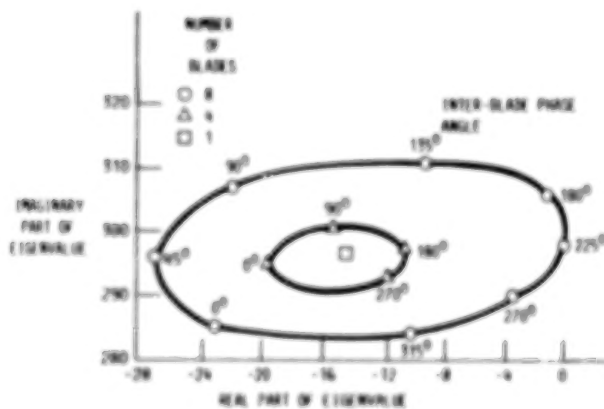
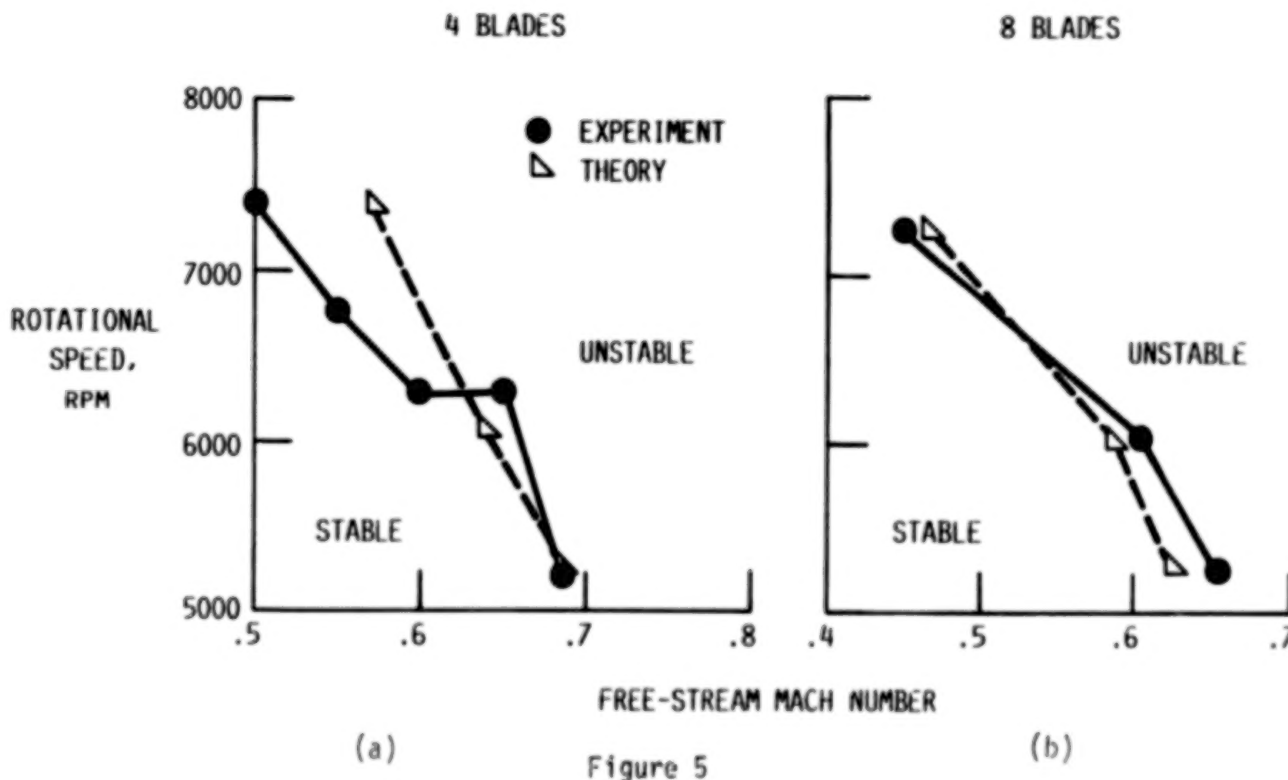


Figure 4 (b)

Comparison of Measured and Calculated Flutter Boundaries for the SR3C-X2 Propfan Model

Theoretical flutter results obtained from the ASTROP3 code have been correlated in figures 5(a) and (b) with flutter data of a wind tunnel propfan model (ref. 5), SR3C-X2, with composite blades. Theoretical results include the effects of centrifugal loads and steady-state airloads. The theory does reasonably well in predicting flutter speeds and slopes of the boundaries. However, the difference between the calculated and measured flutter Mach numbers for the four-blade case is greater than for the eight-blade case. This implies that the theory may be overcorrecting for aerodynamic cascade effects for four blades. Calculated interblade phase angles at flutter (not shown) also compared well with measured values. However, calculated flutter frequencies were about 8% higher than measured.



Evaluation of Two-Dimensional Unsteady Aero for Propfan Flutter Prediction

Actually the ASTROP code was started with two-dimensional unsteady aerodynamic theory (ref. 6) by correcting for blade sweep (ref. 1). The version of the code which uses blade normal modes and two-dimensional unsteady aero theory in a stripwise manner is ASTROP2 (figure 3). The ASTROP3 version uses three dimensional unsteady aero theory. To assess the validity of two-dimensional aerodynamic theory and the associated sweep correction, the real part of the eigenvalue of the critical mode calculated by using both ASTROP2 and ASTROP3 are compared in figure 6. Also included in this figure is the measured flutter mach number. Evidently, the two-dimensional theory is less accurate than three-dimensional theory in predicting flutter Mach number for this case. Correlative studies (not shown) of measured and calculated flutter boundaries were also conducted by varying Mach number, blade sweep, rotational speed, and blade setting angle. The correlation varied from poor to good. In some cases the expected conservative nature of the two-dimensional theory did not prevail, possibly because of the arbitrary nature of the reference line which is employed in the strip-method, and the associated sweep correction.

COMPARISON OF 2-D AND 3-D UNSTEADY AERO FOR PROPFAN FLUTTER PREDICTION

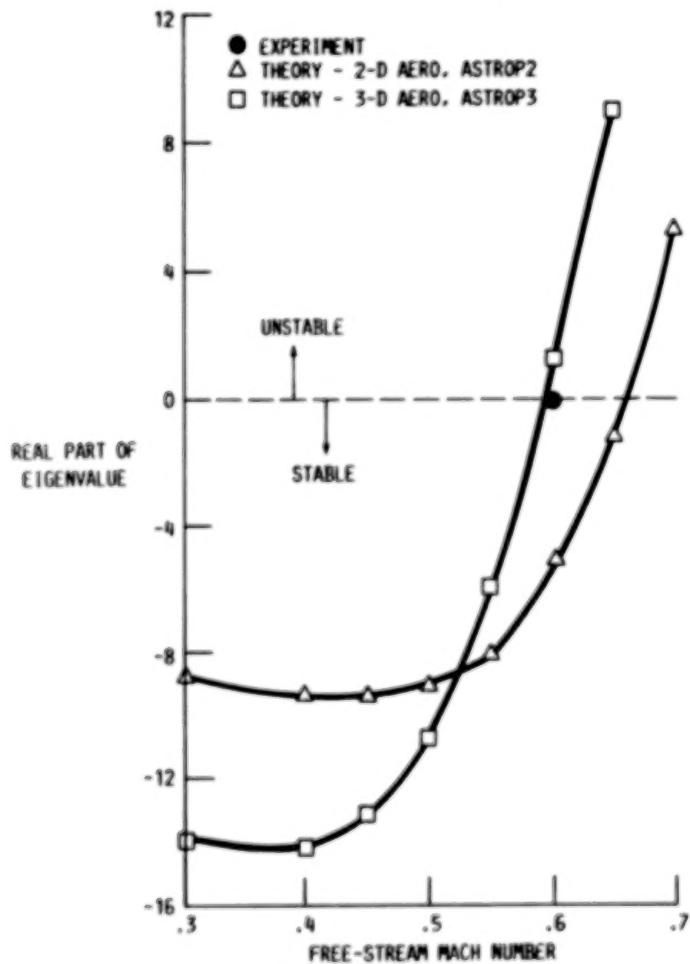
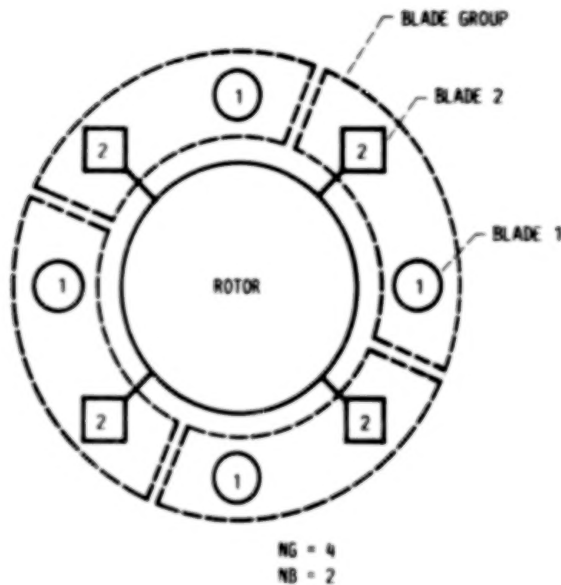


Figure 6

Propfan Blade Mistuning Models

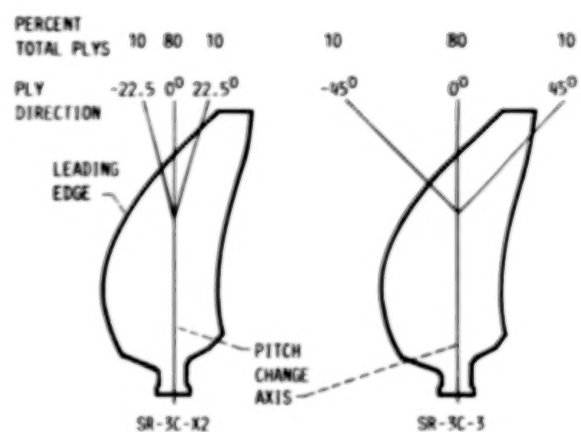
Understanding the effects of blade mistuning on vibration, flutter and forced response of turbomachinery rotors is a current research topic because mistuning affects flutter and response behavior. An analytical and experimental investigation of mistuning in propfan flutter was conducted in ref. 7. A schematic for an eight-bladed mistuned rotor in formulating the analytical model and blade ply directions used in constructing the wind tunnel model are shown in figures 7 (a) and (b), respectively. The analytical model, which is more general than the wind tunnel model, is based on normal modes of a rotating composite blade and subsonic unsteady lifting surface aerodynamic theory. The natural frequencies and mode shapes of the SR3C-X2 and -3 model blades differ because of the ply angle variations between the blades. The first mode frequencies of both the blades are very close and were insensitive to ply angles. However, the average second mode frequency of the SR3C-3 blade is about 12 percent higher than that of the -X2 blade. More details can be found in ref. 7.

BLADE GROUP SCHEMATIC FOR AN EIGHT-BLADED ROTOR



(a)

BLADE PLY DIRECTIONS



(b)

Figure 7

Comparison of Eigenvalues of Tuned and Mistuned Propfan Models

To illustrate the effect of mistuning (which is partly aerodynamic and structural) the calculated real and imaginary parts of eigenvalues of the SR3C-X2 (8-bladed tuned rotor), SR3C-3 (8-bladed tuned rotor), and mixed (mistuned) rotor were compared in figure 8. The mistuning is due to the differences in blade steady-state geometry, frequencies, and mode shapes. The eigenvalues are for all interblade phase angles of the mode with lowest damping. The calculations were performed by treating the SR3C-X2 and -3 rotors as tuned and the mixed rotor as an idealized alternately mistuned rotor--four identical blade pairs with two different blades in each pair. Comparison of root loci indicates that the area of the approximate ellipse for the SR3C-X2 is greater than that of SR3C-3, indicating a stronger aerodynamic coupling between the blades of the SR3C-X2 rotor. The difference in stability of the tuned rotors is due to the difference in blade stiffness and mode shapes because of the different ply angles of the blades. The results also show that mixing the blades significantly affected the eigenvalues and resulted in a rotor with a greater damping than the lowest damped mode of either tuned rotor.

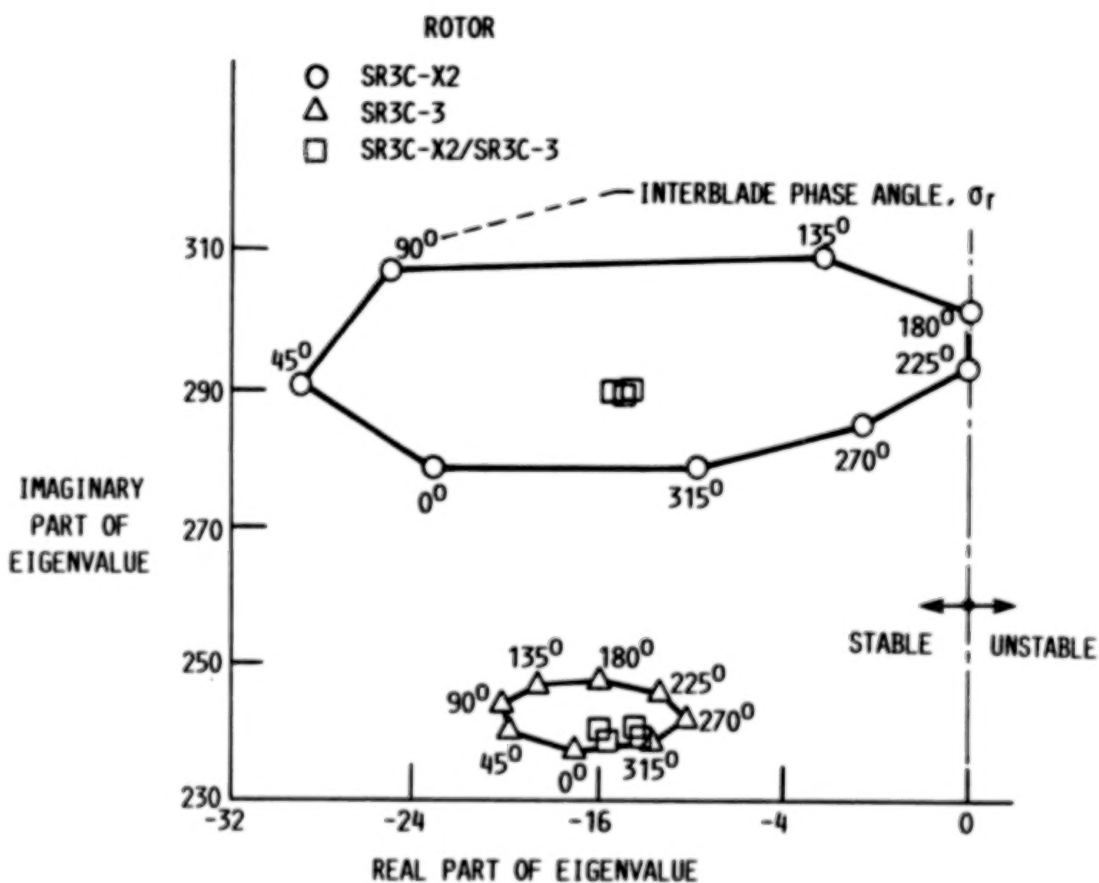


Figure 8

Comparison of Measured and Calculated Flutter Boundaries
for Tuned and Mistuned Propfan Models

Measured and calculated results for the tuned rotor SR3C-X2 and mistuned rotor SR3C-X2/SR3C-3 are compared in figure 9. The calculations for each rotor were made with the calculated modes and frequencies, except that the measured second mode frequency was substituted for the calculated one. The calculated flutter Mach numbers for the SR3C-X2 are less than the measured ones for all rotational speeds. The agreement would be better if the effects of steady airloads and structural damping were included in calculations (see ref. 1 for detailed discussion). The agreement of the mixed rotor is better, but would become unconservative if steady airloads and structural damping were included in the theory. However, the overall agreement between theory and experiment is more than satisfactory. For additional details and results see ref. 7.

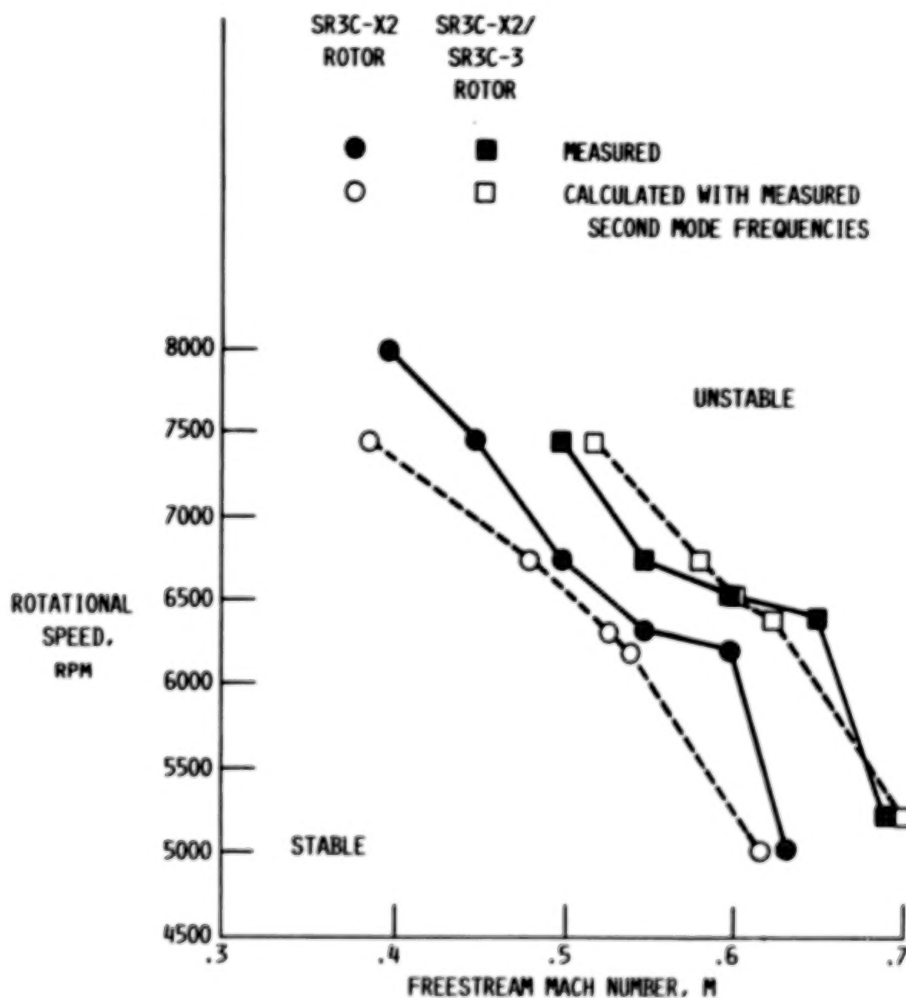
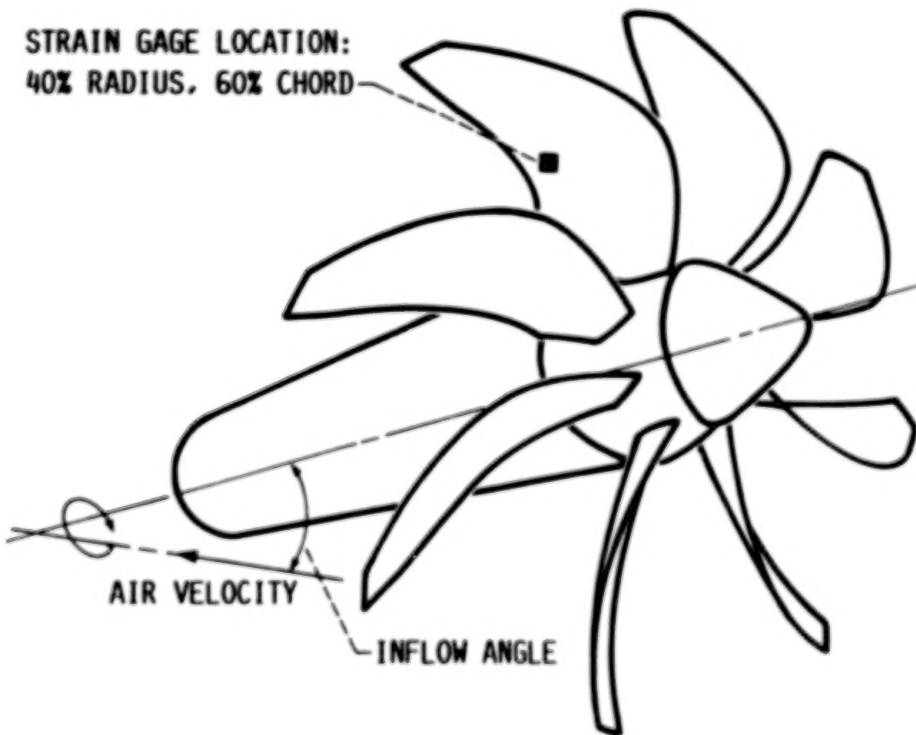


Figure 9

Comparison of Measured and Calculated Vibratory Stress Amplitudes of a Propfan Model

A new feature of the ASTROP3 code under development is the capability to perform a modal forced response vibration analysis of aerodynamically excited propfans. Figure 10 depicts a single-rotation, advanced propfan wind tunnel model (SR5, 10 metallic blades), ref. 8, operating in a generally uniform, steady inflow field, inclined at a small angle with respect to the axis of rotation. Although the absolute inflow field is constant, rotation of the propfan results in velocities with oscillatory components relative to the blades. Under such conditions, ASTROP3 is able to determine the oscillatory loading distributions over the propfan blades at various excitation frequencies and calculate the vibratory displacements and stresses of the propfan. The table shows measured and preliminary calculated one per rev vibratory stress amplitudes for the SR5 blade. Also included in the table are the calculated results from ref. 9 by using a 2-D unsteady aerodynamic theory. Comparison shows that 2-D results are better than 3-D results. The reason for this difference is being investigated.



MEASURED STRESS, PSI	ASTROP3 PREDICTED	REFERENCE 9 PREDICTED
3365	2322	3065

Figure 10

Stall Flutter Analysis Methods

The third feature of the ASTROP code is a stall flutter analysis which is in ASTROPS. Under take-off conditions, the propfan blades operate at high angles of attack and have the potential to stall flutter, triggered by separated flow during part of every cycle of oscillation. Stall flutter speeds are very low and the forces due to vibration at the stall condition (dynamic stall) are an order of magnitude high compared to forces in separated flow with no vibration. Prediction of forces during dynamic stall has been a continuing research effort. Some prediction methods are reviewed in ref. 10, and their classification is shown in figure 11. The Navier-Stokes solvers (N.S.S.), vortex methods, and the zonal methods attempt to solve the fluid mechanics equations in their fundamental form by numerical techniques with varying degrees of simplifications and assumptions. These models require a significant amount of computer time and therefore are not suitable for routine aeroelastic analysis. In semi-empirical models an analytical approximation is attempted to approximately reproduce measurements for example, by way of analytical curve fit to wind tunnel data. The semi-empirical models take less computer time to solve and can be used in a routine aeroelastic analysis.

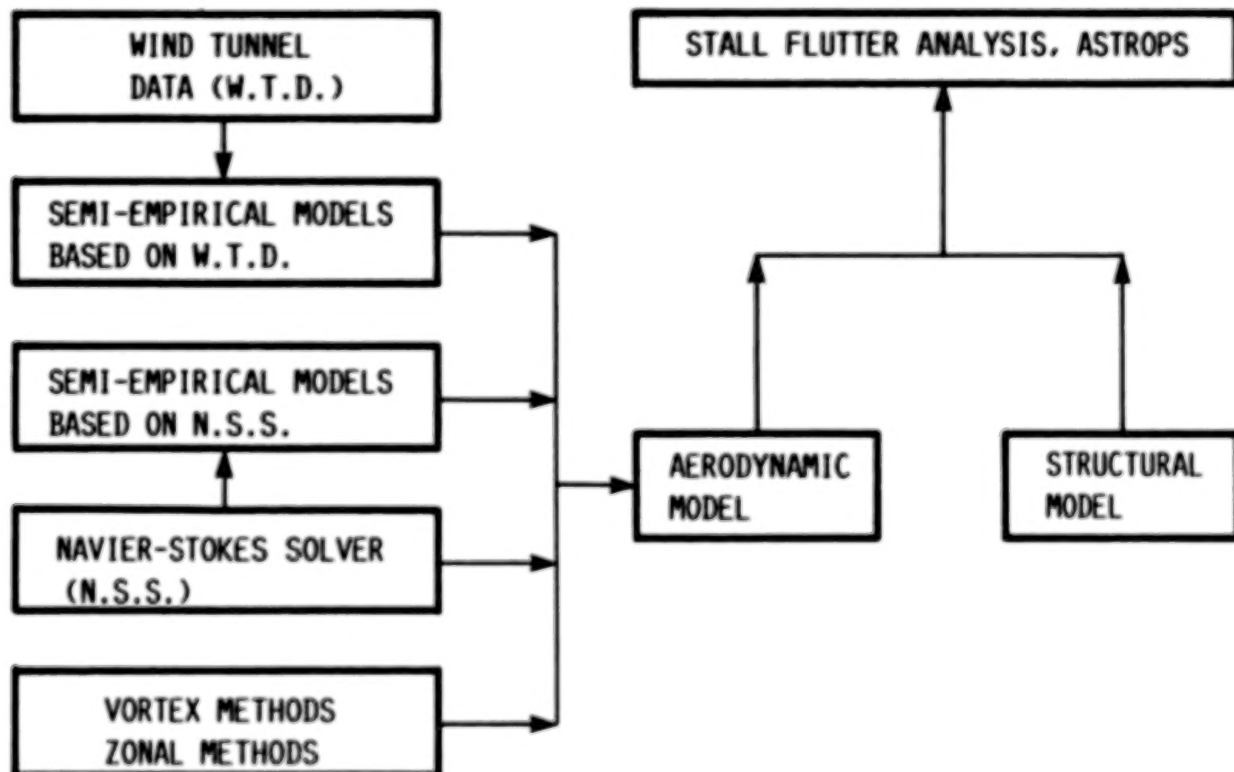


Figure 11

Comparison of Measured and Calculated Stall Flutter Results of an Unswept Propfan Model

Recently two semi-empirical dynamic stall models, designated as model A and model B, were applied to an unswept propfan model (SR-2, 8 metallic blades). The calculated logarithmic decrement of third mode response as a function of blade pitch angle is shown in figure 12. Also included in the figure is the blade pitch angle at which the blade is unstable in a wind tunnel experiment. Model A (ref. 11) incorporates the unsteady effects in stall using only one stall parameter that relates the dynamic stall angle and the non-dimensional rate of angle-of-attack. The stall parameter is given as a function of Mach number and airfoil thickness to chord ratio. Model B (ref. 12) is a synthesized data method to dynamic stall modeling. An analytical curve is fitted for the wind tunnel data obtained from oscillating airfoil tests. The empirical parameters in the model are obtained from this fit. However, experimental dynamic data is not available for propfan airfoil sections (16 series). Therefore, in implementing model B for propfan application, the dynamic data corresponding to NLR-1 airfoil was used, even though the airfoil geometries are different. However, for the case studied here, the Mach number range for which the data available for the NLR-1 airfoil corresponds to the helical Mach number (at zero freestream Mach number) due to rotation of the propfan model. In spite of the differences in dynamic data, the empirical models chosen predicted a qualitative stall flutter behavior for the case studied. Both the models predicted that the stall flutter response occurred in third mode as was found in the experiment at a rotor speed of 8500 rpm. However, the calculated blade pitch angles at which the stall flutter occurred is lower than that of the experiment (30°), model B predicted a closer value (28.25°) compared to that predicted by model A (25°). The calculated frequency at stall flutter condition is about 10% higher than the experimental data.

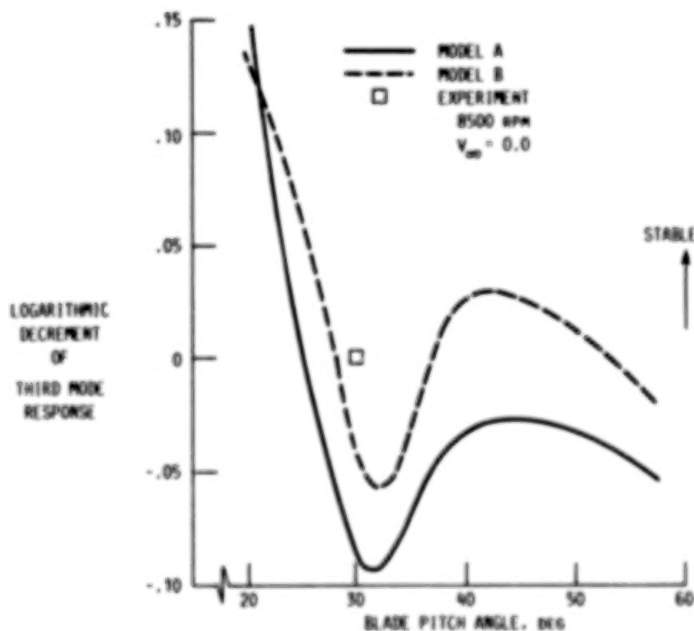


Figure 12

Stall Flutter Analysis with Navier-Stokes Code

A solution procedure is described for determining the two-dimensional, one- or two-degree-of-freedom flutter characteristics of arbitrary airfoils at large angles-of-attack (see ref. 12). The same procedure is used to predict stall flutter including separated flow. This procedure requires a simultaneous integration in time of the solid and fluid equations of motion. The fluid equations are the unsteady compressible Navier-Stokes equations, solved in a body-fitted moving coordinate system using an approximate factorization scheme. The solid equations are integrated in time using an Euler implicit scheme. Several special cases, figures 13-15, are presented to demonstrate the capability of this scheme to predict transonic flutter and stall flutter with large separated flow.

The first case is shown to illustrate the capability of the present solver to predict the highly separated flows. The aerodynamic coefficients of an NACA 0012 airfoil oscillating in pitch at large angle-of-attack is shown and compared with experiment in figure 13. The mean angle and amplitude of oscillation was 15 degrees and 10 degrees respectively. The reduced frequency based on semi-chord was 0.151. The freestream Mach number and Reynolds number were 0.283 and 3.45 million respectively. It is seen from figure 13 that the Navier-Stokes solver produces lift, drag, and moment coefficients which are in a reasonable agreement with the measured ones. The fact that the flow solver is able to capture much of the dynamic stall flow features increases the confidence in the capability of this code for stall flutter predictions.

STALL FLUTTER ANALYSIS WITH NAVIER-STOKES
 CODE: $\alpha = 15 - 10 \cos(\Omega t)$

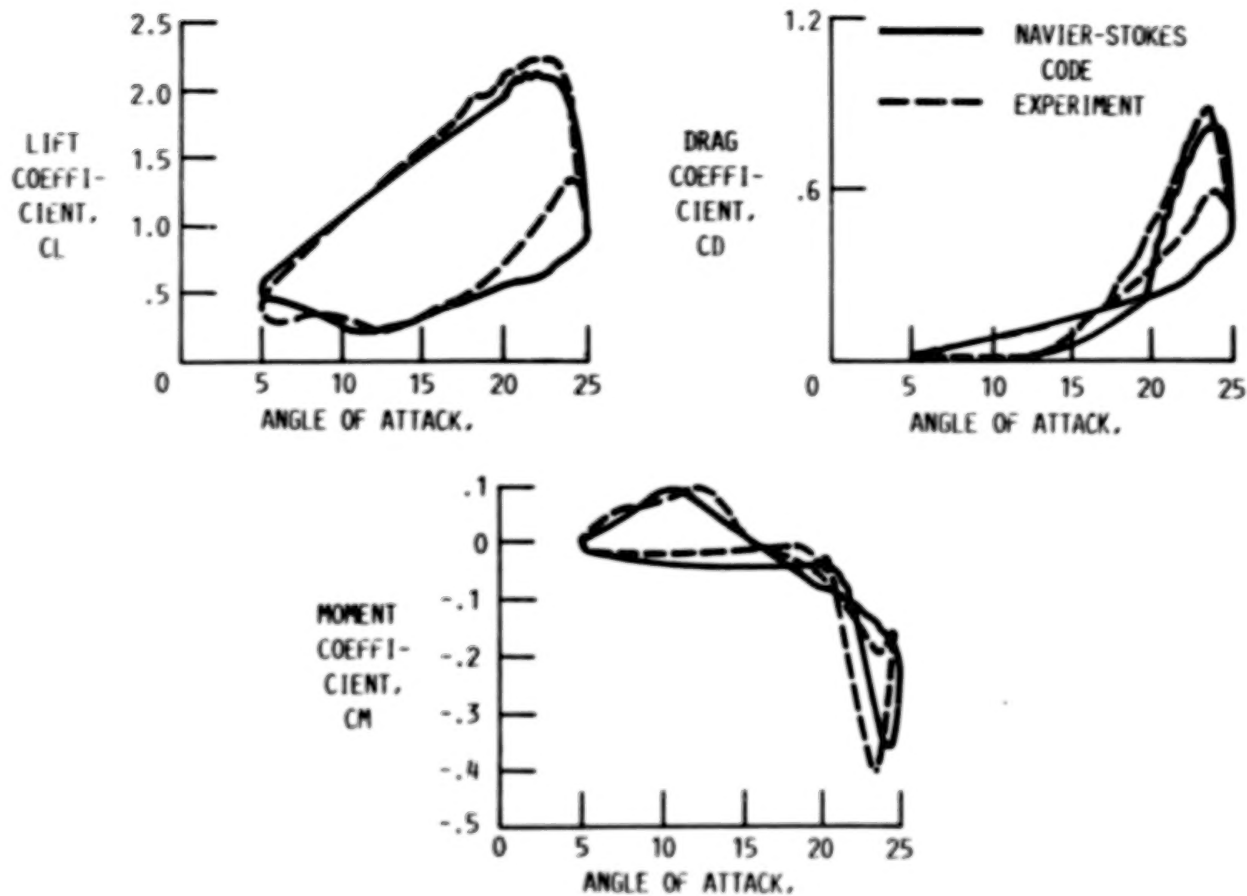


Figure 13

Comparison of Flutter Speeds from Euler, UTRANS2,
and LTRAN2 Codes

A second special case considered for validation of the Navier-Stokes solver is its Euler version to calculate transonic flutter speed. Predicted transonic flutter speeds at various mass-to-air ratios for NACA 64006 airfoil oscillating in pitch and plunge at Mach number 0.85 are shown in figure 14. Several other validation cases are reported in ref. 13. The results from UTRANS2 (ref. 14) and LTRAN2 (ref. 15) are also included. Very good agreement between present Euler and UTRANS2 code results is found. A qualitative agreement between present and LTRAN2 results is found, too.

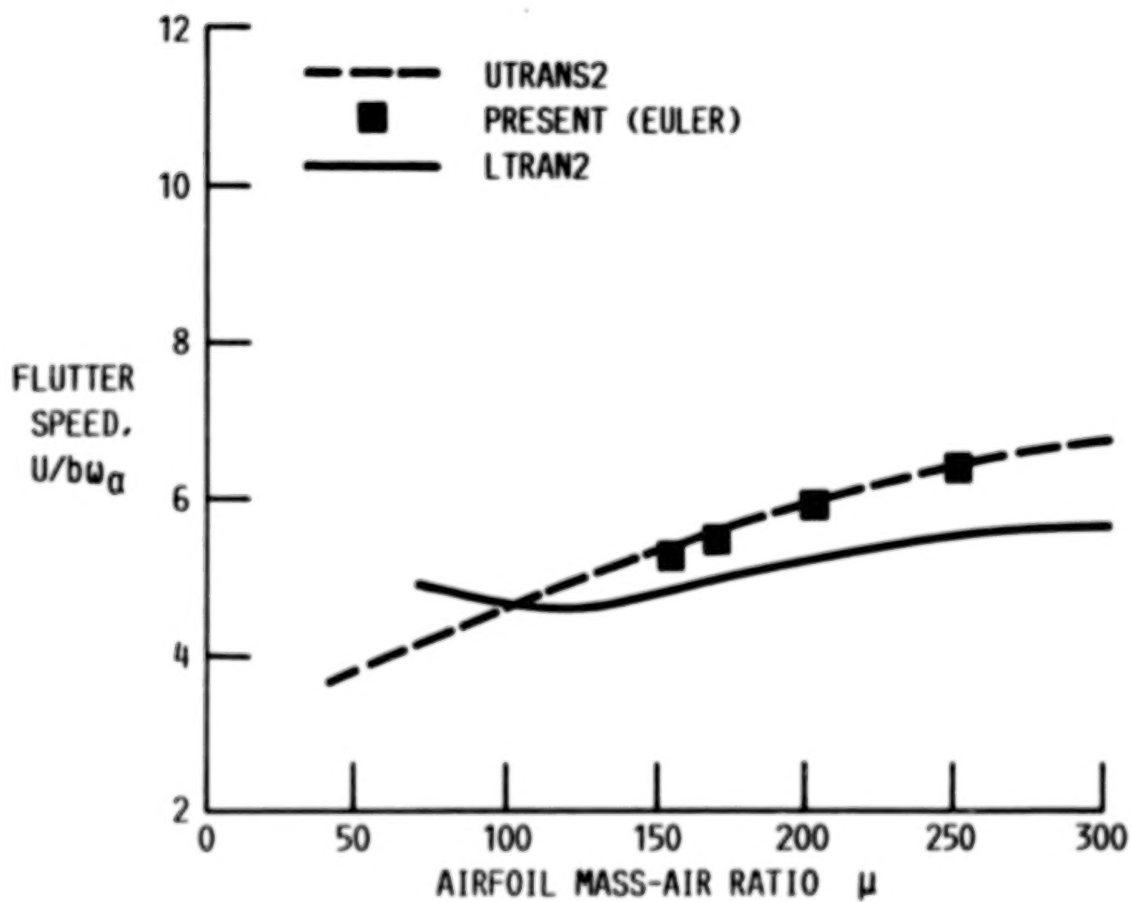


Figure 14

Plunging and Pitching Stall Response

The third case considered with the Navier-Stokes code is the prediction of flutter at large mean angle-of-attack, including flow separations. The time response of plunging and pitching displacements and lift and moment coefficients of an NACA 0012 airfoil is shown in figure 15. The airfoil was initially subjected to a sinusoidal pitching oscillation from 5 to 25 degrees. During the downstroke, around 23.8 degrees, the airfoil was released and was allowed to follow a pitching and plunging motion. The dimensionless speed is varied from 4 to 8. The response of the airfoil is stable when the speed is 4 and is unstable when the speed increases to 8. It was found that the growing response is induced by the separated flow over the airfoil at large angle-of-attack.

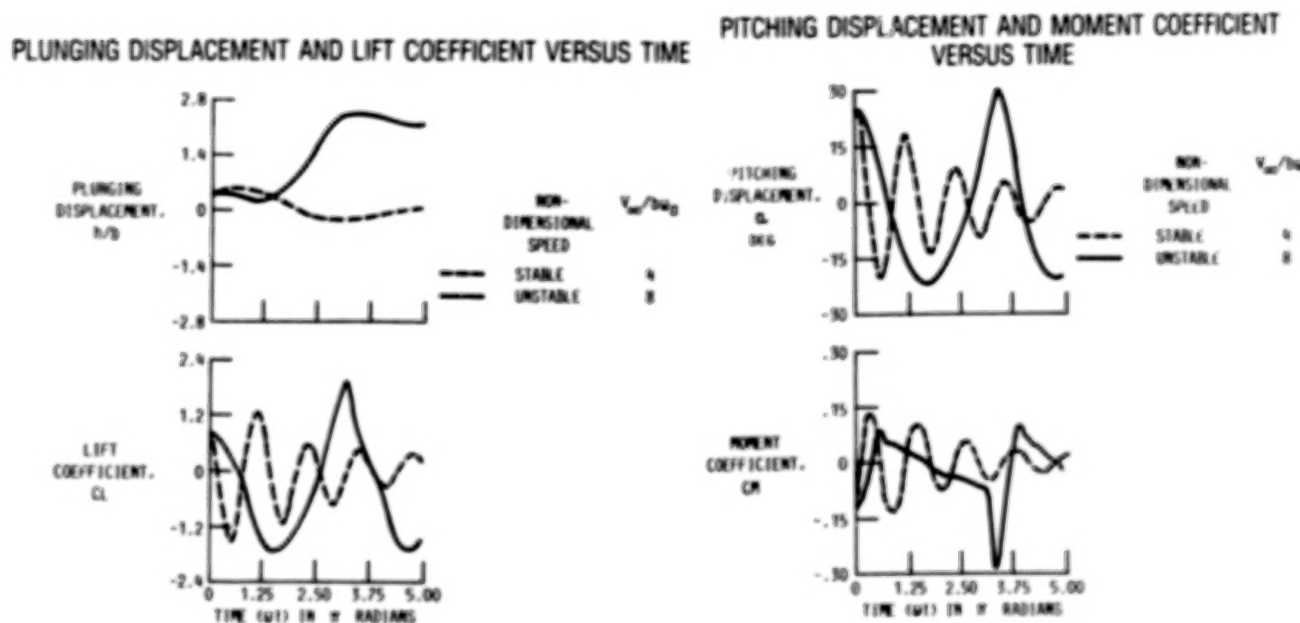


Figure 15

Full Potential Unsteady (Cascade) Aero Model

A compressible, unsteady, full potential, finite difference code is being developed for modeling 2D/3D flow through single rotation propfans and other turbomachinery rotors. The procedure introduces a deforming grid with a uniform shear mesh. The numerical scheme is based on finite volume and implicit time marching technique. The 2-D code is vectorized and verified by applying it to several special cases. Two such cases are shown in figure 16. For comparison, the results from refs. 16 and 17 are also included. Even though a very coarse grid is used in the present calculations, the agreement between the present results and those of refs. 16 and 17 is very good. Validation of 3-D code is in progress.

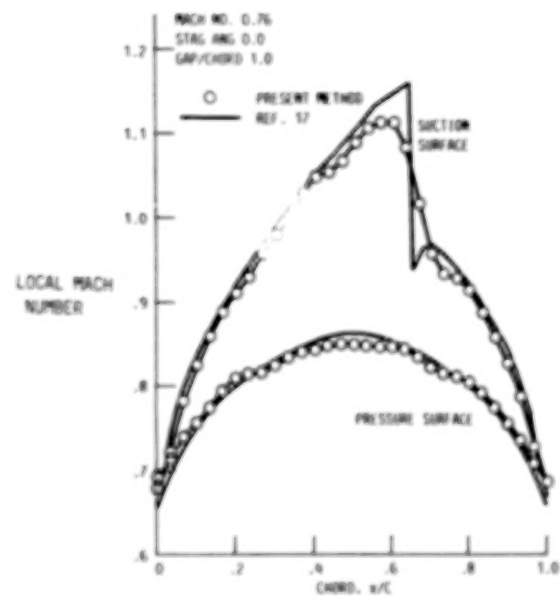
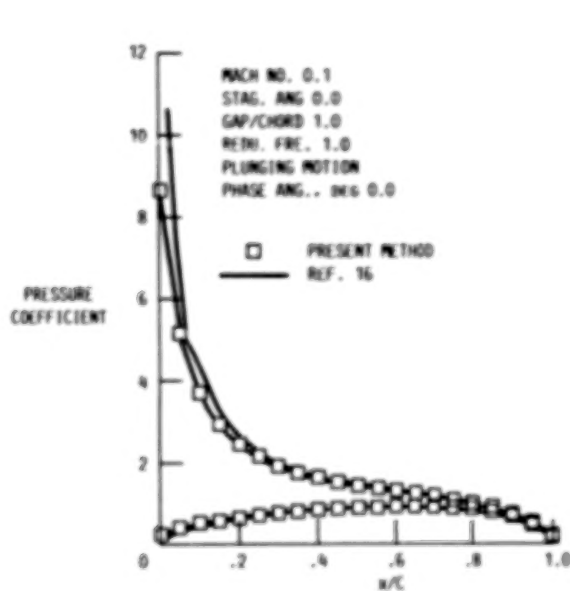


Figure 16

CR Propfan 3-D Steady and Unsteady Aero Model

An incompressible, steady and unsteady aerodynamic model is being developed in ref. 18 for modeling flow through counter rotation propfans. The model is based on time domain solution in conjunction with panel method. This model is applicable for calculating performance and stability of both single and counter rotation propfans including interaction from wing. The code is being verified by applying to several special cases. One such case is shown in figure 17 in which present results are compared with the corresponding ones in ref. 19. See ref. 18 for additional validations and for details. This code will be extended to compressible flow, and, then, will be merged with ASTROP code structural modules to predict flutter of counter rotating propfans.

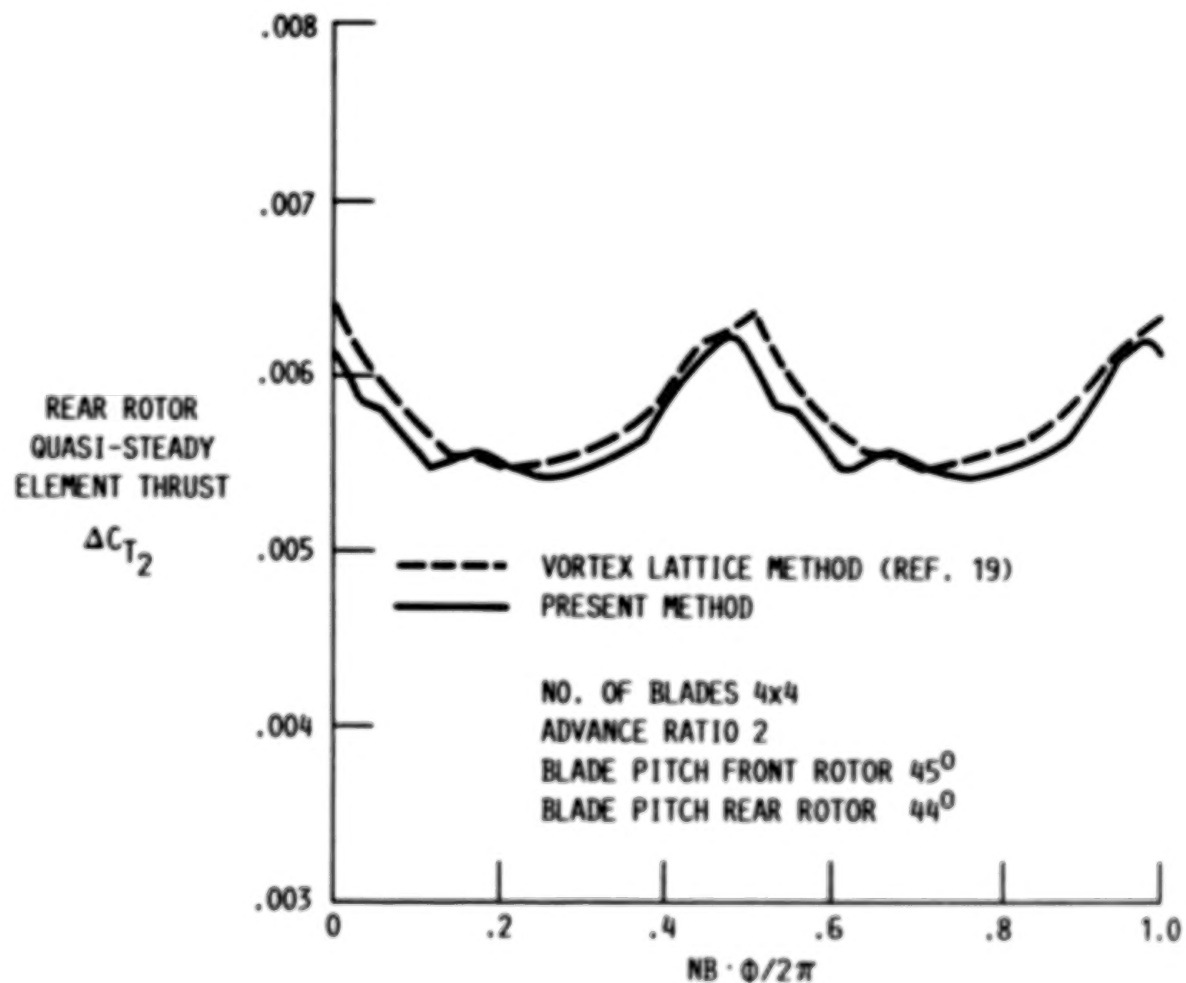
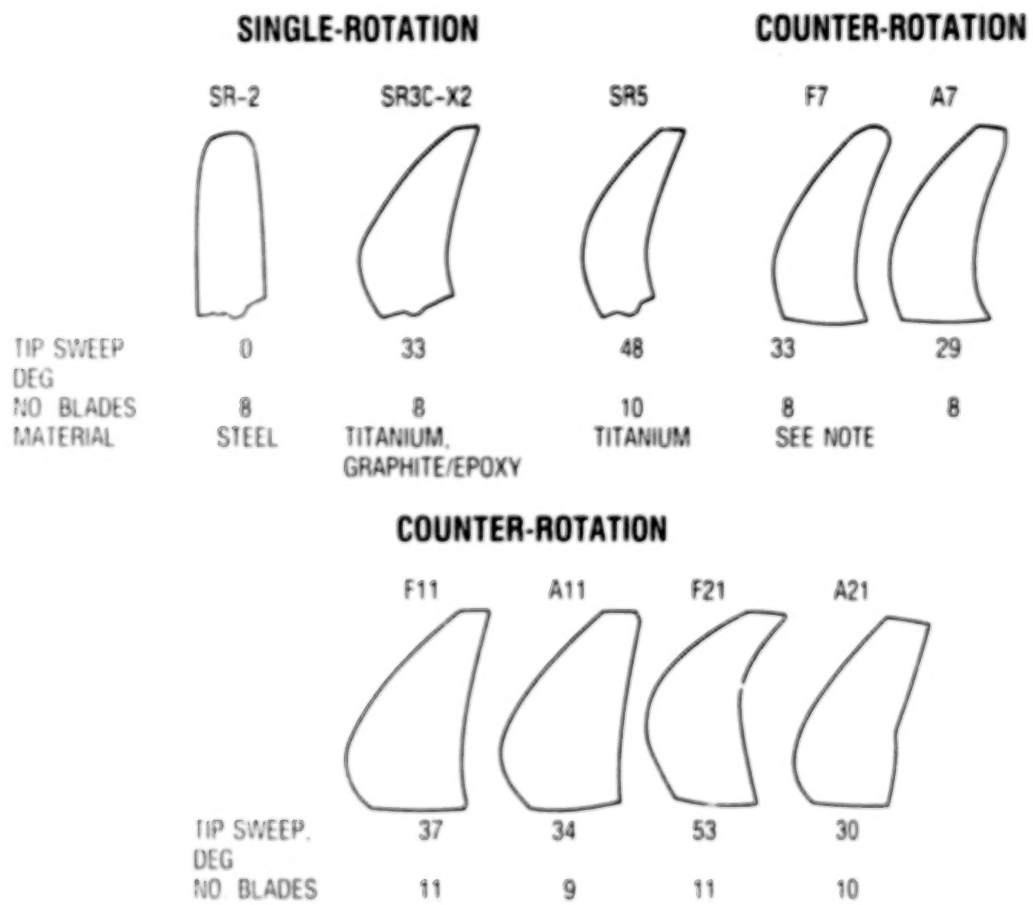


Figure 17

Propfan Wind Tunnel Flutter Models

Figure 18 shows propfan blade wind tunnel models that have had flutter. These blades are not aeroelastically scaled models and were made for aerodynamic performance tests. However, the SR3C-X2 and -3 models were specifically designed for flutter and forced response experiments, respectively. One single rotation model had stall flutter, SR-2. The other two had unstalled flutter SR3C-X2 and SR-5. The flutter data from these models has been used to verify the analysis methods discussed earlier. The three counter-rotation models shown have had unstalled flutter. The correlation of this data with analysis is in progress.



NOTE: ALL CR BLADES HAVE A SPAR OF TITANIUM AND A SHELL OF GRAPHITE/EPOXY

Figure 18

Forced Response of SSME Turbopump Blades

The state-of-the-art in forced response analysis of turbomachinery blading is to simply calculate the blade natural frequencies and try to avoid known forcing frequencies (Campbell Diagram). Forced response calculations are not attempted. This can lead to unexpected blade cracking. The objective of this research is to develop a forced response prediction method for turbopump blades. The flow chart for this method is shown in figure 19. The development will proceed in three parallel, integrated tasks. The first task continues existing in-house research to develop a model (M-STAGE) of the 3D, time-averaged, flow field within a passage of a blade row embedded in a multi-stage machine. This model identifies the distorted (i.e. non-axisymmetric) flow field generated by neighboring blade rows. This information serves as input to Task 2. The second task will develop a model (LINPUT) to predict the unsteady aerodynamic loads generated by the flow distortion. This model will consist of an unsteady, linearized, potential flow solver, and a linearized, convected gust solver. The model will be applicable to thick, highly cambered turbine blades. The third task continues existing in-house research to develop a model (FREPS) for integrated forced response predictions. This model will integrate the M-STAGE model of task 1 with the LINPUT model of task 2 and a structural dynamic model. Two structural dynamic models will be used. Initially, a simplified two degree-of-freedom blade model will be incorporated. This will be followed by a complete modal blade model. The result of this research will be a system to calculate the forced response of a turbopump blade embedded in a multi-stage turbine. The benefit will be a marked reduction in occurrences of unexpected blade cracking. This system will also be applicable to blading in aeronautical propulsion systems.

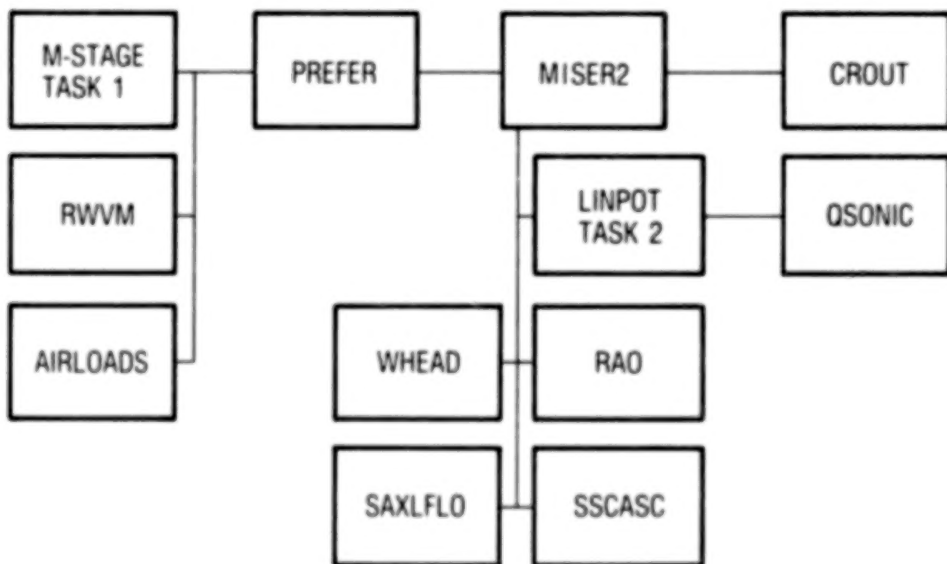
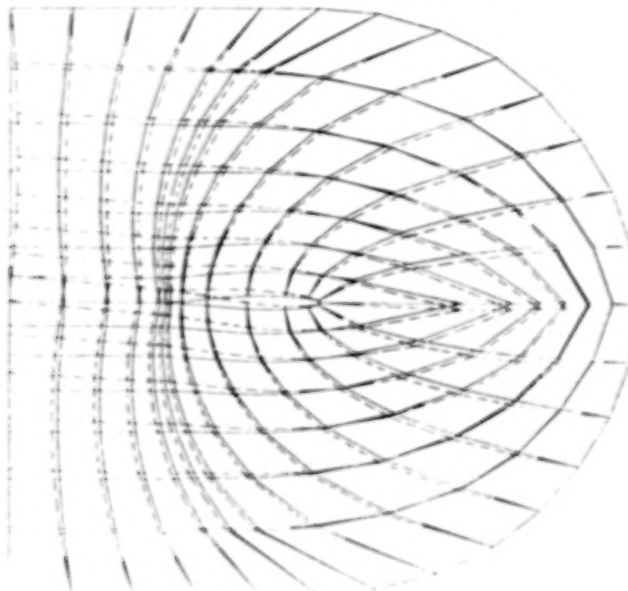


Figure 19

2D Unsteady, Viscous Cascade Aero Model

A compressible, unsteady, full Navier-Stokes, finite difference code has been developed for modeling transonic flow through two-dimensional, oscillating cascades. The procedure introduces a deforming grid (fig. 20) technique to capture the motion of the airfoils. The use of a deforming grid is convenient for treatment of the outer boundary conditions since the outer boundary can be fixed in space, while the inner boundary moves with the blade motion. The code is an extension of the isolated airfoil code developed in reference 20. More results validating the deforming grid technique are presented in reference 21.

2D UNSTEADY VISCOUS CASCADE AERO MODEL



2D UNSTEADY VISCOUS CASCADE AERO MODEL

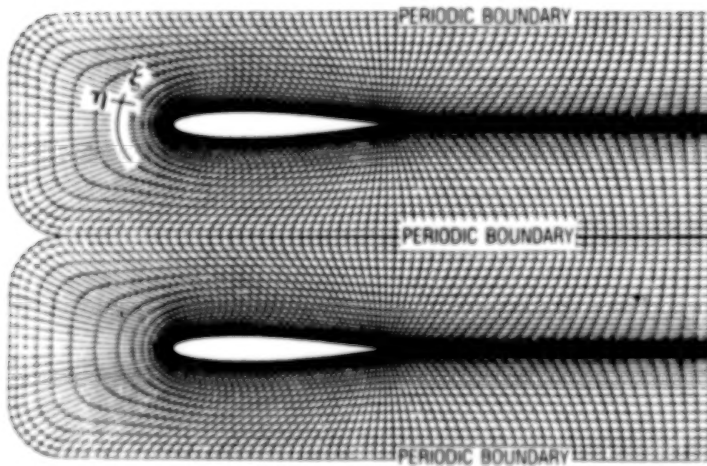


Figure 20

Pressure Coefficients for an NACA 0012 Cascade with Viscous Effects

The deforming grid technique has been used to predict the load histories for a NACA 0012 cascade with zero inter-blade phase angle and zero stagger. Two flow conditions were selected to investigate both subsonic and transonic flow. The cascade has a gap to chord ratio of one, $M = 0.60$ and 0.67 , $Re = 3.21$ million, $\alpha_m = 0.0$ degrees, pitching ± 2.0 degrees, and $k = 0.20$ (reduced frequency based on semi-chord). A Fourier transform on the pressure coefficient distribution was done for the first harmonics. The results are shown in figure 21. Future work will investigate non-zero inter-blade phase angles and will compare predictions with experimental data from the NASA Lewis Transonic Oscillating Cascade Facility.

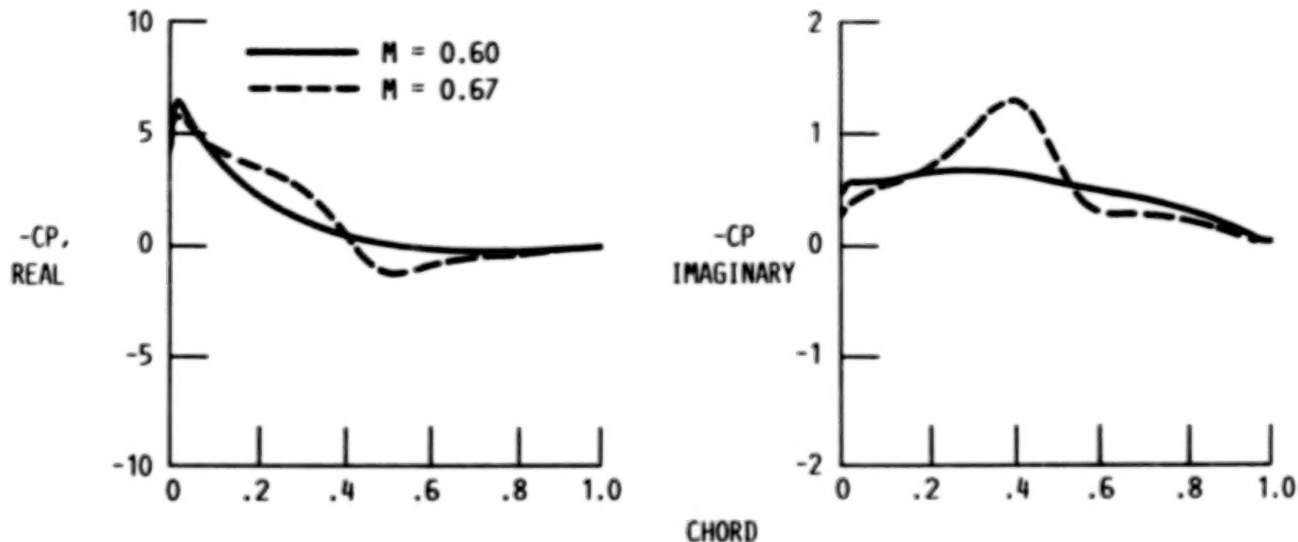


Figure 21

3-D Unsteady Euler Analysis

The three dimensional unsteady Euler analysis for an isolated wing developed in ref. 22 has been recently extended to propfans. This extended version of the code is being utilized to study the effect that propfan angle-of-attack has on the unsteady blade loading of a single rotation propfan design. The code is capable of modeling the complete propfan configuration. The program will be used to predict the unsteady loading on the propfan recently tested in a two-bladed configuration as part of the Large-Scale Advanced Propfan (LAP) program. Part of the objective of this test program was to obtain detailed steady and unsteady blade surface pressure measurements for benchmarking computer models. Presently this computer program assumes that the blades are rigid. It is planned to look at the formulation and coding necessary to allow the blades to respond to the unsteady loading thus allowing the program to be used in aeroelastic forced response predictions. Sample pressure contours on blades of a propfan are shown in figure 22.

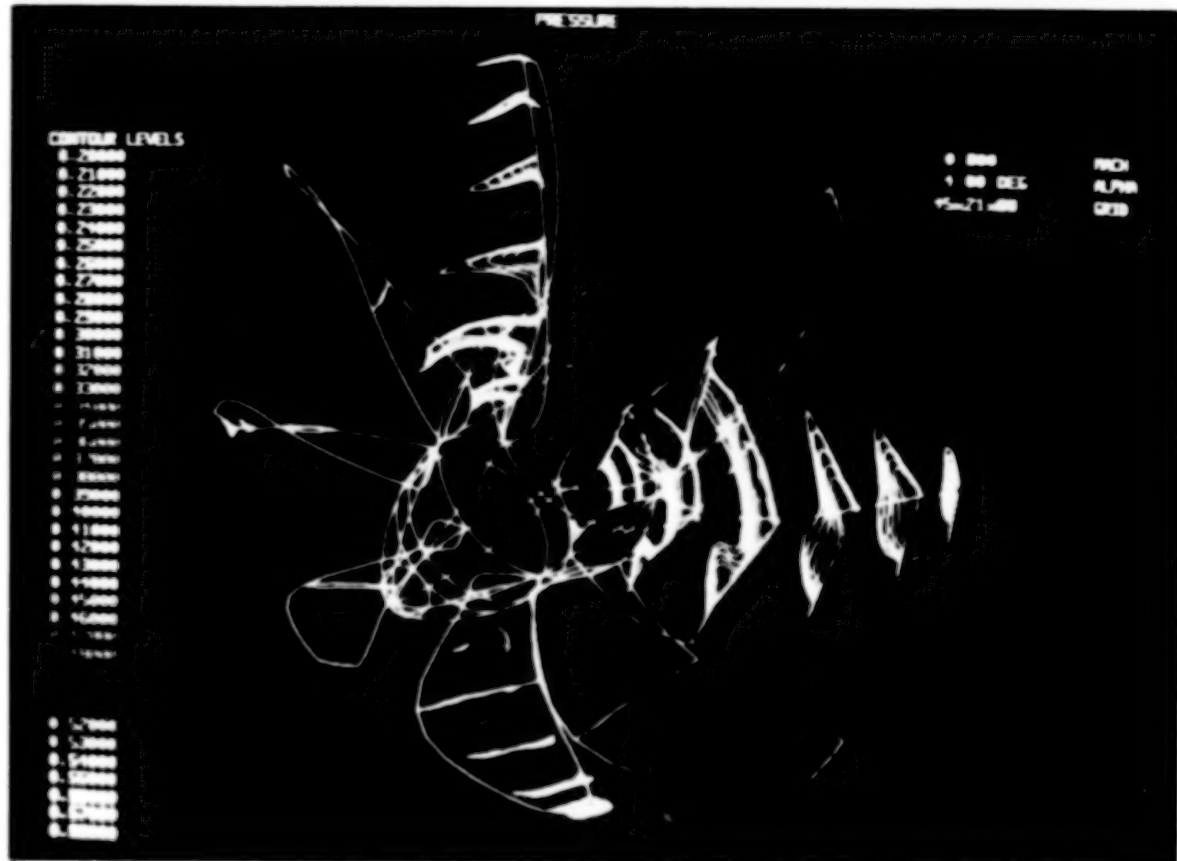


Figure 22

2-D Unsteady Perturbation Analysis for Cascades

In order to study the effect that blade sweep has on the flutter behavior of a cascade of airfoils operating in the transonic flow regime, the linearized unsteady analysis developed in ref. 17 is being utilized. This analysis predicts the unsteady loading resulting from small amplitude harmonic motion of the blades in a two-dimensional cascade operating in an inviscid subsonic or transonic flow. The unsteady potential is obtained from a perturbation analysis applied to the steady flow solution. Thus, the unsteady analysis is able to include the effects of finite mean loading on the unsteady response. At LeRC, the transonic potential code developed in reference 23 is utilized in calculating the steady flow field. Sample unsteady pressures calculated for a cascade of NACA 0012 airfoils (at Mach number 0.6, stagger angle 45° and mean incidence angle 9°) by using the combined code are shown in figure 23. The combination of these steady and unsteady programs allows for the prediction of the flutter behavior of fan and propfan designs which include the effect of realistic reduced frequencies and blade geometries. The resulting computer program will be benchmarked against experimental cascade data and then applied to study the effect that blade sweep has on the flutter behavior of a cascade of airfoils.

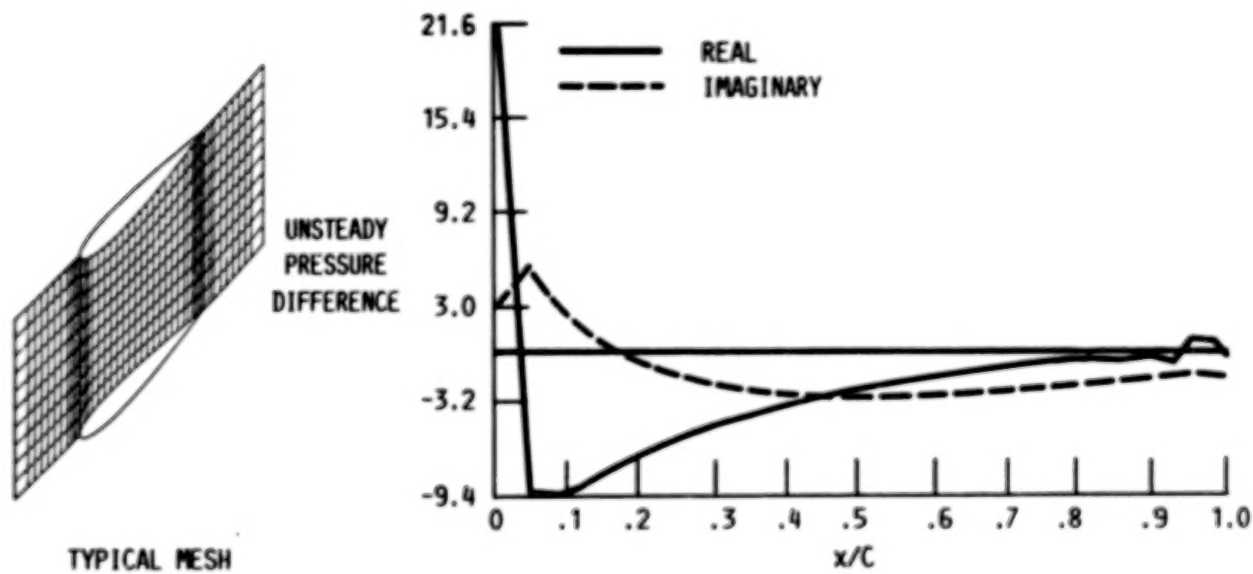
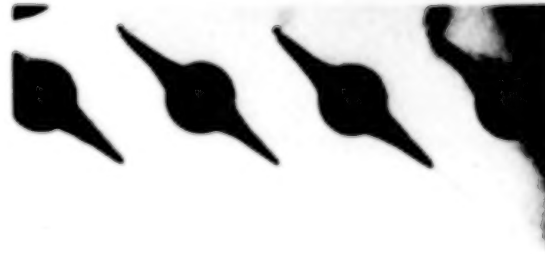
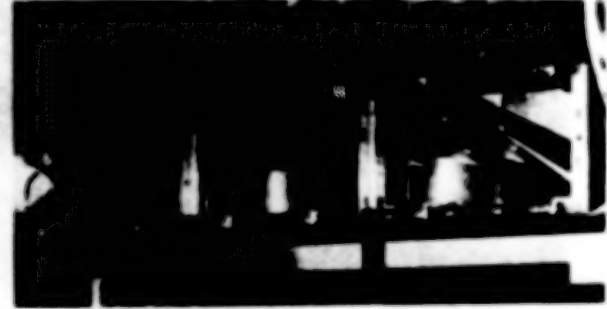


Figure 23

Unsteady Swept Cascade Experiments

The effect of blade sweep on the flutter behavior of a cascade of airfoils is being studied in the transonic oscillating cascade facility, figure 24. This study is being conducted to determine if classical sweep corrections applicable for fixed wing flows are valid for oscillating airfoils in a torsional motion while maintaining a selected interblade phase angle between adjacent blades. The unsteady loading is determined by a number of blade mounted high response pressure transducers. The initial phase of testing will involve the use of unswept airfoils in order to provide a baseline set of data for benchmarking the computer programs to be used in this study. The swept airfoils will then be installed and a series of tests will be run to determine the effect of incidence angle, Mach number, reduced frequency and interblade phase angle on the flutter behavior of the swept cascade.



UNSWEPT BLADE TEST PROVIDES
BASELINE DATA

Figure 24

Three-Dimensional Gust Model for a Propeller Blade

A propeller blade (figure 25) rotating in a nonuniform upstream flow encounters an unsteady flow field, even when the nonuniform upstream flow is steady. For straight bladed propellers, the unsteady flow of the propeller can be approximated by a two-dimensional wing in a three-dimensional gust as shown in figure 25. For small amplitude disturbances, the unsteady flow field may be obtained as a perturbation about the underlying steady flow. The governing equation is a linear, nonconstant coefficient, inhomogenous, convective wave equation, see refs. 24 and 25. A finite difference scheme is used to solve for the perturbation potential. Some sample results are shown in figure 26.

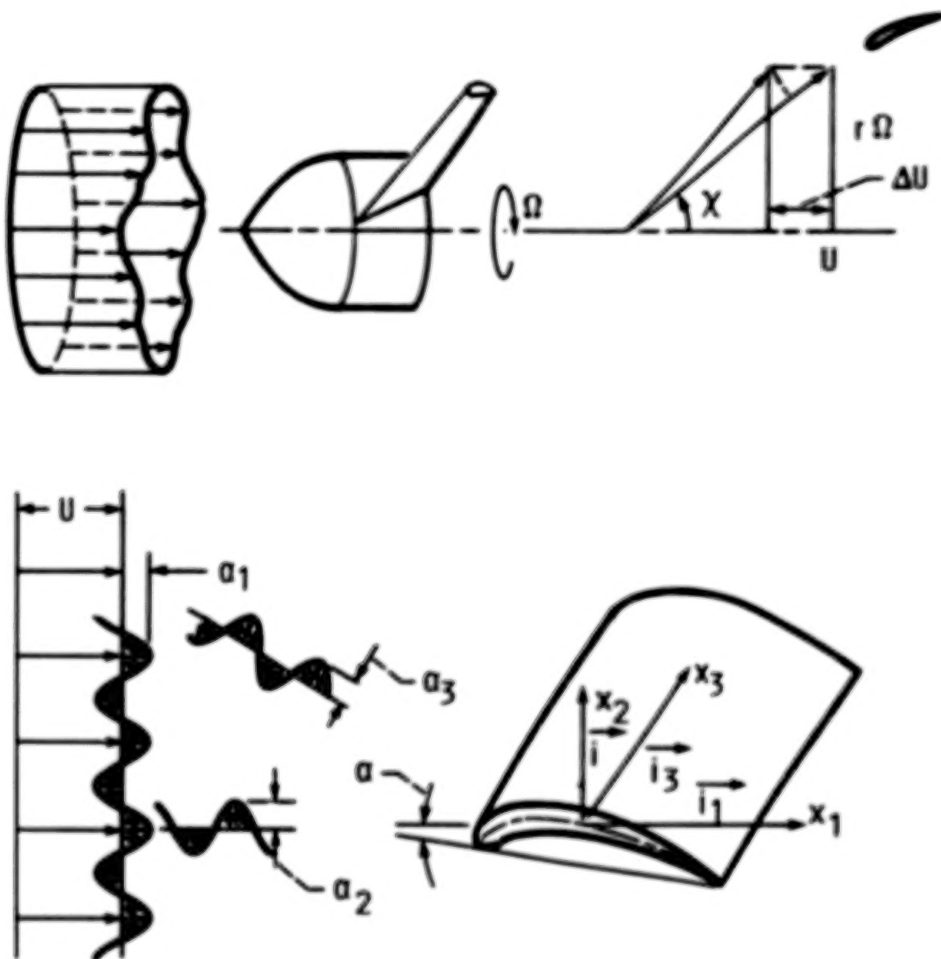


Figure 25

Variation of Unsteady Lift Coefficient
of 12% Thick, Symmetric Joukowski
Airfoil in a Transverse Gust

The governing wave equation for the model described in figure 25 is solved for perturbation potential by using a finite differencing scheme. For a symmetric airfoil in a transverse gust the real and imaginary parts of the lift at Mach number 0.6 and with reduced frequency as parameters are shown in figure 26. Also included in the figure is the corresponding curve for the flat plate. Comparing the flat plate and 12% thick airfoil results, it is observed that the thickness effects on the lift are more significant at low reduced frequencies. Similar comparisons (not shown) are also made at different Mach numbers, and it was found that the thickness effects on lift are more significant at higher Mach numbers.

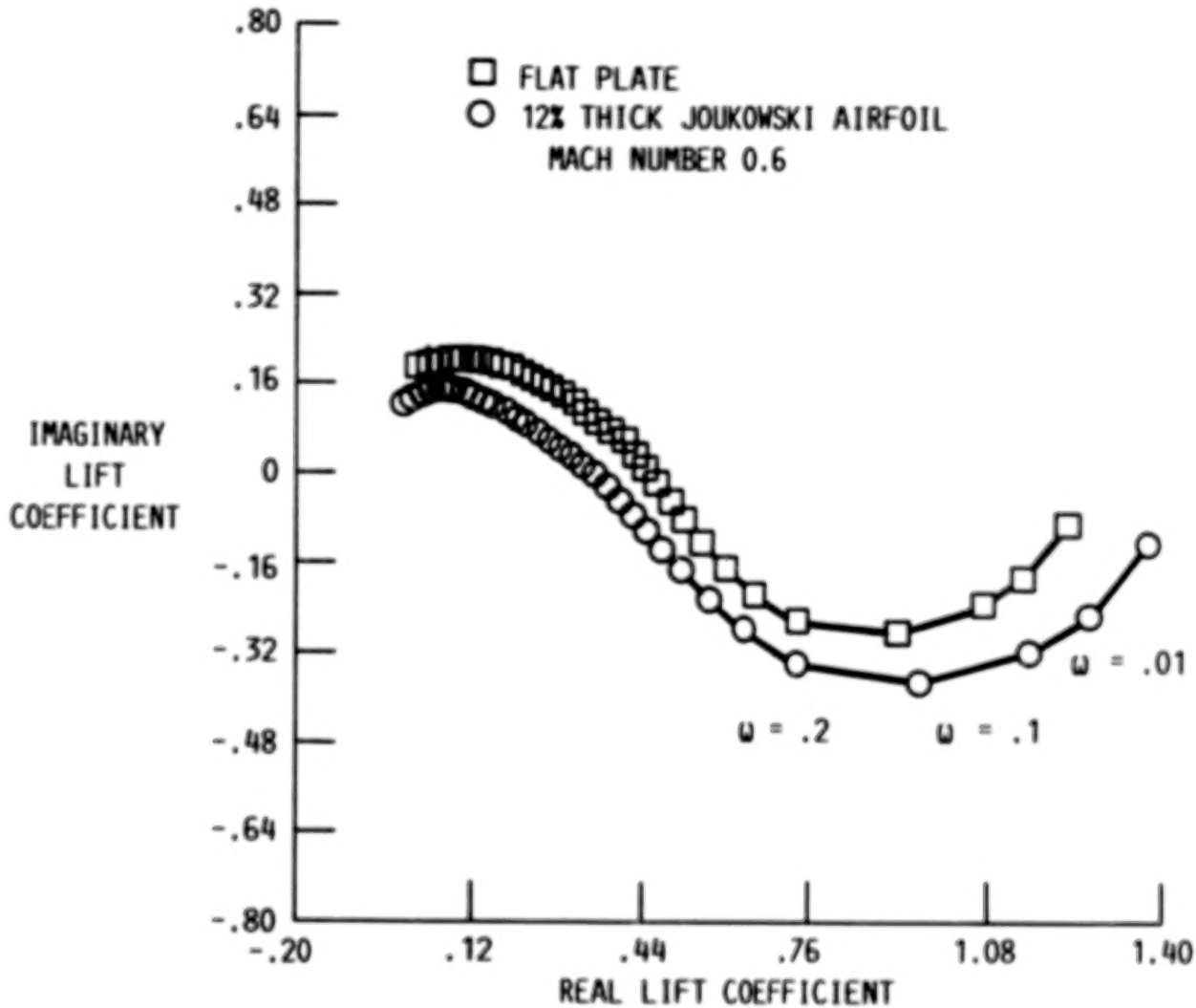


Figure 26

Numerical Simulation of Flow Through
Counter Rotating Propfans - Average
Passage Flow Model

A new analytical model, referred to as "average passage flow model," is being developed in reference 26 for simulating flows through counter rotating propfans. It describes the three-dimensional time-average flow field within a typical passage of a blade run in a multiblade run configuration. The model has been used to examine the flow field generated by a counter rotating propfan configuration (UDF). For example, the pressure field radiated by the aft fan is shown in figure 27. The pressure field is color-coded with a spectrum ranging from blue (low pressure) to green to yellow to red (high pressure). The boundary between green (lower pressure) and yellow-orange (higher pressure) regions is the footprint of the aft propfan trailing-edge shock. The base of the shock lies at approximately three-quarters of the span. From this point it appears to spiral outward beyond the tip of each blade.



Figure 27

Application of "Average Passage Flow Model"
for CR Propfan Noise Prediction

The average passage flow model developed in ref. 26 was merged with an aeroacoustic prediction model for CR propfans developed by Dr. F. Farassat of NASA Langley Research Center. This merger permits the simultaneous evaluation of aerodynamic performance and radiated sound levels. Figure 28 shows a comparison of the predicted sound levels with corresponding measured data of the CR scaled model by Dr. J. H. Dittman of NASA Lewis Research Center. The correlation between theory and experiment is excellent.

2' GE F7/A7, LeRC 8x6 WIND TUNNEL, DESIGN CONDITION (M=0.72)

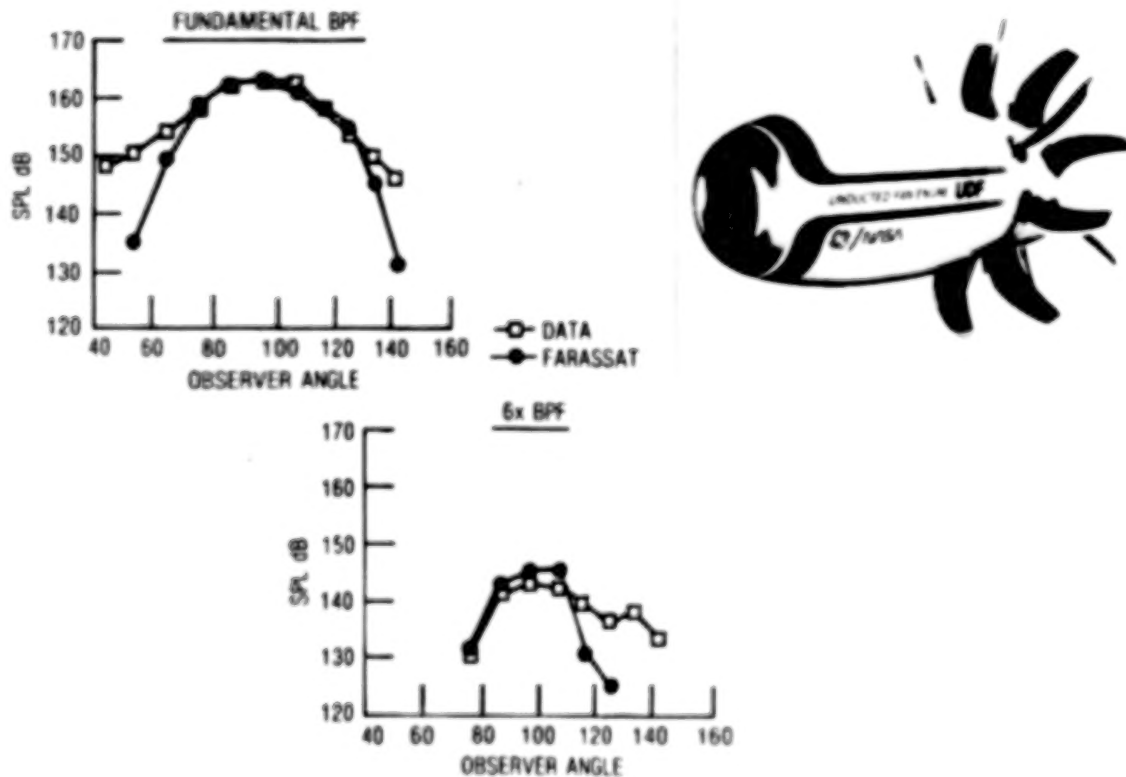


Figure 28

LeRC Groups Involved in Unsteady Aerodynamics and Aeroelasticity

The groups in the unsteady aerodynamics and aeroelasticity effort at LeRC are shown in figure 29. Also listed in the figure are the names of NASA LeRC employees, Support Service Contractors and Grantees, who contributed to the research effort described in the paper.

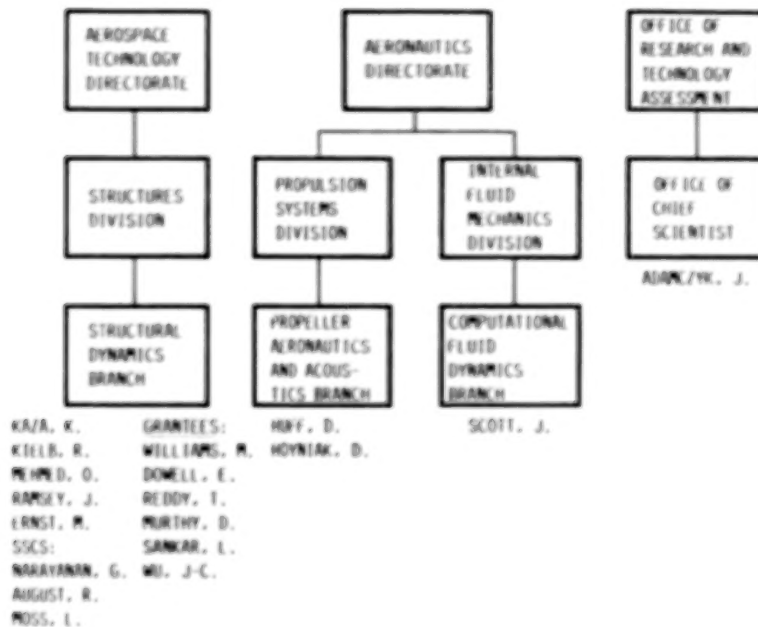


Figure 29

LeRC Unsteady Aerodynamics and Aeroelasticity Effort

The elements of the overall research effort in the subject area are shown in figure 30. These elements cover the development of unsteady aerodynamic models, aeroelastic models (for flutter, forced response and optimization), associated computer programs, and wind tunnel flutter experiments.

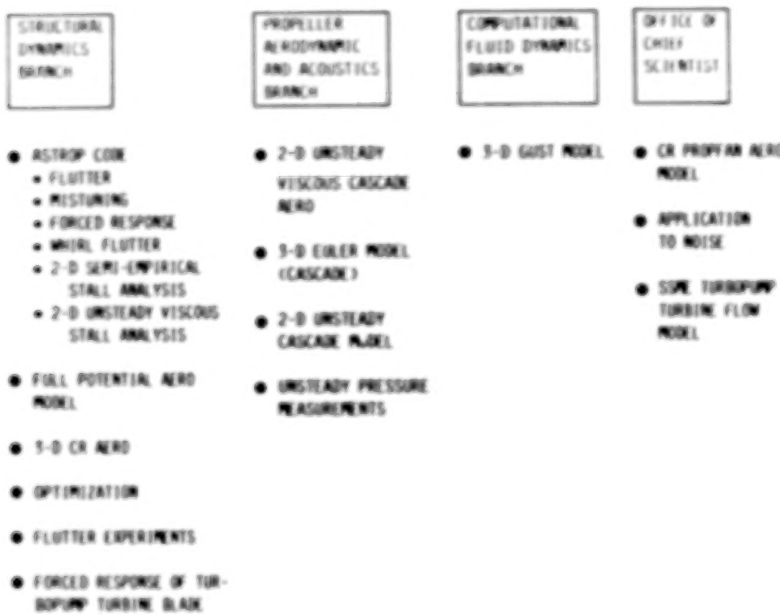


Figure 30

References

1. Kaza, K.R.V., Mehmed, O., Narayanan, G.V., and Murthy, D.V.: Analytical Flutter Investigation of a Composite Propfan Model. NASA TM 88944 1987, AIAA Paper No. 87-0738.
2. Williams, M.H., and Hwang, C.: Three Dimensional Unsteady Aerodynamics and Aeroelastic Response of Advanced Turboprops. AIAA 27th SDM Conference, part II, 1986, pp. 116-124.
3. The Nastran Theoretical Manual, NASA SP-221(06) 1981.
4. Chamis, C.C.: "Integrated Analysis of Engine Structures. NASA TM-82713, 1981.
5. Mehmed, O., and Kaza, K.R.V.: Experimental Classical Flutter Results of a Composite Advanced Turboprop Model. NASA TM-88972, 1986.
6. Rao, B.M., and Jones, W.P.: Unsteady Airloads for a Cascade of Staggered Blades in Subsonic Flow. Unsteady Phenomena in Turbomachinery, AGARD CP-177, AGARD, France, 1976, pp. 32-2 to 32-10.
7. Kaza, K.R.V., Mehmed, O., Williams, M., and Moss, L.: Analytical and Experimental Investigation of Mistuning in Propfan Flutter. NASA TM 88959 1987, AIAA Paper No. 87-0739.
8. Mehmed, O., Kaza, K.R.V., Lubomski, J.F., and Kielb, R.E.: Bending Torsion Flutter of Highly Swept Advanced Turboprop. NASA TM 82975, 1982.
9. Elchuri, V.: Modal Forced Vibration Analysis of Aerodynamically Excited Turbosystems. NASA CR 174966, July 1985.
10. Reddy, T.S.R., and Kaza, K.R.V.: A Comparative Study of Some Dynamic Stall Models. NASA TM 88917, 1987.
11. Gormont, R.E.: A Mathematical Model of Unsteady Aerodynamics and Radial Flow for Application to Helicopter Rotors. USAAMRDL TR-72-67, May 1973.
12. Gangwani, S.T.: Prediction of Dynamic Stall and Unsteady Airloads for Rotor Blades. J. Of American Helicopter Society, Vol. 27, No. 4, October 1982, pp. 57-64.
13. Wu, J.-C., and Kaza, K.R.V., and Sankar, L.N.: A Technique for the Prediction of Airfoil Flutter Characteristics in Separated Flow. AIAA Paper No. 87-0910-CP, 1987.
14. Farr, J.L., Traci, R.M., and Albano, E.D.: Computer Programs for Calculating Small Disturbance Transonic Flows About Oscillating Airfoils. AFFDL-TR-74-135, Nov. 1974.
15. Guruswami, D.M., and Yang, T.Y.: Transonic Time-Response Analysis of Thin Airfoils by Transonic Code LTRAN2. Computers and Fluids, Vol. 9, No. 4, pp. 409-425, 1981.

16. Smith, S.N.: Discrete Frequency Sound Generation in Axial Flow Turbomachines. A.R.C. R&M No. 3709, 1973.
17. Verdon, J.M., and Caspar, J.R.: "A Linearized Unsteady Aerodynamic Analysis for Transonic Cascades. NASA CR 168638.
18. Chen, S.H., and Williams, M.H.: Panel Method for Counter Rotating Propfans. AIAA Paper No. 87-1890, 1987.
19. Lesieur, D.J., and Sullivan, J.P.: Unsteady Forces on Counter-Rotating Propeller Blades. AIAA Paper No. 86-1804, 1986.
20. Sankar, L.N., and Tang, W.: Numerical Solution of Unsteady Viscous Flow Past Rotor Sections. AIAA Paper No. 85-0129.
21. Huff, D.: Numerical Simulations of Unsteady, Viscous, Transonic Flow over Isolated and Cascaded Airfoils Using a Deforming Grid. AIAA Paper No. 87-1316, 1987.
22. Whitefield, D.L., and Janus, J.M.: Three Dimensional Unsteady Euler Equations Solution Using Flux Vector Splitting. AIAA 84-1552, June 1981.
23. Farrel, C., and Adamczyk, J.: Full Potential Solution of Transonic Quasi-Three-Dimensional Flow Through a Cascade Using Artificial Compressibility. Journal of Engineering for Power, Jan. 1982, Vol. 104, pp. 143-153.
24. Goldstein, M.E.: Unsteady Vortical and Entropic Distortions of Potential Flows Round Arbitrary Obstacles. J. Fluid Mech., Vol. 89, Part 3, 1978, pp. 433-468.
25. Atassi, H.M., and Grzedzinski, J.: Unsteady disturbances of Streaming Motions Around Bodies. To appear in J. of Fluid Mechanics, 1987.
26. Adamczyk, J.F.: Model Equations for Simulating Flows in Multistage Turbomachinery. ASME Paper No. 85-GT-226, March 1985.

UNSTEADY AERODYNAMICS OF BLADE ROWS

Joseph M. Verdon
United Technologies Research Center
East Hartford, Ct.

INTRODUCTION

The requirements placed on an unsteady aerodynamic theory intended for turbomachinery aeroelastic or aeroacoustic applications will be discussed along with a brief description of the various theoretical models that are available to address these requirements. The major emphasis is placed on the description of a linearized inviscid theory which fully accounts for the affects of a nonuniform mean or steady flow on unsteady aerodynamic response. Although this linearization has been developed primarily for blade flutter prediction, more general equations will be presented which account for unsteady excitations due to incident external aerodynamic disturbances as well as those due to prescribed blade motions. In this presentation we will focus on the motivation for this linearized unsteady aerodynamic theory, outline its physical and mathematical formulation and present examples to illustrate the status of numerical solution procedures and several effects of mean-flow nonuniformity on unsteady aerodynamic response. This presentation is based on a paper of the same title which is published in full in the Proceedings of the Tenth U. S. National Congress of Applied Mechanics (ref 1).

- **Linearized unsteady aerodynamic analysis**
 - Real blade geometry
 - Mean blade loading
 - Shock phenomena
- **Design applications**
 - Aeroelastic
 - Blade flutter and forced vibration
 - Aeroacoustic
 - Noise generation, transmission and reflection

MAJOR ASSUMPTIONS

The development of theoretical models to predict unsteady flows through turbomachines is a formidable task. The analyst is confronted with determining the time-dependent, three-dimensional flow of a viscous compressible fluid through a geometric configuration of enormous complexity. This task has required the introduction of a considerable number of simplifying assumptions to make the problem mathematically tractable and to render the resulting solutions useful to designers. For the most part, the theoretical formulations that have been developed to predict the unsteady aerodynamic phenomena associated with blade flutter or forced vibration consider the blades of an isolated two-dimensional cascade, neglect viscous effects at the outset and regard unsteady fluctuations to be of sufficiently small amplitude so that a linearized treatment of the unsteady perturbation is justified. In addition the resulting two-dimensional inviscid flow is assumed to remain attached to the blade surfaces, the mean flow is assumed to be at most a small irrotational steady perturbation from a uniform stream at the cascade inlet, and any shocks that might occur are assumed to be of weak to moderate strength and have small curvature.

- **Isolated blade row**
- **Two-dimensional inviscid ($Re \rightarrow \infty$) flow**
- **Small-amplitude periodic unsteady excitations**
- **Attached flow**
- **Irrotational mean flow at Inlet:**
$$\vec{V} = \vec{V}_{\infty} + \nabla \bar{\phi}$$
- **Weak shocks**

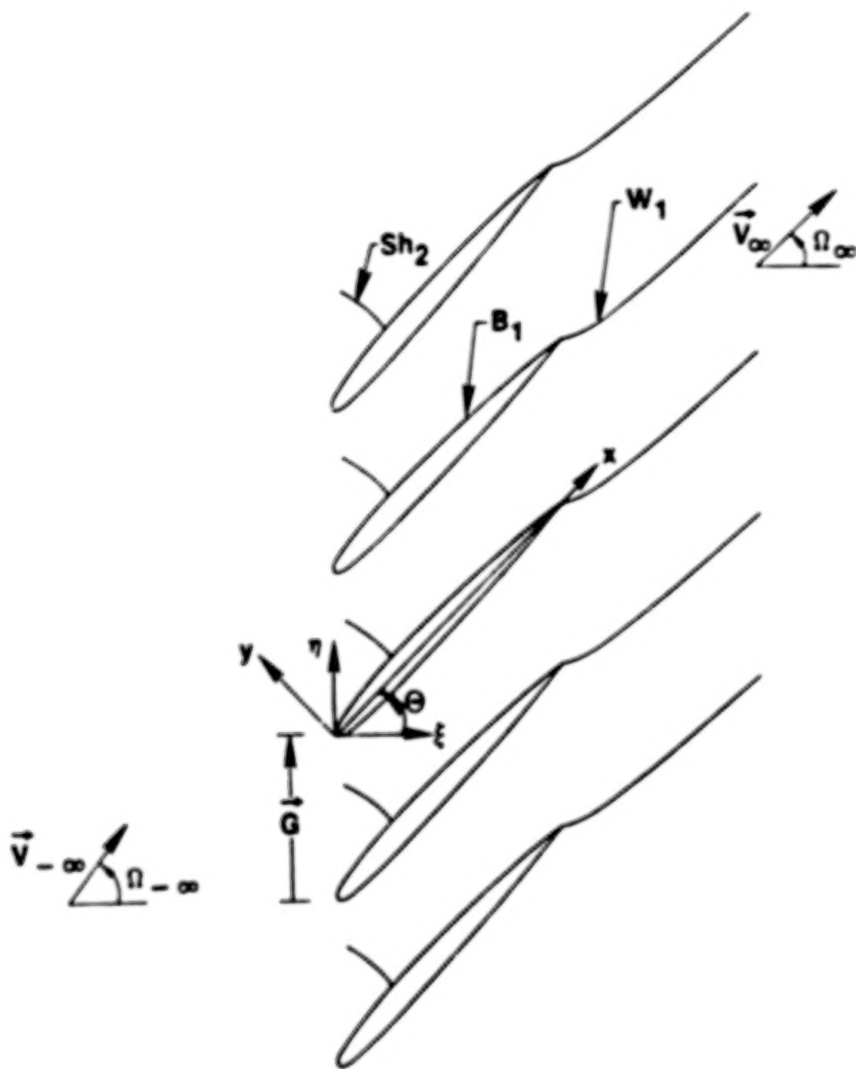
REQUIREMENTS

In general, the unsteady aerodynamic analyses intended for turbomachinery aeroelastic applications must be applicable to fan, compressor and turbine cascades, to subsonic, transonic and supersonic Mach numbers and to moderate through high frequency structural and external aerodynamic excitations. Then, to determine the aeroelastic and aeroacoustic characteristics of the blading such analyses must be capable of predicting the unsteady loads acting on the blades and the amplitude and wave numbers of the acoustic waves which carry energy away from the blade row and the entropic and vortical fluctuations which are convected downstream. These responses arise from the various sources of unsteady excitation including prescribed blade motions, variations in total temperature and pressure ("entropy and vorticity waves") at inlet, and variations in static pressure (acoustic waves) at inlet and exit. For blade flutter applications it is only necessary to predict the unsteady loads acting on the blades as a result of prescribed blade motions; for forced response applications the unsteady blade loads due to incident entropic, vortical and acoustic disturbances are also required. Finally, for aeroacoustic applications the parameters associated with far-field acoustic responses must be determined.

- **Fan, compressor and turbine cascades**
- **Subsonic, transonic, supersonic Mach numbers**
- **Moderate to high excitation frequencies**
- **Response predictions**
 - On blades: surface pressures, global unsteady airloads
 - Far field: outward propagating acoustic waves
vorticity and entropy variations downstream
- **Prescribed excitations**
 - Blade motions (flutter)
 - External aerodynamic disturbances (forced vibration)
 - Vortical and entropic disturbances at inlet
 - Acoustic disturbances at inlet and exit

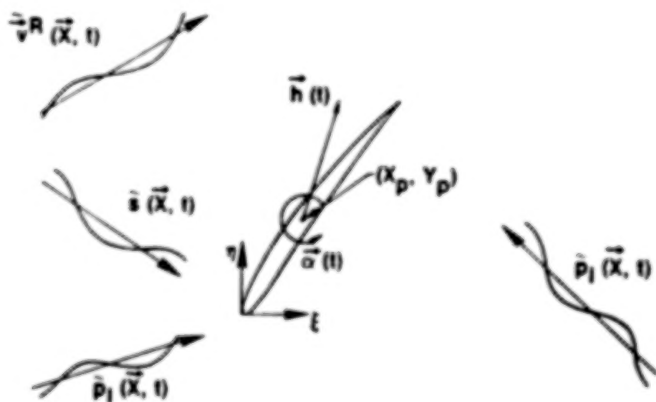
TRANSONIC CASCADE: $M_\infty < M_{-\infty} < 1$

A representative cascade configuration is shown in the figure below which depicts a two-dimensional section of a transonic compressor rotor ($M_\infty < M_{-\infty} < 1$). The cascade stagger angle is denoted by Θ and the blade spacing by G . In the absence of unsteady excitation the blades are identical in shape, equally spaced and their chord lines are oriented at the same angle, Θ , relative to the axial flow direction. The inlet and exit free-stream flows are described by the velocity vectors $\vec{V}_{\mp\infty}$. The free-stream flow angles measured relative to the axial-flow (or ξ -) direction are denoted by $\Omega_{\mp\infty}$. For the configuration illustrated the inlet and exit conditions are such that normal shocks (Sh) emanate from the blade suction surfaces and vortex wakes (W) emanate from the blade trailing edges and extend downstream.



UNSTEADY EXCITATIONS

The unsteady fluctuations in the flow arise from one or more of the following prescribed sources: blade motions, upstream and/or downstream acoustic disturbances which carry energy toward the blade row, and upstream entropic and vortical disturbances which are convected through the blade row by the mean flow. These excitations are assumed to be of small amplitude and periodic in time. The external aerodynamic excitations are also spatially periodic, while the structural excitation is periodic in the "circumferential" or η -direction. For example, we consider blade motions and incident acoustic disturbances as described below. Here \tilde{R} measures the displacement of a point on a moving blade surface relative to its mean or steady-state position, \vec{X} is a position vector, m is a blade number index, t is time, \vec{r}_B is the reference-blade ($m = 0$) complex displacement-amplitude vector, ω and σ are the temporal frequency and interblade phase angle, respectively, of the unsteady excitation and $Re\{ \cdot \}$ denotes the real part of $\{ \cdot \}$. Also, $p_{I,\mp\infty}$ and $\vec{\kappa}_{\mp\infty}$ are the amplitude and wave number, respectively, of an incident pressure fluctuation, $\tilde{p}_I(\vec{X}, t)$, coming from far upstream ($-\infty$) or far downstream ($+\infty$). Note that the interblade phase angle, σ , of an incident disturbance is $\vec{\kappa}_{\mp\infty} \cdot \vec{G}$. The temporal frequency and wave number of an incident vortical or entropic disturbance are related by $\omega = -\vec{\kappa}_{\mp\infty} \cdot \vec{G}$, but a more complicated relationship exists between ω and $\vec{\kappa}_{\mp\infty}$ for an incident pressure disturbance.



Blade motions: $\tilde{R}(\vec{X} + m\vec{G}, t) = Re \left\{ \vec{r}(\vec{X}) \exp [i(\omega t + m\sigma)] \right\}$

Incident disturbances: $\tilde{p}_{I,\mp\infty}(\vec{X}, t) = Re \left\{ p_{I,\mp\infty} \exp [i(\vec{\kappa}_{\mp\infty} \cdot \vec{X} + \omega t)] \right\}$

TIME-DEPENDENT GOVERNING EQUATIONS

The equations governing the fluid motion follow from the integral forms of the mass, momentum and energy conservation laws and the thermodynamic relations for a perfect gas. The former provide a coupled set of corresponding nonlinear differential equations (the Euler equations) in continuous regions of the flow and jump conditions at surfaces across which the inviscid flow variables are discontinuous, i.e., at vortex-sheet wakes and shocks. In continuous regions the energy equation can be replaced by the requirement that the entropy following a fluid particle must remain constant. In addition to the foregoing field equations and jump conditions, the attached flow assumption requires that the unsteady flow must be tangential to the moving blade surfaces and information on the uniform inlet and exit flow conditions and the incident entropic, vortical and acoustic or static pressure disturbances must be specified. The remaining steady and unsteady departures from the uniform inlet and exit conditions must be determined as part of the time-dependent solution. This foregoing aerodynamic problem is a formidable one as it involves a system of nonlinear time-dependent equations with conditions imposed on moving blade, wake and shock surfaces in which the instantaneous positions of the wakes and shocks must be determined as part of the solution. Because of these features and the prohibitive expense that would be involved in obtaining the aerodynamic response information needed for aeroelastic or aeroacoustic applications, the usual approach is to examine limiting forms of the full governing equations with the intention of providing efficient analyses for design applications.

- Integral conservation laws
- Thermodynamic relations



- Euler equations at field points
- Jump conditions at moving shocks ($\tilde{M}_f \neq 0$) and at vortex sheet boundary layers and wakes ($\tilde{M}_f = 0$)
- Flow tangency condition at moving blade surfaces



- Far-field behavior

UNSTEADY AERODYNAMIC LINEARIZATIONS

Because of the complexity of the nonlinear time-dependent unsteady aerodynamic problem, linearized treatments of the unsteady flow are often considered. The major linearizations that have been proposed are the following: classical linearized theory, time-linearized transonic flow theory and the present theory in which unsteady disturbances are regarded as small relative to a fully nonuniform mean flow. The essential differences between these theories arise from the manner in which the steady flow is represented. In classical theory both steady and unsteady departures from a uniform stream are regarded as small and of the same order of magnitude. In time-linearized transonic theory steady and unsteady disturbances are regarded as small and very small, respectively, relative to uniform free-stream flow properties. Finally, in the present linearization no restriction is placed on the steady flow but the unsteady perturbations are assumed to be of small amplitude. The classical theory applies at the (reduced) frequencies of interest for turbomachinery applications, but steady flow variations have no impact on the unsteady response. Time-linearized transonic theory applies at Mach numbers near one and the unsteady perturbation depends on the steady flow, but this theory is formally restricted to low-frequency unsteady motions. The present theory fully includes the effects of nonuniform mean flow and applies throughout the Mach number and frequency range of interest for turbomachinery applications.

● Classical theory

$$\tilde{P}(x, y, t) = P_{-\infty} + \bar{p}(x, y) + \operatorname{Re} \left\{ p(x, y) e^{i\omega t} \right\} + \dots$$

● Time-linearized transonic theory

$$\tilde{P}(x, y, t) = P_{-\infty} + \bar{p}(x, \hat{y}) + \operatorname{Re} \left\{ p(x, \hat{y}) e^{i\omega t} \right\} + \dots$$

● Present theory

$$\tilde{P}(x, y, t) = P(x, y) + \operatorname{Re} \left\{ p(x, y) e^{i\omega t} \right\} + \dots$$

PRESENT LINEARIZATION

The equations governing small-amplitude unsteady departures from a nonuniform mean flow are determined by expanding the various flow variables in asymptotic series in ϵ , where ϵ is a measure of the amplitude of the unsteady excitation. Thus, for example, in the first equation below $\tilde{P}(\vec{X}, t)$ is the time-dependent fluid pressure, $P(\vec{X})$ is the pressure in the steady background flow, $\text{Re}\{p(\vec{X})e^{i\omega t}\}$ is the first-order time-dependent pressure and $p(\vec{X})$ is its complex amplitude. In addition, Taylor series expansions and surface vector relations are used to refer information at a moving blade, wake or shock surface (\mathcal{S}) to the mean position of this surface (S). Equations governing the zeroth-order or steady and the complex amplitudes of the first-order unsteady flow properties are obtained after substituting the foregoing expansions into the full time-dependent governing equations, equating terms of like power in ϵ and neglecting terms of higher than first order in ϵ . It follows from the original assumptions that the steady background flow is governed by a full-potential boundary-value problem and that the complex amplitudes of the unsteady flow properties are governed by a system of time-independent linearized equations with variable coefficients which depend on the underlying mean flow. In the unsteady problem surface conditions can be imposed at the mean surface locations, and in both the steady and first-order unsteady problems the required solution domain can be limited to a single extended blade-passage region.

● Series expansions

$$\tilde{P}(\vec{X}, t) = P(\vec{X}) + \text{Re}\{p(\vec{X})e^{i\omega t}\} + \dots$$

$$\tilde{P}_{\mathcal{S}} = (\tilde{P} + \vec{R} \cdot \nabla \tilde{P} + \dots)_{\mathcal{S}}$$

$$\tilde{\tau}_{\mathcal{S}} = f(\tilde{\tau}_{\mathcal{S}}, \vec{R}) + \dots$$



- Full potential boundary-value problem for steady background flow
- Linear variable-coefficient boundary-value problem for first-order unsteady flow
 - Time-independent
 - Surface conditions at mean surface locations
 - Single extended blade-passage solution domain

THE STEADY BACKGROUND FLOW

As a consequence of our assumptions regarding shocks and the steady flow far upstream of the blade row, the mean or steady background flow through the cascade will be homentropic and irrotational; i.e., $\vec{V} = \nabla\Phi$, where \vec{V} and Φ are the local steady velocity and velocity potential, respectively. The field equations governing the steady flow follow from the mass and momentum conservation laws and the isentropic relations for a perfect gas. Here, $\bar{\rho}$, P , M and A are the local steady density, pressure, Mach number and speed of sound propagation, respectively, and γ is the specific heat ratio of the fluid. Surface conditions for the zeroth-order or steady flow apply at the mean positions of the blade (B), wake (W) and Shock (Sh) surfaces. Blade mean positions are prescribed, but the mean wake, i.e., the stagnation streamlines downstream of the blade row, and shock positions must be determined as part of the steady solution. Since, by assumption, the flow remains attached to the blades, a flow tangency condition applies at blade surfaces. In addition the steady pressure and normal velocity component must be continuous across blade wakes and mass and tangential momentum must be conserved at shocks. Finally, three of the far-field uniform velocity components, or the equivalent information, must be prescribed to completely specify the steady boundary-value problem. The fourth or remaining component can be determined in terms of the three prescribed using the integral form of the mass conservation law.

- **Field equations** : $\nabla \cdot (\bar{\rho} \nabla \Phi) = 0$

$$\bar{\rho}^{(\gamma-1)} = (\gamma M_{-\infty}^2 P/2)^{(\gamma-1)/\gamma} = (M_{-\infty} A)^2 = F(\nabla \Phi)$$

- **Surface conditions**

- **Blades** (B): $\nabla \Phi \cdot \vec{n} = 0$

- **Wakes** (W): $[\nabla \Phi] \cdot \vec{n} = 0, [\Phi] = \text{constant}$

- **Shocks** (Sh): $[\bar{\rho} \nabla \Phi] \cdot \vec{n} = [\Phi] = 0$

- **Far-field conditions**

- **Uniform flow conditions**

- **Analytic solutions for steady disturbances**

THE LINEARIZED UNSTEADY FLOW - I

The field equations governing the first-order unsteady perturbation of a nonlinear homentropic and irrotational steady flow are determined from the full time-dependent mass, momentum and entropy transport equations and the thermodynamic equation relating the entropy, pressure and density of a perfect gas. These equations can be cast in a convenient form by introducing the Goldstein (ref. 2) velocity decomposition, i.e., $\vec{V} = \vec{v}^R + \nabla\phi$. The rotational component of the unsteady velocity (\vec{v}^R) is divergence-free far upstream of the blade row and it is independent of the pressure fluctuation (p); the irrotational component ($\nabla\phi$) is related directly to the unsteady pressure fluctuation. The resulting field equations for the first-order entropy (s), rotational velocity (\vec{v}^R) and velocity potential (ϕ) are given below. First-order partial differential equations describe the transport of entropy and rotational velocity through the blade row. The unsteady potential is governed by a second-order equation, which is locally elliptic at field points at which the local steady Mach number (M) is less than one and locally hyperbolic at those points at which $M > 1$. Note that the rotational velocity provides a forcing function term to the potential equation. Also, if there are no entropy and rotational velocity fluctuations at inlet, then only a single field equation must be solved to determine the unsteady flow.

● Velocity decomposition : $\vec{V} = \vec{v}^R + \nabla\phi$

where $\vec{v}^R = f(s_{-\infty}, \vec{v}_{-\infty}^R, \nabla\Phi)$ and $p = -\bar{\rho} \frac{D\phi}{Dt}$

● Field equations

$$\frac{\bar{D}s}{Dt} = 0$$

$$\frac{\bar{D}}{Dt} (\vec{v}^R - s \nabla\Phi/2) + [(\vec{v}^R - s \nabla\Phi/2) \cdot \nabla] \nabla\Phi = 0$$

$$\frac{\bar{D}}{Dt} (A^{-2} \frac{\bar{D}\phi}{Dt}) - \bar{\rho}^{-1} \nabla \cdot (\bar{\rho} \nabla\phi) = \bar{\rho}^{-1} \nabla \cdot (\bar{\rho} \vec{v}^R)$$

THE LINEARIZED UNSTEADY FLOW 2

Conditions on the linearized unsteady perturbation at Blade (B), wake (W) and shock (Sh) mean positions are obtained in a similar fashion, i.e., by substituting the asymptotic, Taylor and surface-vector series expansions into the full time-dependent surface conditions and equating terms of like order in ϵ . The resulting first-order flow tangency, wake-jump (continuity of normal velocity and pressure) and shock-jump (conservation of mass and tangential momentum) conditions are indicated schematically below. Note that the blade displacement (\vec{r}_B) is prescribed but that the normal(to the shock) component of the shock displacement ($\vec{r}_{Sh} \cdot \vec{n}$) must be determined as part of the unsteady solution. Wake displacements have no impact on the linearized unsteady problem. In addition to the surface conditions, we require information on the unsteady flows far upstream and far downstream from the blade row. In these regions the linearized unsteady equations reduce to the constant coefficient equations of classical linearized theory, and analytic solutions for the velocity potential fluctuations (ϕ^P) due to acoustic response disturbances and the far-downstream potential fluctuations (ϕ^R) associated with the vortical or rotational velocity disturbances can be determined. These analytic far-field solutions can be matched to near-field numerical solutions, and they thereby serve to complete the specification of the linearized unsteady boundary-value problem (ref. 3).

● Surface conditions

- **Blades:** $\phi_n = f(\Phi, \vec{r}_B, \vec{v}^R)$

- **Wakes:** $[\phi_n + \vec{v}_n^R] \cdot [p] = 0$

- **Shocks:** $[F(\Phi)\phi + G(\Phi)\phi_n] = f(\Phi, \vec{r}_{Sh,n}, \vec{v}^R)$

$$\vec{r}_{Sh,n} = -[\phi]/[\phi_n], [s] = [\vec{v}^R] = 0$$

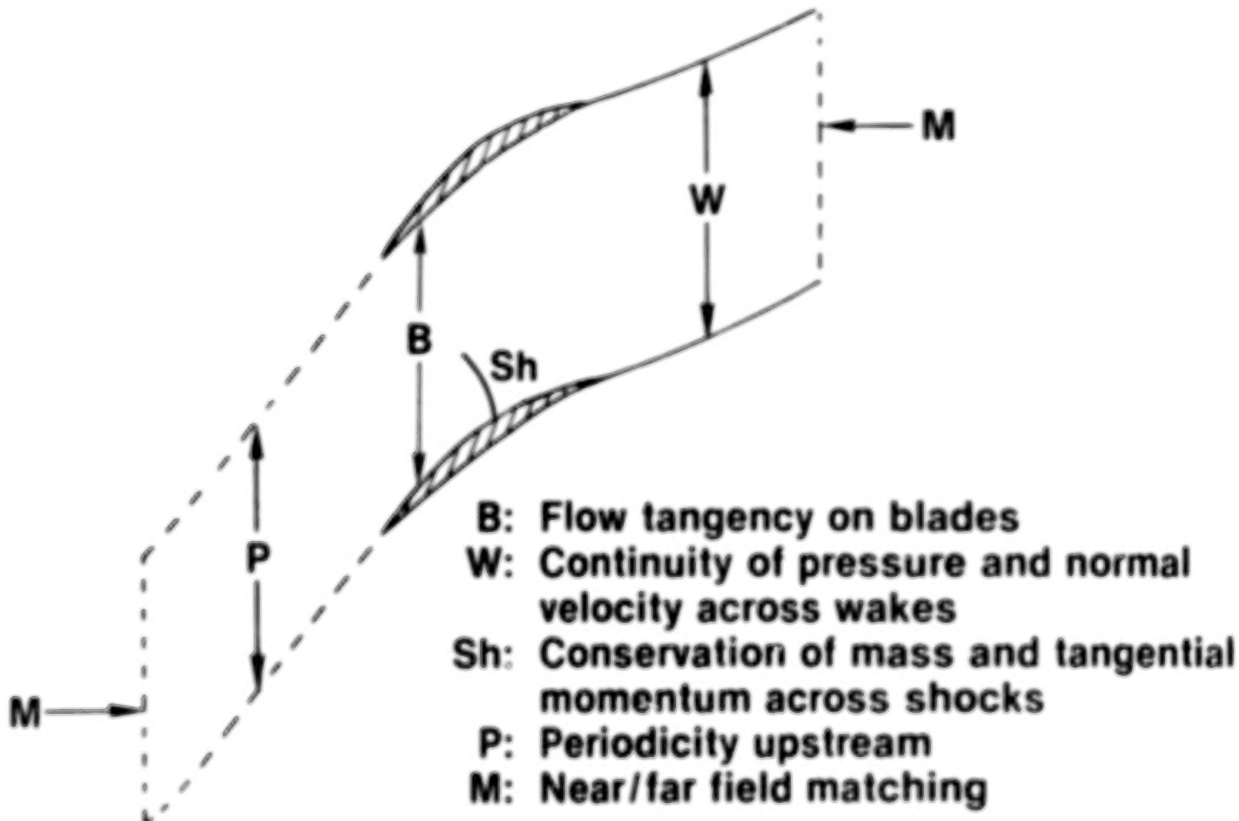
● Far - field conditions

$$s_{-\infty}, \vec{v}_{-\infty}^R \text{ Prescribed}$$

$$\phi_{\infty} = \frac{\phi_{IN}^P + \phi_{OUT}^P}{\text{Prescribed}} + \phi^R$$

NUMERICAL SOLUTION DOMAIN

The foregoing steady and linearized unsteady boundary-value problems account for the effects of blade geometry, mean blade loading and transonic, including moving shock, phenomena on the unsteady fluctuations arising from small-amplitude harmonic excitations. The unsteady equations are linear, time-independent and contain variable coefficients which depend on a fully nonlinear homentropic and irrotational steady background flow. Numerical resolutions of the nonlinear steady and the linearized unsteady problems are required to determine the aerodynamic response information needed for aeroelastic and aeroacoustic applications. Because of the cascade geometry and the assumed form of the unsteady excitations (i.e., periodic in t and η), such resolutions are required only over a single extended blade-passage region. In addition, since analytic far-field unsteady solutions have been determined, the numerical solution domain can be restricted further to a single extended blade-passage region of finite extent in the axial direction as shown below.

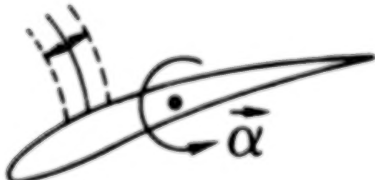


AERODYNAMIC RESPONSE AT A BLADE SURFACE

For aeroelastic and aeroacoustic applications, solutions to the nonlinear steady and the linearized unsteady boundary-value problems are required to predict the unsteady aerodynamic response at a moving blade surface (i.e., the unsteady surface pressures and the global unsteady airloads) and in the far-field (i.e., the unsteady pressure fluctuations), respectively. In particular, the pressure acting at the instantaneous position (\mathcal{B}) of a given blade surface is made up of two components: a harmonic component (p_H) which is determined by the steady (Φ) and the linearized unsteady (ϕ) potentials and the prescribed blade displacement (\vec{r}_B), and an anharmonic component (p_{Sh}) which is caused by the motion ($r_{Sh,B}$) of a shock along the blade surface. The anharmonic pressure is determined by analytically continuing the solution to the steady boundary-value problem from the mean to the instantaneous shock location (ref. 4). Although the pressure disturbance p_B is not everywhere harmonic, its regions of an harmonicity are small. Consequently, the first order global unsteady airloads are harmonic in time (ref. 5). In particular, if each two-dimensional blade section undergoes a pitching oscillation ($\vec{r}_B = \vec{\alpha} \times \vec{R}_p$) about an axis fixed to the blade, the first-harmonic unsteady moment is determined by integrating the product of the first-harmonic component of the unsteady surface pressure and $\vec{R}_p \cdot \vec{\tau}$ over the mean blade surface and subtracting a term consisting of the product of the steady pressure jump across the shock, $\vec{R}_p \cdot \vec{\tau}$ and the shock displacement along the blade surface.

Surface pressure

$$p_B = p_H(\Phi, \phi, \vec{r}_B) + p_{Sh}(\Phi, r_{Sh,B}, t) + \dots$$



Unsteady moment

$$m = \oint p_H \vec{R}_p \cdot d\vec{\tau} - r_{Sh,B} [p_B] (\vec{R}_p \cdot \vec{\tau}) \Big|_B + \dots$$

NUMERICAL RESULTS

At this point we have completed our description of the unsteady aerodynamic model and proceed to present numerical results to partially illustrate the status of numerical procedures for solving the nonlinear steady and linearized unsteady boundary-value problems and to demonstrate several important effects associated with nonuniform steady flow on the aerodynamic response at a moving blade surface. We refer the reader to refs. (6 and 7) for a description of the numerical procedures used. We will present results for two-dimensional compressor- or fan-type cascades operating at subsonic inlet and exit conditions. Theoretical results for steady surface Mach number (M) distributions, first-harmonic unsteady pressure-difference (Δp_H) distributions and unsteady aerodynamic moments (m) will be presented for blades undergoing pure pitching (torsional) motions with $\alpha = 1, 0$ about their midchords. The stability of such motions depends upon the sign of the out-of-phase moment (m_I). If $m_I > 0$, the airstream supplies energy to the blade motion, and this motion is unstable according to linearized theory. We will consider a subsonic cascade of NACA 0012 airfoils to illustrate the effects of a relatively thick, blunt-nosed blade geometry and variable mean incidence on the unsteady response and a subsonic/transonic cascade of 5% thick flat-bottomed double-circular-arc (DCA) airfoils to illustrate the effects of mean blade loading and transonic phenomena on the response at high subsonic inlet Mach number. For purposes of comparison results for flat-plate cascades, operating in uniform mean flows will be included along with those for the NACA 0012 and DCA cascades. The example cascades each have a stagger angle Θ of 45 deg and a unit gap/chord ratio ($G = 1$). The steady flows through the NACA 0012 and DCA cascades have been determined by imposing a zero-load condition at sharp blade edges.

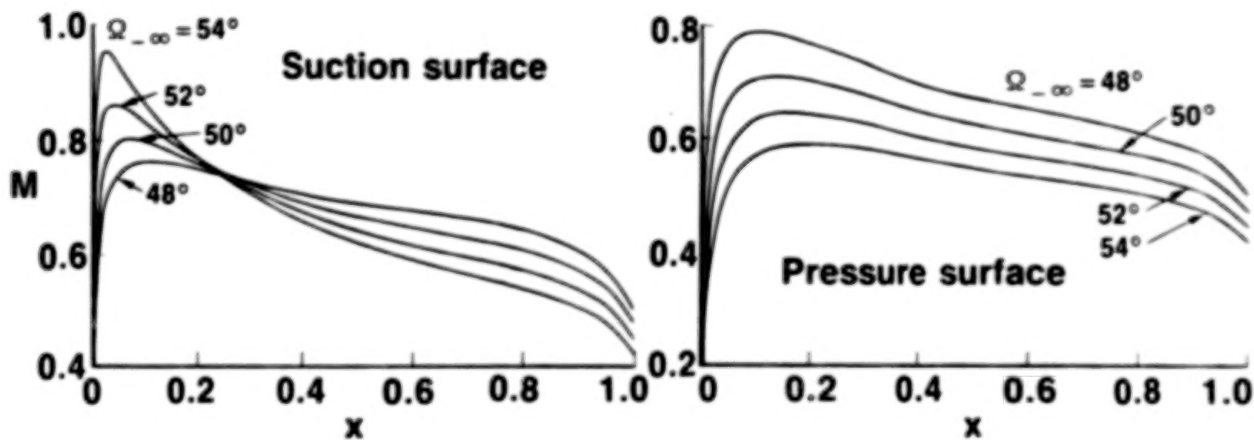
- **Torsional vibrations about midchord: $r_B = (\vec{\alpha} \times \vec{R}_p)$**
- **Response parameters: Δp_H and m**
- **Subsonic flow: NACA 0012 airfoils**
- **Subsonic/transonic flow: DCA airfoils**



AF2
1/2

SUBSONIC FLOW: EFFECT OF INCIDENCE - 1

Steady and unsteady flows through the staggered cascade of modified NACA 0012 airfoils have been determined for an inlet Mach number (M_{∞}) of 0.6 and four inlet flow angles. The predicted surface Mach number distributions for $\Omega_{\infty} = 48, 50, 52$ and 54 deg are shown below. The calculated exit Mach numbers are respectively 0.595, 0.557, 0.522 and 0.490, and in each case the calculated exit flow angle is approximately 47.7 deg. These steady flows are entirely subsonic with a peak Mach number of 0.789 occurring at $x = 0.113$ on the pressure (lower) surface of the blade for $\Omega_{\infty} = 48$ deg, and 0.8, 0.86 and 0.96 occurring at $x = 0.07, 0.05$ and 0.03 on the suction (upper) surface for $\Omega_{\infty} = 50, 52$ and 54 deg, respectively. In each case the mean flow stagnates within 0.2% of blade chord downstream from the leading edge.

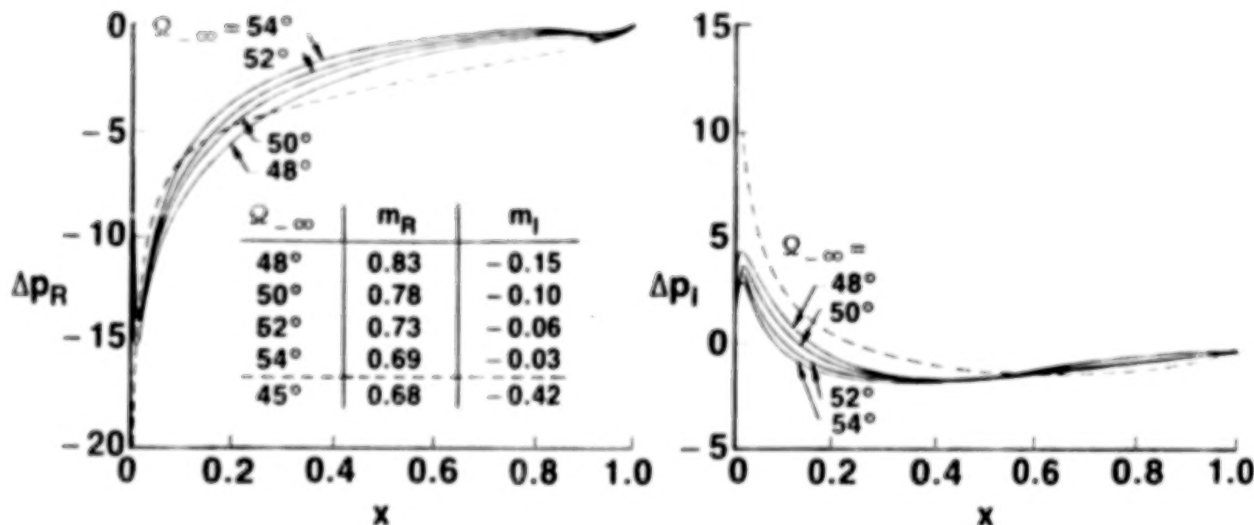


SUBSONIC FLOW: EFFECT OF INCIDENCE - 2

Unsteady response predictions for the NACA 0012 cascade and for a flat-plate cascade operating at $M_{\infty} = 0.6$ and $\Omega_{\infty} = 45^\circ$ are shown on this and the next two figures. Shown below are unsteady pressure-difference distributions and aerodynamic moments for the reference ($m = 0$) NACA 0012 and flat-plate blades undergoing unit-frequency pitching motions at $\sigma = 90$ deg. The unsteady pressure difference is singular and behaves like a multiple of $x^{-1/2}$ near the leading edge of the flat-plate airfoil. In contrast, the unsteady pressure is analytic in the vicinity of the rounded leading edge of the NACA 0012 blade. In this case both the real and imaginary components of the unsteady pressure difference are zero at the leading edge and reach local extrema very close to the leading edge. The results indicate that the coupling between the steady and unsteady flows, due to blade geometry and mean loading, leads to a reduction in the out-of-phase pressure difference, $Im\{\Delta p(x)\}$, over a forward part of the NACA 0012 blade and, therefore, a reduction in the out-of-phase moment opposing the blade motion.

Unsteady pressure difference distributions: NACA 0012 cascade;
 $\Theta = 45^\circ$, $G = 1.0$, $M_{\infty} = 0.6$, $\omega = 1.0$, $\sigma = 90^\circ$.

— NACA 0012 cascade, - - - flat-plate cascade

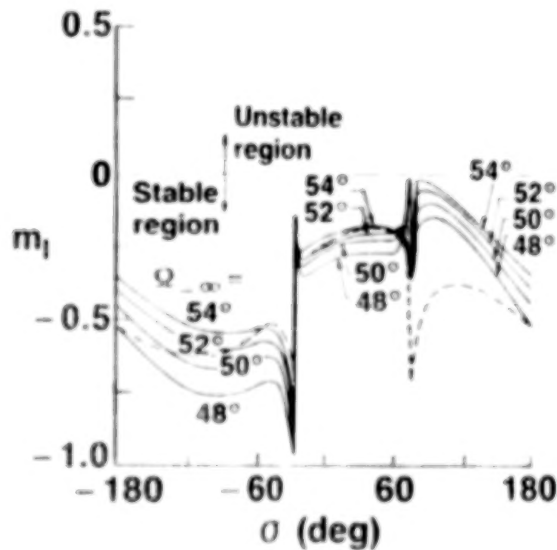
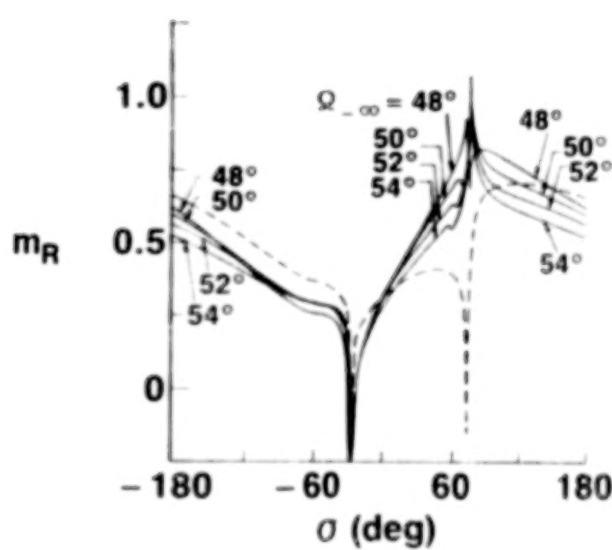


SUBSONIC FLOW: EFFECT OF INCIDENCE - 3

Unsteady moments acting on the reference blade of the NACA 0012 cascade operating at inlet flow angles of 48, 50, 52 and 54 deg and on the reference blade of the flat plate cascade operating at $\Omega_{\infty} = 45$ deg are shown below for blades undergoing unit-frequency torsional vibrations over the entire range of interblade phase angles, i.e., $\sigma \in [-\pi, \pi]$. The abrupt changes in the moment curves are indicative of an acoustic resonance. The blade motions are superresonant (i.e., acoustic response disturbances persist in the far field and carry energy away from the blade row) at interblade phase angles lying between the lowest and highest resonant phase angles and subresonant (acoustic response disturbances attenuate with increasing distance from the blade row) at the interblade phase angles below the lowest and above the highest resonant phase angles. The blade motions considered below are stable but the NACA 0012 results indicate that the effect of mean blade loading tends to be destabilizing. Note that for a given σ the out-of-phase moment moves closer to the stability boundary as the inlet flow angle is increased.

Unsteady moment vs. interblade phase angle: $\Theta = 45^\circ$, $G = 1.0$, $M_{\infty} = 0.6$.

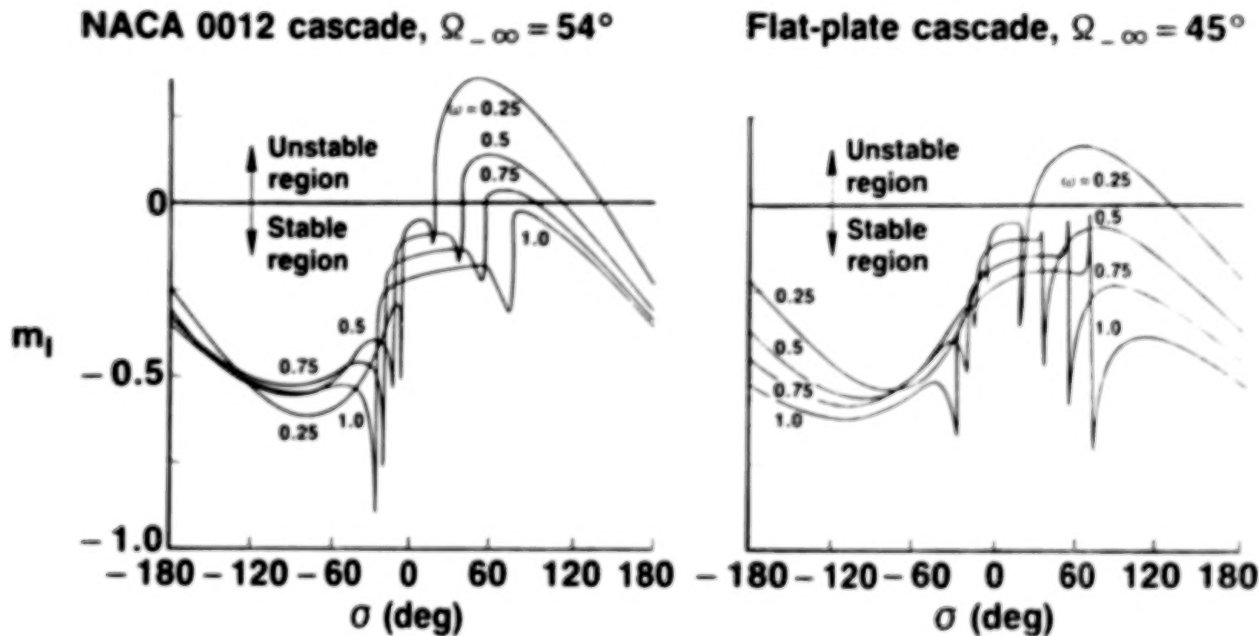
— NACA 0012 cascade, - - - flat-plate cascade



SUBSONIC FLOW: EFFECT OF FREQUENCY

The effect of frequency on the out-of-phase component of the unsteady moment due to torsion about midchord is illustrated below for the NACA 0012 cascade operating at $\Omega_{-\infty} = 54$ deg and for the flat-plate cascade operating at $\Omega_{-\infty} = 45$ deg. The NACA 0012 blades experience a region of subresonant torsional instability for $\omega = 0.25, 0.5$ and 0.75 , with the extent of this region decreasing with increasing frequency. The subresonant torsional motions of the flat-plate cascade are unstable only at the lowest frequency considered, i.e., $\omega = 0.25$. Thus the nonuniform flow through the NACA 0012 cascade extends the frequency range over which the blades are susceptible to a torsional instability.

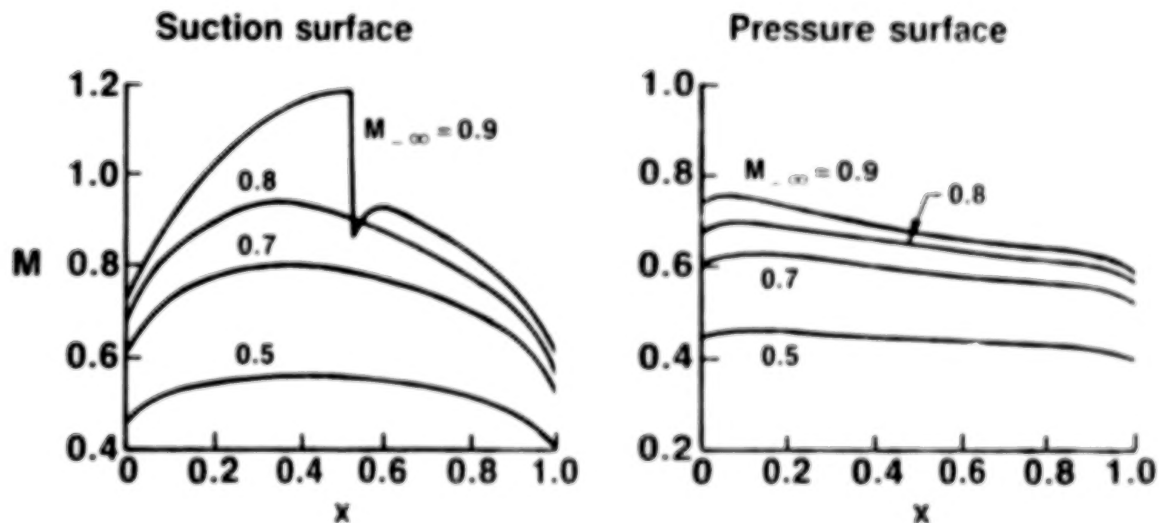
Unsteady moment vs. interblade phase angle:
 $\Theta = 45^\circ$, $G = 1.0$, $M_{-\infty} = 0.6$.



SUBSONIC/TRANSonic FLOW: EFFECT OF MACH NUMBER - 1

We now consider the staggered cascade of sharp-edged double-circular-arc airfoils. In particular, the airfoils have flat lower surfaces, circular arc upper surfaces and maximum thicknesses at midchord of 0.05. Full-potential steady and linearized unsteady flows through this example configuration have been determined for inlet Mach numbers of 0.5, 0.7, 0.8 and 0.9. The steady flows have been determined by imposing a zero-load requirement at blade leading and trailing edges. As a consequence, only the inlet Mach number is prescribed with the remaining inlet and exit parameters determined as part of the steady flow solution. Numerical results for this configuration along with those for a corresponding flat-plate cascade ($\Omega = 45$ deg, $G = 1$) are given in this and in the following three figures. Shown below are the predicted surface Mach number distributions for the example DCA cascade. For the prescribed inlet Mach numbers stated above, the calculated exit Mach numbers are 0.43, 0.57, 0.62 and 0.64, respectively. In addition, the calculated inlet flow angles are 49.0, 49.2, 49.4, and 49.6 deg, respectively, and in each case the calculated exit flow angle is approximately 43.0 deg. The steady flows at $M_{\infty} = 0.5$, $M_{\infty} = 0.7$ and $M_{\infty} = 0.8$ are entirely subsonic with the maximum suction-surface Mach numbers of 0.561, 0.804 and 0.941 occurring at, respectively, 40.8, 38.5 and 36.5% of blade chord downstream from the leading edge. The steady flow at $M_{\infty} = 0.9$ is transonic with the supersonic region extending from 18.5 to 52.5% of blade chord along the suction surface and terminating at a shock discontinuity. The Mach numbers at the foot of the shock are 1.193 on the upstream or supersonic side and 0.871 on the downstream or subsonic side.

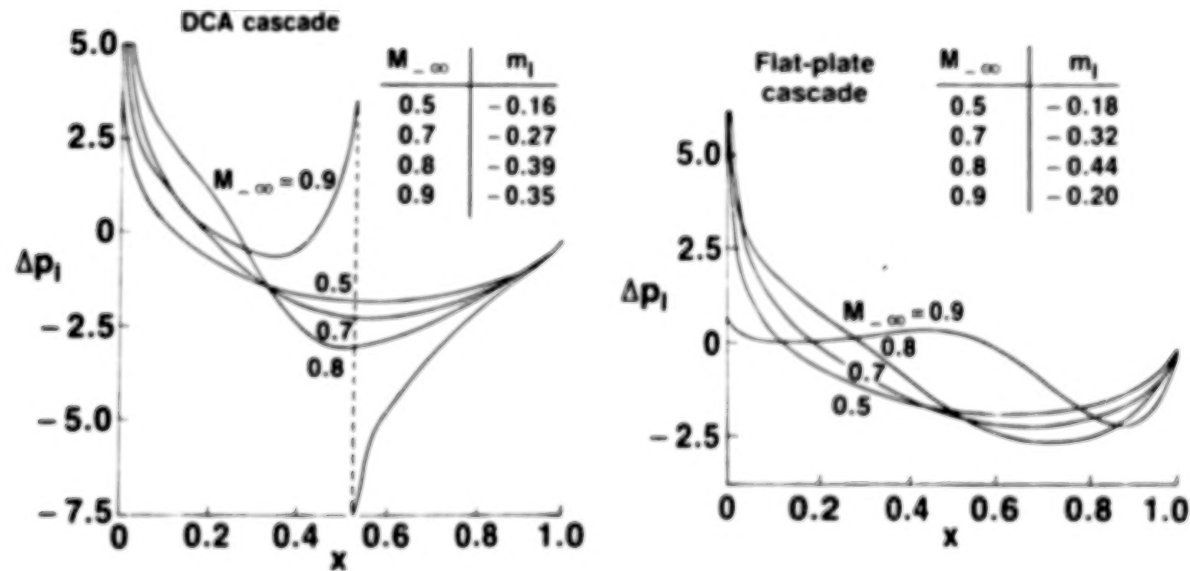
Surface Mach number distributions: DCA cascade; $\Theta = 45^\circ$, $G = 1.0$



SUBSONIC/TRANSonic FLOW: EFFECT OF MACH NUMBER - 2

The effect of Mach number on the response to in-phase ($\sigma = 0$ deg) unit-frequency torsional blade vibrations is illustrated below for the DCA and flat-plate cascades. The blade motions at $\sigma = 0$ deg are superresonant. For the flows at $M_{\infty} = 0.5, 0.7$ and 0.8 two acoustic waves persist in the far field—one upstream and one downstream—and propagate away from the blade row. For the DCA cascade operating at $M_{\infty} = 0.9$ there are three such waves—two upstream and one downstream. Finally, for the flat-plate cascade operating at $M_{\infty} = 0.9$ there are four such waves—two upstream and two downstream. The out-of-phase pressure-difference distributions and unsteady moments for the reference DCA and flat-plate blades reflect this change in character of the acoustic response in the far field, since the trends indicated by the results for $M_{\infty} = 0.5, 0.7$ and 0.8 are not sustained at $M_{\infty} = 0.9$. Also, a comparison of the DCA and flat-plate pressure-difference curves for in-phase motions suggests that the influence of mean flow gradients on the unsteady aerodynamic response becomes more pronounced with increasing Mach number. The pressure difference distributions for the DCA and flat-plate blades are very similar for the two lower inlet Mach number, differ somewhat for $M_{\infty} = 0.8$ and differ substantially for $M_{\infty} = 0.9$. The differences at $M_{\infty} = 0.8$ can be attributed to the relatively large gradients in the subsonic mean flow that occur along the suction surface of each DCA blade. The substantial differences at $M_{\infty} = 0.9$ are caused by the transonic effects associated with the DCA cascade and by the different far-field acoustic response environments produced by the two cascades.

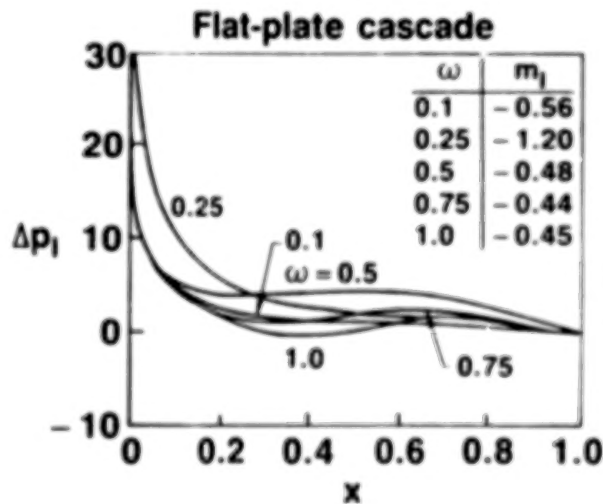
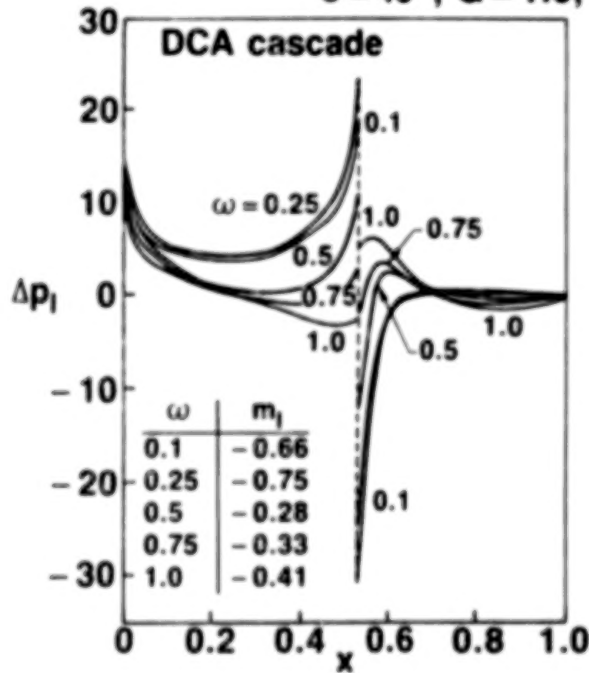
Unsteady pressure-difference distributions and unsteady moments:
 $\Theta = 45^\circ, G = 1.0, \omega = 1.0, \sigma = 0^\circ$.



SUBSONIC/TRANSONIC FLOW: EFFECT OF FREQUENCY

Shown below are first-harmonic, out-of-phase, pressure-difference distributions and aerodynamic moments for the example DCA and flat-plate cascades operating at an inlet Mach number of 0.9. Here the blades are undergoing out-of-phase ($\sigma = 180$ deg) torsional vibrations about midchord at different prescribed frequencies. Recall that for a discontinuous transonic flow there are two contributions to the first-harmonic unsteady moment: one arising from the harmonic unsteady surface-pressure response and the other from the anharmonic surface pressures produced by shock motion. However, for the DCA cascade at $M_{\infty} = 0.9$, the mean shock location is only slightly aft of blade midchord and, therefore, the anharmonic surface pressures make only a small contribution to the unsteady moment. A comparison of the DCA and flat-plate results depicted below indicates the dramatic impact of transonic mean-flow phenomena on unsteady aerodynamic response. A second interesting feature indicated by these results is the change in the unsteady moment behavior as the blade vibration frequency is increased from 0.25 to 0.5. This change occurs because the out-of-phase blade motions of the DCA and flat-plate cascades are subresonant for $\omega = 0.1$ and 0.25 and superresonant for $\omega = 0.5$, 0.75 and 1.0, and this change in the far-field acoustic response has an important impact on the unsteady aerodynamic response at a blade surface.

Unsteady pressure-difference distributions:
 $\Theta = 45^\circ$, $G = 1.0$, $M_{\infty} = 0.9$, $\sigma = 180^\circ$.

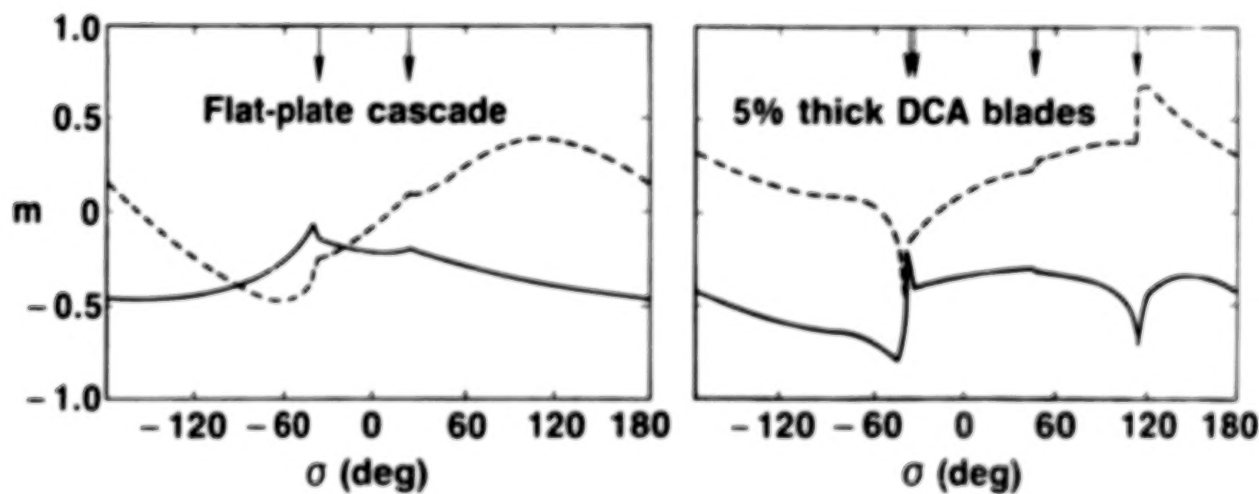


SUBSONIC/TRANSONIC FLOW

Finally, predictions of the aerodynamic moment versus interblade phase angle are shown for unit frequency torsional blade vibrations for the flat-plate and DCA cascades. Here $M_{\infty} = 0.9$ and those angles at which an acoustic resonance occurs are indicated by the arrows at the top of each figure. The unit-frequency torsional blade motions of the two cascades are stable (i.e., $m_I < 0$ for all σ), but the behaviors of the flat-plate and DCA moment responses vs. interblade phase angle are quite different. These differences occur not only because the mean flow through the flat-plate cascade is entirely subsonic while that through the DCA cascade is transonic with a shock discontinuity, but also because of the substantial difference between the exit Mach numbers for the flat-plate ($M_{\infty} = 0.9$) and the DCA ($M_{\infty} = 0.64$) cascades. This difference implies that the two cascades operate in very different far-downstream acoustic response environments over almost the entire range of interblade phase angles.

Unsteady moment vs. interblade phase angle: $---m_R$, $—m_I$

$\Theta = 45^\circ$, $G = 1$, $M_{\infty} = 0.9$, $\omega = 1.0$.



SUMMARY

The linearized unsteady aerodynamic theory outlined above accounts for the effects of real blade geometry, mean blade loading and operation at transonic Mach numbers on the unsteady aerodynamic response produced by the blades of an isolated two-dimensional cascade. This theory has been developed to meet the requirements of turbomachinery aeroelastic designers, but it should also be useful for aeroacoustic design applications. The unsteady flow is regarded as a small perturbation of a fully nonuniform isentropic and irrotational mean or steady flow, which is produced by small-amplitude temporally and spatially (in the cascade direction) periodic structural (blade motions) and external aerodynamic (incident entropic, vortical and acoustic disturbances) excitations. Thus the steady flow is determined as a solution of a full-potential boundary-value problem and the linearized unsteady flow as a solution of a time-independent, linear, variable-coefficient, boundary-value problem in which the variable coefficients depend on the underlying mean or steady flow.

Response predictions have been presented for the blades of compressor- and fan-type cascades undergoing pure torsional motions. In these examples there are no incident entropy or rotational velocity fluctuations and, therefore, only a single field equation must be solved to determine the linearized unsteady flow field. The numerical results demonstrate, to some extent, the status of numerical field methods for solving the nonlinear steady and the linear, variable-coefficient, unsteady, boundary-value problems and illustrate partially the effects of blade geometry, mean incidence, shock phenomena and differences between inlet and exit free-stream conditions on the unsteady response at blade surfaces.

- **Linearized unsteady aerodynamic analysis**
- **Effects of:**
 - **Blade geometry**
 - **Blade loading**
 - **Shocks and their motions**
 - **High frequency unsteady motions**
- **Blade flutter prediction**
- **Subsonic / transonic Mach numbers**

FUTURE DIRECTIONS

Linearizations relative to nonuniform steady flows offer great potential for meeting the needs of aeroelastic (or aeroacoustic) designers for efficient unsteady aerodynamic analyses that contain much of the essential physics associated with turbomachinery flow fields. However, before this potential can be fully realized, significant improvements in numerical solution methods for both the steady and linearized unsteady flows must be achieved so that reliable response information can be provided over the wide range of geometric configurations and flow conditions at which blade vibrations are of practical concern. In particular, unsteady aerodynamic analyses intended for turbomachinery aeroelastic predictions must be applicable to fan, compressor and turbine cascades, low subsonic through low supersonic Mach number operation and moderate through high frequency structural and external aerodynamic excitations. Some needed capabilities include the ability to predict transonic flows (i.e., subsonic flows with imbedded supersonic regions) through fan and compressor cascades operating at high positive or negative mean incidence, supersonic flows with complicated moving shock patterns and the high frequency unsteady flows caused by incident external aerodynamic disturbances. Major advances in our ability to predict turbomachinery aeroelastic and aeroacoustic behavior should result if future research is directed toward including the effects of strong viscous/inviscid interactions and possibly large-scale flow-separations within a linearized unsteady aerodynamic framework. Ultimately, linearized analyses which account for nonuniform steady flow and viscous/inviscid interaction phenomena must be extended to treat three-dimensional flows.

- **Subsonic/transonic flows at high incidence**

- **Forced aerodynamic excitations**

$$\mathcal{L}\phi = f(\vec{v}^R, s)$$

- **Supersonic Mach numbers**

- **Viscous separation phenomena**



REFERENCES

1. Verdon, J. M. : Unsteady Aerodynamics of Blade Rows. In Proceedings of the Tenth U. S. National Congress of Applied Mechanics, J. P. Lamb (ed.), ASME, New York, January 1987, pp. 485-497.
2. Goldstein, M. E. : Unsteady Vortical and Entropic Distortions of Potential Flows Round Arbitrary Obstacles. *Journal of Fluid Mechanics*, vol. 89, part 3, 1978, pp. 433-468.
3. Verdon, J. M. : Linearized Unsteady Aerodynamic Theory. Chapter 2 in AGARD Manual on Aeroelasticity in Axial Flow Turbomachines, vol. I, M. F. Platzer and F. O. Carta (eds.), March 1987.
4. Williams, M. H. : Linearization of Unsteady Transonic Flows Containing Shocks. *AIAA Journal*, vol. 17, no. 4, April 1979, pp. 394-397.
5. Ehlers F. E. and Weatherill, W. H. : A Harmonic Analysis Method for Unsteady Transonic Flow and Its Application to the Flutter of Airfoils. *NASA CR 3537*, May 1982.
6. Caspar, J. R. : Unconditionally Stable Calculation of Transonic Potential Flow Through Cascades Using an Adaptive Mesh for Shock Capture. *Trans. ASME A: Journal of Engineering for Power*, vol. 105, no. 3, July 1983, pp. 504-513.
7. Verdon, J. M. and Caspar, J. R. : A Linearized Unsteady Aerodynamic Analysis for Transonic Cascades. *Journal of Fluid Mechanics*, vol. 149, December 1984, pp. 403-429.

COMPUTATIONAL AEROELASTICITY CHALLENGES AND RESOURCES

**John W. Edwards
NASA Langley Research Center**

TRANSONIC AERODYNAMICS AND FLUTTER

In the past decade there has been much activity in the development of computational methods for the analysis of unsteady transonic aerodynamics about airfoils and wings. The upper left figure illustrates significant features which must be addressed in the treatment of computational transonic unsteady aerodynamics. On the plot of equivalent airspeed versus Mach number, lines of constant altitude are straight lines through the origin with decreasing altitudes represented by steeper slopes. The flight envelope, typically set by the maximum limit speed and a typical flutter boundary curve, characterized by the flutter speed gradually dropping to a minimum in the transonic speed range followed by a rapid upward rise, is shown. The ability to predict this minimum, termed the transonic flutter dip, is of great importance in design, since the flutter boundary must be shown by a combination of analysis and flight test to be outside the flight envelope by a margin of at least 15 percent in equivalent airspeed for military aircraft.

The upper right figure indicates the flow regions for an aircraft on a plot of lift coefficient versus Mach number. Flows which are predominantly attached or separated are designated as type I and III respectively, while mixed attached and separated flows are designated type II. For aeroelastic problems the boundary of the type II flows will be enlarged over that for steady flows since a vibrating airfoil or wing may exhibit alternating attached and separated flow for sensitive conditions. The "picket fence" in the mixed flow region has been added to emphasize the possibility of "nonclassical" aeroelastic effects in this region.

The diagram in the lower left of the figure illustrates the sequence of events occurring in air combat maneuvers. Upon the decision to engage, a maneuver is initiated with the objective of achieving maximum turn rate. This leads, in turn, to pull-up and turn at the structural limit load, decelerating at limit load to the intersection with the maximum lift coefficient curve, holding this "corner" condition until the pointing objective is achieved and completion of engagement and pull-out occurs. These maneuvers, encompassing the complete flight envelope, involve rapid transitions between type I, II, and III flow conditions.

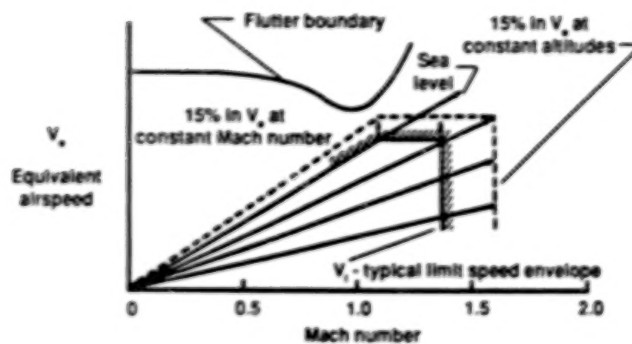
Further features of transonic flutter are illustrated in the lower right diagram. Dynamic pressure at flutter tends to decrease with increasing Mach number to a minimum "critical flutter point" value in the transonic speed range. At subsonic speeds the flow can be reasonably assumed to be attached (type I) at flutter and linear theory is well calibrated for flutter analysis. At transonic speeds the situation is complicated by the onset of flow separation (type II flow) and linear theory must be used with caution. The low damping region indicated in the figure indicates the potential for nonclassical aeroelastic response and instabilities which may be encountered.

References:

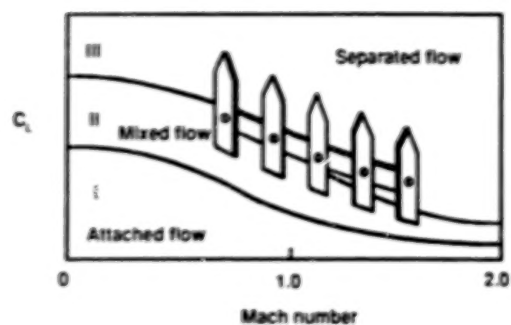
Edwards, J. W.; and Thomas, J. L.: Computational Methods for Unsteady Transonic Flows, AIAA Paper No. 87-0107.

TRANSONIC AERODYNAMICS AND FLUTTER

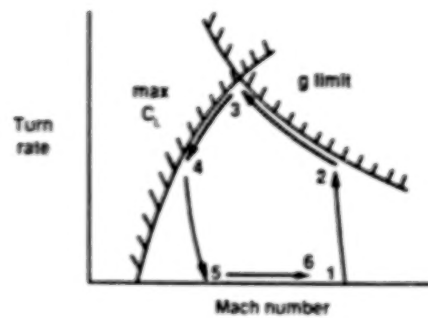
GRAPHICAL REPRESENTATION OF MINIMUM REQUIRED FLUTTER MARGIN



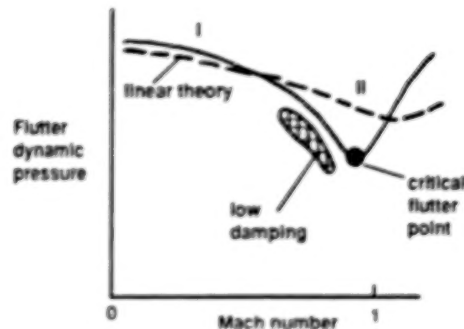
CHARACTERISTICS OF ATTACHED AND SEPARATED FLOW FOR COMPLETE AIRCRAFT



AIR COMBAT DYNAMICS



FEATURES OF TRANSONIC FLUTTER



COMPUTATIONAL AEROELASTICITY CHALLENGES

This figure illustrates several types of aeroelastic response which have been encountered and which offer challenges for computational methods. The four cases illustrate problem areas encountered near the boundaries of aircraft flight envelopes, as operating conditions change from high speed, low angle conditions to lower speed, higher angle conditions. The nonclassical aeroelastic response observed on the DAST ARW-2 wing model (upper left) is a region of high dynamic response at nearly constant Mach number which was encountered at dynamic pressures well below those for which flutter was predicted. The motion is of the limit-amplitude type and the response is believed to be associated with flow separation and reattachment over the supercritical wing (type II flow).

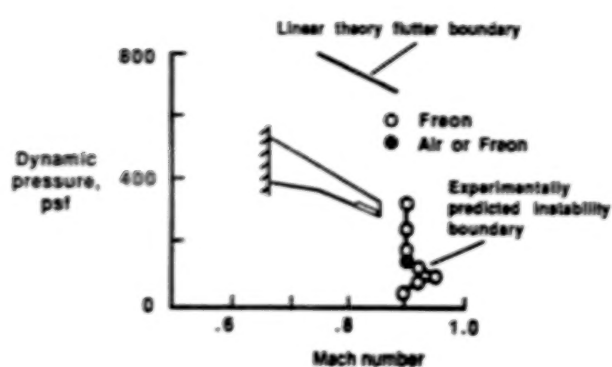
The upper right figure illustrates wing/store limited amplitude oscillations experienced by modern, high performance aircraft under various loading and maneuvering conditions at transonic Mach numbers. Such oscillations can result in limitations on vehicle performance. The conditions for which this response occurs appear to be near the onset of type II mixed flow. The response typically increases for maneuvering flight conditions.

Dynamic vortex-structure interactions causing wing oscillations have been observed on a bomber type aircraft for high wing sweep conditions during wind-up turn maneuvers (lower left). The flow involves the interaction of the wing vortex system with the first wing bending mode and occurs over a wide Mach number range (0.6 - 0.95) at angles of attack of 7 - 9 degrees.

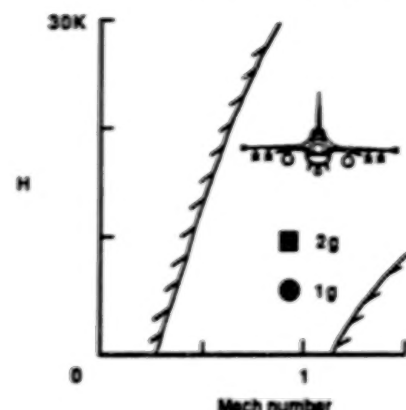
At higher angles, interaction of forebody and wing vortex systems with aft vehicle components results in vortex-induced buffet loads, illustrated in the lower right figure. The figure shows the operating conditions for which tail buffet may occur on a high performance fighter. Buffet of horizontal tails can occur at intermediate angles of attack and is a result of the vortex system encountering the horizontal tail lifting surface. As angle of attack increases, the location of vortex bursting moves upstream in the wake. Loss of lift is associated with the burst location reaching the vicinity of the aircraft, and vertical tail surfaces located in such regions can experience severe dynamic loads.

COMPUTATIONAL AEROELASTICITY CHALLENGES

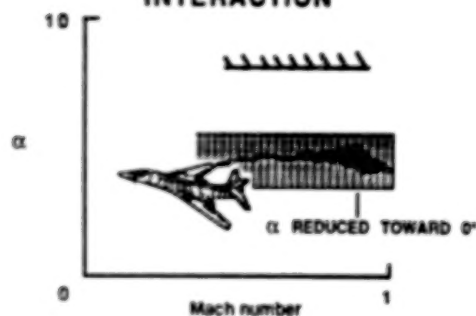
NOVEL SHOCK-INDUCED INSTABILITIES



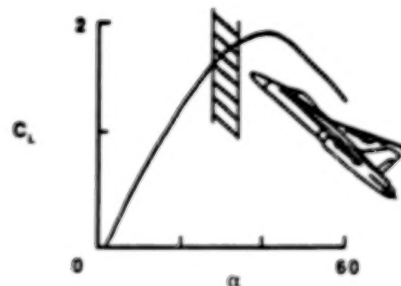
WING/STORE LIMITED AMPLITUDE FLUTTER



DYNAMIC VORTEX-STRUCTURE INTERACTION



VORTEX-INDUCED BUFFET LOADS



COMPUTER RESOURCE REQUIREMENTS FOR FLUTTER ANALYSIS

This table indicates the computer resources required to perform a flutter analysis of a complete aircraft configuration at one Mach number. Time-marching transient aeroelastic response calculations are used to determine the flutter condition. This involves, on average, four response calculations: two to calculate steady flow field conditions and two transient responses bracketing the flutter speed. Modal frequency and damping estimates from the responses are determined and the flutter speed interpolated from the damping estimates. Calculations have been performed for a complete aircraft configuration with a transonic small disturbance (TSD) potential code using 750,000 grid points. The calculation of one flutter point for this case on the CDC VPS-32 computer would require 2.3 CPU hours. Estimates of similar calculations using the full Navier-Stokes equations would require 77.8 CPU hours. Conditions for this estimate are a Reynolds number of 10 million, 7 million grid points and an assumed computational speed of 100 million floating point operations per second (MFLOPS).

References:

Whitlow, Woodrow, Jr.: Computational Unsteady Aerodynamics for Aeroelastic Analysis, NASA TM 100523, December 1987.

COMPUTER RESOURCE REQUIREMENTS TO DETERMINE FLUTTER POINT AT A SPECIFIED MACH NUMBER

(4000 TIME STEPS PER FLUTTER POINT)

<u>CONFIGURATION</u>	<u>FLOW MODEL</u>	<u>GRID POINTS</u>	<u>CPU HOURS (VPS-32)</u>
COMPLETE AIRCRAFT	TSD	0.75M	2.3*
COMPLETE AIRCRAFT	FULL NAVIER-STOKES (RE = 10 MILLION)	7.00M	77.8**

*BASED ON ACTUAL CASES

**ASSUMES COMPUTATIONAL SPEED OF 100 MFLOPS

COMPUTER RESOURCE REQUIREMENTS FOR COMPLETE FLUTTER BOUNDARY

This table summarizes computational requirements for flutter calculations of a wing/body/canard configuration on the CDC VPS-32 computer operating at 100 MFLOPS and on the NAS CRAY II computer operating at 250 MFLOPS. Again, four response calculations per flutter point are assumed. It is assumed that ten flutter points will be calculated to define the flutter boundary versus Mach number. The left hand column indicates the difficulty of the flowfield calculation as defined in figure 1; type I for attached flows, type II for mixed (alternately separated and attached) flows and type III for fully separated flows. The second column indicates the fluid dynamic equation level needed to accurately model the flow physics of the problem. Note that two-dimensional strip boundary layer models are assumed for interactive viscous-inviscid calculations for the potential and Euler equation methods. It is anticipated that potential equation models will be adequate for flutter calculations of type I attached flow conditions and may also be quite useful for some type II mixed flow cases. Full potential equation codes will require about 50 percent more computer resources than TSD methods due to the necessity of conforming, moving grids, among other considerations. Euler equation methods should also be adequate for these conditions and, in addition, be able to treat more difficult type III fully separated flows. Euler equation methods are estimated to require approximately twice the resources of TSD methods. The full Navier-Stokes equations, which should only be required for type II and III flows require approximately 30 times the resources of the Euler equations (at a Reynolds number of 100 million).

WING/BODY/CANARD CONFIGURATION 10 MACH NUMBERS (40 CASES) PER ANALYSIS

$$\text{TIME} = (\text{GRID PTS}) \times \frac{\text{OPS}}{(\text{GRID PTS} \times \text{ITER})} \times (\text{ITER}) / \frac{\text{OPS}}{\text{SEC}}$$

FLOW REGION	FLOW MODEL	VPS-32 (100 MFLOPS)	NAS (250 MFLOPS)
I, MAYBE II	TSD WITH 2-D STRIP BOUNDARY LAYER	30 HOURS	12 HOURS
I, MAYBE II	POTENTIAL WITH 2-D STRIP BOUNDARY LAYER	45 HOURS	18 HOURS
I, II, MAYBE III	EULER WITH 2-D STRIP BOUNDARY LAYER	65 HOURS	26 HOURS
II, III	NAVIER-STOKES (RE = 10 ⁸)	1611 HOURS	644 HOURS



Report Documentation Page

1. Report No. NASA CP-3022, Part 2	2. Government Accession No.	3. Recipient's Catalog No.	
4. Title and Subtitle Transonic Unsteady Aerodynamics and Aeroelasticity - 1987		5. Report Date February 1989	
6. Performing Organization Code			
7. Author(s) Samuel R. Bland, Compiler	8. Performing Organization Report No. L-16532	10. Work Unit No. 505-63-21-01	
9. Performing Organization Name and Address NASA Langley Research Center Hampton, VA 23665-5225	11. Contract or Grant No.	13. Type of Report and Period Covered Conference Publication	
12. Sponsoring Agency Name and Address National Aeronautics and Space Administration Washington, DC 20546-0001	14. Sponsoring Agency Code		
15. Supplementary Notes			
16. Abstract This two-part document contains copies of the text and figures for the papers presented at the Symposium on Transonic Unsteady Aerodynamics and Aeroelasticity - 1987, held at the NASA Langley Research Center on May 20-22, 1987. The papers are grouped in five subject areas as follows: (1) Transonic small disturbance theory for complete aircraft configurations (2) Full potential and Euler equation methods (3) Methods for vortex and viscous flows (4) Aeroelastic applications (5) Experimental results and cascade flows			
17. Key Words (Suggested by Author(s)) Unsteady aerodynamics Transonic aerodynamics Aeroelasticity	18. Distribution Statement Unclassified - Unlimited	Subject Category 02	
19. Security Classif. (of this report) Unclassified	20. Security Classif. (of this page) Unclassified	21. No. of pages 385	22. Price A17

NASA

National Aeronautics and
Space Administration
Code NTT-4
Washington, D.C.
20546-0001

National Aeronautics and
Space Administration
Washington, D.C.
20546

SPECIAL FOURTH CLASS MAIL
BOOK

Postage and Fees Paid
National Aeronautics and
Space Administration
NASA-451

Official Business
Penalty for Private Use \$300



NASA

POSTMASTER: If Undeliverable (Section 158
Postal Manual) Do Not Return

END

DATE FILMED

02-14-92